Project No. 12-3545

Concrete Materials with Ultra-High Damage Resistance and Self-Sensing Capacity for Extended Nuclear Fuel Storage Systems

Fuel Cycle Research and Development

Mo Li
University of California, Irvine

In collaboration with:
University of Houston
University of Colorado, Boulder

John Orchard, Federal POC
Ken Sorenson, Technical POC

NEUP Nuclear Energy University Programs
U.S. Department of Energy

FINAL REPORT

Project Title:	Concrete Materials with Ultra-High Damage Resistance and Self-Sensing Capacity for Extended Nuclear Fuel Storage Systems
Covering Period:	October 1, 2012 – September 30, 2016
Recipient:	University of California, Irvine E4145 Engineering Gateway Irvine, CA 92617-2175
Principal Investigator:	Dr. Mo Li, 949-824-4671, moli@uci.edu
Collaborators:	Dr. Kaspar Willam, 713-743-1461, kwillam@uh.edu Dr. Kalyana Nakshatrala, 713-743-4418, knakshatrala@uh.edu Dr. Yunping Xi, 303-492-8991, yunping.xi@colorado.edu Dr. Dan Naus, 865-574-0657, nausdj@ornl.gov

Project Objective: The objective of this project is to develop a new class of multifunctional concrete materials (MSCs) for extended spent nuclear fuel (SNF) storage systems, which combine ultra-high damage resistance through strain-hardening behavior with distributed multi-dimensional damage self-sensing capacity. The beauty of multifunctional concrete materials is two-fold: *First*, it serves as a major material component for the SNF pool, dry cask shielding and foundation pad with greatly improved resistance to cracking, reinforcement corrosion, and other common deterioration mechanisms under service conditions, and prevention from fracture failure under extreme events (e.g. impact, earthquake). This will be achieved by designing multiple levels of protection mechanisms into the material (i.e., ultra-high ductility that provides thousands of times greater fracture energy than concrete and normal fiber reinforced concrete; intrinsic cracking control, electrochemical properties modification, reduced chemical and radionuclide transport properties, and crack-healing properties). *Second*, it offers capacity for distributed and direct sensing of cracking, strain, and corrosion wherever the material is located. This will be achieved by establishing the changes in electrical properties due to mechanical and electrochemical stimulus. The project will combine nano-, micro- and composite technologies, computational mechanics, durability characterization, and structural health monitoring methods, to realize new MSCs for very long-term (greater than 120 years) SNF storage systems.

Contents

EXECUTIVE SUMMARY

A micromechanics-based framework and rheology design methodology was established in this project for developing ductile strain-hardening cementitious materials (SHCs) that feature strain-hardening behavior with optimized tensile ductility. The framework links measurable parameters at nano- and micro-scales to composite strain-hardening behavior. The framework also took into account the random distribution of flaws and "effective volume" of polymeric fibers, in addition to the interface nanoscale tailoring and matrix microstructure manipulation. According to this analytical framework, we successfully designed and processed SHC materials with tensile ductility two orders higher than SNF concrete and fiber-reinforced concrete, as well as intrinsic crack width control capacity. Through tuning the chemical and physical parameters of SHC at microstructure scales, the "spring law" (fiber bridging stress vs. crack opening relation) of each individual crack was modified to achieve a significant change in the crack width distribution during SHC strain-hardening stage. By this means, the mean crack width was further reduced to 12.5 μm while the tensile strain capacity was increased to above 5%.

The new SHC materials offer great advantage over normal concrete materials, in terms of improved damage resistance and reduced transport properties for SNF storage. The large tensile ductility of SHC overcomes the inherent brittleness of cementitious materials, leading to extraordinary damage tolerance under service loading (e.g. cracking induced deterioration, corrosion-induced concrete spalling and fracture) and extreme loading conditions (e.g. impact, earthquake, accidental loading during transportation). The fracture energy of SHC is two orders higher than current concrete used in SNF storage systems, and one order higher than most FRCs. The intrinsically controlled micro-crack width (mean crack width of 30.0 μm for SHC-1, mean crack width of 12.5 μm for SHC-2) during strain-hardening stage was independent of reinforcing ratio, structural member geometry, applied deformation and loading condition. The tight crack width provides high resistance to chloride diffusion and water permeation, compared to conventional concrete at the cracked stage. It is far below the maximum allowable crack width at the tensile face of reinforced concrete structures as 150 μm for exposure conditions of seawater, seawater spray, wetting, and drying, and 180 μm for deicing chemical exposure, specified by ACI 224R. This indicates that steel reinforcement is not required to control crack width in SHC even for the most stringent allowable crack width requirement.

The newly developed SHCs were further encoded with a robust self-sensing capacity. The self-sensing SHC is called multifunctional strain-hardening cementitious materials (MSC). The fundamental understanding of the electrical, electro-chemical, and electro-mechanical behavior of cementitious was obtained. Electrical impedance spectroscopy and equivalent circuit analysis on various mixtures with different binder ingredients, water/binder ratios, hydration chemistry, incorporation of conductive nano-

materials, age effects, and damage levels were conducted. The results shed light on the age-dependent material electrical properties at composite, component and ingredient levels, which laid the groundwork for the systematic development of MSCs for SNF storage applications. Furthermore, in order to correlate MSC material mechanical behavior (e.g. strain and damage) with electrical response, four-point probing piezoresistivity test method was established. The results revealed the effect of nanomaterials on the electro-mechanical properties of MSC composite material systems.

A new generation of multifunctional strain-hardening cementitious materials was successfully developed in this project. The beauty of MSC is two-fold: *First*, it serves as a major material component for the SNF pool, dry cask shielding and foundation pad with greatly improved resistance to cracking, reinforcement corrosion, and other common deterioration mechanisms under service conditions, and prevention from fracture failure under extreme events (e.g. impact, earthquake). This was achieved through multiple scales of protection mechanisms designed into the MSC material (i.e., ultra-high ductility that provides thousands of times greater fracture energy than concrete and normal fiber reinforced concrete, intrinsic cracking control, electrochemical properties modification, reduced transport properties, and extraordinary energy dissipation capacity). *Second*, it offers capacity for distributed and direct sensing of cracking, strain, and corrosion wherever the material is located. This was achieved by establishing the changes in electrical properties due to mechanical and electrochemical stimulus through experimental studies and analytical modeling. MSCs exhibit strong piezoresistive behavior at both elastic and inelastic stages. The elastic gage factors are 17, 62 and 56 for 2.5%, 5% and 10% MSCs, respectively, The inelastic gage factors are 6413, 4134 and 2236 in average for 2.5%, 5% and 10% MSC specimens, respectively. These gage factors are above the targets set in the proposal for the material development, and are far above the gage factor of 2 (elastic only) for commercial strain gages. Larger gage factors mean that a small change in strain can be reflected as large change in the measured impedance, indicating a higher sensing capacity. Robust strain self-sensing in MSCs can thus be achieved by their large gage factors and strong signal to noise ratios.

In addition to strain self-sensing, damage self-sensing was also accomplished in this project by integrating material development and advanced impedance tomography methods. Algorithms were developed to autonomously measure strain and identify damage based on an analysis of the input-output voltages taken from MSC elements stimulated electrically. This study made it possible to visualize distributed damage (e.g. a defect, a large localized crack, distributed microcracks and embedded steel corrosion) in MSC based upon impedance measurements collected from MSC specimens in a multitude of probe locations. MSC can behave as a damage sensor itself, thus offering spatial data wherever the material is located. This eliminates the need for installing and maintaining a dense array of sensors; instead, inexpensive electrodes can be attached to structural component boundaries to apply electrical input and

measure output signals that collect spatial information throughout the material. This approach allows for spatial sensing inside the material although the electrodes are only required at boundaries.

. To complement MSC material development and characterization, a robust methodology for linear transient diffusion equations was developed. Non-negative methodologies for nonlinear (in particular, semi-linear and quasi-linear) diffusion-type equations were also developed. Mesh restrictions were derived to meet maximum principles and the non-negative constraint for advection-diffusion and linear reactions. Moreover, a state-of-the-art numerical methodology was developed to simultaneously meet the element-wise species balance, the non-negative constraint and avoid node-to-node spurious oscillations. Furthermore, a hierarchy of mathematical models was developed to model various mechanisms of degradation. The models accounted for coupled chemo-thermal-deformation response, which was crucial for mathematical modeling of degradation of materials. This mathematical model was consistently derived using mechanics and thermodynamics principles. In particular, the model satisfies the second law of thermodynamics, which is not the case with some of the current models for degradation. Overall, a comprehensive mathematical model and stable and accurate computational framework that uniquely capture fully coupled deterioration processes were developed through this project.

The self-sensing capacity of MSC was validated both at material and structural element scales. Constitutive models of MSC were established for structural behavior prediction and future structural design. A benchmark problem (i.e. a wall structure under shear) was studied through finite element simulation that incorporates the new MSC constitutive models. The structural simulation results are compared with experimental data.

In addition to the mechanical, electrical and electromechanical behavior, the durability of MSC was characterized. Common deterioration mechanisms in spent nuclear fuel storage systems were studied, including restrained shrinkage cracking, chloride penetration, embedded steel corrosion, freeze and thaw, alkali-silica reaction and elevated temperature effects. The experimental results revealed that MSC had superior durability to conventional concrete, mainly due to its extraordinarily high damage tolerance, chemical stability and low transport properties even under large applied deformation. The improved durability leads to an extended service life for SNF systems when MSC is used in lieu of conventional concrete. Life-cycle analysis was conducted on dry cask systems to compare the newly developed MSCs with existing concrete. The results showed the life cycle cost of a representative dry cask system can be reduced by 30% when MSC is used. It should be noted that the life cycle analysis was based on simple assumption that corrosion is the dominant deterioration mode, and other types of deterioration or failure events will not occur during the structural life cycle. When other deterioration modes and possibilities of natural and man-made hazards are considered, the life cycle cost advantage of SNF systems using MSC will be even more predominant.

1. INTRODUCTION

1.1 Research Significance

The U.S. Department of Energy's termination of the Yucca Mountain repository project means that spent nuclear fuel (SNF) will remain at non-permanent sites for decades longer than expected. As pools at many nuclear reactors began to be filled up with SNF, dry cask storage has become one of the most practical interim storage options. The 1,200+ loaded storage casks at 44 sites today could climb to more than 2,400 casks at 73 sites by 2020 and 9,300 casks by 2055. Licensed for 20 years with possible renewal up to 40 years, it is hoped the dry casks can be used for a greatly extended period, e.g. 300 years[1].

Concrete is a major material component for spent nuclear fuel storage systems that provides radiation shielding in steel-lined concrete pools, concrete dry-storage casks, and foundation pads. The concrete in SNF storage systems is constantly subjected to aging and deterioration under combined thermo-chemo-hygro-mechanical effects, which often causes chemical and physical alteration of the concrete and results in excessive cracking, spalling and loss of strength[2, 3]. SNF storage concrete is also susceptible to impact loads or severely elevated temperatures during accident conditions and extreme events, which can lead to catastrophic fracture failure[4, 5]. Obviously, the long-term durability and safety of concrete structures for spent fuel pools and dry casks are key factors for extended storage of SNF[1]. This goal of extended storage of SNF, however, is currently plagued by two fundamental limitations: quasi-brittle nature of concrete materials, and inadequacies of current health monitoring methods.

Concrete is an inherently quasi-brittle material with low fracture energy on the order of 0.1 kJ/m^2[6]. It is, therefore, highly susceptible to cracking and fracture failure under combined mechanical loads and environmental effects. Cracking causes reduction of concrete member load carrying capacity and greatly impairs the transport properties of concrete. This further leads to other common deterioration mechanisms such as chemical attack, chloride diffusion and corrosion of embedded steel, moisture penetration, radioactive water leakage, and increased radiation levels[7]. The deterioration process is further accelerated when concrete is exposed to neutron or gamma radiation and elevated temperature, which leads to strength loss and brittle fracture failure modes such as spalling. Furthermore, under impact loads during extreme events or accident conditions, the low fracture energy of concrete can result in concrete spalling and fragmentation, loss of bond with reinforcing steel, and catastrophic fracture failure[8]. While short discontinuous fibers (e.g., polymer, glass, carbon, steel) have been used to improve concrete fracture toughness and reduce the crack width, quasi-brittle fracture mode is still prevalent in fiber-reinforced cement or concrete (FRC). FRCs feature a tension-softening behavior, with fracture energy extending to several kJ/m^2. It is noteworthy that FRCs do not fundamentally address the quasi-brittleness of concrete materials; crack width within FRCs is still dependent on applied deformation, loading conditions,

reinforcement ratio and structural geometry, and thus is not an inherent material property. To radically extend concrete service life and improve safety in SNF storage systems, the quasi-brittleness of concrete and FRC must be eliminated. Therefore, a new class of cementitious materials with ductile strain-hardening behavior and fracture energy on the order of 10-100 kJ/m^2 is proposed and developed in this project.

Early detection of cracking and deterioration in SNF pools and dry cask concrete is critical to minimize maintenance costs, prolonging structural service life, ensuring safety and preventing failure. Current management practices rely on regular visual inspections that can be subjective and are limited to accessible locations. While great technological advances have been made in recent years on many fronts in the field of structural health monitoring (SHM), there still remain very few implementations of SHM systems in operational structures. Key flaws still remain[9, 10]: (1) Indirect damage sensing that requires physics-based models to correlate structural response measurements to damage state. Given the many complexities inherent to this inverse problem, robust algorithms that are generically applicable to the SNF storage concrete components do not yet exist. (2) Point-based sensors (e.g., strain gages, thermocouples) that cannot accurately identify spatially distributed damage such as cracking and corrosion. To identify spatially distributed damage, a dense network of point-based sensors is necessary for analytical models to extrapolate the point measurements to predicted component behavior, but highly costly. Engineers have begun to explore spatial or distributed sensing methods such as techniques based on ultrasonic acoustics[11]. While promising, ultrasonic inspection is difficult to apply to concrete structures, and requires expensive and power-hungry instrumentation. Distributed multi-dimensional sensing that provides the spatial resolution necessary to localize and quantify the severity of concrete deterioration and damage is direly needed. Therefore, we developed a new approach to direct and distributed sensing that employs innovative multifunctional strain-hardening cementitious materials.

This project aims to develop a new class of multifunctional strain-hardening cementitious materials (MSCs) that possess intrinsic damage tolerance and self-sensing capacity for extended SNF storage systems. The innovation of multifunctional concrete material is two-fold: *First*, it serves as a major material component for SNF storage systems with greatly improved resistance to cracking, reinforcement corrosion, spalling and other common deterioration mechanisms under service conditions, and prevents fracture failure under extreme events. This is achieved by designing multiple levels of protection mechanisms (e.g., ultra-high fracture energy, ductile strain-hardening behavior, and intrinsically controlled crack width) into the material. *Second*, it offers capacity for distributed and direct sensing of cracking and straining wherever the material is located. This is achieved by establishing the changes in electrical properties due to mechanical and electrochemical stimuli. Using electrical stimulation and advanced modeling methods, multi-dimensional spatial mapping offering a visual depiction of concrete damage and deterioration is gained.

1.2 Research Scope

This final report is organized as follows. In section 2, a class of ductile strain-hardening cementitious materials (SHC) was developed with a set of desirable characteristics that provides ultra-high damage resistance under a SNF storage environment. The micromechanics-based material design theory of SHC was presented. The multi-scale (i.e. microscale, mesoscale, and macroscale) experimental studies on SHC for material development and properties characterization were described.

In Section 3, the newly developed SHC was further tailored and encoded with self-sensing properties. The new self-sensing SHC was named MSC (multifunctional strain-hardening cementitious materials). The MSC material design methodology and the unique electromechanical properties were presented. The strain self-sensing capacity of MSC at elastic and inelastic stages was explored through experimental studies and analytical modeling.

In Section 4, the distributed damage sensing capacity of MSC was explored by electrical impedance tomography. Distributed damage within MSC was successfully visualized through the innovation in material science, the development of advanced algorithms and modeling methods that solve nonlinear inverse problems.

In Section 5, newly developed mathematical and computational models of the coupled deterioration process within MSC were introduced. The mathematical model was fully coupled accounting for deformation, temperature and diffusion while paying attention to the constitutive behavior of cementitious materials. The computational model was capable of simulating various degradation mechanisms.

In Section 6, constitutive models of MSC were established for bridging material properties to structural behavior. Finite element simulation of a wall structure using the new constitutive models was conducted, and compared with experimental data.

In Section 7, the MSC durability characterization results are presented. Life cycle analysis was performed on a representative dry cask system to compared MSC with conventional concrete.

1.3 References

[1] D. Rigby, *Evaluation of the technical basis for extended dry storage and transportation of used nuclear fuel: executive summary*: US Nuclear Waste Technical Review Board, 2010.

[2] S. L. Morton, P. L. Winston, T. Saegusa, K. Shirai, A. Sasahara, and T. Hattori, "Concrete shield performance of the VSC-17 spent nuclear fuel cask," in *International high level radioactive waste management conference*, 2006.

[3] D. Fillmore, *Literature Review of the Effects of Radiation and Temperature on the Aging of Concrete*: United States. Department of Energy, 2004.

[4] D. Aquaro, P. Castrataro, and G. Forasassi, "Impact resistance of a concrete bed for a spent nuclear fuel cask repository," in *16th International Conference on Structural Mechanics in Reactor Technology*.

[5] R. Alvarez, "Spent nuclear fuel pools in the U.S.: reducing the deadly risks of storage " 2011.

[6] Z. P. Bazant and M. Kazemi, "Size dependence of concrete fracture energy determined by RILEM Work-Of-Fracture method," *International Journal of Fracture,* vol. 51, pp. 121-138, 1991.

[7] F. Bangert, S. Grasberger, D. Kuhl, and G. Meschke, "Environmentally induced deterioration of concrete: physical motivation and numerical modeling," *Engineering Fracture Mechanics,* vol. 70, pp. 891-910, 5// 2003.

[8] N. Banthia, S. Mindess, and J. F. Trc, "Impact Resistance of Steel Fiber Reinforced Concrete," *Materials Journal,* vol. 93, 9/1/1996 1996.

[9] D. Adams, *Health Monitoring of Structural Materials and Components: Methods with Applications*. Chichester, UK: John Wiley& Sons, Ltd, 2007.

[10] K. Loh, J. Kim, J. Lynch, N. Kam, and N. Kotov, "Multifunctional layer-by-layer carbon nanotube–polyelectrolyte thin films for strain and corrosion sensing," *Smart Materials and Structures,* vol. 16, p. 429, 2007.

[11] A. Raghavan and C. E. S. Cesnik, "Review of guided-wave structural health monitoring," *Shock and Vibration Digest,* vol. 39, pp. 91-114, 2007.

2. DEVELOPMENT OF STRAIN-HARDENING CEMENTITIOUS MATERIALS FOR SPENT NUCLEAR FUEL STORAGE SYTEMS

2.1 Micromechanics Based Design of Strain-Hardening Cementitious Composites

2.1.1 Scale linking

The tensile strain-hardening behavior of SHC was be realized by tailoring the synergistic interaction between the fibers, matrix, and fiber/matrix interface using micromechanics theory. Scale linking is a fundamental characteristic of the SHC design approach; the theory links the measurable constituent parameters to the cracking propagation mode, and then to conditions for composite tensile strain-hardening behavior. Understanding and tailoring of microscale constituent parameters are the keys to achieving target macroscale composite properties. The macroscale tensile stress-strain relation of SHC is shown in **Figure 2.1**. Compared with normal fiber reinforced concrete (FRC), SHC features a pseudo strain-hardening behavior after the initial elastic stage. During its strain-hardening stage, tensile stress increases with tensile strain in SHC, leading to incredible tensile ductility hundreds of times larger than normal FRC. Such tensile ductility indicates large fracture energy, and is thus crucial for achieving ultra-high damage tolerance to extend service life (against cracking-induced deterioration) and improving safety (against extreme loads) of spent nuclear fuel storage systems.

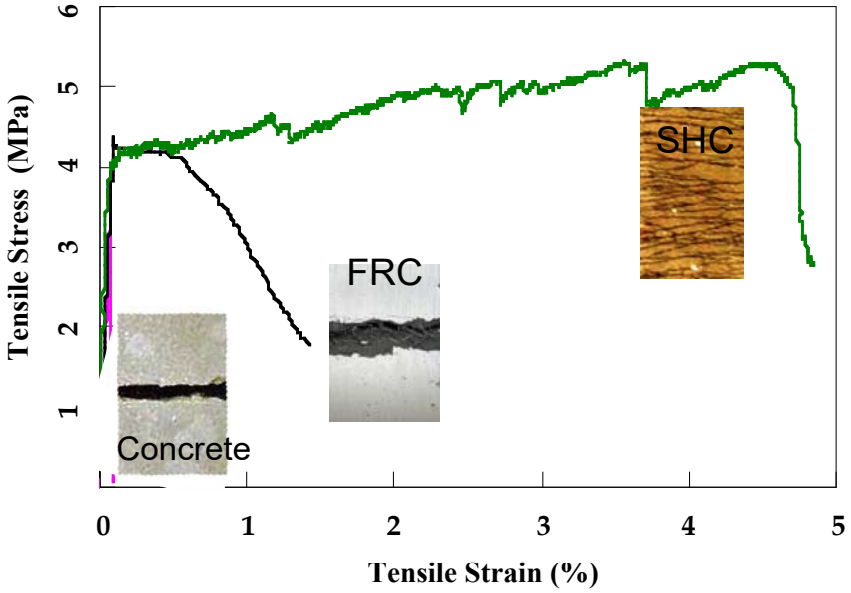

Figure 2.1 Comparison of energy dissipation capacity of shear walls using concrete and MSC under monotonic loading and cyclic loading.

As a composite material, a fiber reinforced cementitious material contains three main components: fibers, matrix (including pre-existing flaws), and fiber/matrix interface. Each of these can be defined by a set of micro-parameters, as summarized in **Table 2.1**. To achieve a ductile tensile strain-hardening behavior at the macroscale ($10^{-2} \sim 10^{-1}$ m) under uniaxial tension, the multiple cracking process needs to be realized instead of localized fracture. Steady-state crack propagation is a necessary condition to ensure multiple cracking, which is governed by the fiber bridging properties across cracks at the mesoscale ($10^{-3} \sim 10^{-2}$ m). The fiber bridging spring law across a crack, quantified by the fiber bridging stress vs. crack opening relationship $\sigma(\delta)$, is the integration of the bridging force contributed by every fiber with different inclination and embedment lengths. For an individual fiber, its bridging force for a given crack opening is determined by its debonding and pullout behavior from the surrounding matrix, and governed by fiber and interface properties at the microscale ($10^{-8} \sim 10^{-5}$ m), as well as by fiber embedment length and inclination angle between the fiber axis and the crack face normal.

Table 2.1: Three components of fiber reinforced cementitious material microstructure and corresponding micro-parameters.

Component	**Micro-Parameters**
Fiber	Length L_f, Diameter d_f, Volume Fraction V_f, Tensile Strength σ_f, Elastic Modulus E_f, Elongation Capacity ε_f,
Matrix	Fracture Toughness K_m, Elastic Modulus E_m, Initial Flaw Size a_0 and Distribution, Tensile Strength σ_m
Fiber/Matrix Interface	Chemical Bond G_d , Frictional Bond τ_0, Slip Hardening Coefficients β_1 and β_1, Snubbing Coefficient η, Fiber Strength Reduction factor f', Cook-Gorden Effect

The micromechanics model links microscale constituent parameters to fiber bridging constitutive behavior on the mesoscale; steady-state crack analysis links fiber bridging properties to tensile strain-hardening behavior on the composite macroscale. This provides a systematic framework for developing strain-hardening cementitious materials with the minimum amount of fibers by strategically tailoring the microstructure at different scales.

2.1.2. Conditions for tensile strain-hardening

As a fiber reinforced brittle mortar matrix composite, its pseudo strain-hardening behavior can only be achieved through the sequential formation of matrix multiple cracking. The fundamental requirement for matrix multiple cracking is that steady-state flat crack propagation prevails under tension. To ensure steady-state cracking, the crack tip toughness J_{tip} must be less than the complementary energy J_b' calculated from the fiber bridging stress σ versus crack opening δ curve, as illustrated in **Figure 2.2** and shown in **Equations 2.1**.

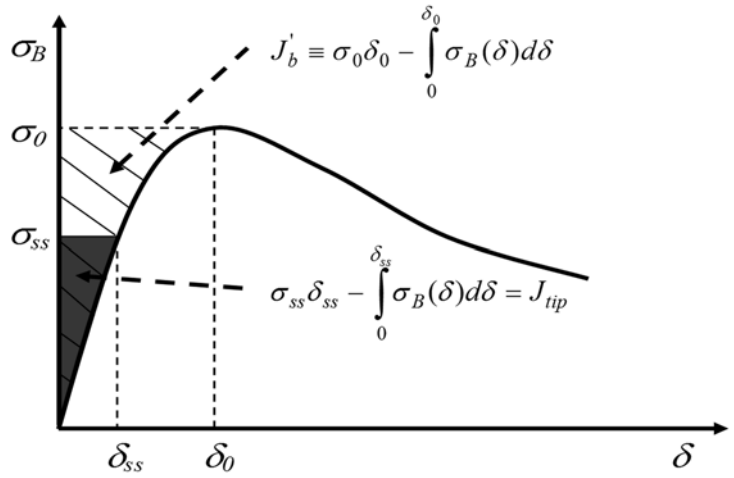

Figure 2.2: Spring law of smeared bridging fibers at one single crack

$$J_{tip} \le \sigma_0\delta_0 - \int_0^{\delta_0} \sigma(\delta)d\delta \equiv J_b' \qquad (2.1)$$

where σ_0 is the maximum fiber bridging stress corresponding to the crack opening δ_0. **Equation 2.1** employs the concept of energy balance during flat crack extension between external work, crack flank energy absorption through fiber/matrix interface debonding and sliding, and crack tip energy absorption through matrix breakdown. This energy-based criterion determines whether the crack propagation mode is steady-state flat cracking or Griffith cracking.

The fiber bridging stress versus crack opening relationship $\sigma(\delta)$, which can be viewed as the constitutive law of fiber bridging behavior, is analytically derived based on fracture mechanics, micromechanics and probabilistic tools. In particular, the energetics of tunnel crack propagation along the fiber/matrix interface is used to model the debonding process of a single fiber from the surrounding cementitious matrix. After debonding is complete the fiber pullout stage begins, and is modeled as slip-hardening behavior with the assumption that non-linear frictional stress increases with slip distance. By these means, the full debonding-pullout process of a single fiber, with given embedment length and

orientation, is quantified as the fiber bridging force vs. fiber displacement relationship. Probabilistic is then introduced to describe the randomness of fiber location and orientation with respect to a crack plane, with the assumption of uniform random fiber distribution. The random orientation of the fibers also necessitates the accounting of the mechanics of interaction between an inclined fiber and the matrix crack. In addition, the snubbing coefficient η and strength reduction factor f' are introduced to account for the interaction between fiber and matrix and the reduction of fiber strength when pulled at an inclined angle. In this way, the σ(δ) curve can be expressible as a function of micromechanics parameters.

Apart from the energy criterion, another condition for pseudo strain-hardening is that the matrix tensile cracking strength σ_c must not exceed the maximum fiber bridging strength σ_0.

$$\sigma_c < \sigma_0 \tag{2.2}$$

where σ_c is determined by the matrix-fracture toughness K_m and pre-existing internal flaw size a_0 and its distribution. σ_0 is the maximum fiber bridging capacity, which is strongly affected by fiber dispersion, and fiber/matrix interfacial bond properties that also influenced by cementitious matrix hydration process and pore structure. While the energy criterion (**Equation 2.1**) governs the crack propagation mode, the strength-based criterion (**Equation 2.2**) controls the initiation of cracks. Satisfaction of both equations is necessary to achieve strain-hardening behavior of cementitious composites; otherwise, the composite behaves as a normal fiber reinforced concrete and tension-softening behavior results, even though a higher amount of fibers are incorporated.

2.1.3. Condition for saturated multiple microcracking

For SHC with pseudo strain-hardening behavior, high tensile strain capacity results from the saturated formation of multiple microcracks. Material tensile strain capacity increases as the number of microcracks increases. While the steady-state cracking criteria (energy criterion, and strength criterion) ensure the occurrence of multiple cracking, it is not directly related to the intensity of multiple cracking. Matrix randomness such as flaws and fiber dispersion uniformity play important roles on the intensity of multiple cracking. Interestingly, the elevated temperature effect will strongly influence both, as observed in this study. The maximum fiber bridging stress σ_0 at the "weakest" section imposes a lower bound of critical flaw size c_{mc}, so that only those flaws larger than c_{mc} can be activated and contribute to multiple cracking. There also exists a minimum crack spacing controlled by interface properties, which imposes an upper bound on the density of multiple cracking.

In this study, the minimum crack spacing x_d for short discontinuous fiber reinforced composites was derived, assuming that the matrix cracking strength is uniform at each section. Under this assumption, the crack spacing between x_d and $2x_d$ was predicted after crack saturation. The minimum crack spacing was determined by the distance necessary for transferring load from the bridging fibers at one crack back

into the matrix through the fiber/matrix interface shear, so that next cracks can be formed. However, a wide distribution far exceeding two times the minimum crack spacing was often observed in our preliminary SHC specimens, due to the variation in matrix properties and non-uniform fiber dispersion. Large crack spacing means that the maximum tensile strain capacity was not achieved (**Figure 2.3**).

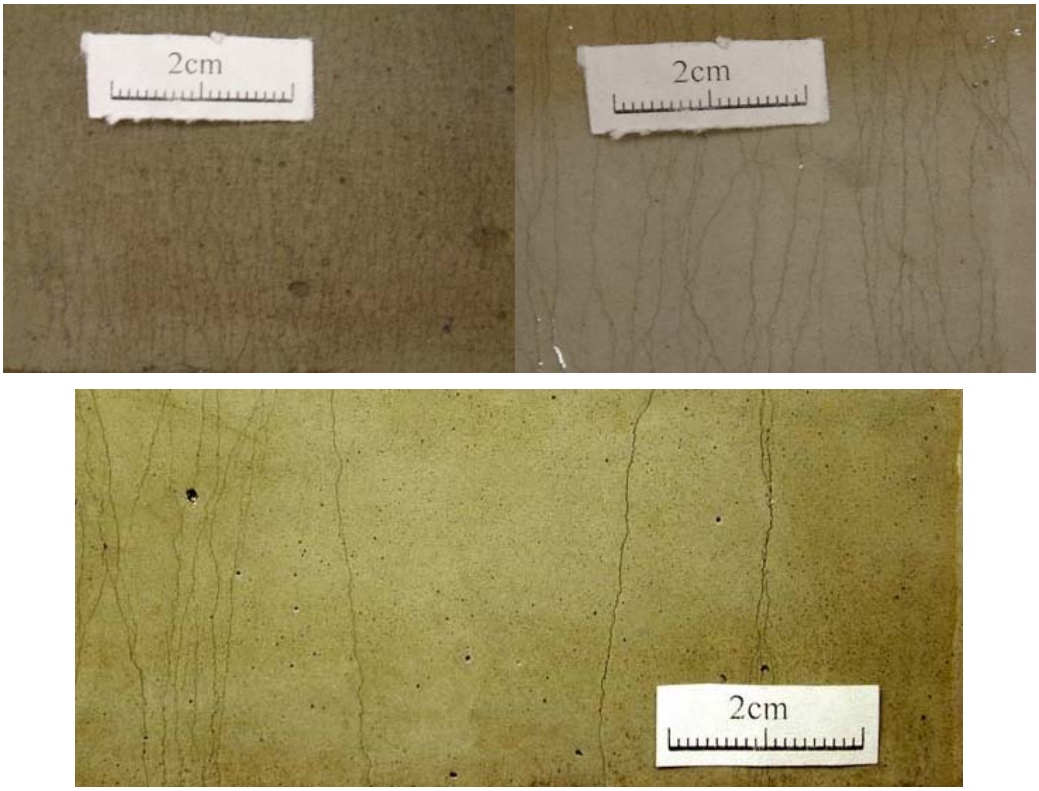

Figure 2.3: Comparison between saturated microcracking (left), less-saturated microcracking (right), and non-saturated microcracking (bottom).

Matrix imperfections, e.g. random distribution of pre-existing flaws, are one cause of the variation in crack spacing and tensile strain capacity. In SHC composites with a quasi-brittle matrix, cracks initiate from pre-existing flaws in the matrix. Examined under an optical microscope, the dominating flaws have sizes below 4-5 mm, depending on the rheology (e.g. plastic viscosity, yield strength) of the fresh material and processing details. The existence of flaws reduces the cracking strength of the cementitious matrix. We computed the effect of initial flaw size on the theoretical cracking strength of an infinite two-dimensional SHC plate under uniaxial tension. The reduction in matrix tensile cracking strength due to the presence of flaws favors the Strength Criterion for Strain-hardening, because the matrix tensile cracking strength σ_c must be lower than the maximum fiber bridging strength σ_0 to satisfy the strength-based strain-hardening criterion. σ_0 can be calculated by taking into account single-fiber debonding and pullout behavior, inclined

angle bridging mechanics, snubbing effect, and the averaging effect of random 3-D fiber dispersion throughout the cross section. It is a function of fiber and fiber/matrix interfacial parameters (**Equation 2.1**), which are temperature dependent and need to be experimentally quantified.

The critical flaw size c_{mc} can be determined as the flaw size that corresponds to the cracking stress σ_0. The critical flaw size is what separates inert and active flaws – only flaws larger than c_{mc} can be activated and contribute to multiple cracking (**Figure 2.4**). The pre-existing flaws in SHC can be entrapped air pores, weak boundaries between phases, and cracks induced by material differential shrinkage, which all possess a random nature and strongly depend on processing details and environmental effects. The number of cracks that can form before reaching the maximum fiber bridging stress may therefore be limited, and can vary significantly from batch to batch. Therefore, a large number of flaws slightly larger than c_{mc} are preferred for saturated multiple cracking and high tensile strain capacity. On the other hand, flaws much larger than c_{mc} will lead to a reduction in the net cross section and fiber bridging stress at the crack section. Under elevated temperature after the fiber melts, a large amount of micro-flaws with very similar sizes will be introduced to the matrix.

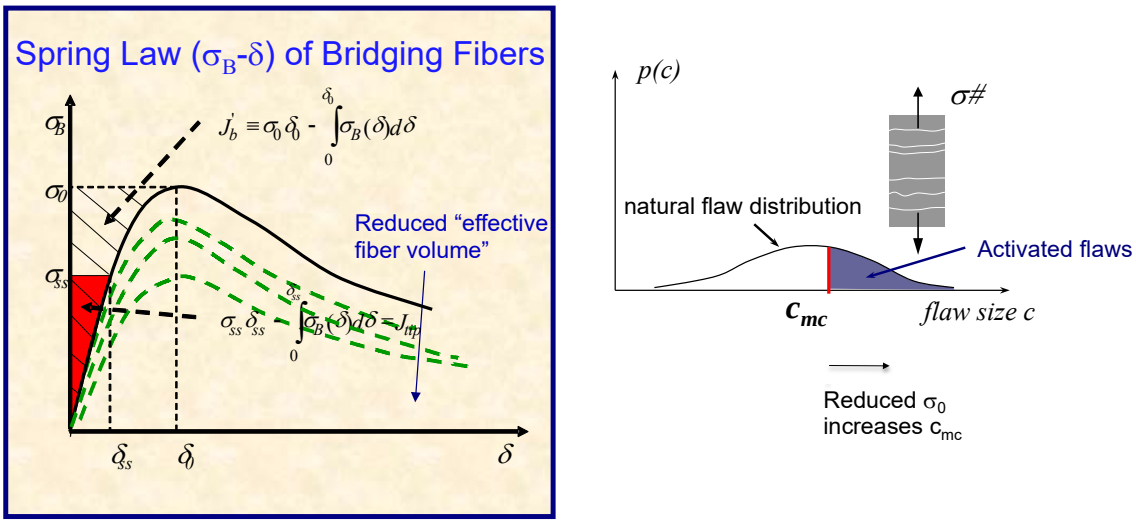

Figure 2.4: Effect of random flaw distribution and fiber bridging capacity on the σ(δ) curve, complementary energy, and critical flaw size.

Fiber dispersion is another contributor to the variation in tensile strain capacity and unsaturated multiple cracking. With a fixed fiber volume percentage, the maximum fiber bridging stress σ_0 at the weakest section is determined by the degree of fiber dispersion uniformity in the composite. Fiber dispersion uniformity is directly influenced by the rheology characteristics, e.g. plastic viscosity and yield stress, of the fresh SHC during processing. It also alters after fibers start to melt after the temperature is

elevated. The total fiber amount, orientation randomness, and uniformity of fiber dispersion determines the maximum bridging stress σ_0, the shape of the $\sigma(\delta)$ curve at the weakest section, and the critical flaw size c_{mc} (**Figure 2.4**). Melting of fibers, degradation of fiber/matrix interface properties, and non-uniform fiber dispersion all lead to a reduction of the value of σ_0 at the weakest section, which increases the critical flaw size c_{mc}. Therefore, less pre-existing flaws with sizes larger than c_{mc} can be triggered and contribute to multiple cracking, resulting in a relatively lower tensile strain capacity. They also shift the $\sigma(\delta)$ curve downward, and may reduce complementary energy J_b' to less than J_{tip}. In this case, the steady-state criteria are violated and tension-softening behavior results. SHC then loses its ductile behavior and becomes a regular FRC material.

2.2. SHC material design, processing, and specimen preparation

Based on the analytical framework in **Section 2.1**, we designed preliminary versions of SHC mixtures (**Table 2.2 and Table 2.3**) by integrating micromechanics theory, rheology control during processing, and micro-structure tailoring. The SHC design theory required the simultaneous satisfaction of steady state cracking criteria and maximized micro-cracking density. The ingredient particle size distribution and the combined amount of water and admixtures were first determined to achieve a homogeneous cementitious composite material at fresh state, with plastic viscosity and yield stress tailored to an optimal level that favored uniform dispersion of micro-scale polyvinyl alcohol (PVA) fibers. Then, the micro-parameters of the hardened material, including matrix properties (e.g., fracture toughness, flaw size distribution, hydration chemistry), the fiber/matrix interfacial properties (e.g., interfacial chemical and frictional bonds, slip-hardening coefficient, fiber debonding and pullout behavior, Cook-Jordan effect), and fiber properties (e.g., aspect ratio, strength, Young's modulus) were tailored to ensure the strain-hardening criteria were satisfied.

The designed SHC-1 binder system contained water, a polycarboxylate-based high range water reducer, Ordinary Portland Cement (OPC) Type I cement, ASTM standard Type F fly ash, and silica sand that served as fine aggregates. The designed SHC-2 binder system contained similar ingredients, except that undensified silica fume and recycled glass bubbles (40 μm diameter) were added. Glass bubbles were incorporated into mix design for two reasons: (a) introduce artificial flaws to the cementitious matrix to maximize multiple microcracking intensity for larger tensile strain capacity, (b) further improve the material resistance to elevated temperature effect. The cementitious ingredients, silica sand, water and admixture together formed the SHC matrix, with tailored toughness and tensile cracking strength satisfying the strain-hardening criteria. Polyvinyl alcohol (PVA) fibers were incorporated into the composite system at a volume fraction of 1.8 %. The PVA fibers were 8 mm long and 39 μm in diameter, with the nominal

tensile strength of 1620 MPa and density of 1300 kg/m^3. Most importantly, the fiber/matrix interfacial bond was strategically tailored at nano-scale so that it can dissipate tremendous energy under loading, while the pullout behavior is controlled to ensure a minimum crack width during multiple microcracking. The complementary energy and the maximum fiber bridging stress were optimized so that they both satisfy the strain-hardening criteria.

Table 2.2: Mixing proportion of SHC-1

Cement	Water	Sand	Fly ash	Superplasticizer	Fiber
Kg/m^3 (lb/ft^3)	Kg/m^3 (lb/ft^3)	Kg/m^3 (lb/ft^3)	Kg/m^3 (lb/ft^3)	Kg/m^3 (lb/ft^3)	Vol-%
266 (16.6)	309 (19.3)	456 (28.5)	956 (59.7)	2.7 (0.168)	1.8

Table 2.3: Mixing proportion of SHC-2

Cement	Water	Sand	Undensified Silica Fume	Glass Bubble	Fly ash	Superplasticizer	Fiber
Kg/m^3 (lb/ft^3)	Kg/m^3 (lb/ft^3)	Kg/m^3 (lb/ft^3)	Kg/m^3 (lb/ft^3)	Kg/m^3 (lb/ft^3)	Kg/m^3 (lb/ft^3)	Kg/m^3 (lb/ft^3)	Vol-%
325 (20.3)	202 (12.6)	325 (20.3)	65 (4.06)	51 (3.4)	33 (2.03)	19.5 (1.22)	1.8

All mixtures were prepared using a 12 L capacity force-based mixer under controlled room temperature 20 ± 1 °C and relative humidity conditions 50 ± 5 % RH. Solid ingredients were first mixed at 100 rpm for one minute. Water and chemical admixtures were then added into the dry mixture and mixed at 150 rpm for three minutes to produce a consistent and uniform. A number of mixtures with the different combinations of water, superplasticizer and viscosity modifying agent were experimented; the yield stress and plastic viscosity of the mortar without fibers were measured using a rotational rheometer and determined based on Bingham model. This information was used to optimize mix design so that optimum plastic viscosity was achieved to favor uniform dispersion of PVA fibers, while optimum yield stress was obtained for the workability and desired self-compacting property of the SHC material.

After the SHC mortar was determined with the target rheological parameters, fibers were

introduced to the material system. The mixtures were then cast into tensile or compression molds. No external vibration was applied. The mixtures flowed under gravity to fill in the molds, and were therefore considered self-compacting. The molds were then covered with plastic sheets, and demolded after 24 hours. Finally, the specimens were moisture-cured in plastic bags at 95±5 % RH and 20±1 °C for 7 days, and air cured at 50±5 % RH and 20±1 °C for 21 days until the age of 28 days when testing started.

2.3 Measurements of micromechanical parameters

The micromechanical parameters described in Table 1 were experimentally and analytically determined for each mixture. Based on the conditions for strain-hardening and saturated multiple cracking, it is evident that high tensile strain capacity requires a high J_b'/J_{tip} ratio and a sufficient number of pre-existing flaws larger than c_{mc}. The matrix toughness J_{tip} and flaw size distribution are matrix properties, while the complementary energy J_b' is mainly controlled by fiber and interface properties.

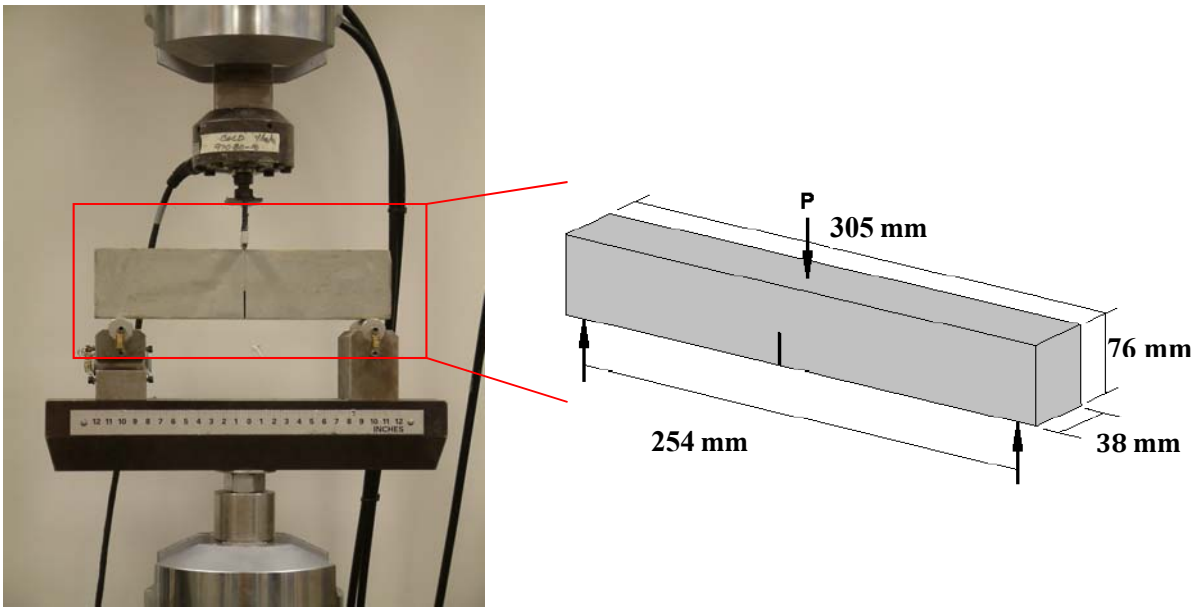

Figure 2.5: Matrix toughness test to characterize J_{tip}.

To experimentally measure J_{tip}, matrix toughness tests were conducted on various mix designs without fibers; therefore it measured the toughness of the cementitious matrix only. This test was similar to ASTM E399[1] "Standard Test Method for Plane-Strain Fracture Toughness of Metallic Materials". The ASTM E399 allowed one to use different geometry specimens, such as bending specimens and compact tension specimens, to measure the K_m value. The cementitious matrix was prepared and cured as described in Section 2.2, except that fibers were not added. The fresh mix was cast into notched beam specimens

measuring 305 mm (12 in.) in length, 76 mm (3 in.) in height, and 38 mm (1.5 in.) in thickness. The matrix fracture toughness K_m was measured by the three point bending test, as shown in **Figure 2.5**. The span of support was 254 mm (10 in.) and the notch depth to height ratio was 0.4. Three specimens were tested for each test series. J_{tip} was calculated from the measured K_m using **Equations 2.3**.

$$J_{tip} = \frac{K_m^2}{E_m} \tag{2.3}$$

To calculate the complementary energy J_b', single crack opening tests were conducted to measure the fiber bridging spring law – the fiber bridging stress versus crack opening relation. Uniaxial tension test was conducted on double-notched specimens (**Figure 2.6**) to measure the tensile stress vs. crack opening relation. The double notches were artificially created to ensure the initiation and propagation of a single crack at the notched cross section.

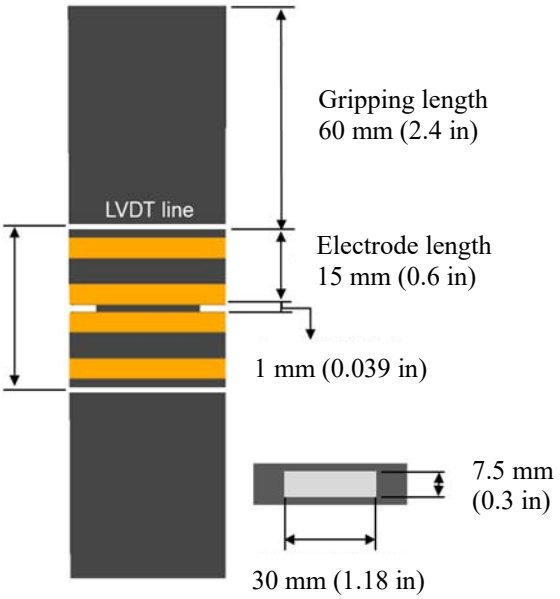

Figure 2.6: Single crack opening test to characterize fiber bridging "spring law" across a crack for calculating J_b'.

The measured fiber bridging spring law across a single crack is shown in Figure 2.7. Processed binary images of the crack at the different opening is shown in Figure 2.8. The crack opening at each loading stage was accurately measured through image processing and digital image correlation technique (See Section 2.4). The fiber bridging stress increased with an initial crack opening, but started decreasing after reaching a peak fiber bridging stress. This phenomenon resulted from the average effect of numerous fibers bridging the crack with the statistically distributed fiber orientation angle and embedment length. Based on the curve, the complementary energy J_b' was calculated and compared with J_{tip} measured through matrix toughness test. **Table 2.4** summarized the results for two mixture designs of SHC. The high J_b'/J_{tip} ratio for

both SHC-1 and SHC-2 indicated that the steady-state cracking criteria were satisfied, and that the materials would macroscopically exhibit tensile strain-hardening behavior.

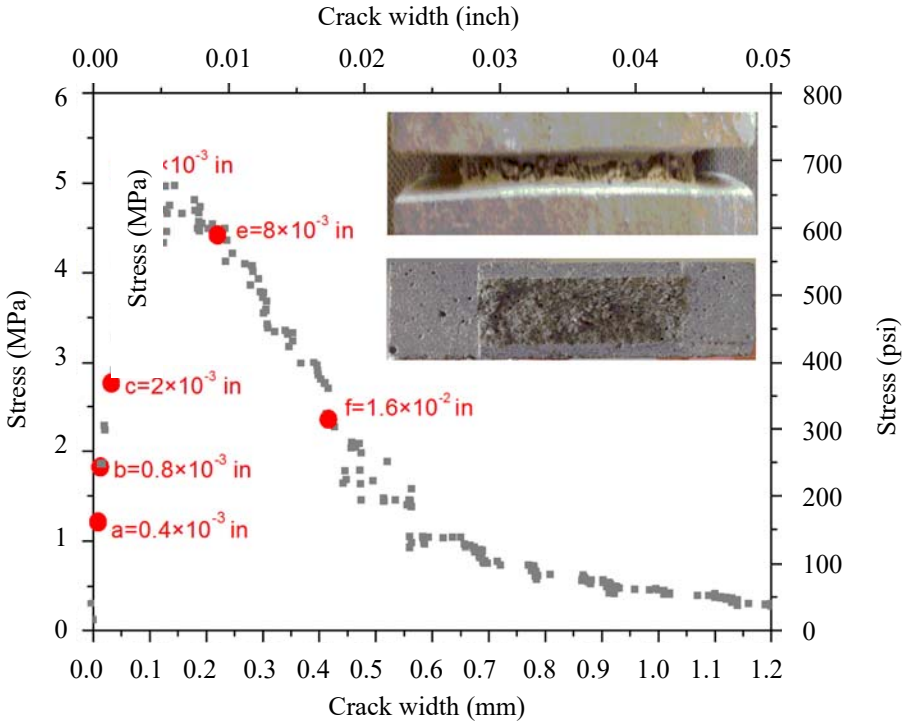

Figure 2.7: Fiber bridging stress vs. crack opening relation (Fiber bridging "spring law").

(a) δ=0.02 mm (0.8×10^{-3} inch)

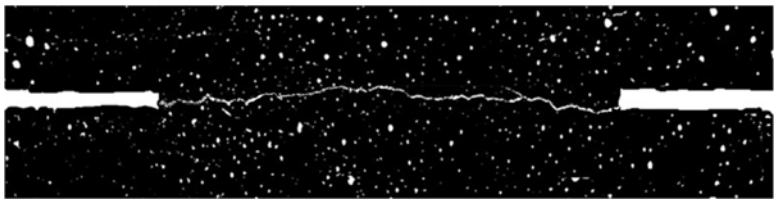

(b) δ=0.05 mm (2×10^{-3} inch)

(c) δ=0.1 mm (4×10^{-3} inch)

(d) δ=0.2 mm (8×10^{-3} inch)

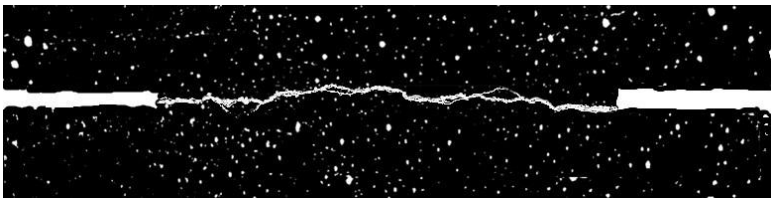

(e) δ=0.4 mm (1.6×10^{-2} inch)

Figure 2.8: Single crack opening at different crack width.

Table 2.4: J_b'/J_{tip} ratios for evaluating strain-hardening energy-criterion

Temp. (°C)	SHC-1			SHC-2		
	J_{tip} (kJ/m^2)	J_b' (kJ/m^2)	$\frac{J_b'}{J_{tip}}$	J_{tip} (kJ/m^2)	J_b' (kJ/m^2)	$\frac{J_b'}{J_{tip}}$
20	0.0123	0.4864	39.6	0.0046	0.4321	94.8

The fiber/matrix interface micro-parameters were experimentally characterized through single fiber pullout test, as shown in **Figure 2.9**. Single fiber pull-out test was conducted on small-scale prismatic specimens with dimensions of 10 mm × 5 mm × 0.5 mm (0.4 in. ×0.2 in. ×0.02 in.). A single fiber was aligned and embedded into the center of SHC mortar prism with an embedment length of 0.5 mm (0.02 in.). Three specimens were tested for each test series. The load P versus displacement δ curve was obtained through quasi-static testing and used to determine the interfacial micro-parameters. These interfacial parameters, along with fiber volume fraction, length and diameter, were used to calculate the fiber bridging law $\sigma(\delta)$ and compared with $\sigma(\delta)$ directly measured through single crack opening test.

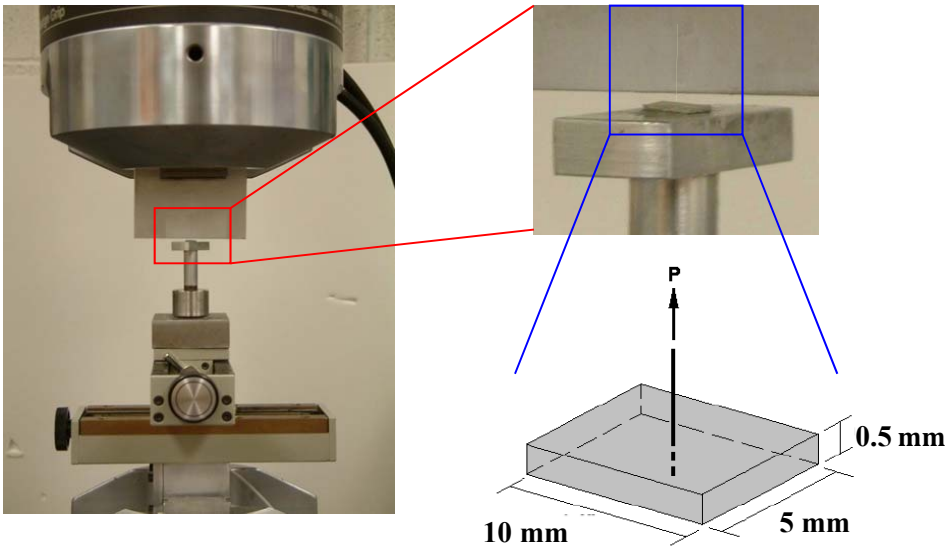

Figure 2.9: Single fiber pullout test to characterize fiber/matrix interfacial bonding micro-parameters.

The general profile of a single fiber pullout curve (P vs. δ) experimentally measured was decomposed into three major regimes. Initially, a stable fiber debonding process occured along the fiber/matrix interface. While the load carried by the fiber increased up to P_a, there was no displacement of the fiber embedded end, $l = l_e$. . The debond length, l_d, increased towards $l_d = l_e$. During this "debonding" stage, the displacement of the fiber end was the sum of the elastic stretching of the debonded fiber segment and of the fiber free length (the portion of the fiber outside the matrix). This debonding process resulted in a tunnel-like crack that propagated stably from the free end towards the embedded end of the fiber. This tunneling process was stable until the tunnel crack tip approached the embedded end of the fiber at which stage it lost stability and the load suddenly dropped from P_a to P_b. At this moment the fiber was held in the matrix only by friction. The chemical debonding energy value, G_d, was calculated from the P_a to P_b difference using Equation 2.4:

$$G_d = \frac{2(P_a - P_b)^2}{\pi^2 E_f d_f^3} \tag{2.4}$$

where E_f is the fiber Young's modulus, and d_f is the fiber diameter.

At the point P_b, the embedded fiber end just completed debonding and the frictional bond strength τ_0 at the onset of fiber slippage was calculated using Equation 2.5:

$$\tau_0 = \frac{P_b}{\pi d_f l_e} \tag{2.5}$$

During the fiber slippage stage, the fiber underwent sliding with slip-hardening, characterized by the positive coefficient β. The β value was calculated from the initial (S' approaching 0) slope of the P versus S' curve using:

$$\beta = (d_f / l_f)[1 / \tau_0 \pi d_f)(\Delta P / \Delta S')\big|_{S'->0} + 1]$$

When the interfacial chemical bond G_d and frictional bond τ_0 were too strong, fiber rupture occurred during pullout state or even debonding stage. This would lead to a low value of J_b' and violation of strain-hardening criteria. On the contrary, when the interfacial bonds were too weak, maximum fiber bridging capacity became lower, leading to the large crack width or even violation of strain-hardening criteria. Therefore, the measurement and evaluation of $G_{d,}$ $\tau_{0,}$ and β values allowed us to tailor these values in this project, to achieve the mixture designs in Tables 2.2 and 2.3 that satisfy strain-hardening criteria.

2.4. SHC uniaxial tensile behavior

To measure the tensile stress-strain relation of designed SHCs, direct uniaxial tension tests were conducted. The direct uniaxial tensile test is considered the most convincing method for evaluating material strain-hardening behavior[2] because some quasi-brittle fiber reinforced brittle matrix composite materials can also show apparent hardening behavior under flexural loading – a phenomenon known as "deflection hardening". The direct uniaxial tension test setup was shown in **Figure 2.10**. The specimen dimensions were 228.6 x 76.2 x 12.7 mm. The both ends of the specimen were wrapped with fiber reinforced plastics to strengthen the end area and facilitate gripping. In this way, multiple cracking was "forced'" to form within the middle gage length of 101.6 mm. Tests were conducted using a 50 kN capacity testing frame under a displacement control rate of 0.0025 mm/s to simulate a quasi-static loading condition. Two external linear variable differential transformers (LVDTs) were attached to the specimen surface with a gage length of 101.6 mm to measure the displacement, which was used to calculate strain. The tensile stress-strain curve of each specimen was determined.

During uniaxial tension tests, digital image correlation (DIC) system was used to characterize the evolution of strain, damage process and final failure. DIC is a technique to track the position of subsets of selected targets in a series of digital images of deformed states relative to an initial undeformed state. For DIC setup, uniform random black speckles were sprayed on the background of the test specimen gauge zone surface. A pair of non-perpendicular 12-megapixel charge-coupled device (CCD) cameras with 24 mm of focal length lenses were mounted on cross-bar of the tripod in order to capture high-resolution images. The distance between cameras, object distance from cameras, and the angle between cameras were adjusted based on target size, available space using DIC system manual. The external sources of fluorescent lights were used to maintain constant optimum illumination of the surface. DIC setup was calibrated by using very

precise calibration panel or calibration cross, and calibration data were captured by the computer. All high-resolution images were collected by a computer having high computing capacity. Afterward, images were post-processed to obtain 3D deformation for crack distribution and crack characterization. The DIC system setup with external lights, DIC inbuilt lights, a pair of cameras, and computer were shown in **Figure 2.11**.

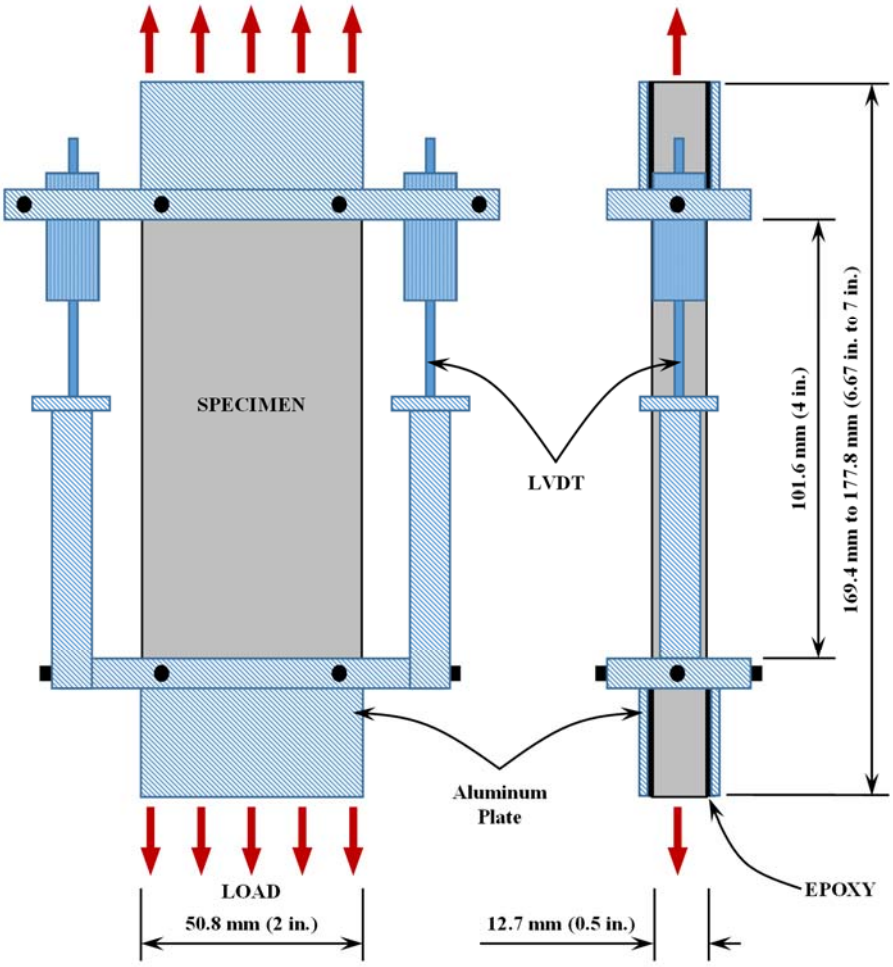

Figure 2.10: Direct uniaxial tension test.

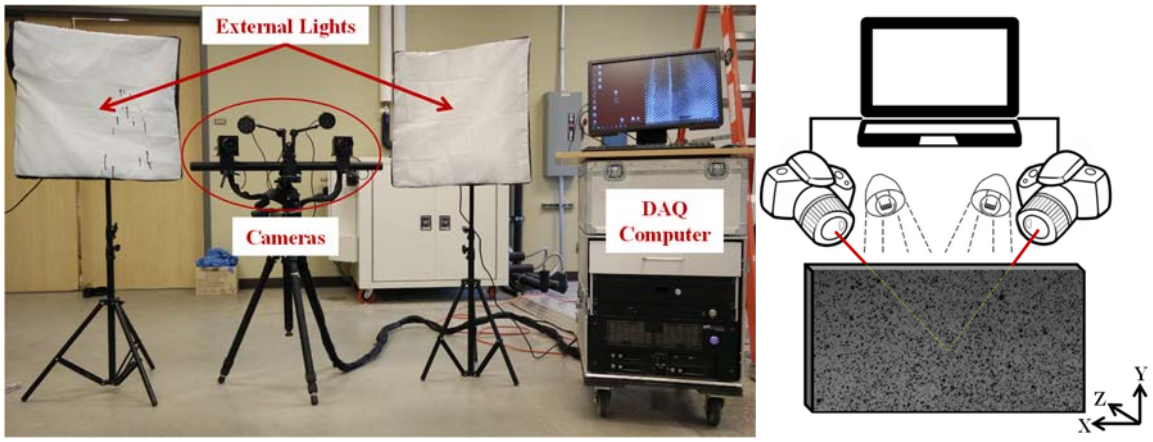

Figure 2.11: DIC setup.

The test results are shown in **Figure 2.12**. Despite the variation in the tensile behavior between SHC-1 and SHC-2 specimens, the tensile stress-strain curve followed the same pattern containing three stages: (1) The initial elastic stage, characterized by Young's modulus. (2) The strain-hardening stage, accompanied by multiple microcracking formations. During this stage, the width of each microcrack remained nearly constant after formation, while the increasing applied strain increases the number of the microcracks. This stage was characterized by first cracking strength (i.e. the stress when the first micro-crack occurs), ultimate tensile strength (i.e. the peak stress), and the strain capacity of the material (i.e. the strain corresponding to peak stress). As this test was conducted under displacement control, each small load "drops" on the curve corresponded to the released energy during the formation of each microcrack. (3) The tension-softening stage, accompanied by the formation of a localized fracture at one of the microcracks and the continuous drop of the ambient load. At the stage, the SHC material behaved the same as tension-softening FRC materials. The results showed that the SHC specimens achieved strain-hardening behavior with tensile strain capacity more than 4% and 5% for SHC-1 and SHC-2 respectively, which is 400 and 500 times, respectively, that of concrete adopted in current SNF systems. The tensile properties of SHC-1 and SHC-2 were summarized in Table Such strain-hardening behavior leads to a high fracture energy that provides ultra-high damage resistance under service or severe loading conditions. Instead of localized fracture that represents a brittle failure mode, SHC has ductile response through the formation of distributed damage. The tensile properties of SHC-1 and SHC-2 are summarized in **Table 2.5**.

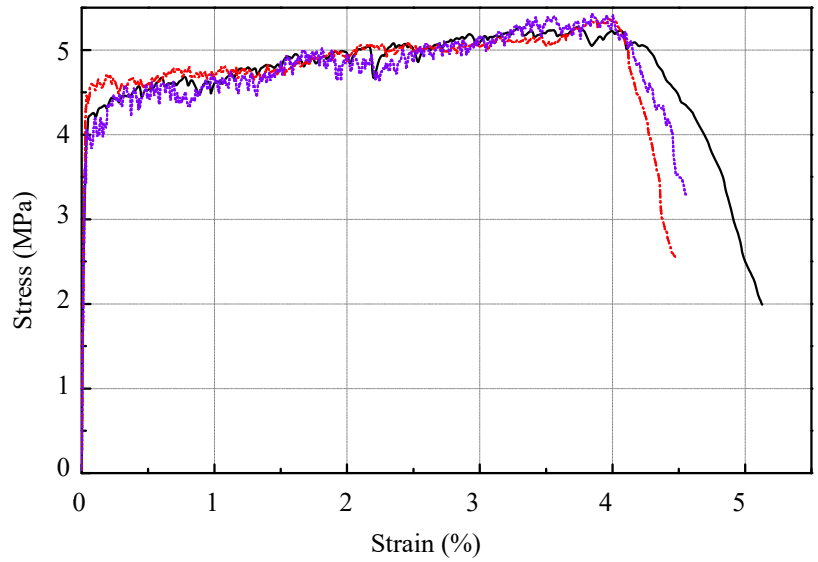

(a)

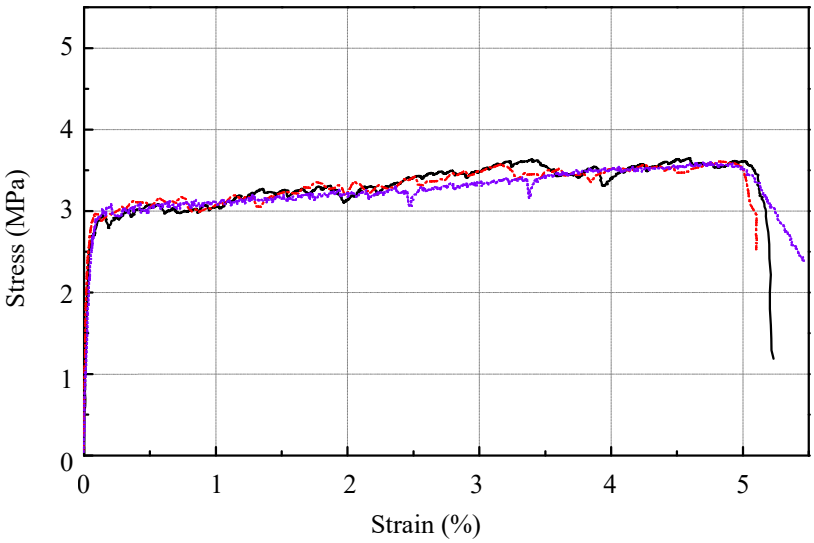

(b)

Figure 2.12: SHC tensile stress-strain curves of: (a) SHC-1, (b) SHC-2.

Table 2.5: Tensile and compressive properties of SHCs

Properties	SHC-1	SHC-2
Mean Tensile Strength (MPa)	5.27	3.49
Mean Tensile Strain (%)	4.21	5.12
Mean Microcrack Width (μm)	30.0	12.5
Mean Compressive Strength (MPa)	57.3	43.8

The multiple microcracking pattern in SHC at maximum tensile strain capacity is shown in **Figure 2.13**. The microcracks have an average width around 30-40 μm for SHC-1, and around 10-20 μm for SHC-

2. The microcracks were hard to see without aid. Special chemicals were applied to the surface of the specimen to better reveal the microcracks. It should be emphasized that these microcracks are "self-controlled", which means their width is independent of specimen geometries, applied load or deformation, and reinforcement ratios, as long as the material is in the strain-hardening stage; increasing strain only increases crack number instead of crack width. The tight self-controlled crack width leads to significantly reduced water permeability, chloride diffusion, and other transport properties of SHC under loading conditions.

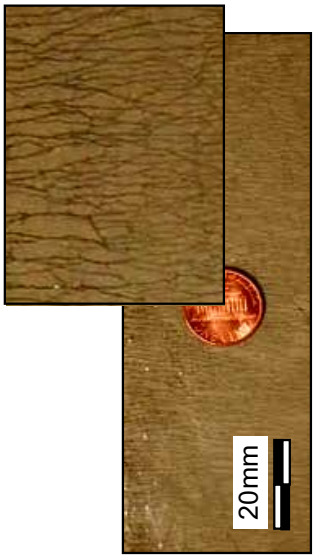

Figure 2.13: Saturated multiple microcracking in SHC.

The multiple microcracking process was captured using DIC, where the different colors showed the different levels of local concentrated strain that indicated cracking (**Figures 2.14** and **2.15**). It should be noted that each "colored line" in the image did not necessarily reflect one single crack; rather, it reflected a number of adjacent microcracks in a local region. It was observed that SHC-2 exhibited more saturated microcracking with tigher crack width than SHC-1. This important finding explained the higher tensile strain capacity of SHC-2 than SHC-1 (5.12% vs. 4.21%) but the smaller average crack width (30-40 μm vs. 10-20 μm). It also validated the micromechanics-based design theory in this study that more tailored flaw distribution in a cementitious matrix of SHC led to better controlled microcracking behavior. To further explain the macroscopic properties of developed SHC at mesoscopic scale, **Figure 2.16** compared the fiber bridging spring law in SHC-1 vs. SHC-2 measured by single crack opening tests. It was seen that the critical crack opening (i.e. crack opening corresponding to the maximum fiber bridging stress) of SHC-2 was lower than SHC-2, leading to the smaller average crack width of SHC-2 than SHC-1.

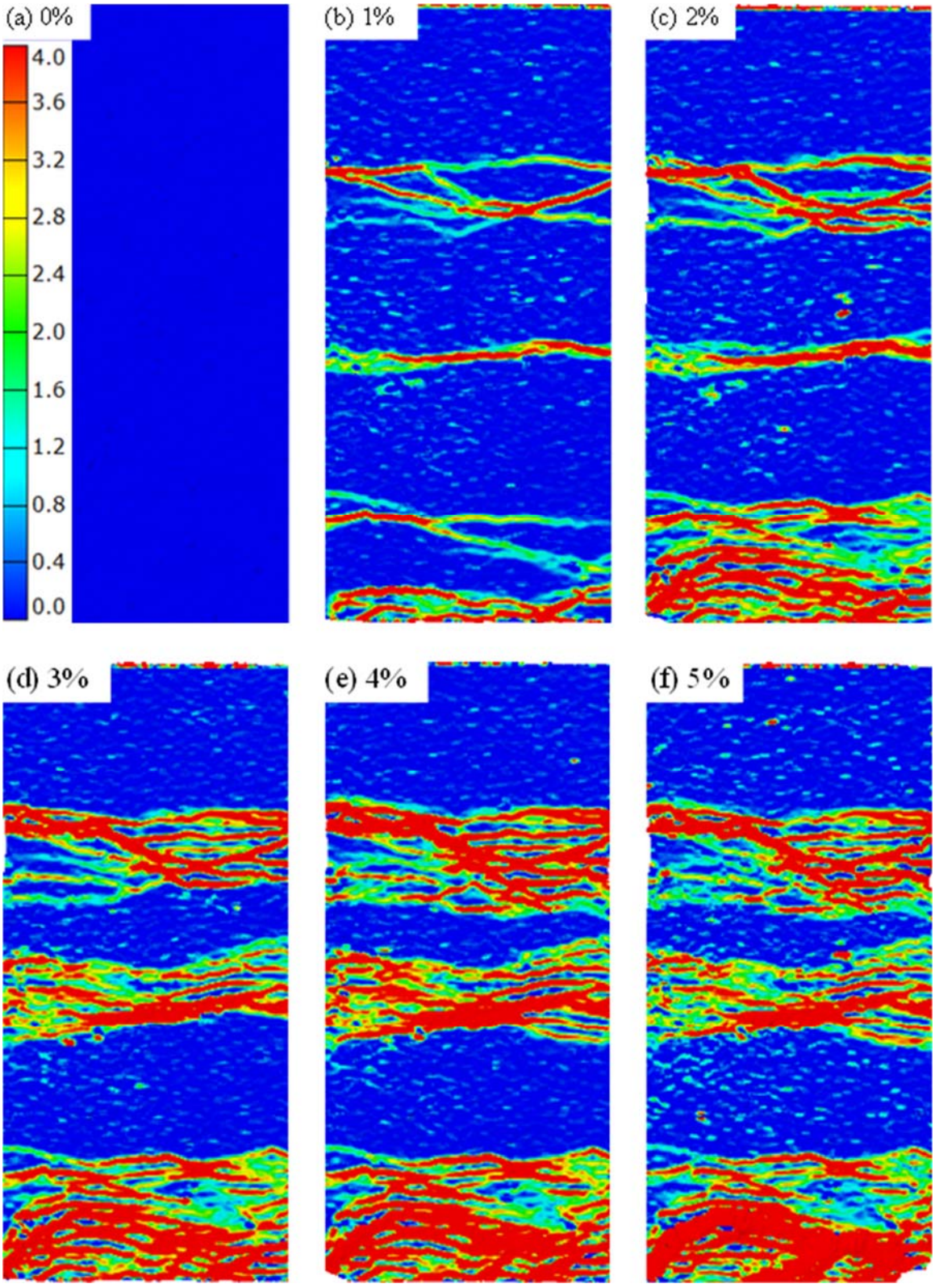

Figure 2.14: DIC images of damage process within SHC-1 as the applied tensile strain increases.

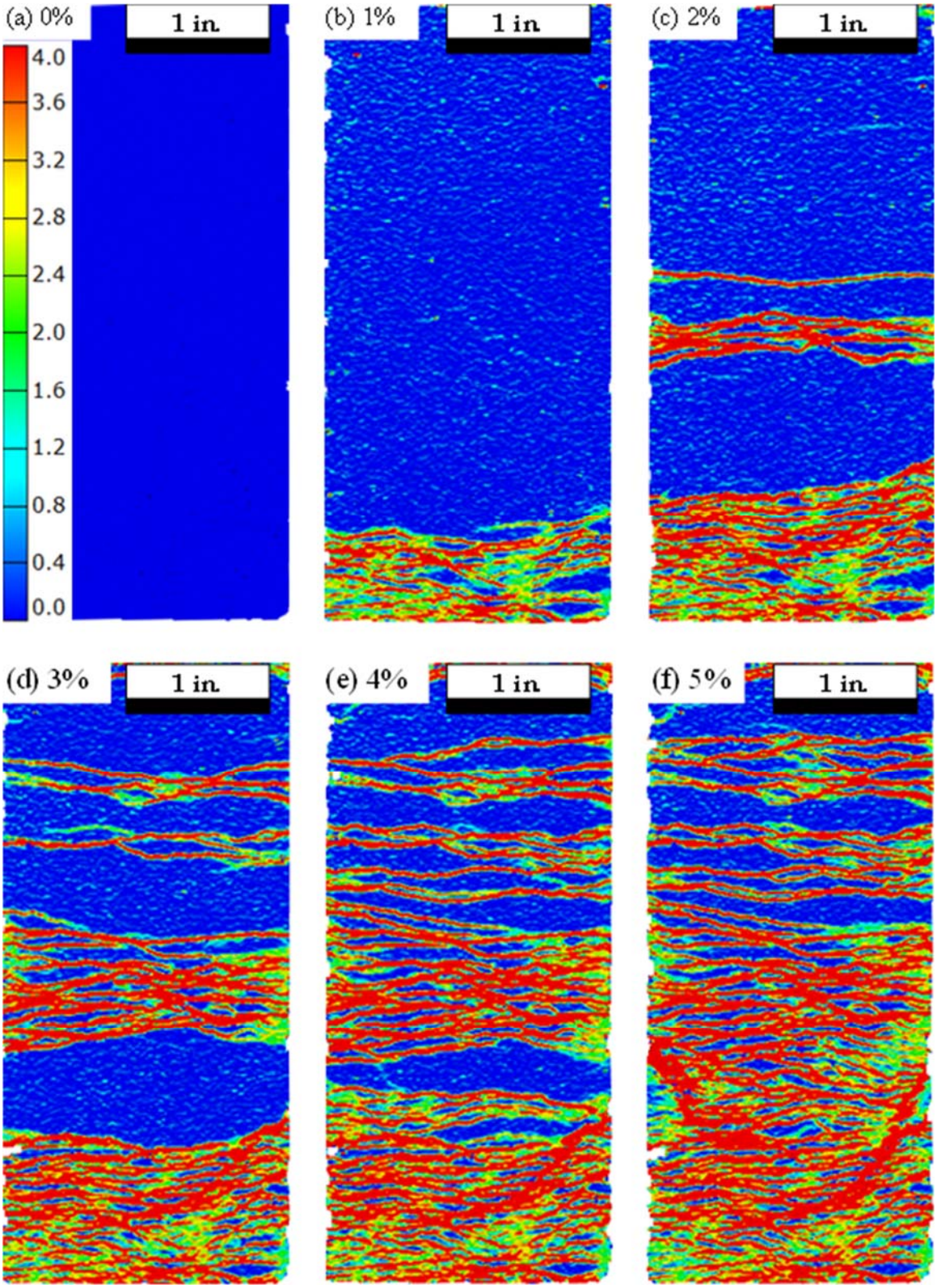

Figure 2.15: DIC images of damage process within SHC-2 as the applied tensile strain increases.

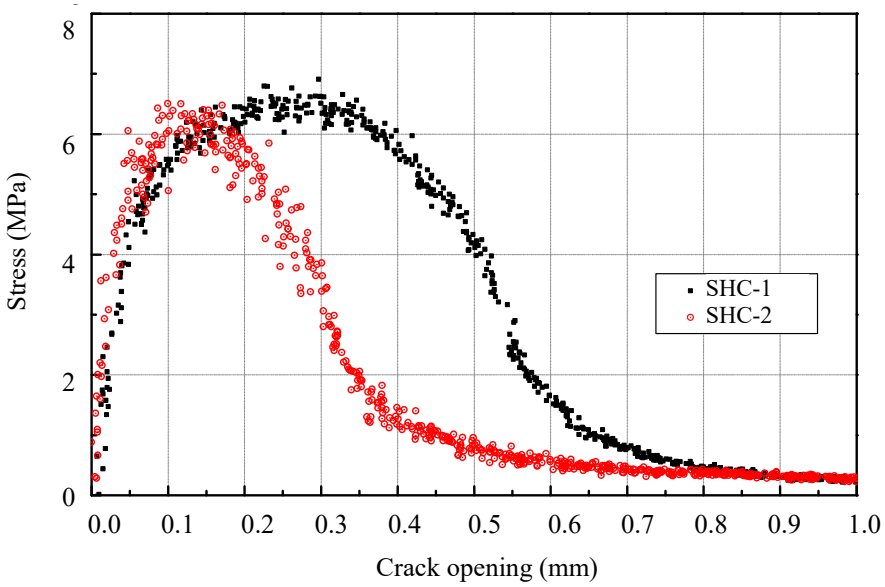

Figure 2.16: Fiber bridging "spring law" of SHC-1 and SHC-2.

2.5. SHC compressive behavior

Compressive testing was carried out according to ASTM C39[3] "Standard Test Method for Compressive Strength of Cylindrical Concrete Specimens" on standard cylinders measuring 75 mm (3 in.) in diameter and 150 mm (6 in.) in length. Tests were conducted on a Tinus Olsen hydraulic test system with 450 kips (2,000 KN) capacity. To ensure that compressive force was uniformly distributed, the test specimens were capped on both ends. Two different types of capping methods were adopted in this study. The first capping method was bonded capping using sulfur-based capping compound conforming ASTM C617[4]. Sulfur was molten and poured into horizontally leveled capping mold, then immediately one end of the cylinder was mounted vertically and waited until the capping material hardened. Similarly, another end was also capped to ensure both capped top and bottom ends of the specimen were smooth and parallel. The leveling of both ends and verticalness of cylinder was ensured by a spirit level. Another method was unbonded capping with neoprene elastomeric pad restrained within steel restrainers conforming ASTM C1231[5]. Elastomer pads of hardness 60 and 70 were used. Compression test results of both SHC-1 and SHC-2 were consistent with either of the capping methods. Un-bonded capping using elastomer pads for capping was a lot faster and easier than bonded capping. Therefore, unbonded capping satisfying ASTM C1231 was used in the rest of compression tests.

The uniaxial compression test was conducted on capped cylinder specimens to measure the load-displacement curves, under displacement control. The displacement rate was set to be 0.2 in/min until the

top loading plate was fully in contact with the specimen; then displacement control testing rate was switched to 0.01 in/min. The specimens were loaded until the load dropped by 20% of the peak load. Three to four specimens were tested for each test scenario. The average compression test results of SHC-1 and SHC-2 is shown in **Error! Reference source not found.**The average compressive strength of SHC was reported to be 57.3 MPa for SHC-1 and 43.8 MPa for SHC-2.

The final compressive failure mode of SHC specimens was compared with control concrete specimens with similar compressive strength (**Figure 2.17**). In contrast with the sudden brittle failure of concrete specimens with splitting cracks (Figure 2.15 (b)), the SHC specimens exhibited ductile failure mode with the final failure plane approximately 45 degree to the axis of the specimen. Such ductility prevents catastrophic failure under compression.

(a) (b)

Figure 2.17: Compressive failure mode of (a) SHC and (b) normal concrete

2.6. SHC flexural behavior under monotonic and cyclic loading

Displacement-controlled four-point bending test was conducted on SHC specimens with geometries and test setup shown in **Figure 2.18**. An LVDT was installed at the midspan of the specimen to measure its vertical deflection. The SHC beam specimen was loaded monotonically until failure with a loading rate of 0.015 mm/s. Under four-point bending, SHC first underwent an elastic stage, followed by a deflection-hardening behavior accompanied by the formation of a number of microcracks on the tensile side of the specimen. This allowed the SHC specimen to undergo a large curvature without fracture failure under excessively applied deformation. The deflection-hardening response of SHC reflected its extraordinary tensile ductility without of the need of steel reinforcements. A highly deformed SHC specimen is shown in **Figure 2.19**. The bending stress vs. displacement relation of SHC is shown in **Figure**

2.20. While the maximum midspan deflection (measured by LVDT and DIC) was around 23 mm, the maximum roller displacement (Δ) was measured as 17.8 mm.

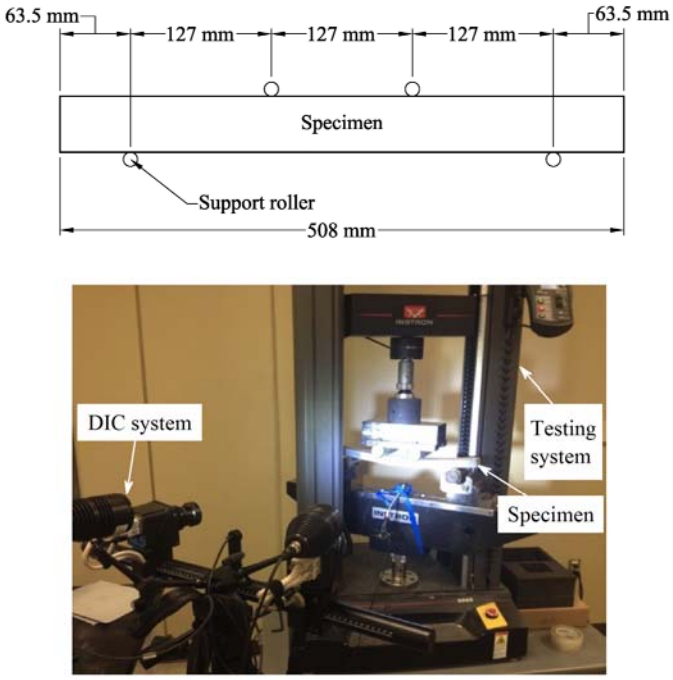

Figure 2.18: Four point bending specimen geometry and test setup.

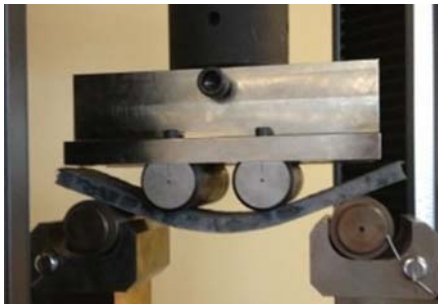

Figure 2.19: A highly deformed SHC specimen under four point bending; no steel reinforcement was used.

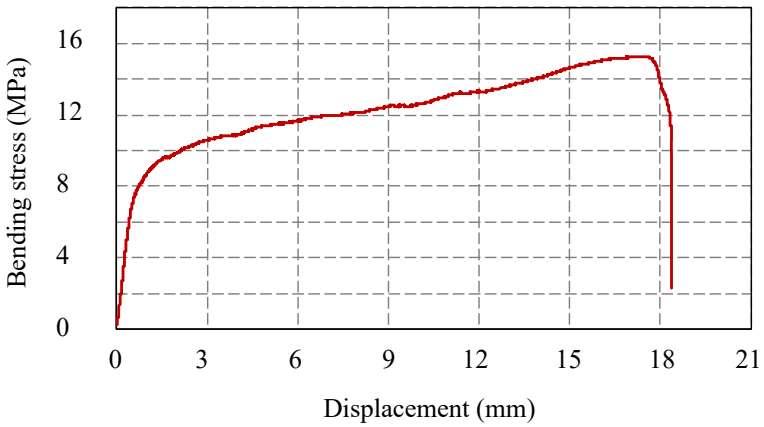

Figure 2.20: SHC bending stress vs. displacement relation.

In the cyclic loading tests, each cycle loaded the specimen with an incrementally increasing deflection value of 1/10 of maximum displacement capacity of SHC beam specimen, which was followed by unloading before starting the next cycle. **Figure 2.21** shows the loading history. The loading and unloading rate was 0.015 mm/s.

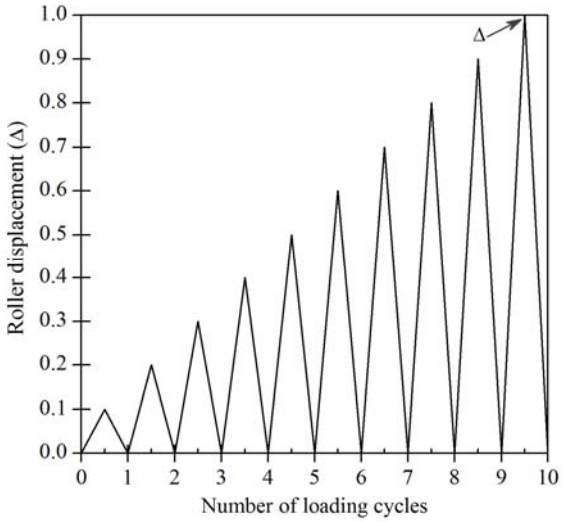

Figure 2.21: The cyclic loading history.

During the testing, a DIC system (**Figure 2.18**) was used to track the surface deformation and strain change of the deformed beam. The DIC is a non-destructive and non-contact measurement tool with many advantages over conventional approaches. It computed the displacement of a regular grid of points on the specimen surface by comparing the digital images of the specimen surface before and after deformation. In this study, the DIC system tracked the full-field deformation, strain and damage from the surface of the specimens during elastic, inelastic and post-cracking stages under cyclic loading. In this way, the DIC

measurements provided information on the spatial strain and damage evolution and recovery of the specimens. The DIC measurements were first verified through comparison with LVDT measurements (**Figure 2.22**).

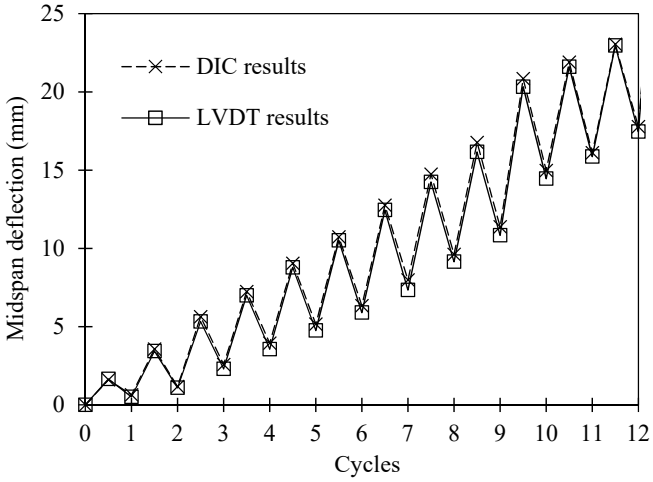

Figure 2.22 Midspan deflection measured by DIC and LVDT.

The SHC beam specimen, even without any steel reinforcement, demonstrated extraordinary ductility and considerable load carrying capacity. Unlike reinforced concrete specimens, no localized fracture was observed. Instead, multiple microcracks were distributed along the tension side of the specimen, with the crack number increasing with increasing deformation during each loading cycle. The large energy dissipation capacity (**Figure 2.23**) of the specimen was solely contributed by SHC itself (i.e. without the need of steel reinforcement). After the initial elastic stage, the beam exhibited a "deflection-hardening" behavior as indicated by the increasing load carrying capacity following each loading cycle. The crack number steadily increased from 14 during the 1st loading cycle to 149 during the 7th loading cycle (**Figure 2.24**). The width of these cracks, however, remained below 30 μm. This distributed damage behavior with self-controlled microcrack width was unique to SHC material. Upon unloading, crack number slightly decreased, whereas the maximum crack width remained almost unchanged. The hysteresis behavior and energy dissipation of SHC were associated with the bridging behavior of short discontinuous fibers with a statistical distribution of embedment lengths and orientations, especially the fiber/cementitious matrix interfacial properties. The large energy dissipation capacity of SHC at mocroscale resulted from its micro- and meso-scale energy dissipation mechanisms. Such large energy dissipation capacity can lead to significant damage tolerance under dynamic loading conditions (e.g. impact, earthquake) or accidental conditions (e.g. during transportation).

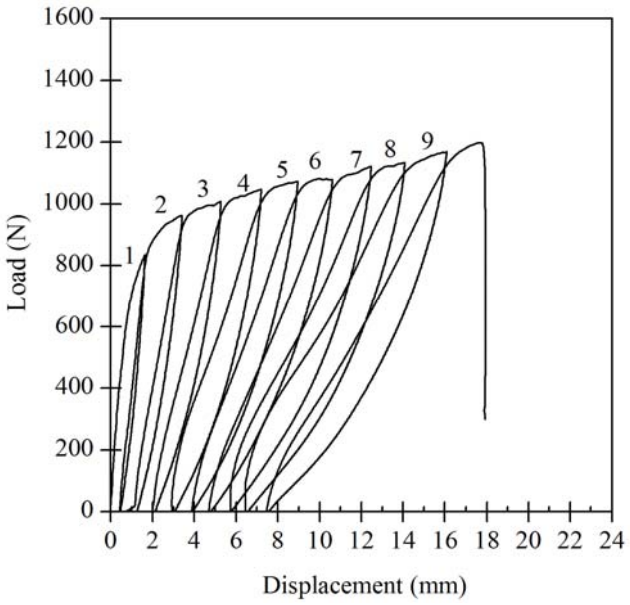

Figure 2.23: Cyclic behavior of SHC under four point bending.

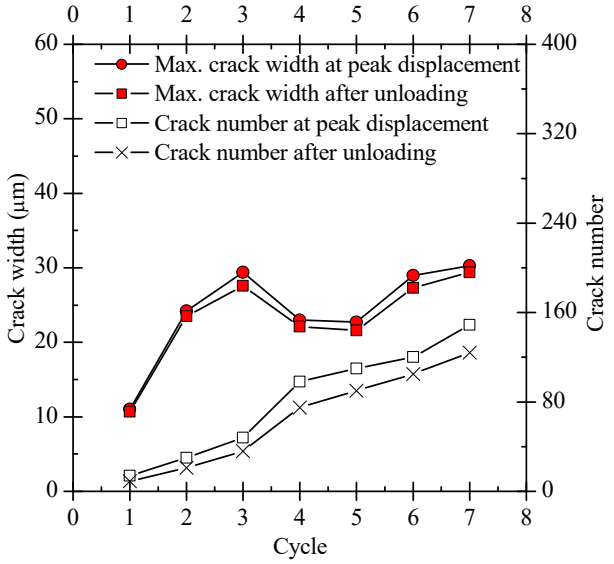

Figure 2.24: SHC crack number and maximum crack width at peak displacement and after unloading for each cycle.

2.7. Summary of accomplishments

A new class of robust strain-hardening cementitious materials (SHCs) for SNF storage systems was successfully developed in this project. The new SHCs uniquely feature the following characteristics:

- Ultra-high ductility with a tensile strain capacity more than 4%, and up to 6.5%. The tensile strain capacity of SHC is more than 400 times that of normal concrete and FRCs.
- The large tensile ductility of SHC overcomes the inherent brittleness of cementitious materials, leading to extraordinary damage tolerance under service loading (e.g. cracking induced deterioration, corrosion-induced concrete spalling and fracture) and extreme loading conditions (e.g. impact, earthquake, accidental loading during transportation). The fracture energy of SHC is two orders higher than current concrete used in SNF storage systems, and one order higher than most FRCs.
- Intrinsically controlled micro-crack width (mean crack width of 30.0 μm for SHC-1, mean crack width of 12.5 μm for SHC-2) during *strain-hardening* stage, which is *independent* of reinforcing ratio, structural member geometry, applied deformation and loading conditions;
- The tight crack width provides high resistance to chloride diffusion and water permeation, compared to conventional concrete at the cracked stage. Maximum allowable crack widths are required in various codes and specifications for the design of reinforced concrete structures exposed to aggressive chloride environments. The allowable maximum crack width ranges from 150 to 300 μm, with the most stringent requirements specified by JSCE[6, 7] and ACI 224R[8]. According to ACI 224R, the maximum crack width at the tensile face of reinforced concrete structures is specified as 150 μm for exposure conditions of seawater, seawater spray, wetting, and drying; and 180 μm for deicing chemical exposure. As the microcrack width of SHC formed during its strain-hardening stage is intrinsically limited to be below 30 μm, which is independent of structural geometry and applied deformation, steel reinforcement is not required to control crack width even for the most stringent allowable crack width requirement;
- Sufficient compressive strength for structural applications including meeting the high strength requirement for seismic applications;
- Large energy dissipation resulted from its hysteresis behavior under cyclic loading.

A micromechanics-based framework and rheology design methodology was established in this project for developing ductile SHCs that feature strain-hardening behavior with optimized tensile ductility. The framework links measurable parameters at nano- and micro-scales to composite strain-hardening behavior. The framework also took into account the random distribution of flaws and “effective volume” of polymeric fibers, in addition to the interface nanoscale tailoring and matrix microstructure manipulation. According to this analytical framework, we successfully designed and processed SHC materials with tensile ductility two orders higher than SNF concrete and fiber-reinforced concrete, as well as intrinsic crack width control capacity. Through tuning the chemical and physical parameters of SHC at microstructure scales, the “spring law” (fiber bridging stress vs. crack opening relation) of each individual crack was modified

(e.g. from SHC-1 to SHC-2) to achieve a significant change in the crack width distribution during SHC strain-hardening stage. By this means, the mean crack width was further reduced to 12.5 μm while the tensile strain capacity was increased to above 5%.

The new SHC materials offer great advantage over normal concrete materials, in terms of improved damage resistance and reduced transport properties for SNF storage.

2.8. References

[1] ASTM, "Standard Test Method for Plane-Strain Fracture Toughness of Metallic Materials," in *ASTM E399-90*, ed, 1997, p. 31.

[2] H. Stang, "Scale Effects in FRC and HPRFCC Structural Elements," in *High Performance Fiber Reinforced Cementitious Composites*, Naaman, 2003, pp. 245-258.

[3] ASTM, "Standard Test Method for Compressive Strength of Cylindrical Concrete Specimens," in *C39/C39M-16b*, ed: ASTM, 2016, p. 7.

[4] ASTM, "Standard Practice for Capping Cylindrical Concrete Specimens," in *C617/C617M-15*, ed: ASTM, 2015, p. 6.

[5] ASTM, "Standard Practice for Use of Unbonded Caps in Determination of Compressive Strength of Hardened Cylindrical Concrete Specimens," in *C1231/C1231M-15*, ed: ASTM, 2015, p. 5.

[6] JSCE, "Recommendations for Design and Construction of High Performance Fiber Reinforced Cement Composites with Multiple Fine Cracks(HPFRCC)," in *Concrete Engineering Series 82*, ed, 2008.

[7] JSCE, "Standard Specifications for Concrete Structures "Design"," ed: Japan Society of Civil Engineering, 2007.

[8] ACI, "Control of Cracking in Concrete Structures," in *224R-01*, ed: ACI Committee 224, 2001, p. 46.

3. DEVELOPMENT OF MULTIFUNCTIONAL STRAIN-HARDENING CEMENTITIOUS MATERIAL WITH SELF-SENSING CAPACITY

3.1 Introduction

The newly designed SHCs were further tailored in this project to achieve novel self-sensing properties, turning it into a multifunctional strain-hardening cementitious material (MSC). The focus was on strain sensing as well as distributed damage sensing.

To achieve the objective, the multi-point probing of SHC materials was explored with different chemical compositions and physical parameters, which revealed their effects on the complex impedance (under a wide range of frequencies) and the electromechanical behavior of SHC. The correlation between the electrical properties and mechanical and environmental stimuli was established. A number of challenges were successfully addressed for the development of MSC, including the following:

- The piezoresistivity test method needs to be robust by removing the electrical and electromagnetic influence due to the testing frame and ambient environment on the impedance measurements. The test results should reflect *true* material properties.
- The electrode and electrode/specimen interface effects need to be removed to obtain more accurate readings to reflect MSC material properties.
- Tailoring the electrical properties of MSC should not sacrifice the tensile ductility of MSC due to the violation of aforementioned strain-hardening conditions.
- A minimum gage factor of 5 during elastic straining stage, and a minimum gage factor of 20 during inelastic straining (i.e., strain-hardening) stages need to be achieved in MSC.
- The crack propagation within MSC needs to be carefully controlled within MSC so that a robust damage sensing capacity can be established.
- The impact of environmental factors on MSC electromechanical properties need to be understood.

Cementitious materials are heterogeneous in terms of their microstructure and physiochemical properties. SEM image of cement paste (**Figure 3.1**) shows that the microstructure of the cementitious material is highly complex. Besides ingredients such as sand, coarse aggregates, pozzolans, etc, cement paste microstructure includes several parts: pores, cement hydration products, outer products, and unhydrated clinkers. Pores include capillary pores, entrapped air voids, and the entrained air system. Hydrated cement particles consist of high-density C-S-H, and in some cases an interior core of unhydrated cement. The outer product can be solid C-S-H gel, gel pores, calcium hydroxide, calcium sulfoaluminate phases. Humidity exists in pore solution and C-S-H layer solution. For pore humidity, there are different ions inside: Na^+, K^+, Ca^+, $SO_4{}^{2-}$, OH^-, etc. For pore solution or gel pore solution, the conductivity is

higher than 10 S/m [1, 2] after 1 day curing. The conductivity of C-S-H and other solid phase composites is several thousand times lower than that of the pore solution [3]. Under an applied steady electric field, the ions in pore water are mobilized to create the electrical current. The electrical response of a cementitious material strongly depends on its heterogeneous microstructure, including the distribution and connectivity of pores, the interconnecting layers of C-S-H gels, and their interfaces.

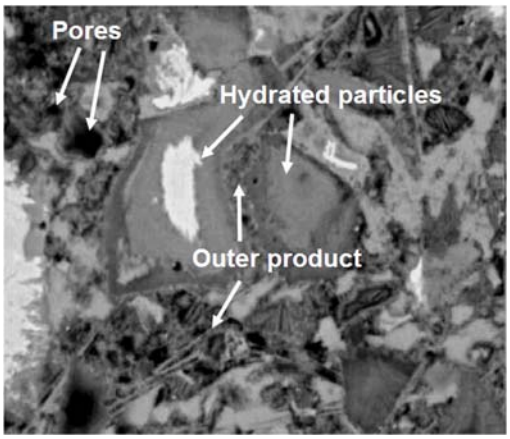

Figure 3.1. Backscattered SEM image of cementitious paste showing the main microstructural features.[4]

The microstructure of cementitious materials is not only heterogonous, but also age-dependent. **Figure 3.2** shows the typical plot of porosity change in terms of concrete age. In addition to aging effect, humidity content within pores also changes from time to time, due to cement hydration process as well as ambient relative humidity changes in the exposure environment.

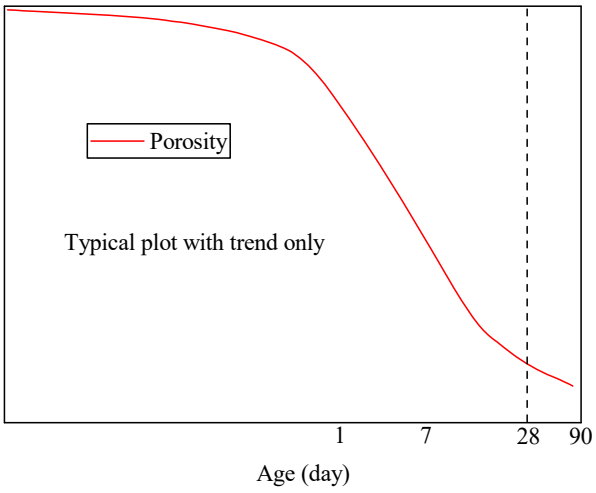

Figure 3.2. Porosity change with concrete age.

In this study, electrical impedance spectroscopy (EIS) was conducted on cementitious material specimens with two variables: age and composition. The electrical response of porous cementitious materials with a wide frequency from 1HZ to 1MHZ reflected the movement of ions in the pore solution and hence was linked to microstructure characterization. Using the improved EIS method throughout the following experiments, the cementitious material electrical properties were accurately characterized. In order to fundamentally understand the electrical behavior, especially the complex impedance of cementitious materials, EIS and equivalent circuit analysis were performed on various mixtures with different binder ingredients, water/binder ratios, incorporation of conductive nano-materials, and age effects. The equivalent circuit model was further refined to better reflect the contribution of different phases, interfaces, components and ingredients on the electrochemical behavior of the material. The results shed light on the age-dependent material electrical properties at the composite, component and ingredient levels, which laid the groundwork for the systematic development of self-sensing strain-hardening cementitious materials for SNF storage applications. A comprehensive electrical impedance study, coupled with equivalent circuit analysis, allowed us to tailor the MSC material physical and chemical parameters to exhibit a strong correlation between complex impedance and material strain, crack width, damage level, and healing.

The significance of this study was three-fold: First, it allowed us to understand the true electrical behavior of the material at the component, phases, microstructure, mesostructure, and composite scales. This laid out the groundwork for systematically tailoring the MSC at different scales so that the material can behave as versatile piezoresistive sensors, connecting mechanical or electrochemical stimulus to different electrical responses. Second, through material tailoring, strain sensing became possible through establishing strong gage factors at elastic, inelastic, and tension softening stages. Finally, sensing of damage was achieved for the first time, which can capture crack opening and distributed damage evolution. Further efforts were made on improving these properties. A series of MSC were further designed, guided by the EIS results, the equivalent circuit model parameter studies, and micromechanics-based model that evaluated the strain-hardening criteria of MSC. Meanwhile, the material design also took into account the effect of chemical composition and hydration products on the rheology of the MSC material during fresh state, and their consequent effects on the dispersion of particles as well as the age-dependent microstructure evolution within MSC during hardened state.

3.2 Electrical impedance spectroscopy on cementitious materials

3.2.1 EIS principle and test setup

Impedance spectroscopy is a relatively new and powerful method for characterizing electrical properties of materials and their interfaces with electrodes. It can be adopted to investigate the dynamics of bound or mobile charge in the bulk or interfacial regions of solid or liquid materials, including ionic, semiconducting, dielectric and mixed electronic-ionic materials. Its fundamental theory can be shown below. For ideal Ohms law:

$$R = \frac{E(t)}{I(t)} \tag{3.1}$$

With small excitation signal, a sinusoidal potential excitation is applied. The response to this potential is an AC current signal, containing excitation frequency and harmonics. The excitation signal, expressed as a function of time, has the form of:

$$E(t) = E_0 \cos(\omega t) \tag{3.2}$$

$$I(t) = I_0 \cos(\omega t - \phi) \tag{3.3}$$

For a linear system, the impedance is written as:

$$Z(t) = \frac{E(t)}{I(t)} = \frac{E_0 \cos(\omega t)}{I_0 \cos(\omega t - \phi)} = Z_0 \frac{\cos(\omega t)}{\cos(\omega t - \phi)} \tag{3.4}$$

With Euler's relationship

$$\exp(i\phi) = \cos\phi + i\sin\phi \tag{3.5}$$

$$E(t) = E_0 \exp(i\omega t) \tag{3.6}$$

$$I(t) = I_0 \exp(i\omega t - i\phi) \tag{3.7}$$

Then impedance can be re-written as a complex number:

$$Z = \frac{E}{I} = Z_0 \exp(i\phi) = Z_0(\cos\phi + i\sin\phi) \tag{3.8}$$

When the complex number is plotted on the complex Coordinate, Nyquist plot is obtained. To experimentally measure impedance response of cementitious materials, AC-Impedance spectroscopy technology was utilized to capture data. This study focused on a wide frequency range (1HZ – 1MHZ) AC-IS results of cementitious material with different proportions of ingredients and age variation from 14 days to 180 days.

Four-point probe method was adopted for EIS, as shown in **Figure 3.3(a)**. Four copper electrodes were applied on the surface of the specimen. Electrodes were parallel to each other with distances shown in

Figure 3.3(b). Two outer electrodes were connected to positive polar of Current and Gen Output connectors of impedance analyzer, which were used to inject current into the specimen and collect output current data. High and Low voltage connectors were connected to the two inner electrodes to measure the voltage existing between electrodes. Collected current data, as well as reference voltage data, provided impedance information of the specimen within the gage length. The specimen had the thickness of 12.7mm, the width of 51 mm and length of 254 mm. The gauge length between two internal electrodes was 102 mm.

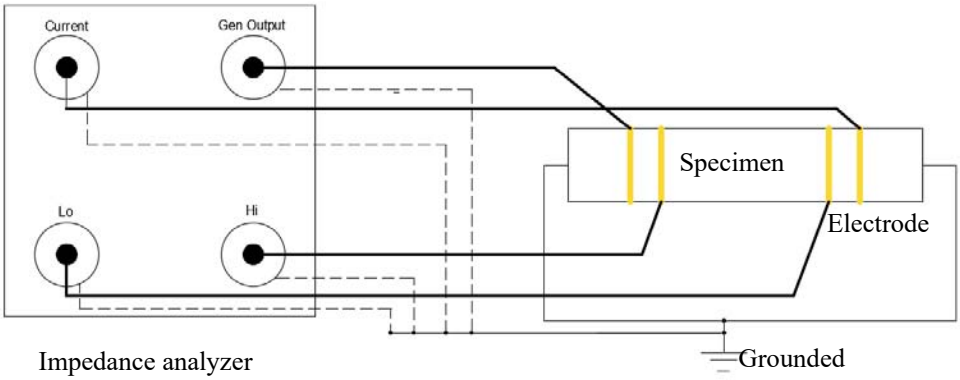

(a)

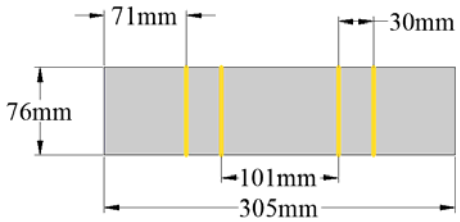

(b)

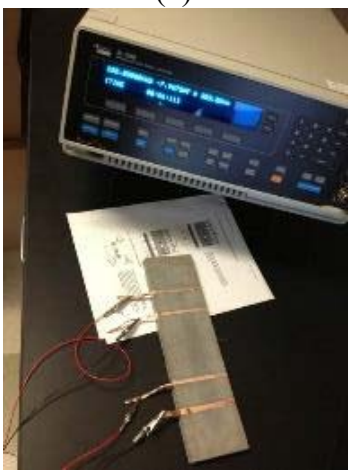

(c)

Figure 3.3. EIS test setup: (a) measurement circuit details; (b) specimen details; (c) four-point probe with

copper electrodes.

.

EIS measurement is sensitive to environmental conditions, such as humidity, temperature, and different outer common electrical signal. It was thus important to verify the accuracy of EIS setup in this project before using the technique to measure the electrical response of cementitious specimens. First, constant resistor measurement (273 Ohms) was used. Four-point probe method was adopted. Bode plot of impedance magnitude and phase degree (**Figure 3.4 (a)**) showed that below 1 MHZ, phase degree was constant as zero degree and impedance magnitude was constant as 270 Ohms. This means the EIS setup measured the real electrical property of a pure resistor. Second, shorten circuit measurement was used. The leads of EIS system were twisted together to provide shortened circuit. It is shown in **Figure 3.4 (b)** that while the phase degree was not constant, impedance magnitude was almost zero from 0.01 Hz to 100,000 Hz, and slightly increased to 0.5 ohms beyond 100,000 Hz. Both verification methods proved that with relatively lower alternate voltage and appropriate frequency selection, the EIS setup established in this project was able to provide accurate measurements to reflect real specimen electrical response. The EIS test framework is shown in **Figure 3.5**.

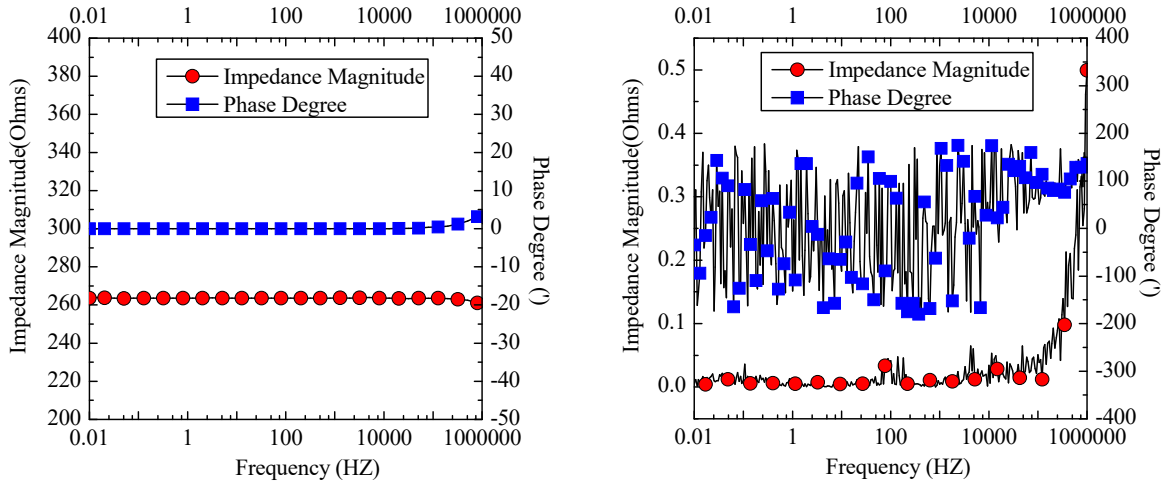

Figure 3.4. EIS verification: (a) constant resistor measurement (273ohms); (b) shorten circuit measurement.

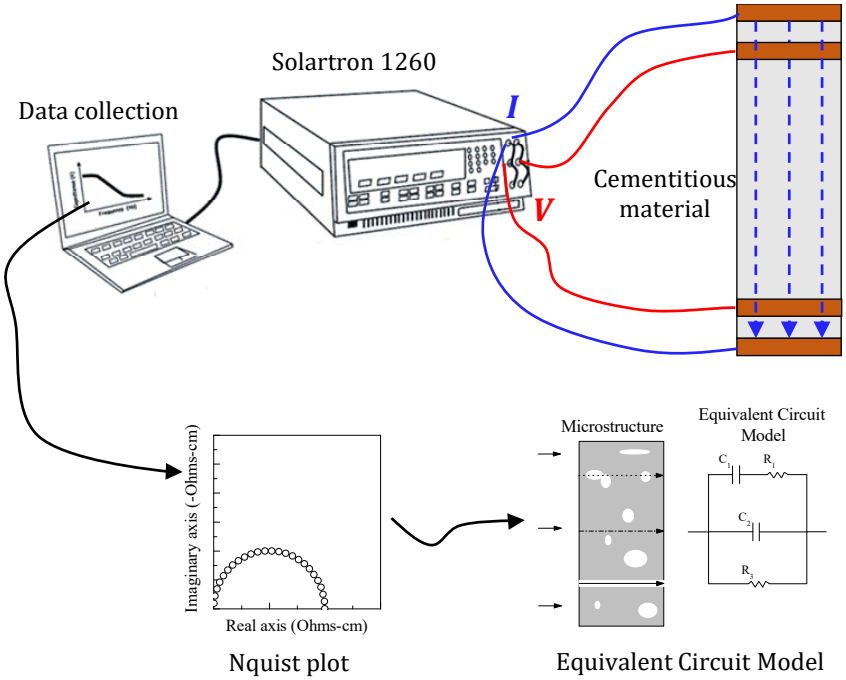

Figure 3.5. EIS measurements and equivalent circuit modeling on cementitious specimens.

3.2.2 Materials

EIS specimens were made of different mixture designs shown in **Table 3.1**. C stands for cement; F stands for fly ash; W stands for water; S stands for silica sand; P stands for PVA fiber; CB stands for carbon black nanoparticles. 1% and 4% mean the volume proportions of carbon black. 0.28 and 0.21 are water/binder ratios. Eight specimens were tested for each mixture design.

For each specimen, impedance was measured as a function of frequency in the range of 1Hz to 10MHz. The phase shift and amplitude, or real and imaginary parts, of the current at each frequency was measured. Data collection rate was 35 point per decade. EIS was performed on the specimens at 7, 14, 21, 28, 42, 63 and 180 days to consider age effect.

Table 3.1: Cementitious specimens with different ingredient proportions.

Specimen no.	Composition & Description	Specimen no.	Composition & Description
1	C+W (0.21)	7	C+W+CB1% (0.28)
2	C+W (0.28)	8	C+W+CB4% (0.28)
3	C+W+S (0.21)	9	C+W+S+F(0.28)
4	C+W+S (0.28)	10	C+W+F+S+PVA
5	C+W+F (0.28)		
6	C+W+F+S+ +CB1%		

3.2.3 EIS test results

The effects of specimen age on complex impedance of cementitious materials are shown in **Figures 3.6-3.15** for different mixture proportions. For each mixture design, the results were plotted as impedance magnitude vs. frequency. It was found that impedance increased with specimen age, and the increase became more significant after 28 days. This was the case for all mixture designs. This change of electrical response of cementitious materials was due to the hydration process that led to a decrease in pore water and an increase in the nonconductive path formed by increasing amount of hydration products.

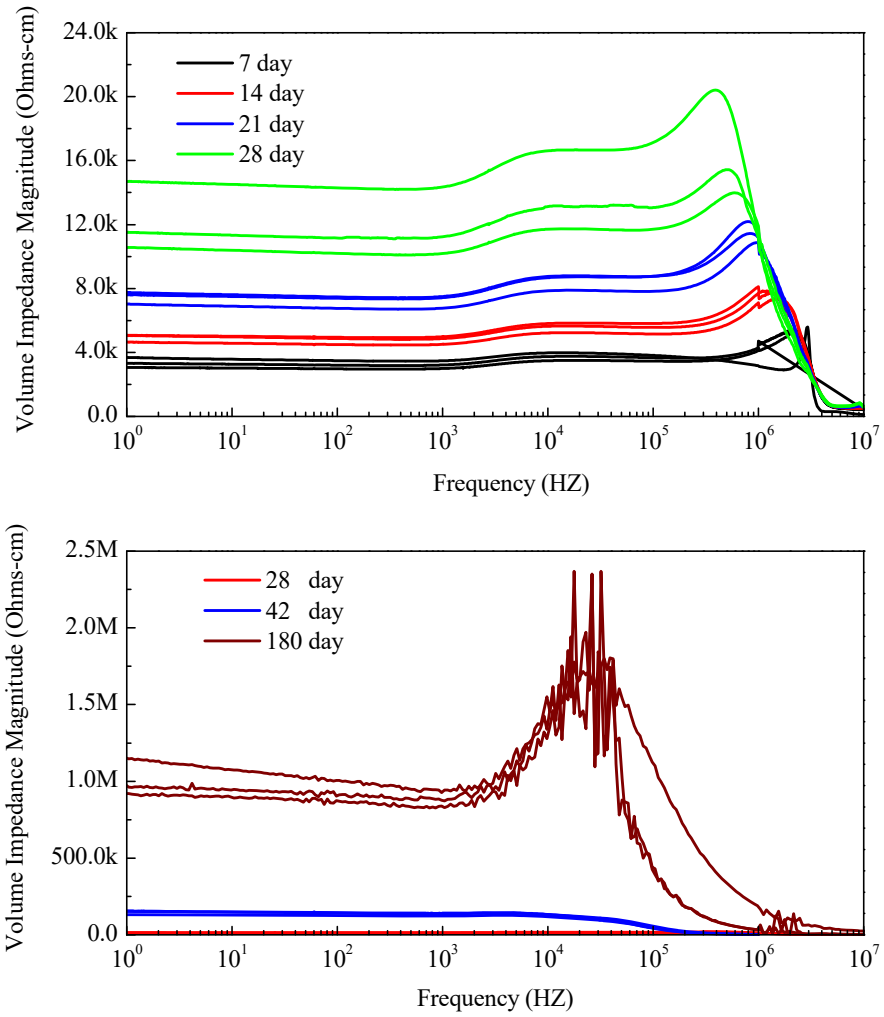

Figure 3.6. Bode plot for C+W (0.21).

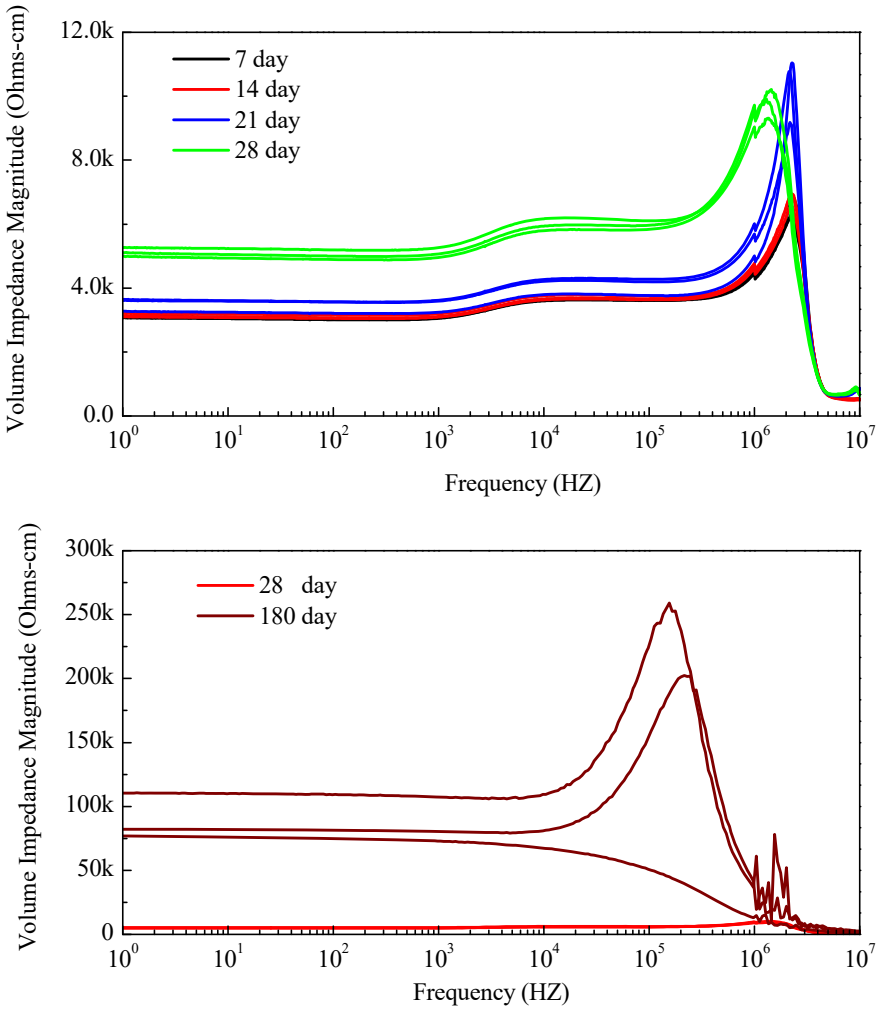

Figure 3.7. Bode plot for C+W (0.28).

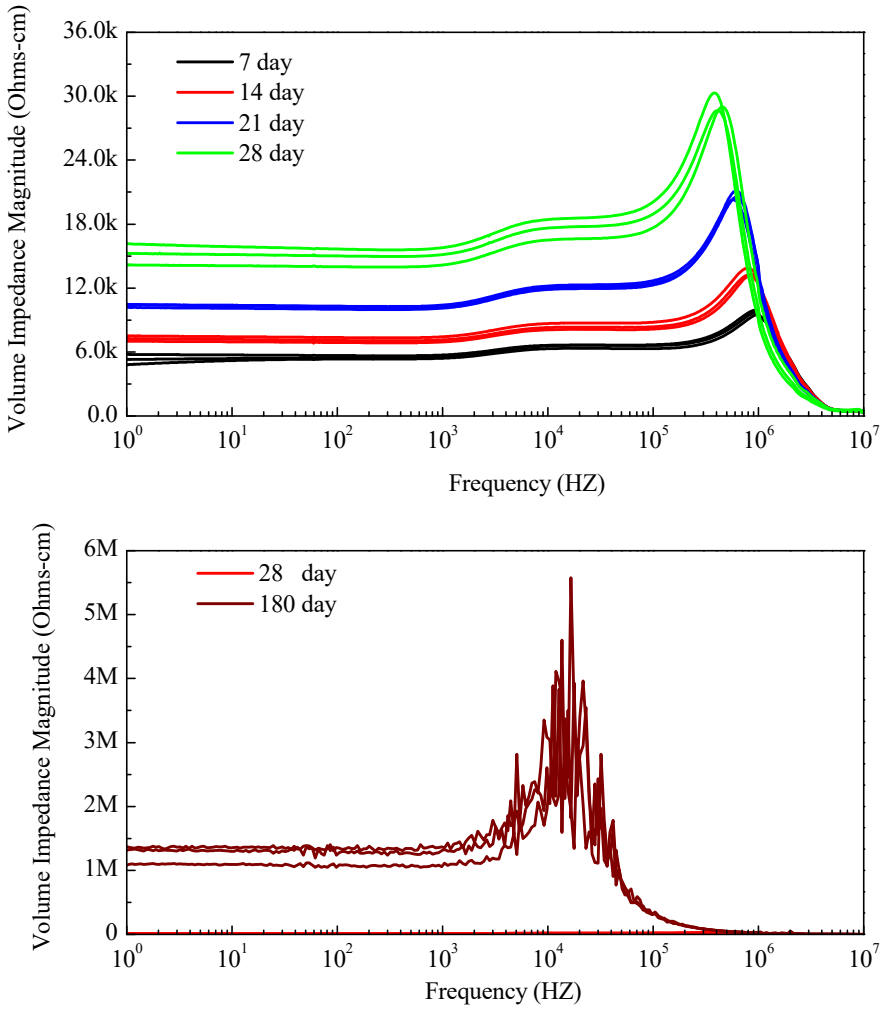

Figure 3.8. Bode plot for C+W+S (0.21).

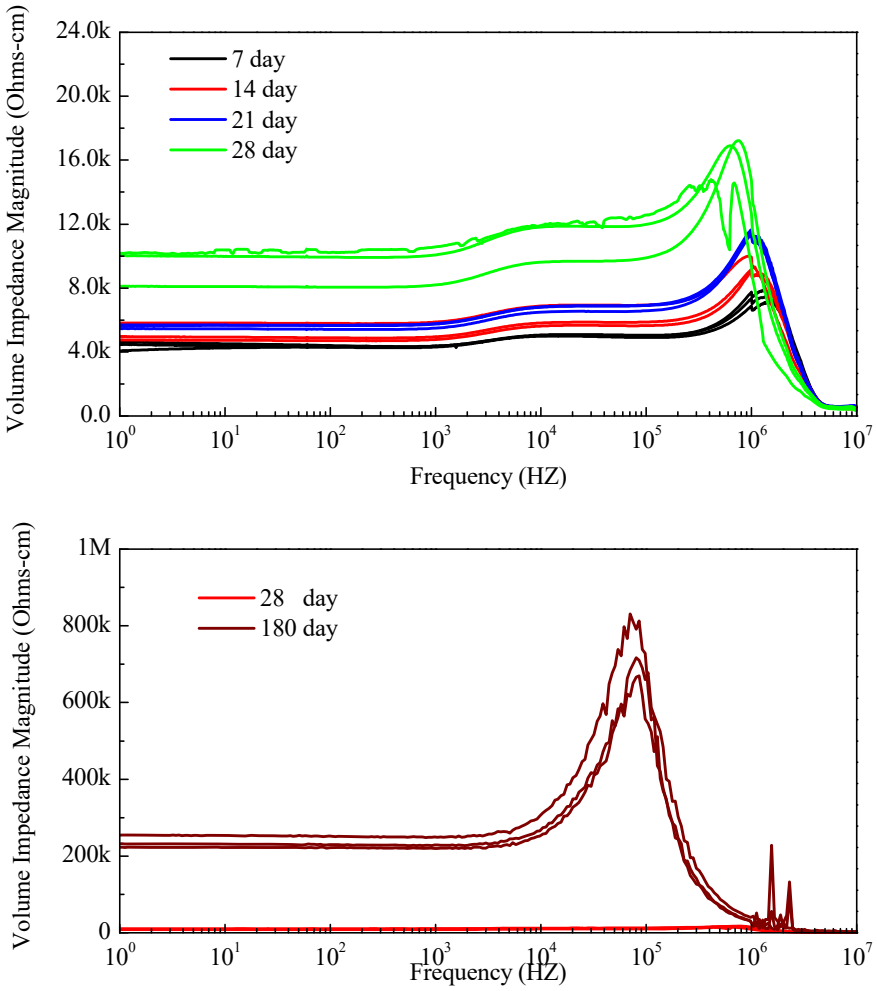

Figure 3.9. Bode plot for C+W+S (0.28).

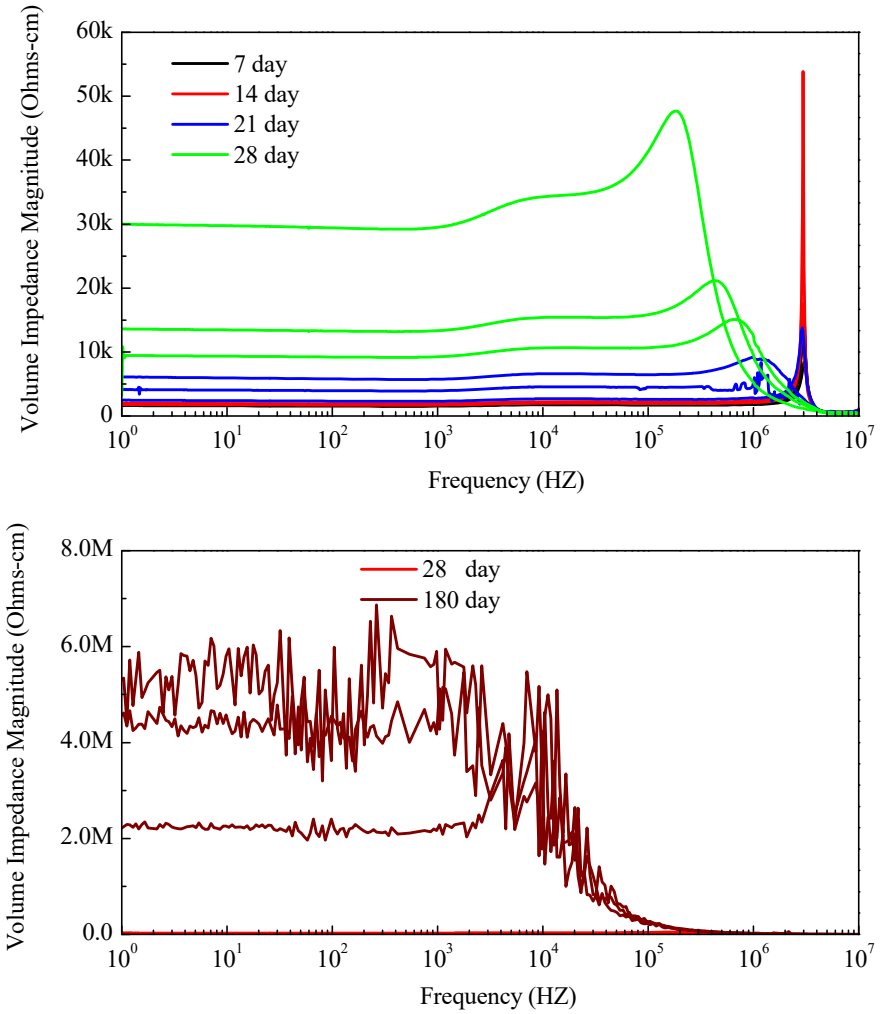

Figure 3.10. Bode plot for C+W+F (0.28).

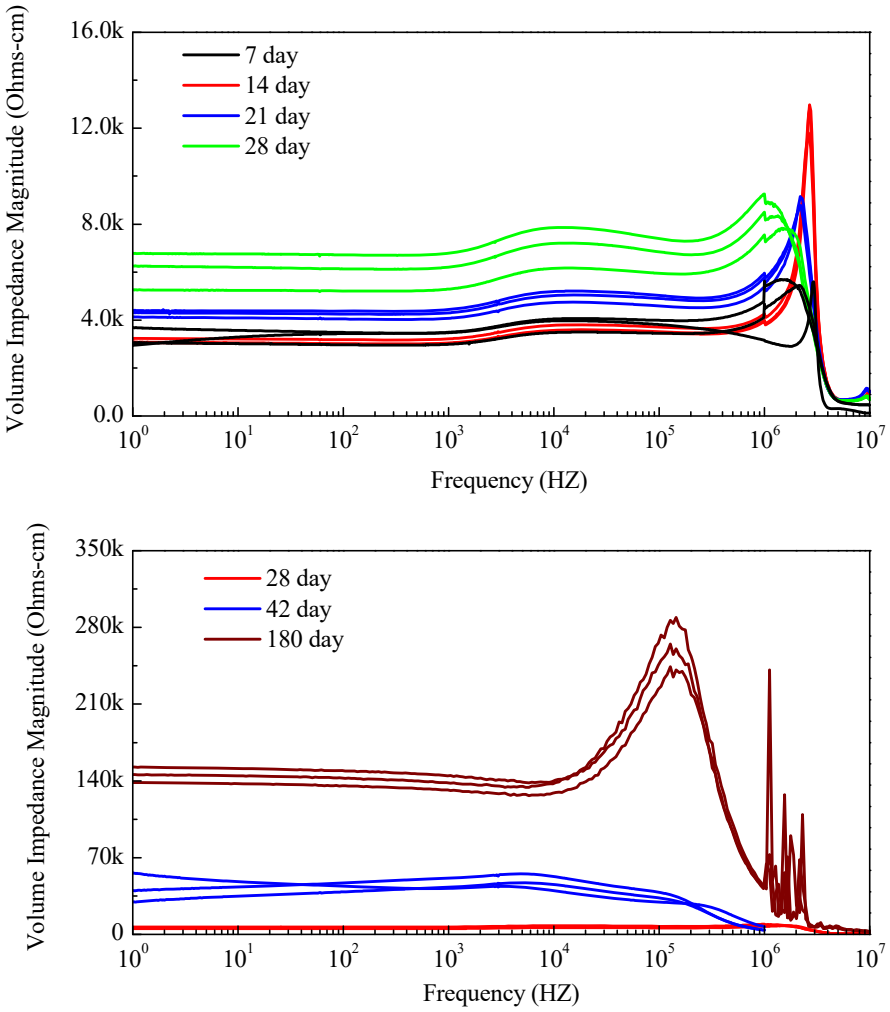

Figure 3.11. Bode plot for CB+C 1%.

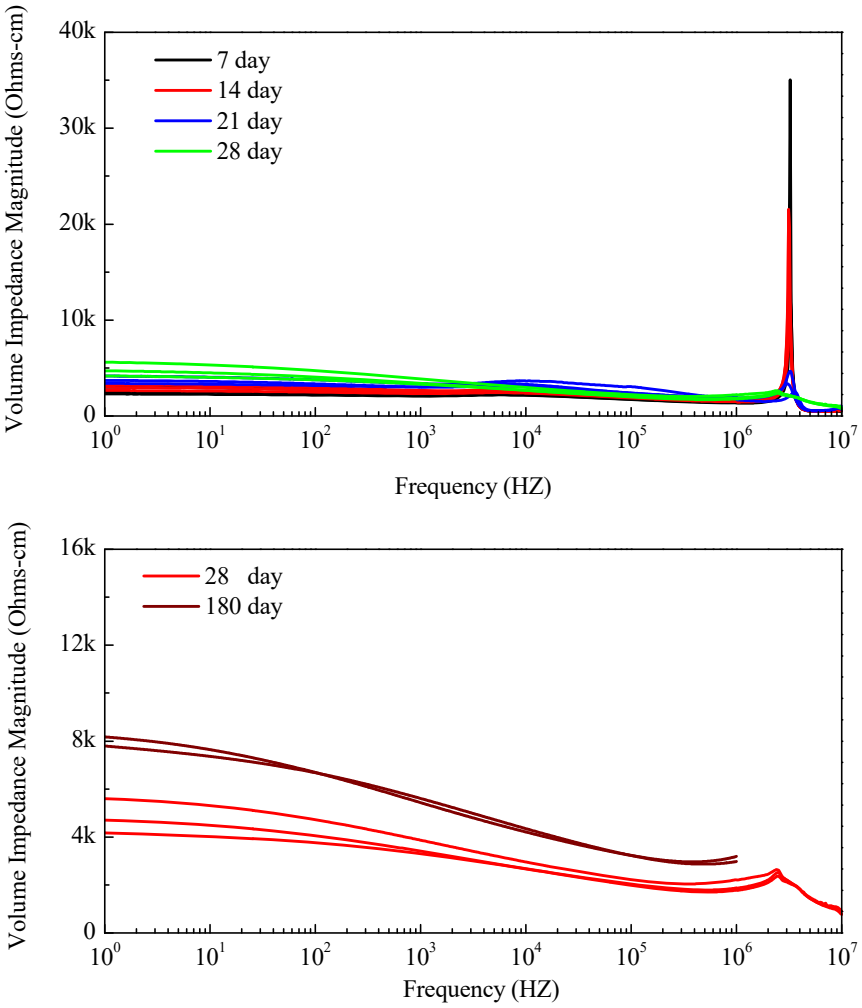

Figure 3.12. Bode plot for CB+C 4%.

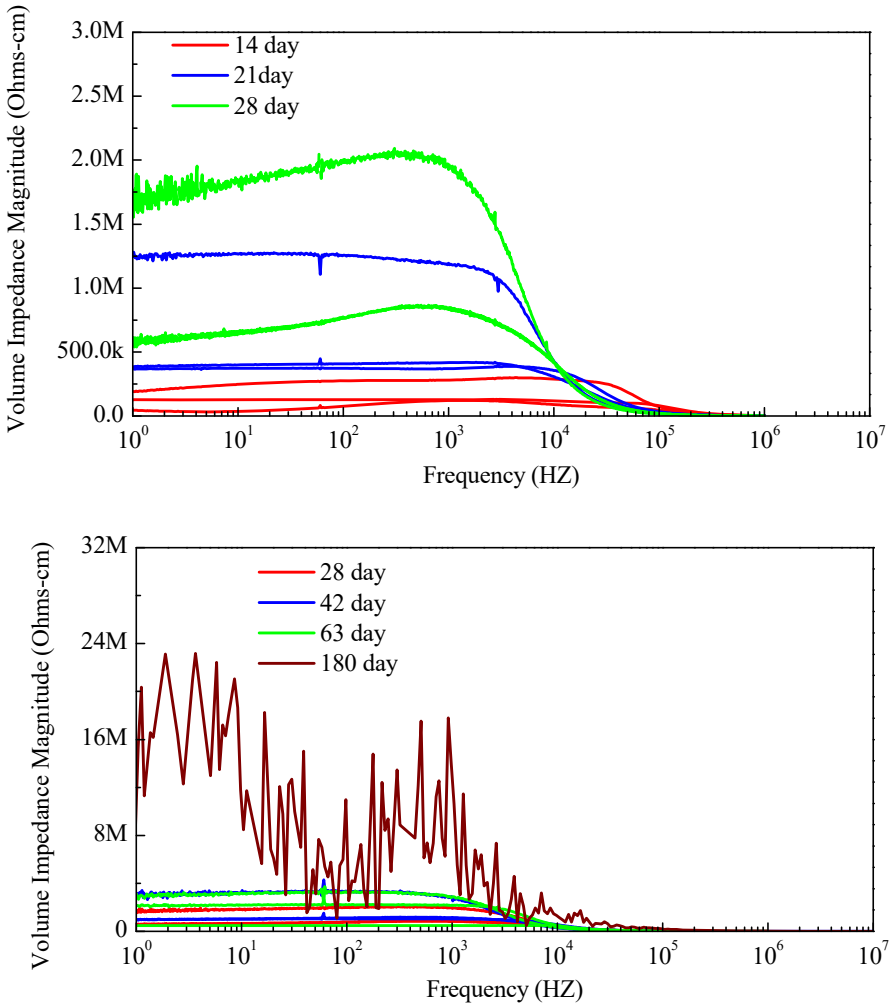

Figure 3.13. Bode plot for C+W+S+F.

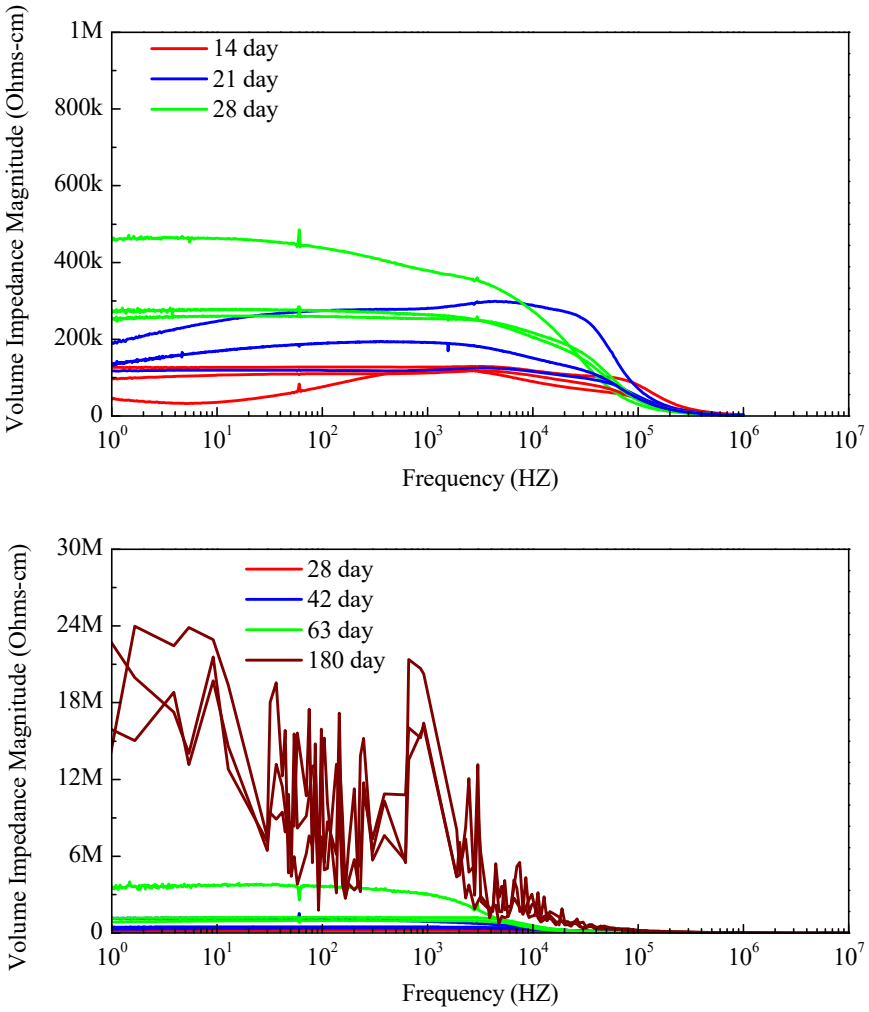

Figure 3.14. Bode plot for C+W+S+F+P.

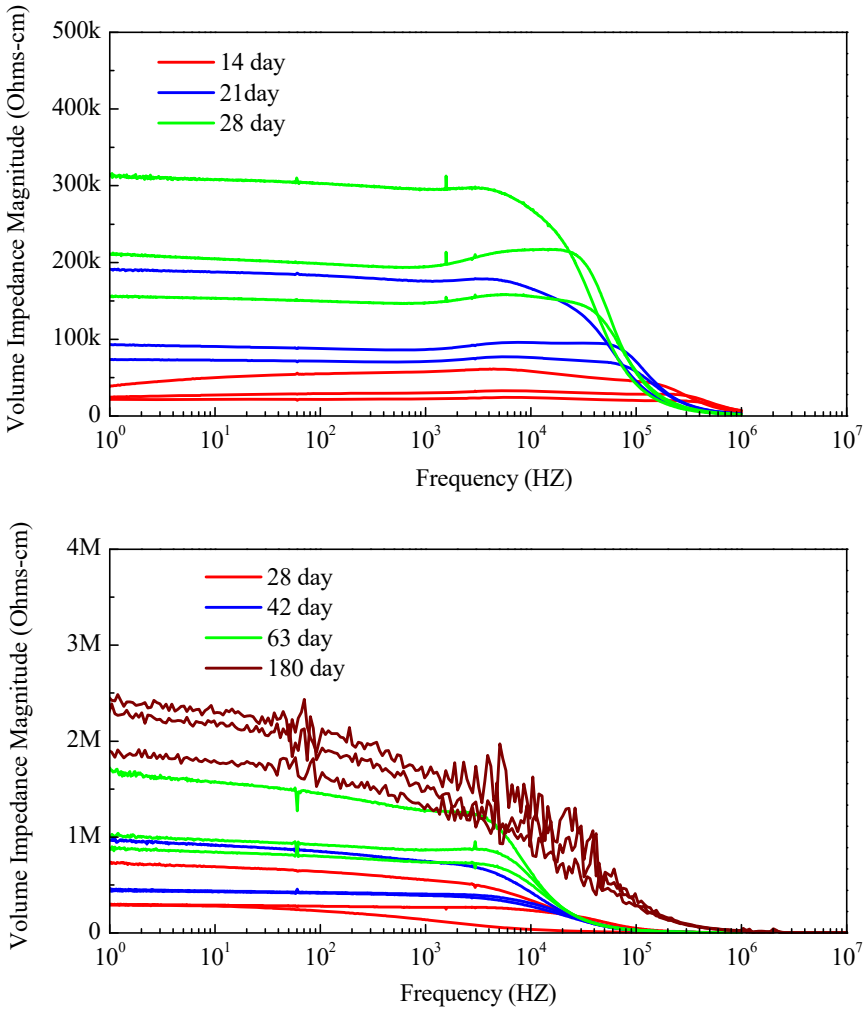

Figure 3.15. Bode plot for C+W+S+F+CB1%.

The effects of water/binder ratios on complex impedance of cementitious materials are shown in the bode plots in **Figures 3.16 and 3.17** for different specimen ages. Two water/binder ratios were investigated: 0.21 and 0.28. It was found that for earlier ages, the water/binder ratio had less effect than later ages. At the age of 7 days, complex impedance 0.21 and 0.28 water/binder ratios did not show any significant difference. At lower frequency, the impedance of C+W 0.21 specimens was slightly higher than that of C+W 0.28. After the age of 14 days, the impedance difference between C+W 0.21 and C+W 0.28 specimens became more and more significant. The specimens with lower water/binder ratio exhibited higher impedance magnitude. For specimen age of 180 days, the impedance magnitude of C+W 0.21 specimens were more than 10 times higher than C+W 0.28 specimens. The trend was similar for C+W 0.28 specimens with a higher water/binder ratio.

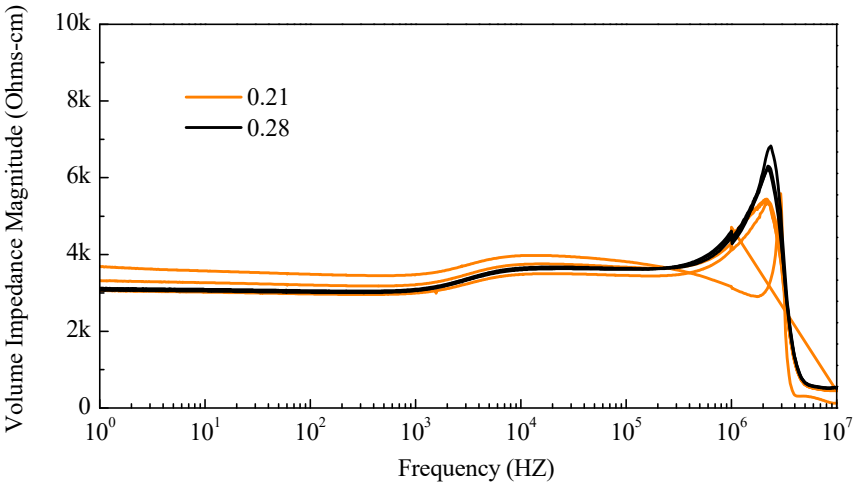
Volume Impedance Magnitude (Ohms-cm)
10k
8k
6k
4k
2k
0
0.21
0.28
10^0 10^1 10^2 10^3 10^4 10^5 10^6 10^7
Frequency (HZ)

(a)

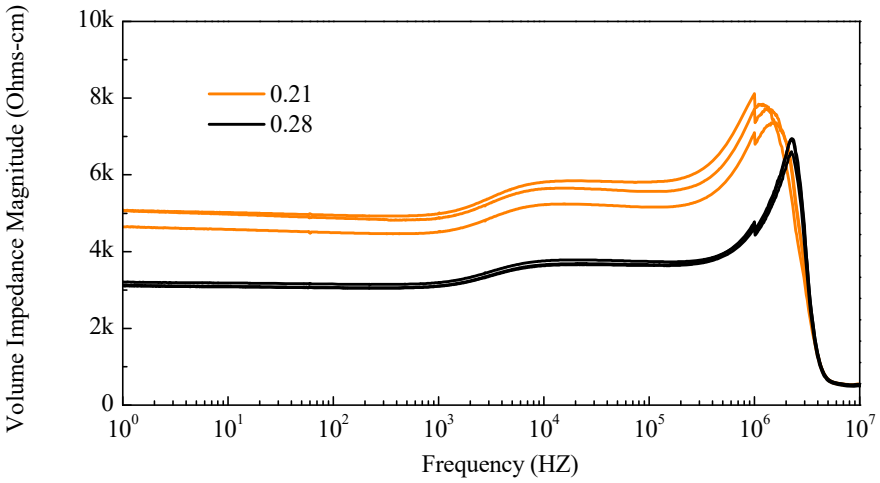
Volume Impedance Magnitude (Ohms-cm)
10k
8k
6k
4k
2k
0
0.21
0.28
10^0 10^1 10^2 10^3 10^4 10^5 10^6 10^7
Frequency (HZ)

(b)

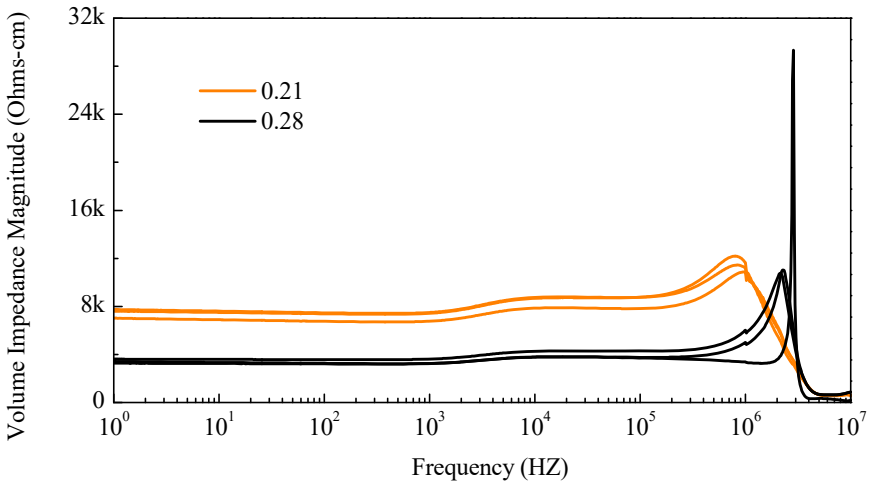
Volume Impedance Magnitude (Ohms-cm)
32k
24k
16k
8k
0
0.21
0.28
10^0 10^1 10^2 10^3 10^4 10^5 10^6 10^7
Frequency (HZ)

(c)

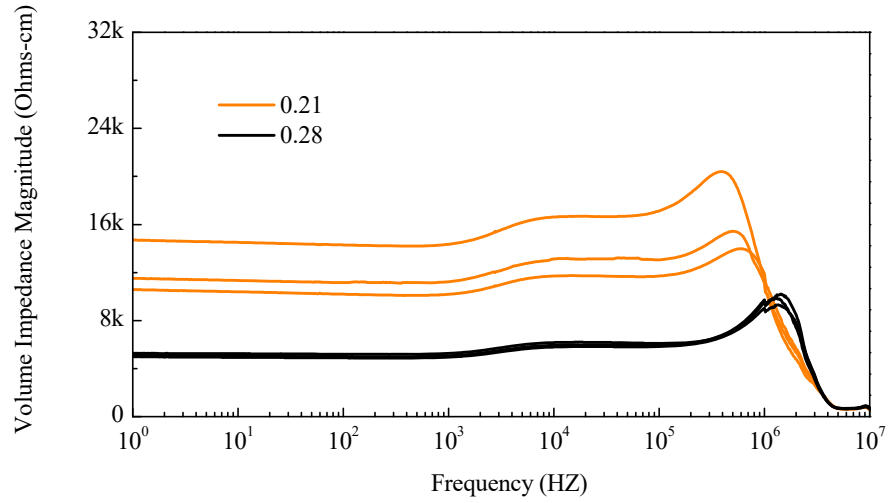

(d)

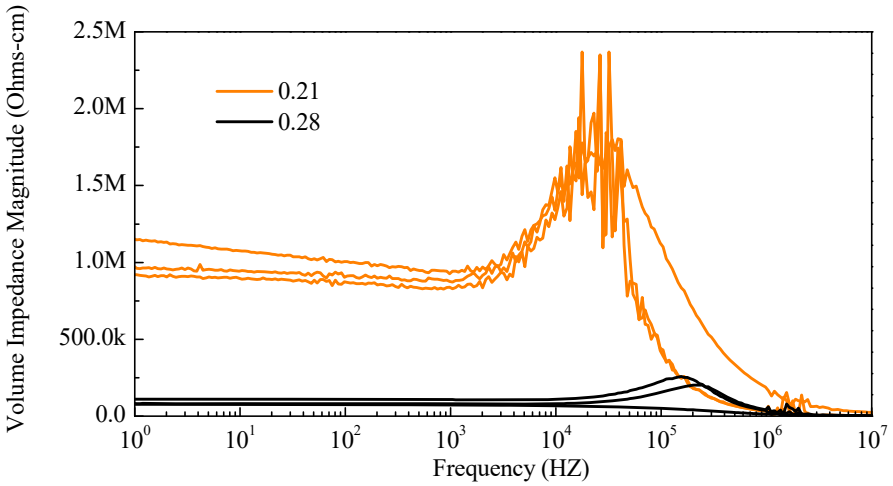

(e)

Figure 3.16. Bode plots of C+W specimens with water/binder ratios of 0.21 and 0.28, at ages of (a) 7 days, (b) 14 days, (c) 21 days, (d) 28 days, and (e) 180 days.

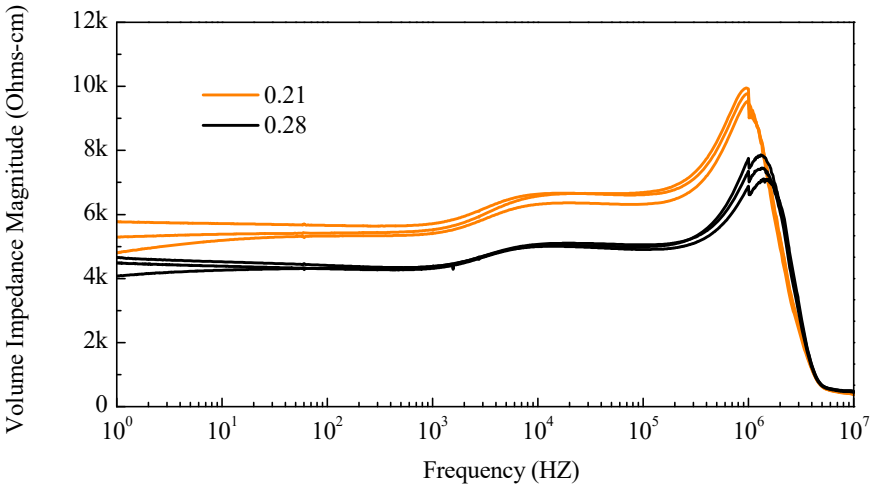
Volume Impedance Magnitude (Ohms-cm)
12k
10k
8k
6k
4k
2k
0
0.21
0.28
10^0 10^1 10^2 10^3 10^4 10^5 10^6 10^7
Frequency (HZ)

(a)

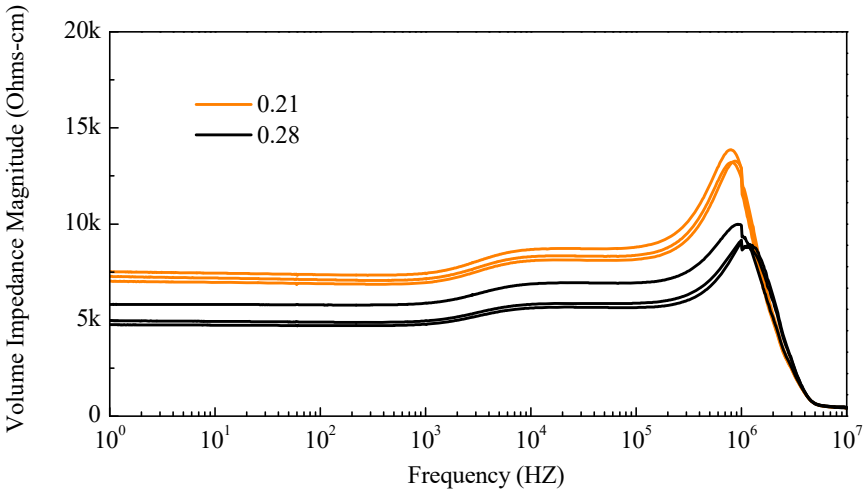
Volume Impedance Magnitude (Ohms-cm)
20k
15k
10k
5k
0
0.21
0.28
10^0 10^1 10^2 10^3 10^4 10^5 10^6 10^7
Frequency (HZ)

(b)

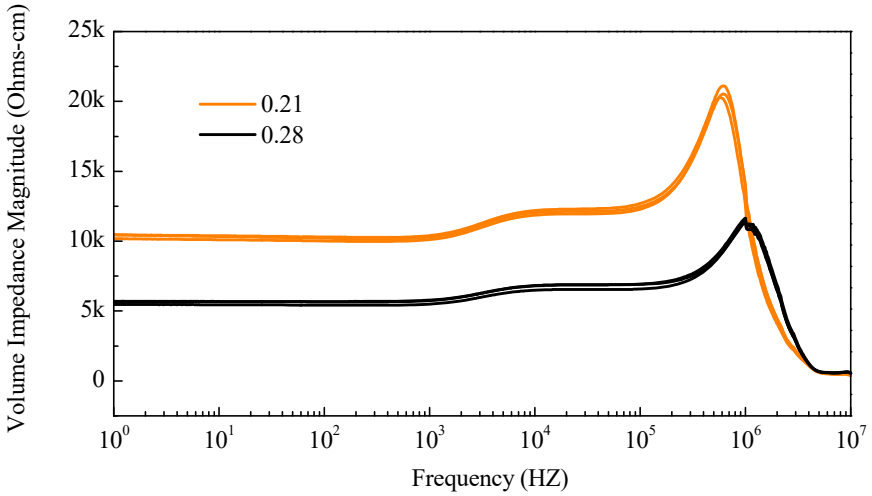
Volume Impedance Magnitude (Ohms-cm)
25k
20k
15k
10k
5k
0
0.21
0.28
10^0 10^1 10^2 10^3 10^4 10^5 10^6 10^7
Frequency (HZ)

(c)

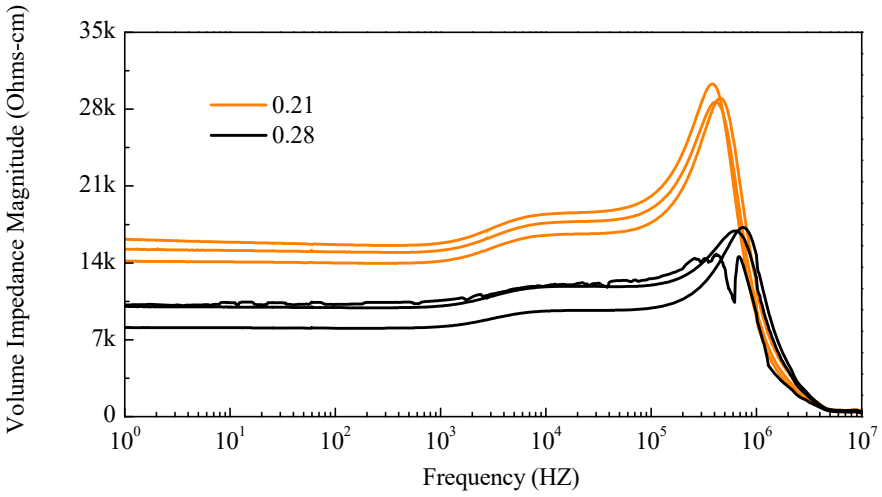

(d)

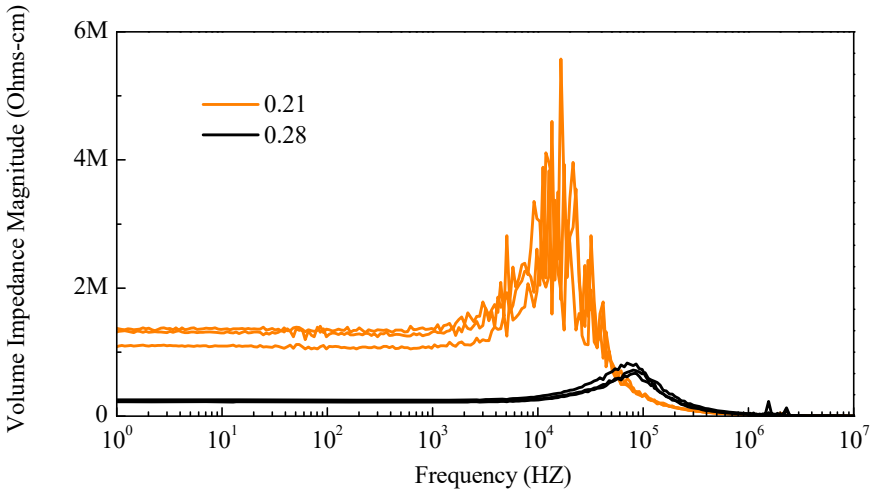

(e)

Figure 3.17. Bode plots of C+W+S specimens with water/binder ratios of 0.21 and 0.28, at ages of (a) 7 days, (b) 14 days, (c) 21 days, (d) 28 days, and (e) 180 days.

The effects of fine aggregates, i.e. sands, on complex impedance of cementitious materials are shown in the bode plots in **Figures 3.18 and 3.19** for different specimen ages. Two scenarios were investigated: with and without sand. For all specimen ages, and for two different water/binder ratios, the presence of sands in the cementitious material led to an increase in impedance magnitude; such increase was more prominent for later ages. The results elucidated the role of silica sands as nonconductive paths for a wide range of frequencies in cementitious materials.

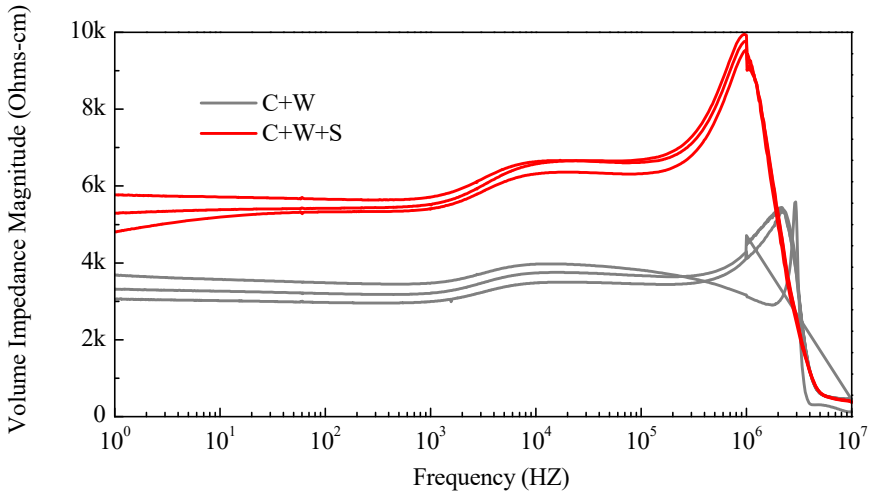
Volume Impedance Magnitude (Ohms-cm)
10k
8k
6k
4k
2k
0
C+W
C+W+S
10^0 10^1 10^2 10^3 10^4 10^5 10^6 10^7
Frequency (HZ)

(a)

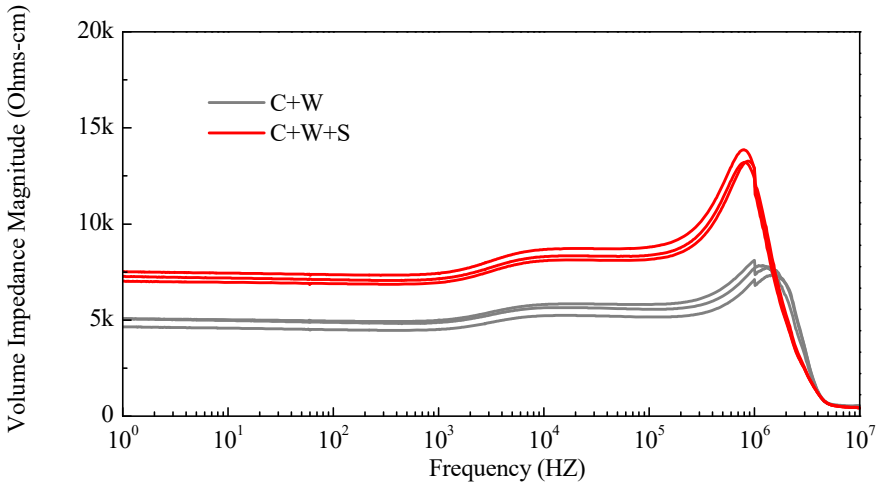
Volume Impedance Magnitude (Ohms-cm)
20k
15k
10k
5k
0
C+W
C+W+S
10^0 10^1 10^2 10^3 10^4 10^5 10^6 10^7
Frequency (HZ)

(b)

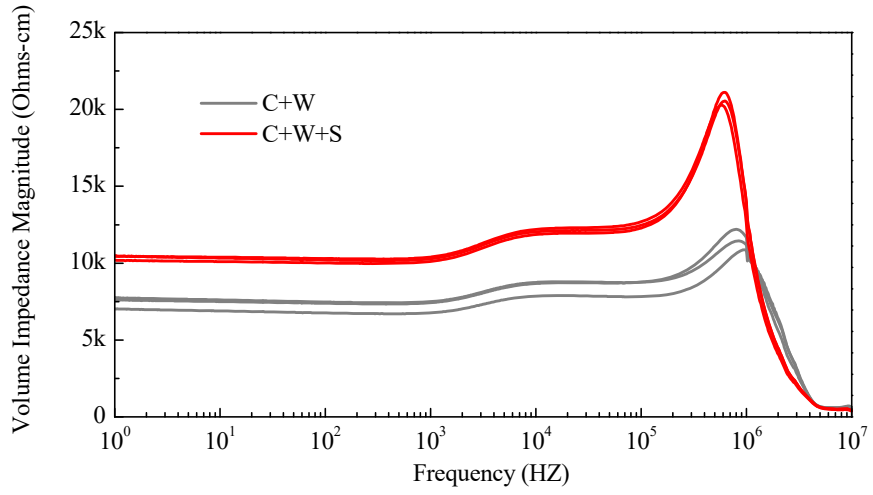
Volume Impedance Magnitude (Ohms-cm)
25k
20k
15k
10k
5k
0
C+W
C+W+S
10^0 10^1 10^2 10^3 10^4 10^5 10^6 10^7
Frequency (HZ)

(c)

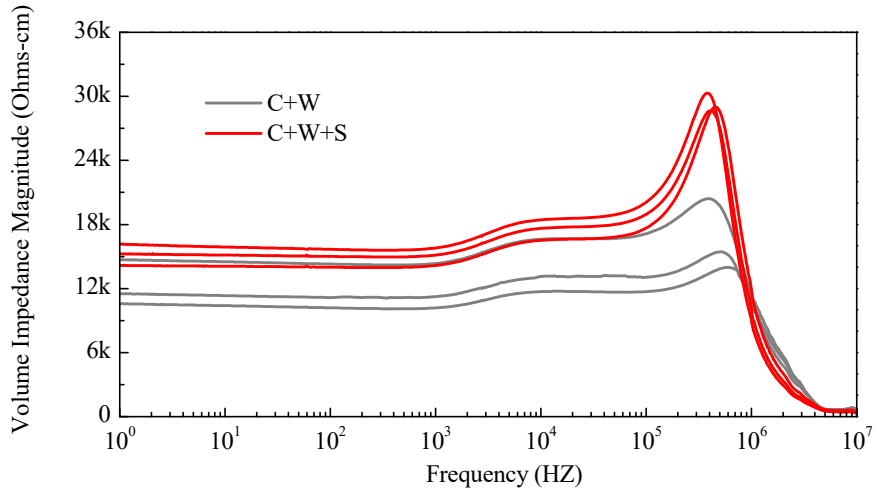

(d)

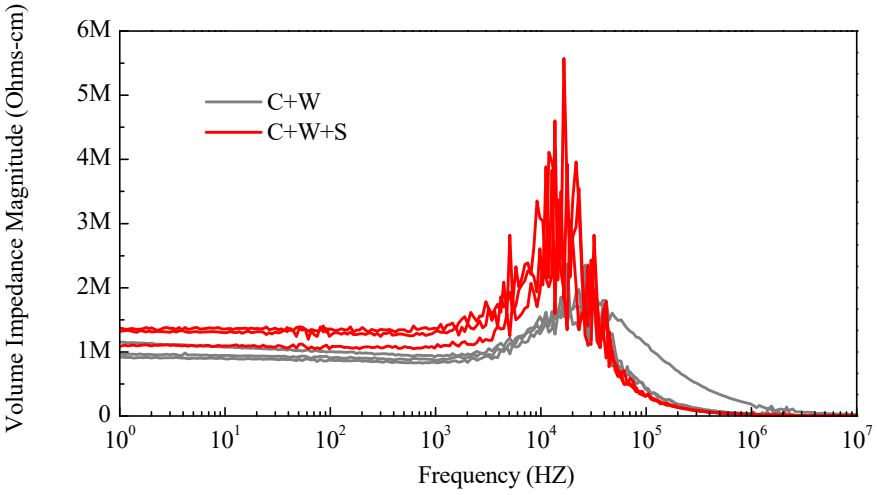

(e)

Figure 3.18. Bode plots of C+W+S 0.21 specimens and C+W 0.21 specimens, at ages of: (a) 7 days, (b) 14 days, (c) 21 days, (d) 28 days, and (e) 180 days.

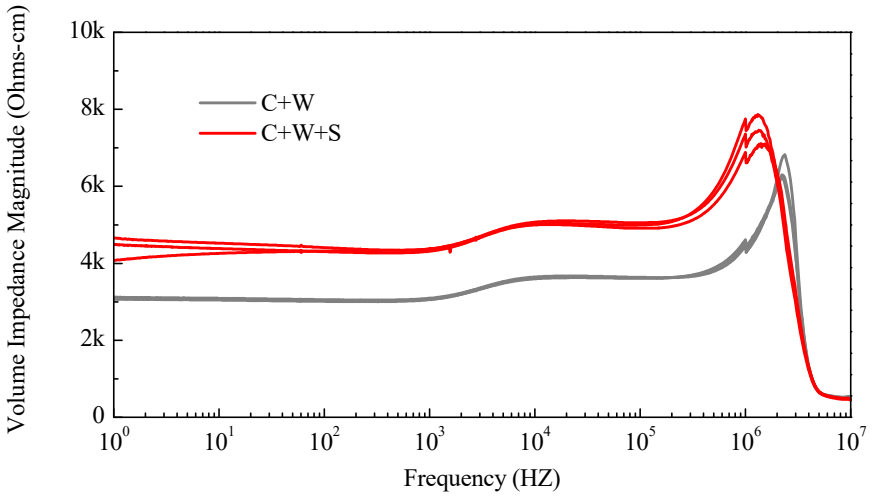
Volume Impedance Magnitude (Ohms-cm)
10k
8k
6k
4k
2k
0
C+W
C+W+S
10^0 10^1 10^2 10^3 10^4 10^5 10^6 10^7
Frequency (HZ)

(a)

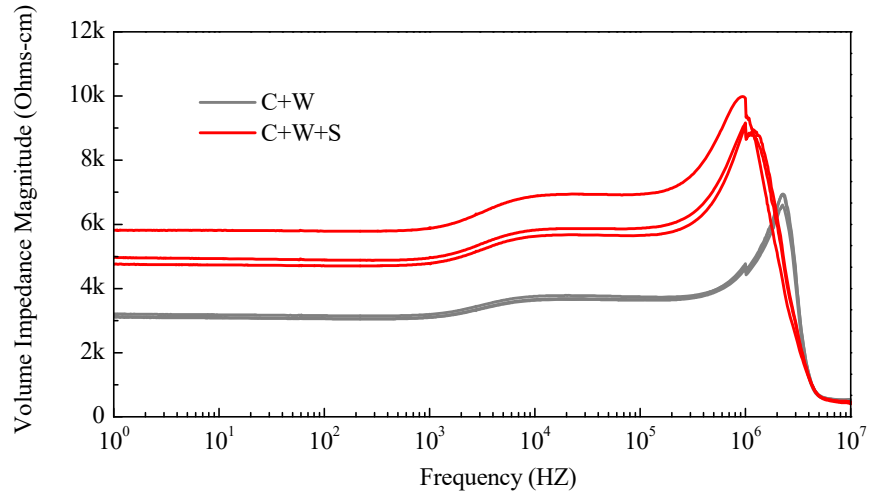
Volume Impedance Magnitude (Ohms-cm)
12k
10k
8k
6k
4k
2k
0
C+W
C+W+S
10^0 10^1 10^2 10^3 10^4 10^5 10^6 10^7
Frequency (HZ)

(b)

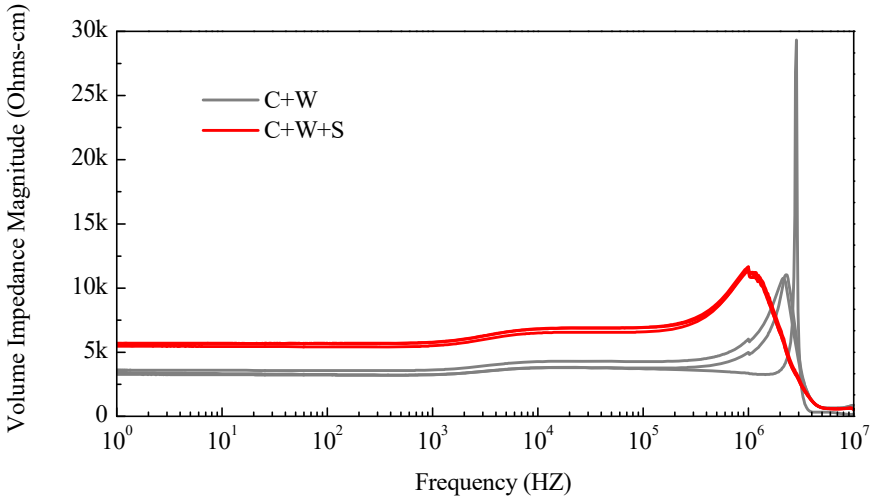
Volume Impedance Magnitude (Ohms-cm)
30k
25k
20k
15k
10k
5k
0
C+W
C+W+S
10^0 10^1 10^2 10^3 10^4 10^5 10^6 10^7
Frequency (HZ)

(c)

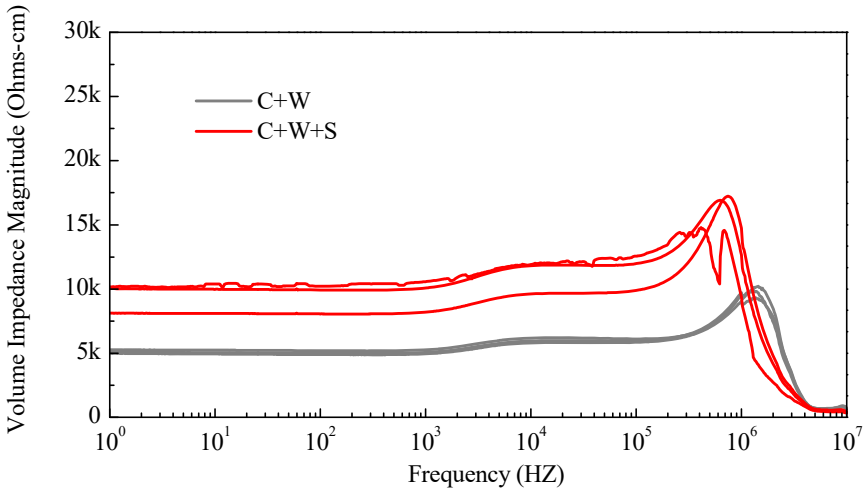

(d)

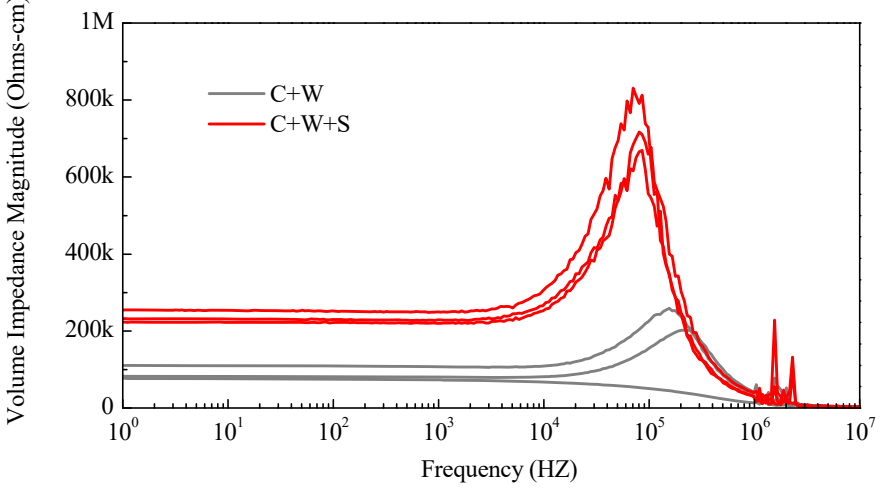

(e)

Figure 3.19. Bode plots of C+W+S 0.28 specimens and C+W 0.28 specimens, at ages of (a) 7 days, (b) 14 days, (c) 21 days, (d) 28 days, and (e) 180 day.

The effects of fly ash on complex impedance of cementitious materials are shown in the bode plots in **Figure 3.20** at different specimen ages. Two scenarios were investigated: with and without fly ash. It was found that the effect of fly ash on electrical response of cementitious materials was different from sand. At the ages of 7 days and 14 days, specimens with fly ash exhibited lower impedance magnitudes. The difference became negligible at the age of 21 days. At the age of 28 days and 180 days, specimens with fly ash exhibited higher impedance magnitudes with larger variation and noise. The impedance magnitude of C+W+F 0.28 specimens was more than 40 times larger than that of C+W 0.28 specimens.

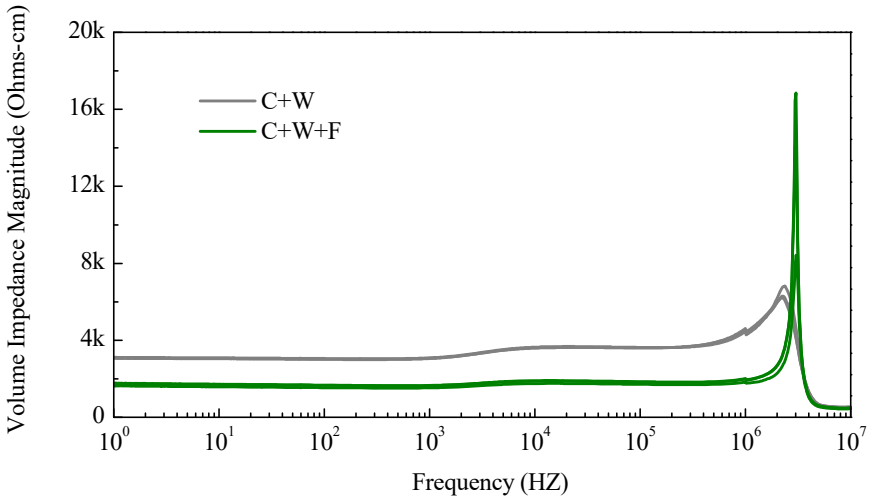
Volume Impedance Magnitude (Ohms-cm)
20k
16k
12k
8k
4k
0
C+W
C+W+F
10^0 10^1 10^2 10^3 10^4 10^5 10^6 10^7
Frequency (HZ)

(a)

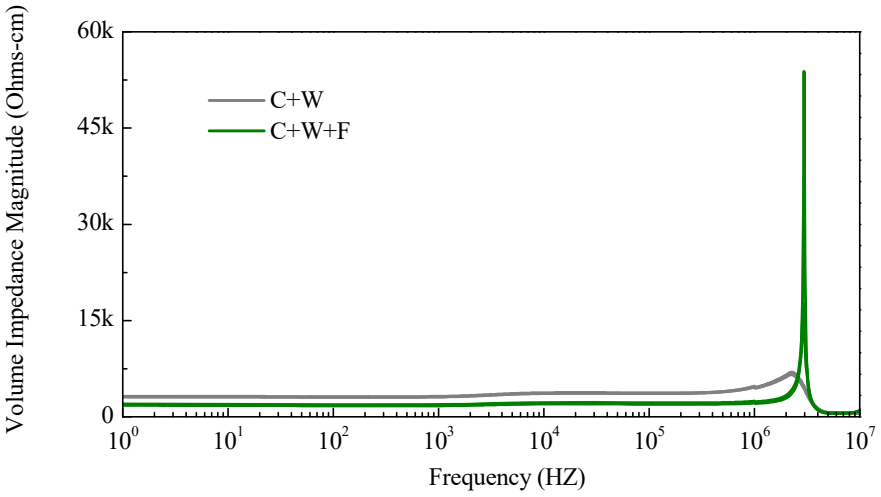
Volume Impedance Magnitude (Ohms-cm)
60k
45k
30k
15k
0
C+W
C+W+F
10^0 10^1 10^2 10^3 10^4 10^5 10^6 10^7
Frequency (HZ)

(b)

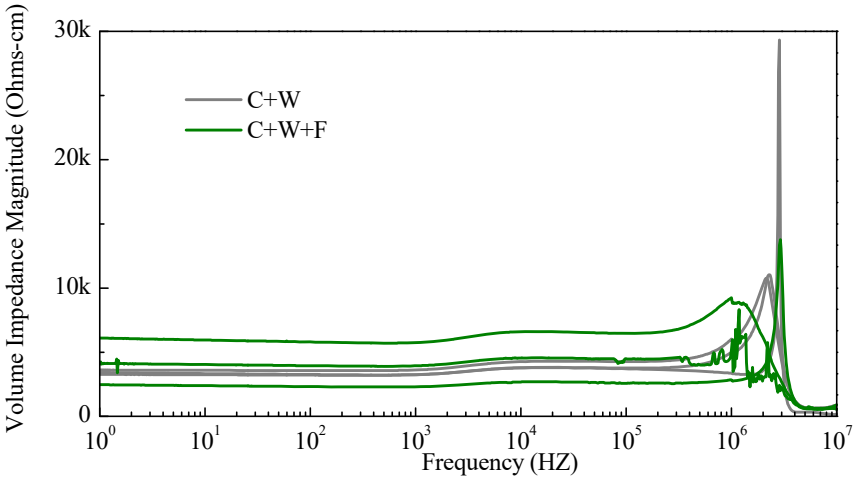
Volume Impedance Magnitude (Ohms-cm)
30k
20k
10k
0
C+W
C+W+F
10^0 10^1 10^2 10^3 10^4 10^5 10^6 10^7
Frequency (HZ)

(c)

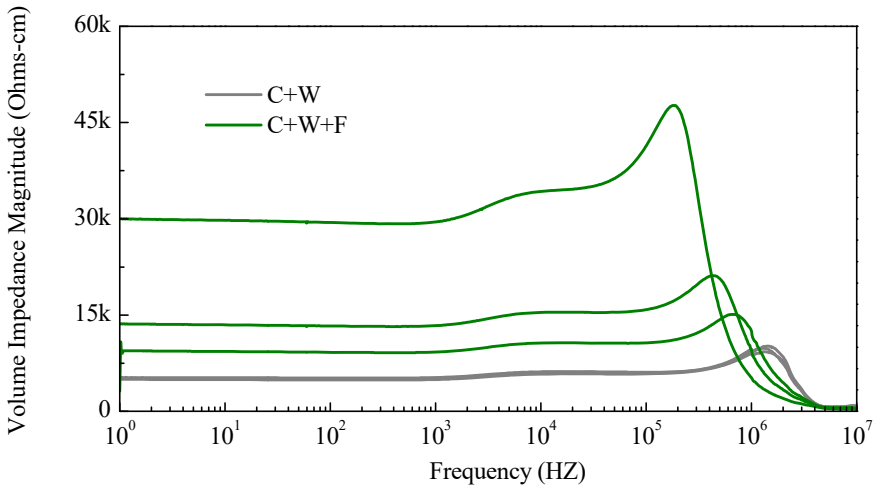

(d)

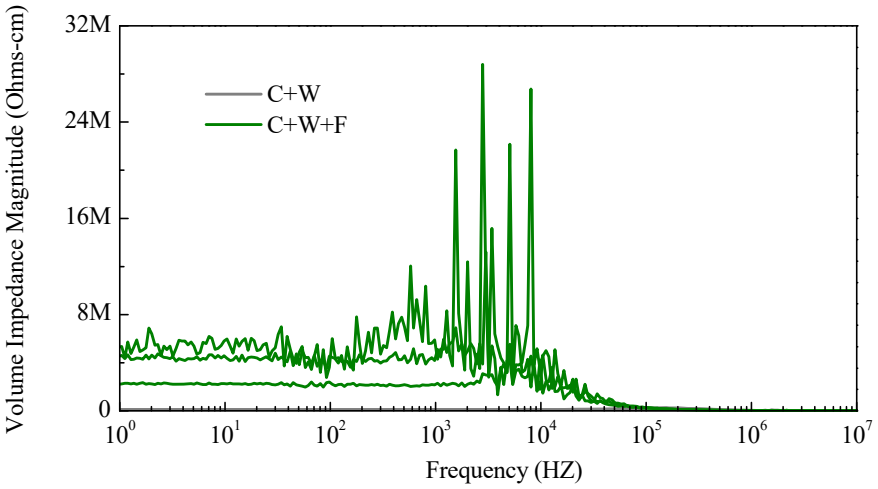

(e)

Figure 3.20. Bode plots of C+W 0.28 specimens and C+W+F 0.28 specimens, at ages of (a) 7 days, (b) 14 days, (c) 21 days, (d) 28 days, and (e) 180 days.

The effects of PVA fibers on complex impedance of cementitious materials are shown in the bode plots in **Figure 3.21** at different specimen ages. Two scenarios were investigated: with and without PVA fibers. The specimens with PVA fibers exhibited higher impedance magnitudes at early ages. At later ages, i.e. 63 days and 180 days, no obvious difference was observed. In fact, the variation in the impedance results made it difficult to conclude that specimens with PVA fibers had higher impedance magnitude at most of the frequencies than specimens without fibers.

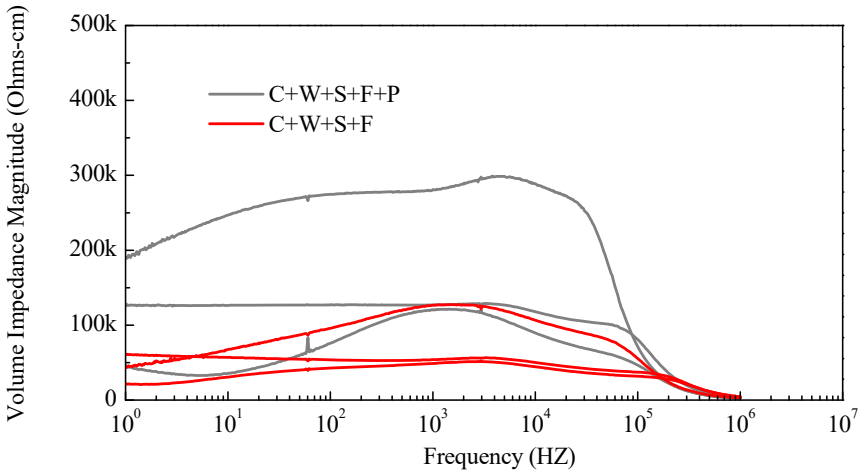
Volume Impedance Magnitude (Ohms-cm)
500k
400k
300k
200k
100k
0
C+W+S+F+P
C+W+S+F
10^0 10^1 10^2 10^3 10^4 10^5 10^6 10^7
Frequency (HZ)

(a)

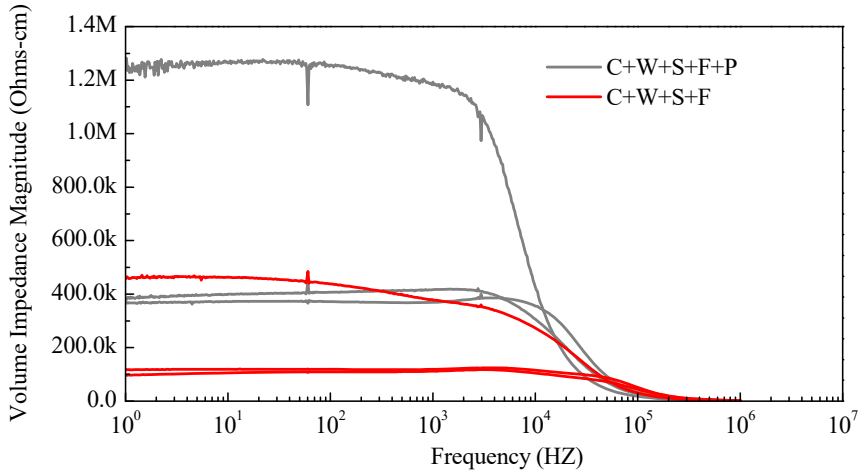
Volume Impedance Magnitude (Ohms-cm)
1.4M
1.2M
1.0M
800.0k
600.0k
400.0k
200.0k
0.0
C+W+S+F+P
C+W+S+F
10^0 10^1 10^2 10^3 10^4 10^5 10^6 10^7
Frequency (HZ)

(b)

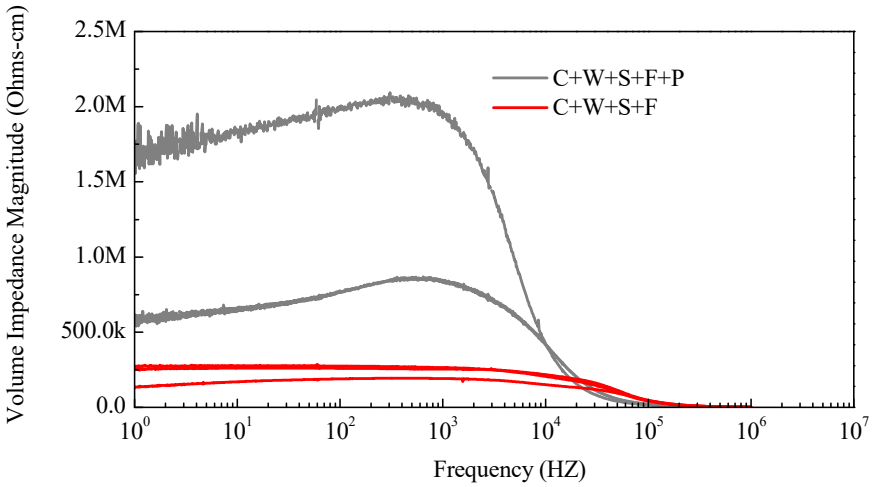
Volume Impedance Magnitude (Ohms-cm)
2.5M
2.0M
1.5M
1.0M
500.0k
0.0
C+W+S+F+P
C+W+S+F
10^0 10^1 10^2 10^3 10^4 10^5 10^6 10^7
Frequency (HZ)

(c)

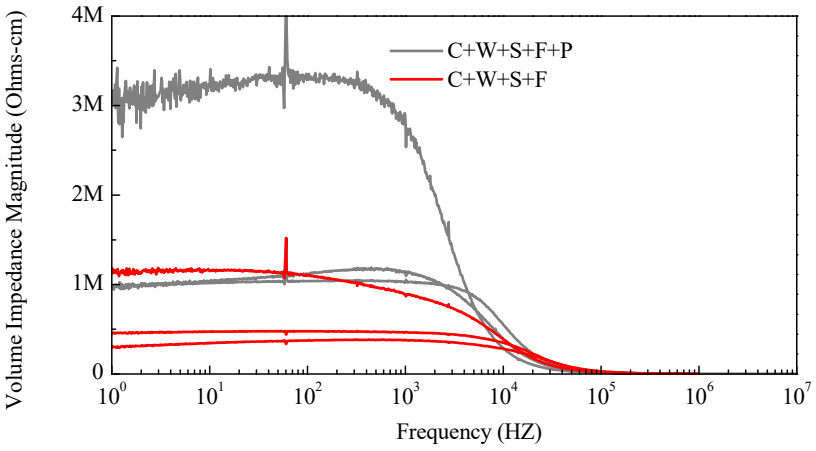

(d)

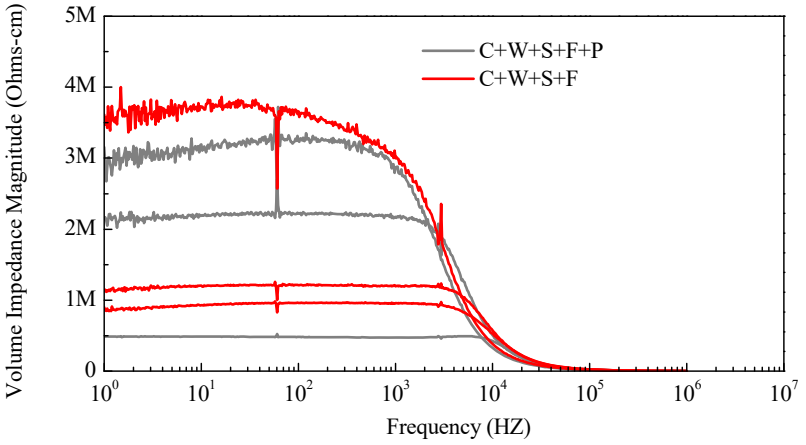

(e)

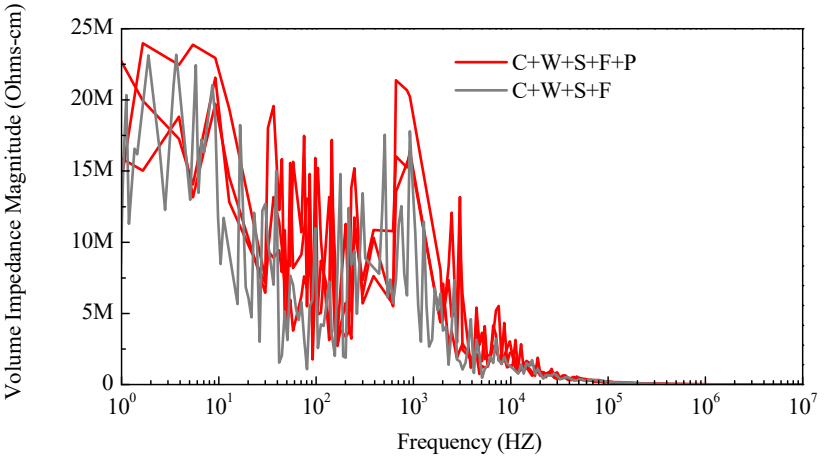

(f)

Figure 3.21. Bode plots of C+W+S+F 0.28 specimens and C+W+F+S+P 0.28 specimens, at ages of (a) 14 days, (b) 21 days, (c) 28 days, (d) 42 days, (e) 63 days and (f) 180 days.

The effects of conductive nanoparticles, e.g. carbon black nanoparticles, on the complex impedance of cementitious materials are shown in the bode plots in **Figure 3.22** at different specimen ages. Three scenarios were investigated: 0%, 1% and 4% addition of carbon black nanoparticles. It was found that the addition of carbon black nanoparticles reduced impedance magnitudes, especially at later ages. Most interesting, the specimens with 4% of carbon black nanoparticles showed negligible age effect on impedance magnitudes. At the age of 180 days, the impedance magnitude of specimens with 4% of carbon black nanoparticles was three orders lower than specimens without and with 1% carbon black nanoparticles.

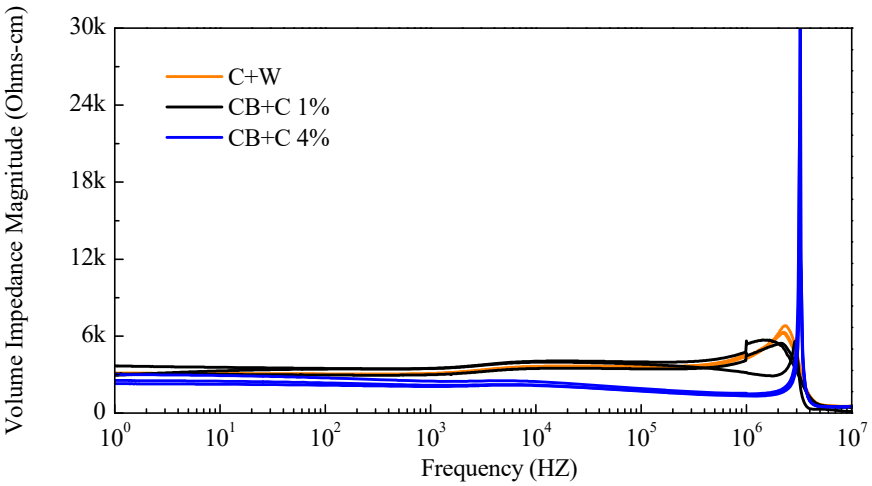

(a)

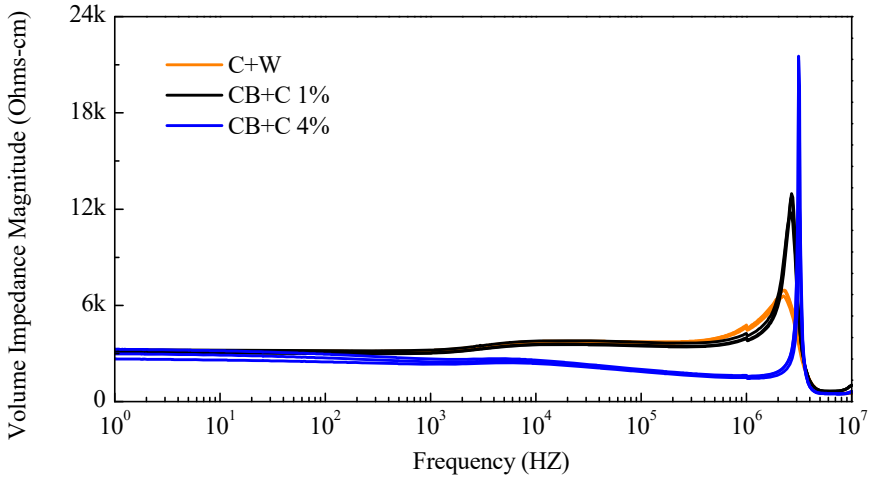

(b)

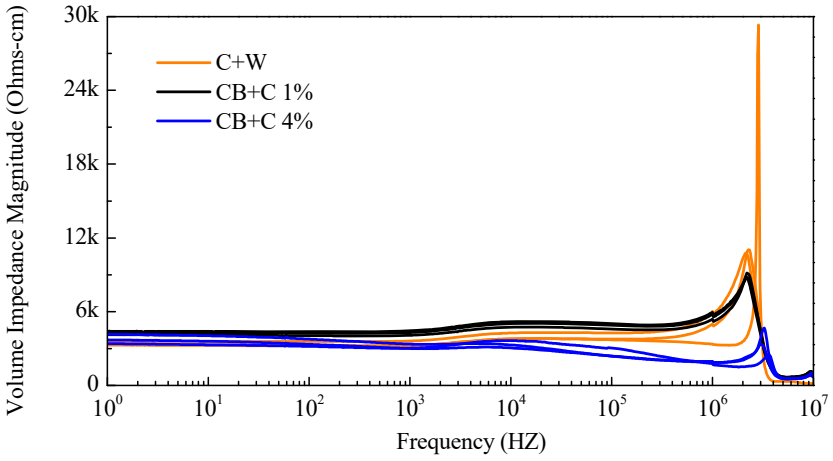

(c)

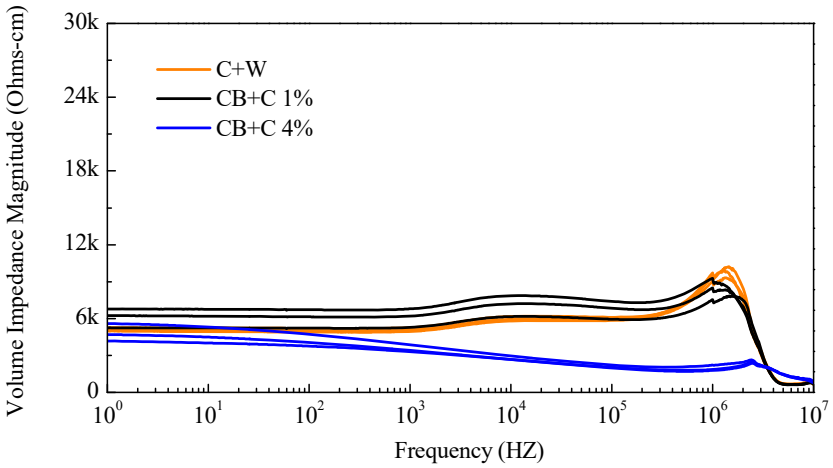

(d)

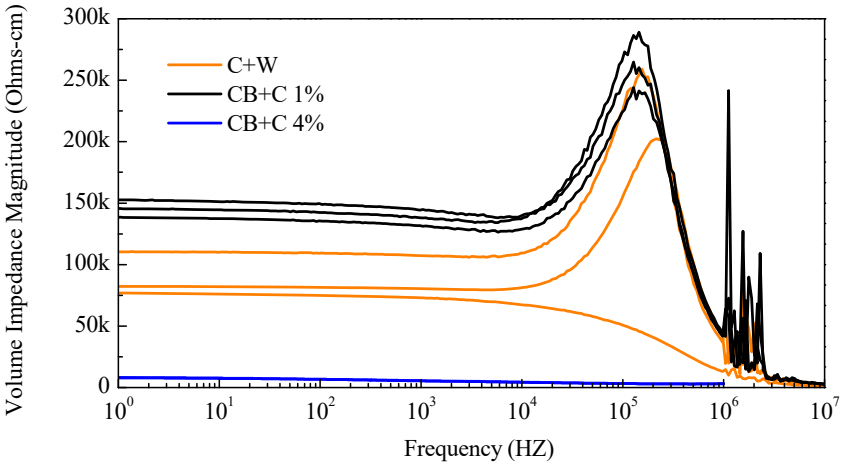

(e)

Figure 3.22. Bode plot comparison for C+W specimen, CB+C 1% specimen, and CB+C 4% specimen. (a) 7day, (b) 14 day, (c) 21 day, (d) 28 day, and (f) 180 day.

The impedance magnitude changes with specimen age for all mixture designs at fixed frequency of 1,500 Hz were plotted in **Figure 3.23.** The 180-day impedance magnitude of different mixture designs was further compared in **Figure 3.24**. Based on the electrical impedance spectroscopy studies, the following conclusions were drawn:

- Material composition, proportion, and age all contributed to the changes of complex impedance at a wide range of excitation frequencies. Material aging led to increased impedance magnitude, indicating the effect of hydration process on the change of the material microstructure, which subsequently resulted in less conductive paths within the cementitious material.
- Water/binder ratio played an important role on the electrical response of cementitious materials. A higher water/binder ratio led to lower impedance magnitude. This difference was small at specimen early age due to a lower hydration degree and thus higher amount of pore water containing ions that can be mobilized to generate current; however, the difference became significantly large at later ages of cementitious materials, as the hydration process consumed more water.
- Silica sand dispersed in cementitious matrix acted as nonconductive paths, leading to increases in impedance magnitude for a wide range of excitation frequencies, and for both early and later ages.
- Fly ash had an age-dependent effect on the impedance magnitude: specimens with fly ash exhibited lower impedance at earlier ages, but higher impedance at later ages compared with specimens without fly ash. This effect was due to the lower hydration rate at earlier ages and increased pozzolanic reaction at later ages.
- Introducing PVA fibers into cementitious materials led to an increase of impedance; such increase was more significant at earlier ages and became negligible at later ages. In addition, the bode plots of specimens with PVA fibers had higher noise, probably due to the increased porosity and nonhomogeneity of material microstructure.
- Adding conductive carbon black nanoparticles into cementitious materials was an effective way to reduce impedance magnitude while minimizing the effect of age on the electrical response of cementitious materials.

Based on the important findings from the comprehensive EIS studies, the initial MSC material composition and proportion design was formulated. Especially, carbon black nanoparticles were incorporated at different percentages into the cementitious material design to explore the resulting material electromechanical behavior.

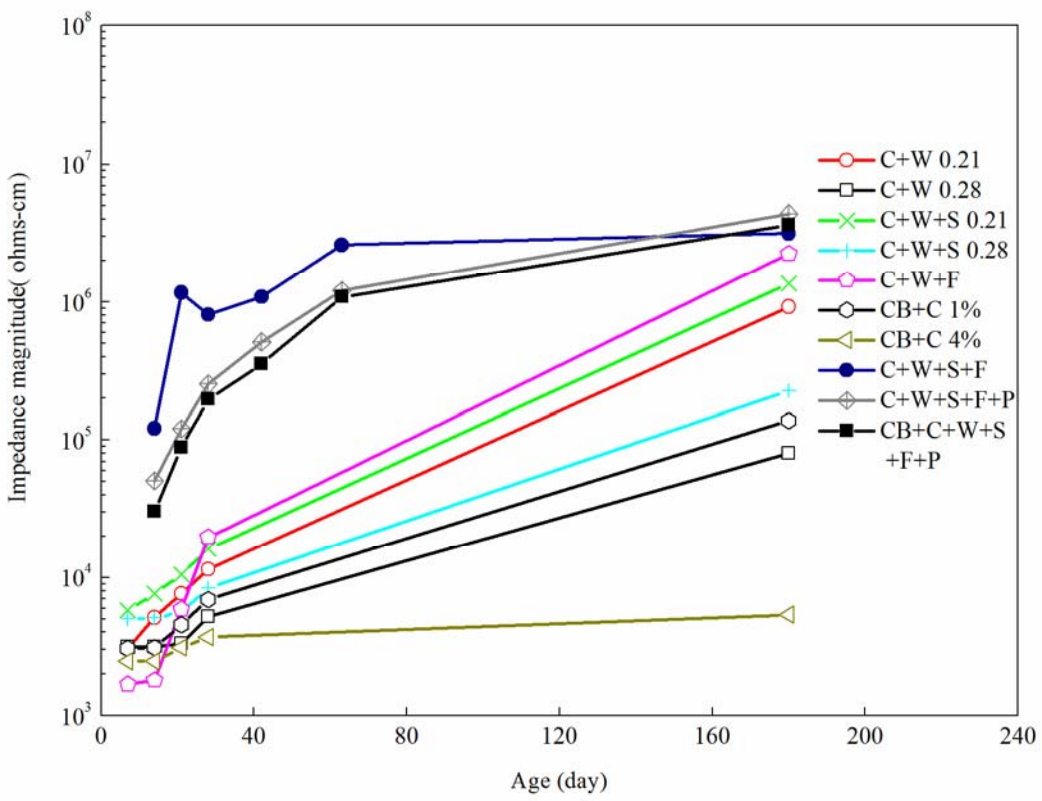

Figure 3.23. Impedance magnitude change with age of different cementitious material designs.

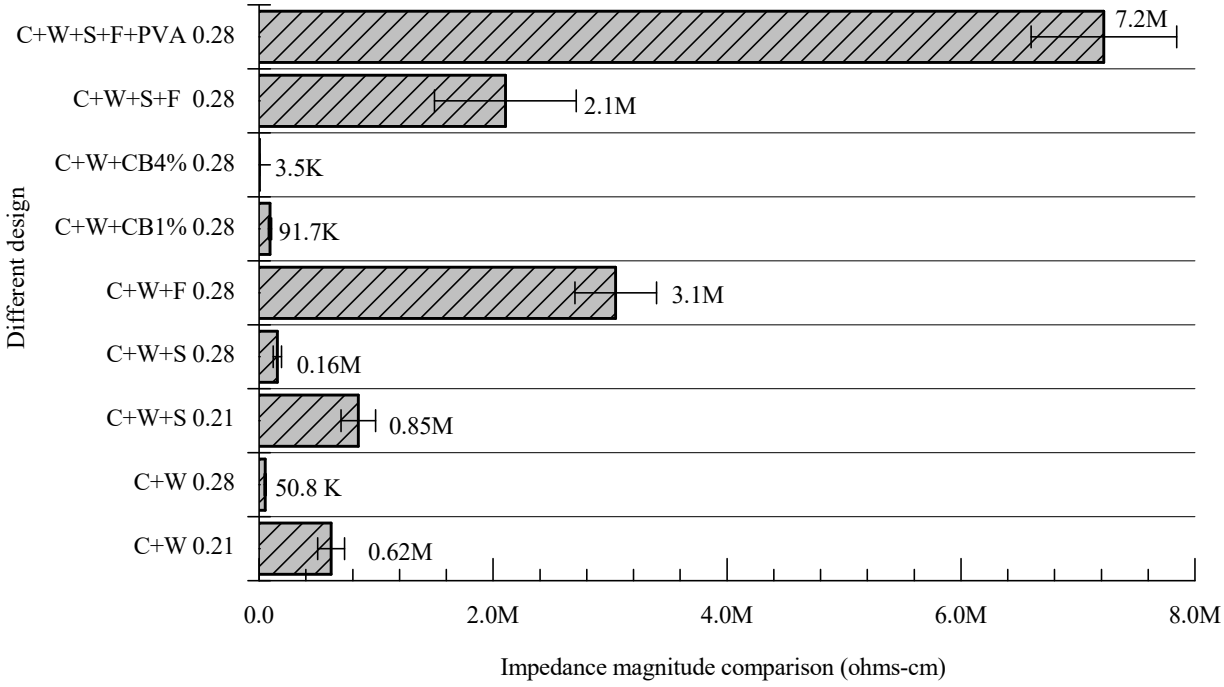

Figure 3.24. 180-day impedance magnitude of different cementitious material designs.

3.3 Nyquist plot and equivalent circuit model

New equivalent circuit model was developed in this project to represent the physical processes in the cementitious material that led to its electrical response. In this model, the material impedance is expressed as:

$$Z = \frac{1}{\frac{1}{R_1} + \frac{1}{R_2 + \frac{1}{j\omega C_1}} + j\omega C_2} \qquad (3.9)$$

Where Z stands for the impedance of cementitious material; R_1 is the resistor that describes continuous conductive paths; R_2 and C_1 are the resistor and constant phase element (imperfect capacitor) that describe discontinuous conductive paths; C_1 is the constant phase element (imperfect capacitor) that describes insulted paths; j is the imaginary unit; ω is the radial frequency.

The modeled results were plotted as Nyquist plot in **Figures 3.25-3.29**. Parameter studies were conducted, including cement/binder ratio (**Figure 3.25**), effect of sands (**Figure 3.26**), effect of fly ash and carbon black nanoparticles (**Figure 3.27**), effect of PVA fibers (**Figure 3.28**), and age (**Figure 3.29**). The modeling results generated clear understanding on how different physical and chemical parameters affected the complex electrical properties of cementitious materials. The modeling results were compared with nyquist plot of experimental results measured by EIS in **Figure 3.30**, showing good agreement. **Figure 3.31** shows the material composition effect on conductive path resistance R_1,, calculated based on the equivalent circuit model. **Figure 3.32** shows the age effect on conductive path resistance R_1.

To summarize, the comprehensive EIS experimental study, coupled with new equivalent circuit modeling in this project, generated significant insights on the physical and chemical mechanisms that affect the AC response and complex impedance of cementitious materials. Such knowledge was generated for the first time, and was critical for guiding us to tailor most critical parameters for achieving new generation of cementitious materials with robust self-sensing capacity. This study took into account of the heterogeneous nature of cementitious materials, as well as its complex microstructure and interfaces, which were generally neglected by DC measurements.

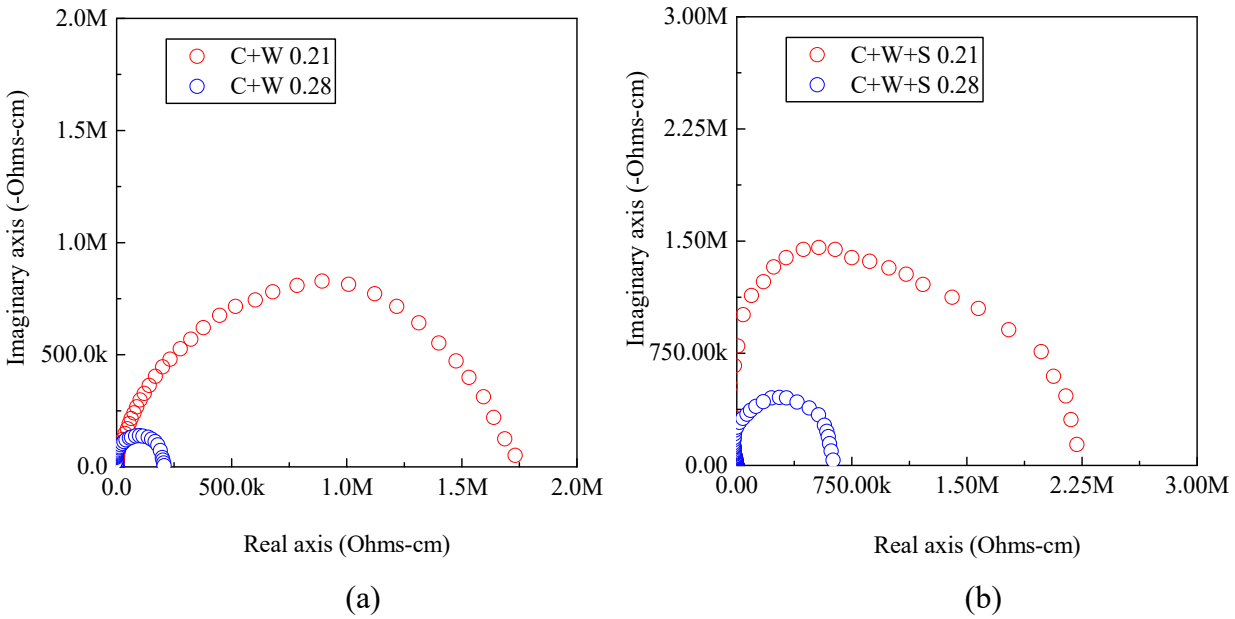

Figure 3.25. Equivalent circuit model Nyquist plot of (a) C+W 0.21 and C+W 0.28; (b) C+W+S 0.21 and C+W+S 0.28 at age of 180 days.

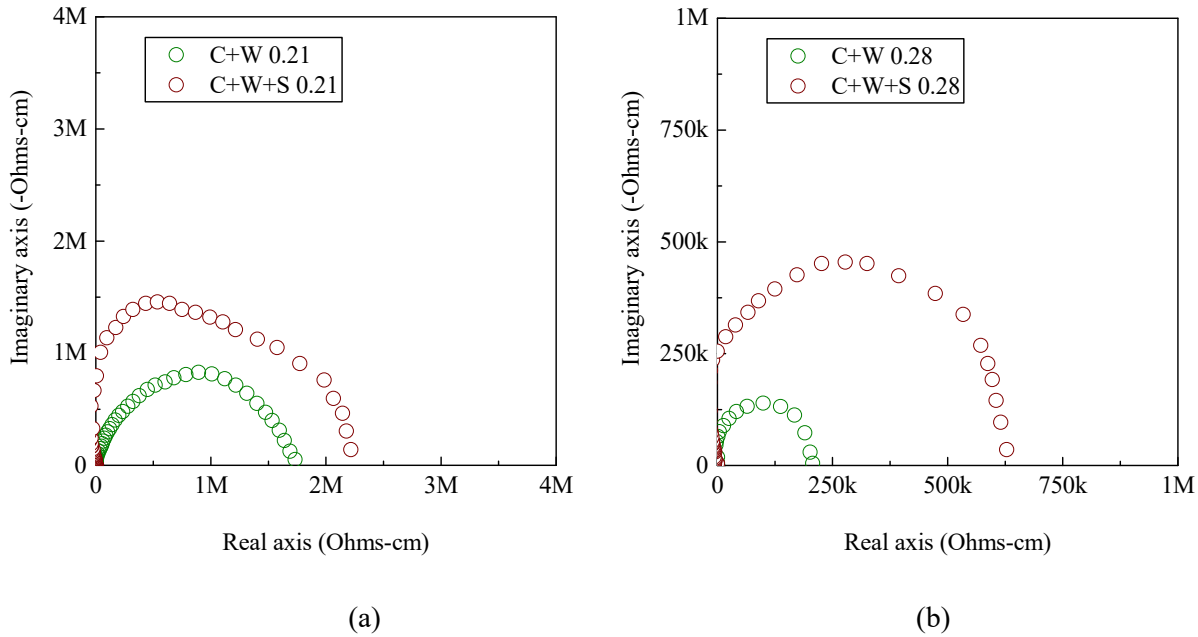

Figure 3.26. Equivalent circuit model Nyquist plot of (a) C+W 0.21 and C+W+S 0.21; (b) C+W 0.28 and C+W+S 0.28 at age of 180 days.

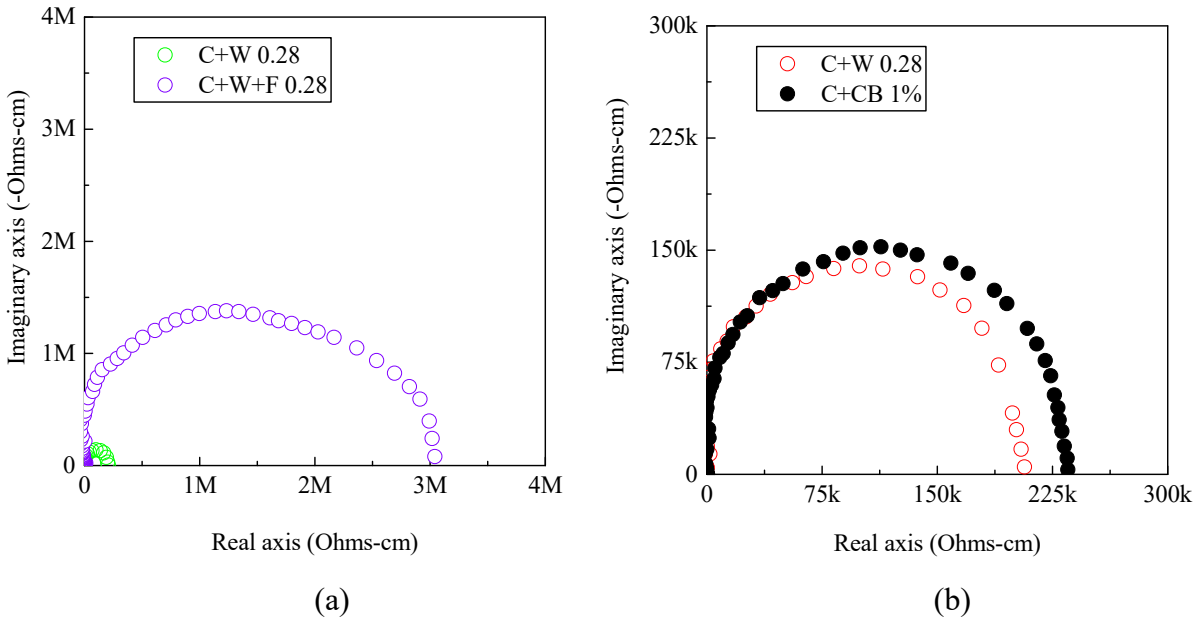

Figure 3.27. Equivalent circuit model Nyquist plot of (a) C+W 0.28 and C+W+F 0.28; (b) C+W 0.28 and C+CB 1% at age of 180 days.

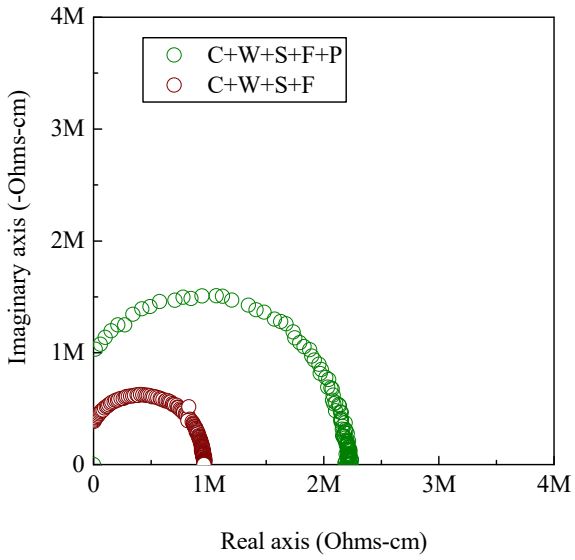

Figure 3.28. Equivalent circuit model Nyquist plot of C+W+S+F and C+W+S+F+P at age of 180 days.

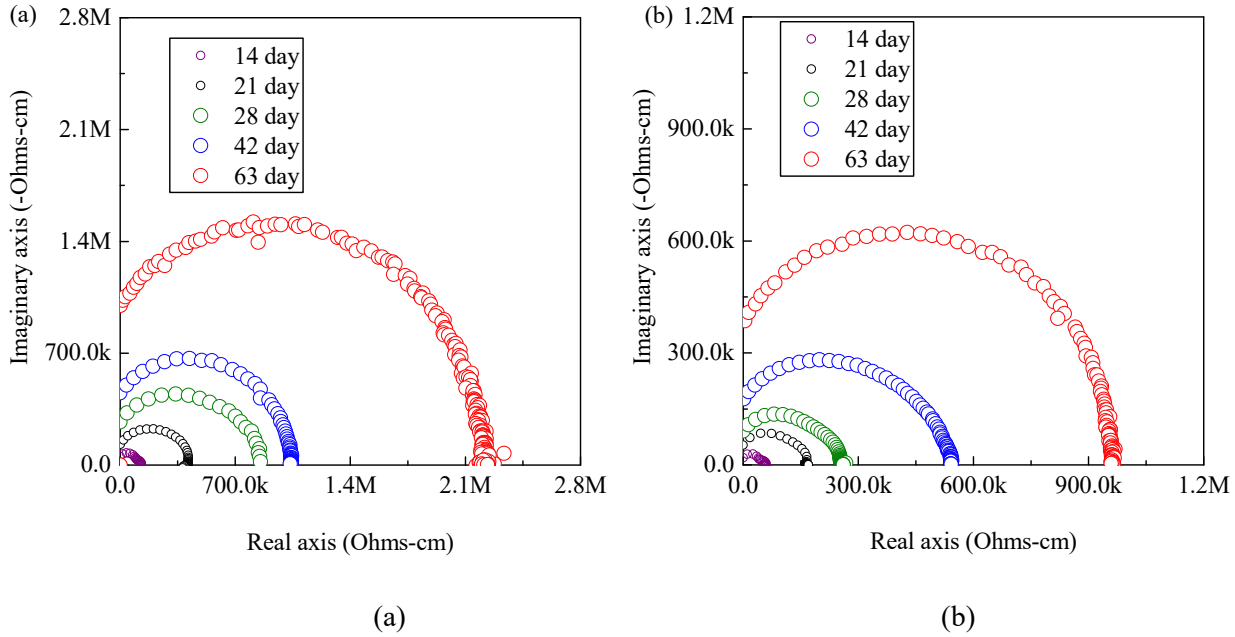

(a) (b)

Figure 3.29. Equivalent circuit model Nyquist plot of (a) C+F+S+W+P and (b) C+F+S+W at different ages.

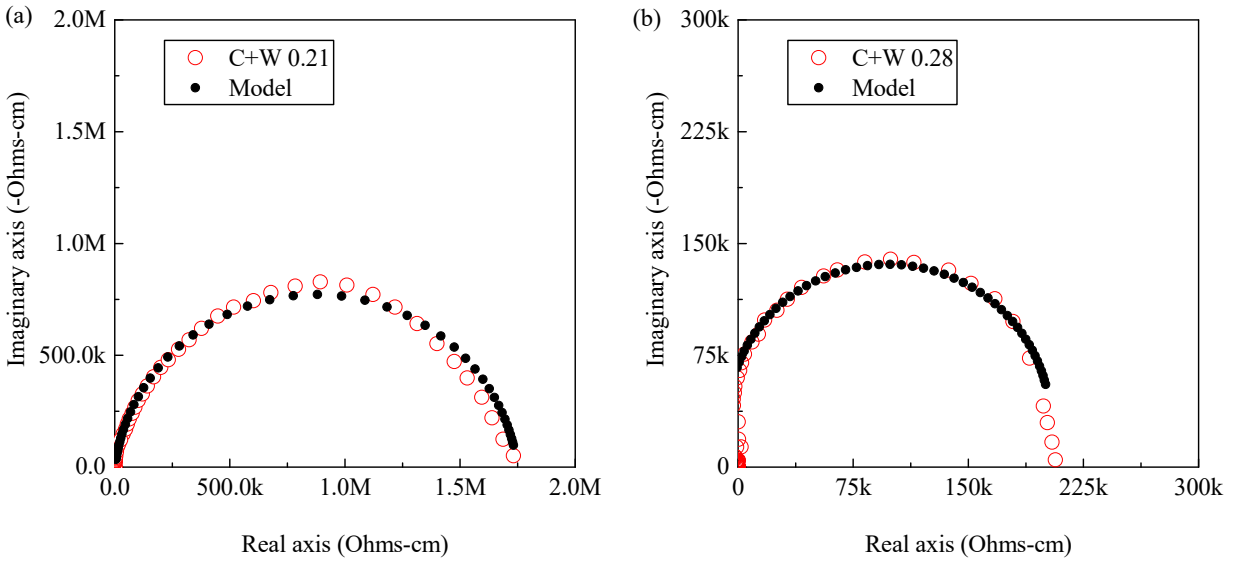

(a) (b)

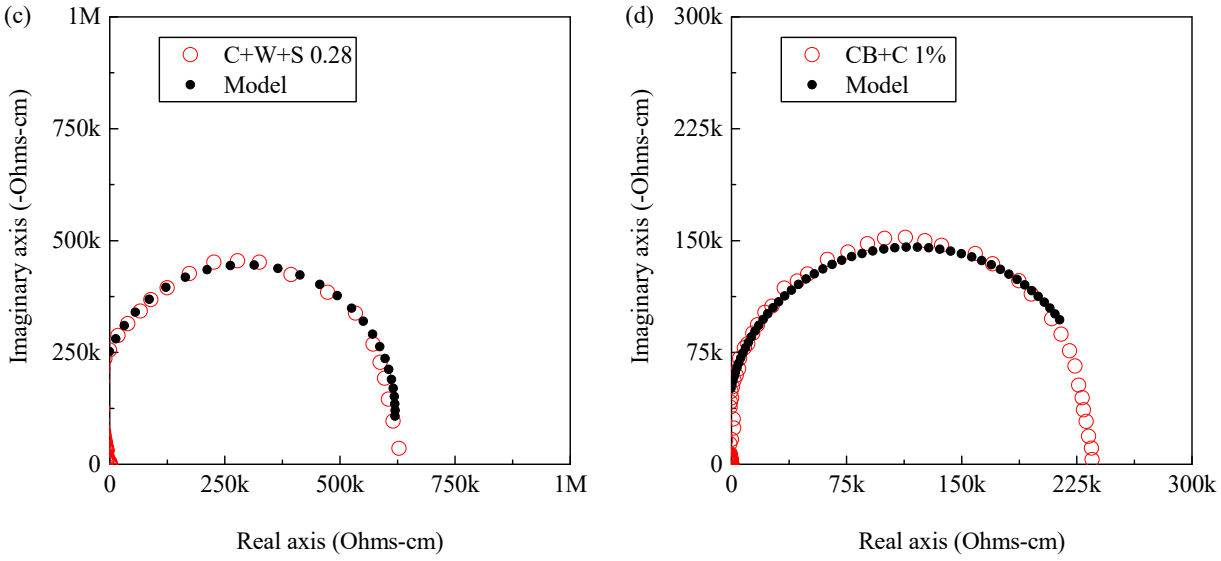

(c) (d)

Figure 3.30. Nyquist plot of EIS measurements and equivalent circuit model for (a) C+W 0.21, (b) C+W 0.28, (c) C+W+S 0.28, and (d) CB+C 1%.

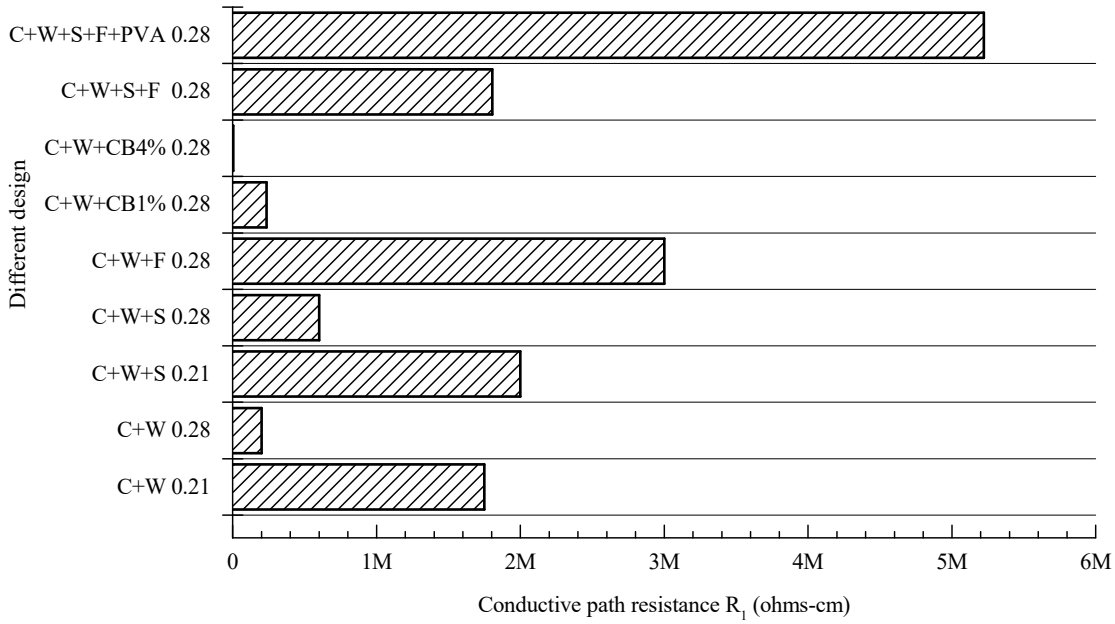

Figure 3.31. Effect of material composition on continuous conductive path R_1 at age of 180 days.

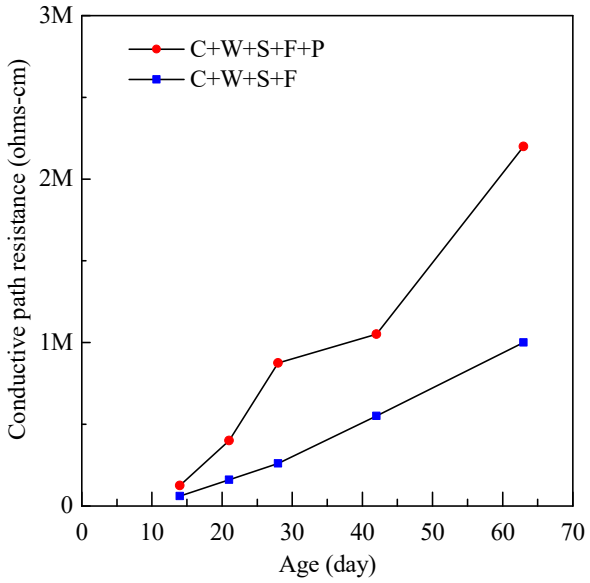

Figure 3.32. Effect of material age on continuous conductive path R_1.

3.4 Doping SHC with carbon black nanoparticles

Carbon black nanoparticles were well dispersed into the developed SHCs (see **Section 2**) with four different percentages of total material volume: 0%, 2.5%, 5% and 10%. The fresh mixtures were cast into coupon specimens (152mm × 51mm × 25.4mm). Specimens were demolded and moisture-cured at a temperature of 20 ± 1 °C and a relative humidity of 50 ± 5% till the age of 42 days. The specimens were then exposed to outdoor environment to simulate field condition for 14 days. Scanning electron microscopy with energy dispersive X-ray analysis (SEM/EDX) was performed on small samples taking from the cured specimens. As shown in **Figure 3.33**, carbon black nanoparticles were well dispersed in the cementitious binder.

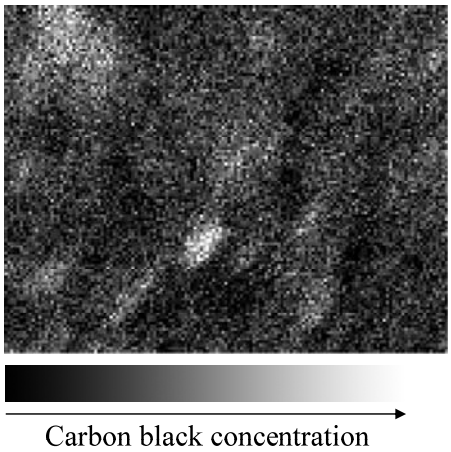

Figure 3.33. SEM/EDX of carbon black nanoparticles dispersed in cementitious matrix.

EIS was then performed on the specimens to measure the phase shift and amplitude, including the real and imaginary parts. Data collection rate was 35 point per decade. Equivalent circuit modeling was also conducted, which took into account of the conductive paths formed by adjacent carbon black nanoparticles, discontinuous paths, and insulated paths within the cementitious microstructure. The EIS experimental results are compared with equivalent circuit modeling results in **Figure 3.34**, showing good agreement. In these figures, the dual-arc behavior was observed. The rightmost arc in all curves was associated with the electrode interface response and did not reflect the material properties. The left arc reflected the cementitious material properties, which was used to calibrate the equivalent circuit model parameters. The effect of increasing carbon black dosage on the impedance spectra was clearly observed: the diameter of the left arc significantly decreased with increasing amount of carbon black nanoparticles; the center of the left arc shifted more to the left.

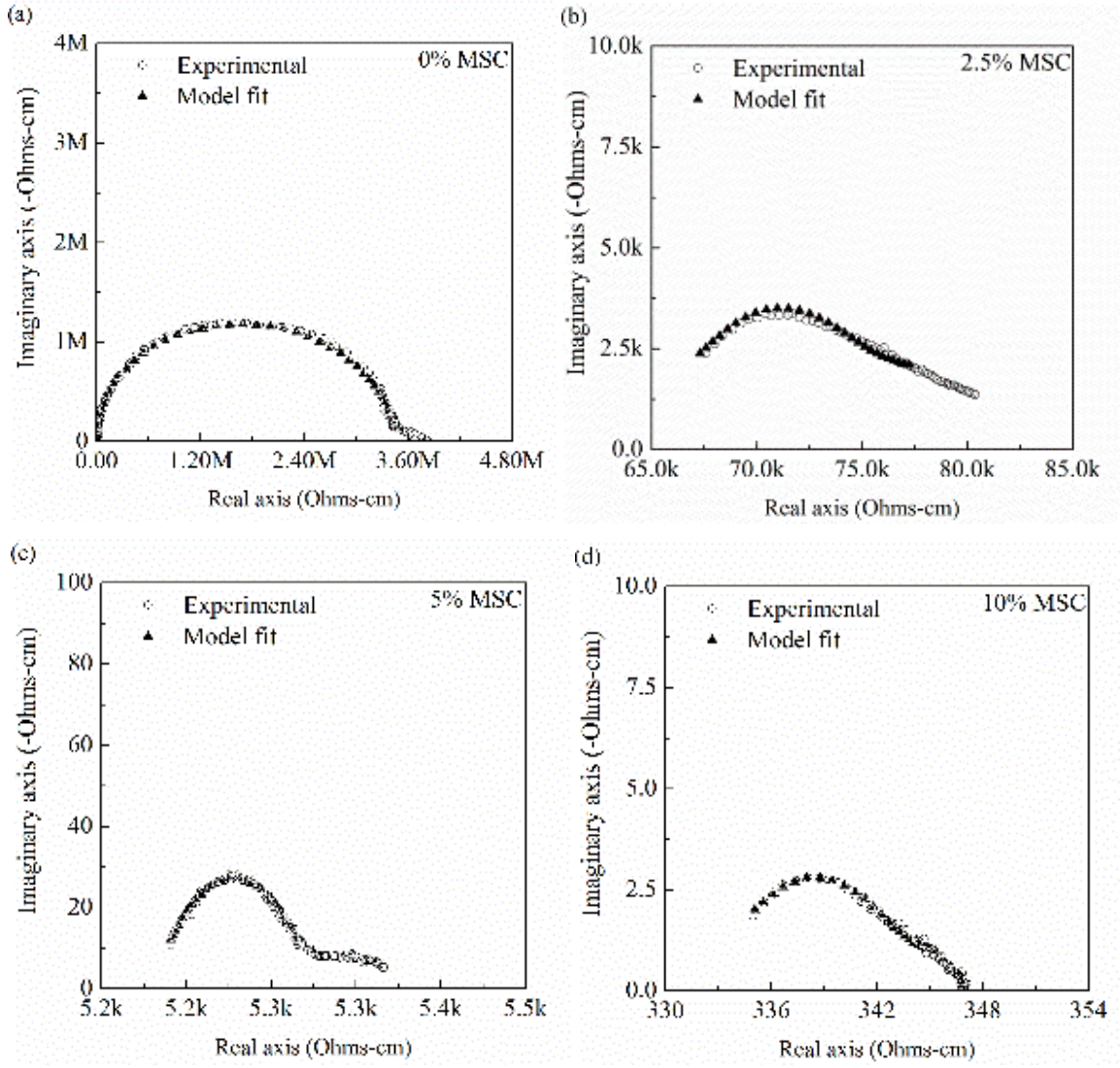

Figure 3.34. EIS Nyquist plot and equivalent circuit model results.

The resistance of R_1, R_2 and capacitance of C_1 obtained from the Nyquist plot and equivalent circuit model enabled us to obtain critical information on conductive paths and discontinuous conductive paths. Conductive paths and discontinuous conductive paths contributed significantly to the bulk impedance of cementitious materials and provided the potential for piezoresistivity. For example, under compressive force, discontinuous conductive paths can turn into conductive paths, resulting in a decrease in bulk impedance. Under tensile force, some of the conductive paths can become discontinuous conductive paths, leading to an increase in bulk impedance. The effects of carbon black nanoparticle dosage on dielectric parameters R_1, R_2 and C_1 are shown in **Figure 3.35**. R_1 and R_2 decreased exponentially with increasing amount of carbon black nanoparticles, while C_1 increased exponentially. This indicated that increasing carbon black nanoparticles led to the increase of conductive paths and discontinuously conductive paths within the SHC materials, presenting a material tailoring strategy for achieving self-sensing capacity.

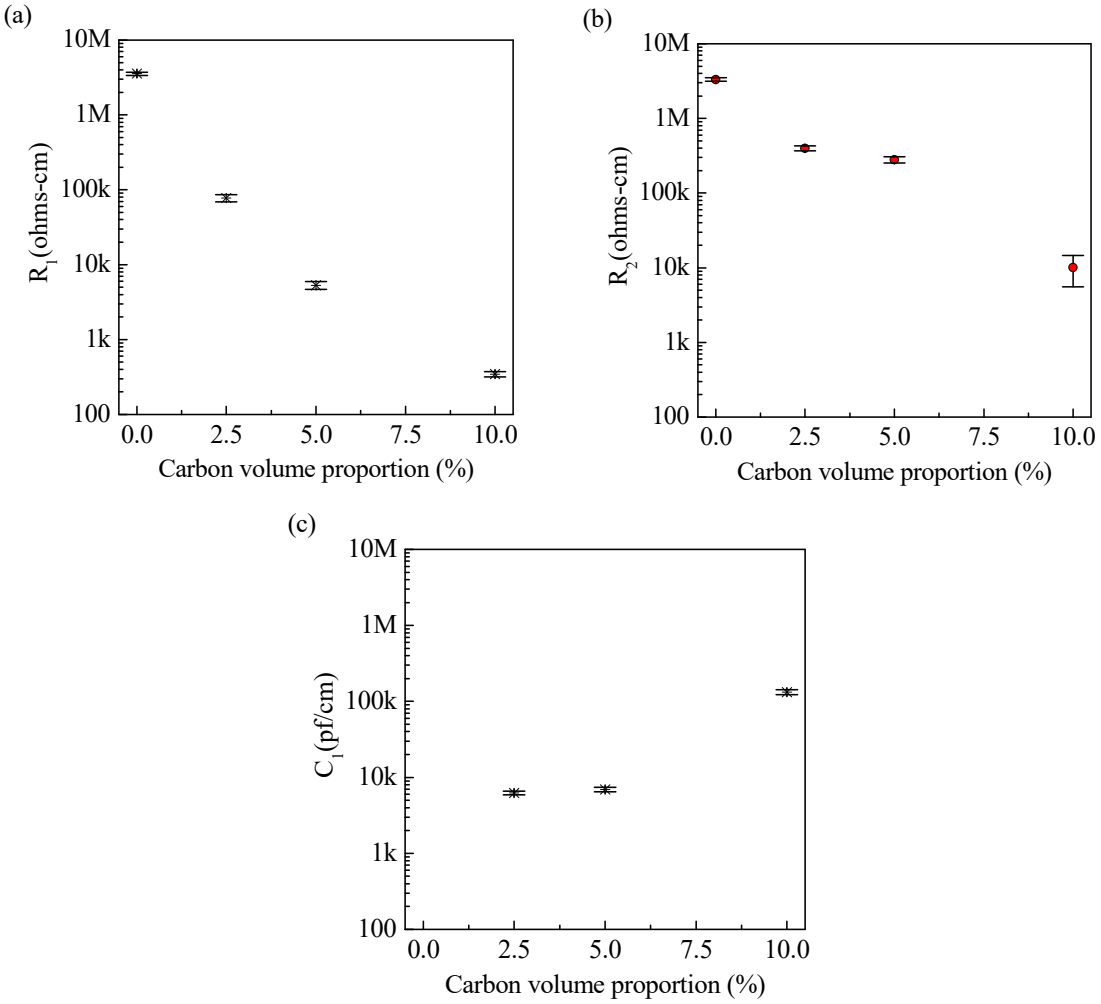

Figure 3.35. Effect of carbon black nanoparticles on physical parameters of conductive paths and discontinuous conductive paths.

3.5 Re-evaluation of strain-hardening criteria

While incorporating carbon black nanoparticles into SHC improved its electrical properties, it had a negative impact on SHC mechanical behavior. Uniaxial tension tests conducted on SHC with different amount of carbon black nanoparticles showed that the both tensile strength and tensile strain capacity decreased with increasing amount of carbon black nanoparticles (**Figure 3.36**).

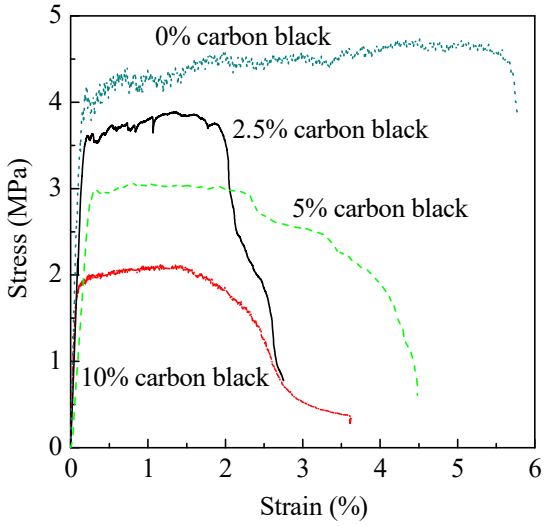

Figure 3.36. Effect of carbon black nanoparticles on tensile stress-strain relation of SHC.

In order to explain the macroscopic phenomenon, the strain-hardening criteria was re-evaluated for SHCs incorporting carbon black nanoparticles. Single crack opening test was performed on double-notched specimens with geometry of 50.8 mm ×12.7 mm ×76.2 mm (**Figure 3.37**). Test was conducted with displacement control at a displacement rate of 8.5×10^{-5} mm/ second. Four specimens were tested for each scenario. From the single crack test results, the complementary energy J_b' was calculated. To measure matrix crack tip energy $J_{tip,}$ The matrix toughness test setup is shown in **Figure 3.38**. The specimens were prepared without fibers. After mixing, the fresh slurry was cast into beam specimens that were 305 mm long, 50.8 mm deep and 25.4 wide. After curing for 42 days, a sharp notch was made on the mid-span of the specimen, with notch depth around 25.4 mm. The matrix fracture toughness K_m was measured by the three-point bending test. Four specimens were tested for each test series, J_{tip} was calculated from the measured K_m based on **Equations 3.10** and **3.11**.

$$J_{tip} \le \sigma_0 \delta_0 - \int_0^{\delta_0} \sigma(\delta) d\delta \equiv J_b' \tag{3.10}$$

$$J_{tip} = \frac{K_m^2}{E_m} \tag{3.11}$$

Where is the maximum bridge stress corresponding to the opening σ_m, K_m is the matrix-fracture toughness, and E_m is the matrix Young's modulus.

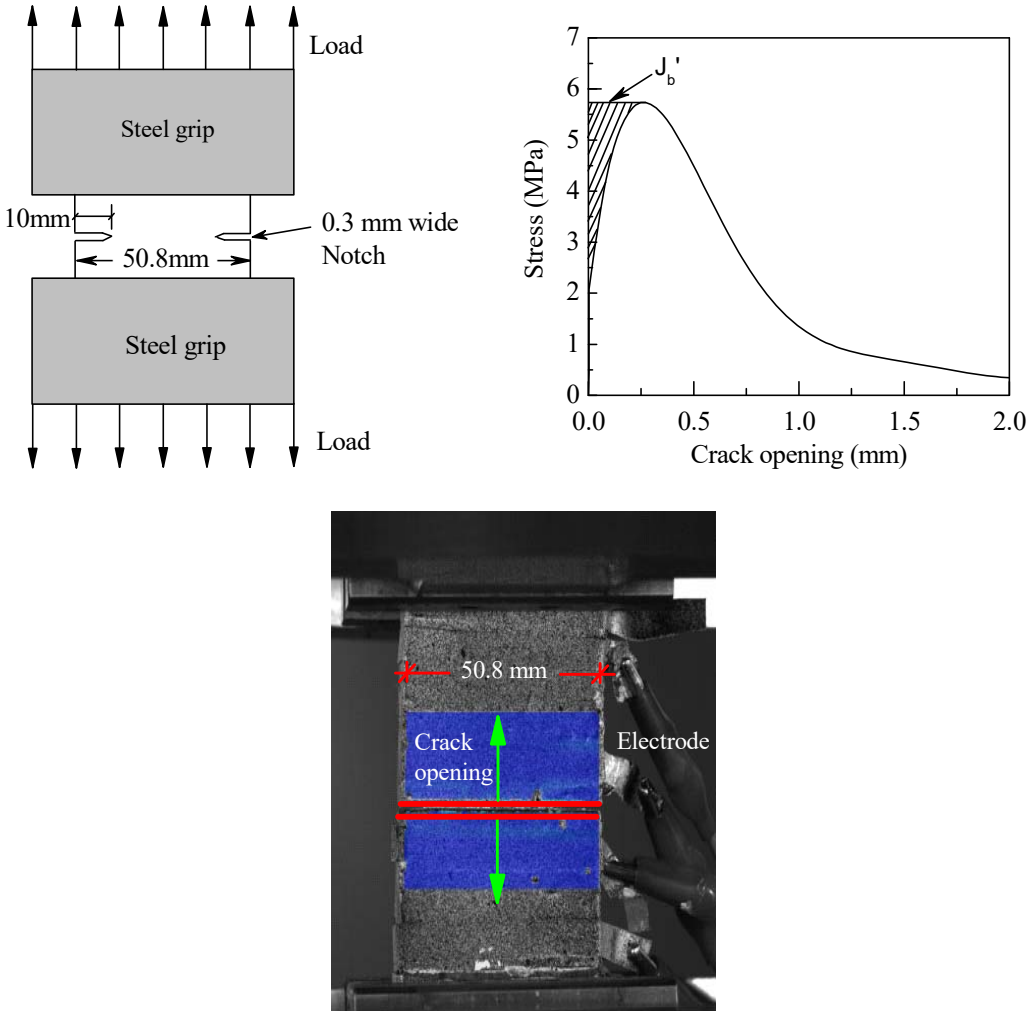

Figure 3.37. Single crack opening test and J_b' calculation.

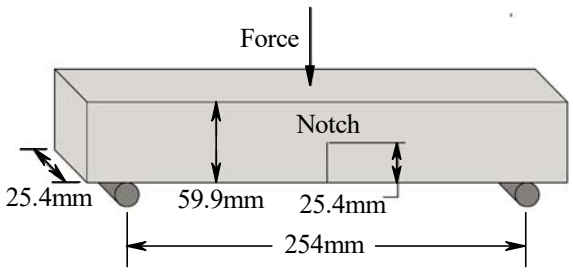

Figure 3.38. Matrix toughness test.

Table 3.2: Proposed Multifunctional Strain-hardening Cementitious Composites design.

Design	Water	Cement	Sand	Fly ash	Silica fume	Carbon Black	Superplasticizer	Fiber
	kg/m^3	kg/m^3	kg/m^3	kg/m^3	kg/m^3	kg/m^3	kg/m^3	Vol-%
0% MSC	312	292	456	935	0	0	2.7	2
2.5% MSC	277	243	380	584	113	12.5	2.7	2
5% MSC	296	243	380	600	115	25	2.7	2
10% MSC	313	243	380	611	117	51	2.7	2

The pseudo strain-hardening index J_b'/J_{tip} was calculated the control mixture design as well as mixture designs containing 2.5%, 5% and 10% carbon black nanoparticles by total volume of cementitous mateirals. The results are shown in **Figure 3.39**. Two conclusions were drawn: (1) the pseudo strain-hardening index was larger than 1 for mixture designs with 2.5%, 5% and 10% carbon black nanoparticles, indicating that 2.5% MSC, 5% MSC and 10% MSC were all able to achieve strain-hardening behavior. (2) There was an upper threshold of the carbon black amount that could be incorporated; higher amount of carbon black nanoparticles could lead to a deterioration of tensile strain capacity due to a lower value of $J_b'/J_{tip,}$ leading to a tension softening behavior.

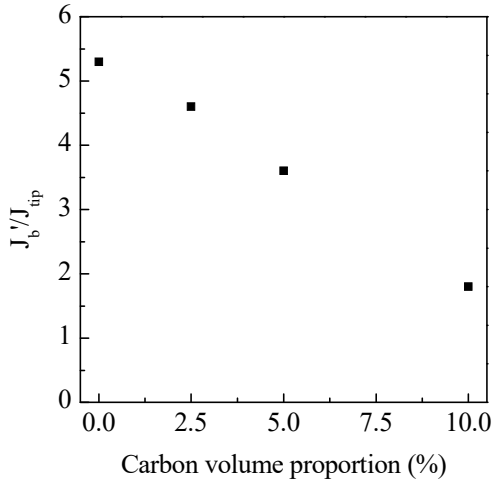

Figure 3.39. Pseudo Strain-hardening index (J_b'/J_{tip}) for 0%, 2.5%, 5% and 10% MSC.

3.6 Tensile properties of MSC

The tensile properties of MSCs in **Table 3.2** were measured by direct uniaxial tension test. The tensile stress-strain curves are shown in **Figure 3.40**. All specimens exhibited tensile strain-hardening behavior with tensile strain capacity larger than 3%. The 5% MSC had a tensile strain capacity larger than

4%, while the 2.5% and 0% MSC had tensile strain capacity larger than 5%. With higher amount of carbon black nanoparticles, the tensile strength of MSC decreased. Nevertheless, all MSC material exhibited large tensile ductility that was hundreds times more than normal concrete or fiber reinforced concrete. After the initial elastic stage, the MSC materials underwent a pseudo strain-hardening stage accompanied by steady-state microcracking with intrinsically controlled crack width. Such unique strain-hardening behavior suppressed localized fracture prevalent in cementitious materials.

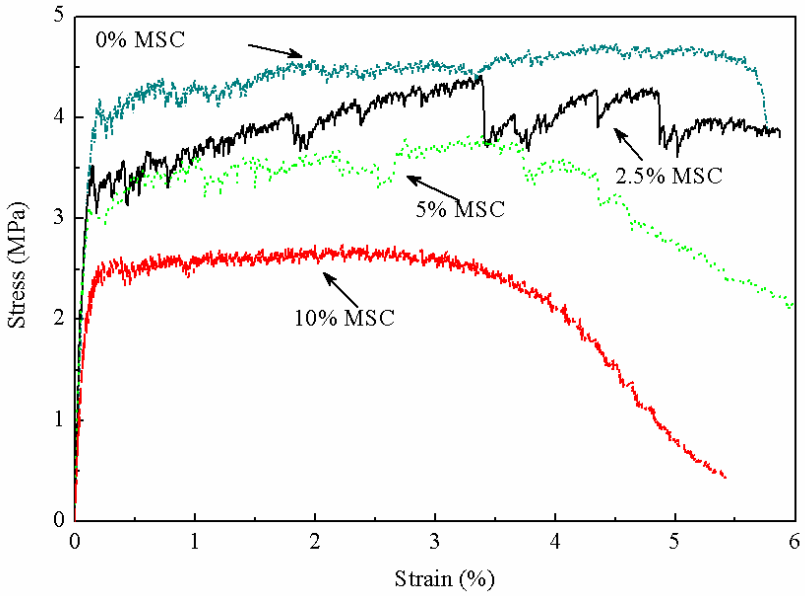

Figure 3.40. Tensile stress-strain relation of 0%, 2.5%, 5% and 10% MSC.

3.7 Electrical properties of MSC

The electrical responses of MSCs were measured using four-point AC probing electrical impedance spectroscopy. The results are shown in **Figure 3.41**. The impedance magnitude was plotted against excitation frequency. It was clearly observed that increasing the amount of carbon black nanoparticles greatly reduced impedance magnitude for a wide frequency range. Compared with the control specimen (0% MSC), the impedance magnitude was reduced by 2 order, 3 orders and 4 orders of magnitude lower for 2.5% MSC, 5% MSC and 10% MSC respectively.

In order to test the uniformity that the electrical properties measured for MSCs, EIS was conducted on specimens with different gauge lengths (**Figure 3.42**). Frequency range from 10e2 HZ to 10e4 HZ was chosen for uniformity analysis. The measured impedance data were transformed into sheet resistivity unit to exclude geometry influence on the electrical properties. The test results are shown in **Figure 3.43**. It was observed that specimens containing carbon black nanoparticles exhibited better uniformity that was barely influenced by the gage length.

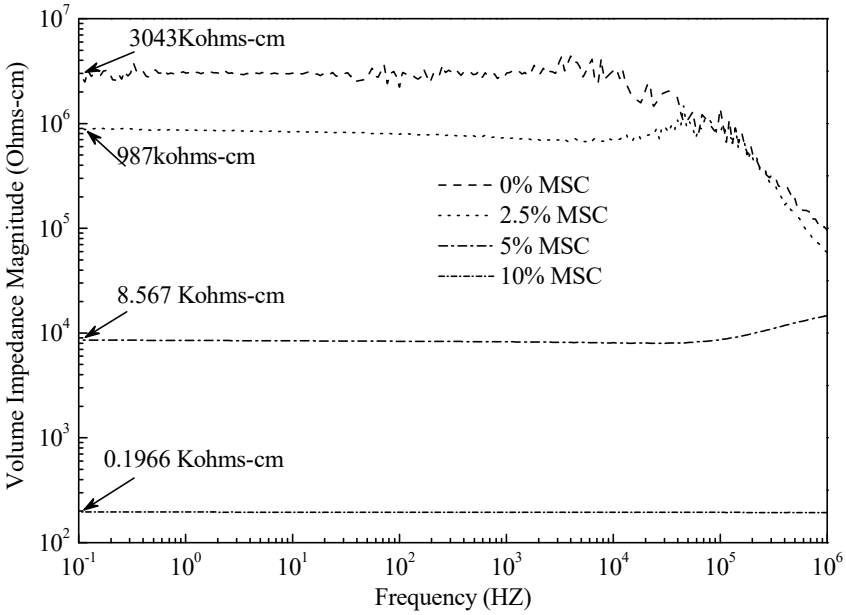

Figure 3.41. Bode plots of 0%, 2.5%, 5% and 10% MSC.

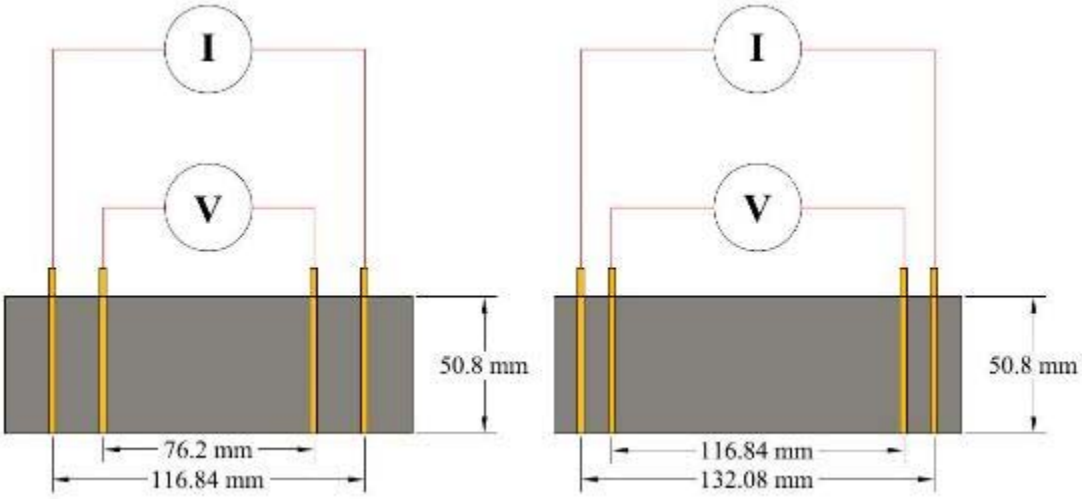

Figure 3.42. Uniformity tests with different gage lengths.

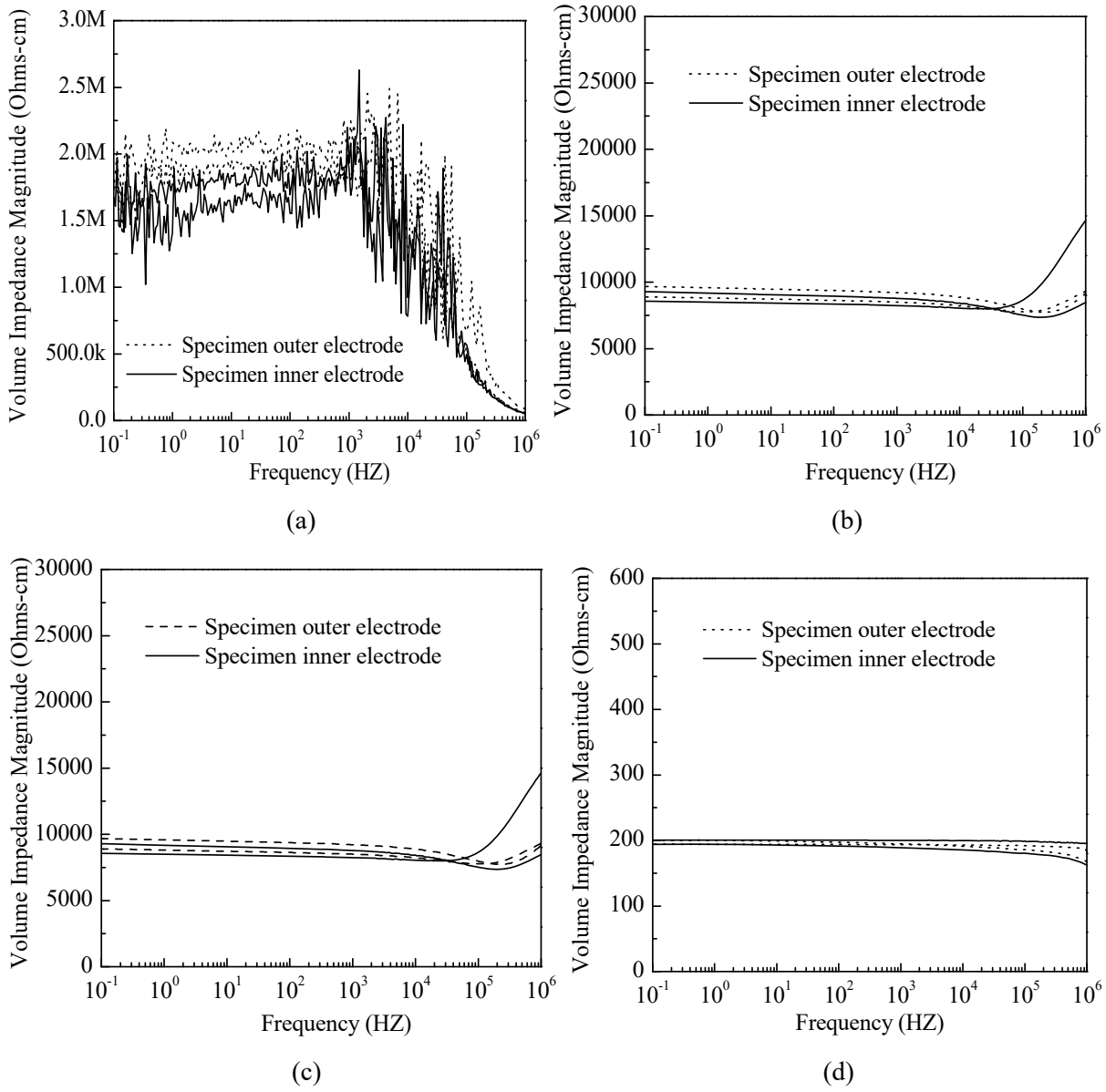

Figure 3.43. Uniformity test results. (a) 0% MSC; (b) 2.5% MSC; (c) 5% MSC; (d) 10% MSC.

3.8 Piezoresistive behavior of MSC

The piezoresistive behavior of MSC was measured using four-point AC probing electrical impedance spectroscopy while the specimen was loaded in uniaxial tension or uniaxial compression. Piezoresistive effect refers to the change in electrical resistivity due to mechanical strain. The uniaxial tension test setup is shown in **Figure 3.44**. The uniaxial tension test setup is shown in **Figure 3.45**. The test was conducted with displacement control with a loading rate of 0.005mm/s. Two LVDTs were attached to both sides of the specimen to measure displacement, while the force was recorded by the testing system. During testing, impedance change was measured at a fixed frequency (1500 HZ).

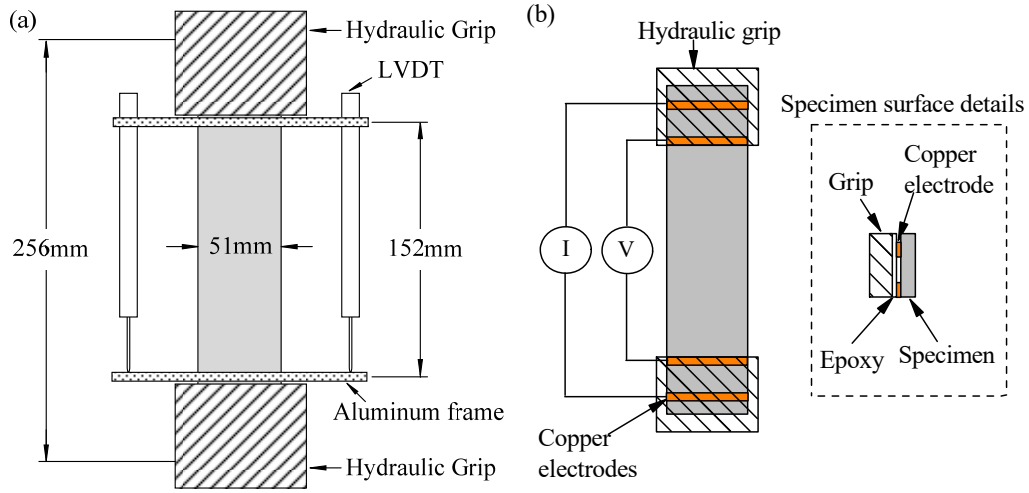

Figure 3.44. Measuring piezoresistive behavior of MSC under uniaxial tension. (a) Test setup; (b) Specimen details.

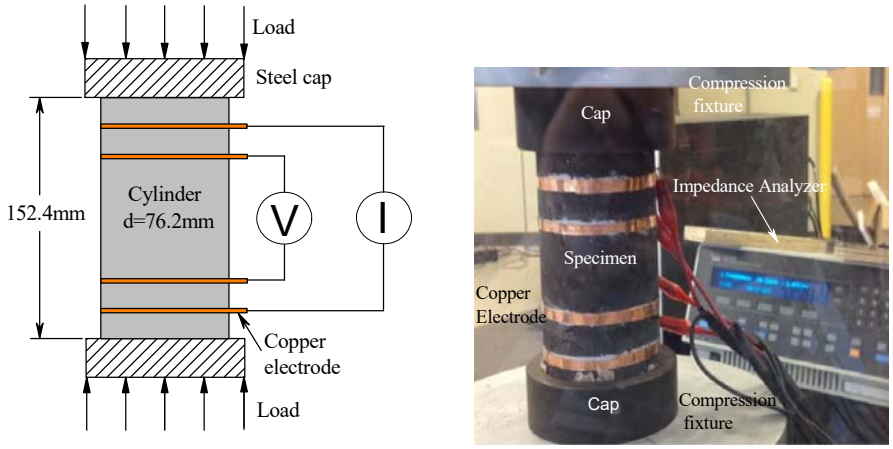

Figure 3.45. Measuring piezoresistive behavior of MSC under uniaxial compression.

Figure 3.46 shows the piezoresistive behavior of 0%, 2.5%, 5% and 10% MSCs under cyclic uniaxial tension within elastic range. The impedance magnitude change was plotted against change of tensile strain. The fractional change in impedance magnitude is defined as:

$$I_f = \frac{\Delta I}{I_i} \tag{3.12}$$

Where I_f is the fractional change in impedance magnitude, I_i is the initial impedance magnitude at zero strain, and ΔI is the change in impedance magnitude.

For the 0% MSC specimens, which served as control specimens, no obvious linear relation between strain and fractional change in impedance magnitude was observed. A large noise was also seen. When the carbon black nanoparticles content increased, linear relation was observed between the fractional change in impedance magnitude and strain. With increasing elastic strain, the impedance magnitude increased in a linear manner; when the material was unloaded with decreasing elastic strain, the impedance magnitude decreased in a linear manner correspondingly. Such piezoresistive behavior under cyclic tension was significant, especially for 5% and 10% MSCs. Noise in impedance data was also minimized in 5% and 10% MSC. The results clearly revealed that by tailoring the piezoresistive behavior of MSC through nanoparticles and micromechanics-based material design, self-sensing of elastic strain under cyclic tension was successfully achieved.

Based on the test results, gage factors and the signal to noise ratios were calculated. Gage factor was defined in **Equation 3.13**, where I_f is the fractional change in impedance magnitude and ε_t is the tensile strain. The value of gage factor indicates the effectiveness of strain-sensing capacity.

$$\alpha = \frac{I_f}{\varepsilon_t} \tag{3.13}$$

The signal to noise ratio is defined as the power of the signal to the power of noise, as shown in **Equation 3.14**, where P_{signal} is the power of the signal and P_{noise} is the power of noise.

$$SNR_{db} = 10\log_{10}\left(\frac{P_{signal}}{P_{noise}}\right) \tag{3.14}$$

Compared with control 0% MSC specimens, the 2.5%, 5% and 10% MSC specimens all surpassed the target gage factor of 5 during elastic straining stage. The gage factors are 45 ± 23, 268 ± 16 and 95 ± 9 for 2.5%, 5% and 10% MSCs, respectively, indicating the strong tensile strain-sensing capacity of the three versions of MSC materials within elastic range. Specially, the 5% MSC achieved the largest gage factor and strongest signal to noise ratio.

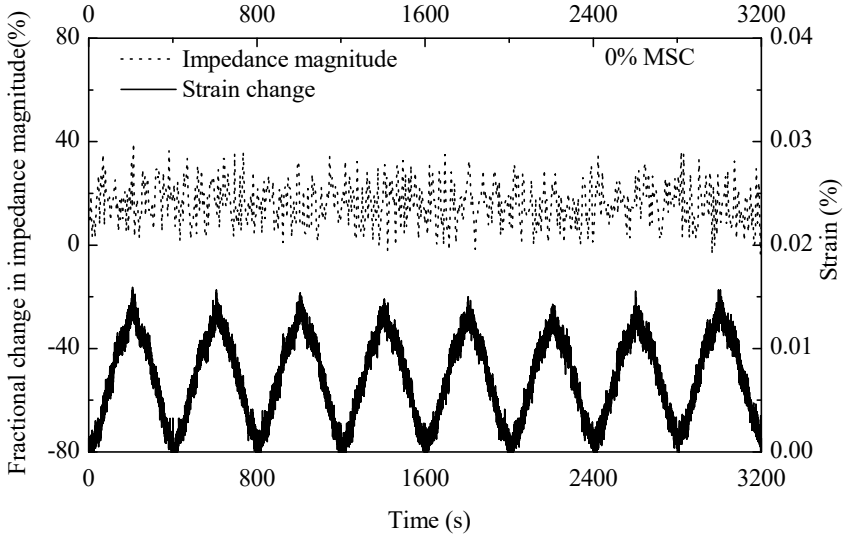
0% MSC
Impedance magnitude
Strain change
Fractional change in impedance magnitude(%)
Strain (%)
Time (s)
0
800
1600
2400
3200
80
40
0
-40
-80
0.04
0.03
0.02
0.01
0.00

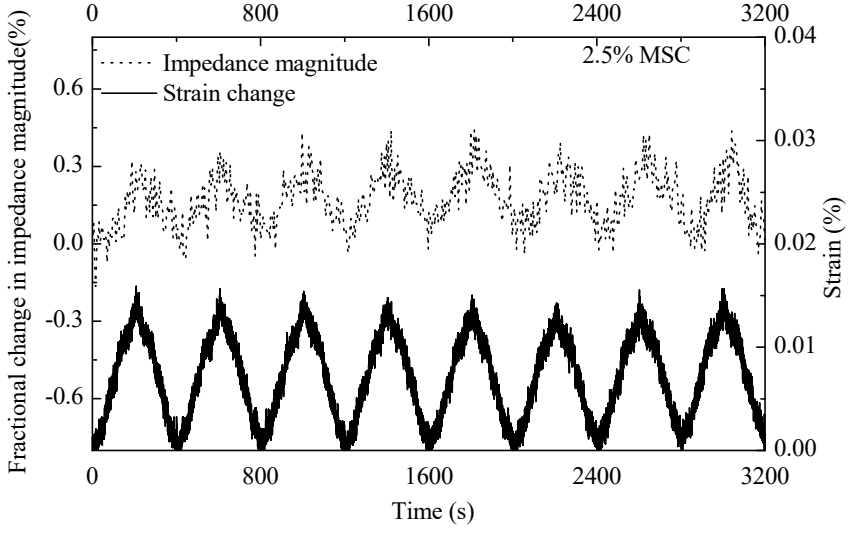
2.5% MSC
Impedance magnitude
Strain change
Fractional change in impedance magnitude(%)
Strain (%)
Time (s)
0
800
1600
2400
3200
0.6
0.3
0.0
-0.3
-0.6
0.04
0.03
0.02
0.01
0.00

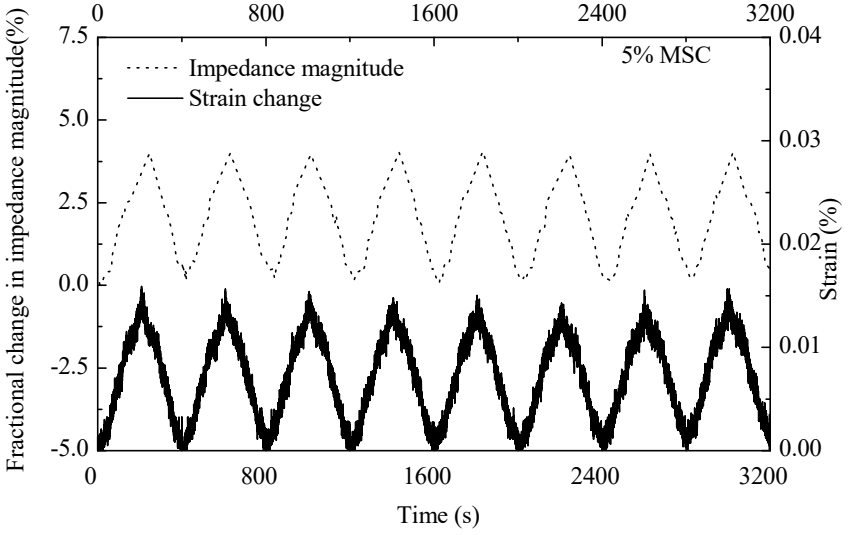
5% MSC
Impedance magnitude
Strain change
Fractional change in impedance magnitude(%)
Strain (%)
Time (s)
0
800
1600
2400
3200
7.5
5.0
2.5
0.0
-2.5
-5.0
0.04
0.03
0.02
0.01
0.00

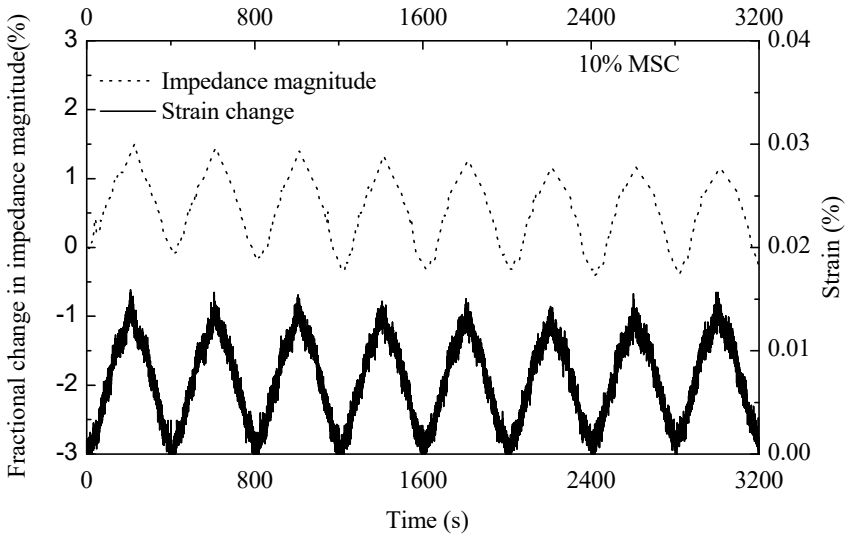

Figure 3.46. Piezoresistive behavior of MSCs during elastic stage under tension.

Table 3.3. Gage factor and Signal-noise ratio comparison for MSCs under tension.

Material	0% MSC	2.5% MSC	5% MSC	10% MSC
Gage factor	N/A	45 ± 23	268 ± 16	95 ± 9
Signal to noise ratio (db)	0	8.34	19.4	17.6

Figure 3.47 shows the piezoresistive behavior of 0%, 2.5%, 5% and 10% MSCs under cyclic uniaxial compression within elastic range. The impedance magnitude change was plotted against change of compressive strain. For the 0% MSC specimens, which served as control specimens, a correlation between strain and fractional change in impedance magnitude was observed, but the pattern of such correlation was inconsistent. Robust sensing of strain through measuring impedance changes was thus difficult to achieve in the control 0% MSC. For the 2.5%, 5% and 10% MSCs, consistent linear relation between impedance magnitude change and compression strain existed during both loading and unloading stages during each loading cycle. Gage factor for each material was calculated and compared in **Table 3.4**. The 2.5%, 5% and 10% MSC specimens all surpassed the target gage factor of 5 during elastic straining stage. The gage factors are 17 ± 3.4, 62 ± 5 and 56 ± 4 for 2.5%, 5% and 10% MSCs, respectively, indicating the strong compression strain-sensing capacity of the three versions of MSC materials within elastic range. Specially, the 5% MSC achieved the largest gage factor and strongest signal to noise ratio.

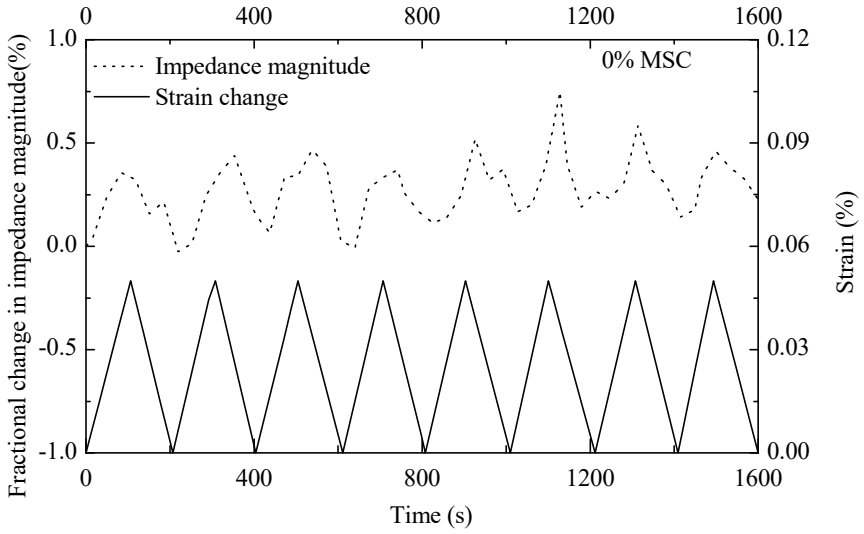
0% MSC
Impedance magnitude
Strain change
Fractional change in impedance magnitude(%)
Strain (%)
Time (s)

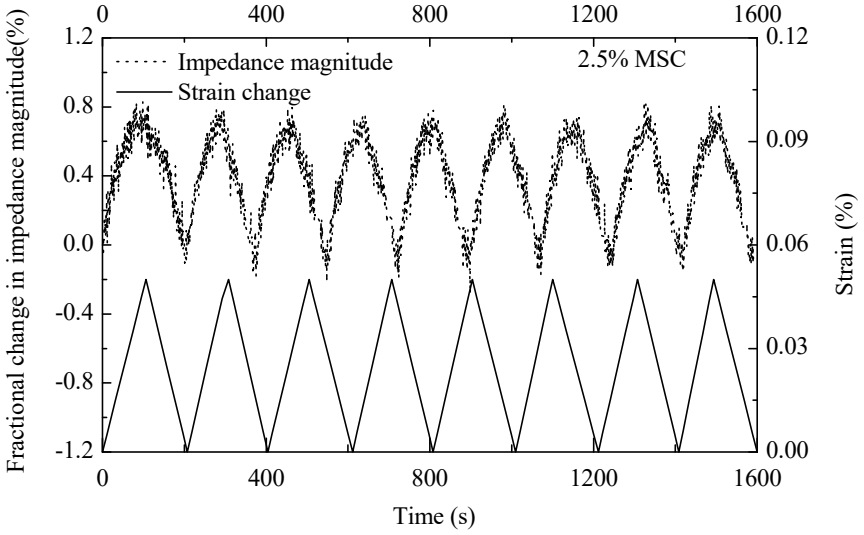
2.5% MSC
Impedance magnitude
Strain change
Fractional change in impedance magnitude(%)
Strain (%)
Time (s)

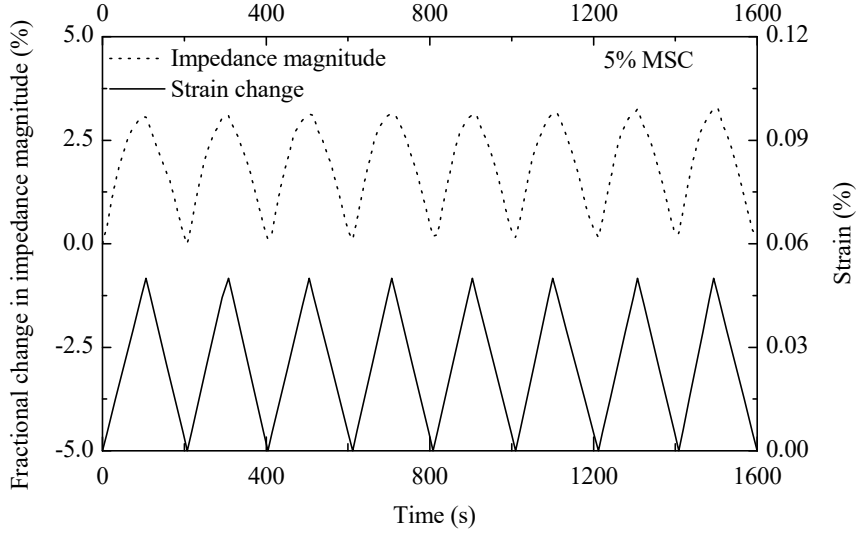
5% MSC
Impedance magnitude
Strain change
Fractional change in impedance magnitude (%)
Strain (%)
Time (s)

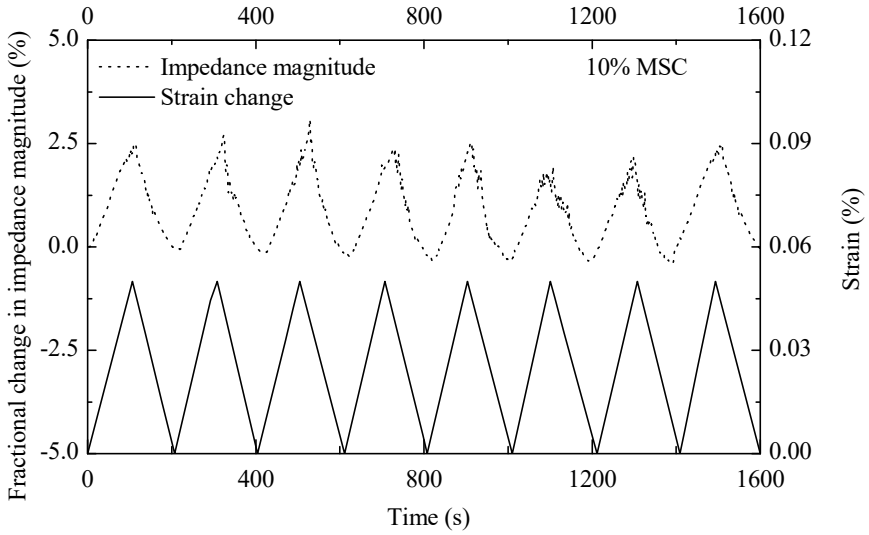

Figure 3.47. Piezoresistive behavior of MSCs during elastic stage under compression.

Table 3.4. Gage factor and Signal-noise ratio comparison for MSCs under compression.

Material	0% MSC	2.5% MSC	5% MSC	10% MSC
Gage factor	8.4±2.67	13.7±4.8	62.4±6.7	54.0±5.5
Signal to noise ratio (db)	7.6	12.4	18.6	17.7

The piezoresistive behavior of MSC beyond its elastic stage, and during inelastic strain-hardening stage followed by tension-softening stage was also measured. The results are shown in **Figure 3.48**, which plotted the fractional change of impedance magnitude with increasing tensile strain till the localized fracture failure occurred in the specimen. For all MSC specimens, they exhibited three distinguishable stages in their tensile stresss-strain curves: (1) elastic stage, (2) strain-hardening stage, which started when the first microcrack occurred and ends when localized fracture took place at one of the many microcracks formed during this stage, and (3) tensile-softening stage, which corresponds the localized fracture process. During the elastic stage, there was no cracking. During the strain-hardening stage, steady-state crack propagation prevailed. The number of microcracks increased with increasing tensile strain while the width of each microcrack merely changed. During the tensile-softening stage, crack opening increased at the single final failure crack with increasing strain, and the total number of total cracks did not change. Interestingly, this unique damage process within MSCs was well reflected in their electrical responses. As shown in **Figure 3.48**, there was a general trend of increasing impedance magnitude due to increasing strain, indicating a strong piezoresistive behavior during the three stages. For the control 0% MSC, large noise was observed in the impedance data, but a nearly linear increasing trend during strain-hardening and tension-softening

stages was clear. For the 2.5%, 5% and 10% MSC specimens, the noise in the impedance data was significantly reduced, indicating more homogeneous electrical properties of the materials. Moreover, a nonlinear relation between fractional impedance magnitude change and tensile strain during strain-hardening stage and tension-softening stage was found in the 2.5%, 5% and 10% MSCs, which was different from the nearly linear relation for the 0% MSC. At the larger strains, the fractional increase in impedance magnitude became faster than at the smaller strains. This unique phenomenon was due to the change in the dielectric effect of matrix cracks during the multiple cracking process, and the change in the contact impedance between fibers and cementitious matrix; both of which were dictated by the fiber bridging law across cracks. As a result, the 2.5%, 5% and 10% MSCs not only can reliably "self-sense" *strain change* with reduced noise, but also can "self-sense" *strain level*. The change of nonlinear relation between impedance magnitude and strain during elastic, strain-hardening and tension-softening stages also made it possible for damage-level sensing in addition to strain sensing.

Figure 3.48 also plotted the fitted results for fractional impedance magnitude change vs tensile strain. A three-degree polynomial function was used, as defined in **Equation 3.15**.

$$I_f = a\varepsilon_t^3 + b\varepsilon_t^2 + c\varepsilon_t \tag{3.15}$$

Where I_f is the fractional change in impedance magnitude, and ε_t is the tension strain. The curve fitting parameters are summarized in **Table 3.5**.

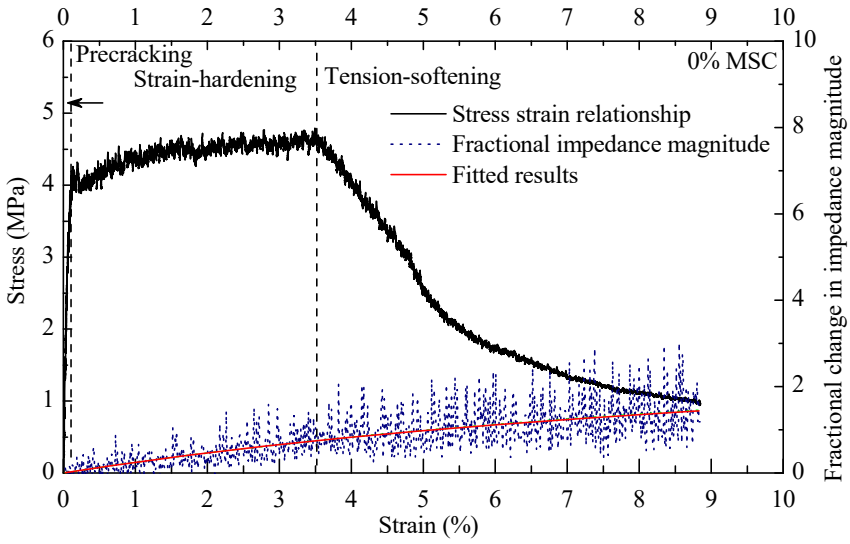

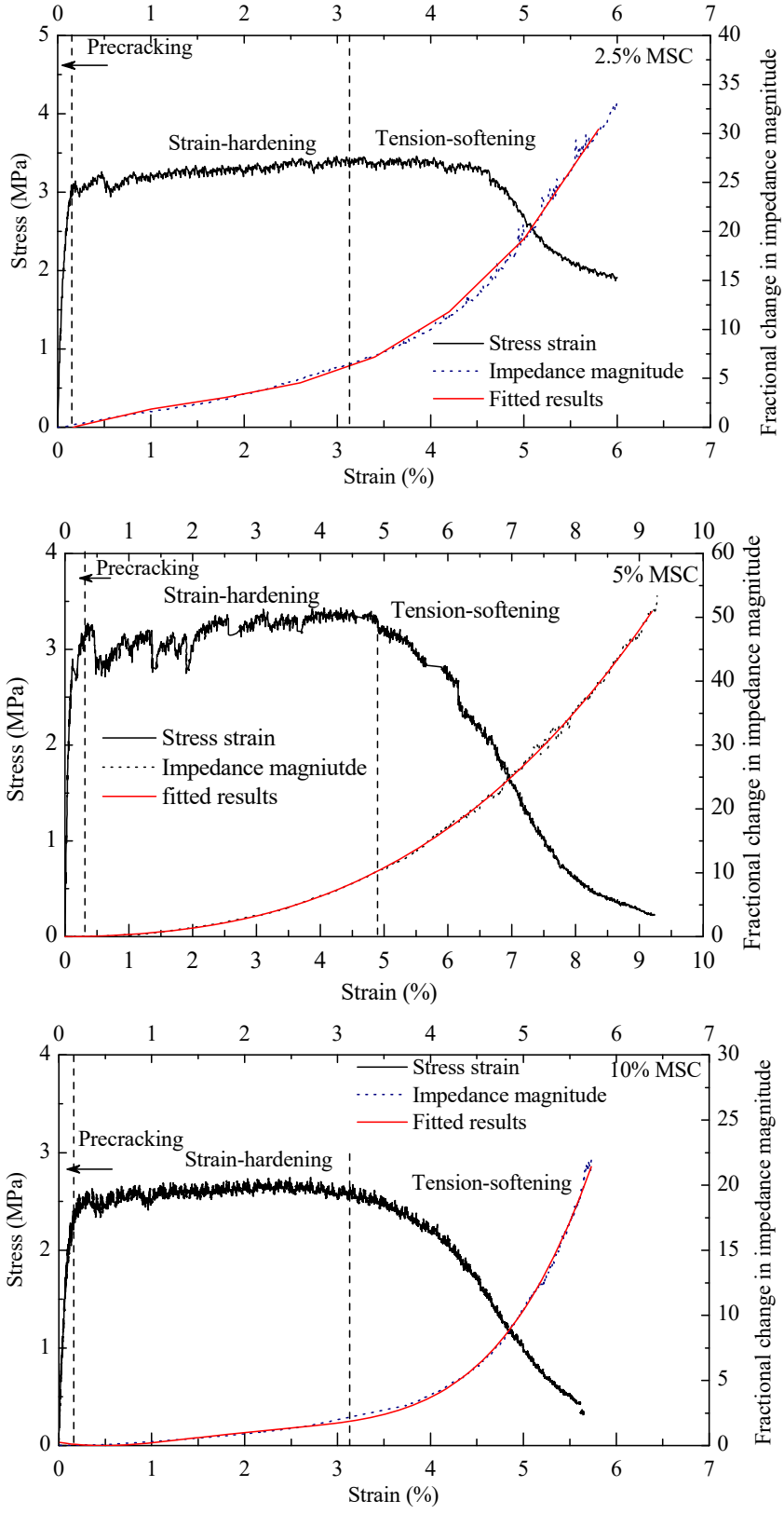

Figure 3.48. Piezoresistive behavior of MSCs under uniaxial tension

Table 3.5. Fractional impedance magnitude change vs. tensile strain curve fitting parameters.

Material	a	b	c
0% MSC	522	-159	26
2.5% MSC	278394	-12814	340
5% MSC	42865	1948	11.6
10% MSC	365112	-20671	359.3

Table 3.6. Electromechanical properties of MSCs.

Material	Specimen number	First cracking strain (%)	Ultimate strength (MPa)	Strain-hardening capacity (%)	Strain-hardening gage factor
0% MSC	1	0.14	4.2	3.6	803
	2	0.1	4.4	4.2	932
	3	0.12	3.9	4.6	743
	4	0.15	4.0	3.8	782
2.5% MSC	1	0.17	3.2	4.5	6574
	2	0.18	3.1	4.8	6210
	3	0.20	3.0	3.9	6000
	4	0.14	3.4	4.1	6870
5% MSC	1	0.18	2.5	5.0	4017
	2	0.19	2.8	4.7	4200
	3	0.22	3.0	5.2	4501
	4	0.16	2.7	4.4	3821
	1	0.21	2.0	3.2	2208
	2	0.19	1.9	3.0	1982

10% MSC	3	0.23	2.2	3.1	2453
	4	0.23	2.1	2.9	2301

The electromechanical properties of MSCs are summarized in **Table 3.6**. The strain-hardening gage factors were determined based on Equation 3.16, as shown in **Figure 3.49**.

$$I_f = s_f \varepsilon_t^2 \tag{3.16}$$

Where I_f is the fractional change in impedance magnitude, S_f is defined as the strain-hardening gage factor, and ε_t is the tension strain. Similar as the elastic gage factor, the strain-hardening gage factor is a critical parameter for strain sensing during the strain-hardening stage of the MSC material to predict strain level based on measured impedance change. A higher the strain-hardening gage factor means a stronger piezoresistive behavior of the MSC material during strain-hardening stage, making it a more sensitive to self-sense strain. The calculated strain-hardening gage factor for MSCs are summarized in **Table 3.6**. It was seen that 2.5% MSC has the highest strain-hardening gage factor and the 0% MSC has the lowest strain-hardening gage factor. For all the 2.5%, 5% and 10% MSC specimens, inelastic (i.e. strain-hardening) gage factors were all well above the target values of 15 set in the proposal. The inelastic gage factors are 6413, 4134 and 2236 in average for 2.5%, 5% and 10% MSC specimens, respectively. Therefore, we have successfully achieved robust strain-sensing in the newly developed MSC materials with large gage factors both at elastic and inelastic stages.

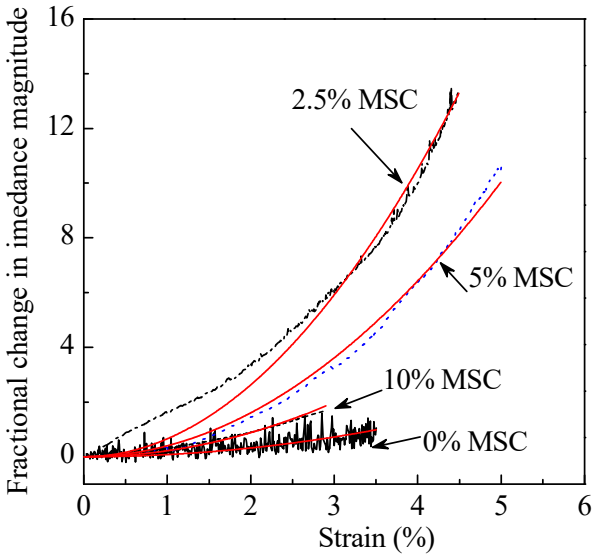

Figure 3.49. Determining MSC gage factors during strain-hardening stage

3.9 Effect of damage level on MSC complex impedance

Impedance spectroscopy at frequencies of 1 HZ to 1 MHZ were conducted on the MSC specimens at different damage levels on tensile, in order to demonstrate the effect of microcracking damage on the complex impedance of self-sensing MSC. The data for 5% MSC is shown in **Figure 3.50**. Eight damage levels were considered, corresponding to 0%, 1%, 2%, 3%, 4%, 5%, 6%, and 7% applied tensile strain. It should be noted that an applied tensile strain level larger than 1% were considered to be extremely high in cementitious materials; large cracking and concrete material failure is inevitable at such high tensile strain levels, and the structure relies on steel reinforcement to prevent failure. Due to the large tensile strain capacity of MSCs, the cementitious material itself can resist extraordinarily large applied tensile strains without failure; instead, the damage level within MSCs increased in form of multiple steady-state microcracking. The change in damage level in MSCs can also be self-sensed through complex measured impedance data, as shown in the Nyquist plot in **Figure 3.50**. With increasing strain level, the increased multiple cracking damage within MSC specimens were shown. It was obvious that increasing microcracking damage level in MSC increased the radius of the high-frequency arc of the Nyquist plot and shifted the center of the arc to the right. Moreover, equivalent circuit model parameters were extracted from the EIS data in **Figure 3.50**. The resistivity of resistor element in the equivalent circuit model was calculated and plotted against tensile strain in **Figure 3.51**. Based on the sudden change of the slope in the measured resistivity increase vs. strain, the localized fracture failure can be identified. The results clearly showed that the damage level in MSC, including the increased multiple microcracking process during strain-hardening stage and the localized fracture failure that initiates the tension-softening stage, can be successfully self-sensed by the newly developed MSCs in this project.

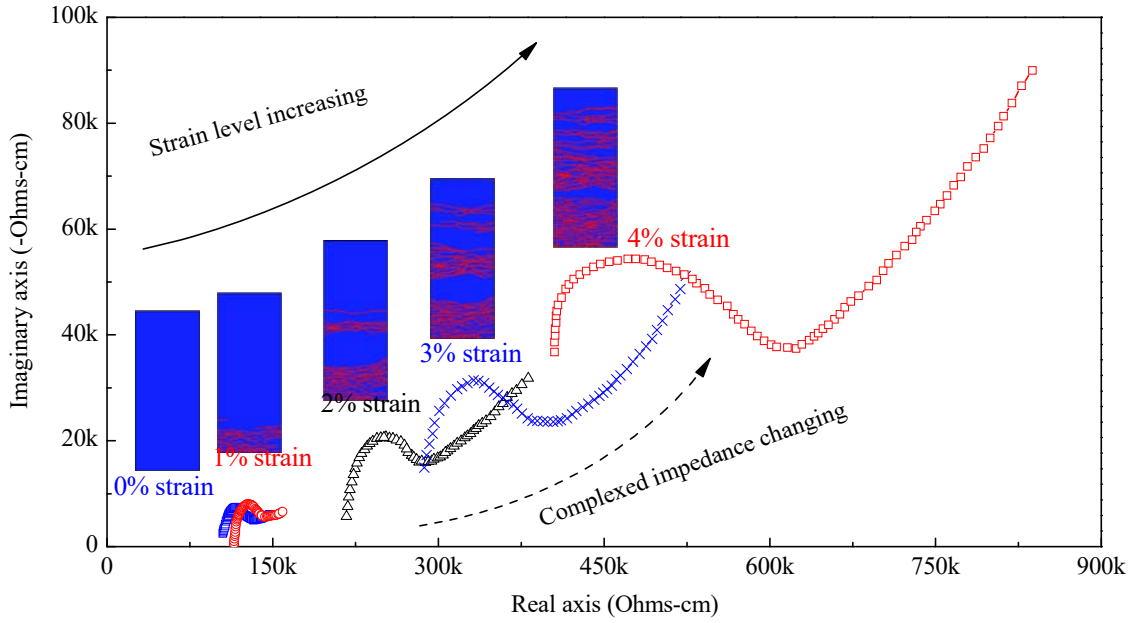

(a)

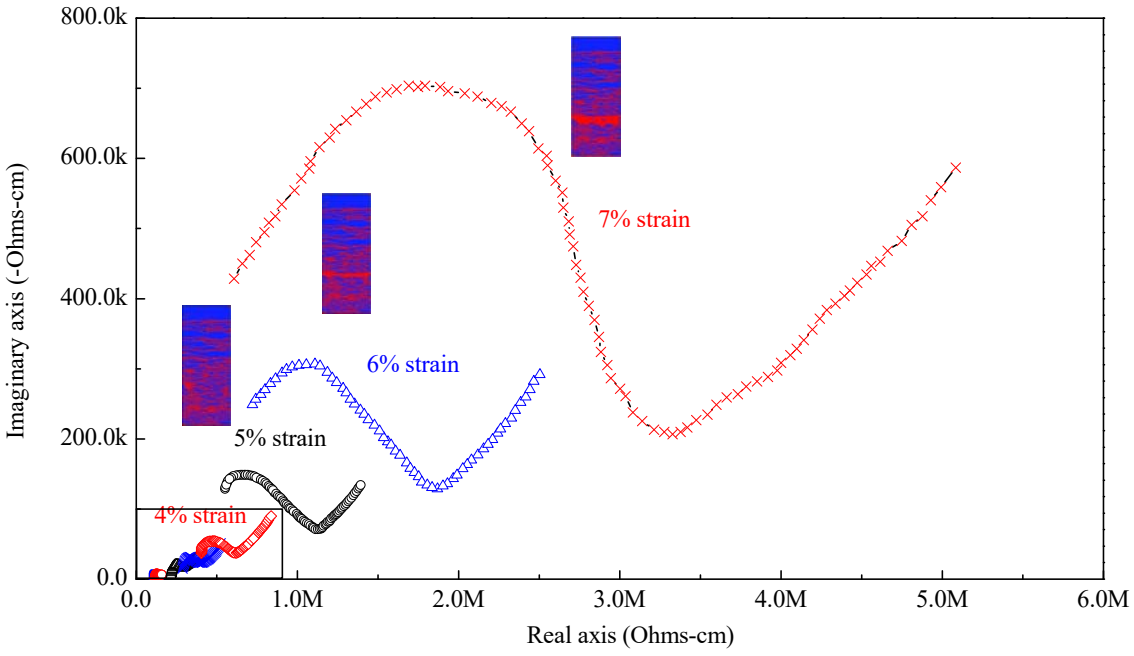

(b)

Figure 3.50. Effect of material damage process on the complex impedance (a) multiple microcracking during strain hardening; (b) localized fracture during tension softening

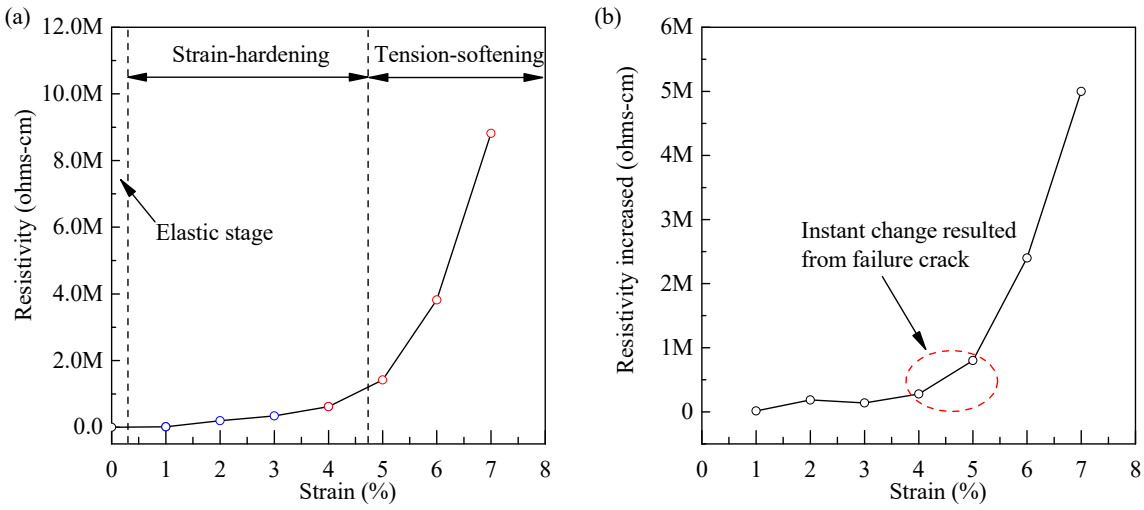

Figure 3.51. Resistivity of the resistor element in MSC vs. tensile strain.: (a) resistivity vs. tensile strain; (b) resistivity change vs. tensile strain.

3.10 Summary of accomplishments

A new generation of multifunctional strain-hardening cementitious materials (MSCs) for SNF storage systems was successfully developed. The MSCs uniquely possess extraordinary damage tolerance and self-sensing capacity. With a tensile strain capacity of more than 4%, MSCs exhibit strong piezoresistive behavior at both elastic and inelastic stages. The elastic gage factors are 17, 62 and 56 for 2.5%, 5% and 10% MSCs, respectively, higher than the elastic target gage factor of 5 specified in the proposal. The inelastic gage factors are 6413, 4134 and 2236 in average for 2.5%, 5% and 10% MSC specimens, respectively, far above the target inelastic gage factor of 20 specified in the proposal. These gage factors are also well above the gage factor of 2 (elastic only) for commercial strain gages. Larger gage factors mean that a small change in strain can be reflected as large change in the measured impedance, indicating a higher sensing capacity. Robust strain self-sensing in MSCs was achieved based on their large gage factors and strong signal to noise ratios.

A fundamental understanding of the electrical, electro-chemical, and electro-mechanical behavior of cementitious materials was obtained. Electrical impedance spectroscopy and equivalent circuit analysis on various mixtures with different binder ingredients, water/binder ratios, hydration chemistry, incorporation of conductive nano-materials, age effects, and damage levels revealed the age-dependent material electrical properties at composite, component and ingredient levels. The equivalent circuit model was well validated by the experimental data. The results laid the groundwork for the systematic

development of MSCs for SNF storage applications. A comprehensive electrical impedance study, coupled with equivalent circuit analysis, allowed us to tailor the MSC material physical and chemical parameters to exhibit strong correlation between complex impedance and material strain, crack width, damage level, and healing. Furthermore, in order to correlate MSC material mechanical behavior (e.g. strain and damage) with electrical response, a four-point probing piezoresistivity test method was established. The results also revealed the effect of conductive nanoparticles on the electromechanical properties of MSC composite material systems.

The significance of this study was three-fold: First, it allowed us to understand the true electrical behavior of the material at component, phases, microstructure, mesostructure, and composite scales. This made it possible for systematically tailoring the MSC at different scales so that the material can to behave as versatile piezoresistive sensors, connecting mechanical or electrochemical stimulus to different electrical responses. Second, through material tailoring, strain sensing became possible through establishing strong gage factors at elastic, inelastic, and tension softening stages. Finally, sensing of damage as well as healing was achieved for the first time, which can capture crack opening, distributed damage evolution, and autogenously healing processes. Further efforts were made on improving these properties. A series of MSC were further designed, guided by the EIS results, the equivalent circuit model parameter studies, and micromechanics-based model that evaluated the strain-hardening criteria of MSC. Meanwhile, the material design also took into account the effect of chemical composition and hydration products on the rheology of the MSC material during fresh state, and their consequent effects on the dispersion of particles as well as the age-dependent microstructure evolution within MSC during hardened state.

In addition to experimental development and characterization, analytical models were established on the electromechanical behavior of MSC at multiple scales: (a) the change in contact impedance due to fiber debonding and pullout behavior at microscale, (b) the impedance vs. crack opening relation at mesoscale, and (c) the impedance vs. strain and damage level relation at macroscale. The multi-scale model coupled micromechanics with equivalent circuit modeling, and was validated by multi-scale experimental data. The multi-scale model elucidated the fundamental mechanisms that were responsible for the unique electromechanical behavior of MSCs at elastic, strain-hardening and tension softening stages.

3.11 References

[1] C. B. J., "Microstructure studies of hydrating portland cement-based materials using impedance spectroscopy," Ph.D, Civil Engineering, Northwestern University, Evanston, Illinois, 1993.

[2] F. Rajabipour, "Fundamental Investigations on Utilizing Electrical Sensing to Improve Life Cycle Modeling of Concrete Structures," Master of Science, Civil Engineering, Purdue University, 2003.

[3] H. Ma, D. Hou, J. Liu, and Z. Li, "Estimate the relative electrical conductivity of C–S–H gel from experimental results," *Construction and Building Materials,* vol. 71, pp. 392-396, 11/30/ 2014.

[4] n. University. *The science of concrete*.

4. DISTRIBUTED DAMAGE SELF-SENSING IN MSC THROUGH IMPEDANCE TOMOGRAPHY

4.1 Introduction

Through engineering conductive nanomaterials into the strain-hardening cementitious composite materials, the elastic and inelastic strain, and damage process, were strongly correlated to electrical conductivity change through large gage factors. To render the electromechanical sensing method proposed herein attractive for industrial adoption, algorithms are needed to autonomously measure strain and identify damage based on an analysis of the input-output voltages taken from MSC elements stimulated electrically. In this project, imaging techniques first developed for the biomedical and geophysics fields were adopted and modified to assist in performing electrical impedance tomography (EIT) on MSC specimens. This task made it possible to visualize material conductivity in three dimensions based upon voltage measurements collected in MSC specimens in a multitude of probe locations. Conductivity reconstruction was a difficult nonlinear inverse problem defined by an underdetermined set of linear equations based on the Poisson equation. Finite element models (FEM) that describe the forward problem and the backward problem were implemented.

In a spent nuclear fuel storage system, the functionality and effectiveness of components that provide radiation shielding, as well as those related to overall structural integrity are ensured by periodic visual inspections and measurements taken with portable equipment and instrumentation. Dry cask storage systems must have the ability for continuous monitoring of temperature, pressure, structure stability, leakage, and degradation, following NRC regulations[1, 2].

For overpack, visual inspection[3] is the main method carried out on the accessible concrete surfaces. Practically, crack comparators and remote portable cameras are set up to measure the extent of the concrete surface damage. Visual inspection of in-service concrete structures needs to follow ACI 201.1R(ACI, 2008a)[4]. Based on the ACI code[5], the frequency of visual inspection on a concrete surface is once per 5 years for structures exposed to the natural environment (direct and indirect). Inspection of air vents is required daily for most Dry Cask Storage Systems(DCSSs). Routine weekly or monthly inspection of the DCSS exterior should also be carried out[6]. The limitations for visual inspection are obvious. The subsurface cracking, internal delamination, voids, and corrosion of the steel reinforcement cannot be detected by visual inspection. It is difficult to conduct a qualitative study with visual inspection and to discern trends in data. The regular visual inspections are known to be highly subjective, labor-intensive, and limited to accessible locations. Taking digital images of suspected regions and the application of image processing techniques (e.g. digital image correlation technique) is limited to surface features. While great technological advances have been made in recent years on many fronts in the field of structural health

monitoring (SHM), there still remain very few implementations of SHM systems in operational structures. The main limitations are **indirect damage sensing** and **point-based sensing**. Sensors in common use do not detect damage directly. Complex physics-based models are needed to correlate structural response measurements to damage states. Robust algorithms that are generically applicable to the nuclear structural concrete components do not yet exist. Furthermore, the widely used sensors are point-based sensors that cannot accurately identify spatially distributed damage or deterioration such as cracking and corrosion. A dense network of point-based sensors is necessary for analytical models to extrapolate the point measurements to predicted component behavior, but highly costly. Distributed and direct sensing that provides the spatial resolution necessary to localize and quantify the severity of concrete damage and deterioration is direly needed.

In this project, the innovative multifunctional strain-hardening and self-sensing concrete (MSC) was integrated with advanced electrical impedance tomography (EIT) algorithms for achieving distributed and direct damage sensing in concrete structures. Using electrical stimulation and advanced modeling methods, spatial mapping offering a visual depiction of concrete performance over time was gained. MSC can behave as a sensor itself, thus offering spatial data wherever the material is located. This eliminates the need for installing and maintaining a dense array of sensors; instead, inexpensive electrodes can be attached to structural component boundaries to apply electrical input and measure output signals that collect spatial information throughout the material. This approach allows for spatial sensing inside the material although the electrodes are only required at boundaries.

4.2 Complete Electrode Model

The complete electrode model is the means by which the boundary electrodes are accurately modeled. In the current study, the common used mesh generator Netgen is used to create the meshes by performing a mixture of advancing front surface meshing and Delaunay tessellation followed by mesh optimization. Once the model is created, it is necessary to establish mathematical formulae relating the physical conditions imposed at the boundary to the electric field in the interior.

Based on Maxwell's equations for electro-magnetics, the flux of electric field E through a closed surface equals the total charge density inside divided by ϵ_0 constant, as shown in the **Equation 4.1**. In the following equations, E is the electric field, B is the magnetic field, ρ is the charge density, j is the current density, ν is the outward unit normal vector, c is the speed of the light, and ε_0 is the constant.

$$\nabla \cdot E = \frac{\rho}{\varepsilon_0} \tag{4.1}$$

In addition, the negative rate of change of the flux of B through the loop can be expressed as **Equation 4.2**,

$$\nabla \times E = -\frac{\partial \beta}{\partial t} \tag{4.2}$$

The flux of *B* through a closed surface is equal to zero,

$$\nabla \bullet B = 0 \tag{4.3}$$

Then,

$$\nabla \times B = \frac{j}{\varepsilon_0} + \frac{\partial E}{\partial t} \tag{4.4}$$

As for EIT technology, the excitation signal believed as quasi-static as the driving patterns are time harmonic at a low frequency. In computation, the static conditions are assumed as static, assuming measurements are conducted instantaneously. The magnetization components are neglected,

$$\frac{\partial B}{\partial t} \approx 0 \quad \text{and} \quad \frac{\partial E}{\partial t} \approx 0 \tag{4.5}$$

Then

$$\nabla \times E = 0 \tag{4.6}$$

Therefore, when the curl of the vector E is equal to zero, then there exists a scalar u whose gradient is equal to that vector,

$$E = -\nabla u \tag{4.7}$$

Then assuming static current signal injected, **Equation 4.5**. becomes:

$$\nabla \times B = \frac{j}{\varepsilon_0} \tag{4.8}$$

In these conditions, the current density can be assumed to be time invariant. If I_n^d is the nth current pattern driven into the volume, from a boundary electrode surface s then

$$I_n^d = \int_s j \cdot v ds \tag{4.9}$$

Based on the charge conservation law,

$$\int_s j \cdot dS = -\frac{d}{dt}(Q_\Omega) \tag{4.10}$$

The charge in the interior of the volume Q_Ω can be expressed as

$$Q_\Omega = \int_\Omega \rho dV \tag{4.11}$$

Combining equation **Equation 4.9**, **Equation 4.10, Equation 4.11**.

$$\nabla \cdot j = -\frac{\partial \rho}{\partial t} \tag{4.12}$$

Since there are no current sources in the interior of the volume and E does not change with time, **Equation 4.12** becomes,

$$\nabla \cdot j = 0 \tag{4.13}$$

In a linear isotropic medium, the current density and the electric field are related by the approximation

$$j \approx \gamma E \approx (\sigma + i\omega\varepsilon)E \tag{4.14}$$

Then

$$\nabla \cdot \gamma E = 0 \tag{4.15}$$

Combine **Equation 4.15** and **Equation 4.7**, it yields the laplacian elliptic partial differential equation,

$$\begin{aligned} \nabla \cdot \gamma(-\nabla u) &= 0 \\ \nabla \cdot \gamma(\nabla u) &= 0 \end{aligned} \tag{4.16}$$

The complete electrode model consists of the partial differential **Equation 4.16** and the following boundary conditions

$$\int_{el} \sigma(x) \frac{\partial u(x)}{\partial \bar{n}} dS = I_l, \quad l = 1,...N_{el} \tag{4.17}$$

$$u(x) + z_l \sigma(x) \frac{\partial u(x)}{\partial \bar{n}} = U_l, \quad x \; belongs \; to \; \partial\Omega, l = 1,...N_{el} \tag{4.18}$$

$$\sigma(x) \frac{\partial u(x)}{\partial \bar{n}} = 0, \quad x \; belongs \; to \; \partial\Omega \setminus \bigcup_{l=1}^{N_{el}} e_l \tag{4.19}$$

Where U_l is the (RMS) potential on l^{th} the electrode, I_l denotes the RMS of the electric current applied to the electrode e_l, z_l is the constant impedance between the l^{th} electrode and the domain Ω, and $\bar{n}$ is the unit normal pointing outward from the boundary $\partial\Omega$. In addition to boundary conditions, the charge conservation law has to be obeyed. Thus **Equation 4.20** needs to be satisfied:

$$\sum_{l=1}^{N_{el}} I_l = 0 \tag{4.20}$$

Further, the potential reference level needs to be fixed,

$$\sum_{l=1}^{N_{el}} U_l = 0 \tag{4.21}$$

4.3 Forward problem with Finite element method

Finite element approximation for the complete electrode model is employed to tackle the forward questions. Firstly, the weak form is derived for Galerkin method.

$$\phi_i(x,y,z) = \begin{cases} 1 & \text{on vertex } i, \\ 0 & \text{otherwise.} \end{cases} \tag{4.22}$$

Then u_h can be expressed as

$$u_h = \sum_{i=1}^{n} U_i \phi_i \tag{4.23}$$

Where U_i is the value of the potential at the vertex i and n the number of vertices in the model. For the FEM derivations, the discrete conductivity distribution vector $\gamma \in \mathbb{C}^n$ is taken as

$$\gamma = \sum_{i=1}^{k} \gamma_i \psi_i \tag{4.24}$$

Where,

$$\psi_i(x,y,z) = \begin{cases} 1 & \text{on element } i, \\ 0 & \text{otherwise.} \end{cases} \tag{4.25}$$

Combining **Equation 4.22** and **Equation 4.23** leads to

$$\iiint_{\Omega} \gamma \cdot \nabla \phi_i \cdot \nabla u_h dx\, dy\, dz = 0 \qquad i = 1, \ldots n \tag{4.26}$$

Applying Green's second identity on **Equation 4.26**,

$$\iiint_{\Omega} \gamma \cdot \nabla \phi_i \cdot \nabla u_h dx\, dy\, dz = \iint_{\partial\Omega} \gamma \phi_i \nabla u_h ds \tag{4.27}$$

Where

$$\nabla u_h = \frac{\partial u_h}{\partial v} \tag{4.28}$$

Then **Equation 4.28** becomes

$$\iiint_{\Omega_E} \gamma \left(\frac{\partial \phi_i}{\partial x} \frac{\partial u_h}{\partial x} + \frac{\partial \phi_i}{\partial y} \frac{\partial u_h}{\partial y} + \frac{\partial \phi_i}{\partial z} \frac{\partial u_h}{\partial z}\right) dx\, dy\, dz = \iint_{\partial\Omega_E} \gamma \phi_i \frac{\partial u_h}{\partial v} ds \tag{4.29}$$

For $i = 1, \ldots, 4$, and plugging in the boundary condition yields,

$$\iiint_{\Omega_E} \gamma \left(\frac{\partial \phi_i}{\partial x} \frac{\partial u_h}{\partial x} + \frac{\partial \phi_i}{\partial y} \frac{\partial u_h}{\partial y} + \frac{\partial \phi_i}{\partial z} \frac{\partial u_h}{\partial z}\right) dx\, dy\, dz = \iint_{\partial\Omega_E} \phi_i \frac{1}{z_l} (V_l - u_h) ds \tag{4.30}$$

Where z_l is the contact impedance of electrode l and V_l the potential measured on it. And then, substituting u_h from **Equation 4.28** leads to

$$\iiint_{\Omega_E} \gamma\left(\frac{\partial \phi_i}{\partial x}\frac{U_j \partial \phi_j}{\partial x} + \frac{\partial \phi_i}{\partial y}\frac{U_j \partial \phi_j}{\partial y} + \frac{\partial \phi_i}{\partial z}\frac{U_j \partial \phi_j}{\partial z}\right) dx\, dy\, dz = \iint_{\partial\Omega_E} \phi_i \frac{1}{z_l}(U_j \partial \phi_j - V_l) ds \quad (4.31)$$

Generalizing equations for the n'th element, the global conductance matrix is assembled by evaluating the following entries for each of the elements. These entries formalized as local matrices $A_m \in \mathbb{C}^{4\times4}$, $A_z \in \mathbb{R}^{4\times4}$ and $A_v \in \mathbb{R}^4$ arise from the various factors of generalization equation and depend on the actual location of the element.

If $U \in \mathbb{C}^4$ is the vector of the potential values at $n_1, \cdots, n_4$, in each element the following relation holds

$$(A_m + A_z)U = A_v V_l \quad (4.32)$$

For a finite set of current patterns I^d, the forward problem is formulated as a system of linear equations

$$\begin{bmatrix} A_M + A_Z & A_V \\ A_V^* & A_D \end{bmatrix} \begin{bmatrix} U \\ V_L \end{bmatrix} = \begin{bmatrix} 0 \\ I^d \end{bmatrix} \quad (4.33)$$

A set of driving current patterns is shown below:

$$I^d = [I_1^d \; I_2^d \; \dots \; I_k^d] \quad (4.34)$$

Where $U \in \mathbb{R}^{L\times k}$ the conservation of charge theorem imposes

$$\int_{\partial\Omega} j = \sum_{i=1}^{k} I_i^d = 0 \quad (4.35)$$

Given a finite element model with known admittivity distribution and a set of current patterns the potential at the vertices of the model and the boundary electrodes can be calculated from equation 34. Expressing above equation in a more condensed form, the forward problem becomes

$$Au = b \quad (4.36)$$

It has an algebraic solution

$$u = A^{-1}b \quad (4.37)$$

The forward problem can be solved either directly or iteratively. In this study, it is solved iteratively. In this study, the iterative schemes for the forward problem are the linear preconditioned conjugate gradients iteration, designed for solving the LS problem.

This iterative algorithm generates a sequence of solutions which minimize the least squares residual

$$\arg_u \min \frac{1}{2} \| Au - b \|_2^2 \tag{4.38}$$

It is known that the rate of convergence can be drastically improved when the system is properly preconditioned. If $M \in \mathbb{R}^{n+L \times n+L}$ is a proper preconditioned, the modified forward problem becomes

$$M^{-1} A u = M^{-1} b \tag{4.39}$$

Which has a solution identical to the original problem, only this time the convergence depends on the properties of the $M^{-1}A$ matrix than A alone.

The preconditioner is selected in a way that

$$\begin{aligned} M^{-1} A &\approx I \\ cond(M^{-1}A) &< cond(A) \end{aligned} \tag{4.40}$$

Where I is the identity matrix.

4.4 Inverse problem

In order to solve the inverse problem, second derivative terms from the Taylor expansion of the nonlinear forward problem are eliminated, so that problems are inversed into well posed problem. The other approach is using some Tikhonov type regularization to obtain a step solution within the Newton-Raphson algorithm, considering a linearized form of the inverse problem.

In principle, for the inverse admittivity problem the aim is to obtain a stable solution $\xi*$ which minimizes the residual error

$$f(\xi) = \frac{1}{2}(F(\xi) - V)^*(F(\xi) - V) = \frac{1}{2} \| F(\xi) - V \|_2^2 \tag{4.41}$$

Where $F(\xi) : \mathbb{C}^n \to \mathbb{C}^m$ is the nonlinear forward operator in a problem with n parameters and m measurements.

Let $D(\xi) = F(\xi) - V$, the Taylor series of $D(\xi)$ is

$$D(\xi + h) = D(\xi) + D'(\xi)h + \frac{1}{2} D''(\xi)h^2 + O(h^3) \tag{4.42}$$

The first method involves neglecting second order terms in above equation

$$\begin{aligned} D(\xi) &= -D'(\xi)h \\ h_{NR} &= -(D'(\xi))^{-1} D(\xi) = F'(\xi)(V - F(\xi)) \end{aligned} \tag{4.43}$$

Finally arriving the Newton-Raphson iterative solution

$$\xi_{k+1} = \xi_k + F'(\xi_k)^{-1}(V - F(\xi_k)) \tag{4.44}$$

Where $F'(\xi_k)$ is the Jacobian matrix. And then

$$\begin{aligned} \nabla f &= D'(\xi) * D(\xi) = F'(\xi) * (F(\xi) - V) \\ Hf &= D'(\xi) * D'(\xi) + D''(\xi) * D(\xi) \\ &= F'(\xi) * F'(\xi) + \sum_i F_i''(\xi)(F(\xi) - V) \end{aligned} \tag{4.45}$$

The second derivative terms in **Equation 4.45** can be neglected. Therefore, we can assume

$$\sum_i F_i''(\xi)(F(\xi) - V) = 0 \tag{4.46}$$

Then

$$f(\xi + h) = f(\xi) + F'(\xi) * (F(\xi) - V)h + \frac{1}{2} F'(\xi) * F(\xi)h^2 = 0 \tag{4.47}$$

Setting the gradient of equation to zero yields

$$h \cdot \nabla f = F'(\xi) * (F(\xi) - V)h + hF'(\xi) * F(\xi) = 0 \tag{4.48}$$

From where the step h is derived as

$$h = F'(\xi)^{\dagger}(V - F(\xi)) \tag{4.49}$$

Where $F'(\xi)^{\dagger}$ is Moore-Penrose generalized inverse of $F'(\xi)$. Then

$$\begin{aligned} h_{GN} &= F'(\xi)^{\dagger}(V - F(\xi)) \\ \xi_{k+1} &= \xi_k + h_{GN} \end{aligned} \tag{4.50}$$

Then

$$\sum_i F_i''(\xi)(F(\xi) - V) = \lambda I \tag{4.51}$$

And then the residual error becomes

$$f(\xi + h) = f(\xi) + F'(\xi) * (F(\xi) - V)h + \frac{1}{2}(F'(\xi) * F(\xi) + \lambda I)h^2 = 0 \tag{4.52}$$

And setting the gradient to zero, which leads to the Tikhonov regularization solution

$$h = (F'(\xi) * F(\xi) + \lambda I)^{-1} F'(\xi) * (V - F(\xi)) \tag{4.53}$$

Substituting this result into the newton-raphson formula gives the Levenberg-Marquardt method

$$\begin{aligned} h_{LM} &= (F'(\xi) * F(\xi) + \lambda I)^{-1} F'(\xi) * (V - F(\xi)) \\ \xi_{k+1} &= \xi_k + h_{LM} \end{aligned} \tag{4.54}$$

Therefore, the inverse problem can be approximately solved with Finite element method.

Figure 4.1 shows the adjacent electrical impedance tomography measurement approach.

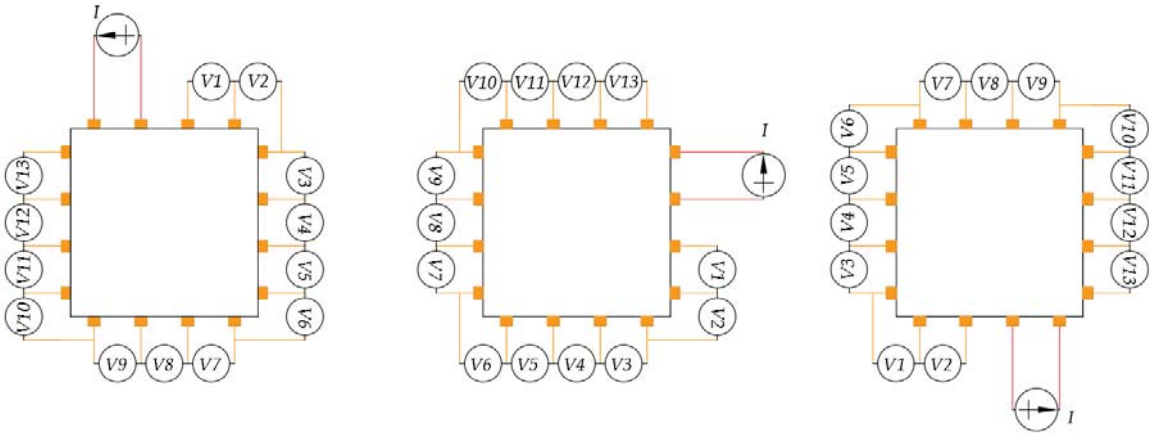

Figure 4.1: Electrical impedance tomography measurement approach.

4.5 Forward problem calculation and corresponding inverse problem calculation

4.5.1 Forward problem calculation

Forward problem was first studied to provide fundamental information for the inverse problem computation. The panel specimen was simulated with Finite Element Method (FEM). As shown in **Figure 4.2**, the panel specimen was simplified as a 2D specimen. The Specimen conductivity was considered as constant 1S/m. With 1 *V* voltage applied on the specimen from different probes, the voltage distribution on the specimen was plotted in **Figure 4.2**. **Figure 4.2** demonstrating 4 types of current injection pattern. The feasibility of FEM method for normal panel specimen was verified.

A panel specimen with a hole drilled in the middle was simulated with FEM. **Figure 4.3** demonstrated the 2D model with a hole in the middle and the corresponding FEM mesh. It was shown that compared with **Figure 4.2**. The voltage distribution on the specimen was different indicating the EIT method was feasible to perform on the panel specimen.

In addition, a panel specimen with a notch on one side of the specimen was simulated. Voltage distributions with nine current inject pattern were plotted in **Figure 4.3**. Compared with **Figure 4.2 and 4.3**, the voltage distribution was totally different. Therefore, it was concluded that with current injection through the boundary, the captured voltage distribution as able to reflect the damage condition.

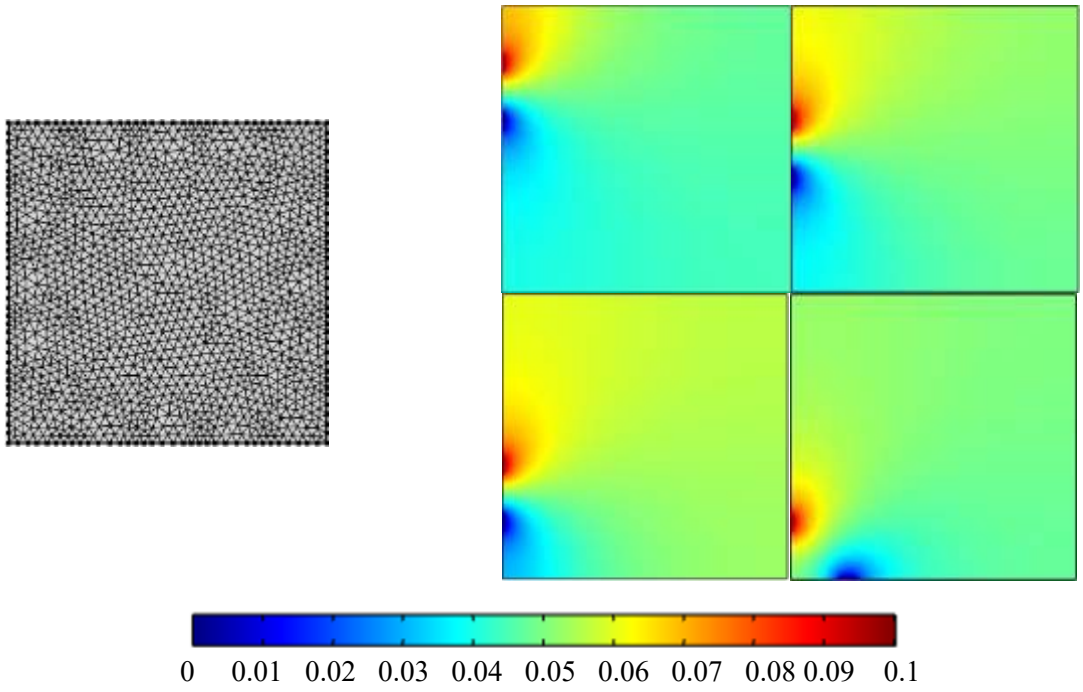

Figure 4.2: Electrical potential distribution in panel specimen. The FEM model and four current injection pattern.

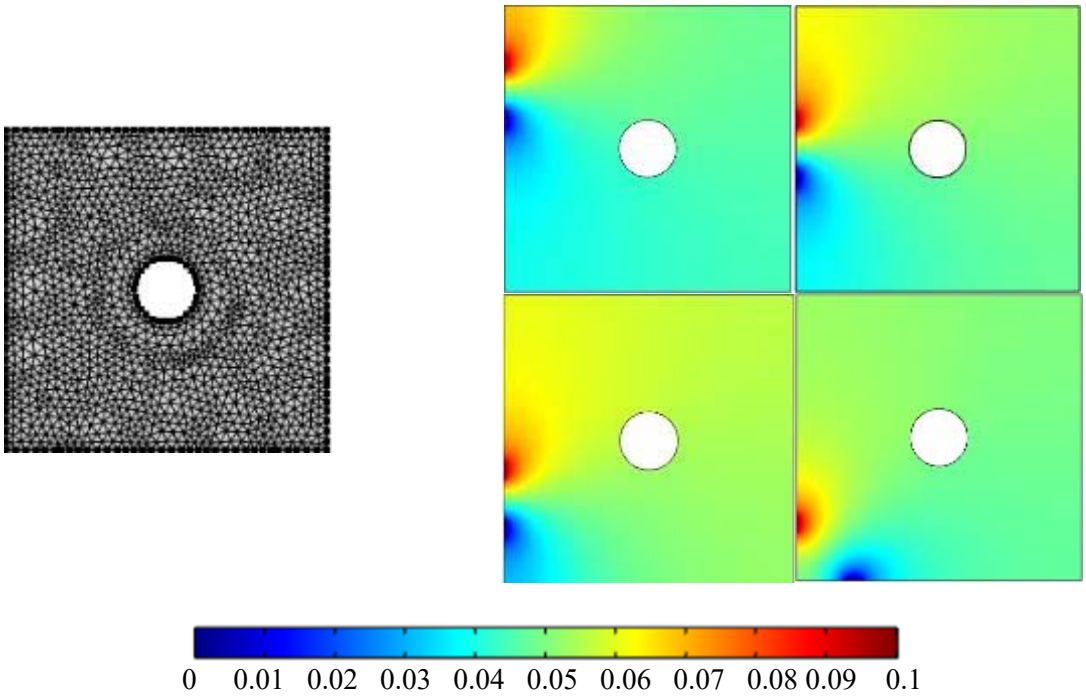

Figure 4.3: Electrical potential distribution in panel with hole in the middle.

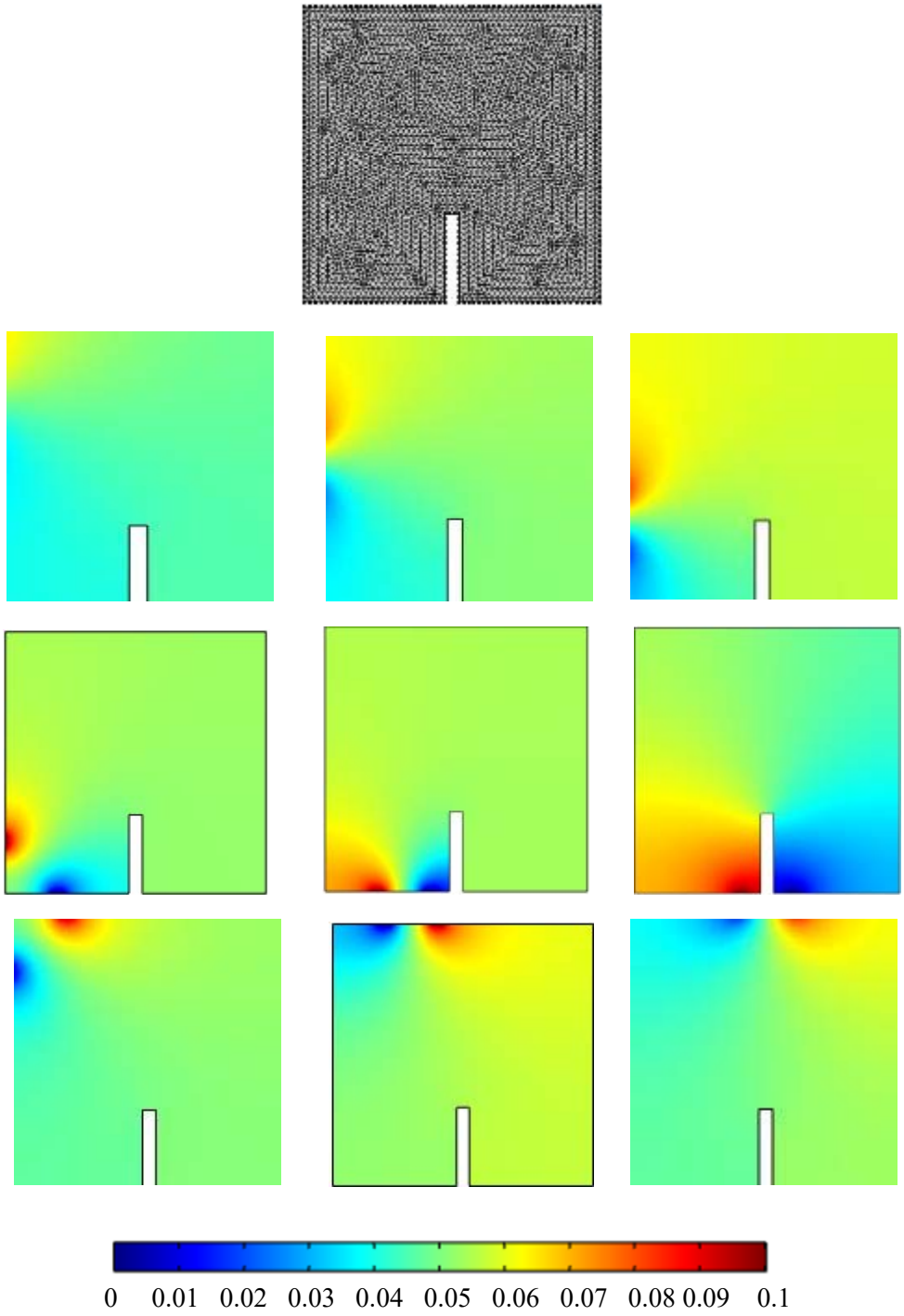

Figure 4.4: Electrical potential distribution in a panel with the notch.

Next, the three-dimensional FEM image reconstruction was conducted. **Figure 4.5** shows the simulated specimen with a length of 6 inch and width of 2 inch. The copper electrodes were wrapped on the two ends of the specimen. The simulated current was injected via top electrodes, and the bottom electrode was grounded.

Then voltage distribution was able to reflect the resistivity distribution in the specimen. The finite element mesh for specimen without cracks and with simulated cracks is shown in **Figure 4.5**. The voltage distribution along the specimen is illustrated in the figure. Then voltage differences between simulation without cracks and simulation with cracks are compared in **Figure 4.6**. It was found that the potential distribution was able to capture damage.

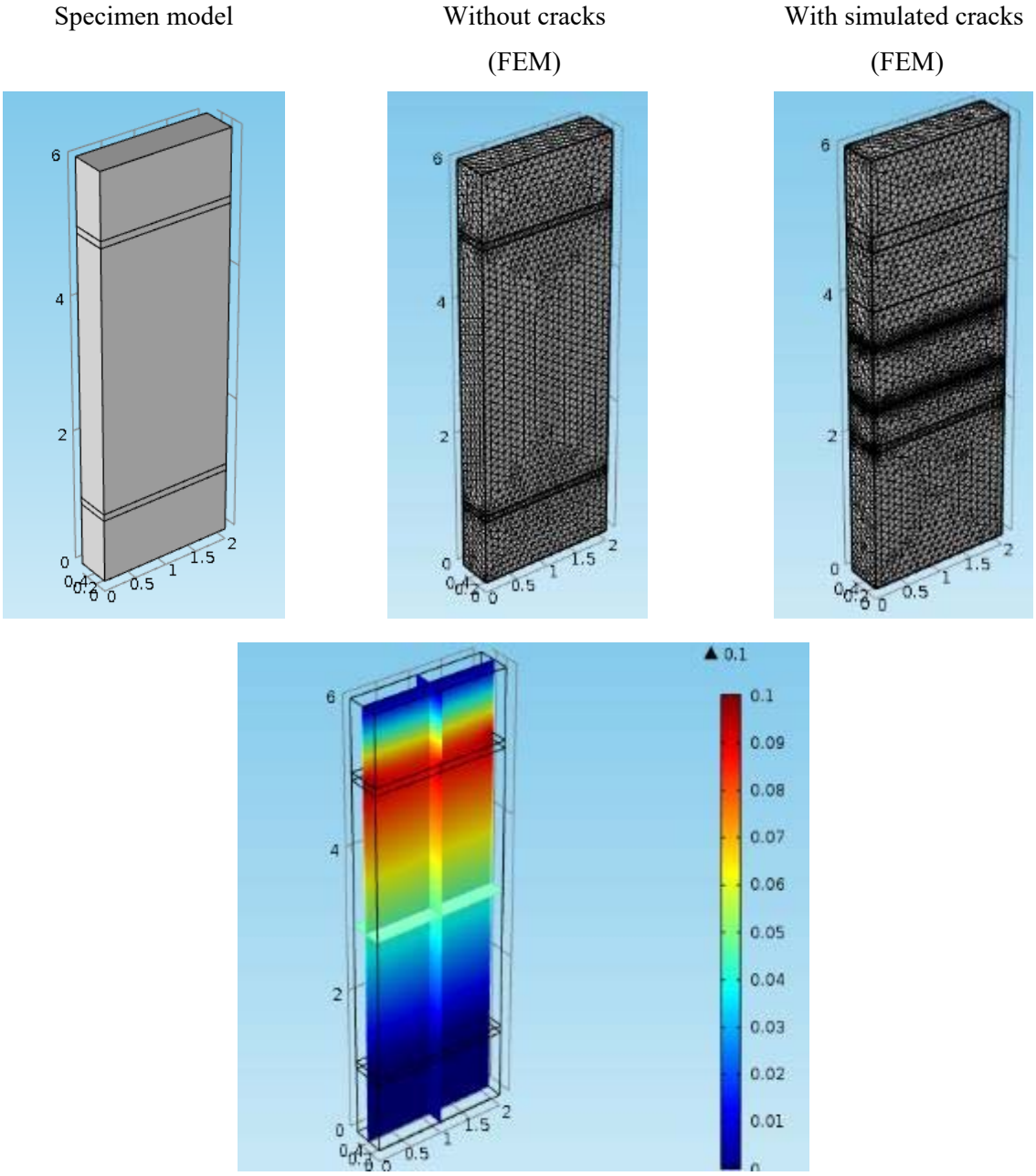

Figure 4.5: Panel specimen with copper electrodes.

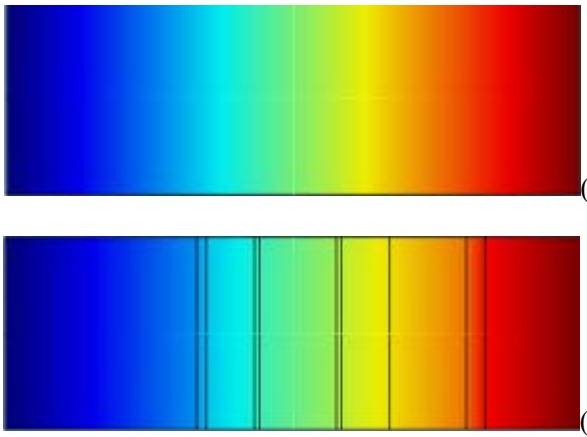

Figure 4.6: Potential distribution for (a) specimen without crack, (b) specimen with crack.

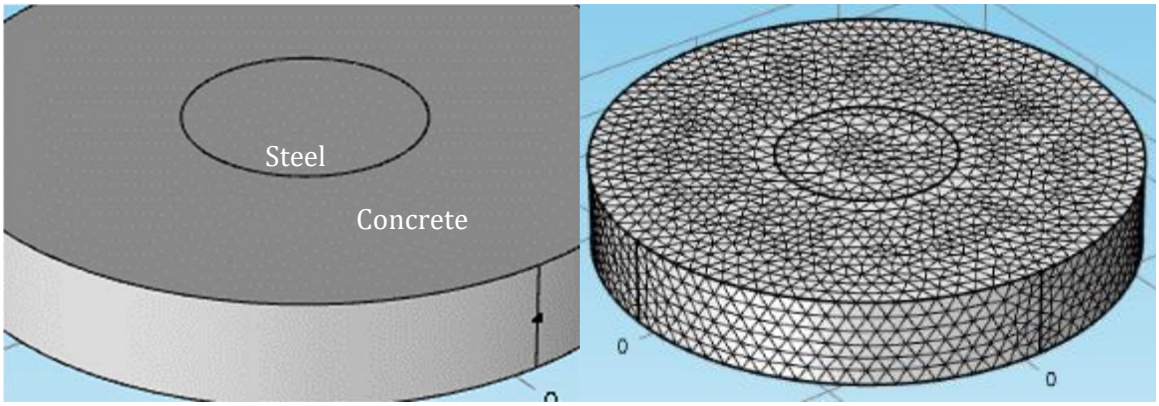

Figure 4.7: Model for concrete with steel.

Electrical impedance tomography to image the condition of embedded steel in concrete and MSC was also studied. As shown in **Figure 4.7**, a steel rod was embedded in a cylindric cementitious sample. The electrical current was injected from one side and the other side was grounded. After computation, the 3D results were shown in **Figure 4.8(a)**. The results were also demonstrated by 2D plot in **Figure 4.8(b) and (c)**. It was observed that the voltage distribution was different between specimens with and without steel reinforcement. It was thus concluded EIT is a feasible method to characterize crack development and steel reinforcement conditions in cementitious materials.

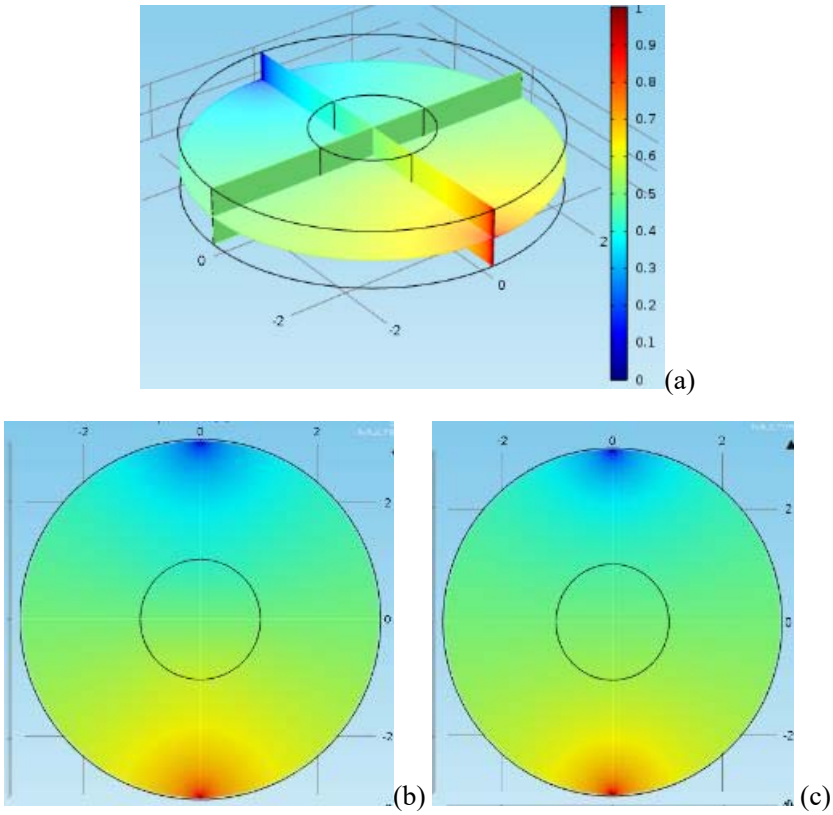

Figure 4.8: Potential distribution for (a) 3D model Comparison for (b) specimen with steel, (c) specimen without steel.

4.5.2 Inverse problem calculation

The inverse computation was carried out. The image reconstruction problems from boundary measurements are in general nonlinear and ill-posed, which are typically solved using a finite element forward model and regularized Newton's method to solve the inverse problem. Currently, there are no commercially available finite element programs for EIT image reconstruction based on complete electrode model.

In this project, the Netgen Mesh Generator was used to generate finite element mesh. NETGEN is an automatic 3d tetrahedral mesh generator. It accepts input from constructive solid geometry (CSG) or boundary representation (BRep) from STL file format.

After generating the finite element mesh, computation was chosen to evaluate different algorithms and to validate the feasibility of the image reconstruction method. The specimen with one center hole is shown in **Figure 4.9**. The electrode number is 16.

The meshing for the specimen is shown in **Figure 4.10**. The conductivity of the specimen was assumed to be uniformly constant. There were 16 electrodes simulated. All 6400 elements were triangular elements. The hole and notch were applied with resistivity ten times more than that of the specimen.

As shown in **figure 4.9**, for the right specimen, the middle part of the specimen was applied with higher resistivity. Then forward computation was conducted and image reconstruction followed using different algorithms: (1) one step Gauss-Newton reconstruction (Tikhonov prior), (2) one step Gauss-Newton reconstruction (NOSER prior), (3) one step Gauss-Newton reconstruction (Laplace filter prior), (4) one step Gauss-Newton reconstruction (automatic hyperparameter selection), and (5) total variation reconstruction. The same simulation experiments were performed on a specimen with a side notch (see **Figure 4.12**), and on a specimen with distributed microcracking damages (see **Figure 4.13**).

The image reconstruction results were plotted in **Figure 4.11**, **Figure 4.12**, and **4.13.** It is shown that the different image reconstruction algorithms provided different image reconstruction quality. For this scenario, total variation reconstruction provided the best results. It was found that the square hole and notch were plotted with EIT image reconstruction. Even for the distributed damages on the specimen, the image reconstruction accurately located damage and identified damage size, as shown in **Figure 4.13**.

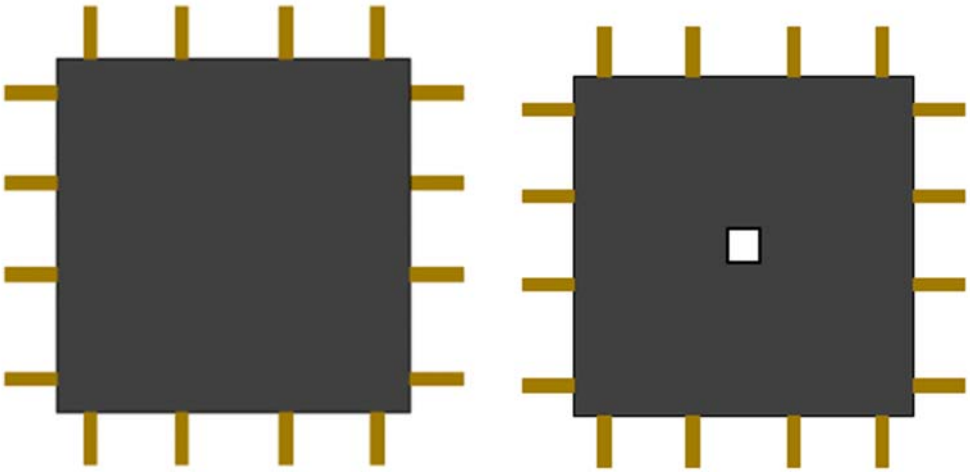

Figure 4.9: Specimen illustration and specimen with a square hole in the middle.

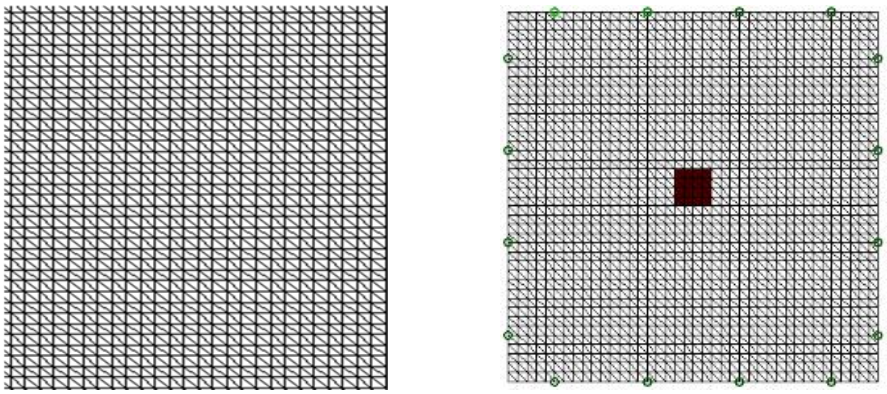

Figure 4.10: FEM model: Specimen illustration and specimen with a square hole in the middle.

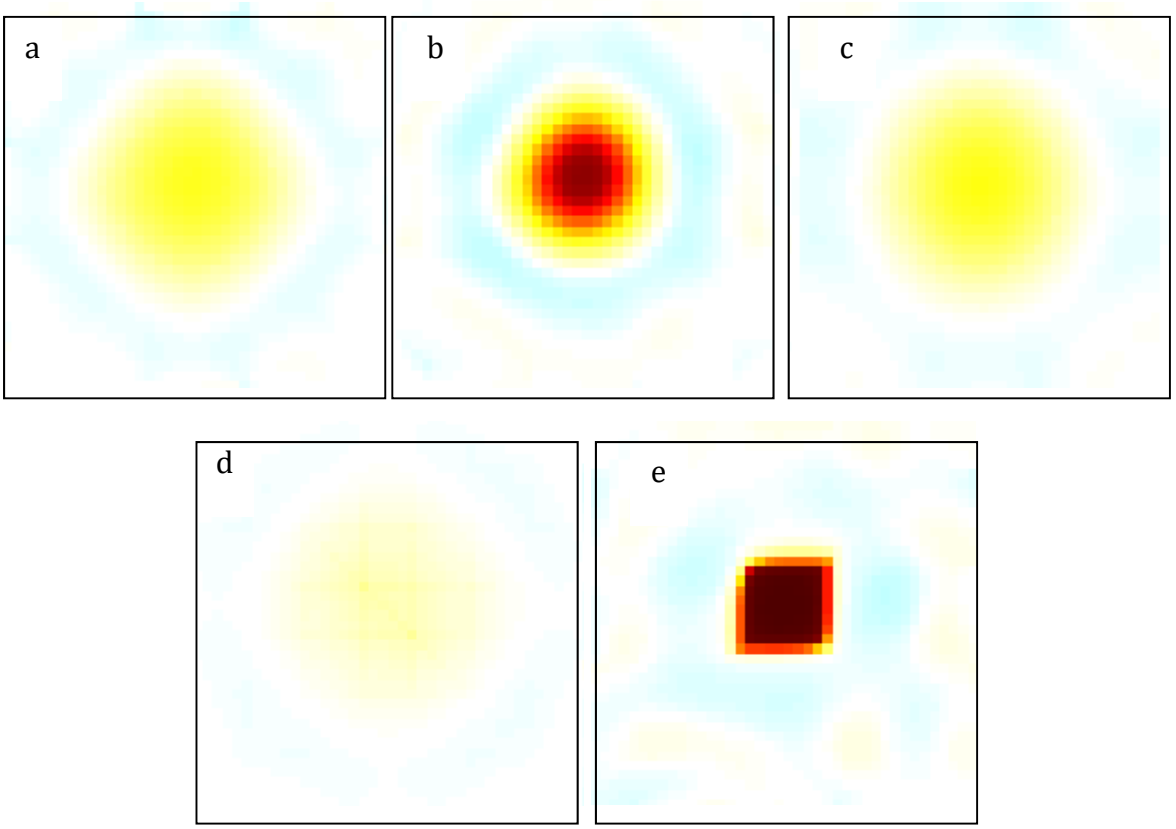

Figure 4.11: Reconstructed images using different algorithms. (a) One step Gauss-Newton reconstruction (Tikhonov prior); (b). One step Gauss-Newton reconstruction (NOSER prior); (c). One step Gauss-Newton reconstruction (Laplace filter prior); (d). One step Gauss-Newton reconstruction (automatic hyperparameter selection); (e). Total variation reconstruction.

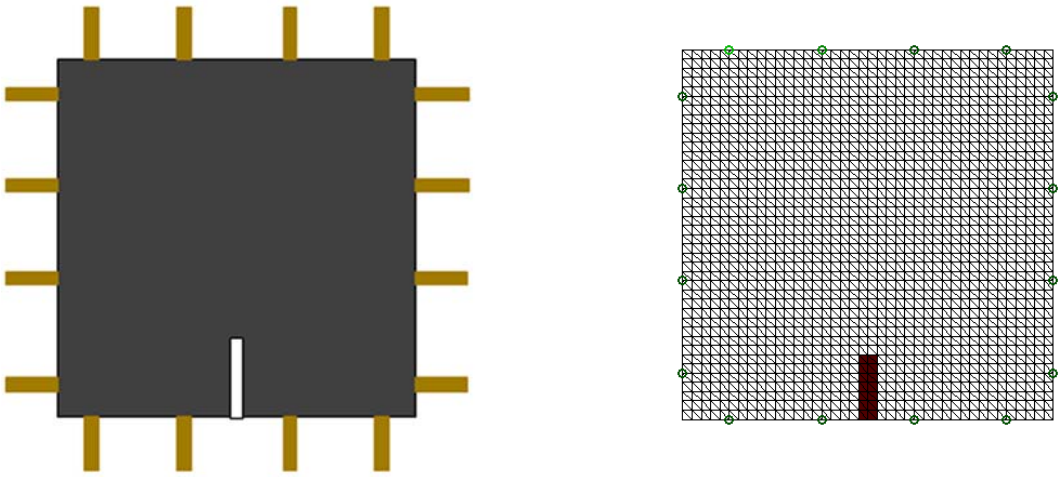

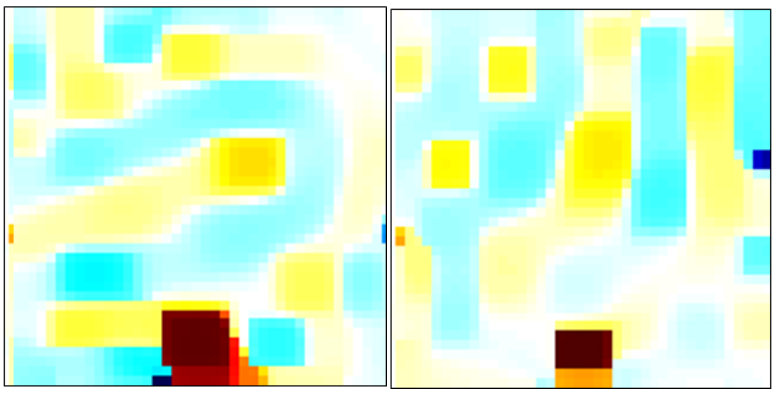

Figure 4.12: Specimen with notch and image reconstruction.

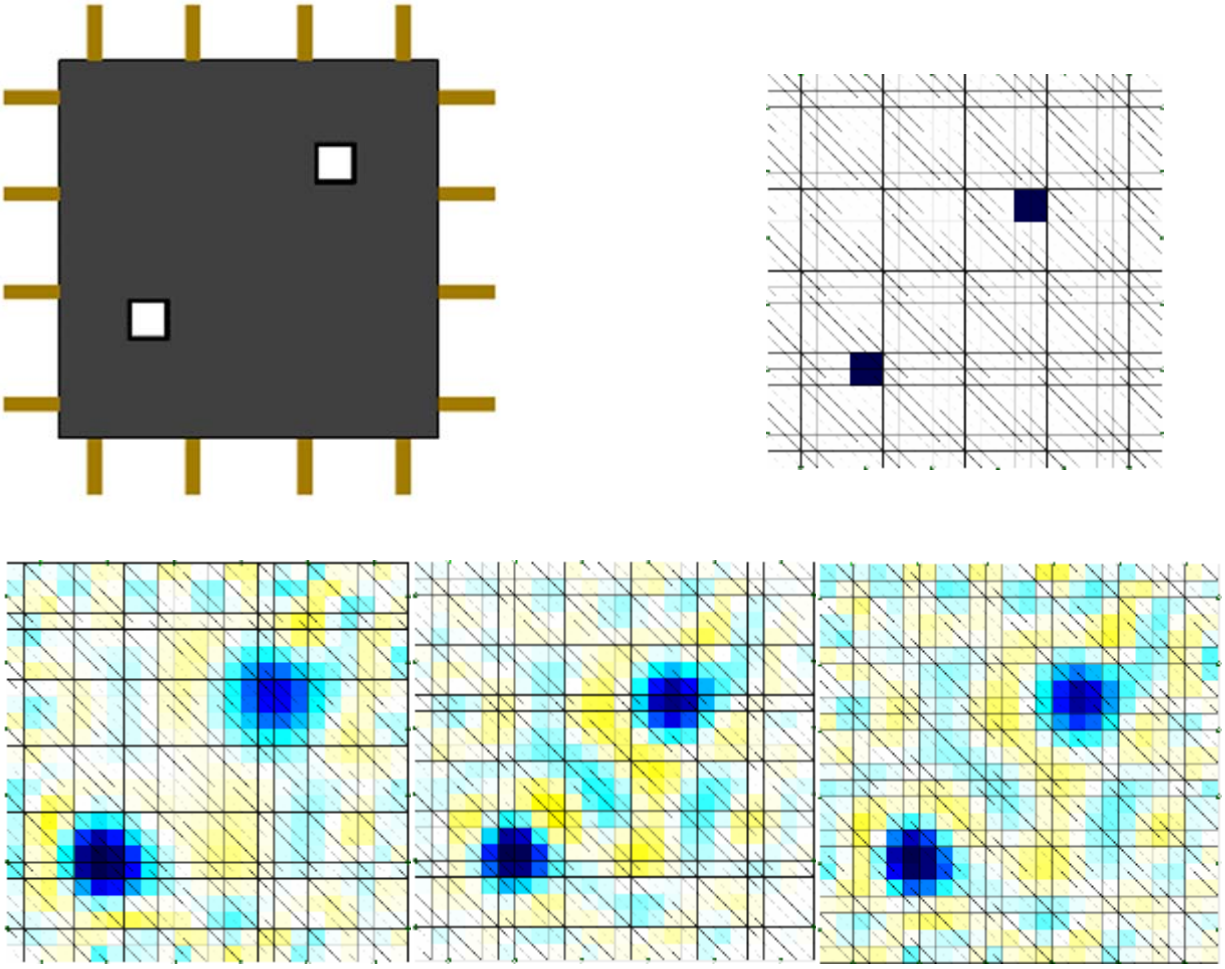

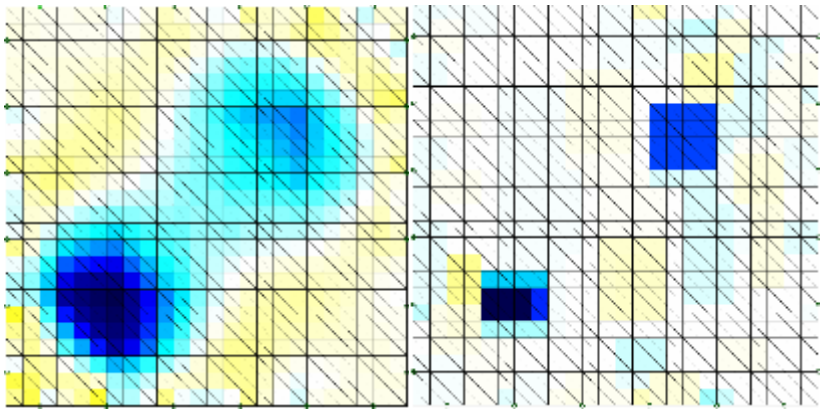

Figure 4.13. Reconstructed images using different algorithms for distributed damage. (a) One step Gauss-Newton reconstruction (Tikhonov prior); (b). One step Gauss-Newton reconstruction (NOSER prior); (c). One step Gauss-Newton reconstruction (Laplace filter prior); (d). One step Gauss-Newton reconstruction (automatic hyperparameter selection); (e). Total variation reconstruction.

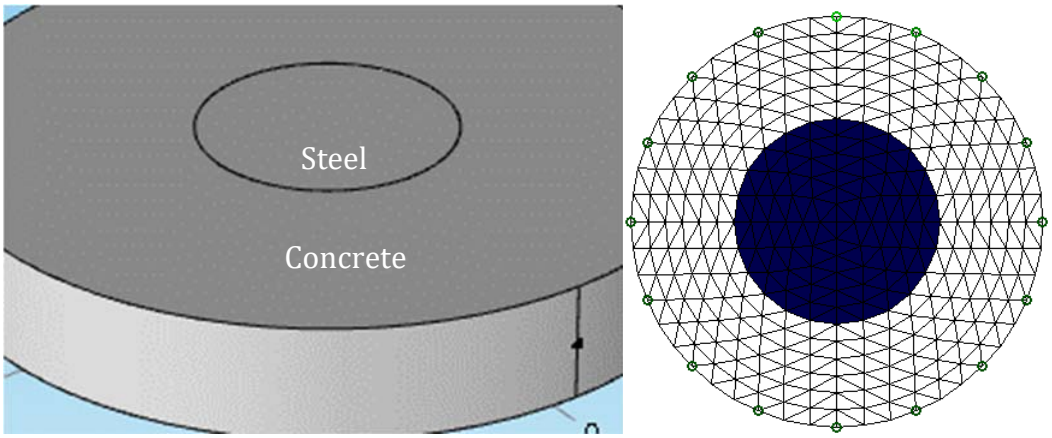

Figure 4.14: Concrete with steel model for image reconstruction.

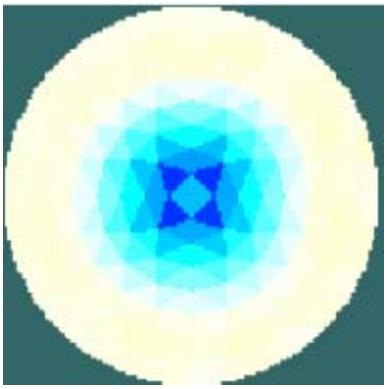

Figure 4.15: Reconstructed images of the model in **Figure 4.14**.

As shown in **Figure 4.14**, a reinforced concrete specimen was simulated. The forward finite element computation was first performed. The simulated measurements were stored for image construction. **Figure 4.15** shows the reconstructed images based on the simulated measurements. It wasfound that the image reconstruction well reflected the presence of steel in the concrete.

4.6 EIT test and results

In this project, the image reconstruction method for electrical impedance tomography on MSC and cementitious materials in general was established. Based on the image reconstruction algorithm, finite element method was conducted to validate the feasibility of the image reconstruction. In addition, electrical impedance tomography experiment was designed in conjunction with LabVIEW software. The MSC material was tailored to reduce the effect of environmental factors on the damage self-sensing sensitivity. The strain-sensing and damage-sensing behavior of MSC under complicated combined loading condition were studied. Example results are shown in sections 4.6.2- 4.6.4. The other results will be shown in two separate journal papers are submitted for publication.

4.6.1 EIT test setup

The framework of EIT method and experimental setup is shown in **Figure 4.16**. A variety of scenarios were investigated, including MSC specimens containing a hole as defect, and subjected to multiple microcracking under different levels of loading conditions. Control concrete specimens were also studied for comparison purpose.

The EIT system built in PI's lab included a data acquisition system, a data processing system, data collection LabVIEW code, and the specimen in interest (**Figure 4.16**). A matrix/multiplexer switch was used to handle the switching of both current injection and voltage measurement. The current injection and voltage measurements can be switched from one pair of channels to the other pair. The current and voltage signals were transported independently so that noise was minimized. The system automatically controlled the switch from one measurement to another. For 16 channels output, the entire scan was approximately 30 seconds. For 32 channels output, the entire scan was approximately 120 seconds. However, when the current was changed with different frequency, the scan time became different. For the lower frequency current injection, the scan time was longer. It was reasonably assumed that electrical properties of MSC did not vary significantly over the scan period. The short scan time made it possible to satisfy the instant scan assumption. AC current source was adopted. With injected current, the voltage was measured and recorded with a data acquisition system.

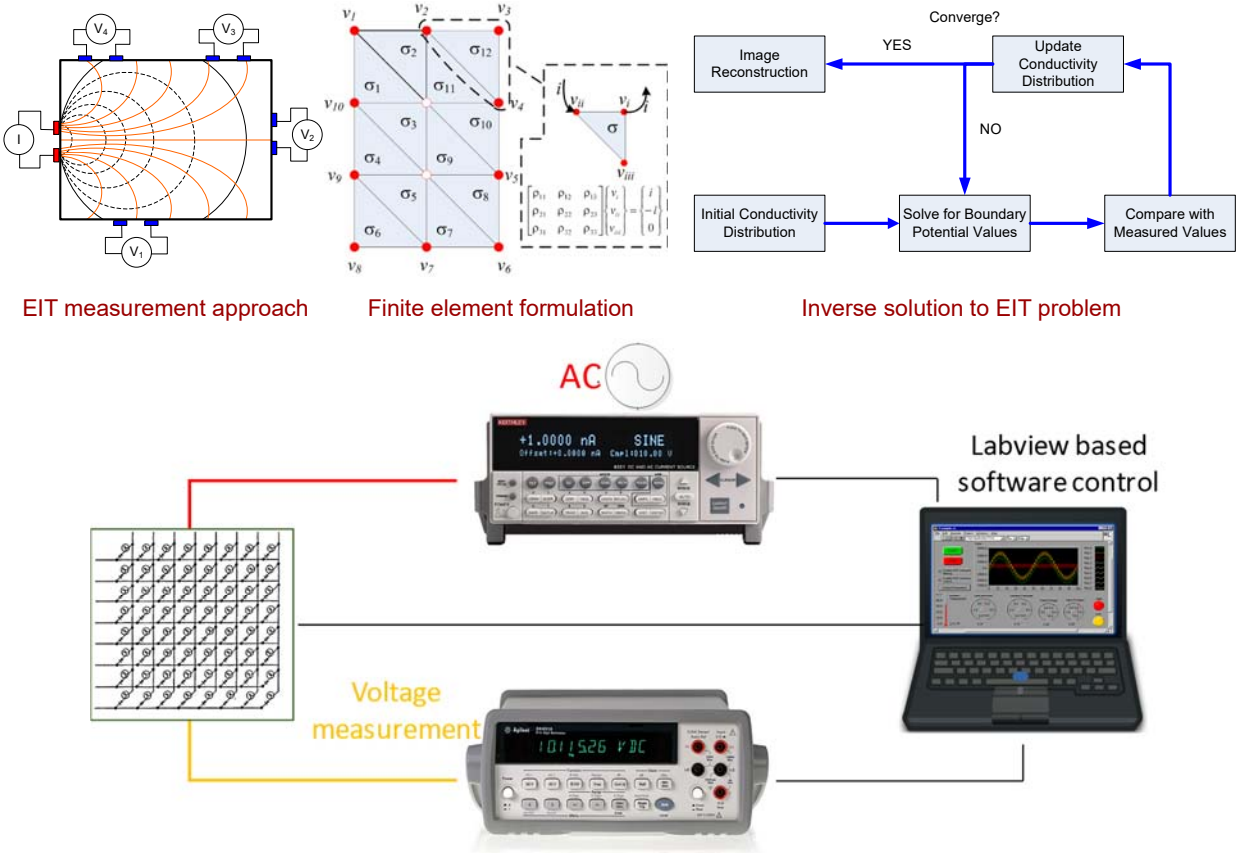

Figure 4.16: EIT test setup.

4.6.2 EIT image reconstruction on panel specimen with a center hole

Figure 4.17 shows the tested specimen with 16 electrodes made of copper tape and conductive silver paste. EIT data collection was conducted on the specimen. 208 data were collected. The Same procedure was repeated for three times. The average of the three scans was utilized as the undamaged EIT data. The specimen was then drilled with a cetner hole with the diameter of 5 mm. Thereafter, another three repeated EIT scans were conducted on the specimen containing the center hole. With the collected data, image reconstruction was conducted. **Figure 4.18** shows the image reconstruction results. Different algorithms were used to reconstruct the image of the distributed damage (i.e. the hole). It was found that while most of the algorithms were able to identify the damage, they did have different sensitivity or accuracy.

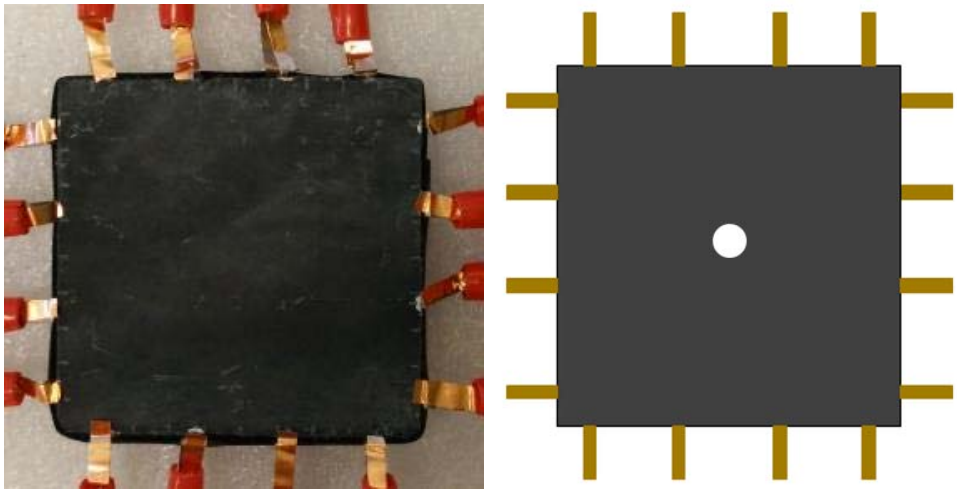

Figure 4.17: Specimen with middle hole.

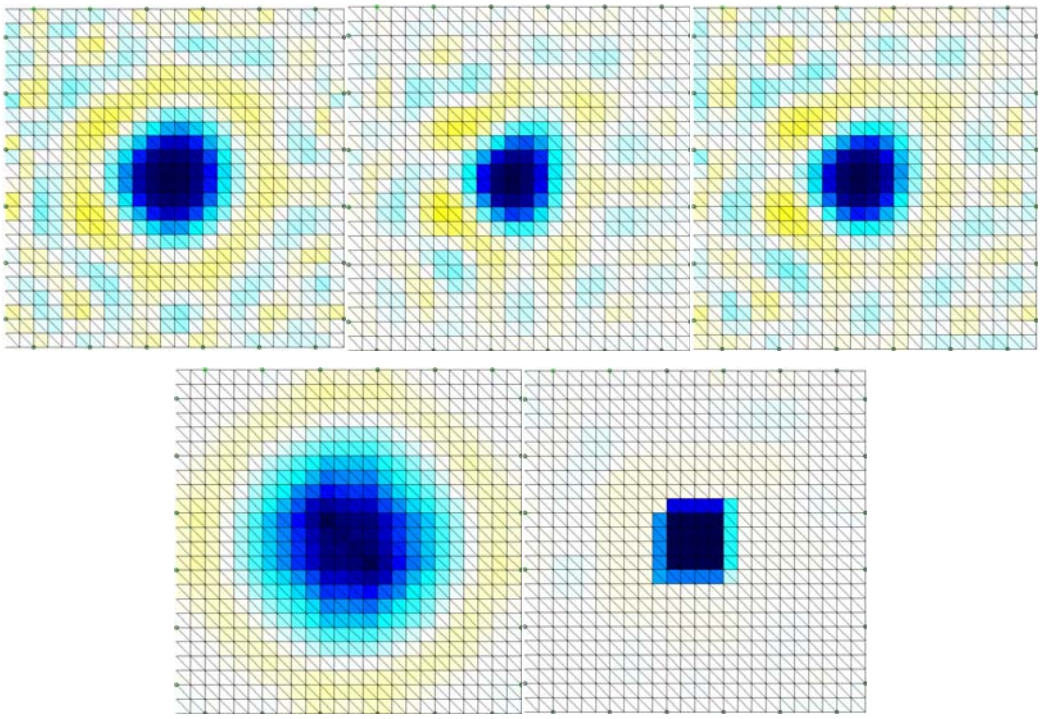

Figure 4.18. Reconstructed EIT images using different algorithm: (a) One step Gauss-Newton reconstruction (Tikhonov prior), (b) One step Gauss-Newton reconstruction (NOSER prior), (c) One step Gauss-Newton reconstruction (Laplace filter prior), (d) One step Gauss-Newton reconstruction (automatic hyperparameter selection) and (e) Total variation reconstruction.

EIT was performed on MSC specimens in comparison with control concrete specimens. The purpose was to reveal the damage self-sensing capacity of MSC that was not possessed by normal concrete

specimens. **Figure 4.19** shows the specimen configuration prepared for the EIT experiment. 32 copper electrodes were attached to the surface of the specimen. In the first scenario, the specimen made of MSC or normal concrete contains a central hole. After the data were collected from EIT measurements, the data was used to reconstruct the damage information within the specimens.

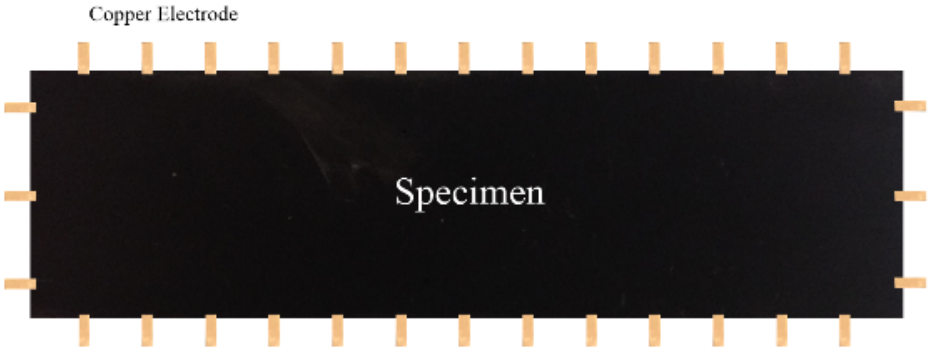

Figure 4.19: 5% MSC specimen with electrodes.

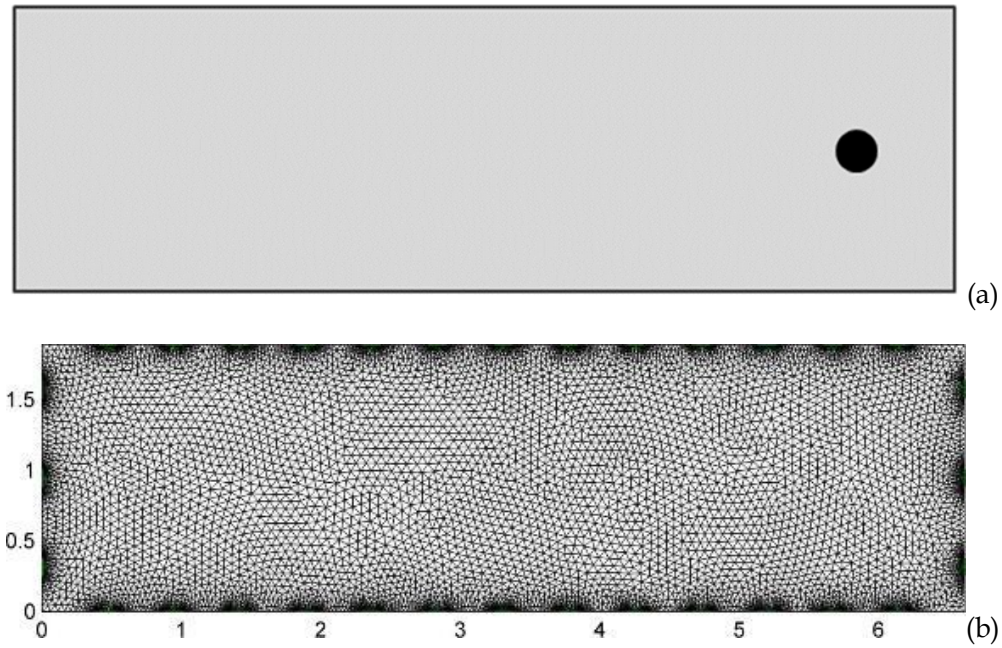

Figure 4.20. (a) Damage location and size; (b) FEM mesh for the specimen.

To reconstruct the damage image, inverse finite element problems needed to be solved. The meshing of the specimen for inverse image reconstruction is shown in **Figure 4.20**. In the physical model, the electrode potentials measured from copper electrodes were correlated to the impedance distribution within and throughout the specimen.

The damage image reconstruction results are shown in **Figure 4.21**. It was clearly shown that the normal concrete specimen failed to identify the millimeter-scale defect through the EIT method. In contrast,

the newly developed MSC specimen was able to accurately identify the distributed damage within the specimen, validating its damage self-sensing capacity. It should be noted that although the data were collected only from specimen boundaries, the distributed damage inside the specimen was located; the image reconstruction clearly reflected the location and the shape of the damage.

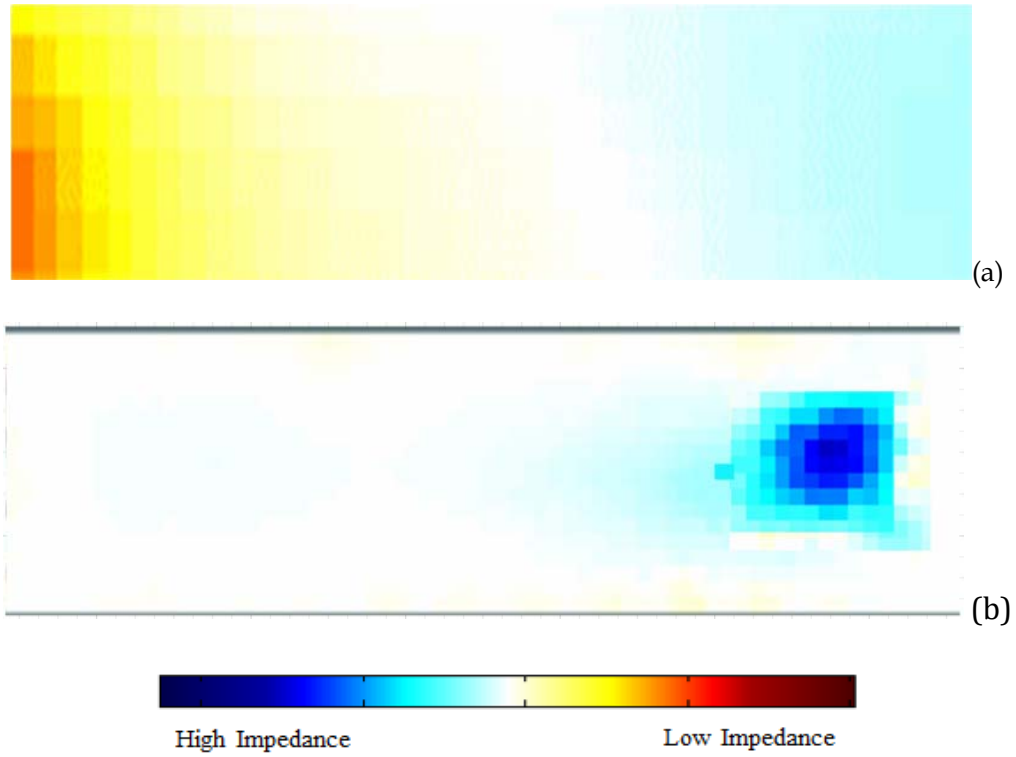

Figure 4.21. Image reconstruction comparison for (a) normal concrete, and (b) 5% MSC material.

4.6.3 EIT image reconstruction on coupon specimen with damage

In addition to identifying a millimeter-scale defect (e.g. a hole), the capability of identifying distributed micro-scale cracks in MSC was studied. **Figure 4.22** shows the test setup and the framework of EIT image reconstruction on coupon specimens with a number of microcracks formed under loading. Two materials were studied: MSC with self-sensing capacity, and SHC without self-sensing capacity. SHC was chosen over normal concrete as the control material because it was impossible to generate microcracks in concrete specimens due to the brittleness of concrete materials, thus making it impossible to evaluate the capacity for sensing microcracks. Once casted and cured, the coupon specimens were gripped on a hydraulic testing frame to performed uniaxial tension test. EIT was performed on the specimens before the tension test, and after the tension test which introduced a number of microcracks into the specimens. Each

microcrack had a width below 30 micron. The difference in the collected impedance data before and after damage was used for image reconstruction. In this study, the image reconstruction esd based on difference image reconstruction. Difference image reconstruction means that there were two sets of measurements. The first set of measurements was the original measurement or reference measurement, which was conducted before damage occured. The second set of measurements were measurement after damage. The damage pattern and image reconstruction of SHC specimens (without self-sensing capacity) are shown in **Figure 4.23** and **4.24**. The damage pattern and image reconstruction of MSC specimens (with self-sensing capacity) are shown in **Figure 4.25** to **Figure 4.28**.

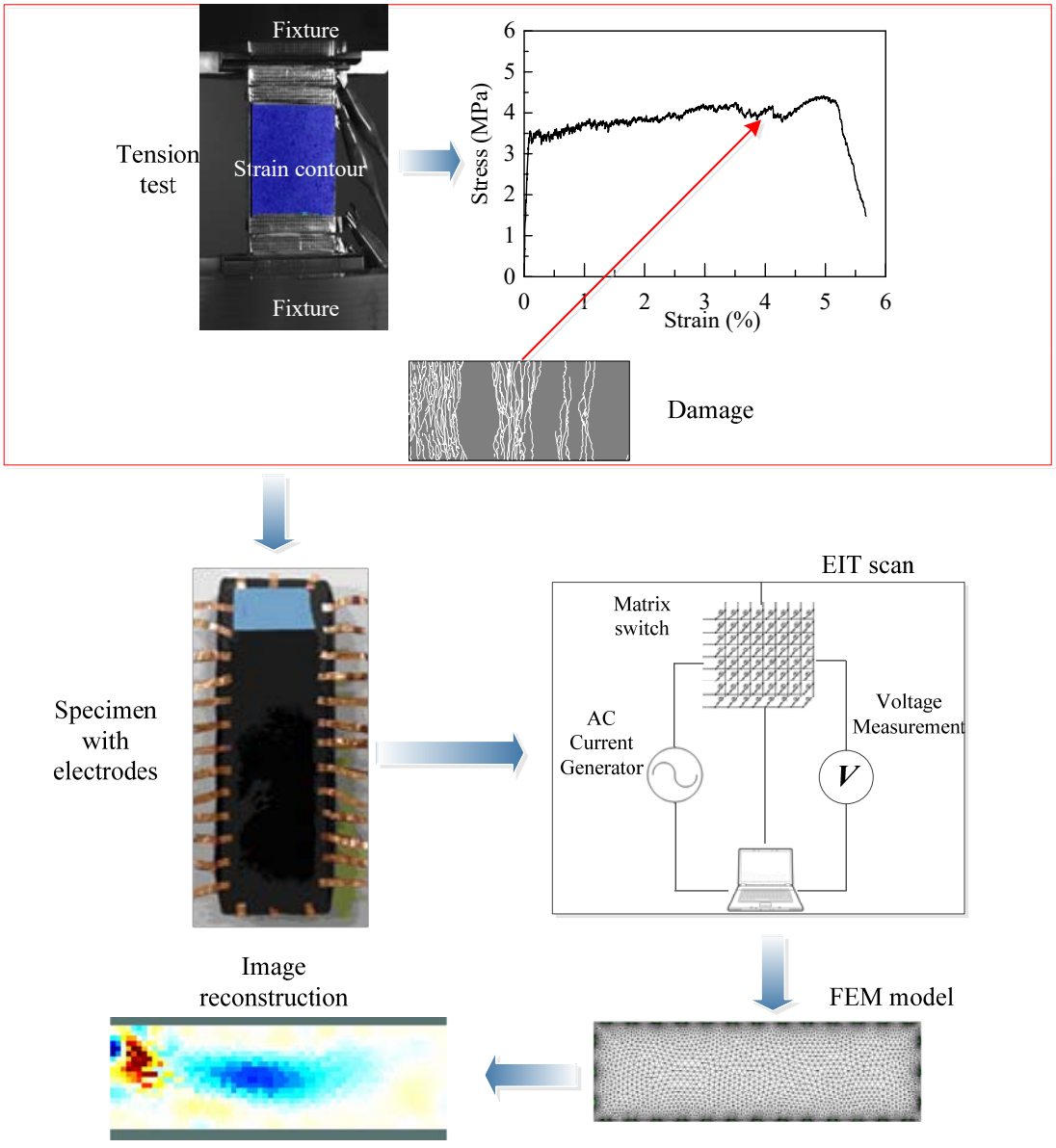

Figure 4.22: Electrical Impedance Tomography image reconstruction of real damage pattern.

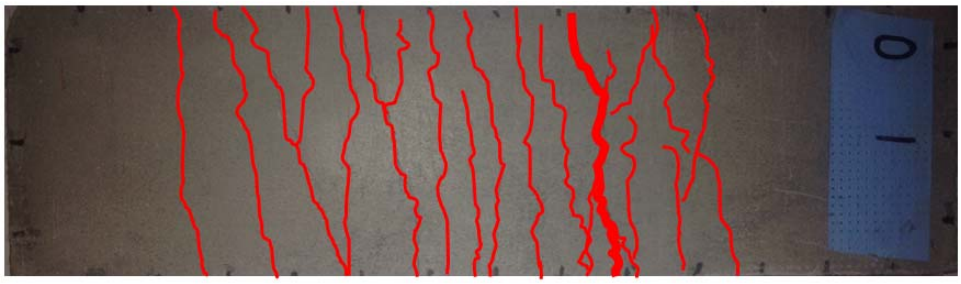

Figure 4.23. Damage pattern of normal SHC material.

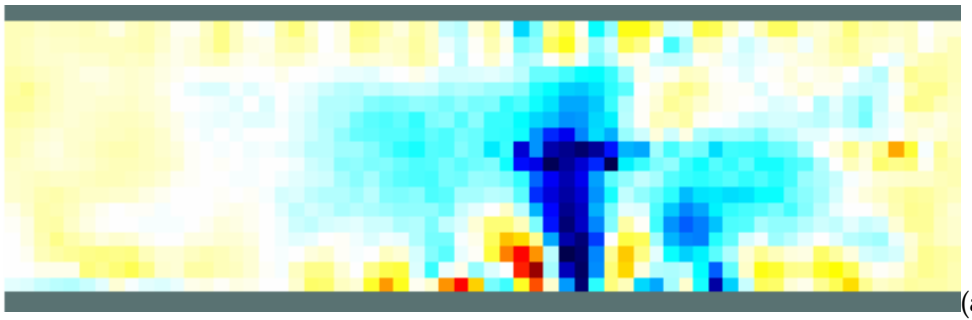

(a)

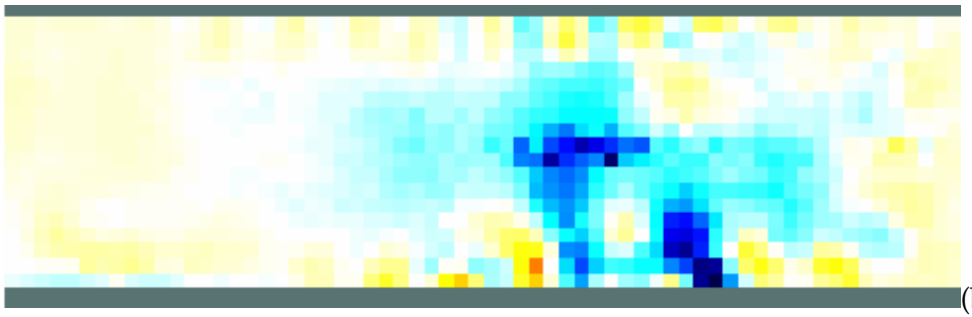

(b)

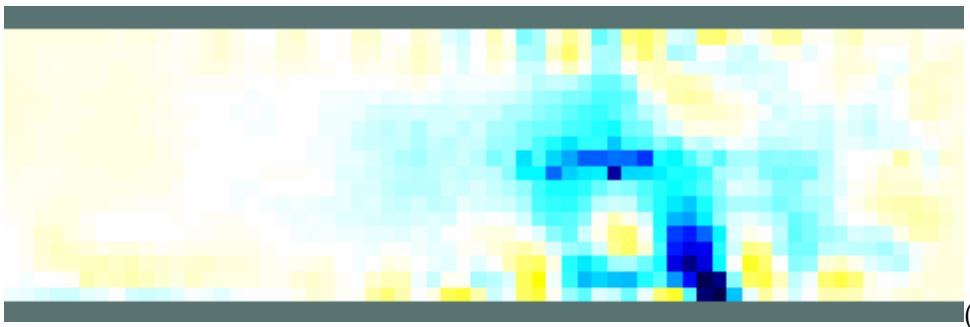

(c)

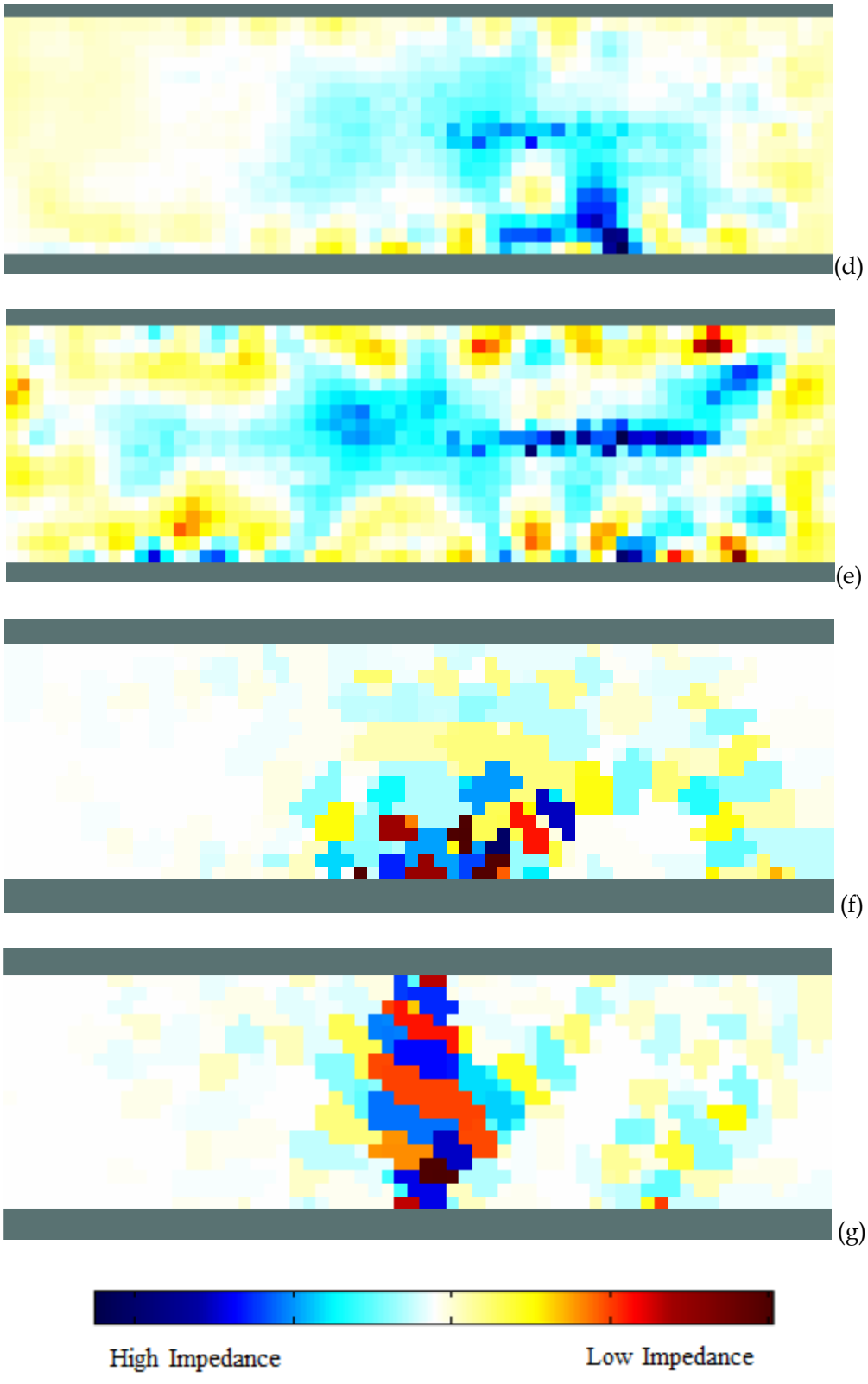

Figure 4.24. Image reconstruction of damage within normal SHC material with collected for different frequency (a) 1 HZ; (b) 10 HZ; (c) 100 HZ; (d) 1000 HZ; (e) 10000 HZ; (f) 100000 HZ; (g) 100000 HZ.

Figure 4.23 shows that under uniaxial tension test, a number of microcracks formed in the SHC specimen. The red color indicated microcracks under the surface of the specimen. **Figure 4.24** shows the image reconstruction of damage pattern for the SHC specimen with a frequency range from 1 HZ to 1MHZ. It was clearly shown that the reconstructed image failed to locate the damage in an accurate way.

Figure 4.25 shows the damage pattern in the 5% MSC material. A number of microcracks with width smaller than 30 micron formed in the 5% MSC specimen during the tension test. **Figure 4.26** shows the image reconstruction of damage pattern for the MSC specimen with a frequency range from 1 HZ to 1MHZ. It was shown that for data collected at 1Hz, 10 HZ, 100 HZ, 1,000 HZ and 10,000 HZ, the reconstructed images clearly revealed the location and intensity of the distributed microcracking damage. However, EIT performed at the very high frequencies (i.e. 100,000HZ and 1,000,000 HZ) were not able to identify the microcracking damage.

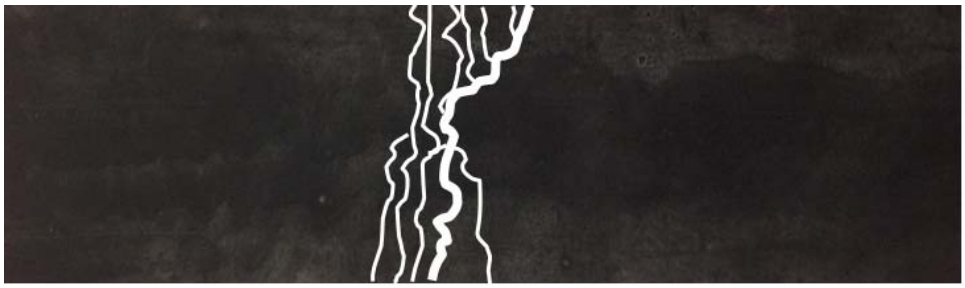

Figure 4.25: Damage pattern illustration of 5% MSC material specimen No.(1) .

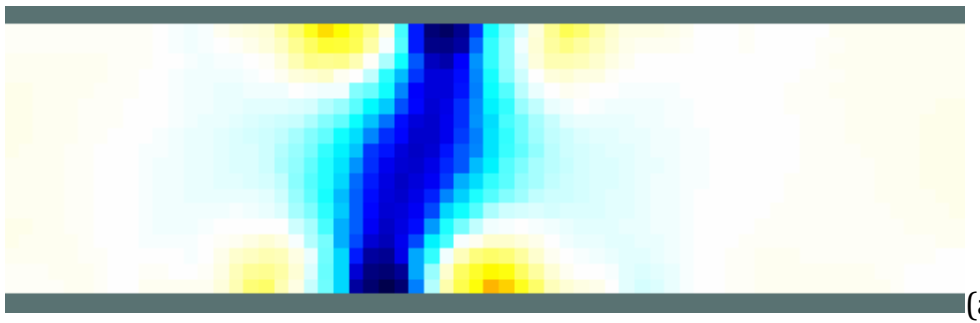

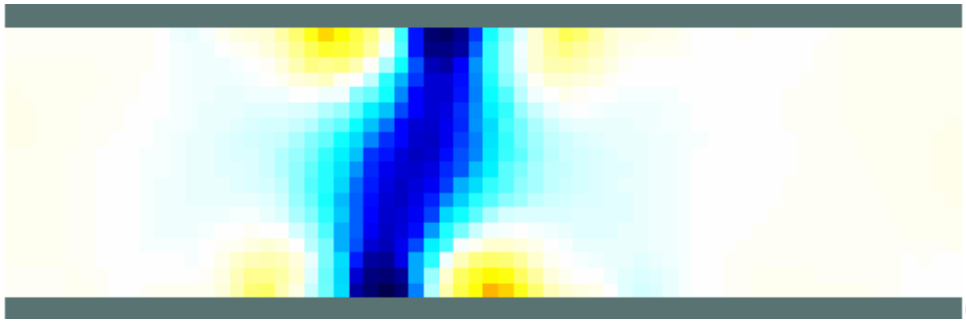

(c)

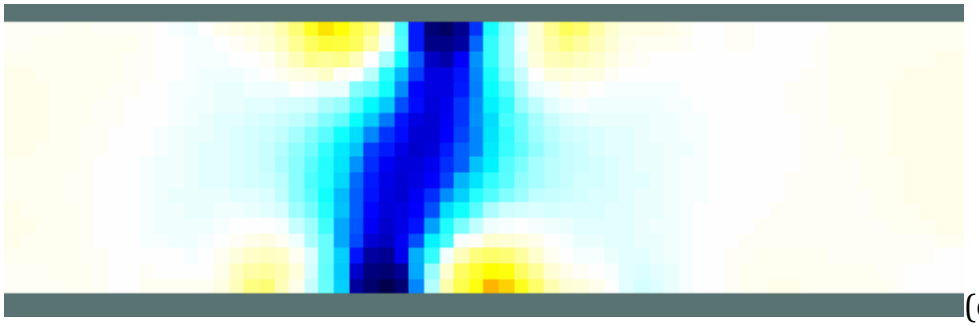

(d)

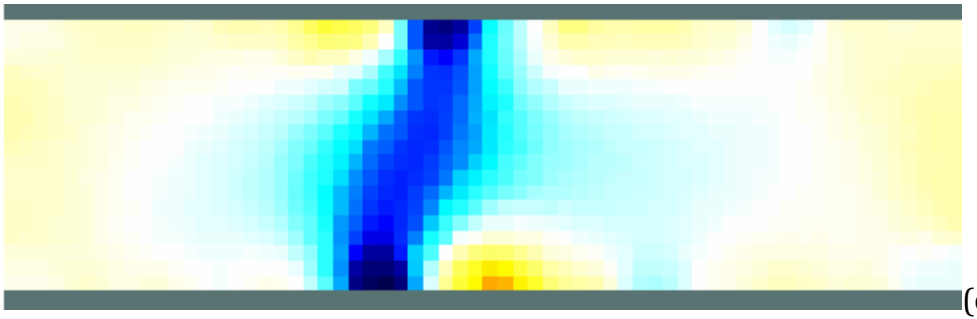

(e)

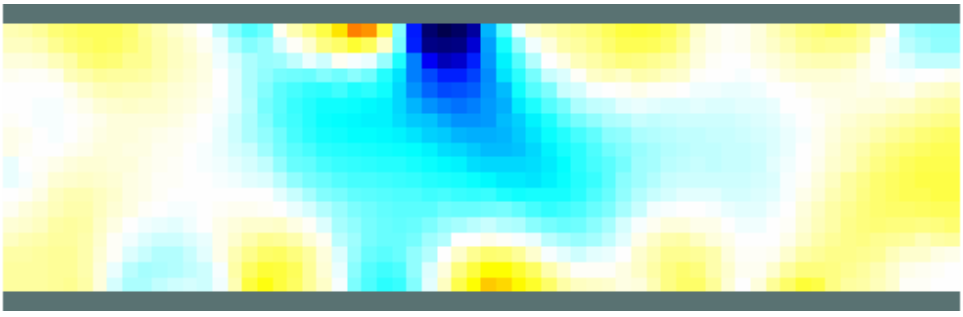

(f)

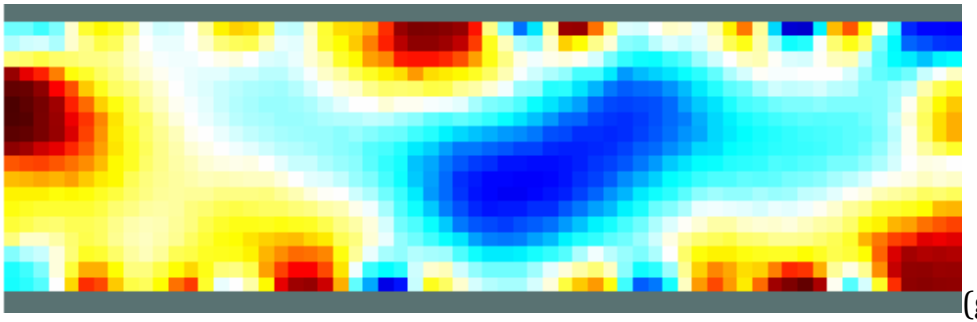

(g)

Figure 4.26: Image reconstruction of damage within 5% MSC material specimen No.(1) with collected for different frequency (a) 1 HZ; (b) 10 HZ; (c) 100 HZ; (d) 1000 HZ; (e) 10,000 HZ; (f) 100,000 HZ; (g) 1,000,000 HZ.

Figure 4.27 shows the damage pattern in a different specimen made of 5% MSC. The specimen contained a number of microcracks with width smaller than 30 μm and a localized failure crack with a width of 380 μm. **Figure 4.28** shows the image reconstruction of damage pattern for the MSC specimen with a frequency range from 1 HZ to 1MHZ. It was seen that for data collected at 1Hz, 10 HZ, 100 HZ, 1,000 HZ and 10,000 HZ, the reconstructed images clearly revealed the location and intensity of the distributed microcracking as well as the localized crack. It was also found that EIT performed at the very high frequencies (i.e. 100,000HZ and 1,000,000 HZ) were not able to identify the microcracking damage.

Figure 4.27: Damage pattern illustration of 5% MSC material specimen No.(2).

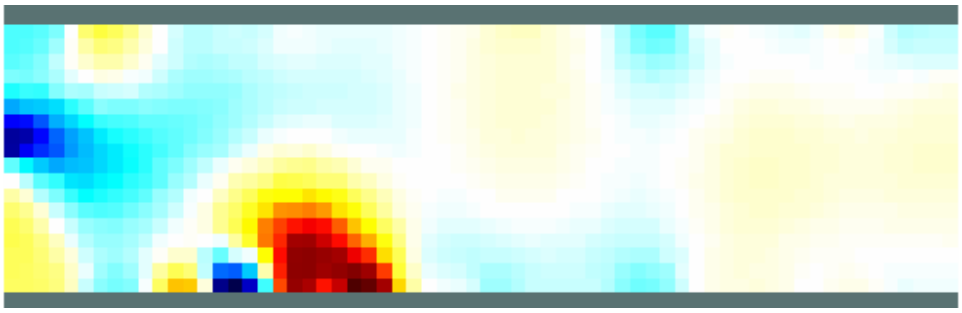

(a)

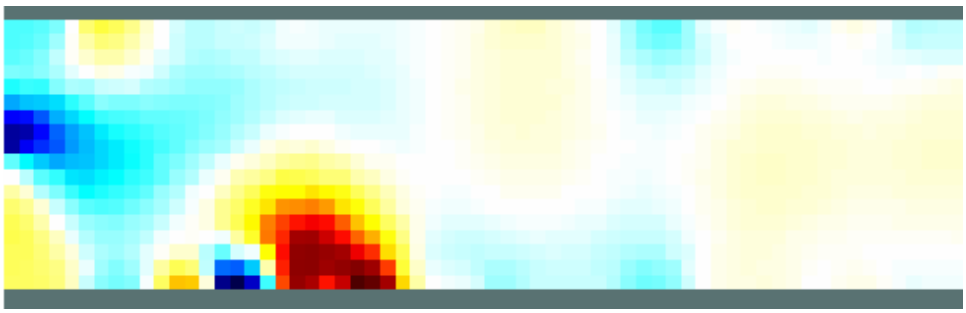

(b)

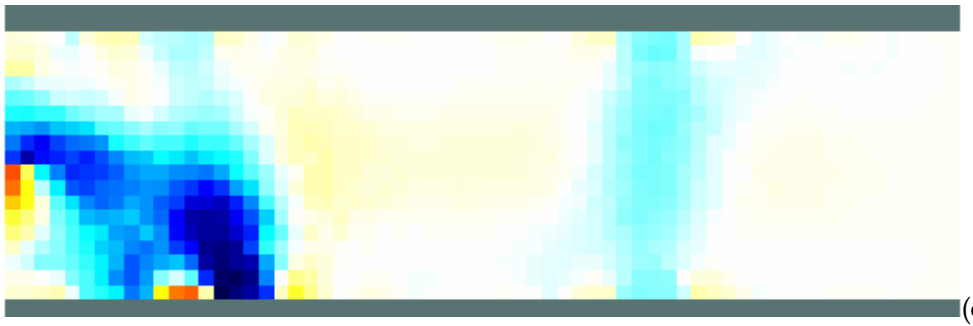
(c)


(d)

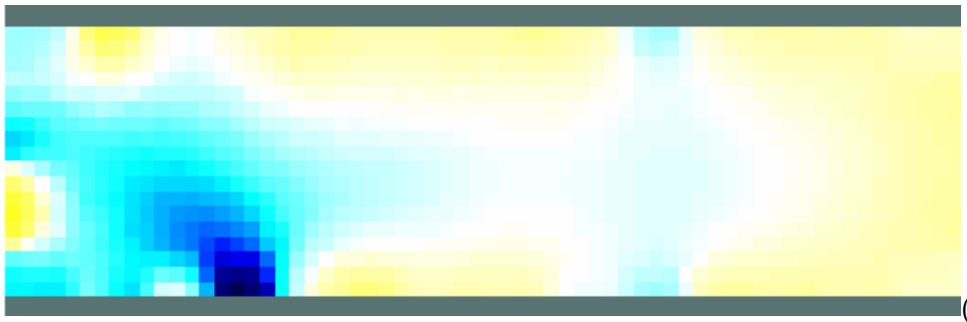
(e)

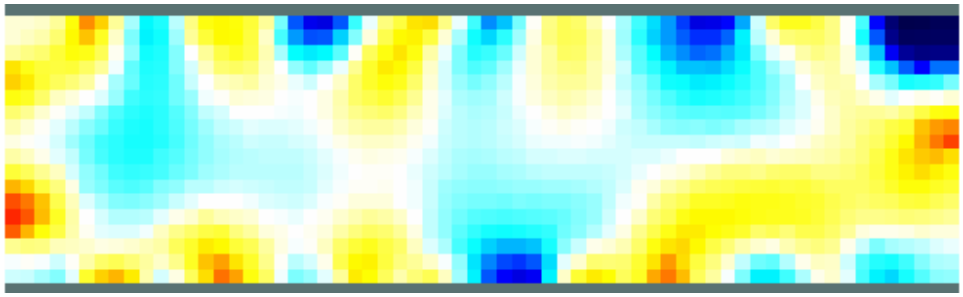
(f)

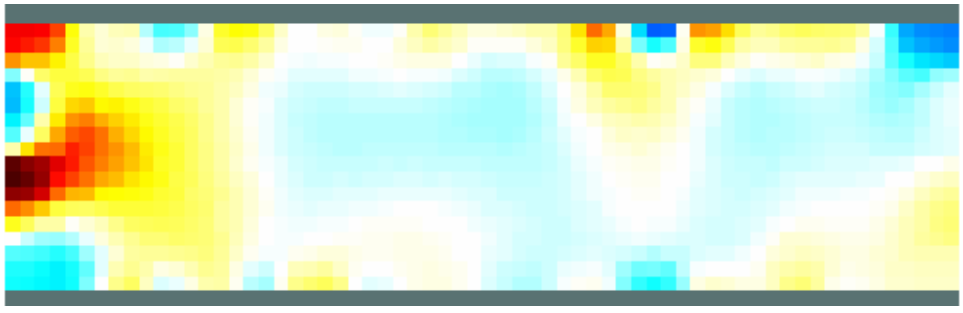
(g)

Figure 4.28: Image reconstruction of damage within 5% MSC material specimen No.(2) with collected for different frequency (a) 1 HZ; (b) 10 HZ; (c) 100 HZ; (d) 1000 HZ; (e) 10,000 HZ; (f) 100,000 HZ; (g) 1,000,000 HZ.

Figure 4.29 shows the damage pattern in the third specimen made of 5% MSC. This specimen was loaded to larger strain that induced higher level of damage in form of larger number of microcracks. In addition, there was a corner "crash" on the specimen which made the damage pattern more complex. **Figure 4.30** shows the image reconstruction of damage pattern for the MSC specimen with a frequency range from 1 HZ to 1MHZ. It was seen that for data collected at 1Hz, 10 HZ, 100 HZ, 1,000 HZ and 10,000 HZ, the reconstructed images clearly revealed the location and intensity of the distributed microcracking as well as the corner damage. For example, for the results based on EIT conducted at 1,000 Hz, the location and intensity of damage were accurately revealed by the difference in colors seen for the microcracks region and for he corner damage region. Similar as other results, EIT performed at the very high frequencies (i.e. 100,000HZ and 1,000,000 HZ) was not able to identify damage.

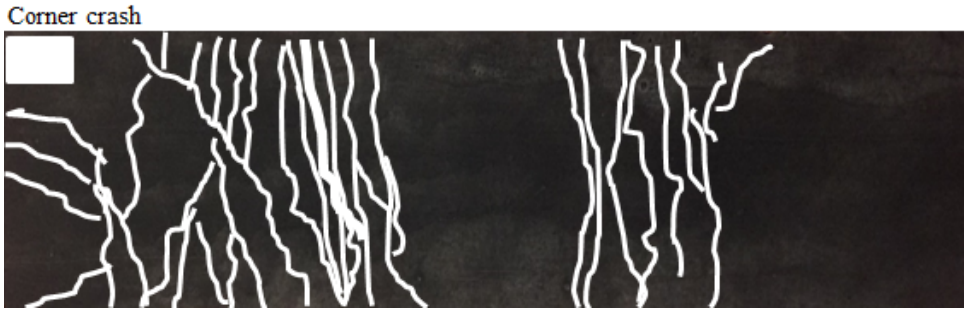

Figure 4.29: Damage pattern illustration of 5% MSC material specimen No.(3).

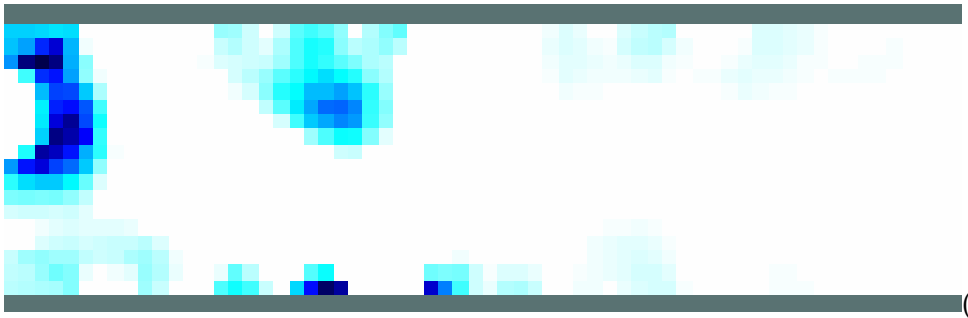

(a)

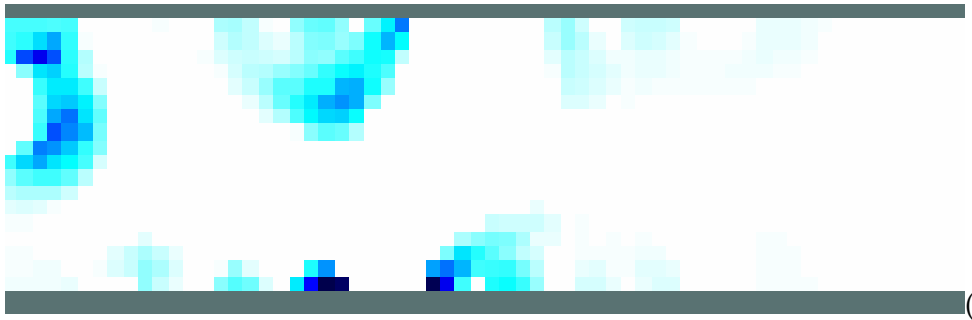

(b)

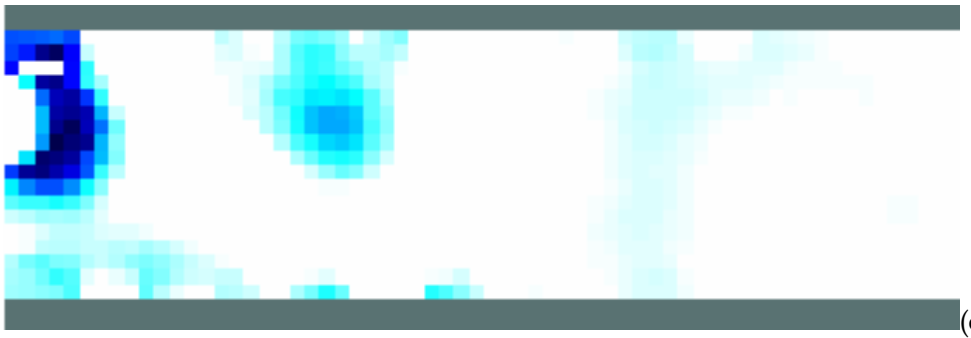

(c)

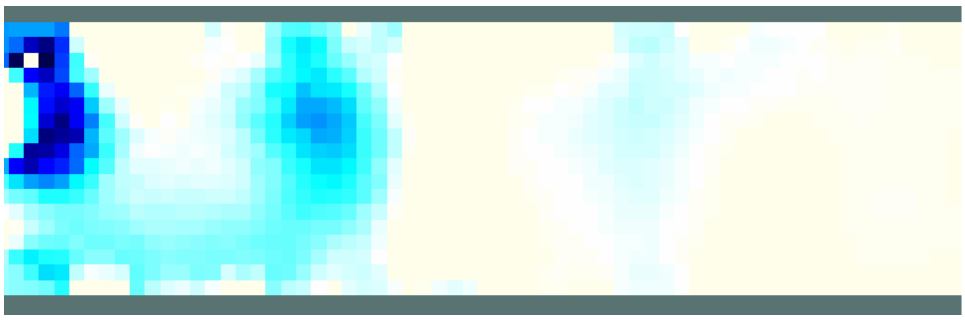

(d)

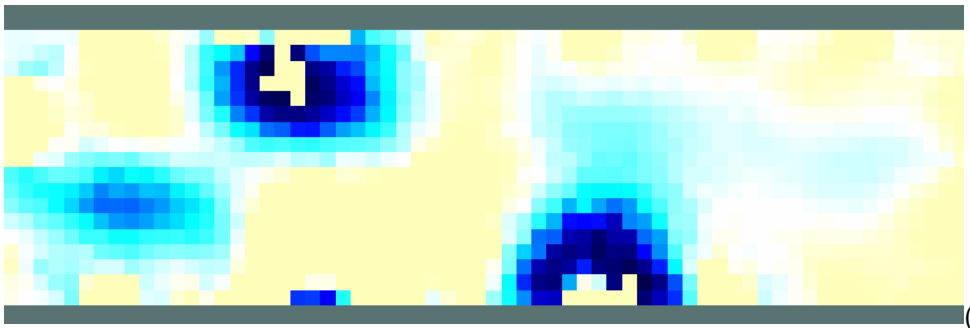

(e)

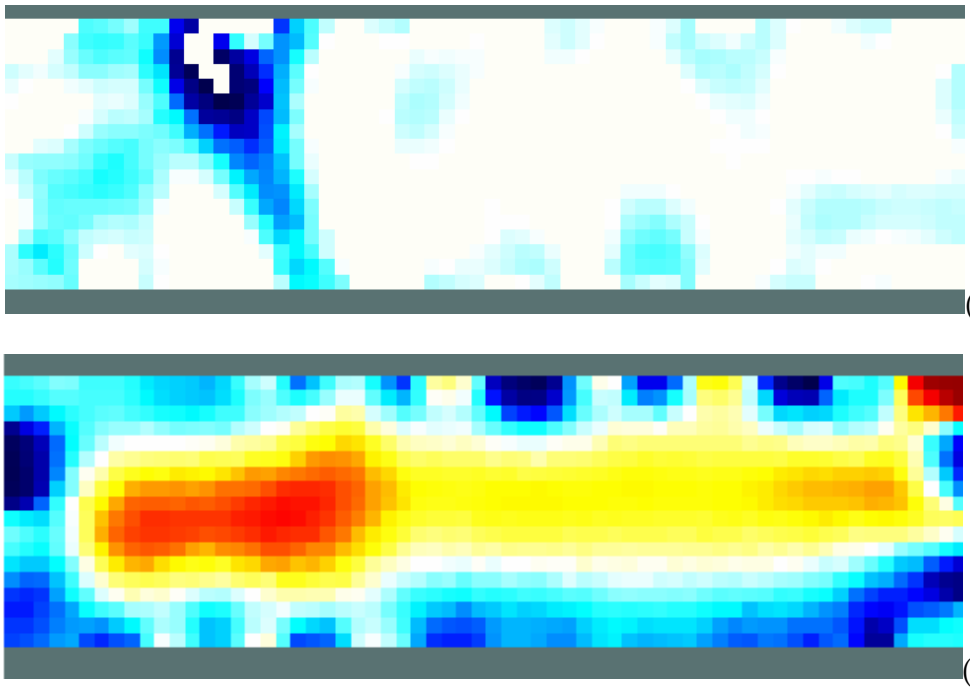

Figure 4.30. Image reconstruction of damage within 5% MSC material specimen No.(3) with collected for different frequency (a) 1 HZ; (b) 10 HZ; (c) 100 HZ; (d) 1000 HZ; (e) 10,000 HZ; (f) 100,000 HZ; (g) 1,000,000 HZ.

In the 5th scenario, the specimen was loaded gradually to different strain levels evaluate the capability of EIT to reconstruct progressive damage. **Figure 4.31** shows the tensile strain levels where the test paused for EIT to be conducted. **Figure 4.32** shows the specimen before testing. There were 32 electrodes attached onto the sides of the specimen. The test was paused at 0.5%, 1%, 2%, and 3% tensile strain for EIT scan.

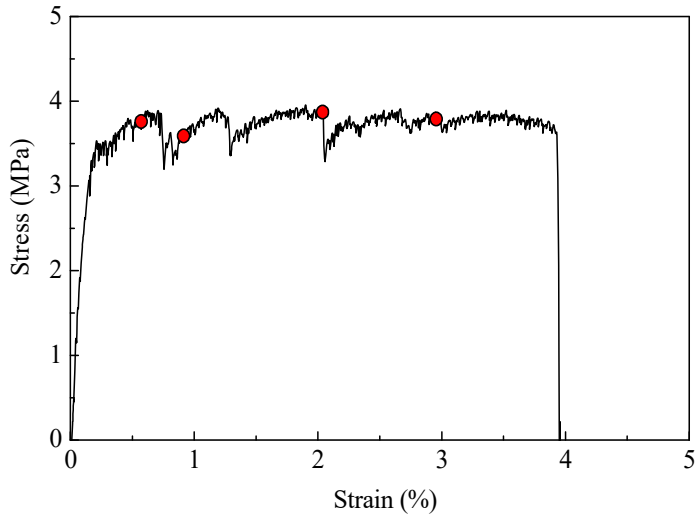

Figure 4.31: Uniaxial tensile test results and EIT scan point.

Figure 4.32. Specimen before damage with 32 electrodes.

Figures 4.33 to 4.36 show the image reconstructions for damage caused by 0.5%, 1%, 2%, and 3% applied strain, respectively. The real damage patterns captured by a microscope are also shown in the figures. The results clearly show that the damage pattern, location and intensity change with progressive loading applied to the MSC specimen were clearly captured by data collected from MSC specimen boundaries, validating the direct and distributed damage self-sensing capacity of MSC even at microcrack levels.

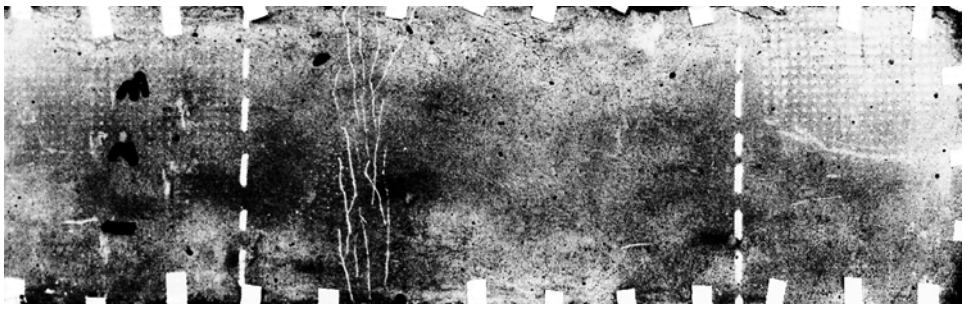

(a)

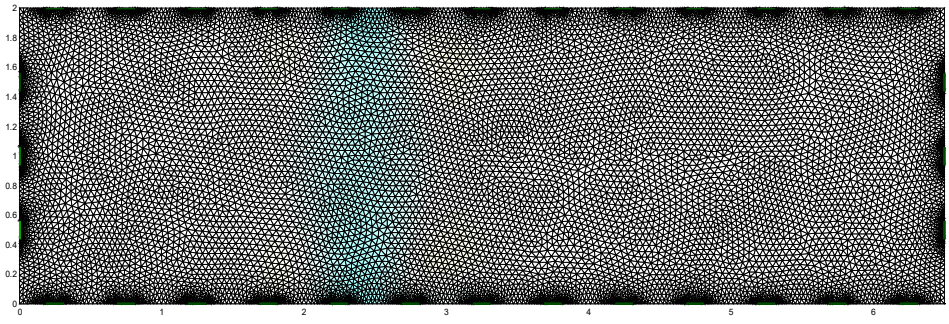

(b)

Figure 4.33: Image reconstruction at 0.5% strain. (a) real damage. (b) image reconstruction.

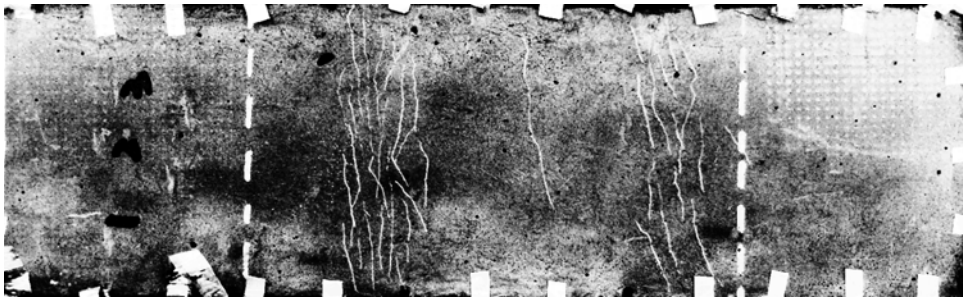

(a)

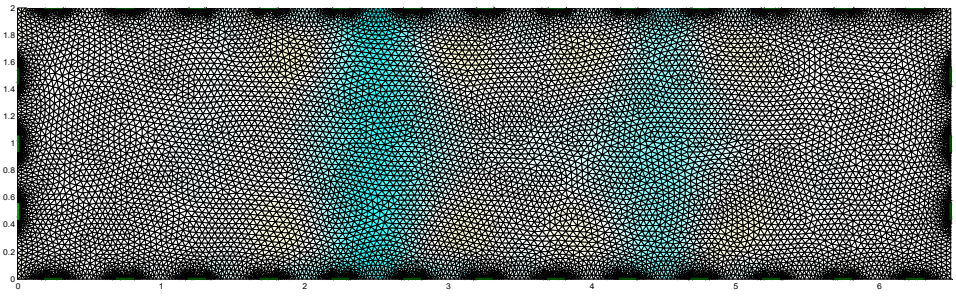

(b)

Figure 4.34: Image reconstruction at 1% strain. (a) real damage. (b) image reconstruction.

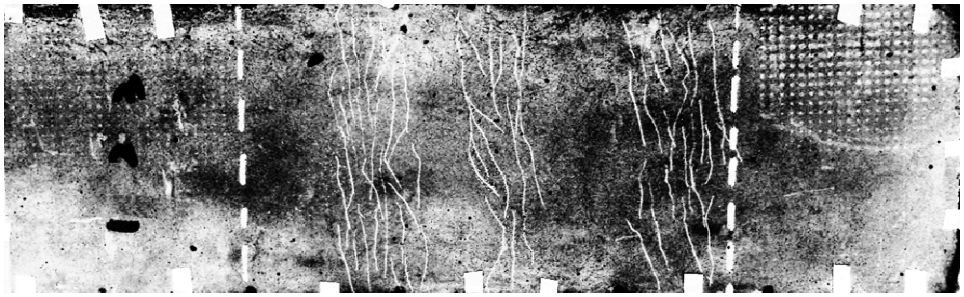

(a)

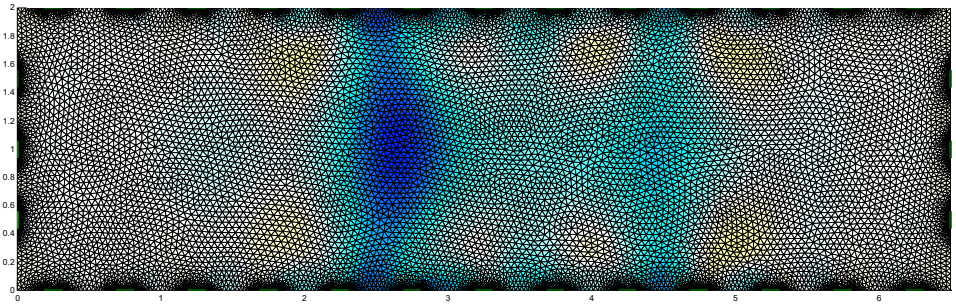

(b)

Figure 4.35: Image reconstruction at 2% strain. (a) real damage. (b) image reconstruction.

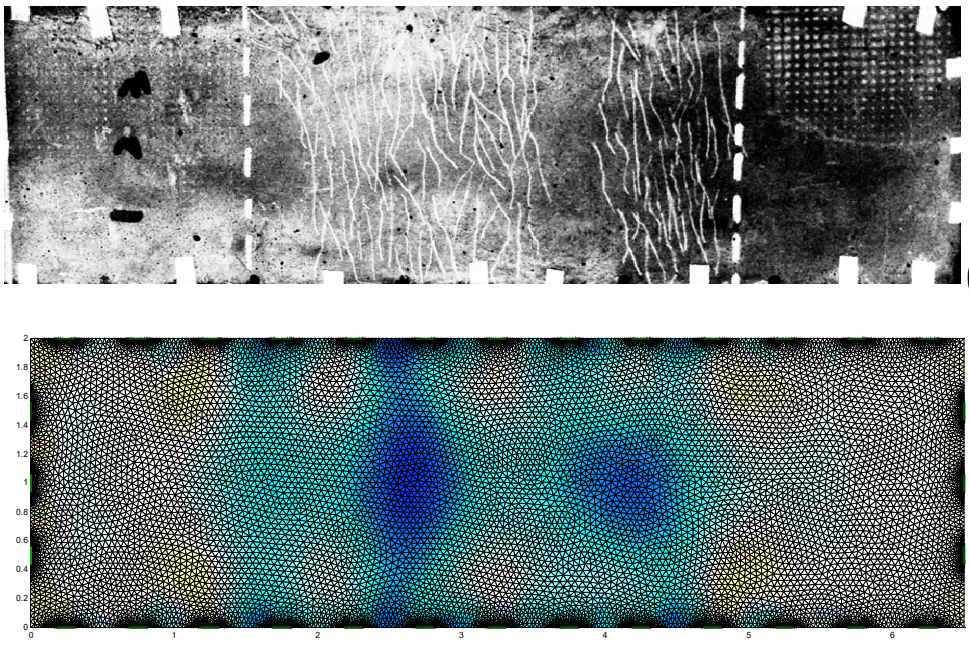

Figure 4.36: Image reconstruction at 3% strain. (a) real damage. (b) image reconstruction.

4.6.4 EIT image reconstruction on beam specimen with damage

In this section, the damage sensing in MSC was studied at structural element scale using a beam specimen subjected to bending load. **Figure 4.38** shows the test setup and specimen details of the beam made of MSC material. The dimensions of beam specimen are 4 in. × 4 in. ×16 in. The specimens were air cured for 28 days, and then subjected to three-point bending (**Figure 4.38)**. The layout of the electrodes are shown in **Figure 4.38 (c)**. 27 circle electrodes were attached to the specimen surface. In real applications, these electrodes can be easily sprayed onto structural service in the region of interests. Maintaining these electrodes is not a concern, because its easy and inexpensive to install or uninstall the electrodes wherever needed. The current was first injected into 1-2 electrodes and then the voltage was measured via 1-2 electrodes, 2-3 electrodes, 3-4 electrode and so on. Thereafter, the current was injected into 2-3 electrodes and the voltage was measured with the same pattern.

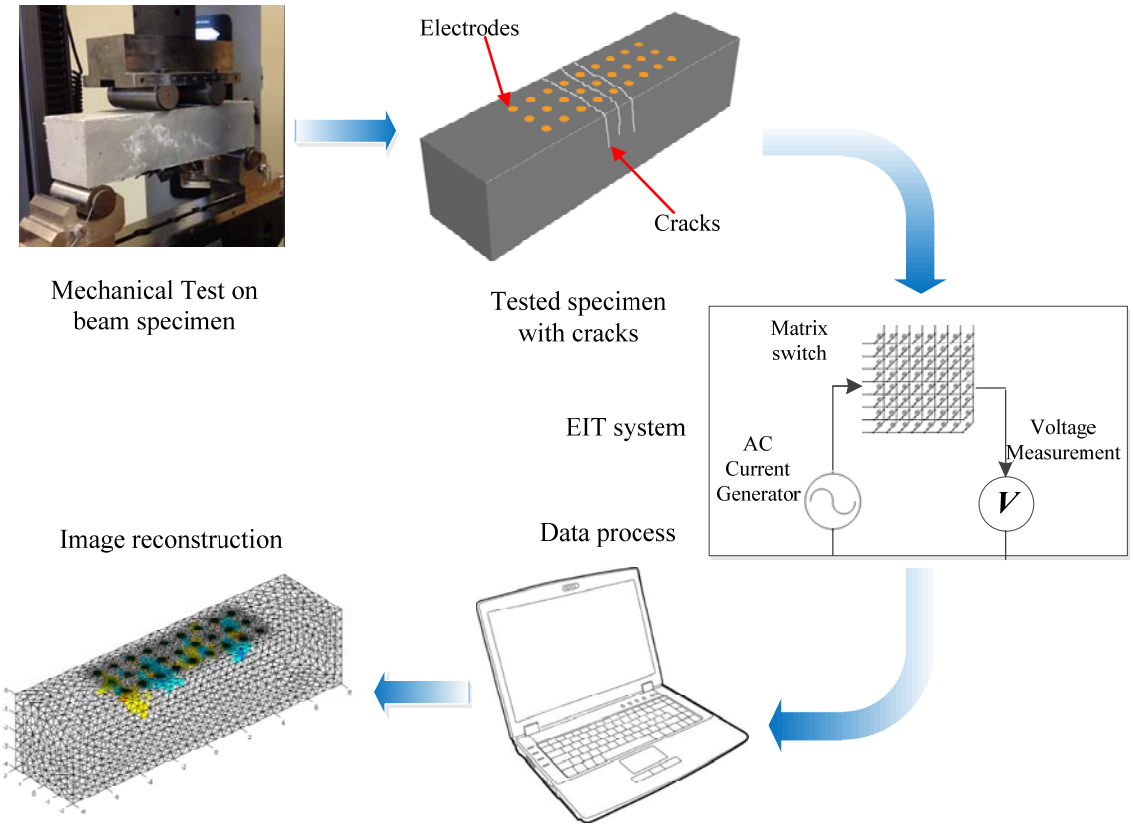

Figure 4.37: EIT image reconstruction on beam specimen.

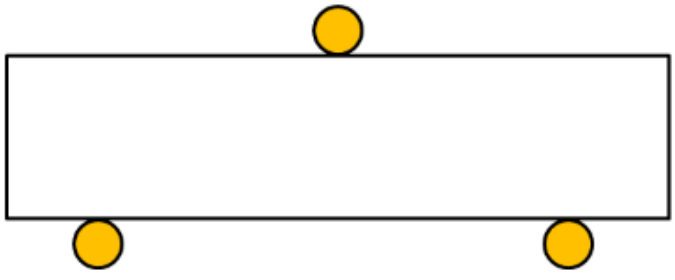

(a)

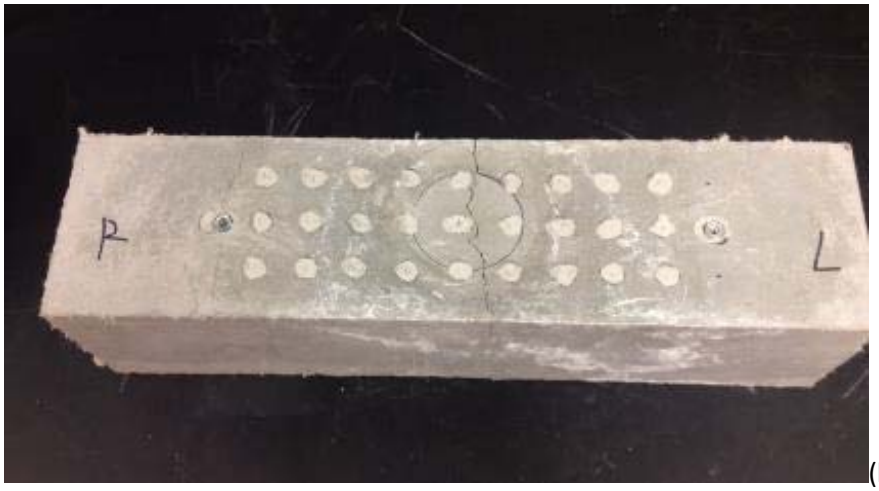

(b)

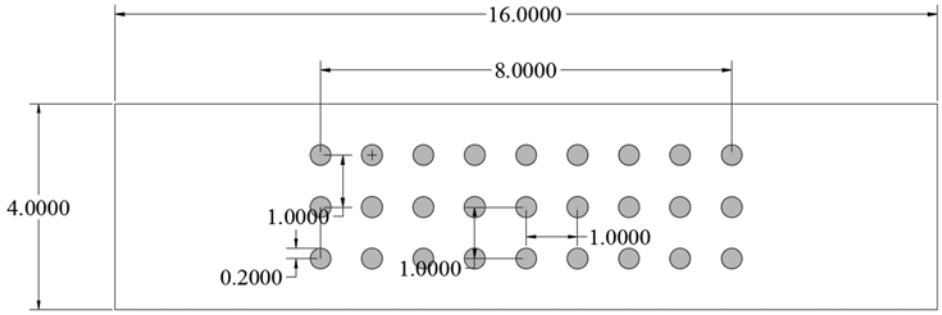

(c)

Figure 4.38 Test setup and specimen details for structural sensing test.

The finite element model of the beam is shown in **Figure 4.39**. 27 surface electrodes were simulated. The mesh size effect was also studied. Data collection was performed at a wide range of low and high frequencies (i.e. 1 Hz, 10 Hz, 100 Hz, 1,000 Hz, 10,000 Hz, 100,000 Hz and 1,000,000 Hz). **Figure 4.40** shows the real damage pattern on the surface and inside of the specimen. There existed one bending crack with a depth around 1.5 inch. The reconstructed image is shown in **Figure 4.41**. The results shown that the bending crack was successfully "sensed" in three dimensions by EIT performed on the MSC specimen with frequency up to 10,000 HZ.

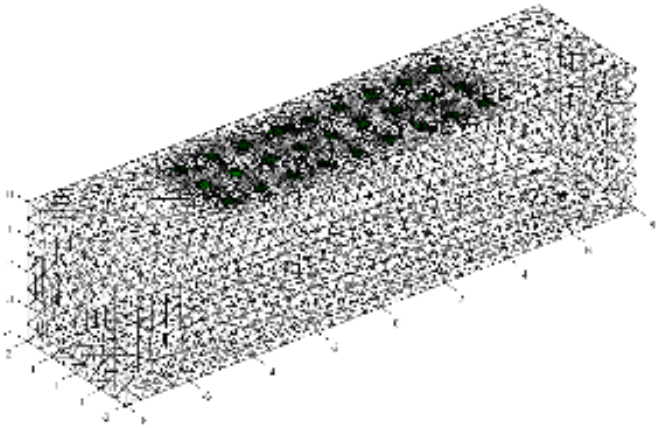

Figure 4.39. Finite element model for resistivity reconstruction.

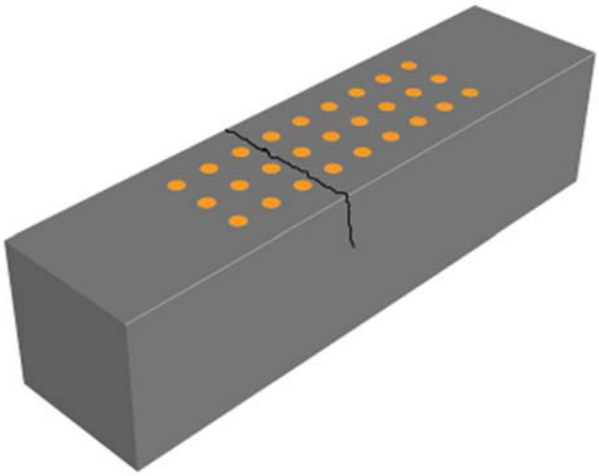

Figure 4.40: Damage location on the surface of the specimen.

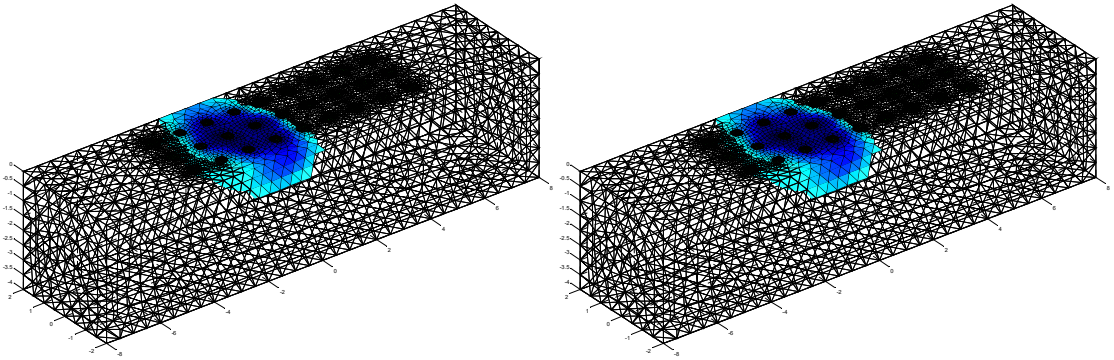

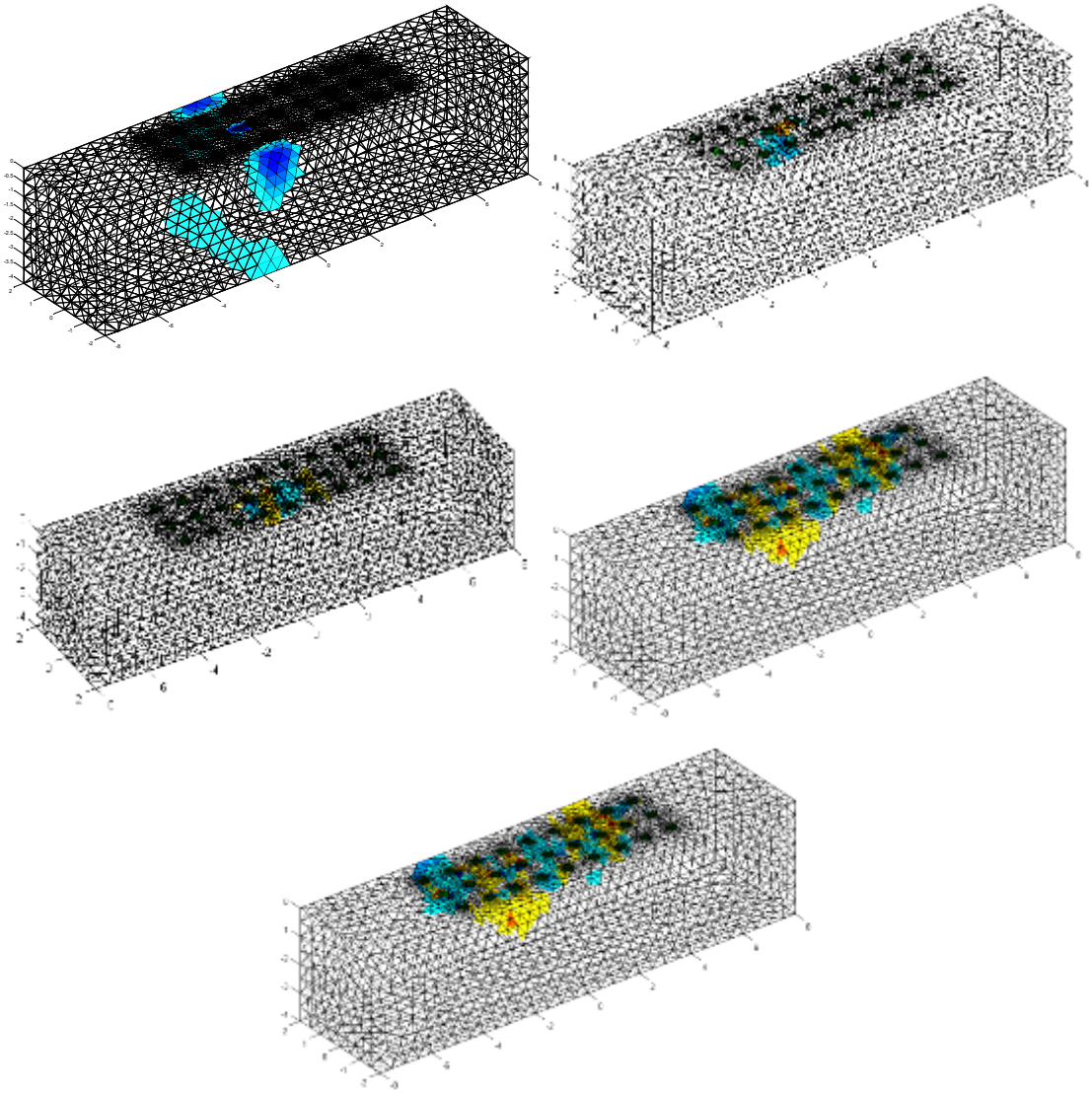

Figure 4.41. MSC image reconstruction (7 results indicate 1 HZ, 10 HZ, 100 HZ, 1,000 HZ, 10,000 HZ, 100,000 HZ, 1,000,000 HZ)

4.7 Summary of accomplishments

This study made it possible to visualize distributed in MSC based upon impedance measurements collected from MSC specimens in probe locations at boundaries. A variety of damage scenarios were investigated, including (1) a millimeter-scale defect, (2) a number of distributed microcracks, (3) a localized single crack, (4) a mix of localized crack and multiple distributed microcracks, (5) a mix of multiple distributed microcracks and corner damage, (6) progressive damage levels, and (7) three-dimensional bending crack. Sensing the damage location and density in MSC was successfully accomplished for the variety of scenarios at a wide frequency range.

The damage self-sensing capacity of MSC was achieved through integrating material innovation with algorithms development for effective and accurate image reconstruction. Advances have been made on the fronts of materials science and engineering, EIT probing and imaging methods, and FEM method. Such interdisciplinary nature of this study was unique, which made it possible for accomplishing the fundamental development of new generation of MSC materials that can also be readily be applied for industrial adoption. This can lead to a new paradigm for future design of self-sensing structures, such as self-sensing spent nuclear fuel storage systems, which can survive harsh environments and extreme conditions with long life, and can also self-sense damage to provide early warning. MSC behaves as damage-tolerant materials as well as a damage sensor itself, thus offering spatial data wherever the material is located. This eliminates the need for installing and maintaining a dense array of sensors; instead, inexpensive electrodes can be attached to structural component boundaries to apply electrical input and measure output signals that collect spatial information throughout the material. This approach allows for spatial sensing inside the material although the electrodes are only required at boundaries.

4.8 References

[1] N. E. D. A. N. Laboratory, "Dry Cask Storage Inspection and Monitoring," 2012.

[2] IAEA, "Operation and Maintenance of Spent Fuel Storage and Transportation Casks/Containers," 2007.

[3] A. H. Chowdhury, L. Caseres, Y.-M. Pan, G. Oberson, and C. Jones, "Expert Panel Workshop on Concrete Degradation in Spent Nuclear Fuel Dry Cask Storage System-Summary Report," 2016.

[4] ACI, "Guide for Conducting a Visual Inspection of Concrete in Service," ed, 2008.

[5] ACI, "Evaluation of Existing Nuclear Safety-Related Concrete Structures," ed, 2010.

[6] A. N. Laboratory, "NRC Job Code V6060: Extended In-Situ and Real Time Monitoring Task 3: Long-Term Dry Cask Storage of Spent Nuclear Fuel," 2012.

[7] T. K. Bera and J. Nagaraju, "A MATLAB-Based Boundary Data Simulator for Studying the Resistivity Reconstruction Using Neighbouring Current Pattern," *Journal of Medical Engineering,* vol. 2013, pp. 1-15, 2013.

5. MATHEMATICAL AND COMPUTATIONAL MODELING OF DETERIORATION PROCESSES

Please see appendix.

6. CONSTITUTIVE MODELING OF MSC AND BENCHMARK PROBLEM

6.1 Introduction

In order to predict performance of structures made of MSC, this study developed new constitutive models of MSC that took into account the unique tensile strain-hardening behavior. The models were incorporated into finite element simulation to study a benchmark problem – a shear wall subjected to earthquake loading. The benchmark problem was chosen to study a structure made of new MSC subjected to complex loading condition under an extreme loading event (e.g. earthquake) which is expected during the long life cycle of spent nuclear fuel storage systems. In a general sense, the shear wall can represent the wall element in dry casks, nuclear reactors and other nuclear engineering structures.

In the past two decades, a significant amount of research in developing constitutive models of reinforced concrete has been performed. The cyclic softening membrane model (CSMM) developed by Mansour et al [4] is the most recent model to predict shear behavior of structural panels under cyclic shear loading. Zhong [5]implemented the model into a finite element program called SCS using OpenSees frame work. The SCS has an excellent capability to predict behavior of a series of shear walls tested by Gao[5]. In this study, the CSMM based finite element program was modified to account for MSC tensile strain-hardening properties. The seismic performance of shear walls with MSC material was studied. The effects of tension and compression properties, energy dissipations, pinching characteristics on the seismic performance of MSC shear walls were critically examined.

6.2 Cyclic Softening Membrame Model (CSMM)

This section aims at expanding the scope of the CSMM model originally developed for reinforced concrete to account for the unique tensile strain-hardening effect of MSC. In order to develop the so-called MSC-CSMM model, the basic principles of the CSMM model for reinforced concrete is presented below.

6.2.1 Formulation of CSMM

6.2.1.1. Coordinate Systems in CSMM

Three Cartesian coordinates, x-y, 1-2, and x_{si}-y_{si}, are defined in the reinforced concrete elements, as demonstrated in **Fig. 6.1**. Coordinate x-y defines the local coordinate of the elements. Coordinate 1-2 represents the principal stress directions of the applied stresses that has an angleθ_1 with respect to the x-axis. Steel bars can be oriented in different directions in the elements. Coordinate x_{si}-y_{si} indicates the direction of the 'i^{th}' group of rebars, where the 'i^{th}' group of rebars are located in the direction of axis x_{si} with an angleθ_{si} to the x-axis. The stress and strain vectors in x-y coordinates and 1-2 coordinates are

denoted as $[\sigma_x, \sigma_y, \tau_{xy}]^T$,$[\varepsilon_x, \varepsilon_y, 0.5\gamma_{xy}]^T$, $[\sigma_1, \sigma_2, \tau_{12}]^T$ and $[\varepsilon_1, \varepsilon_2, 0.5\gamma_{12}]^T$, respectively.

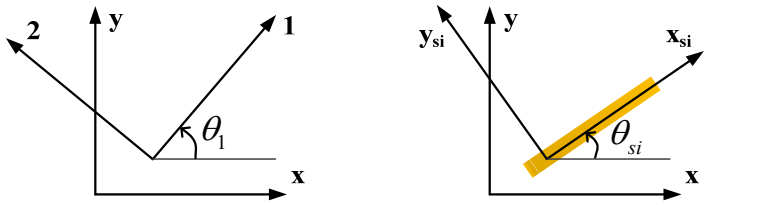

(a) Applied principal stresses in local coordinate

(b) Reinforcement component in local coordinates

Figure 6.1: Cyclic stress-strain relationship of material.

6.2.1.2. Equilibrium and Compatibility Equation

The applied stresses in the x-y coordinate (σ_x, σ_y and τ_{xy}) are related to the internal concrete stresses (σ^c_x, σ^c_y and τ^c_{xy}) in the principal stress directions, and the steel bar stresses (f_{si}) in the bar directions by the following equilibrium equation:

$$\begin{Bmatrix} \sigma_x \\ \sigma_y \\ \tau_{xy} \end{Bmatrix} = \left[T\left(-\theta_1\right)\right] \begin{Bmatrix} \sigma_1^c \\ \sigma_2^c \\ \tau_{12}^c \end{Bmatrix} + \sum_i \left[T\left(-\theta_{si}\right)\right] \begin{Bmatrix} \rho_{si} f_{si} \\ 0 \\ 0 \end{Bmatrix} \tag{6.1}$$

whereρ_{si} is the steel ratio in the "ith" direction; [T(-θ_1)] and [T(-θ_{si})] are the transformation matrices from the 1-2 coordinate and the x_{si}-y_{si} coordinate to the x-y coordinate, respectively.

The relationships between the biaxial steel strains (ε_{si}) in the x_{si}-y_{si} coordinate and the biaxial concrete strains (ε_1 and ε_2) in the 1-2 coordinate are defined by the following compatibility equation:

$$\begin{Bmatrix} \varepsilon_{si} \\ \varepsilon_{si'} \\ 0.5\gamma_{si} \end{Bmatrix} = \left[T\left(\theta_{si} - \theta_1\right)\right] \begin{Bmatrix} \varepsilon_1 \\ \varepsilon_2 \\ 0.5\gamma_{12} \end{Bmatrix} \tag{6.2}$$

6.2.1.3. Uniaxial strain and Biaxial strain

In reality, uniaxial tests are usually performed in laboratory to determine material properties. There is no such exprimental biaxial constitutive material model for the biaxial strains in **Equation (6.2)**. In order to solve problems in 2-D dimension, the biaxial strains need to be converted to uniaxial strains so that the unixial constitutive material model tested in laboratory can be used. The uniaxial strains are related to the biaxial strainsby the Poisson Ratios of cracked concrete:

$$\begin{Bmatrix} \overline{\varepsilon}_1 \\ \overline{\varepsilon}_2 \\ 0.5\gamma_{12} \end{Bmatrix} = [V] \begin{Bmatrix} \varepsilon_1 \\ \varepsilon_2 \\ 0.5\gamma_{12} \end{Bmatrix}; \; [V] = \begin{bmatrix} \dfrac{1}{1-\nu_{12}\nu_{21}} & \dfrac{\nu_{12}}{1-\nu_{12}\nu_{21}} & 0 \\ \dfrac{\nu_{21}}{1-\nu_{12}\nu_{21}} & \dfrac{1}{1-\nu_{12}\nu_{21}} & 0 \\ 0 & 0 & 1 \end{bmatrix} \tag{6.3}$$

In **Equation (6.3)**, $\nu_{12}$is the ratio of the resulting tensile strain increment in the principal 1-direction to the source compressive strain increment in the principal 2-direction, and $\nu_{21}$is the ratio of the resulting compressive strain increment in the principal 2-direction to the sourcetensile strain increment in the principal 1-direction. Values for $\nu_{12}$and $\nu_{21}$for reinforced concrete elements were derived from the panel tests by Zhu and Hsu[6].

6.2.1.4. Uniaxial constitutive model for concrete and embedded steel

The cyclic uniaxial constitutive relationships of concrete with embedded mild steel barswere proposed by Mansour [7]. The characteristics of these concrete constitutive laws include: (1) the softening effect on the concrete in compression due to the tensile strain in the perpendicular direction; (2) the softening effect on the concrete in compression under reversed cyclic loading; (3) the opening and closing of cracks, which are taken into account in the unloading and reloading stages, as shown **Figure 6.2(a)**. The smeared yield stress of embedded mild steel bars is lower than the yield stress of bare steel bars and the hardening ratio of steel bars after yielding is calculated from the steel ratio, steel strength and concrete strength. The unloading and reloading stress-strain curves of embedded steel bars take into account the Bauschinger effect, as shown in **Figure 6.2(b)**.

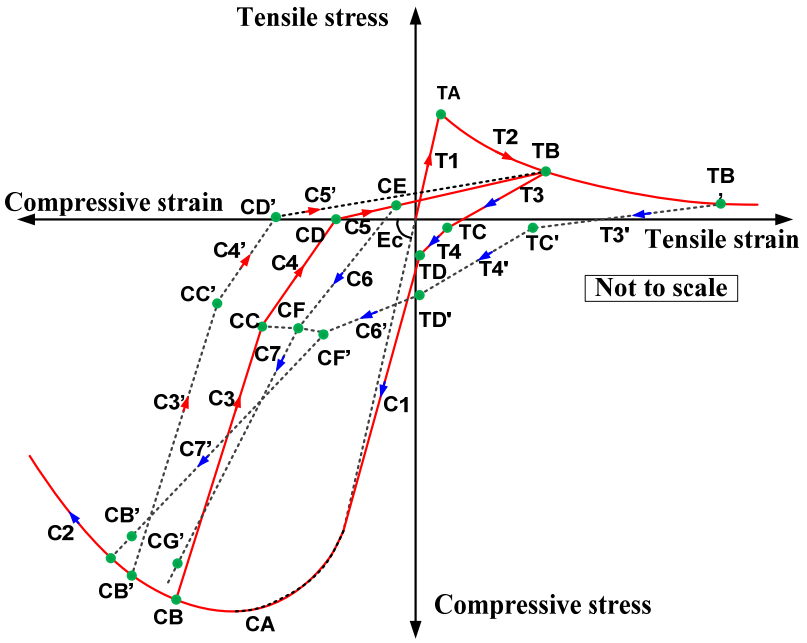

(a) Concrete

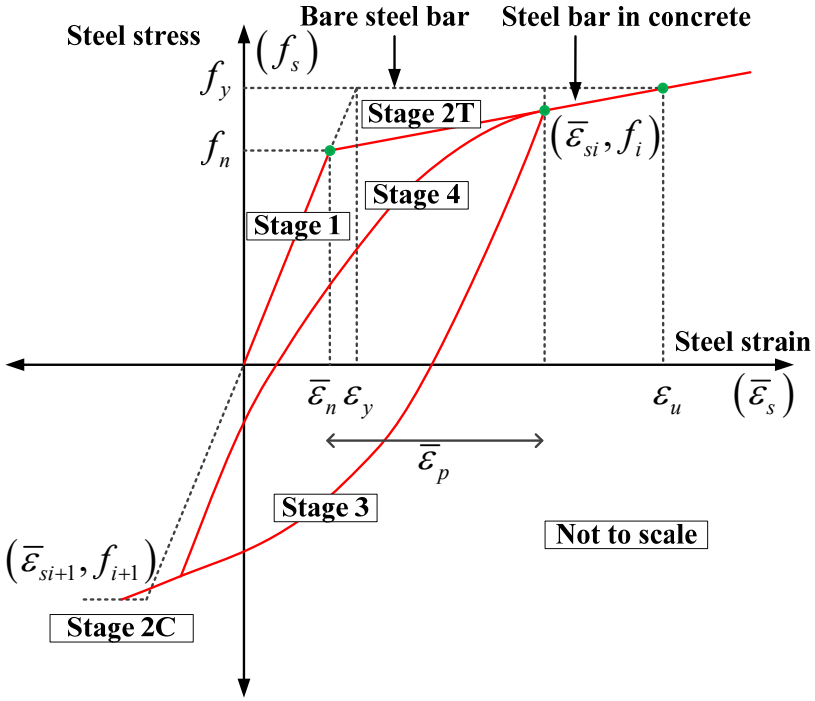

(b) Steel

Figure 6.2: Cyclic stress-strain relationship of materials.

6.2.1.5. Finite Element Implementation

The constitutive laws discussed before are combined with the equilibrium and compatibility equations to form a tangent stiffness matrix [*D*] for element. The detail of the derivation of the matrix [*D*] is presented in Zhong [5].The formulation to determine [*D*] is given as follows:

$$[D] = \partial \begin{Bmatrix} \sigma_x \\ \sigma_y \\ \tau_{xy} \end{Bmatrix} / \partial \begin{Bmatrix} \varepsilon_x \\ \varepsilon_y \\ 0.5\gamma_{xy} \end{Bmatrix} \tag{6.4}$$

[*D*] is evaluated by:

$$[D] = [T(-\theta_1)][D_c][V][T(\theta_1)] + \sum_i [T(-\theta_{si})][D_{si}][T(\theta_{si} - \theta_1)][V][T(\theta_1)] \tag{6.5}$$

In **Equation (6.5)**, [*V*]is the matrix defined in **Equation (6.3)** which translates the biaxial strains into uniaxial strains using the Hsu/Zhu ratios. [D_c] and [D_{si}] are the uniaxial tangential constitutive matrix of concrete and the uniaxial tangential constitutive matrix of steel, respectively. [D_c] and [D_{si}] are defined as follows:

$$[D_c] = \begin{bmatrix} \bar{E}_1^c & \dfrac{\partial \sigma_1^c}{\partial \bar{\varepsilon}_2} & 0 \\ \dfrac{\partial \sigma_2^c}{\partial \bar{\varepsilon}_1} & \bar{E}_2^c & 0 \\ 0 & 0 & G_{12}^c \end{bmatrix}; \; [D_{si}] = \begin{bmatrix} \rho_{si}\bar{E}_{si} & 0 & 0 \\ 0 & 0 & 0 \\ 0 & 0 & 0 \end{bmatrix} \tag{6.6}$$

In **Equation (6.6)**, $\bar{E}_1^c$, $\bar{E}_2^c$ and $\bar{E}_{si}$ are the tangential stiffness of uniaxial moduli of concrete and reinforcement which are computed at a stress/strain state. The derivatives of stress over strain $\partial\sigma^c_1/\partial\varepsilon_2$ and $\partial\sigma^c_2/\partial\varepsilon_1$ can be obtained by using the uniaxial constitutive relationships and taking into account the states of the concrete stresses and uniaxial strains in the 1-2 directions[5]. G_{12}^c is the shear modulus of concrete and is evaluated by the following equation.

$$G_{12}^c = \frac{\sigma_1^c - \sigma_2^c}{\varepsilon_1 - \varepsilon_2} \tag{6.7}$$

6.2.2 Program SCS and Validation

6.2.2.1. Implementation

OpenSees stands for Open System for Earthquake Engineering Simulation [8]. OpenSees has been developed in the Pacific Earthquake Engineering Center (PEER) and is an object-oriented framework for simulation applications in earthquake engineering using finite element methods. An object-oriented

framework is a set of cooperating classes that can be used to generate software for a specific class of problem, such as finite element analysis. The framework dictates overall program structure by defining the abstract classes, their responsibilities, and how these classes interact. OpenSees is a communication mechanism for exchanging and building upon research accomplishments, and has the potential for a community code for earthquake engineering because it is an open source.

Using the OpenSees as the finite element framework, a nonlinear finite element program titled Simulation of Concrete Structures (SCS) was developed for the simulation of reinforced concrete structures subjected to monotonic and reversed cyclic loading [9]. To create SCS program, the CSMM is implement OpenSees, three new material modules, namely SteelZ01, ConcreteZ01 and RCPlaneStress were developed. SteelZ01 and ConcreteZ01 are the uniaxial material modules, in which the uniaxial constitutive relationships of steel and concrete specified in the CSMM are defined, as shown Error! Reference source not found... The RCPlaneStress is implemented with the quadrilateral element to represent the four-node reinforced concrete membrane elements. The uniaxial materials of SteelZ01 and ConcreteZ01 are related with material RCPlaneStress to determine the material stiffness matrix of membrane reinforced concrete in RCPlaneStress.

6.2.2.2. Validation

OpenSees stands for Open System for Earthquake Engineering Simulation [8]. OpenSees has been developed in the Pacific Earthquake Engineering Center (PEER) and is an object-oriented framework for simulation applications in earthquake engineering using finite element methods. An object-oriented framework is a set of cooperating classes that can be used to generate software for a specific class of problem, such as finite element analysis. The framework dictates overall program structure by defining the abstract classes, their responsibilities, and how these classes interact. OpenSees is a communication mechanism for exchanging and building upon research accomplishments, and has the potential for a community code for earthquake engineering because it is an open source.

Nine different framed shear walls were tested by Gao[10] to evaluate the seismic performance of shear walls under constant axial load and reserved cyclic loading. In this article, two of these shear walls are selected for analysis. The wall dimensions were 914.4 mm by 914.4 mm with a thickness of 76.2 mm. The cross section of the boundary columns was 152.4 mm square. The details of the reinforcement of the specimen are illustrated in **Figure 6.3(a).** The bottom left and right corner of the specimens were supported by a hinge and a roller, respectively. **Table 6.1** gives the material properties, reinforcement ratio and axial load ratio of each specimen. As noted from the table, the concrete strengths used in the two specimens are very close. Specimen SW13 has less reinforcement ratio and lower axial load ratio than Specimen SW4.

As observed from the test results, Specimen SW13 has ductile behavior and Specimen SW4 has brittle behavior [10].

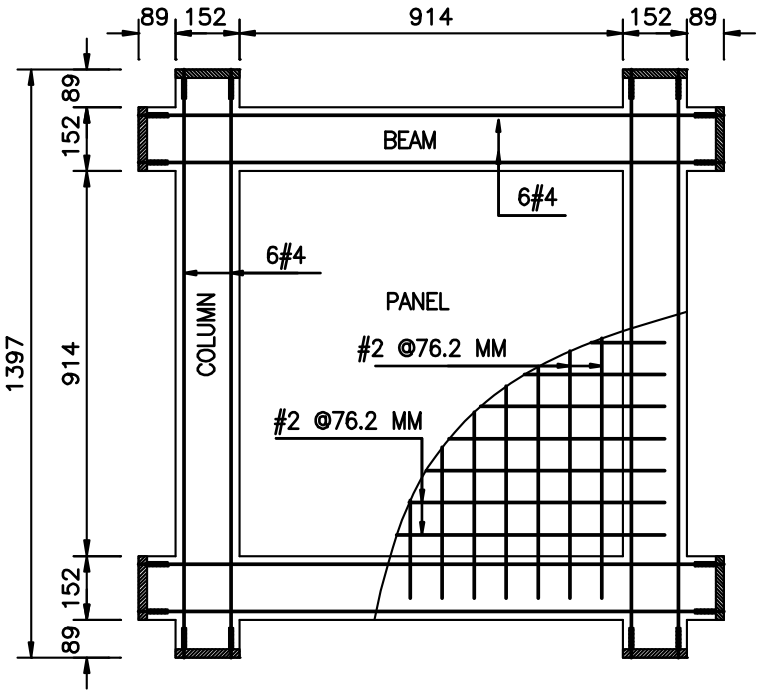

(a) Details of shear walls

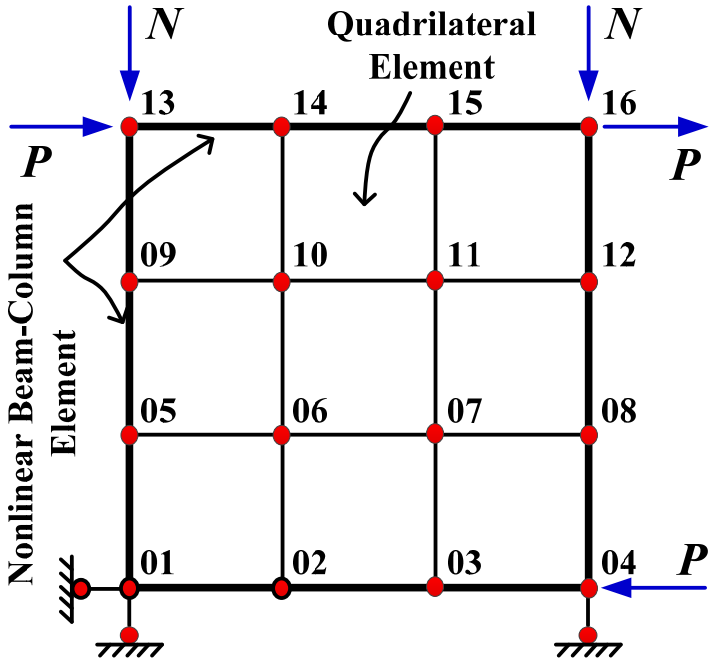

(b) FEM modeling of shear walls

Figure 6.3: Frame shear walls [10].

Finite element analyses were conducted on the shear walls named SW4 and SW13. The two specimens were modeled by the finite element mesh, as illustrated in **Figure 6.3(b).** The wall panel are simulated by RCPlaneStress quadrilateral elements, mentioned above. The boundary columns and beams are simulated with NonlinearBeamColumn element, which are available elements in OpenSees. The axial loads acting on the columns were applied as vertical nodal forces which remain constant in the analysis. The comparison of the analytical result with test data of the shear force-drift relationship of the structures is illustrated in **Figure 6.4.** The analytical result is shown to provide a good correlation with experimental data. The primary backbone curves, the initial stiffness, the yield point, the peak strength, the descending branch, and the failure characteristics of the analytical result matches very closely with experimental data.

Table 6.1 Dimensions and properties of specimens

Specimen name	f_c' (MPa)	Column & beam			Wall panel		Vertical Load	
		Hoop steel (mm)	Long. steel	Long. steel (%)	Panel steel (mm)	Panel steel (%)	P (kN)	P/Po Ratio
SW4	49.51	#3@63.5	6#4	3.33	#2@152.4	0.23	534	0.46
SW13	56.91	#2@63.5	6#4	3.33	W2@152.4	0.55	89	0.07

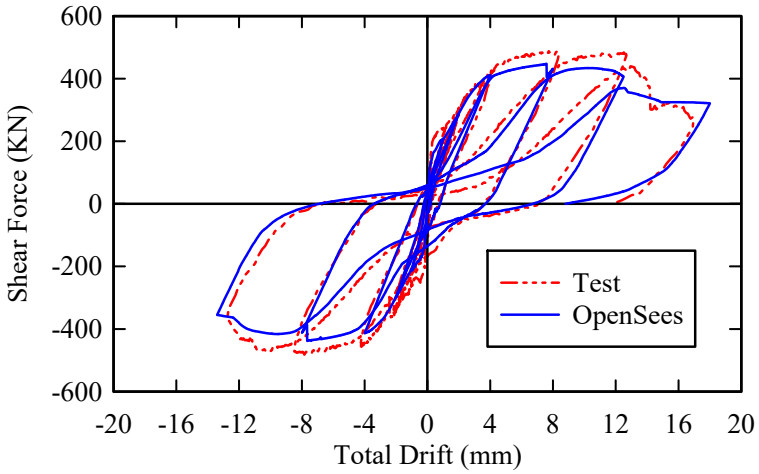

(a) Shear Wall SW13

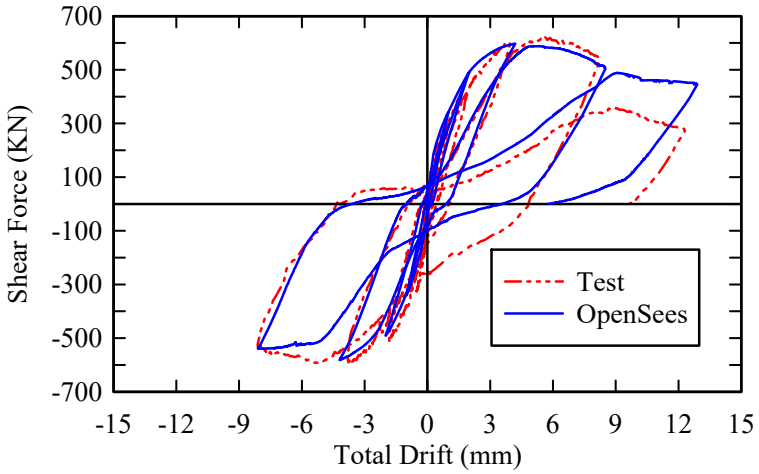

(b) Shear Wall SW4

Figure 6.4: Seismic behavior of shear walls under cyclic loading.

6.3 Constitutive models of Multifunctional Strain-hardening Cementitious Composites

To expand the CSMM model to account for the tensile strain-hardening behavior, the constitutive laws of normal concrete in CSMM is modified following two beneficial characteristics of MSC. First, the tension stiffening of normal concrete is replaced by the tensile strain-hardening behavior of MSC, as shown in **Figure 6.5 (a).** Second, the strain at maximum compression stress of MSC is modified to be higher than concrete, as shown in **Figure 6.5 (b).**

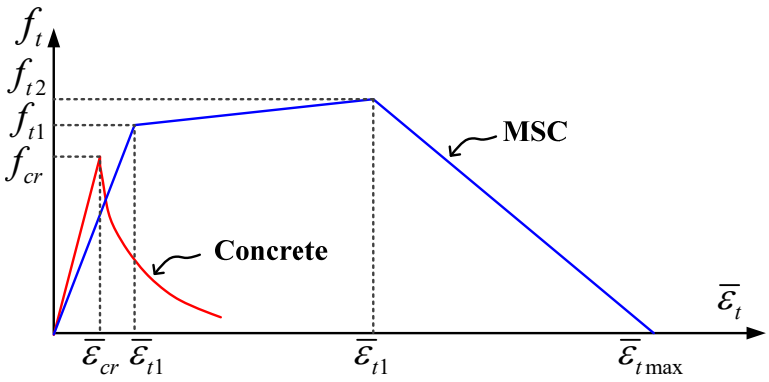

(a) In tension

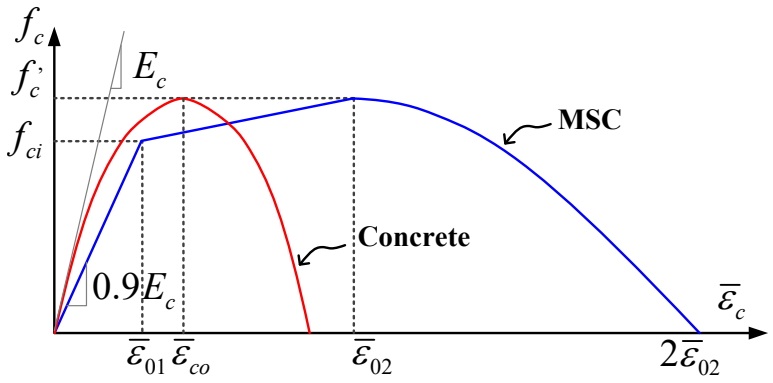

(b) In compression

Figure 6.5: Smeared uniaxial stress-strain relationships of concrete and MSC.

The behavior of MSC subjected to shear is considered for the softening effect because the biaxial state of stress is different than the uniaxial behavior so that the compressive strength is a function of the lateral strain. The softened stress-strain relationship of MSC is proposed in this section, as shown in **Figure 6.6**. The softening effect of MSC is expected to be different from the concrete elements due to the unique multiple microcracking pattern of MSC. The softening effect of for MSC is considered in this model.

As shown in **Figure 6.6**, the compressive stress-strain curve of MSC in a 2-D element subjected to shear exhibits three characteristics. First, the peak point is reduced or 'softened' in both strain and stress. Second, the ascending branch is expressed by a bi-linear curve. Third, the descending curve is a parabolic curve which intersects the horizontal axis at a large strain of $4\overline{\varepsilon}_{02}$.

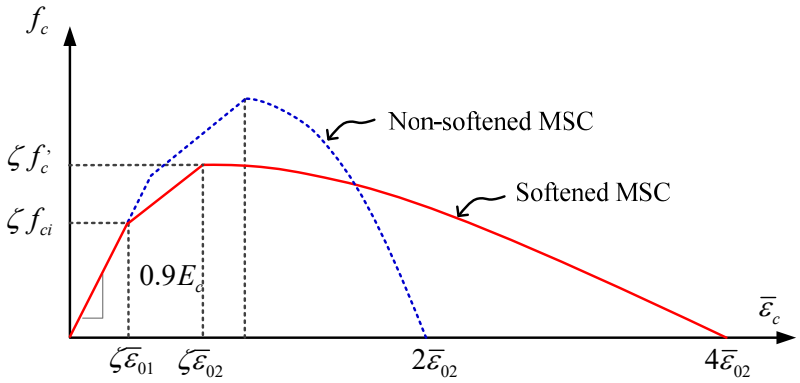

Figure 6.6: Softening stress-strain relationship of MSC.

The ascending branch of the softened stress-strain curve of MSC can be expresses as:

$$f_c = E_{ecc}\overline{\varepsilon}_c \quad \varepsilon_c \le \zeta\overline{\varepsilon}_{01} \tag{6.8}$$

$$f_c = \zeta\left(f_{ci} + \frac{f_c^{/} - f_{ci}}{\bar{\varepsilon}_{02} - \bar{\varepsilon}_{01}}\left(\bar{\varepsilon}_c - \bar{\varepsilon}_{01}\right)\right) \quad \zeta\bar{\varepsilon}_{01} \le \varepsilon_c \le \zeta\bar{\varepsilon}_{02} \qquad (6.9)$$

The descending branch of the softened stress-strain curve of MSC can be expresses as:

$$f_c = \zeta f_c^{/}\left(1 - \left(\frac{\bar{\varepsilon}_c/\zeta\bar{\varepsilon}_{02} - 1}{4/\zeta - 1}\right)^2\right) \quad \varepsilon_c \ge \zeta\bar{\varepsilon}_{02} \qquad (6.10)$$

Where $\bar{\varepsilon}_{02}$ is the strain at peak stress f_c'. This value for MSC is usually greater than that for concrete. In this section, $\bar{\varepsilon}_{02}$ is taken as 0.005 in most of analysis cases. ζ is the softened coefficient. Notice that both peak stress f_c' and the equivalent strain at peak point $\bar{\varepsilon}_{02}$ are multiplied by ζ to achieve the effect of stress softening and strain softening, respectively. $\bar{\varepsilon}_{01}$is the strain at the stress f_{ci}, which is defined as the limit stress for the elastic zone of MSC, and is taken as $0.8f_c'$. $E_{ecc}$is the initial modulus of MSC, taken as 90 percent of the initial modulus of concrete with the same strength.

6.4 Seismic behavior of Reinforced MSC shear walls

The proposed MSC-CSMM was implemented in SCS program. The SCS program with MSC is utilized to perform similar analyses of the two shear walls SW4 and SW13 mentioned in the previous section. In all analyses, the maximum compressive stresses, the tensile stresses at cracking and the tensile strains at cracking of MSC are defined the same as the values used with concrete in **Section 6.2**.The ultimate point of the response curve is defined at the point of 80% of the structure's maximum shear capacity. Some of important aspects of the results obtained from the analyses are discussed to evaluate the effect of MSC on the seismic performance of the shear wall structures.

6.4.1 Seismic response of shear walls under monotonic loading

The results from the analyses of monotonic loading are presented in **Figure 6.7**. It is very interesting to see the very big difference between these two sets of curves. Before the cracking point, MSC shear walls and concrete shear walls have almost identical stiffness. After the cracking point, the stiffness of all shear walls decreases, the stiffness of MSC shear walls is higher than that of concrete walls. The similarity of stiffness before cracking can be explained by two reasons. Firstly, these values of maximum compressive stresses, tensile stresses at cracking and the tensile strains at cracking are similar. Secondly, the initial stiffness of the compressive stress-strain curve of MSC is defined very close to the initial stiffness of concrete. The difference of the stiffness between MSC shear walls and concrete shear walls after cracking can be explained by the dissimilarity of the tensile stress-strain curve of MSC and concrete after cracking. After cracking, the tensile stress of concrete decreases and is usually neglected. The tensile stress of MSC,

however, maintains its value or increases steadily due to the elastic-hardening property of MSC. This tensile stress contributes in increasing the shear force capacity of MSC shear walls.

In both cases of SW4 and SW13, the peak strength and ultimate displacements or total drifts of MSC shear walls are greater than concrete shear walls. As shown in **Figure 6.7a**, the peak strength increases about 30% and the displacement increase approximately three times. It is noted that, in the case of SW13, the curve is ductile with the use of original concrete and it becomes much more ductile the use of with MSC. In the case of SW4, the behavior of wall which is originally brittle becomes a little ductile when MSC is used, as shown in **Figure 6.7b.**

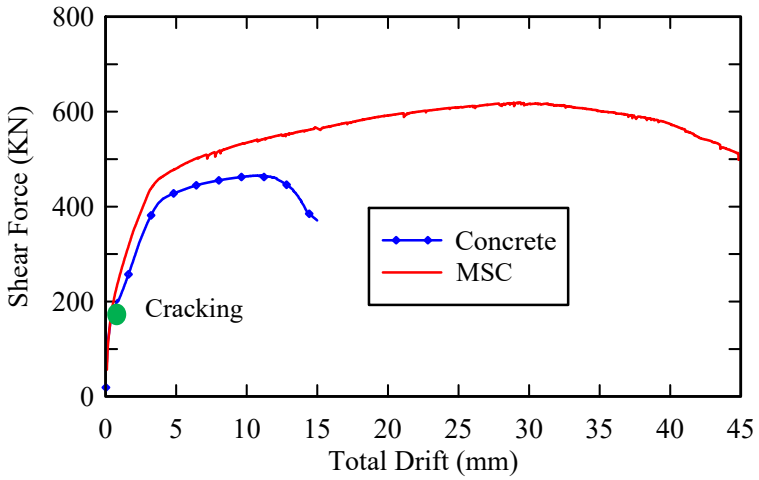

(a) Shear Wall SW13

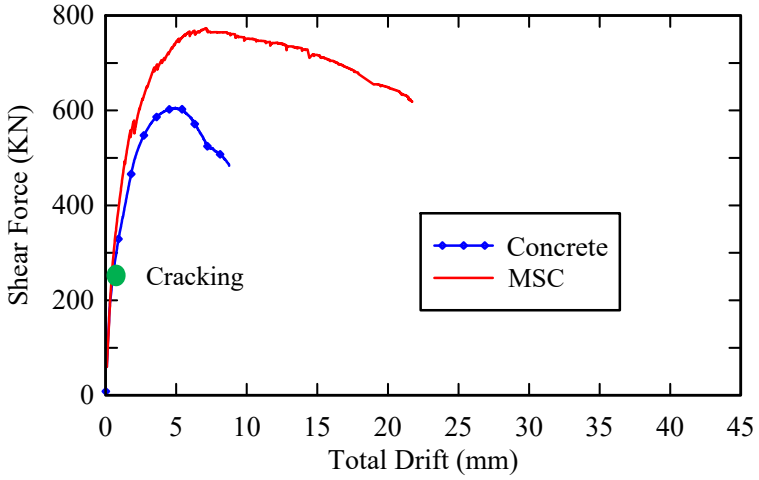

(b) Shear Wall SW4

Figure 6.7: Seismic responses of shear walls using different material under monotonic loading.

6.4.2 Seismic response of shear walls under cyclic loading

The results from the analyses of cyclic loading are presented in **Figure 6.8**. The stiffness, peak strength, and maximum displacement of the shear walls increase significantly similar to the case of monotonic loading. For the sake of the higher ductility, the shear walls can sustain more cycles of loading. Therefore, the energy dissipation capacity is sustainably increased.

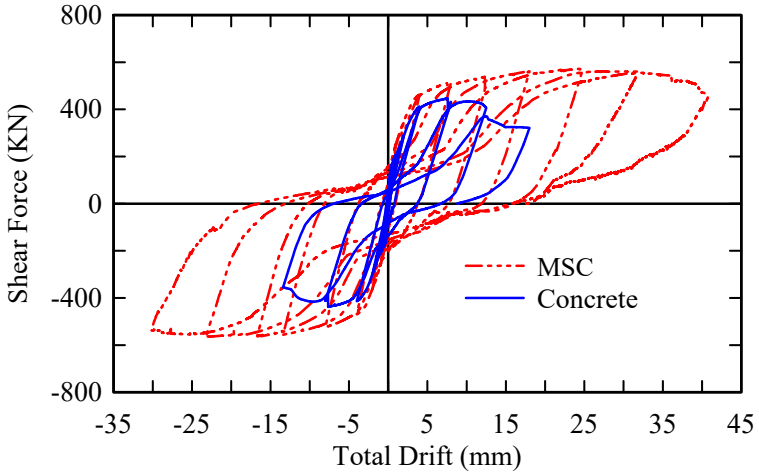

(a) Shear Wall SW10

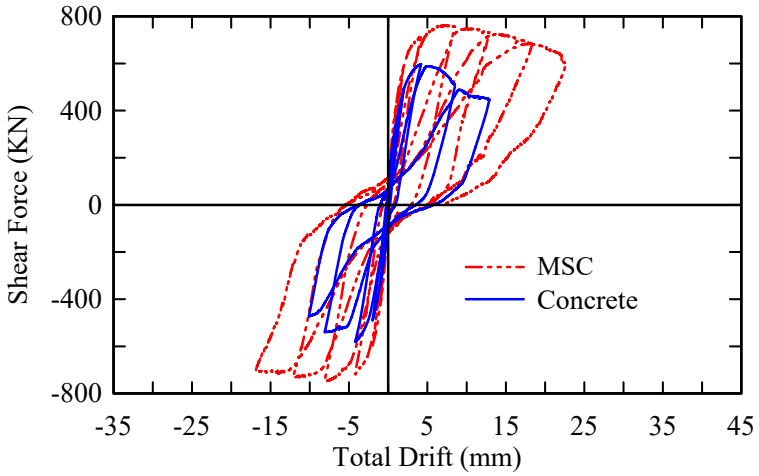

(b) Shear Wall SW4

Figure 6.8: Seismic responses of shear walls using different material under cyclic loading.

6.4.3 Effect of strain at maximum strength εo

Unlike tensile property, not many studies have been done to investigate the compressive property of MSC. The MSC is assumed to have a similar characteristic in compression as confined concrete which is more ductile than ordinary concrete [11].It is noted from analysis, when the ascending part of the force-

displacement curve is affected mostly by the tensile property of material, the descending part is controlled by the compressive property, in that, the train at peak compressive stress is the dominant parameter.

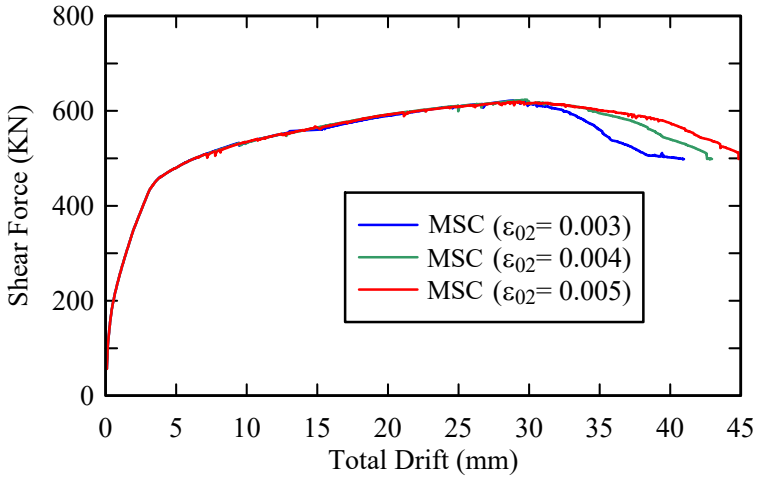

(a) Shear Wall SW13

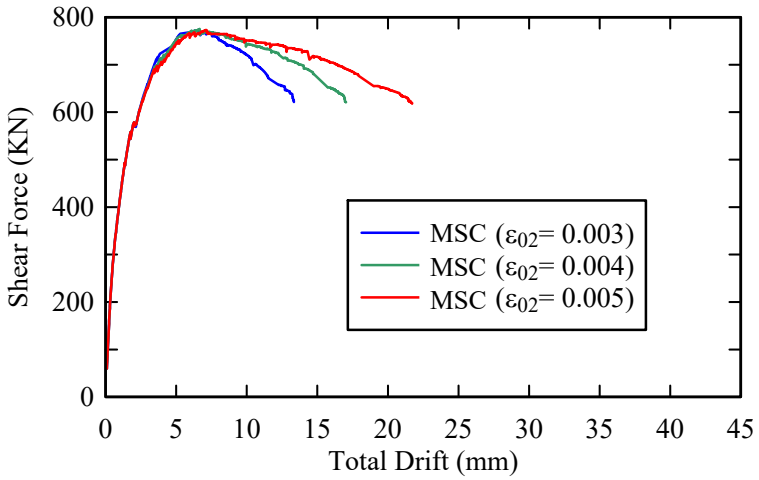

(b) Shear Wall SW4

Figure 6.9: Seismic responses of shear walls using MSC material with different values of strain at peak strength.

Error! Reference source not found. shows the results of the same shear walls using MSC material with different values of the trains at peak compressive stress. As the strain at peak compressive stress increases, the stiffness of the descending part increases and the wall has more ductility. For the case of ductile shear wall SW13, this change has little contribution in the overall response of the wall. However, this change makes big improvement in the case of SW4 because it original behavior with concrete is brittle. In other words, the ductility of material in compression becomes more important in case of brittle structures and more attention is need.

6.4.4 Pinching effect

As shown in **Figure 6.8**, the pinching effect of MSC shearwalls is not much improved compared with concrete shear walls. Since tensile property of MSC is very ductile, it is expected to enhance the ductility in tensile principal direction; as a result, the pinching effect of the shearwalls will be increased like the use of steel in principal direction [4]. However, although the tensile strain is large, but the tensile stress is small, it cannot have big influence to help enhance pinching effect on the shear walls.

6.4.5 Energy dissipation capacity

Error! Reference source not found. shows the difference in term of energy dissipation capacity between concrete walls and MSC structures analyzed in Sections 6.4.1 and 6.4.2. It can be seen that for both analyzed cases of monotonic and cyclic loading, the dissipated energy of MSC shearwalls is approximately four times greater than concrete shear walls.

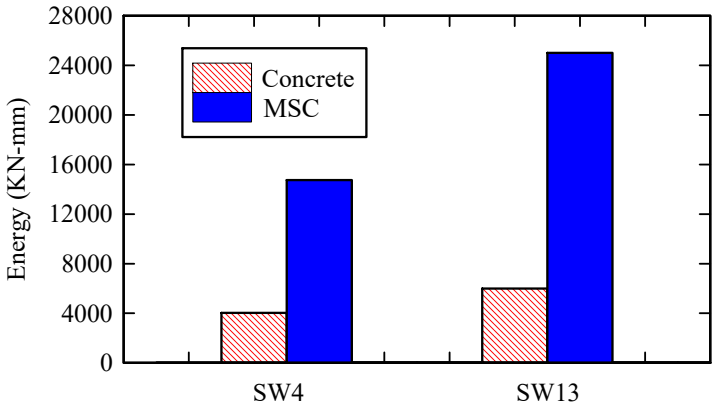

(a) Monotonic loading

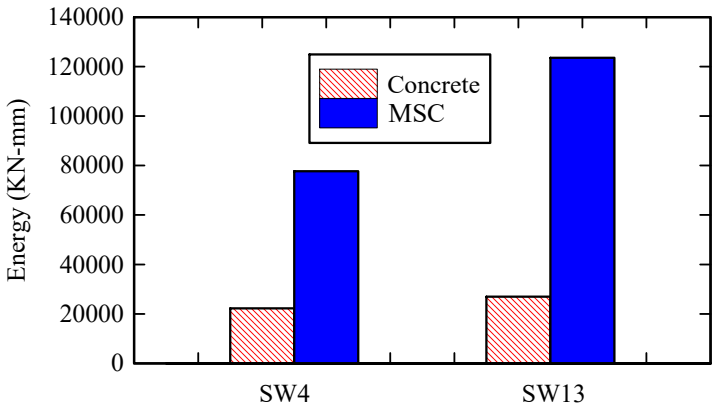

(b) Cyclic loading

Figure 6.10: Comparison of energy dissipation capacity of shear walls using concrete and MSC under monotonic loading and cyclic loading.

6.5. Summary of accomplishments

In the section, the seismic performance of a reinforced MSC shear wall was studied as a benchmark problem. A new Cyclic Softening Membrane Model for MSC was developed. The constitutive model links material properties of MSC to structural behavior. The seismic response of MSC shear walls under monotonic and cyclic loading, including pinching effect and energy dissipation capacity were critically examined. It was concluded that MSC shear walls had superior performance and safety than normal reinforced concrete shear walls under seismic loading. Compared with reinforced concrete shear walls, reinforced MSC shear walls had significantly larger shear capacity, ductility, and energy dissipation capacity. MSC shear walls were also able to survive more cycles than concrete shear walls under cyclic loading.

6.6. References

[1] T. T. C. Hsu and Y. L. Mo, *Unified Theory of Concrete Structures*: John Wiley & Sons, 2010.

[2] V. C. Li, D. K. Mishra, A. E. Naaman, J. K. Wight, J. M. LaFave, H. C. Wu*, et al.*, "On the shear behavior of engineered cementitious composites," *Advanced Cement Based Materials,* vol. 1, pp. 142-149, 3// 1994.

[3] M. Li and V. C. Li, "Influence of Material Ductility on Performance of Concrete Repair," *ACI Materials Journal,* vol. 106, pp. 419-428, 2009.

[4] M. Mansour and T. T. C. Hsu, "Behavior of reinforced concrete elements under cyclic shear. II: Theoretical model," *Journal of Structural Engineering,* vol. 131, pp. 54-65, 2005.

[5] J. Zhong, "Model-based Simulation of Reinforced Concrete Plane Stress Structures," University of Houston, Houston, 2005.

[6] R. R. H. Zhu and T. T. C. Hsu, "Poisson effect in reinforced concrete membrane elements," *ACI structural journal,* vol. 99, pp. 631-640, 2002.

[7] M. Mansour, Y. H. Lee, and T. T. C. Hsu, "Cyclic stress-strain curves of concrete and steel bars in membrane elements," *Journal of Structural Engineering, ASCE,* vol. 127, pp. 1402-1411, 2001.

[8] OpenSees, "Annual workshop on open system for earthquake engineering simulation," in *Pacific Earthquake Engineering Research Center*, UC Berkeley, 2013.

[9] Y. L. Mo, J. Zhong, and T. T. C. Hsu, "Seismic simulation of RC wall-type structures," *Engineering Structures,* vol. 30, pp. 3167-3175, 2008.

[10] X. D. Gao, "Framed shear walls under cyclic loading," University of Houston, Houston, 1999.

[11] V. C. Li, M. Lepech, and G. Fischer, "General design assumptions for engineered cementitious composites (ECC)," in *International RILEM Workshop on High Performance Fiber Reinforced Cementitious Composites in Structural Applications*, Honolulu, Hawaii, 2006, pp. 269-277.

7. DURABILITY CHARACTERIZATIONS AND LIFE-CYCLE ANALYSIS

7.1 Introduction

The objective of this task was to compare the newly developed MSCs with existing concrete through durability characterization and life-cycle analysis. Life-cycle modeling represents a comprehensive analytic tool for evaluation and management of SNF storage systems with regard to long-term economic and environmental indicators. New service life and deterioration models developed within this project were critical to facilitate life cycle assessment of both existing and new designs of dry casks using MSCs. Data collected from experimental characterization and computational modeling provided deterioration measures and input for predictive service life modeling and life estimation. The service life prediction was integrated with maintenance and repair schedules to develop a life cycle analysis framework that considered material production, construction, use and end-of-life stages.

A durability-based, lifetime optimization methodology for planning the inspection and repair of structures that deteriorate over time was introduced and illustrated in the event trees. The life cycle model was based on minimizing the expected total life-cycle cost while maintaining an allowable lifetime reliability for the structure. This method took into consideration (1) the quality of inspection techniques with different detection capabilities, (2) maintenance and repair frequencies, and (3) the time value of money. In addition, the sensitivity analysis was performed to study different sustainability indicators.

7.2 Durability Characterization

7.2.1 Chloride penetration and corrosion

Corrosion of reinforcing steel and other embedded metals is the leading cause of deterioration in concrete. When steel corrodes, the resulting rust occupies a greater volume than the steel. This expansion creates tensile stresses in the concrete, which can eventually cause cracking and spalling.

The corrosion of steel reinforcement is complex, but basically, it is an electro-chemical reaction similar to that of a simple battery. Concrete is capable of conducting electric current and acts as the electrolyte with the circuit being completed by the bar through which the electrons can flow. However, the highly alkaline environment (pH is typically over 12) provided by good quality concrete produces a protective layer around the steel preventing the flow of current. This is known as passivation.

In dense concrete, the embedded steel reinforcement is normally protected from corrosion due to the formation of a passive layer over the steel surface in the highly alkaline concrete environment. However, the breakdown of the passive film occurs either due to the carbonation which reduces the pH of the pore water to a non-protective level or by the presence of the significant quantities of chloride ions at reinforcement level in concrete[1-3]. Chloride ions are considered to be the primary cause of rebar corrosion

in concrete. The source of chloride may be internal and/or external. The chloride introduced into concrete at the time of preparation, i.e. from mixing water, chloride contaminated aggregates, chloride containing admixtures, etc. is known as internal chloride. On the other hand, chloride entering into hardened concrete by the application of deicing salts in bridge decks and parking structures, from sea water in marine structures, and from soil and ground water containing chloride salts is known as external chloride.

Carbonation occurs when carbon dioxide from the air penetrates the concrete and reacts with hydroxides, such as calcium hydroxide, to form carbonates. In the reaction with calcium hydroxide, calcium carbonate is formed. This reaction reduces the pH of the pore solution to as low as 8.5, at which level the passive film on the steel is not stable. Carbonation is generally a slow process. The amount of carbonation is significantly increased in concrete with a high water-to-cement ratio, low cement content, short curing period, low strength, and highly permeable or porous paste.

MSC specimens were prepared from 4-inch diameter cylinders with 8-inch height, which were casted according to ASTM C192 without tamping. These specimens were cut using wet masonry saw to the thickness of 2 in. ± 0.04 in. tolerance (**Figure 7.1**).

Figure 7.1. Cylinder specimens for rapid chloride penetration test

Prior to the rapid chloride penetration measurement, specimens were conditioned in a vacuum desiccator (**Figure 7.2**) using a vacuum pump for 3 hours, introducing negative pressure to >0.95 bar into the chamber. Distilled water was then instilled into the vacuum system until the entire specimen was immersed in water, the pumping was continued for another hour. The vacuum was vented and the specimens remained immersed in distilled water for another 18 hours. After conditioning, concrete samples were installed in between measuring cells. Distilled water from specimen conditioning was poured into the measuring cells to confirm that no leakage occurs on the cells before they are filled with proper solutions.

Figure 7.2. Conditioning of specimens with a vacuum desiccator

Approximately 250 mL of solutions was poured into respective measuring cells, 3% sodium chloride solution on the anode and 0.3M sodium hydroxide solution on the cathode. These two measuring cells were connected to a power supply through the electrodes (**Figure 7.3**). With the flow of electric current that was maintained under 60V DC potential for 6 hours period, anionic chloride was repelled from the anodic side into the specimen. In the case of a higher penetrability specimen, a larger number of ions were transported into the material, which created a higher conductivity between the anode and cathode, indicated by a larger current reading.

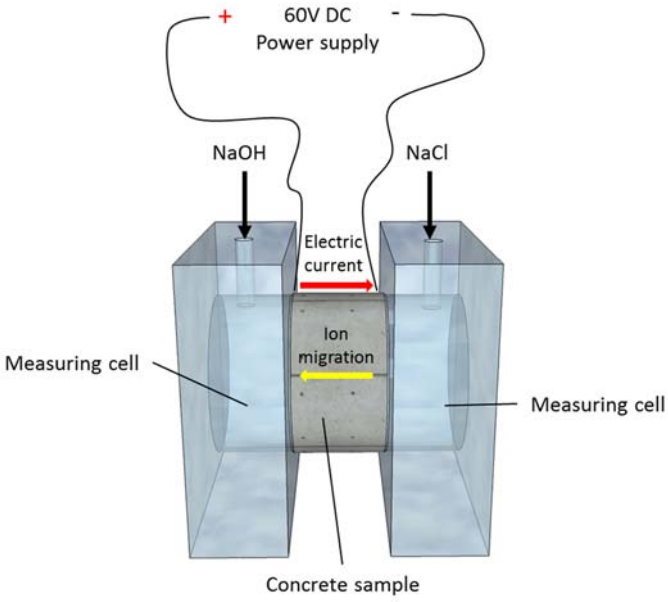

Figure 7.3. Rapid chloride penetration test

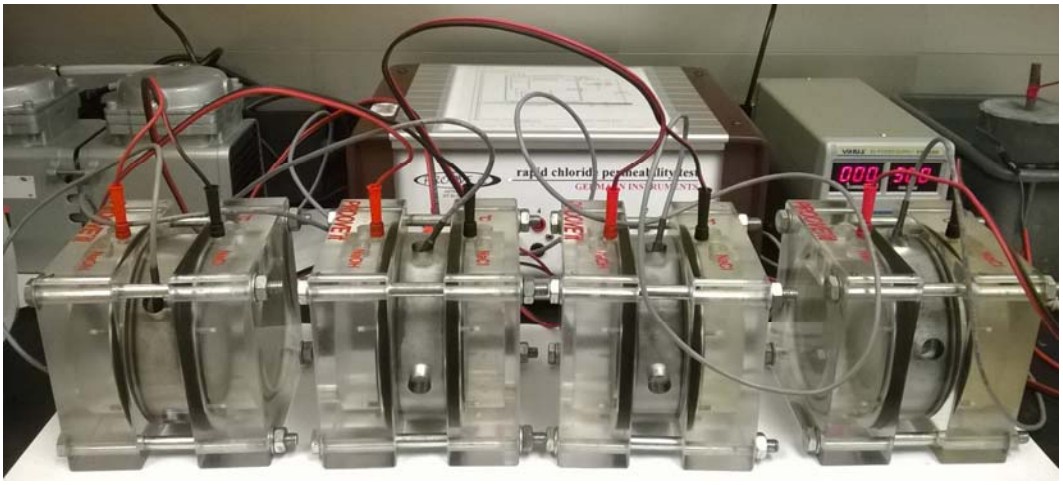

Figure 7.4. Rapid chloride permeability test measurement in progress

The rapid chloride permeability test was performed on MSC and conventional concrete specimens at 28 days and 90 days (**Figure 7.4**). Measurement of the current through the distilled water-saturated concrete sample was obtained every five minutes for a total of 6 hours. The total charge passed through the sample can be obtained by an integration of the current over time, as expressed in **Equation 7.1**:

$$Q = \int_0^T I(t)\, dt \tag{7.1}$$

Where

Q = charge passed (Coulombs)

I = electrical current (A)

T = current testing time (s)

T = total testing period (6 hours)

Since the measurement was performed in 72 steps of 5 minutes interval yielding a total of 6 hours, integration can be done in a simplified calculation shown in **Equation 7.2**:

$$Q = 150^{(sec)} \frac{(I_5 + 2I_{10} + 2I_{15} + \ldots + 2\,I_{350} + 2\,I_{355} + I_{360})^{(mA)}}{1000} \tag{7.2}$$

MSC rapid chloride permeability measurement resulted in an average of 48.87 Coulombs of charge passed at 90 days, which was categorized as negligible; 203.52 Coulombs at 28 days, which was categorized as very low; while conventional concrete samples resulted in an average of 4748.16 Coulombs and 3207.89 Coulombs at 28 days and 90 days, respectively. The results are shown in Table 7.1.

Conductivity of the concrete was calculated by **Equation 7.3**

$$\sigma = \frac{Q}{V}\frac{L}{t A} \tag{7.3}$$

Where

σ = bulk conductivity (Siemens/meter)

V = applied voltage (V)

L = length of the specimen (m)

A = specimen cross sectional area (m^2)

t = total measurement period (s)

As the experiment proceeds, more ions migrated into the concrete causing an increase in the conductivity of the specimen. However, the net change in conductivity during the test also depended on the amount of chloride ions binding to the concrete matrix which decreased conductivity, and a possible increase in the temperature (due to the application of high voltage), which decreased the conductivity according to **Equation 7.4**

$$\rho(T) = \rho_0[1 + \alpha(T - T_0)] \tag{7.4}$$

Where

ρ = resistivity at temperature T (**Ω**)

ρ_0 = resistivity at temperature T_0 (**Ω**)

α = temperature coefficient of resistivity

T = temperature (ºC)

T_0 = fixed ambient temperature (ºC)

The net conductivity was observed to decrease slightly for MSC, and increased slightly for conventional concrete due to the net interaction of the aforementioned reasons. The calculated bulk conductivity was 22.96 mS/m and 15.51 mS/m for control concrete at 28 and 90 days, and 0.98 mS/m and 0.24 mS/m for MSC at 28 and 90 days, respectively.

Table 7.1. Total charge passed and conductivity in rapid chloride permeability test

Properties	Age	MSC	Control Concrete
Charge passed (Coulombs)	28 days	515	4750
	90 days	73.4	3210
Conductivity (millisiemens/meter)	28 days	2.13	23.0
	90 days	0.84	15.51

Accelerated corrosion test was performed using a standard procedure with a 30V DC capacity potentiostat (constant voltage source). Electromigration of chloride ions from the solution into concrete specimen hastened the corrosion and expansion of steel rebar. Localized expansion of rebar generated tensile stress on concrete specimen that resulted in cracking. A crack in the concrete allowed exposure of the steel bar to the solution provides a shorter electrical path. This phenomenon resulted in a current increase that can be a failure indicator even without the appearance of a visible crack on the concrete specimen. The experimental setup was adopted from Florida DoT standard for accelerated corrosion test.

The theory of the accelerated corrosion test relies on basic theory of electrolysis in electrochemistry. When two different metals are connected to a power supply and immersed in an aqueous electrolyte, the more reactive electrode loses electrons and corrode, as shown in **Figure 7.5**. In this case, the iron electrode was more reactive than the copper electrode, and elemental iron readily lost their electrons to become aqueous iron ions.

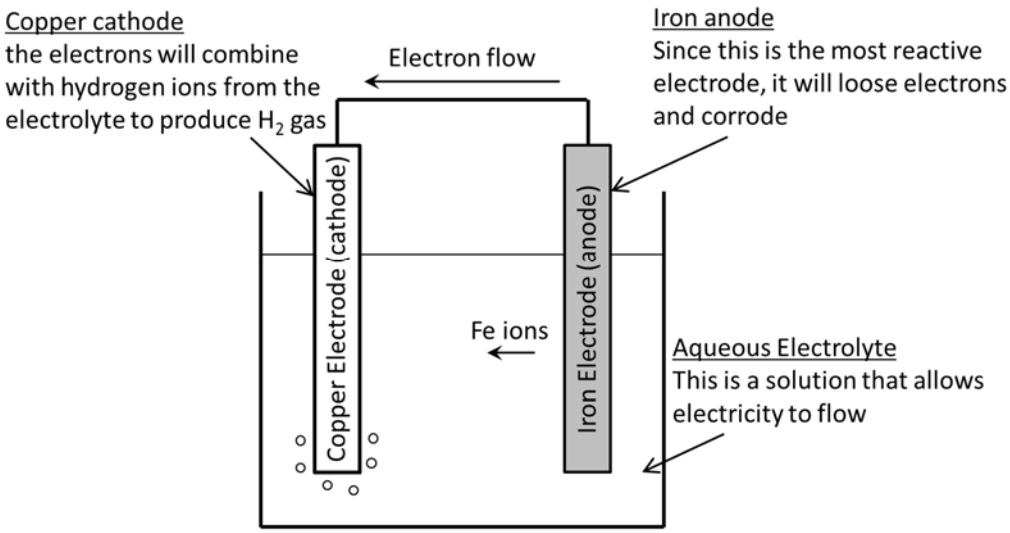

Figure 7.5. Electrochemical cell of copper and iron

Chloride ions migration from the solution to the rebar through the porous concrete specimen caused oxidation in the steel that manifests in volume expansion thus creating a tensile stress in the embedded rebar, leading up to cracks in the concrete. In order to accelerate the corrosion process, electrochemical process is used to enhance the efficiency of chloride ions to attach themselves onto the steel bar. Since sodium chloride dissociates into positive sodium ions and negative chloride ions when dissolved in water, the negative charge of chloride is used by attaching the steel bar to a positive voltage source. The higher the voltage of the steel bar, the faster and larger are amount of chloride ions that are attracted and react to the steel bar.

The standardized procedure for accelerated corrosion test is to embed a bar through the center of a concrete cylinder with diameter 4 inches and height 5.75 inches, suspended at 1.75 inches height from the

cylinder base. Test setup is shown in Figure 76. In this experiment, the specimen was moist cured for 14 days upon demolding, and partially submersed in a 5% sodium chloride solution with 6V DC applied electric field to facilitate the initiation of corrosion. The steel bar concrete complex using rebar with diameter 0.375in similar to the ties used in the SC-UHPC beam is electrically connected to the cathode and a 2 inch wide, 0.063in thick stainless steel strip was selected as anode due to its stable behavior compared to the rebar electrode (**Figure 7.7**).

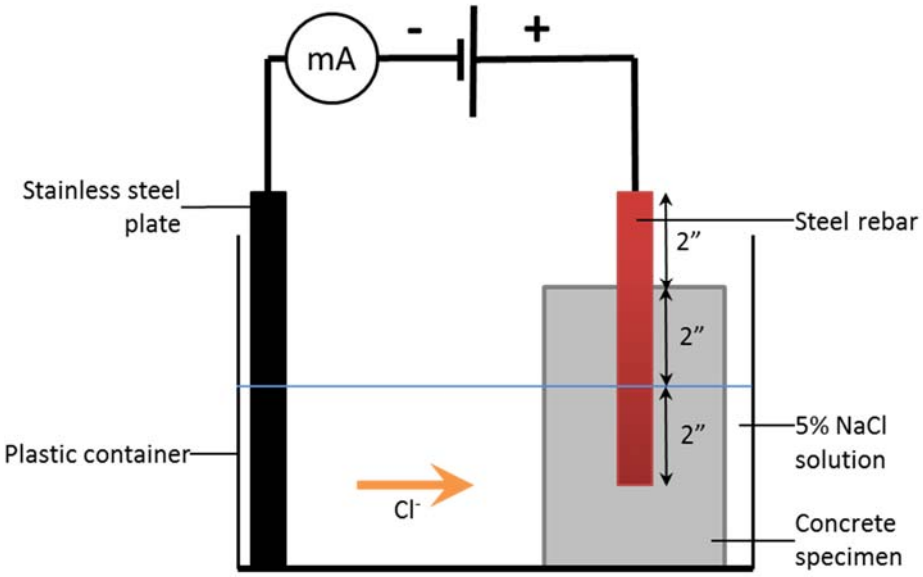

Figure 7.6. Accelerated corrosion test setup

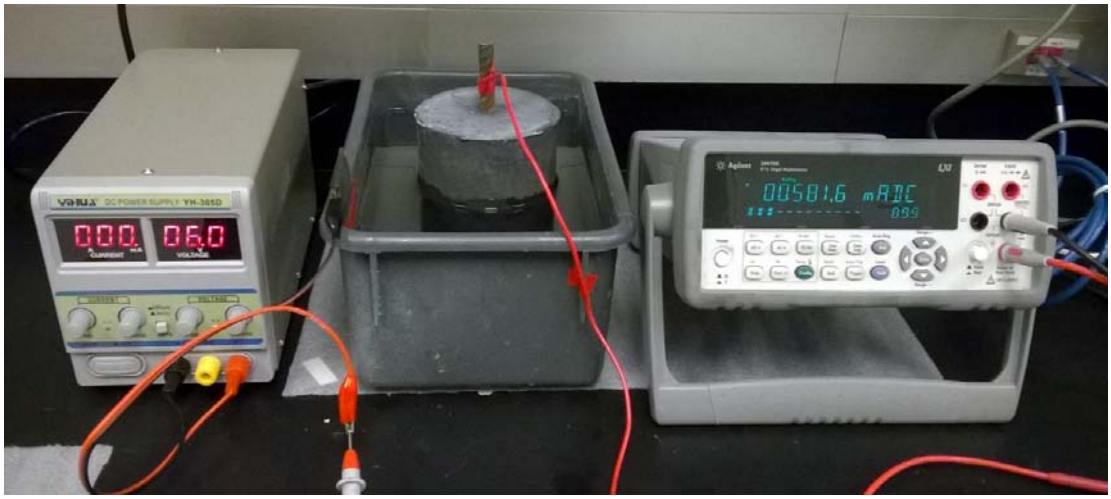

Figure 7.7. Accelerated corrosion test on a MSC

Through chloride diffusion test and accelerated corrosion test in this study, it was found that both corrosion initiation time and propagation time were prolonged by MSC in comparison with control concrete. Through the multiple microcracking behavior and self-controlled crack width of the new MSC, the chloride diffusion rate was significantly slowed down, through prolonging the corrosion initiation time. In addition, the strain-hardening behavior and tensile ductility of the MSC were able to accommodate the expansion and resulting tensile strain during the corrosion stage, providing extra spalling resistance. Furthermore, microcracking behavior in MSC led to a microcell corrosion mechanism, in contrast with the localized macrocracking behavior and macrocell corrosion mechanism in concrete, thus prolonging the corrosion propagation time. The three levels of corrosion protection offered by MSC (i.e. prolonged corrosion initiation and propagation stages, and spalling resistance) led to prolonged service life of the overpack in dry casks, and significantly reduced maintenance and repair intervals. The improved service life was considered in the life cycle analysis.

7.2.2 Freeze and thaw

Concrete materials that are saturated or nearly saturated with water can be damaged by repeated freezing and thawing cycles. Because water expands when freezing, fully or mostly saturated concrete will experience internal stresses from the expanding ice during a cooling event. If the pressure developed exceeds the tensile strength of the concrete, the cavity will dilate and rupture. The accumulative effect of successive freeze-thaw cycles and disruption of paste and aggregate can eventually cause expansion and crack, scaling, and crumbling of the concrete[4, 5].

Freezing and thawing testing was conducted on non-air-entrained MSC and non-air-entrained normal concrete prisms over 15 weeks based on ASTM C666A. After 5 weeks (110 cycles of freezing and thawing), the non-air-entrained concrete specimens had severely deteriorated. The non-air-entrained MSC specimens survived 330 cycles with no degradation of dynamic modulus. The freeze-thaw durability factor of MSC was calculated as 100, far larger than 10 for the non-air-entrained concrete.

7.2.3 Restrained shrinkage cracking

Shrinkage of concrete, when constrained, often causes early-age cracking in concrete. The tensile ductility of MSC is two orders higher than its shrinkage strain measured in this task. Therefore, ECC can accommodate the restrained shrinkage deformation to suppress localized cracking. Shrinkage ring tests were conducted to simulate the shrinkage of a freshly cast MSC layer constrained by a steel ring, following AASHTO T334-08. The standard steel ring had an outer diameter 12 in. and wall thickness of 0.5 in (**Figures 7.8** and **7.9**). The inner and outer faces were machined smooth and polished to minimize friction between the concrete layer and the steel ring. Once the control concrete or MSC were casted around the

steel ring, the specimens were demolded 24 hours after casting. Top surfaces of the specimens were lined with silicone sealant to prevent water from evaporating from the top surface. **Figure 7.10** shows the specimens after casting. Curing with wet burlap was done right after the specimen hardened to mimic the condition on site. The burlap was kept wet for three days prior to its removal (**Figure 7.11**). Then the specimen was exposed to ambient temperature between 21ºC to 24ºC and humidity 40% to 60%. Crack formation and development in the rings was visually monitored periodically using a portable microscope microscope.

In contrast with the localized cracking in the control concrete specimens, whose crack width increased as the shrinkage strain increased with time, the MSC layer exhibited a number of distributed microcracks with crack width under 30 micron. The width of these microcracks did not increase as the shrinkage strain increased with time; instead, the number of microcracks increased. The results indicated that MSC does not require steel reinforcement to control shrinkage cracking.

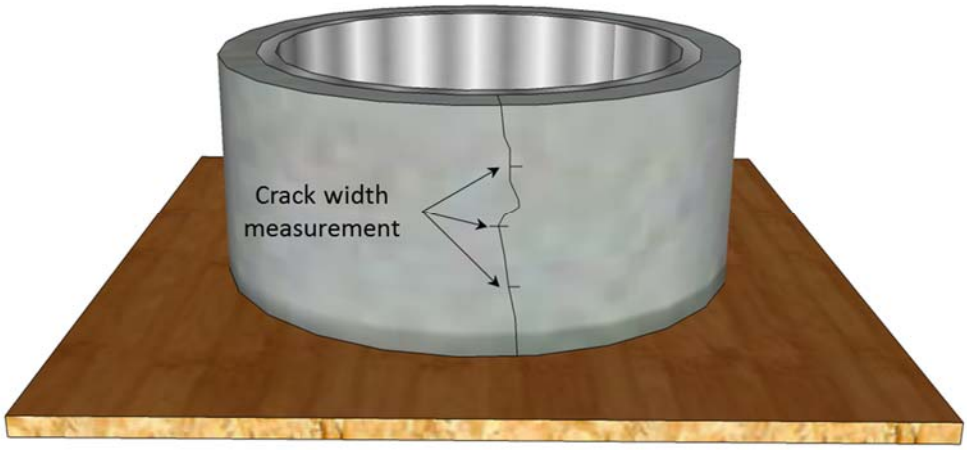

Figure 7.8. Test setup for crack width measurement of restrained shrinkage test

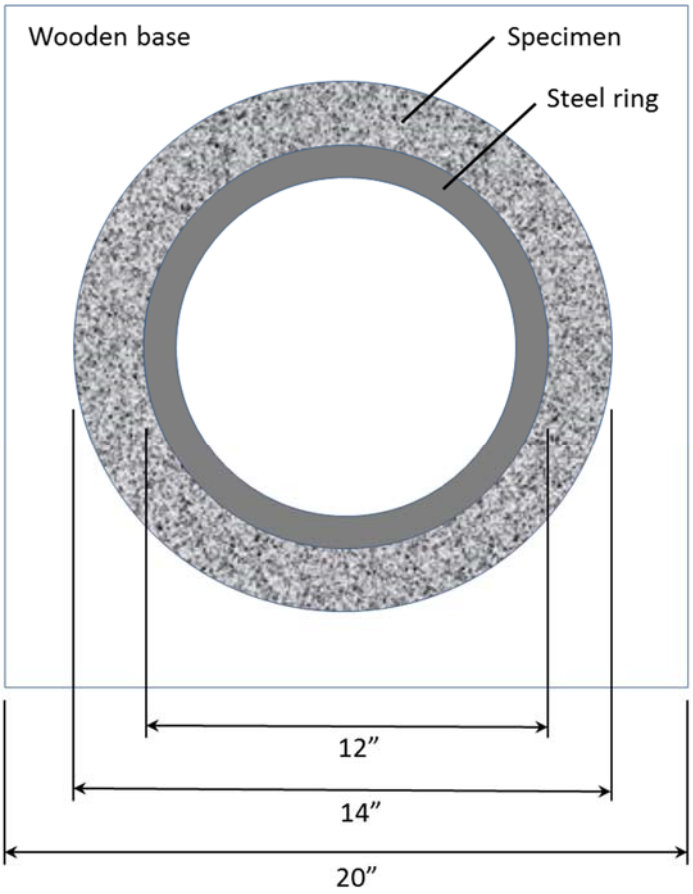

Figure 7.9 Specimen dimension for restrained shrinkage test**.**

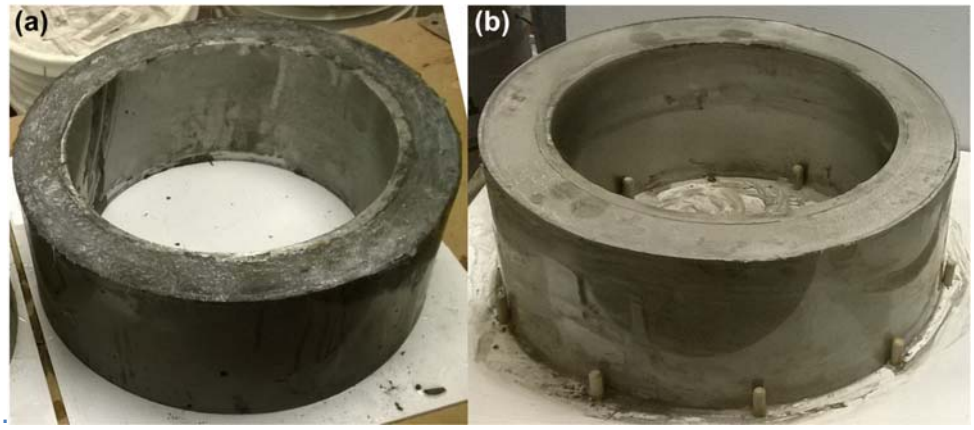

Figure 7.10: Casted restrained shrinkage specimens of (a) MSC and (b) control concrete.

Figure 7.11: Specimen moisture-curing with a burlap

7.2.4 Alkali-silica reaction

Alkali-silica reaction is the most common form of alkali-aggregate reaction in concrete. Alkali-silica reaction is a chemical reaction between hydroxyl ions in the alkaline cement pore solution in the concrete and reactive forms of silica present in some aggregates (e.g., opal, chert, chalcedony, tridymite, cristobalite, strained quartz)[6]. The resulting chemical reaction produces an alkali-silica gel that swells with the absorption of moisture, and this swelling exerts an expansive pressure within the concrete, resulting in internal damage that manifests as characteristic map cracking on the surface concrete[7].

The primary factors influencing the initiation and propagation of alkali-silica reaction include: a) a sufficiently high alkali content of the cement (or alkali from other sources such as deicing salts, seawater, and groundwater); b) a reactive aggregate; and c) available moisture, generally accepted to be relative humidity greater than 80 percent. In general, ASR can cause serviceability issues and can also exacerbate other deterioration mechanisms.

The alkali silica reaction resistance and potential degradation of MSC was characterized in this task. To promote alkali silica reaction, ASTM C1260-94 and ASTM C1293 were followed. Specimens were exposed to 1 M NaOH solution. Measurements were taken at 7, 28, and 56 days, followed by measurements at 3, 6, 9, and 12 months. Selected samples were impregnated with epoxy and then surface polished to 0.25 microns to be analyzed using scanning electron microscopy with a back-scatter sensor to identify the location of the gel and how fibers confine the microstructure to prevent the overall expansion. **Figure 7.12** and **7.13** show the severe deterioration of the control concrete specimen due to ASR, while the MSC did not exhibit any deterioration.

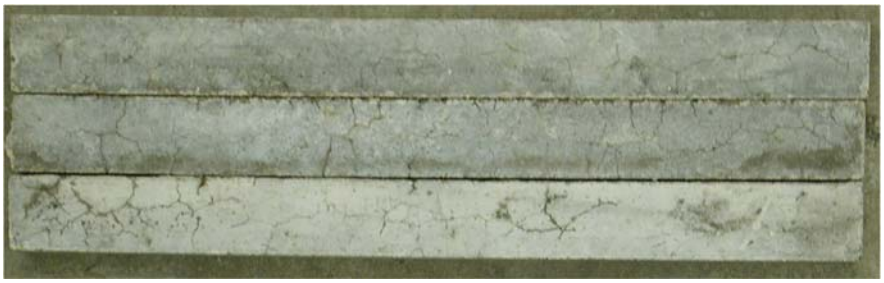

(a) Control concrete specimen

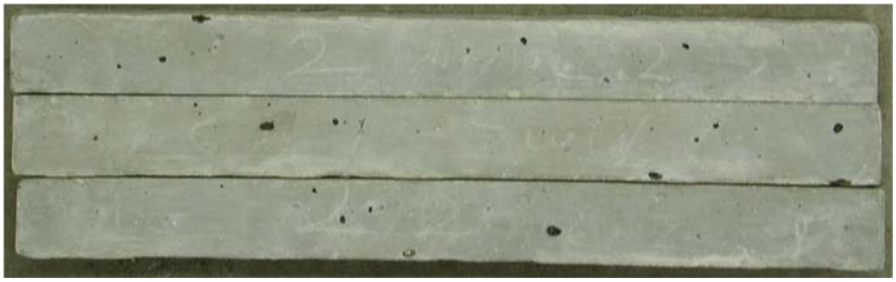

(b) MSC specimen

Figure 7.12: Alkali-silica reaction resistance of MSC.

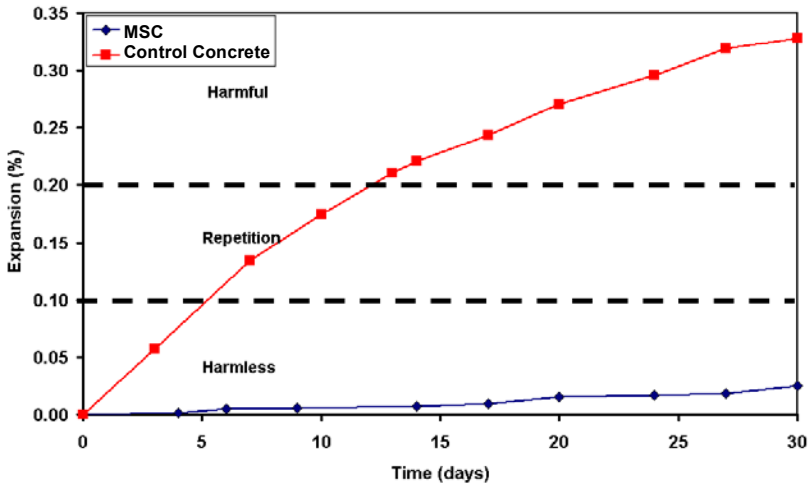

Figure 7.13: Time-dependent alkali-silica reaction expansion of MSC compared to control concrete

7.3 Service life prediction of reinforced concrete structures

LCCA estimated initial construction costs, protection costs, and future repair costs to compute the costs over the design life of the structure. A number of models for predicting the service life of concrete structures for estimating life-cycle costs have been developed recently. The corrosion of embedded steel

reinforcement in concrete due to the penetration of chlorides from deicing salts, groundwater or seawater is the most prevalent form of deterioration in concrete structures. Deterioration of reinforced concrete structures due to chloride ingress followed by reinforcement corrosion is the principal factor that has been used to mathematically predict service life in practical solutions.

The initiation period, t_i, defines the time takes for sufficient chlorides to penetrate the concrete cover and accumulate in sufficient quantity at the depth of the embedded steel to initiate corrosion of the steel. Specifically, it represents the time taken for the critical threshold concentration of chlorides, C_t, to reach the depth of cover, x_d. This study predicts the initiation period assuming diffusion to be the dominant mechanism. Fick's second law is the governing differential equation:

$$\frac{dC}{dt} = D \cdot \frac{d^2C}{dx^2} \tag{7.5}$$

where C = chloride content, D = apparent diffusion coefficient, x = depth (from the exposed surface), and t = time.

The chloride diffusion coefficient is a function of both time and temperature, and it is governed by the following relationship to account for time-dependent changes in diffusion:

$$D(t) = D_{ref} \cdot (\frac{t_{ref}}{t})^m \tag{7.6}$$

where D(t) = diffusion coefficient at time t, D_{ref} = diffusion coefficient at time t_{ref} (= 28 days), and m = constant (depending on mix proportions).

The temperature dependent changes in diffusion is determined by:

$$D(T) = D_{ref} \cdot \exp[\frac{U}{R} \cdot (\frac{1}{T_{ref}} - \frac{1}{T})] \tag{7.7}$$

where D(T) = diffusion coefficient at time t and temperature T, U = activation energy of the diffusion process (35000 J/mol), R = gas constant, and T = absolute temperature.

The chloride exposure conditions (e.g., the rate of chloride build up at the surface and maximum chloride content) are selected by the model based on the type of structure, the type of exposure (e.g., to marine or deicing salts) and the geographic location (as shown in **Figure 7.14**). The solution is carried out using a finite difference implementation of Fick's second law (**Equation 7.5**) where the value of D is modified at every time step using **Equation 7.6** and **7.7**.

In this study, the effects of temperature, corrosion inhibitors, and the addition of silica fume and fly ash on the permeability and diffusivity of concrete were considered. In addition, the influence of crack on the diffusion coefficient was also accounted for. Crack width was selected as the main test variable. when a crack occurs in the cover concrete, the corrosion of the steel reinforcement may be accelerated because the deterioration causing factors can pass through the crack. In recent years the effect of cracking on the

penetration of concrete has been the subject of numerous investigations [8-11], All of these studies have clearly indicated that the presence of cracks could contribute to an increase in the diffusion coefficient. A comparison of diffusion coefficients for cracked and uncracked concrete shows an increase in the diffusion coefficient for cracked concrete by one or two orders of magnitude, with wider cracks resulting in higher values.

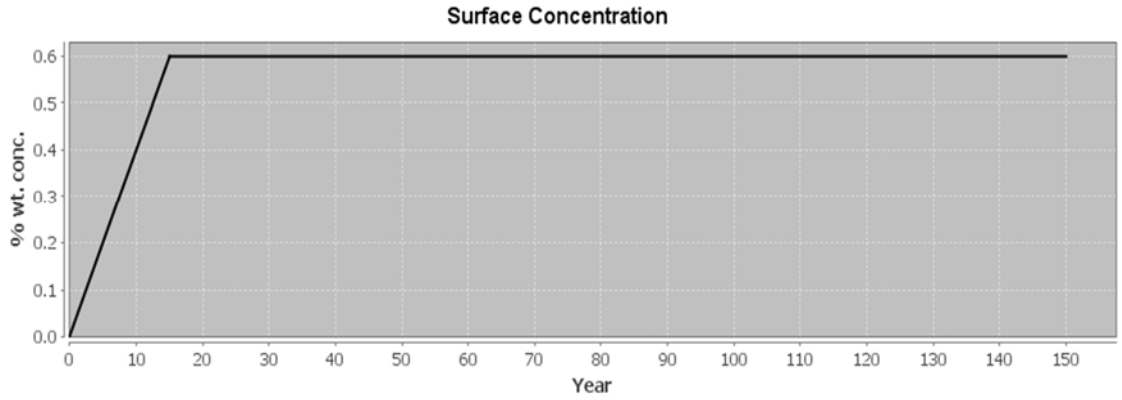

Figure 7.14: The chloride exposure conditions

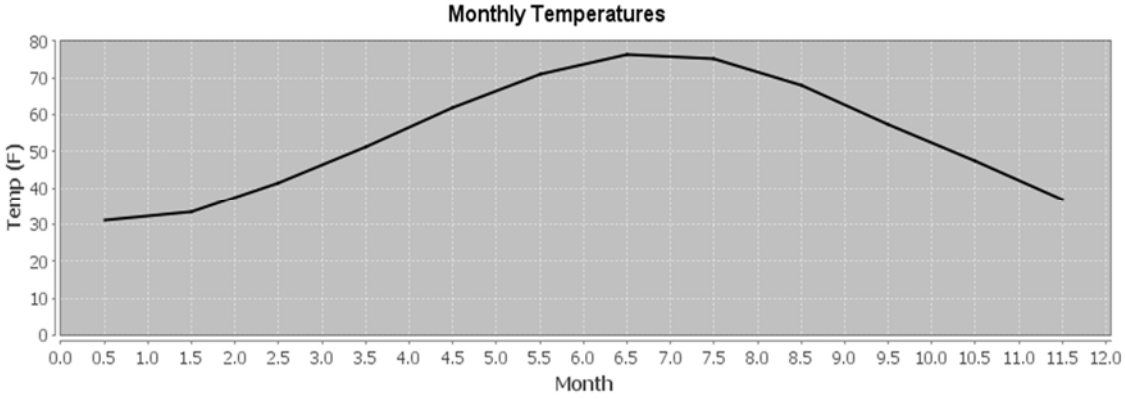

Figure 7.15: Monthly temperatures conditions

The diffusion coefficients of concrete do not increase with increasing crack widths up to the so-called "threshold crack width," while, over this threshold value, the diffusion coefficients start to increase. The threshold crack width is found to be around 30~80 μm based on the present test data. After this threshold, the chloride diffusion coefficient through cracked concrete is proportional to the crack width. MSC is a fiber-reinforced cement-based composite material micromechanically tailored to achieve high ductility and multiple cracking under tensile and shear loading. The characteristic strain-hardening after first cracking is accompanied by multiple microcracking. Even at ultimate load, the crack width remains on

the order of about 30 μm. This tight crack width is self-controlled and, whether the composite is used in combination with conventional reinforcement or not, it is a material characteristic independent of reinforcing bar reinforcement ratio. In contrast, normal concrete and fiber-reinforced concrete rely on steel reinforcement for crack width control, and the crack width can easily go up to hundreds of microns. **Fig. 7.16** [11, 12] shows the relationship between the effective diffusion coefficient of chloride ions and the beam deformation level for mortar and specimens with strain-hardening behavior measured by the PI. MSC falls within this category. Despite the same or higher magnitude of imposed overall deformation and higher crack density, the MSC specimens reveal a effective diffusion coefficient considerably lower than that of the reinforced mortar because of the tight crack width control.

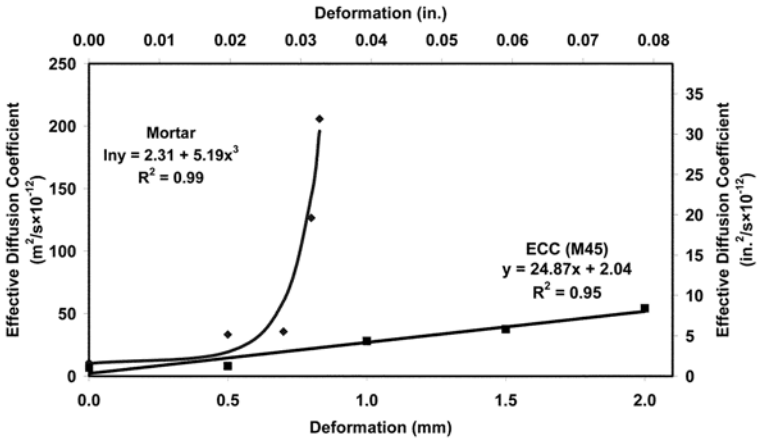

Fig. 7.16 Diffusion coefficient versus preloading deformation level for ECC and mortar [11, 12]

Once the corrosion of rebar starts, corrosion product (rust) is formed and deposited on the surface of rebar. The formation of rust is controlled by the corrosion rate (c_r), which can be determined theoretically by Faraday's law or experimentally by the galvanostatic pulse method.

7.4 Durability based LCCA model

7.4.1 System definition

The typical DCSS designs analyzed in this study are constructed upon an existing reinforced concrete overpack (MAGNASTOR) originally built by NAC INTERNATIONAL, INC[13]. **Figure 7.17** and **Table 7.1** illustrates the structures of the different types of the overpack system. Two types of materials system, normal concrete and MSC, respectively, are assessed in this study. The material mixtures and durability parameters are shown in **Table 7.2**.

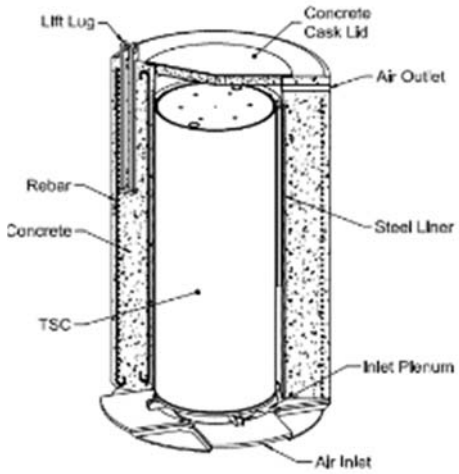

Figure 7.17: Details of the overpack structure[13].

Table 7.1 Dimension and Volume of the concrete cylinder.

Type of Structure	**Cylinder**
Wall Depth	25 in.
Total Length	200 ft
Reinf. Depth	2.5 in.
Vol. of Concrete	5524 cub. yd

Table 7.2 Material composition and chloride diffusion parameters

	Normal Concrete	**MSC**
water cement ratio	0.4	0.3
Fly ash (%)	0	40%
Average crack width (μm)	30	100
D_{28} (in*in/sec)	1.231E-8	7.085E-9
m	0.2	0.44
Hydration (yrs)	25	25
Ct (% wt. conc)	0.05	0.05
Prop. (yrs)	20	20
Rebar volume	5.2%	5.2%

Rebar type	Epoxy coated	Epoxy coated

7.4.2 Life Cycle Assessment Model

If all attributes and consequences of a decision concerning a structure can be expressed in monetary terms, then an optimal decision will be the one that minimizes the life-cycle cost of the structure. Generally, if the benefits of each alternative are the same, then the expected life-cycle cost up to time T, LCC(T), may be represented as

$$LCC(T) = C_I + C_M(T) + C_{IN}(T) + C_R(T) \qquad (7.8)$$

where C_I is the initial material and construction costs, $C_M(T)$ is the expected cost of maintenance, $C_{IN}(T)$ indicates the cost of inspections, and $C_R(T)$ is the repair cost. Costs and benefits may occur at different times so in order to obtain consistent results it is necessary for all costs and benefits to be discounted to a present value. Discount rates are influenced by a number of economic, social and political factors and thus can be quite variable.

Figure 7.18: Timeline and maintenance schedule for construction activities.

The total life-cycle costs are calculated as the sum of the initial construction costs and the discounted future repair costs over the life of the structure. These are typically construction and preservation costs, including material costs, equipment rental and operating costs, and labor costs. The initial construction costs are simply the cost of the concrete + the cost of the steel (or other reinforcement) plus the cost of any surface protection (membrane or sealer). Future repair costs are calculated on a "present worth" basis using the inflation rate, i, and the real discount rate, r.

The discount rate is a central element to economic analysis, and can significantly influence LCCA results. Historical trends over the last several years indicate that the real time value of money ranges approximately between 3% and 5%[14]. In the LCCA model, a real discount rate is used. Real discount

rates reflect the true time value of money with no inflation premium. The real discount rate of 4% for all costs was estimated based on values recommended by the U.S. Office of Management and Budget (OMB).

Table 7.3 Economic parameters

Concrete &Steel		**Repair**	
Concrete ($/cub.yd)	76.76	Repair ($/sq.ft)	37.16
MSC ($/cub.yd)	195.85	Area to repair (%)	10
Vol. of Concrete	5524 cub. yd	Repair interval	10(Normal)/20(MSC)
Steel ($/lb)	0.45	Repair Qtty	7159 sq.ft
Rebar Qtty(lb)	2170424		

7.5 Results and discussions

7.5.1 Service life prediction results

Figure 7.19 displays the change in chloride concentration over time on the surface of the rebar. The chloride concentration exponentially grows during service life. It can be also seen that under service condition, it takes around 60 years for the chloride concentration reaching the threshold for the initiation of corrosion, while for MSC system, the corrosion point has been greatly extended to about 170 years. This can be mainly attributed to the tightly cracking control property of MSC materials. The large cracks in normal concrete due to structural loads would significantly accelerate the chloride transport, thereby influence the deteriorate rate of structures. **Figure 7.20** shows the service life of each materials mix, dividing the total into the initiation period and propagation period.

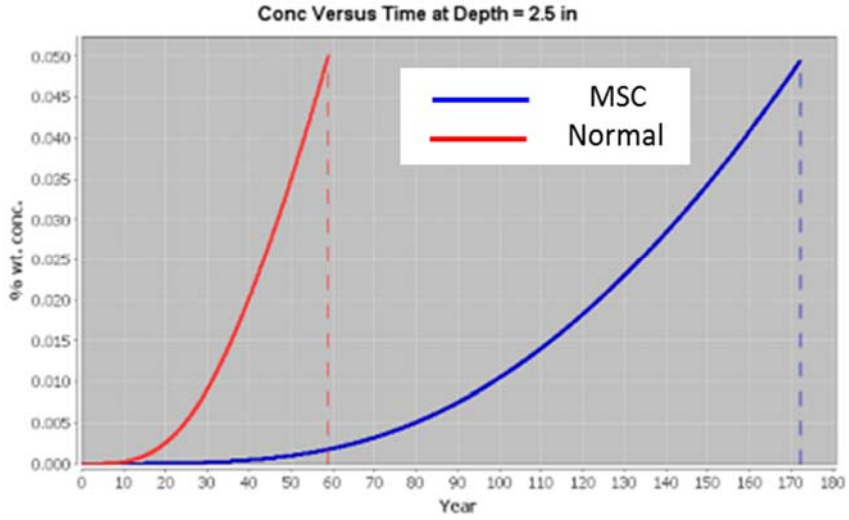

Figure 7.19 Chloride concentration at rebar as a function of time.

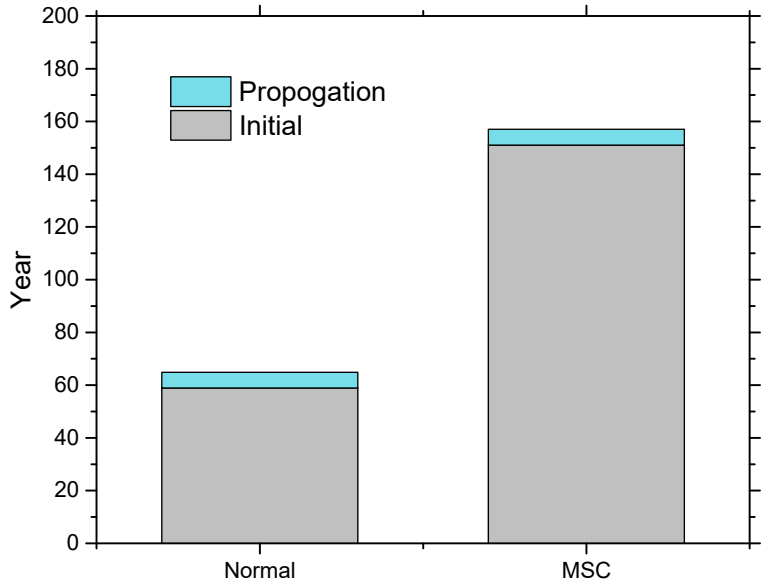

Figure 7.20 Predicted service life for the first time repair event.

Figure 7.21 and **7.22** use color to show how the chlorides diffuse through the concrete over the initiation period. On the left-hand-side of this cross-section is a color scale of chloride concentrations, expressed as either % wt. of concrete. At the point of initiation, the color at the outer edge of the reinforcing steel should correspond to the Ct, which is 0.5% wt in this study.

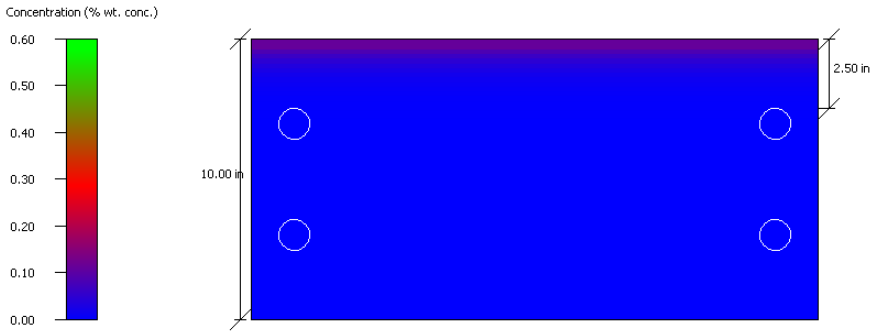

(a) 15 years

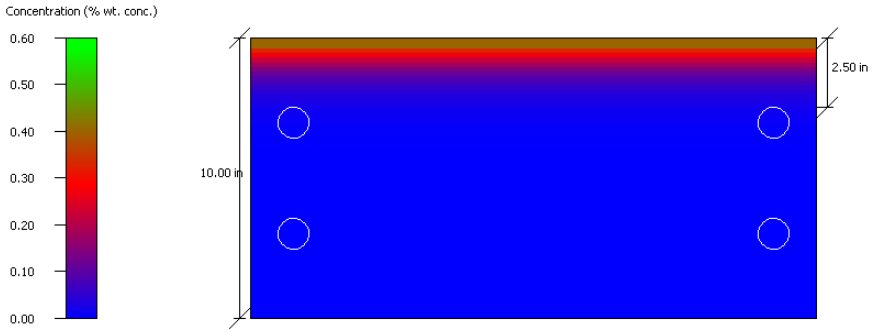

(b) 30 years

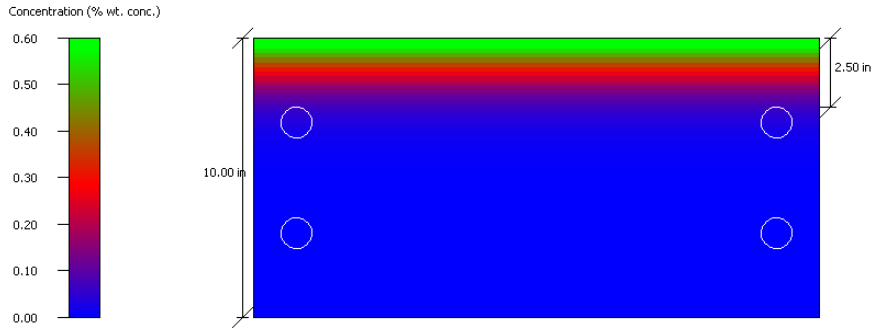

(c) 50 years

Figure 7.21: Chloride distribution on the cross section of normal concrete materials.

(a) 50 years

(b) 100 years

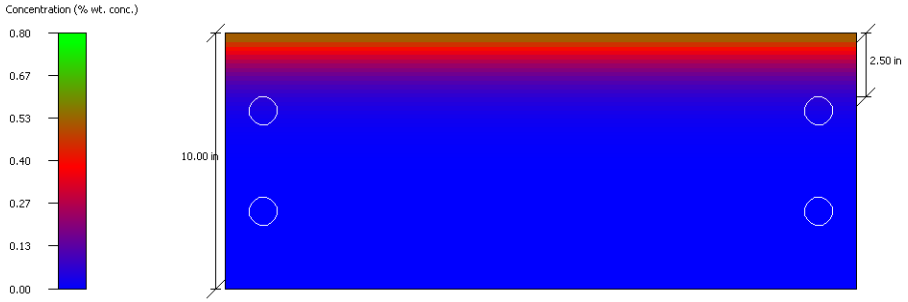

(c) 150 years

Figure 7.22: Chloride distribution on the cross section of MSC materials.

Figure 7.23 shows the concrete's diffusivity over time. In a typical analysis, this graph shows that the diffusivity decreases over time (this is modeled through the "m" term described above); on the other hand, the diffusivity oscillates annually, due to the annual changes in temperature (diffusivity increases with temperature).

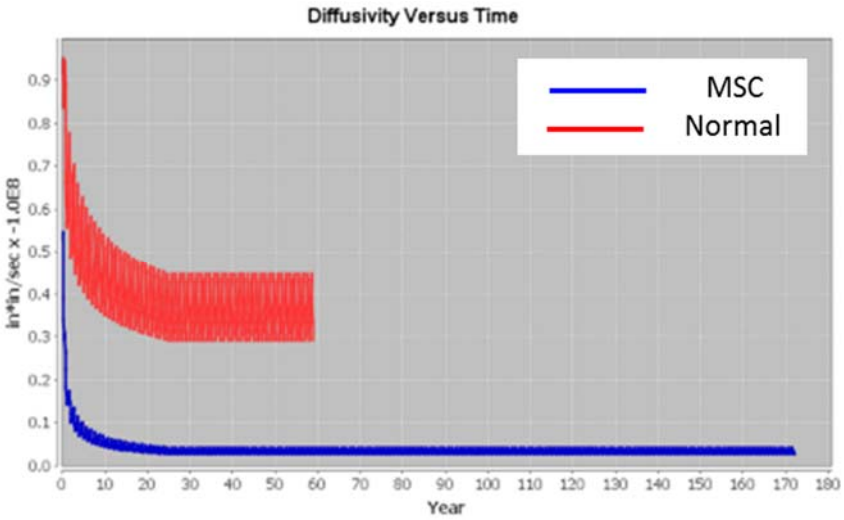

Figure 7.23: The change of diffusion coefficient versus time.

7.5.2 Life cycle cost analysis results

Figure 7.24 gives the life cycle cost for each materials system. It shows that the MSC overpack system increases the initial costs at year one of the life cycle. The MSC system is about 40% higher for initial cost than the conventional system in year 1. By the end of life cycle, however, the total cost of the normal concrete system is significantly higher than MSC system. The MSC system saves about 30% of total cost comparing with normal concrete.

Figure 7.25 displays the present value of all costs, by year, over the analysis period. The values are created by summing all costs that occur in a given year and then discounting this value to the next year using the real discount rate specified in the previous section. It can be seen that by the year 100 of the life cycle, the conventional system exceeds the total life cycle cost of MSC system. These results show that assessing costs from a life cycle perspective is important for long-live systems. While initial costs would suggest the normal concrete is more economical than the MSC system, total life cycle costs show a 30% advantage for the MSC materials by the end of 300 years.

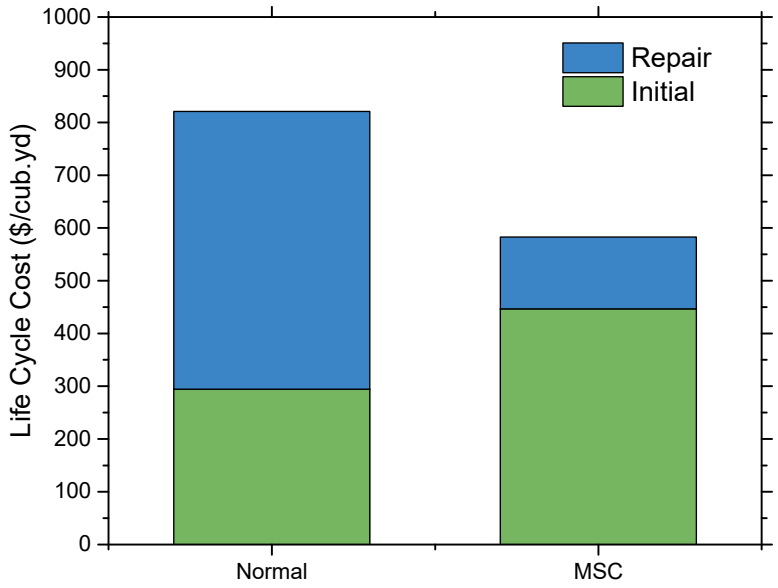

Figure 7.24: Life cycle costs.

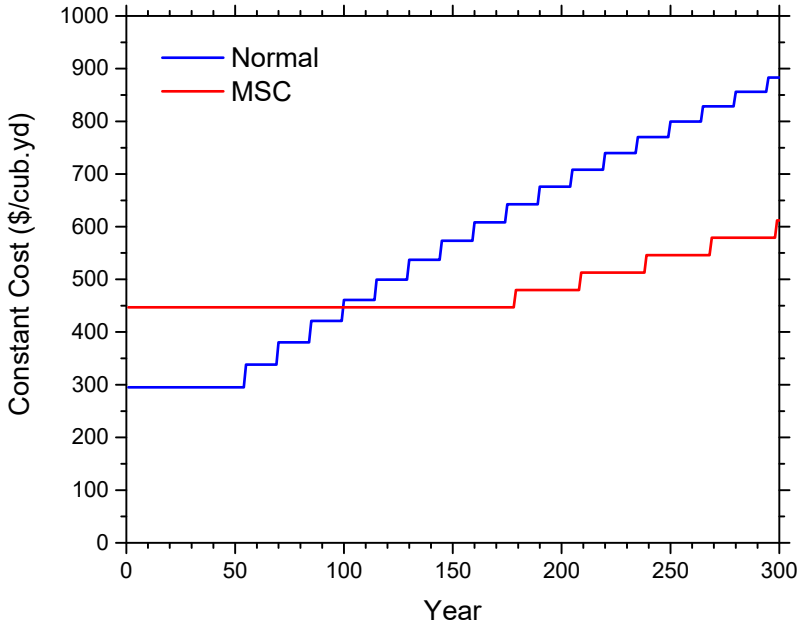

Figure 7.25: Cumulated costs during service life.

7.5.3 Sensitivity analysis

Sensitivity analysis is the calculating procedure used for prediction of the effect of changes in the key input data on output results. In this procedure input parameters are altered one by one from initial values in order to determine their impact on the analysis outcomes. This, if necessary, prevents unwanted alterations of outcome variables. This procedure is often used in investment decision making related with

the investment project evaluation under conditions of uncertainty. Uncertainty in cost parameters and the future conditions of inflation ratio, repair interval, and repair cost can affect the outcomes of LCCA.

Figure 7.26 shows that the repair cost significantly affects the life cycle costs. The total life cycle cost increases as the repair cost grows. And the repair related costs have a more significant impact on the conventional concrete system than the SHC system. When the repair cost is lower than 8 $/cub.yd, the normal concrete system still costs less than SHC system even though the later system can greatly reduce repair events. As the repair cost pass this threshold, the normal concrete costs surpass SHC system for the total life cycle. This difference becomes more obvious as the repair cost increases.

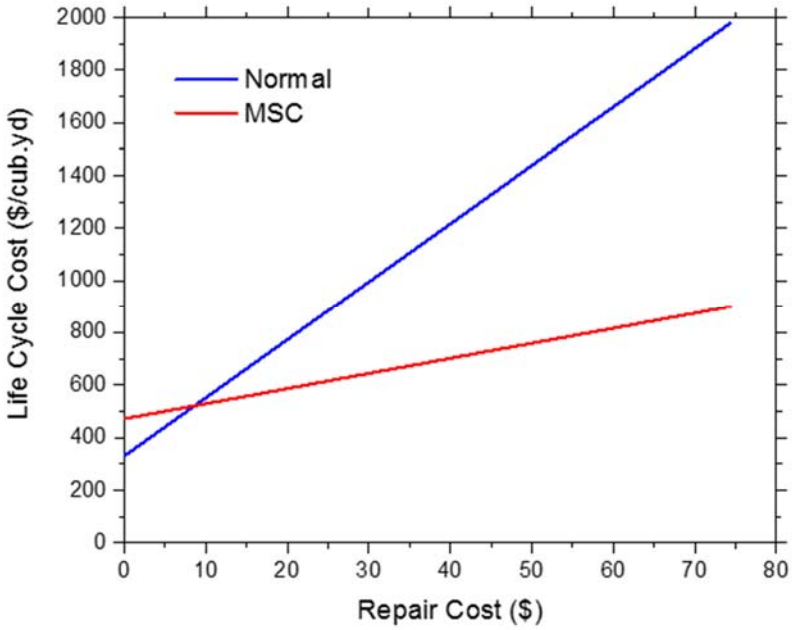

Figure 7.26: The impact of a repair cost on life cycle cost.

Repair interval is another important parameter that can change total cost in LCCA. **Figure 7.27** shows the influence of repair interval on the life cycle costs. It can be seen that the repair frequency strongly influences the total life cycle costs, especially when the repair interval is shorter than 5 years. This result indicates that the quality of repair significantly affects the life cycle cost. For normal concrete, due to the natural brittleness, most often drying shrinkage of "new" repair material restrained by "old" concrete substrate causes cracking of the repair material, combined with interface delamination between the repair and the concrete substrate, which may also introduce chlorides, oxygen, moisture, alkali or acid into the repaired concrete structure and accelerate further deterioration. MSC is a material micromechanically designed with high ductility and toughness indicated by multiple micro-cracking behaviors. Experimental study on a layered repair system verified that the high ductility of MSC can relieve shrinkage induced

stresses in the repair layer and at the MSC/concrete interface, thereby suppressing large surface cracks and interface delamination.

Figure 7.28 shows the development of total life cycle cost net present value depending on the material system and the discount rate applied when calculating the net present value costs. The figure shows that increasing the discount rate reduces the differences of facility life-cycle costs net present values for two selected material systems. At discount rate of 7.0 %, there is almost no difference in the facility life cycle cost net present values for those two systems. This suggests the selection of a discount rate can be a key parameter in determining the results of a comparative LCCA, and can have a significant effect on long-term investment decisions. The sliding discount rate affects the conventional design results more greatly than the MSC design because the conventional design requires more repair in later years when compared to the MSC system.

Figure 7.29 provides the initiation time for rebar corrosion as a function of average crack width under service condition. It can be noticed that when the crack width is small enough, usually below 50 microns, the chloride induced service life reduction is negligible. However, once the crack width is larger than this threshold, the diffusivity of concrete is approximately proportional to the crack width. As a result, the initiation time of corrosion dramatically declined. When the crack width reaches 200 microns, it only takes about 20 years for chloride concentration passing C_t.

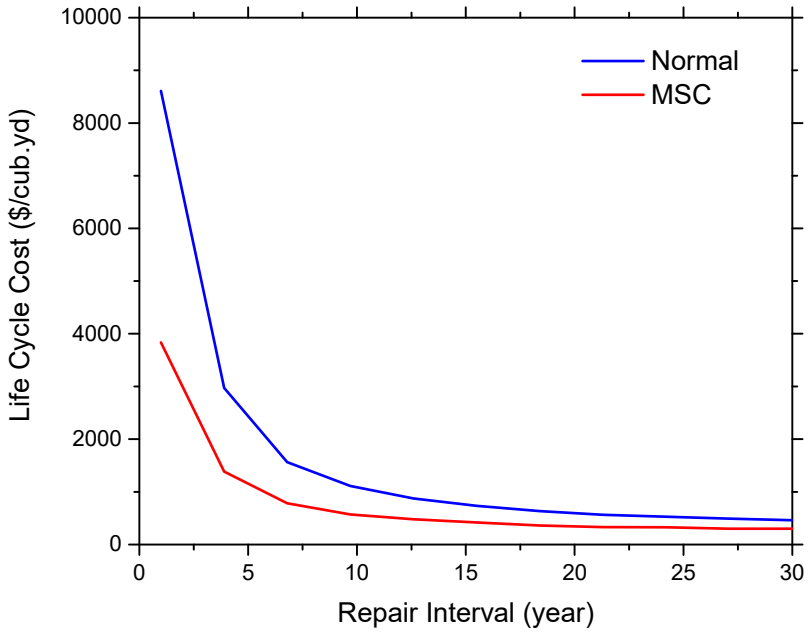

Figure 7.27: The impact of repair interval on the life cycle cost.

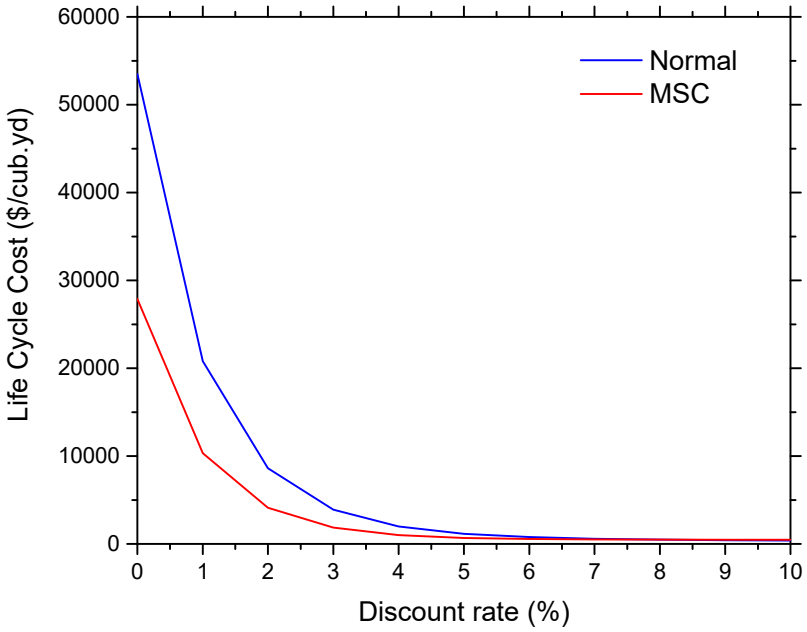

Figure 7.28: Discount rate variation from 0-4% and the corresponding life cycle cost.

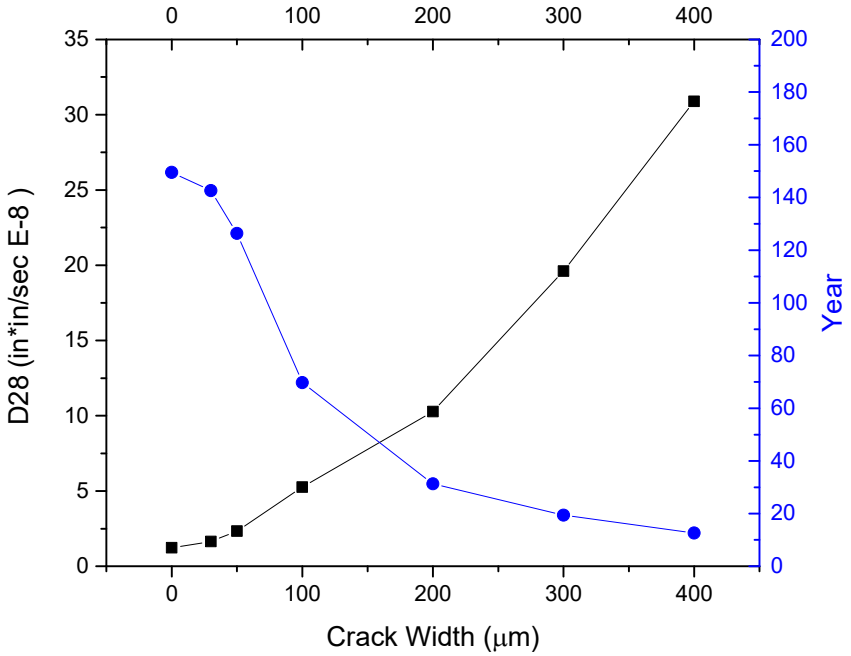

Figure 7.29: initiation time for rebar corrosion

7.6 Summary of accomplishment

The durability of MSC was characterized. Common deterioration mechanisms in spent nuclear fuel storage systems were studied, including restrained shrinkage cracking, chloride penetration, embedded steel corrosion, freeze and thaw, and alkali-silica reaction and elevated temperature effect. The details study of

elevated temperature effect is reported in a published journal paper [15] and a Ph.D. dissertation [16] advised by PI. The experimental results revealed that MSC had superior durability to conventional concrete, mainly due to its extraordinarily high damage tolerance, chemical stability and low transport properties even under large applied deformation. The improved durability leads to an extended service life for SNF systems when MSC is used in lieu of conventional concrete.

A framework for LCCA that assesses the life cycle cost concrete overpack of dry cask system was proposed. Two potential material designs were evaluated and compared using this LCCA framework: a conventional concrete design, and a new MSC design. Life-cycle analysis was conducted on dry cask systems to compare the newly developed MSCs with existing concrete. The results showed the life cycle cost of a representative dry cask system can be reduced by 30% when MSC is used. It should be noted that the life cycle analysis was based on simple assumption that corrosion is the dominant deterioration mode, and other types of deterioration or failure events will not occur during the structural life cycle. When other deterioration modes and possibilities of natural and man-made hazards are considered, the life cycle cost advantage of SNF systems using MSC will be even more predominant.

7.7. References

[1] A. M. Neville, *Properties of concrete*, 1995.

[2] J. G. Cabrera, "Deterioration of concrete due to reinforcement steel corrosion," *Cement and Concrete Composites,* vol. 18, pp. 47-59, 1996/01/01 1996.

[3] A. Steffens, D. Dinkler, and H. Ahrens, "Modeling carbonation for corrosion risk prediction of concrete structures," *Cement and Concrete Research,* vol. 32, pp. 935-941, 6// 2002.

[4] W. A. Cordon, *Freezing and thawing of concrete;: Mechanisms and control*, 1966.

[5] W. Sun, R. Mu, X. Luo, and C. Miao, "Effect of chloride salt, freeze–thaw cycling and externally applied load on the performance of the concrete," *Cement and Concrete Research,* vol. 32, pp. 1859-1864, 12// 2002.

[6] A. E. K. Jones and L. A. Clark, "The effects of ASR on the properties of concrete and the implications for assessment," *Engineering Structures,* vol. 20, pp. 785-791, 1998/09/01 1998.

[7] S. Chatterji, N. Thaulow, and A. D. Jensen, "Studies of alkali-silica reaction. Part 4. Effect of different alkali salt solutions on expansion," *Cement and Concrete Research,* vol. 17, pp. 777-783, 1987/09/01 1987.

[8] C.-M. Aldea, S. P. Shah, and A. Karr, "Effect of Cracking on Water and Chloride Permeability of Concrete," *Journal of Materials in Civil Engineering,* vol. 11, 1999.

[9] I. S. Yoon, E. Schlangen, M. R. d. Rooij, and K. v. Breugel, "The Effect of Cracks on Chloride Penetration into..." *Key Engineering Materials,* vol. 348-349, pp. 769-772, 2007.

[10] S. Jacobsen, J. Marchand, and L. Boisvert, "Effect of cracking and healing on chloride transport in OPC concrete," *Cement and Concrete Research,* vol. 26, pp. 869-881, 1996/06/01 1996.

[11] A. Djerbi, S. Bonnet, A. Khelidj, and V. Baroghel-bouny, "Influence of traversing crack on chloride diffusion into concrete," *Cement and Concrete Research,* vol. 38, pp. 877-883, 6// 2008.

[12] M. L. Mustafa Sahmaran and C. L. Victor, "Transport Properties of Engineered Cementitious Composites under Chloride Exposure," *Materials Journal,* vol. 104, 11/1/2007 2007.

[13] C. W. Pennington, "NAC's Modular, Advanced Generation, Nuclear All-purpose STORage (MAGNASTOR) system: new generation multipurpose spent fuel storage for global application," presented at the The 14th international symposium on the packaging and transportation of radioactive materials. Conference proceedings, 2004.

[14] S. E. Chang and M. Shinozuka, "Life-cycle cost analysis with natural hazard risk. journal of infrastructure systems," *Journal of Infrastructure Systems,* vol. 2, pp. 118-126, 1996.

[15] Bhat, P., Chang, V., **Li, M.** (2014). Effect of Elevated Temperature on Strain-Hardening Engineered Cementitious Composites. *Construction and Building Materials, 69*, 370-380.

[16] Bhat, P., Cementitious Materials with Ultra-High Damage Tolerance for Hazard Mitigation, Ph.D. Dissertation, 2016.

APPENDIX

Task 4: Mathematical and Computational Modeling of Deterioration Process

Senior personnel
Dr. Kalyana Babu Nakshatrala
University of Houston
e-mail: knakshatrala@uh.edu

Funded student on the project
Maruti Kumar Mudunuru (Ph.D. student)

Covering Period: October 1, 2012 through September 30, 2013
Date of Report: October 20, 2013

ID #: RPA-12-3545, Yearly Report Y1

SUMMARY & PLANS

The following are the on-going or completed research tasks. We also briefly discuss our future plans. We also provided journal papers, conferences talks and awards that have resulted from this research funding.

(I) ***Numerical methodology for transient diffusion equation to meet maximum principles and the non-negative constraint:*** One of main tasks on the numerical modeling front is to the develop numerical methodologies for satisfying maximum principles and the non-negative constraint for transient problems.

(a) In the first year, we have *finished* the development of a robust methodology for linear transient diffusion equations. The research is also submitted for review to an international journal. We have briefly outlined this research component in this yearly report.

(b) We have just started developing non-negative methodologies for nonlinear (in particular, semi-linear and quasilinear) diffusion-type equations. The transport in sophisticated degradation models will be nonlinear transient diffusion-type equations. This part of work will be finished by the end of year #2, and we plan to include the results in the subsequent quarterly reports.

(II) ***Deriving mesh restrictions to meet maximum principles:*** We have made a great progress on deriving mesh restrictions to meet maximum principles and the non-negative constraint for advection-diffusion and linear reactions. Our plan is to finish this part of the research and submit the research findings to a peer-reviewed journal by the end of this year (2013). Some of the main findings are provided in this yearly report.

(III) ***On achieving element-wise species balance and enforcing maximum principles for advection-diffusion-reaction equations:*** We have been developing a state-of-the-art numerical methodology to simultaneously meet the element-wise species balance, the non-negative constraint and avoid node-to-node spurious oscillations. The numerical methodologies have been derived. We also obtained some preliminary results. Currently, we are in the process of developing a computer code to be able to solve large-scale realistic problems. To complete this research task, it make take two quarters. It is worth saying that this component of the research is truly transformative research and will greatly enhance simulation capabilities for a wide variety of fields including degradation of materials, contaminant transport. In this yearly report, we have provided the numerical methodologies, and some preliminary numerical results.

(IV) ***Deriving a chemo-thermal-deformation model for degradation studies:*** We have been developing a hierarchy of mathematical models to model various mechanisms of degradation. The models will account for coupled chemo-thermal-deformation response, which is crucial for mathematical modeling of degradation of materials. As discussed in our proposal, this mathematical model in consistently derived using mechanics and thermodynamics principles. In particular, the model will satisfy the second law of thermodynamics, which is not the case with some of the current models for degradation. After this model is derived, we need to develop a computational framework to solve the resulting nonlinear partial differential equations, which will be another research task, as outlined in the proposal. We will report our research progress on this task in subsequent quarterly reports.

Conferences & Invited Talks

C1. "*Numerical modeling of diffusive-reactive systems*;" K.B. Nakshatrala, *ASME International Mechanical Engineering Congress & Exposition*, Houston, Texas, November 9–15, 2012.

C2. "*Modeling moisture degradation of structural members*;" M.K. Mudunuru, and K.B. Nakshatrala, *ASME International Mechanical Engineering Congress & Exposition* (Special session on *Environmental effects and failure of engineering structures*), Houston, Texas, November 9–15, 2012.

C3. "*On achieving element-wise species balance and enforcing non-negative constraint for advection-diffusion equation*;" M.K. Mudunuru, and K.B. Nakshatrala, *American Geophysical Union Fall Meeting*, San Francisco, California, December 3–7, 2012.

C4. "*Least-squares finite element formulations for flow problems*;" J.N. Reddy, K.B. Nakshatrala, and J. Chang, *American Geophysical Union Fall Meeting*, San Francisco, California, December 3–7, 2012. [An invited talk]

C5. "*Optimization-based methodology for enforcing maximum principles and the non-negative constraint*;" K.B. Nakshatrala, *American Geophysical Union Fall Meeting*, San Francisco, California, December 3–7, 2012.

C6. "*A robust non-negative numerical framework for diffusion-controlled bimolecular-reactive systems*;" M.K. Mudunuru, K.B. Nakshatrala, and A.J. Valocchi; SIAM Conference on Computational Science and Engineering (SIAM CSE13), Boston, February 25–March 1, 2013.

C7. "*Importance of non-negative numerical solution for mixing-controlled reactive transport*;" A.J. Valocchi, and K.B. Nakshatrala, *SIAM Conference on Mathematical & Computational Issues in the Geosciences*, University of Padova, Italy, June 17–20, 2013.

C8. "*On modeling thermal and moisture degradation of materials and structures*;" M.K. Mudunuru, C. Xu, and K.B. Nakshatrala, US National Congress on Computational Mechanics, Raleigh, North Carolina, July 22–25, 2013.

C9. "*On mesh restrictions for advective-diffusive-reactive systems to achieve non-negative solutions*;" M.K. Mudunuru, and K.B. Nakshatrala, *US National Congress on Computational Mechanics*, Raleigh, North Carolina, July 22–25, 2013.

C10. "*A new framework for coupling flow and deformation of the porous solid*;" M.J. Martinez, D.Z. Turner, and K.B. Nakshatrala, *US National Congress on Computational Mechanics*, Raleigh, North Carolina, July 22–25, 2013.

C11. "*Importance of non-negative numerical solutions in degradation modeling, groundwater modeling, and reactive transport*;" K.B. Nakshatrala, US National Congress on Computational Mechanics, Raleigh, North Carolina, July 22–25, 2013.

Peer-Reviewed Journal Papers

P1. "*A numerical framework for diffusion-controlled bimolecular-reactive systems to enforce maximum principles and the non-negative constraint*;" K.B. Nakshatrala, M.K. Mudunuru, and A.J. Valocchi; *Journal of Computational Physics*, 253: 278-307, 2013.

P2. "*A numerical methodology for enforcing maximum principles and the non-negative constraint for transient diffusion equations*;" K.B. Nakshatrala, H. Nagarajan, and M. Shabouei; *International Journal for Numerical Methods in Fluids*, under review, 2013.

P3. "*On mesh restrictions to satisfy maximum principles, comparison principles, and the non-negative constraint for a general linear second-order elliptic equation*;" M.K. Mudunuru, and K.B. Nakshatrala; *under preparation*, 2013. [*will be submitted soon to a journal*]

P4. "*On achieving element-wise species balance and enforcing maximum principles for advection-diffusion-reaction equations under the finite element method*;" M.K. Mudunuru, and K.B. Nakshatrala; *under preparation*, 2013. [*will be submitted soon to a journal*]

Awards / Honors

A1. Maruti Kumar Mudunuru won travel award from SIAM to attend 2013 SIAM Conference on Computational Science and Engineering (CSE13). The conference held from February 25–March 1, 2013. The award is based on the abstract: "*A robust non-negative numerical framework for diffusion-controlled bimolecular-reactive systems*." The award consisted of cash award and waiver of conference registration fee.

A2. Maruti Kumar Mudunuru won travel grant from the U.S. Association for Computational Mechanics to attend US National Congress on Computational Mechanics (USNCCM) 2013. The conference will be from July 22–25, 2013. The award is based on the abstract: "*On mesh restrictions for advective-diffusive-reactive systems to achieve non-negative solutions*," M.K. Mudunuru, and K.B. Nakshatrala. The award consisted of cash award and waiver of conference registration fee.

Mini-symposia organization at national/international conferences

M1. "*Flow and transport in heterogeneous porous media*," Organizers: K.B. Nakshatrala (Chair), D.Z. Turner, M. Martinez, and S. Karra, ASME International Mechanical Engineering Congress and Exposition (IMECE), Houston, November 9–15, 2012.

M2. "*Environmental effects and fatigue of engineering structures / materials*," Organizers: K. B. Nakshatrala (Chair), and K.J. Willam, ASME International Mechanical Engineering Congress and Exposition (IMECE), Houston, November 9–15, 2012.

M3. "*Multifunctional composite materials*," Organizers: M. Li (Chair), K.B. Nakshatrala, C. Vipulanandan, and D. Jack, *ASME International Mechanical Engineering Congress and Exposition (IMECE)*, Houston, November 9–15, 2012.

M4. "*Recent advances in theoretical, numerical and experimental methods in flow and transport in porous media*," Organizers: S. Karra (Chair), K.B. Nakshatrala, A. Cortis, and S. Anwar, American Geophysical Union Fall Meeting, San Francisco, December 3–7, 2012.

M5. "*Flow and transport in heterogeneous porous media*," Organizers: K.B. Nakshatrala (Chair), D.Z. Turner, M. Martinez, and S. Karra, 12th US National Congress on Computational Mechanics, Raleigh, North Carolina, July 22–25, 2013.

M6. "*Mathematical and numerical modeling of degradation of materials and structures*," Organizers: K.B. Nakshatrala (Chair), R. Duddu, J.N. Reddy, and K.J. Willam, 12th US National Congress on Computational Mechanics, Raleigh, North Carolina, July 22–25, 2013.

A Report on Research Task #4.1

Enforcing maximum principles and the non-negative constraint for transient linear diffusion equations

1. INTRODUCTION AND MOTIVATION

Certain quantities (e.g., concentration of a chemical species and absolute temperature) naturally attain non-negative values. A violation of the non-negative constraint for these quantities will imply violation of some basic tenets of Physics. It is, therefore, imperative that such physical constraints are met by mathematical models and by their associated numerical formulations. Herein, we shall focus on two popular transient mathematical models, in which physical restrictions like the non-negative constraint play a central role. The first model is based on Fick's assumption (commonly referred to as Fick's law) and balance of mass. Fick's assumption is a simple constitutive model to describe the diffusion of a chemical species in which the flux is proportional to the negative gradient of the concentration. The second model is based on Fourier's assumption and balance of energy, which describes heat conduction in a rigid conductor. Both these constitutive models combined with their corresponding balance laws give rise to transient diffusion-type equations, which are parabolic partial differential equations.

There has been tremendous progress in Applied Mathematics for these type of equations with respect to existence and uniqueness results, qualitative behavior of solutions, estimates, and other mathematical properties [**79, 32**]. In particular, it has been shown that transient diffusion-type equations satisfy the so-called maximum principles [**79**]. It will be shown in a subsequent section that the non-negative constraint can be shown as a consequence of maximum principles under certain assumptions. Analytical solutions to several problems have been documented in various monographs (e.g., see references [**19, 77**]). However, it should be noted that most of these solutions are for isotropic and homogeneous media, and for simple geometries. For problems involving anisotropic and heterogeneous media, and complex geometries; finding analytical solutions is not possible, and one has to resort to numerical solutions. Obtaining physically meaningful numerical solutions for transient diffusion equation that satisfy maximum principles and the non-negative constraint is the main aim of this research. It is well-known (and will be discussed in subsequent sections) that many popular numerical schemes (including the ones that are based on the finite element method) do not satisfy maximum principles and the non-negative constraint. Even for isotropic diffusion, stringent restrictions on the time step and the computational mesh are necessary to meet these important mathematical properties.

The usual approach of solving linear second-order parabolic partial differential equations under the finite element method is to employ Galerkin formalism for spatial discretization. Several theoretical results (which include convergence proofs, a-priori estimates) for this approach can be found

in the literature (e.g., see Reference [**30**]). But it has been adequately documented in the literature that this approach will not satisfy maximum principles and the non-negative constraint (for example, see Reference [**45**]). Thus, there is a need to develop new methodologies that will satisfy important mathematical properties like maximum principles and the non-negative constraint, and thereby improve the overall predictive capabilities of current numerical schemes.

1.1. Maximum principles for transient systems. Transient diffusion equations fall in the realm of parabolic partial differential equations (PDEs), whereas steady-state diffusion equations are elliptic PDEs. A noticeable difference in maximum principles for parabolic PDEs and the corresponding ones for elliptic PDEs is that, in the case of a parabolic PDE, the maximum can occur either on the boundary of the domain or in the initial conditions. On the other hand, for a second-order elliptic PDE, the classical maximum principle says that the maximum occurs on the boundary of the domain (under some appropriate conditions on the input data and domain). A more precise mathematical treatment in Section 2.

Several papers have also addressed maximum principles for transient systems (i.e., parabolic problems) in numerical setting. Herrera and Valocchi [**48**] have employed flow-oriented derivatives with backward Euler to obtain non-negative solutions in the context of finite difference and finite volume methods. One method that is commonly employed in the area of subsurface hydrology is by Chen and Thomee [**22**]. This method is based on the standard single-field formulation but employs lumped capacity matrix. (By the standard single-field formulation we refer to the formulation obtained by employing the semi-discrete approach using method of vertical lines at integral time steps, and Galerkin formalism for spatial discretization. See Appendix for more details of this formulation.) It is noteworthy that lumping capacity matrix approach is commonly considered as a variational crime [**53**]. Reference [**13**] also alters the capacity matrix to preserve positivity for parabolic problems but restricts to isotropic diffusion. Other notable works are [**86, 83, 33, 31**], which all focused on getting restrictions on the mesh (and in some cases on the time step) to meet maximum principles. More importantly, they did not consider anisotropy, and such restrictions are not possible for anisotropic and heterogeneous medium.

There are several papers that considered consistent capacity matrices, but derived restrictions on the time step to satisfy maximum principles [**68, 92, 57, 45, 51**]. A striking difference between the time step restrictions with respect to numerical stability and maximum principles is that numerical stability places an upper bound on the selection of the time step whereas maximum principles place a lower bound on the selection of the time step. The time step is selected based on the following inequality:

$$0 < \Delta t^{\text{MP}}_{\text{crit}} \leq \Delta t \leq \Delta t^{\text{stability}}_{\text{crit}} \tag{1.1}$$

where $\Delta t^{\text{stability}}_{\text{crit}}$ is the critical time step to obtain stable results, and $\Delta t^{\text{MP}}_{\text{crit}}$ is the critical time step to satisfy maximum principles. It should be however mentioned that these works on deriving time step restrictions have considered one-dimensional problems or isotropic media, and these conditions are not applicable otherwise. To the best of our knowledge, none of the prior works presented a methodology for transient anisotropic diffusion equations to satisfy maximum principles and the non-negative constraint on general computational grids with no further restrictions on the time step.

1.2. Our approach and main contributions of this report. Herein, we shall employ the Rothe method (or the method of horizontal lines) [**88**] to solve transient anisotropic diffusion equation. There are several papers in the literature that have employed Rothe method to solve parabolic equations [**45, 15, 60, 21**]. These papers, except for Reference [**45**], did not apply the Rothe method in the context of maximum principles. Although Reference [**45**] addressed maximum principles by using the Rothe method, but the formulation is restricted to isotropic diffusion. In addition, Reference [**45**] employed techniques from stabilized methods, which is different from the approach taken in this research. In the proposed formulation, the temporal discretization using the Rothe method will give rise to inhomogeneous elliptic partial differential equation, which is solved using the approach presented in our earlier paper [**73**]. An attractive aspect of the proposed methodology is that there are no additional restrictions on the time step to meet maximum principles.

1.3. An outline and notation used in this report. The remainder of this report is organized as follows. In Section 2, we present governing equations for transient anisotropic diffusion, and discuss maximum principles and the non-negative constraint. In Section 3, we derive a methodology for enforcing maximum principles and the non-negative constraint for transient anisotropic diffusion equation using the method of horizontal lines. In Section 4, we illustrate the performance of the proposed formulation using representative numerical examples. Finally, conclusions are drawn in Section 5.

The symbolic notation adopted in this report is as follows. Repeated indices do not imply summation. (That is, we do not employ Einstien's summation convention.) We shall employ the standard notation for open, closed and half-open intervals [**11**]:

$$(a,b) := \{\mathrm{x} \in \mathbb{R} \;\big|\; a < \mathrm{x} < b\},\ [a,b] := \{\mathrm{x} \in \mathbb{R} \;\big|\; a \leq \mathrm{x} \leq b\},$$
$$(a,b] := \{\mathrm{x} \in \mathbb{R} \;\big|\; a < \mathrm{x} \leq b\},\ [a,b) := \{\mathrm{x} \in \mathbb{R} \;\big|\; a \leq \mathrm{x} < b\} \tag{1.2}$$

Similar to our earlier paper [**73**], we shall make a distinction between vectors in the continuum and finite element settings. We also make a distinction between second-order tensors in the continuum setting versus matrices in the context of the finite element method. The continuum vectors are denoted by lower case boldface normal letters, and second-order tensors will be denoted by upper case boldface normal letters (for example, vector $\mathbf{x}$ and second-order tensor $\mathbf{D}$). In the finite element context, we shall denote the vectors using lower case boldface italic letters, and the matrices are denoted using upper case boldface italic letters. For example, vector $\boldsymbol{v}$ and matrix $\boldsymbol{K}$. Other notational conventions adopted in this report are introduced as needed.

2. GOVERNING EQUATIONS: TRANSIENT ANISOTROPIC DIFFUSION

Let $\Omega \subset \mathbb{R}^{nd}$ be a bounded open set, where "nd" denotes the number of spatial dimensions. The boundary is denoted by $\partial\Omega$, which is assumed to be piecewise smooth. A spatial point is denoted by $\mathbf{x} \in \overline{\Omega}$. The gradient and divergence with respect to $\mathbf{x}$ are denoted by grad$[\cdot]$ and div$[\cdot]$, respectively. Let $t \in [0, \mathcal{I}]$ denote the time, where $\mathcal{I} > 0$ denotes the length of the time interval. The concentration of an inert chemical species is denoted by $c(\mathbf{x}, t)$. The (spatial) boundary is divided into two parts: Γ^{D} and Γ^{N} such that $\Gamma^{\mathrm{D}} \cup \Gamma^{\mathrm{N}} = \partial\Omega$ and $\Gamma^{\mathrm{D}} \cap \Gamma^{\mathrm{N}} = \emptyset$. Γ^{D} is that part of the boundary on which Dirichlet boundary condition (i.e., the concentration) is prescribed, and Γ^{N} is the part of the boundary on which Neumann boundary condition (i.e., the flux) is prescribed. The

unit outward normal to the boundary is denoted by $\hat{\mathbf{n}}(\mathbf{x})$. The governing equations for transient anisotropic diffusion can be written as follows:

$$\frac{\partial c(\mathbf{x},t)}{\partial t} - \text{div}[\mathbf{D}(\mathbf{x})\text{grad}[c(\mathbf{x},t)]] = f(\mathbf{x},t) \quad \text{in } \Omega \times (0,\mathcal{I}) \tag{2.1a}$$

$$c(\mathbf{x},t) = c_p(\mathbf{x},t) \quad \text{on } \Gamma^{\text{D}} \times (0,\mathcal{I}) \tag{2.1b}$$

$$\hat{\mathbf{n}}(\mathbf{x}) \cdot \mathbf{D}(\mathbf{x})\text{grad}[c(\mathbf{x},t)] = q_p(\mathbf{x},t) \quad \text{on } \Gamma^{\text{N}} \times (0,\mathcal{I}) \tag{2.1c}$$

$$c(\mathbf{x},t=0) = c_0(\mathbf{x}) \quad \text{in } \Omega \tag{2.1d}$$

where $\mathbf{D}(\mathbf{x})$ is the diffusivity tensor, $f(\mathbf{x},t)$ is the volumetric source/sink, $c_p(\mathbf{x},t)$ is the prescribed concentration on the boundary, $q_p(\mathbf{x},t)$ is the prescribed flux on the boundary, and $c_0(\mathbf{x})$ is the prescribed initial condition. The diffusivity tensor is symmetric, and is assumed to be bounded above and uniformly elliptic. That is, there exists two constants $0 < \xi_1 \leq \xi_2 < +\infty$ such that

$$\xi_1 \mathbf{y}^{\text{T}}\mathbf{y} \leq \mathbf{y}^{\text{T}}\mathbf{D}(\mathbf{x})\mathbf{y} \leq \xi_2 \mathbf{y}^{\text{T}}\mathbf{y} \quad \forall \mathbf{x} \in \Omega \text{ and } \forall \mathbf{y} \in \mathbb{R}^{nd} \tag{2.2}$$

The above initial boundary value problem given by equations (2.1a)–(2.1d) is a *linear parabolic partial differential equation*. From the theory of partial differential equations, such equations are known to satisfy maximum principles under appropriate regularity assumptions on the input data and the domain [**85, 66**].

REMARK 2.1. *It should be noted that a consequence of Fickian/Fourier mathematical model is that a thermal/chemical disturbance at a point will be felt at other points instantaneously. This is because of the parabolic nature of the resulting partial differential equations. To put it differently, these mathematical models predict that the information travels at infinite speed, which is against the current accepted laws of Physics. Several modifications have been suggested in the area of heat conduction to have finite speeds for thermal disturbances, and most of these models are hyperbolic partial differential equations. Some notable works on this topic are by Maxwell* [**65**]*, Catteneo* [**20**]*, and Gurtin and Pipkin* [**40**]*. A more detailed discussion with respect to finite speed thermoelasticity can be found in Reference* [**55**]*. It is noteworthy that hyperbolic partial differential equations do not possess maximum principles "similar" to the ones possessed by elliptic and parabolic partial differential equations. This area of research is far from settled, and is beyond the scope of this paper.*

2.1. Maximum principles for parabolic equations. Maximum principles for parabolic partial differential equations can be traced back to Levi [**61**] and Picone [**82**]. A brief history and other references on maximum principles for parabolic partial differential equations can be found in the book by Protter and Weinberger [**85**]. Herein, we shall employ an approach similar to that of Nirenberg [**76**]. Before we state a maximum principle for linear parabolic partial differential equations, we shall introduce relevant notation and definitions. The parabolic cylinder is defined as $\Omega_{\mathcal{I}} := \Omega \times (0,\mathcal{I})$. The parabolic boundary is defined as follows:

$$\Gamma_{\mathcal{I}} := \left\{ (\mathbf{x},t) \in \overline{\Omega}_{\mathcal{I}} \;\middle|\; \mathbf{x} \in \partial\Omega \text{ or } t = 0 \right\} \tag{2.3}$$

The parabolic cylinder and parabolic boundary are pictorially described in Figure 1. Let $C^m(\Omega)$ denotes the set of functions defined on Ω that are continuously differentiable up to m-th order. We

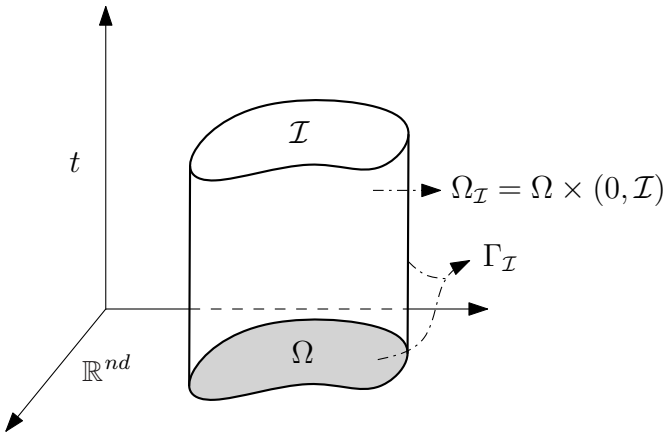

FIGURE 1. A pictorial description of parabolic cylinder $\Omega_{\mathcal{I}}$ and parabolic boundary $\Gamma_{\mathcal{I}}$.

shall introduce the following function space with differing smoothness in the $\mathbf{x}$- and t-variables:

$$C_1^2(\Omega_{\mathcal{I}}) := \left\{ c : \Omega_{\mathcal{I}} \to \mathbb{R} \mid c, \frac{\partial c}{\partial x_i}, \frac{\partial^2 c}{\partial x_i \partial x_j}, \frac{\partial c}{\partial t} \in C(\Omega_{\mathcal{I}}); i, j = 1, \cdots, nd \right\} \tag{2.4}$$

THEOREM 2.2 (maximum principle). *Let $c(\mathbf{x}, t) \in C_1^2(\Omega_{\mathcal{I}}) \cap C(\overline{\Omega}_{\mathcal{I}})$ satisfy $\partial c/\partial t - \mathrm{div}[\mathbf{D}(\mathbf{x})\mathrm{grad}[c]] \geq 0$ in $\Omega_{\mathcal{I}}$. Then $c(\mathbf{x}, t)$ achieves its minimum on the parabolic boundary of $\Omega_{\mathcal{I}}$. That is,*

$$\min_{(\mathbf{x},t)\in\overline{\Omega}_{\mathcal{I}}} c(\mathbf{x}, t) = \min_{(\mathbf{x},t)\in\Gamma_{\mathcal{I}}} c(\mathbf{x}, t) \tag{2.5}$$

PROOF. A proof can be found in standard books on partial differential equations (e.g., see [**85, 66, 32**]). □

REMARK 2.3. *The above maximum principle implies that if one has volumetric source everywhere and at all times (i.e., $f(\mathbf{x}, t) \geq 0$) then the minimum will occur on the boundary of the domain or in the initial condition. A logically equivalent statement of the above theorem can be written as follows: If $c(\mathbf{x}, t)$ satisfies $\partial c/\partial t - \mathrm{div}[\mathbf{D}(\mathbf{x})\mathrm{grad}[c]] \leq 0$, the maximum occurs on the parabolic boundary. That is,*

$$\max_{(\mathbf{x},t)\in\overline{\Omega}_{\mathcal{I}}} c(\mathbf{x}, t) = \max_{(\mathbf{x},t)\in\Gamma_{\mathcal{I}}} c(\mathbf{x}, t) \tag{2.6}$$

Maximum principles play a central role in the study of partial differential equations. Many uniqueness theorems and powerful estimates for elliptic and parabolic partial differential equations utilize some form of maximum principles [**36, 79**]. Maximum principles also have important physical implications in mathematical modeling, as they place restrictions on physical quantities. One such implication is the non-negative constraint. We now show that, under certain assumptions, the non-negative constraint is a consequence of the maximum principle given by Theorem 2.2. For the present discussion, let us assume that $\Gamma^{\mathrm{D}} = \partial\Omega$ (that is, we prescribe Dirichlet boundary conditions on the whole boundary). If $f(\mathbf{x}, t) \geq 0$ (i.e., we have volumetric source), $c_p(\mathbf{x}, t) \geq 0$ (i.e., we have non-negative prescribed Dirichlet boundary conditions on the whole boundary), and $c_0(\mathbf{x}) \geq 0$ (i.e., we have non-negative prescribed initial concentration); then the maximum principle given by Theorem 2.2 implies that the quantity $c(\mathbf{x}, t)$ is non-negative in the whole domain and at all times.

That is,

$$c(\mathbf{x}, t) \geq 0 \quad \forall \mathbf{x} \in \overline{\Omega} \text{ and } \forall t \in [0, \mathcal{I}] \tag{2.7}$$

It should be noted that the above discussion on maximum principles and the non-negative constraint is in continuum setting. For most practical problems (which will involve complex geometries and spatially varying coefficients), it is not possible to find analytical solutions. Therefore, one has to resort to numerical solutions. This leads to the following questions, which are central to this paper. *Whether numerical formulations satisfy maximum principles and the non-negative constraint for transient diffusion equation. If so, under what conditions? If not, is it possible to fix a given numerical formulation to meet these important principles?* This area of research is popularly referred to as discrete maximum principles.

REMARK 2.4. *Some recent efforts* [**64, 75, 73**] *have addressed similar questions with respect to maximum principles and the non-negative constraint, but all these studies have considered* steady *diffusion equation.*

2.2. Discrete maximum principles. The discrete analogy of maximum principles is commonly referred to as *discrete maximum principles* (DMP). Some main factors which affect numerical solutions with respect to discrete maximum principles are:

(i) topology of the domain (e.g., shape of the domain, features like holes in the domain),
(ii) type of mesh (e.g., Delaunay, well-centered, structured vs. unstructured),
(iii) element type (simplicial vs. non-simplicial elements),
(iv) mesh size (i.e., aspect ratio),
(v) medium properties (e.g., anisotropy, heterogeneity),
(vi) order of approximation (i.e., low-order vs. high-order), and
(vii) temporal discretization (e.g., time stepping scheme, selection of the time step).

The first six factors are equally applicable to steady anisotropic diffusion equation. Systematic studies on the effect of first five factors on maximum principles and the non-negative constraint can be found in references [**75, 73, 70**]. Reference [**80**] discusses in detail about the sixth factor. The last factor (in combination with other six factors) is the subject matter of this paper.

This leads to the problem statement of this paper: *Develop a finite element methodology for linear transient tensorial diffusion equation that satisfies maximum principles and the non-negative constraint on general computational grids for low-order finite elements with no additional restrictions on the time step.* To the best of our knowledge, such a methodology does not exist in the literature. In the next section, we shall extend the optimization-based methodologies that are presented in references [**75, 73**] for steady diffusion equations to transient diffusion equation. We shall explicitly enforce constraints on the nodal concentrations to satisfy maximum principles and the non-negative. We shall restrict to low-order finite elements, which include two-node line element, three-node triangular element, four-node quadrilateral element, four-node tetrahedron element, eight-node brick element, and six-node wedge element. However, it should be noted that the proposed methodology is *not* applicable to high-order elements, as enforcing non-negative constraints at nodes does not imply non-negative concentrations throughout the domain for high-order elements (e.g., three-node line element, six-node triangular element) [**80**].

3. PROPOSED METHODOLOGY: DERIVATION AND IMPLEMENTATION DETAILS

Herein, we shall employ the method of horizontal lines (also known as the Rothe method) [**88**] as opposed to the commonly employed method of vertical lines [**53**]. The method of horizontal lines is a discretization sequence in which the time is discretized first followed by spatial discretization. To this end, we shall define two sets of time levels: *integral* and *weighted* time levels. The time interval of interest $[0, \mathcal{I}]$ is divided into N non-overlapping subintervals such that

$$[0, \mathcal{I}] = \bigcup_{n=1}^{N} [t_{n-1}, t_n] \tag{3.1}$$

where t_n $(n = 0, \cdots, N)$ are referred to as integral time levels. For convenience, we shall assume that the time step Δt to be uniform, which implies that

$$\Delta t = \frac{\mathcal{I}}{N} \text{ and } t_n = n\Delta t \tag{3.2}$$

However, it should be noted that the proposed methodology can be easily extended to non-uniform time steps. We shall apply the method of horizontal lines at weighted time levels, which are defined as follows:

$$t_{n+\eta} := (1-\eta)t_n + \eta t_{n+1} \tag{3.3}$$

where the parameter $\eta \in [0, 1]$. The concentration and its rate at integral time levels are respectively denoted as follows:

$$c^{(n)}(\mathbf{x}) = c(\mathbf{x}, t = t_n) \tag{3.4a}$$

$$v^{(n)}(\mathbf{x}) = \frac{\partial c}{\partial t}(\mathbf{x}, t = t_n) \tag{3.4b}$$

The following notation is used to denote quantities at weighted time levels:

$$c^{(n+\eta)}(\mathbf{x}) := (1-\eta)c^{(n)}(\mathbf{x}) + \eta c^{(n+1)}(\mathbf{x}) \approx c(\mathbf{x}, t_{n+\eta}) \tag{3.5a}$$

$$v^{(n+\eta)}(\mathbf{x}) := (1-\eta)v^{(n)}(\mathbf{x}) + \eta v^{(n+1)}(\mathbf{x}) \approx \frac{\partial c}{\partial t}(\mathbf{x}, t = t_{n+\eta}) \tag{3.5b}$$

$$c_p^{(n+\eta)}(\mathbf{x}) := c_p(\mathbf{x}, t_{n+\eta}) \tag{3.5c}$$

$$f^{(n+\eta)}(\mathbf{x}) := f(\mathbf{x}, t_{n+\eta}) \tag{3.5d}$$

$$q_p^{(n+\eta)}(\mathbf{x}) := q_p(\mathbf{x}, t_{n+\eta}) \tag{3.5e}$$

3.1. Derivation. In designing the proposed methodology, attention will be exercised on two different aspects. The first aspect is to make sure that the non-negative constraint and maximum principles are preserved after both temporal and spatial discretizations. The second aspect is to achieve numerical stability in solving the resulting differential-algebraic equations. As we shall see in subsection 3.2, we will be adding additional equations in the form of lower and upper bounds (i.e., inequality constraints). This implies that we will be dealing with differential-algebraic equations. It is important to note that numerical time integration schemes that are designed for ordinary differential equations may not be stable and accurate for solving differential-algebraic equations. This point has been discussed adequately in the literature (e.g., see references [**10, 42, 43**]). An important work on numerical time integration of differential-algebraic equations is by Petzold [**81**],

and the title of this paper ("Differential/algebraic equations are not ODEs") succinctly summarizes the above discussion.

We shall employ the generalized-α method for temporal discretization. The generalized-α method was first proposed for second-order transient systems in Reference [**23**], and later modified for first-order transient systems in Reference [**58**]. After applying the generalized-α method to the governing equations (2.1a)–(2.1c), we obtain the following equations:

$$v^{(n+\alpha_m)}(\mathbf{x}) - \mathrm{div}[\mathbf{D}(\mathbf{x})\mathrm{grad}[c^{(n+\alpha_f)}]] = f^{(n+\alpha_f)}(\mathbf{x}) \quad \text{in } \Omega \tag{3.6a}$$

$$c^{(n+\alpha_f)}(\mathbf{x}) = c_p^{(n+\alpha_f)}(\mathbf{x}) \quad \text{on } \Gamma^{\mathrm{D}} \tag{3.6b}$$

$$\hat{\mathbf{n}}(\mathbf{x}) \cdot \mathbf{D}(\mathbf{x})\mathrm{grad}[c^{(n+\alpha_f)}] = q_p^{(n+\alpha_f)}(\mathbf{x}) \quad \text{on } \Gamma^{\mathrm{N}} \tag{3.6c}$$

where the parameters $\alpha_m,\ \alpha_f \in [0,1]$. In addition, we have the following relationship:

$$c^{(n+1)}(\mathbf{x}) = c^{(n)}(\mathbf{x}) + \Delta t \left((1-\gamma) v^{(n)}(\mathbf{x}) + \gamma v^{(n+1)}(\mathbf{x}) \right) \tag{3.7}$$

where the parameter $\gamma \in [0,1]$. The initial condition takes the following form:

$$c^{(0)}(\mathbf{x}) = c_0(\mathbf{x}) \quad \text{in } \Omega \tag{3.8}$$

REMARK 3.1. *Many popular time stepping schemes are special case of generalized-α method. For example, forward Euler ($\alpha_m = 1, \alpha_f = 1, \gamma = 0$), trapezoidal rule ($\alpha_m = 1, \alpha_f = 1, \gamma = 1/2$), and backward Euler ($\alpha_m = 1, \alpha_f = 1, \gamma = 1$).*

Herein, we shall take $\alpha_m = \gamma$. This selection is intended to inherit the non-negative property for the resulting time discrete equations. The time discrete equations in terms of concentration take the following form: Find $c^{(n+\alpha_f)}(\mathbf{x})$ such that we have

$$\frac{1}{\alpha_f \Delta t} c^{(n+\alpha_f)}(\mathbf{x}) - \mathrm{div}[\mathbf{D}(\mathbf{x})\mathrm{grad}[c^{(n+\alpha_f)}]] = f^{(n+\alpha_f)}(\mathbf{x}) + \frac{1}{\alpha_f \Delta t} c^{(n)}(\mathbf{x}) \quad \text{in } \Omega \tag{3.9a}$$

$$c^{(n+\alpha_f)}(\mathbf{x}) = c_p^{(n+\alpha_f)}(\mathbf{x}) \quad \text{on } \Gamma^{\mathrm{D}} \tag{3.9b}$$

$$\hat{\mathbf{n}}(\mathbf{x}) \cdot \mathbf{D}(\mathbf{x})\mathrm{grad}[c^{(n+\alpha_f)}] = q_p^{(n+\alpha_f)}(\mathbf{x}) \quad \text{on } \Gamma^{\mathrm{N}} \tag{3.9c}$$

The above boundary value problem (3.9a)–(3.9c) is a second-order inhomogeneous elliptic partial differential equation with Dirichlet and Neumann boundary conditions. Specifically, equation (3.9a) is the well-known steady-state anisotropic diffusion equation with decay, as $\alpha_f \Delta t$ will be always positive. The decay coefficient can be identified as $1/(\alpha_f \Delta t)$, and the volumetric source term is $f^{(n+\alpha_f)}(\mathbf{x}) + \frac{1}{\alpha_f \Delta t} c^{(n)}(\mathbf{x})$. This boundary value problem is also known to satisfy maximum principles and the non-negative constraint. The selection $\alpha_m = \gamma$ made it possible to preserve maximum principles and the non-negative constraint by ensuring the decay coefficient to be positive, and the volumetric source at discrete time levels to be non-negative.

It should be emphasized that an arbitrary temporal discretization will not preserve maximum principles and the non-negative constraint. An important aspect is to ensure is that the resulting equation after a temporal discretization of transient diffusion equation (2.1a) is a diffusion equation with decay instead of a Helmholtz equation. Diffusion equation with decay takes the following form:

$$\alpha(\mathbf{x}) c(\mathbf{x}) - \mathrm{div}[\mathbf{D}(\mathbf{x})\mathrm{grad}[c]] = f(\mathbf{x}) \tag{3.10}$$

with $\alpha(\mathbf{x}) \geq 0$. If $\alpha(\mathbf{x}) < 0$, the equation is referred to as Helmholtz equation. It should be noted that Helmholtz equation does not have a maximum principle similar to the one possessed

by diffusion equation with decay [**36**]. Hence, in order to preserve maximum principles and the non-negative constraint, the temporal discretization based on the method of horizontal lines should be carried out in such a way that the resulting decay coefficient is non-negative.

Recently, Nagarajan and Nakshatrala [**73**] have proposed a procedure for enforcing maximum principles and the non-negative constraint for steady diffusion with decay equation, which we shall modify to solve equations (3.9a)–(3.9c). We start by applying Galerkin formalism to equations (3.9a)–(3.9c). The corresponding weak form takes the following form: Find $c^{(n+\alpha_f)}(\mathbf{x}) \in \mathcal{P}_{n+\alpha_f}$ such that we have

$$\begin{aligned}\int_\Omega w(\mathbf{x})\frac{1}{\alpha_f \Delta t}c^{(n+\alpha_f)}(\mathbf{x})\,\mathrm{d}\Omega + \int_\Omega \mathrm{grad}[w]\cdot\mathbf{D}(\mathbf{x})\mathrm{grad}\left[c^{(n+\alpha_f)}\right]\,\mathrm{d}\Omega \\ = \int_\Omega w(\mathbf{x}) f^{(n+\alpha_f)}(\mathbf{x})\,\mathrm{d}\Omega + \int_\Omega w(\mathbf{x})\frac{1}{\alpha_f\Delta t}c^{(n)}(\mathbf{x})\,\mathrm{d}\Omega \\ + \int_{\Gamma^{\mathrm{N}}} w(\mathbf{x}) q_p^{(n+\alpha_f)}(\mathbf{x})\,\mathrm{d}\Gamma \quad \forall w(\mathbf{x}) \in \mathcal{Q} \end{aligned} \tag{3.11}$$

where the function spaces $\mathcal{P}_{n+\alpha_f}$ and $\mathcal{Q}$ are defined as follows:

$$\mathcal{P}_{n+\alpha_f} := \left\{ c(\mathbf{x}) \in H^1(\Omega) \;\middle|\; c(\mathbf{x}) = c_p^{(n+\alpha_f)}(\mathbf{x}) \text{ on } \Gamma^{\mathrm{D}} \right\} \tag{3.12a}$$

$$\mathcal{Q} := \left\{ w(\mathbf{x}) \in H^1(\Omega) \;\middle|\; w(\mathbf{x}) = 0 \text{ on } \Gamma^{\mathrm{D}} \right\} \tag{3.12b}$$

After executing the usual steps of the finite element method, the above weak form (3.11) can be converted to a system of linear equations of the following form:

$$\boldsymbol{K}\boldsymbol{c}^{(n+\alpha_f)} = \boldsymbol{f}^{(n+\alpha_f)} \tag{3.13}$$

where "$ndofs$" denotes the number of (free) degrees-of-freedom, $\boldsymbol{c}^{(n+\alpha_f)} \in \mathbb{R}^{ndofs}$ denotes the unknown vector containing nodal concentrations at the weighted time level $t_{n+\alpha_f}$, $\boldsymbol{f}^{(n+\alpha_f)} \in \mathbb{R}^{ndofs}$ is a known vector, and $\boldsymbol{K}$ is a symmetric and positive definite matrix. It will be shown in a subsequent section that the finite element solution obtained by solving the system of linear equations (3.13) may not satisfy maximum principles and the non-negative constraint. Using optimization-based techniques, we now modify the above solution procedure to meet these important physical constraints.

3.2. Enforcing maximum principles and the non-negative constraint. We shall denote the standard inner product on finite dimensional Euclidean spaces by $\langle \cdot ; \cdot \rangle$. We shall use the symbols $\preceq$ and $\succeq$ to denote component-wise inequalities for vectors. That is, for given any two (finite dimensional) vectors $\boldsymbol{a}$ and $\boldsymbol{b}$

$$\boldsymbol{a} \preceq \boldsymbol{b} \quad \text{means that} \quad a_i \leq b_i \;\forall i \tag{3.14}$$

Similarly, one can define the symbol $\succeq$. The optimization problem can then be written as follows:

$$\underset{\boldsymbol{c}^{(n+\alpha_f)} \in \mathbb{R}^{ndofs}}{\text{minimize}} \quad \frac{1}{2}\left\langle \boldsymbol{c}^{(n+\alpha_f)}; \boldsymbol{K}\boldsymbol{c}^{(n+\alpha_f)} \right\rangle - \left\langle \boldsymbol{c}^{(n+\alpha_f)}; \boldsymbol{f}^{(n+\alpha_f)} \right\rangle \tag{3.15a}$$

$$\text{subject to} \quad c_{\min}^{(n+\alpha_f)}\mathbf{1} \preceq \boldsymbol{c}^{(n+\alpha_f)} \preceq c_{\max}^{(n+\alpha_f)}\mathbf{1} \tag{3.15b}$$

where $\mathbf{1}$ is a vector containing ones of size $ndofs \times 1$, and $c_{\min}^{(n+\alpha_f)}$ and $c_{\max}^{(n+\alpha_f)}$ are respectively the lower and upper bounds. For enforcing maximum principles, $c_{\min}^{(n+\alpha_f)}$ and $c_{\max}^{(n+\alpha_f)}$ can be taken as

follows:

$$c_{\min}^{(n+\alpha_f)} := \min\left\{\min_{\mathbf{x}\in\Omega}\ c_0(\mathbf{x}),\ \min_{\mathbf{x}\in\partial\Omega}\ c_p^{(n+\alpha_f)}(\mathbf{x})\right\} \tag{3.16a}$$

$$c_{\max}^{(n+\alpha_f)} := \max\left\{\max_{\mathbf{x}\in\Omega}\ c_0(\mathbf{x}),\ \max_{\mathbf{x}\in\partial\Omega}\ c_p^{(n+\alpha_f)}(\mathbf{x})\right\} \tag{3.16b}$$

For problems involving only the non-negative constraint, one can employ the following:

$$c_{\min}^{(n+\alpha_f)} = 0 \text{ and } c_{\max}^{(n+\alpha_f)} = +\infty \tag{3.17}$$

Alternatively, for enforcing the non-negative constraint, one can replace the constraint (3.15b) with the following:

$$\mathbf{0} \preceq \boldsymbol{c}^{(n+\alpha_f)} \tag{3.18}$$

where $\mathbf{0}$ denotes the vector of size $ndofs \times 1$ containing zeros. It should be noted that the above optimization problem (3.15) belongs to *quadratic programming*. Since, for the problem at hand, the matrix $\boldsymbol{K}$ is positive definite (which makes the objective function (3.15a) convex) the optimization problem belongs to *convex quadratic programming*. A sound mathematical theory is already in place for studying convex quadratic programming [**16**], and several efficient algorithms are available in the literature [**78, 95, 16**]. In this paper, we shall employ the built-in optimization solver available in MATLAB [**7**]. Some other popular packages that can handle convex quadratic programming optimization problems are GAMS [**6**], TAO [**72**], and DAKOTA [**8**].

Once the nodal concentrations are obtained at weighted time level, one can obtain the nodal concentrations at integral time levels as follows:

$$\boldsymbol{c}^{(n+1)} = \frac{\boldsymbol{c}^{(n+\alpha_f)} - (1-\alpha_f)\boldsymbol{c}^{(n)}}{\alpha_f} \tag{3.19}$$

Although $\boldsymbol{c}^{(n+\alpha_f)} \succeq \mathbf{0}$, the nodal concentrations at integral time levels based on equation (3.19) need not be non-negative if $\alpha_f \neq 1$. To put it differently, one is assured of satisfying maximum principles and the non-negative constraint under the proposed methodology if $\alpha_m = \gamma \in (0, 1]$ and $\alpha_f = 1$. If needed, calculate nodal rate of concentrations using the following expression:

$$\boldsymbol{v}^{(n+1)} = \frac{\boldsymbol{c}^{(n+1)} - \boldsymbol{c}^{(n)} - (1-\gamma)\Delta t\boldsymbol{v}^{(n)}}{\gamma\Delta t} \tag{3.20}$$

It should also be emphasized that explicit schemes (i.e., the forward Euler) cannot be employed under the proposed methodology to meet maximum principles and the non-negative constraint. The various steps involved in the numerical implementation of the proposed methodology to satisfy maximum principles and the non-negative constraint are summarized in Algorithm 1, which could serve as a quick reference during computer code design and implementation.

4. A REPRESENTATIVE NUMERICAL RESULT

In this section, we shall illustrate the performance of the proposed methodology for enforcing maximum principles and the non-negative constraint using a representative two-dimensional problem. It should be, however, noted that the proposed methodology is equally applicable for solving three-dimensional problems. We do not solve any three-dimensional problem here as, in comparison with one- and two-dimensional problems, there are no additional difficulties other than the usual book keeping that is associated with most three-dimensional problems. In our numerical

Algorithm 1 Implementation of the proposed methodology based on $\alpha_f = 1$.

1: Input: Initial condition $c(\mathbf{x})$, Dirichlet boundary conditions $c_p(\mathbf{x}, t)$, Neumann boundary conditions $q_p(\mathbf{x}, t)$, time step Δt, total time of interest $\mathcal{I}$, $\alpha_m = \gamma \in (0, 1]$.
2: Construct initial nodal concentrations $\boldsymbol{c}^{(0)}$
3: Set $\boldsymbol{c}^{(n)} \longleftarrow \boldsymbol{c}^{(0)}$, $t \longleftarrow 0$, $n \longleftarrow 0$
4: **while** $t < \mathcal{I}$ **do**
5: Calculate $c_{\min}^{(n+1)}$ and $c_{\max}^{(n+1)}$ (see equations (3.16)–(3.17))
6: Call non-negative solver to obtain $\boldsymbol{c}^{(n+1)}$

$$\begin{aligned} \underset{\boldsymbol{c}^{(n+1)} \in \mathbb{R}^{ndofs}}{\text{minimize}} \quad & \frac{1}{2}\langle \boldsymbol{c}^{(n+1)}; \boldsymbol{K}\boldsymbol{c}^{(n+1)} \rangle - \langle \boldsymbol{c}^{(n+1)}; \boldsymbol{f}^{(n+1)} \rangle \\ \text{subject to} \quad & c_{\min}^{(n+1)} \mathbf{1} \preceq \boldsymbol{c}^{(n+1)} \preceq c_{\max}^{(n+1)} \mathbf{1} \end{aligned}$$

7: If needed, obtain rate of nodal concentrations at integral time levels (but need to choose $\gamma > 1/2$ to obtain stable results for the rates)

$$\boldsymbol{v}^{(n+1)} = \frac{\boldsymbol{c}^{(n+1)} - \boldsymbol{c}^{(n)} - (1-\gamma)\Delta t \boldsymbol{v}^{(n)}}{\gamma \Delta t}$$

8: Set $\boldsymbol{c}^{(n)} \longleftarrow \boldsymbol{c}^{(n+1)}$, $t \longleftarrow t + \Delta t$, $n \longleftarrow n + 1$
9: **end while**

simulations we have employed low-order finite elements, and have taken $\alpha_f = 1$. It is assumed that $\alpha_m = \gamma = 1$, unless stated otherwise.

4.1. Transient anisotropic diffusion in square plate with a hole. The computational domain is given by $\Omega := (0, 1) \times (0, 1) - [0.45, 0.55] \times [0.45, 0.55]$. The initial concentration in the domain is taken to be zero (i.e., $c_0(\mathbf{x}) = 0$). The volumetric source is zero (i.e., $f(\mathbf{x}, t) = 0$). The inner hole is prescribed with a constant concentration of unity, and the outer hole is prescribed with a constant concentration of zero. The diffusivity tensor is taken as follows:

$$\mathbf{D}(\mathbf{x}) = \mathbf{R}\mathbf{D}_0\mathbf{R}^{\mathrm{T}} \tag{4.1}$$

where $\mathbf{D}_0$ and the rotation tensor are, respectively, defined as follows:

$$\mathbf{D}_0 = \begin{pmatrix} k_1 & 0 \\ 0 & k_2 \end{pmatrix} \tag{4.2a}$$

$$\mathbf{R} = \begin{pmatrix} +\cos(\theta) & -\sin(\theta) \\ +\sin(\theta) & +\cos(\theta) \end{pmatrix} \tag{4.2b}$$

with the values $k_1 = 10$, $k_2 = 10^{-3}$ and $\theta = -\pi/6$. Using the maximum principle given by Theorem 2.2, it can be concluded that the concentration in the domain should be between zero and unity. This test problem is used to illustrate the following aspects:

(i) The numerical results from COMSOL [**71**] (which is a popular commercial finite element software package) do not satisfy the maximum principle and the non-negative constraint for transient anisotropic diffusion.

(ii) The proposed methodology satisfies the maximum principle and the non-negative constraint even on unstructured meshes with no additional restrictions on the time step.

(iii) The approach of using the backward Euler time stepping scheme with lumped capacity matrix does not guarantee non-negative solutions in the case of anisotropic diffusion.

Using numerical simulations it has been found that the transient solution is very close to the steady-state solution for time greater than 0.05. Therefore, the time steps for this test problem are chosen to be smaller than or equal to 0.05 so that they are appropriate for transient analyses.

We first show the results obtained using COMSOL [**71**]. Two different meshes are employed in the numerical simulations, which are shown in Figure 2. The variation of the minimum concentration with time is shown in Figure 3, and the numerical results from COMSOL did not satisfy the non-negative constraint. Figures 4 and 5 show the spread of the violation of the non-negative constraint and the concentration profiles using COMSOL for four-node structured mesh and three-node unstructured mesh, respectively. From these figures, the following two observations can be made:

(a) The magnitude of the violation of the non-negative constraint increases as the time step decreases.

(b) The violation reaches a steady-state value after sufficient time, which is around $t = 0.05$ for this problem. It should be emphasized that this steady-state value for minimum concentration is a significant non-negative number, and the violation of the non-negative constraint is nearly 5%.

The aforementioned problem is also solved using the proposed methodology. Figure 6 shows the unstructured computational meshes used in the numerical simulation. The concentration profiles obtained under the proposed methodology using these computational meshes are shown in Figures 7 and 8. Clearly, the proposed methodology satisfies the maximum principle and the non-negative constraint at all time levels. Figure 9 clearly shows that the approach of employing the backward Euler time stepping scheme with lumped capacity matrix is not sufficient to meet the maximum principle and the non-negative constraint in the case of transient anisotropic diffusion. This approach will work in the case of transient isotropic diffusion provided some restrictions on the mesh are met.

5. CONCLUDING REMARKS

We have presented a novel methodology for transient anisotropic diffusion equations that satisfies maximum principles and the non-negative constraint on computational grids with *no additional restrictions on the time step*. The methodology has been developed using the method of horizontal lines, and techniques from convex programming. We have shown that the semi-discrete procedure based on the standard single-field formulation gives unphysical negative concentrations and violates maximum principles. Using several representative numerical examples we have shown that the proposed methodology satisfies maximum principles and the non-negative constraint on general computational grids with anisotropic and heterogeneous diffusion. The proposed methodology performs gives physically meaningful non-negative concentrations even on coarse computational grids and for small time steps.

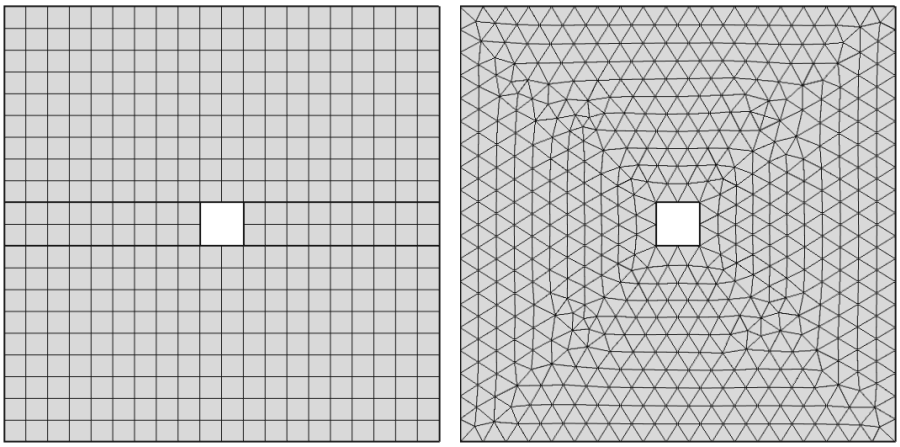

FIGURE 2. Anisotropic diffusion in a square plate with a hole: This figure shows the meshes employed in the numerical simulations using COMSOL [**71**]. The left figure shows a structured mesh based on four-node quadrilateral elements, and the right figure shows an unstructured mesh based on three-node triangular elements.

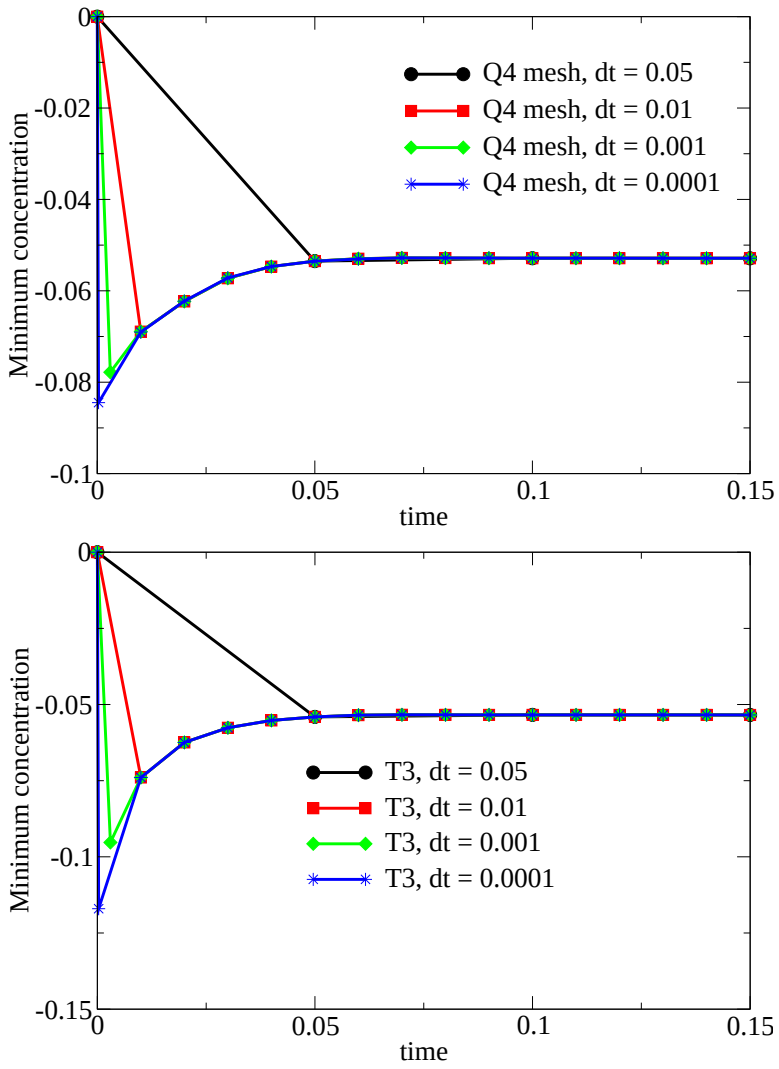

FIGURE 3. Anisotropic diffusion in square plate with a hole: This figure shows the variation of minimum concentration with time under the meshes shown in Figure 2. COMSOL [**71**] is employed in the numerical simulation. The solution is very close to the steady-state response for time greater than 0.05.

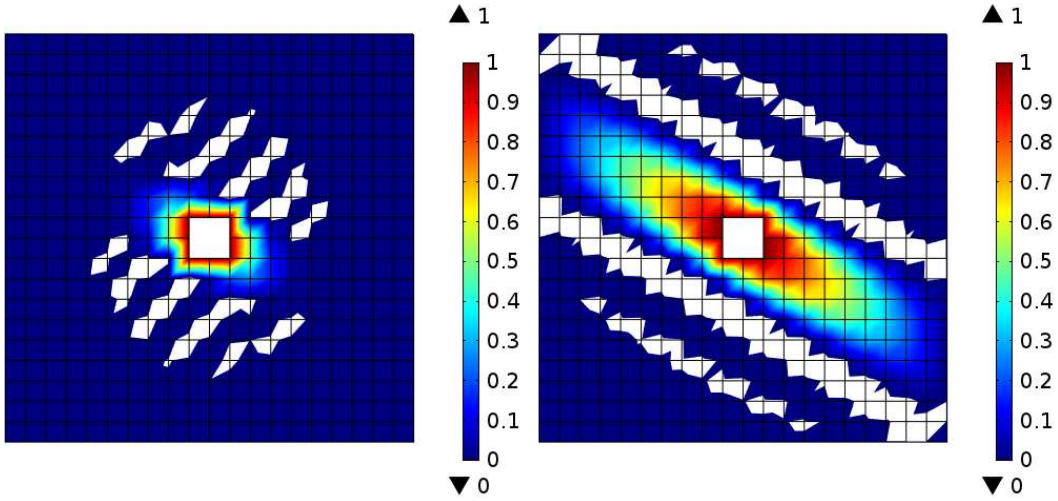

(a) $\Delta t = 0.0001$, $t = 3\Delta t$ (minimum = -0.08447) (b) $\Delta t = 0.0001$, t = 0.05 (minimum = -0.05351)

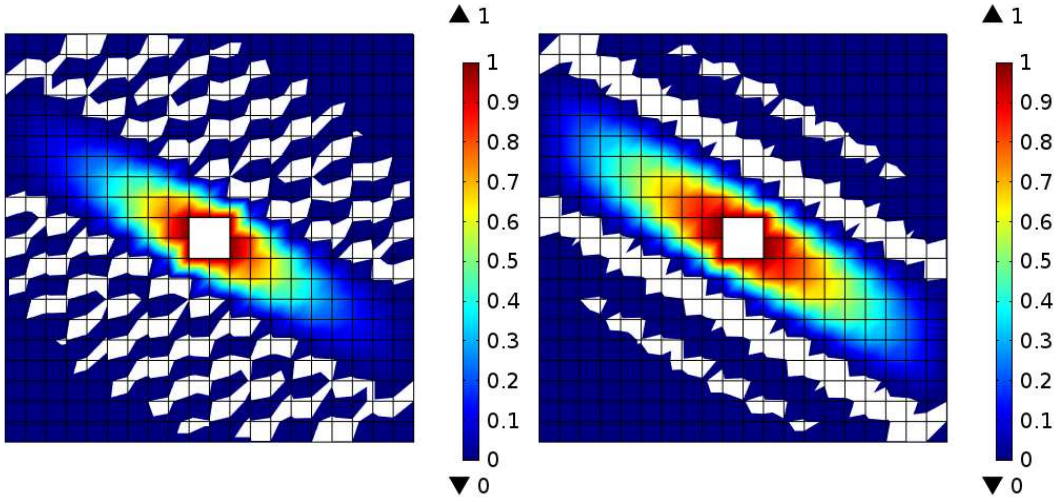

(c) $\Delta t = 0.001$, $t = 3\Delta t$ (minimum = -0.07781) (d) $\Delta t = 0.001$, t = 0.05 (minimum = -0.05350)

FIGURE 4. Anisotropic diffusion in square plate with a hole: Concentration profiles using COMSOL [**71**] by employing *structured four-node quadrilateral mesh*. The finite element mesh is also shown. The numerical results clearly violated the non-negative constraint for the concentration. The regions that violated the non-negative constraint are indicated in white color.

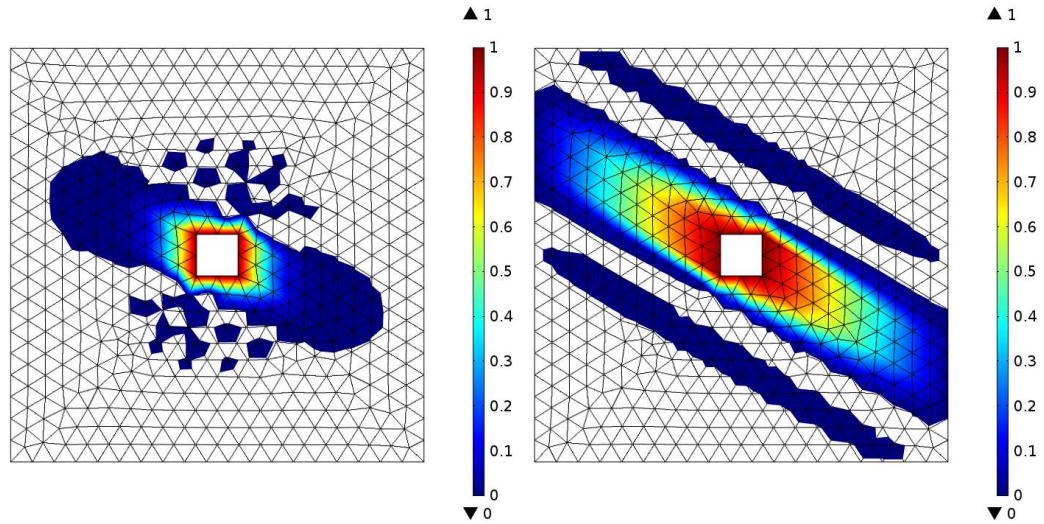

(a) $\Delta t = 0.0001$, $t = 3\Delta t$ (minimum = -0.1170) (b) $\Delta t = 0.0001$, t = 0.05 (minimum = -0.05406)

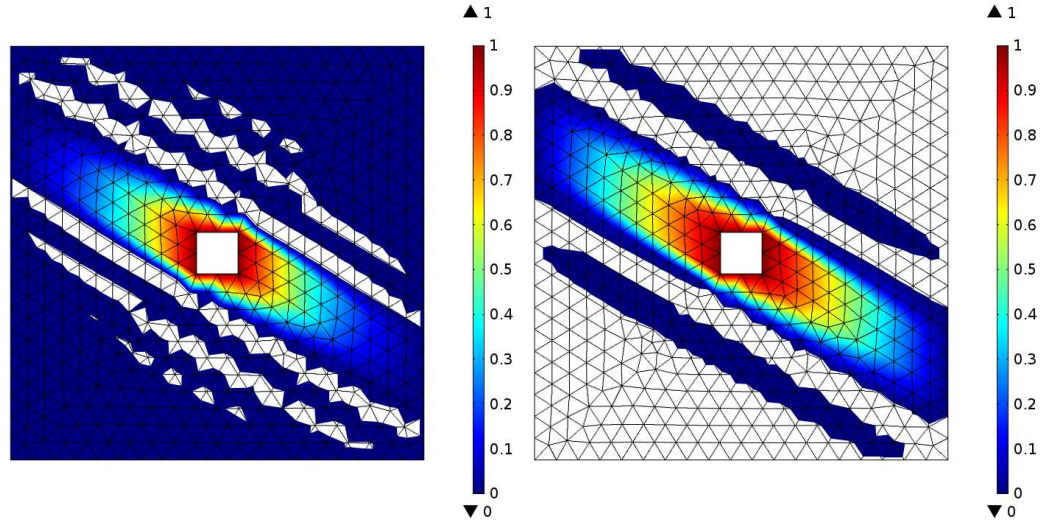

(c) $\Delta t = 0.001$, $t = 3\Delta t$ (minimum = -0.09527) (d) $\Delta t = 0.001$, t = 0.05 (minimum = -0.05406)

FIGURE 5. Anisotropic diffusion in square plate with a hole: Concentration profiles using COMSOL [**71**] by employing *unstructured three-node triangular mesh*. The finite element mesh is also shown. The numerical results clearly violated the non-negative constraint for the concentration. The regions that violated the non-negative constraint are indicated in white color.

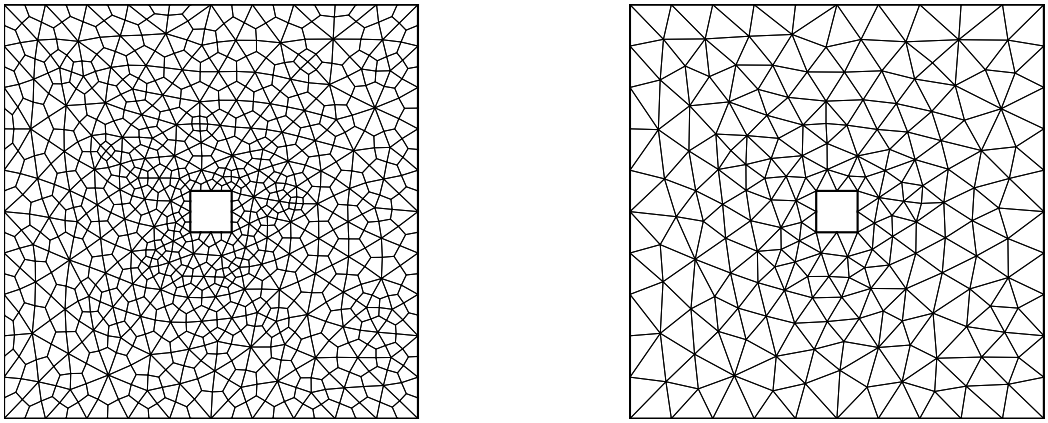

FIGURE 6. Anisotropic diffusion in a square plate with a hole: This figure shows the meshes employed in the numerical simulations using the proposed numerical methodology. The left figure shows an unstructured mesh based on four-node quadrilateral elements, and the right figure shows an unstructured mesh based on three-node triangular elements. The meshes are generated using GMSH [**1**].

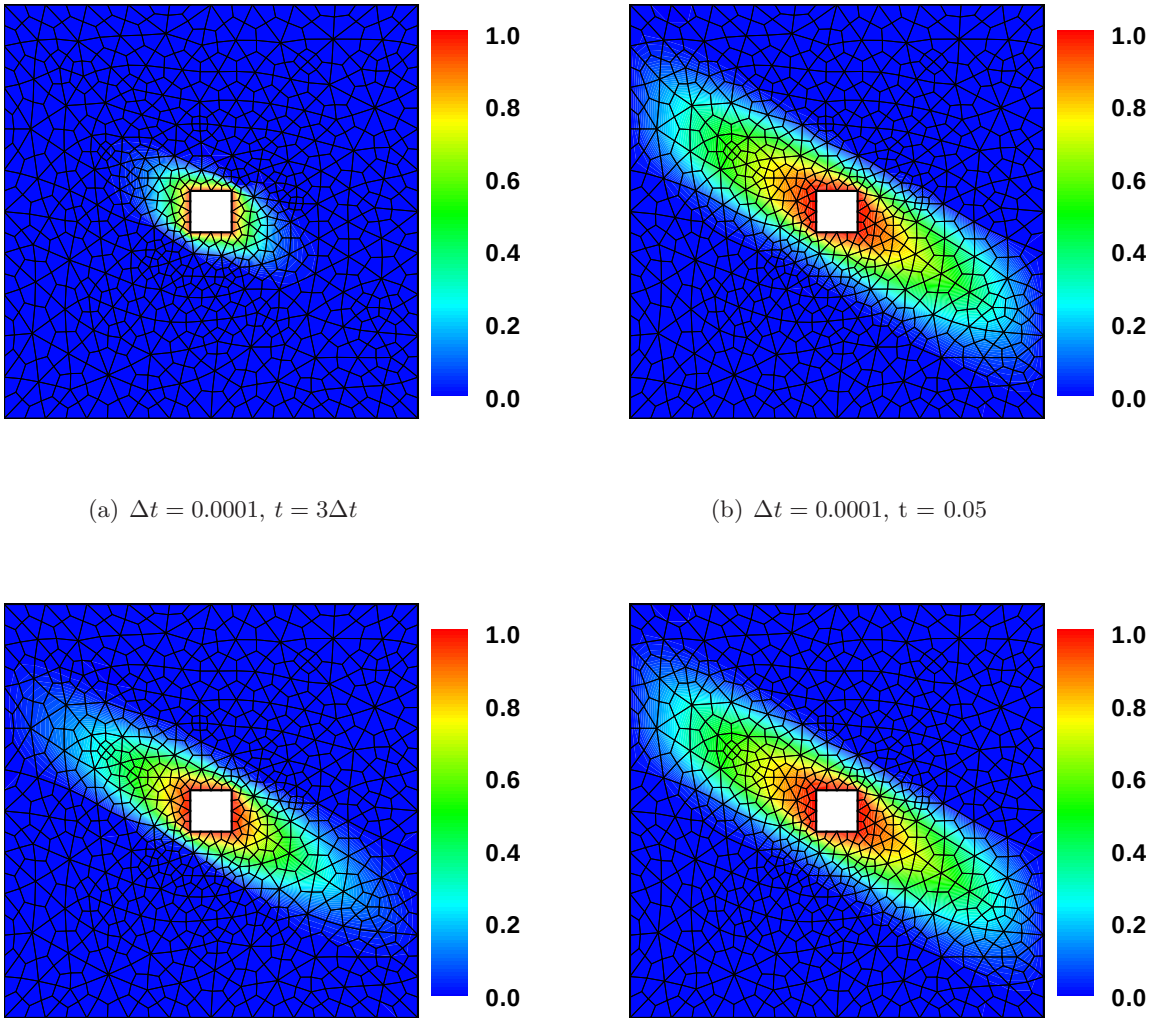

(a) $\Delta t = 0.0001$, $t = 3\Delta t$

(b) $\Delta t = 0.0001$, t = 0.05

(c) $\Delta t = 0.001$, $t = 3\Delta t$

(d) $\Delta t = 0.001$, t = 0.05

FIGURE 7. Anisotropic diffusion in square plate with a hole: Concentration profiles using the proposed methodology by employing *unstructured four-node triangular mesh*, which is shown in figure 6(a). The numerical results satisfy the maximum principle and the non-negative constraint. The numerical results are visualized using Tecplot [**2**].

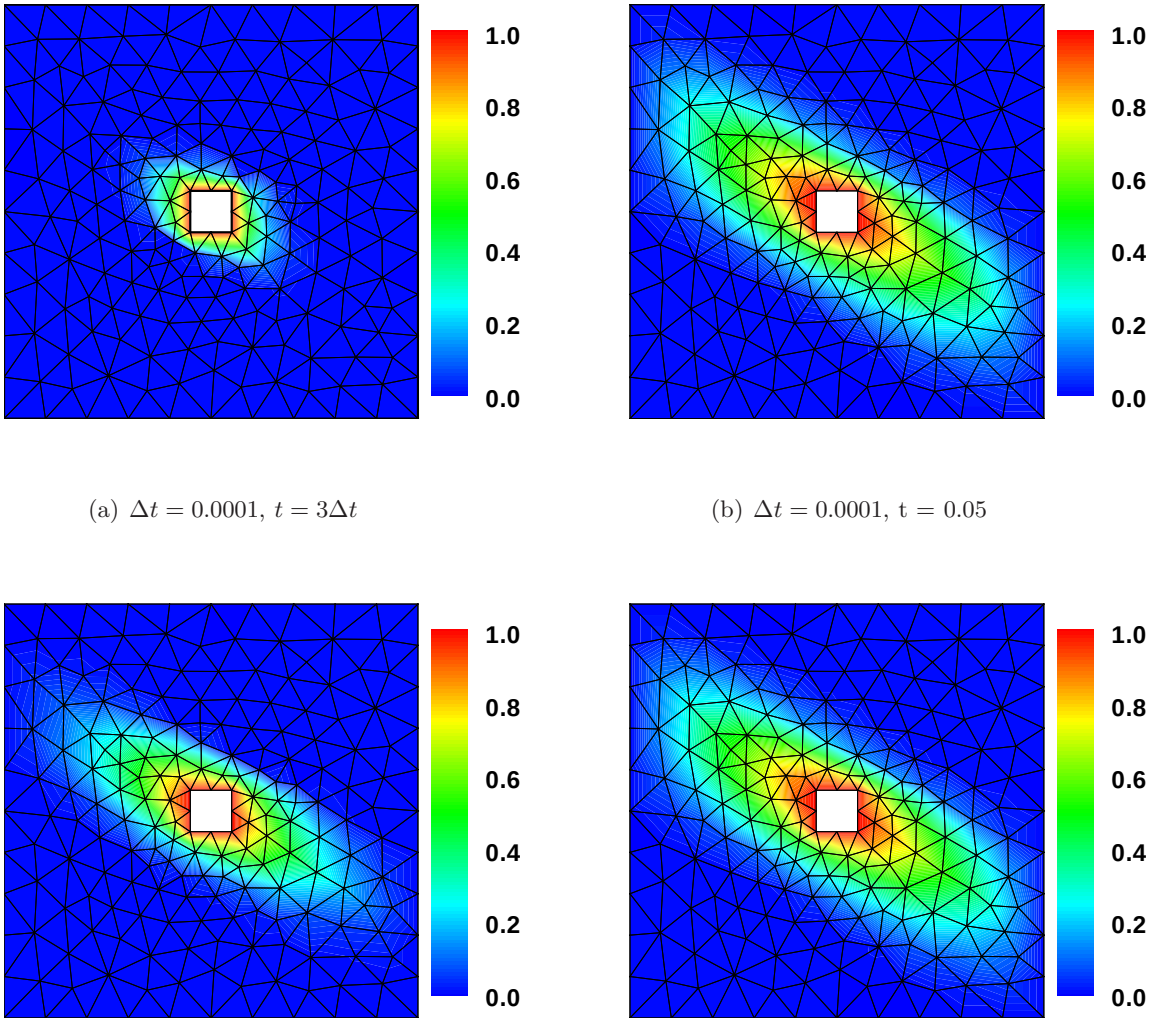

(a) $\Delta t = 0.0001$, $t = 3\Delta t$

(b) $\Delta t = 0.0001$, t = 0.05

(c) $\Delta t = 0.001$, $t = 3\Delta t$

(d) $\Delta t = 0.001$, t = 0.05

FIGURE 8. Anisotropic diffusion in square plate with a hole: Concentration profiles using the proposed methodology by employing *unstructured three-node triangular mesh*, which is shown in figure 6(b). The numerical results satisfy the maximum principle and the non-negative constraint. The numerical results are visualized using Tecplot [**2**].

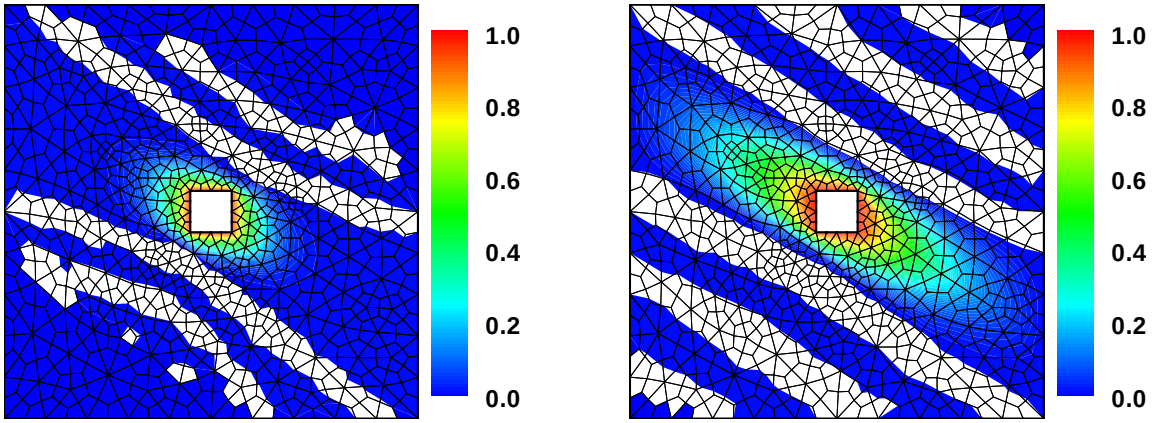

(a) $\Delta t = 0.0001$, $t = 3\Delta t$ (minimum = -0.01024)

(b) $\Delta t = 0.001$, $t = 3\Delta t$ (minimum = -0.03603)

FIGURE 9. Anisotropic diffusion in square plate with a hole: This figure shows the concentration profiles obtained using the backward Euler time stepping scheme ($\alpha_f = \alpha_m = \gamma = 1$) and lumped capacity matrix approach. The unstructured four-node quadrilateral mesh shown in figure 6(a) is used in the numerical simulation. Clearly, the numerical results do not satisfy the maximum principle and the non-negative constraint. In the case of isotropic diffusion, employing the backward Euler time-stepping scheme with lumped capacity matrix approach can be employed to satisfy maximum principles and the non-negative constraint (with some restrictions on the mesh). As it is evident from this figure, meeting these conditions is not sufficient in the case of transient anisotropic diffusion. The regions of the violation of the non-negative constraint are shown in white color. The numerical results are visualized using Tecplot [**2**].

A Report on Research Task #4.2

On achieving element-wise species balance and enforcing maximum principles for advection-diffusion-reaction equations

6. MOTIVATION BEHIND THE RESEARCH

Many phenomena in mathematical physics and engineering science are modeled using advection-diffusion-reaction (ADR) equation [**37, 27, 91, 28**]. For example, ADR equations naturally arise in many chemical, biological, and technological important processes such as degradation / healing of materials under extreme environmental conditions, coupled chemo-thermo-mechano-diffusion problems arising in nuclear industry, contaminant transport in heterogeneous anisotropic porous media, turbulent mixing in atmospheric sciences, diffusion-controlled biochemical reactions with applications to medicine, ionic mobility in chemical and biological sciences, transport and dispersion of injected tracers in hydrogeological systems. In addition, advection-diffusion-reaction equation serves as a good mathematical model in the field of numerical analysis, as it offers various challenges in obtaining stable and accurate numerical solutions [**69, 56, 54, 67**].

The typical unknown in these equations will be concentration. It should be noted the physical quantities like concentration of a chemical species or absolute temperature naturally attain non-negative values. In certain constitutive models, these quantities satisfy the so-called diffusion-type equations, which are either elliptic or parabolic partial differential equations. These elliptic/parabolic PDEs satisfy important mathematical properties like maximum principles, comparison principles, the non-negative constraint, and monotone property [**79**]. Any robust and reliable numerical formulation needs to satisfy these mathematical properties and the physical constraints like the non-negative constraint. In the literature, it is well-documented that traditional numerical methods perform poorly for advection-dominated ADR equations (e.g., see reference [**29**]). In the past few decades, considerable progress has been made in trying to capture various localized phenomena and obtain sufficiently accurate numerical solution for ADR equations on coarse grids. It is then natural to ask: "*why there is a need for yet another numerical formulation for ADR equation*?"

The three main challenges to solve an ADR equation are in capturing localized phenomena and avoiding node-to-node spurious oscillations, in satisfying the non-negative constraint and maximum principles, and in satisfying element-wise (or local) species balance. It should be emphasized that the current numerical formulations do not meet one or more of the aforementioned features. This sets up the main objective of this research work, which is to develop a finite element methodology for advection-diffusion-reaction equations that possesses the following desirable properties:

(i) No spurious node-to-node oscillations in the entire domain.
(ii) Captures the interior and boundary layers for advection-dominated problems.

(iii) Satisfies discrete maximum principles and the non-negative constraint.
(iv) Satisfies element-wise species balance.
(v) Gives sufficiently accurate solutions even on coarse computational grids[1].

6.1. An outline of the report. The remainder of the report is organized as follows. The governing equations for ADR systems are presented in Section 7. In Section 8, we propose an optimization-based mixed finite element method to satisfy discrete maximum principles and element-wise species balance. This involves minimizing a least-squares functional subject to a set of constraints. In Section 9, we perform numerical h-convergence of the proposed methodology. Finally, conclusions are drawn in Section 10.

The standard symbolic notation is adopted in this report. We shall denote scalars by lowercase English alphabet or lowercase Greek alphabet (e.g., concentration c). We shall make a distinction between vectors in the continuum and finite element settings. Similarly, a distinction is made between second-order tensors in the continuum setting versus matrices in the context of the finite element method. The continuum vectors are denoted by lower case boldface normal letters, and the second-order tensors will be denoted using upper case boldface normal letters (e.g., vector $\mathbf{x}$ and second-order tensor $\mathbf{D}$). In the finite element context, we shall denote the vectors using lower case boldface italic letters, and the matrices are denoted using upper case boldface italic letters (e.g., vector $\boldsymbol{v}$ and matrix $\boldsymbol{K}$). Other notational conventions adopted in this report are introduced as needed.

7. GOVERNING EQUATIONS: ADVECTION-DIFFUSION-REACTION SYSTEM

Let $\Omega \subset \mathbb{R}^{nd}$ be a bounded open domain, where "nd" denotes the number of spatial dimensions. The boundary of the domain is denoted by $\partial\Omega$, which is assumed to be piecewise smooth. Mathematically, $\partial\Omega := \overline{\Omega} - \Omega$, where a superposed bar denotes the set closure. A spatial point is denoted by $\mathbf{x} \in \overline{\Omega}$. The gradient and divergence operators are, respectively, denoted by grad$[\cdot]$ and div$[\cdot]$. Let $c(\mathbf{x})$ denote the concentration field. The boundary is divided into two parts: Γ^c and Γ^q such that $\Gamma^c \cup \Gamma^q = \partial\Omega$ and $\Gamma^c \cap \Gamma^q = \emptyset$. Γ^c is that part of the boundary on which the concentration is prescribed, and Γ^q is the part of the boundary on which the total flux is prescribed. The governing equations take the following form:

$$\alpha(\mathbf{x})c(\mathbf{x}) + \text{div}\,[c(\mathbf{x})\mathbf{v}(\mathbf{x}) - \mathbf{D}(\mathbf{x})\text{grad}[c(\mathbf{x})]] = f(\mathbf{x}) \quad \text{in } \Omega \tag{7.1a}$$

$$c(\mathbf{x}) = c^{\text{p}}(\mathbf{x}) \quad \text{on } \Gamma^c \tag{7.1b}$$

$$(c(\mathbf{x})\mathbf{v}(\mathbf{x}) - \mathbf{D}(\mathbf{x})\text{grad}[c(\mathbf{x})]) \cdot \mathbf{n}(\mathbf{x}) = q^{\text{p}}(\mathbf{x}) \quad \text{on } \Gamma^q \tag{7.1c}$$

where $\mathbf{n}(\mathbf{x})$ is the unit outward normal to the boundary, $\mathbf{v}(\mathbf{x})$ is the known velocity field, $\alpha(\mathbf{x})$ is the decay co-efficient, $f(\mathbf{x})$ is the prescribed volumetric source, $\mathbf{D}(\mathbf{x})$ is the anisotropic diffusivity tensor, $c^{\text{p}}(\mathbf{x})$ is the prescribed concentration, and $q^{\text{p}}(\mathbf{x})$ is the prescribed total flux. The diffusivity tensor is assumed to be symmetric, uniformly elliptic and bounded above.

[1]One may expect some subjectivity in calling a mesh to be coarse. But in a subsequent section, we will define precisely what is meant by a "coarse mesh" for advection-diffusion-reaction equations in terms of P-matrices.

7.1. Single-field Galerkin formulation. Let us define the following function spaces, which will be used in the remainder of this report:

$$\mathcal{C} := \left\{ c(\mathbf{x}) \in H^1(\Omega) \;\middle|\; c(\mathbf{x}) = c^{\mathrm{p}}(\mathbf{x}) \text{ on } \Gamma^c \right\} \tag{7.2a}$$

$$\mathcal{W} := \left\{ w(\mathbf{x}) \in H^1(\Omega) \;\middle|\; w(\mathbf{x}) = 0 \text{ on } \Gamma^c \right\} \tag{7.2b}$$

$$\mathcal{Q} := \left\{ \mathbf{q}(\mathbf{x}) \in \left(H^1(\Omega) \right)^{nd} \right\} \tag{7.2c}$$

where $H^1(\Omega)$ is a standard Sobolev space [**32**]. Given two fields $a(\mathbf{x})$ and $b(\mathbf{x})$ on K, the standard L_2 inner product over K is denoted as follows:

$$(a; b)_K = \int_K a(\mathbf{x}) \cdot b(\mathbf{x}) \, \mathrm{d}K \tag{7.3}$$

The subscript for the inner product will be dropped if $K = \Omega$. The single-field Galerkin formulation for advection-diffusion with (linear) decay reads as follows: Find $c(\mathbf{x}) \in \mathcal{C}$ such that we have

$$(w; \alpha c) + (w; \mathrm{div}[\mathbf{v}c]) + (\mathrm{grad}[w]; \mathbf{D}\mathrm{grad}[c]) = (w; f) \quad \forall w(\mathbf{x}) \in \mathcal{W} \tag{7.4}$$

It is well-known that the single-field Galerkin formulation does not perform well, as it produces spurious node-to-node oscillations on coarse grids [**29**]. The formulation also violates the non-negative constraint and maximum principles for anisotropic medium, and does not possess element-wise species balance property.

8. PROPOSED NUMERICAL METHODOLOGY: DMP AND ELEMENT-WISE SPECIES BALANCE

Let the computational domain Ω be discretized into a set of "*Nele*" non-overlapping open sub-domains, which will be referred to as elements. We shall denote the mesh discretization by $\mathcal{T}_h$. The *mesh parameters* for a given $\Omega_e \in \mathcal{T}_h$ are defined as follows:

$$\mathcal{T}_h = \bigcup_{e=1}^{Nele} \overline{\Omega}_e \tag{8.1a}$$

$$h = \max_{\Omega_e \in \mathcal{T}_h} \left\{ \mathrm{diam}(\Omega_e) \right\} \tag{8.1b}$$

$$\mathrm{diam}(\Omega_e) = \text{the longest edge of mesh cell } \bar{\Omega}_e \tag{8.1c}$$

where a superposed bar denotes the set closure. The boundary of Ω_e is denoted as $\partial\Omega_e := \overline{\Omega}_e - \Omega_e$. We now present a finite element methodology to obtain numerical solutions for ADR equations that satisfies maximum principles and element-wise species balance.

8.1. First-order mixed formulation. We shall rewrite the governing equations for ADR in first-order mixed form, which take the following form:

$$\mathbf{q}(\mathbf{x}) - \mathbf{v}(\mathbf{x})c(\mathbf{x}) + \mathbf{D}(\mathbf{x})\mathrm{grad}[c] = \mathbf{0} \quad \text{in } \Omega \tag{8.2a}$$

$$\mathrm{div}[\mathbf{q}(\mathbf{x})] = f(\mathbf{x}) - \alpha(\mathbf{x})c(\mathbf{x}) \quad \text{in } \Omega \tag{8.2b}$$

$$c(\mathbf{x}) = c^{\mathrm{p}}(\mathbf{x}) \quad \text{on } \Gamma^c \tag{8.2c}$$

$$\mathbf{q}(\mathbf{x}) \cdot \mathbf{n}(\mathbf{x}) = q^{\mathrm{p}}(\mathbf{x}) \quad \text{on } \Gamma^q \tag{8.2d}$$

The various components of the proposed computational framework for ADR equations are as follows:

(i) Construct a least-squares functional for the above first-order equations
(ii) Use low-order finite element interpolation for $c(\mathbf{x})$ and $\mathbf{q}(\mathbf{x})$
(iii) Enforce maximum principle as constraint: $c_{\min} \leq c \leq c_{\max}$ in $\overline{\Omega}$
(iv) Enforce local mass balance: $\mathrm{div}[\mathbf{q}] = f(\mathbf{x}) - \alpha(\mathbf{x})c(\mathbf{x})$ in each mesh cell Ω_e

$$\int_{\partial\Omega_e} \mathbf{q}(\mathbf{x}) \cdot \mathbf{n}(\mathbf{x}) \, \mathrm{d}\Gamma = \int_{\Omega_e} f(\mathbf{x}) \, \mathrm{d}\Omega - \int_{\Omega_e} \alpha(\mathbf{x})c(\mathbf{x}) \, \mathrm{d}\Omega$$

We now construct various least-squares functionals and analyze the influence of various constraints on the performance of these least-squares. Hsieh and Yang [**52**] have proposed a similar least-squares functionals for a different set of first-order mixed form of isotropic advection-diffusion equations. Even for isotropic case, they did not consider the effects of maximum principles and element-wise (or local) species balance on the performance of these least-squares. In this report, we investigate how do these least-squares functionals perform when one includes anisotropy, heterogeneity, linear reaction term, non-solenoidal velocity field, and influence of constraints.

8.2. Weighted primitive LSFEM. The weighted primitive least-squares functional $\mathfrak{F}_{\mathrm{Prim}}(c, \mathbf{q}) : \mathcal{C} \times \mathcal{Q} \to \mathbb{R}$ based on L_2–norm is given by:

$$\begin{aligned}
\mathfrak{F}_{\mathrm{Prim}}(c, \mathbf{q}) := & \frac{1}{2}\Big\| \mathbf{A}(\mathbf{x})\big(\mathbf{q}(\mathbf{x}) - c(\mathbf{x})\mathbf{v}(\mathbf{x}) + \mathbf{D}(\mathbf{x})\mathrm{grad}[c(\mathbf{x})]\big) \Big\|_{\Omega}^2 \\
& + \frac{1}{2}\Big\| \beta(\mathbf{x})\big(\alpha(\mathbf{x})c(\mathbf{x}) + \mathrm{div}[\mathbf{q}(\mathbf{x})] - f(\mathbf{x})\big) \Big\|_{\Omega}^2 \\
& + \frac{1}{2}\Big\| \mathbf{q}(\mathbf{x}) \cdot \mathbf{n}(\mathbf{x}) - q^{\mathrm{p}}(\mathbf{x}) \Big\|_{\Gamma^q}^2
\end{aligned} \tag{8.3}$$

where the second-order tensor $\mathbf{A}(\mathbf{x})$ and the scalar function $\beta(\mathbf{x})$ are the weights, and are defined as follows:

$$\mathbf{A}(\mathbf{x}) = \begin{cases} \mathbf{I} & \text{LS Type-1} \\ \mathbf{D}^{-1/2}(\mathbf{x}) & \text{LS Type-2} \end{cases} \tag{8.4a}$$

$$\beta(\mathbf{x}) = \begin{cases} 1 & \text{LS Type-1} \\ \begin{array}{ll} 1 & \text{if } \alpha(\mathbf{x}) = 0 \\ \alpha^{-1/2}(\mathbf{x}) & \text{if } \alpha(\mathbf{x}) \neq 0 \end{array} & \text{LS Type-2} \end{cases} \tag{8.4b}$$

8.3. Weighted stabilized LSFEM. The weighted stabilized least-squares functional $\mathfrak{F}_{\mathrm{Stab}}(c, \mathbf{q}) : \mathcal{C} \times \mathcal{Q} \to \mathbb{R}$ based on L_2–norm is given by:

$$\begin{aligned}
\mathfrak{F}_{\mathrm{Stab}}(c, \mathbf{q}) := & \frac{1}{2}\Big\| \mathbf{A}(\mathbf{x})\big(\mathbf{q}(\mathbf{x}) - c(\mathbf{x})\mathbf{v}(\mathbf{x}) + \mathbf{D}(\mathbf{x})\mathrm{grad}[c(\mathbf{x})]\big) \Big\|_{\Omega}^2 \\
& + \frac{1}{2}\Big\| \beta(\mathbf{x})\big(\alpha(\mathbf{x})c(\mathbf{x}) + \mathrm{div}[\mathbf{q}(\mathbf{x})] - f(\mathbf{x})\big) \Big\|_{\Omega}^2 \\
& + \frac{1}{2}\Big\| \mathbf{q}(\mathbf{x}) \cdot \mathbf{n}(\mathbf{x}) - q^{\mathrm{p}}(\mathbf{x}) \Big\|_{\Gamma^q}^2 \\
& + \frac{1}{2} \sum_{\Omega_{\mathrm{e}} \in \mathcal{T}_h} \tau_{\Omega_{\mathrm{e}}} \Big\| \mathrm{div}\big[c(\mathbf{x})\mathbf{v}(\mathbf{x}) - \mathbf{D}(\mathbf{x})\mathrm{grad}[c(\mathbf{x})]\big] + \alpha(\mathbf{x})c(\mathbf{x}) - f(\mathbf{x}) \Big\|_{\Omega_{\mathrm{e}}}^2
\end{aligned} \tag{8.5}$$

where the element dependent stabilization parameter $\tau_{\Omega_{\mathrm{e}}} \geq 0$ is given as:

$$\tau_{\Omega_{\mathrm{e}}} = c_{\Omega_{\mathrm{e}}} h_{\Omega_{\mathrm{e}}}^2 \tag{8.6}$$

8.4. Weighted streamline diffusion LSFEM. The weighted streamline diffusion least-squares functional $\mathfrak{F}_{\text{StrDif}}(c,\mathbf{q}) : \mathcal{C} \times \mathcal{Q} \to \mathbb{R}$ based on L_2–norm is given by:

$$\begin{aligned}\mathfrak{F}_{\text{StrDif}}\,(c,\mathbf{q}) := \frac{1}{2}\sum_{\Omega_{\text{e}}\in\mathcal{T}_h} \Big\|\mathbf{A}(\mathbf{x})\big(\mathbf{q} - c\mathbf{v} + \mathbf{D}\text{grad}[c] - \delta_{\Omega_{\text{e}}}\mathbf{v}\,(\text{div}[c\mathbf{v} - \mathbf{D}\text{grad}[c]])\,\big)\Big\|^2_{\Omega_{\text{e}}} \\ + \frac{1}{2}\sum_{\Omega_{\text{e}}\in\mathcal{T}_h} \Big\|\beta(\mathbf{x})\big(\alpha c + \text{div}[\mathbf{q}] - f - f_{\delta_{\Omega_{\text{e}}}}\big)\Big\|^2_{\Omega_{\text{e}}} \\ + \frac{1}{2}\sum_{\Omega_{\text{e}}\in\mathcal{T}_h\big|_{\Gamma^q}} \Big\|\mathbf{q}\cdot\mathbf{n} - q^{\text{p}} - \delta_{\Omega_{\text{e}}}\mathbf{v}\cdot\mathbf{n}\,(f-\alpha c)\Big\|^2_{\Omega_{\text{e}}}\end{aligned} \tag{8.7}$$

where the element dependent streamline diffusion parameter $\delta_{\Omega_{\text{e}}} \leq 0$ and the term $f_{\delta_{\Omega_{\text{e}}}}$ is given as follows:

$$\delta_{\Omega_{\text{e}}} = -\frac{\breve{c}_{\Omega_{\text{e}}} h^2_{\Omega_{\text{e}}}}{\|\mathbf{D}\|_\infty} \tag{8.8a}$$

$$f_{\delta_{\Omega_{\text{e}}}} = \delta_{\Omega_{\text{e}}}\big(\text{grad}[f-\alpha c]\cdot\mathbf{v} + \text{div}[\mathbf{v}]\;(f-\alpha c)\,\big) \tag{8.8b}$$

8.5. Weighted negatively stabilized streamline diffusion LSFEM. The weighted negatively stabilized streamline diffusion least-squares functional $\mathfrak{F}_{\text{NgStb}}(c,\mathbf{q}) : \mathcal{C} \times \mathcal{Q} \to \mathbb{R}$ based on L_2–norm is given by:

$$\begin{aligned}\mathfrak{F}_{\text{NgStb}}\,(c,\mathbf{q}) := \frac{1}{2}\sum_{\Omega_{\text{e}}\in\mathcal{T}_h} \Big\|\mathbf{A}(\mathbf{x})\big(\mathbf{q} - c\mathbf{v} + \mathbf{D}\text{grad}[c] - \delta_{\Omega_{\text{e}}}\mathbf{v}\,(\text{div}[c\mathbf{v} - \mathbf{D}\text{grad}[c]])\,\big)\Big\|^2_{\Omega_{\text{e}}} \\ + \frac{1}{2}\sum_{\Omega_{\text{e}}\in\mathcal{T}_h} \Big\|\beta(\mathbf{x})\big(\alpha c + \text{div}[\mathbf{q}] - f - f_{\delta_{\Omega_{\text{e}}}}\big)\Big\|^2_{\Omega_{\text{e}}} \\ + \frac{1}{2}\sum_{\Omega_{\text{e}}\in\mathcal{T}_h\big|_{\Gamma^q}} \Big\|\mathbf{q}\cdot\mathbf{n} - q^{\text{p}} - \delta_{\Omega_{\text{e}}}\mathbf{v}\cdot\mathbf{n}\,(f-\alpha c)\Big\|^2_{\Omega_{\text{e}}} \\ + \frac{1}{2}\sum_{\Omega_{\text{e}}\in\mathcal{T}_h} \tau_{\Omega_{\text{e}}}\Big\|\text{div}\big[c\mathbf{v} - \mathbf{D}\text{grad}[c]\big] + \alpha c - f\Big\|^2_{\Omega_{\text{e}}}\end{aligned} \tag{8.9}$$

where the element dependent parameters $\tau_{\Omega_{\text{e}}} \leq 0$ and $\delta_{\Omega_{\text{e}}} \leq 0$ are given as:

$$\delta_{\Omega_{\text{e}}} = -\frac{\tilde{c}_{\Omega_{\text{e}}} h^2_{\Omega_{\text{e}}}}{\|\mathbf{D}\|_\infty} \tag{8.10a}$$

$$\tau_{\Omega_{\text{e}}} = -\tilde{\tilde{c}}_{\Omega_{\text{e}}} h^2_{\Omega_{\text{e}}} \tag{8.10b}$$

In the subsequent sections, we will present representative numerical results for steady-state advection-diffusion-reaction equations. In particular, we shall consider several canonical problems that exhibit localized phenomena such as steep interior and boundary layers. The performance of the four least-squares formulations (primitive, stabilized, streamline diffusion, and negatively stabilized streamline diffusion) are analyzed when subjected to the non-negative constraint and the local species balance constraint.

9. NUMERICAL h-CONVERGENCE STUDY

Consider the computational domain to be a unit square $\Omega = (0,1) \times (0,1)$. The diffusivity D is assumed to be a constant. The velocity field is taken as $\mathbf{v}(\mathbf{x}) = \hat{\mathbf{e}}_y$. The boundary conditions can be written as follows:

$$c(\mathbf{x}) = \begin{cases} \sin(\pi x) & \text{for } y = 0 \\ 0 & \text{for } x = 0 \text{ or } x = 1 \text{ or } y = 1 \end{cases} \tag{9.1}$$

A pictorial description of the boundary value problem is given in Figure 10. Using the method of manufactured solutions, we construct the analytical solution to the concentration field. The corresponding analytical solution for $c(\mathbf{x})$ which satisfies the boundary conditions given by equation (9.1) is as follows [**35**]:

$$c(x,y) = \frac{\sin(\pi x)}{e^{m_2 - m_1} - 1} \left(e^{m_2 - m_1} e^{m_1 y} - e^{m_2 y} \right) \tag{9.2}$$

where

$$m_1 = \frac{1 - \sqrt{1 + 4\pi^2 D^2}}{2D} \tag{9.3a}$$

$$m_2 = \frac{1 + \sqrt{1 + 4\pi^2 D^2}}{2D} \tag{9.3b}$$

By using equation (9.2), we calculate the corresponding flux vector and volumetric source . The analytical expressions for $\mathbf{q}(\mathbf{x})$ and $f(\mathbf{x})$ are given as follows:

$$\mathbf{q}(x,y) = \begin{pmatrix} -\frac{D\pi \cos(\pi x)}{e^{m_2 - m_1} - 1} \left(e^{m_2 - m_1} e^{m_1 y} - e^{m_2 y} \right) \\ \frac{\sin(\pi x)}{e^{m_2 - m_1} - 1} \left((1 - m_1 D)\, e^{m_2 - m_1} e^{m_1 y} - (1 - m_2 D)\, e^{m_2 y} \right) \end{pmatrix} \tag{9.4a}$$

$$f(x,y) = \frac{\sin(\pi x)}{e^{m_2 - m_1} - 1} \Big(\left(m_1 - m_1^2 D + \pi^2 D \right) e^{m_2 - m_1} e^{m_1 y} - \left(m_2 - m_2^2 D + \pi^2 D \right) e^{m_2 y} \Big) \tag{9.4b}$$

In the present study we have taken $D = 1$. *From figures 11–14, one can conclude that the performance of four-node quadrilateral finite element mesh is much better than that of the three-node triangle finite element mesh. The proposed methodology works well.*

10. CONCLUDING REMARKS

We have presented a methodology for advection-diffusion equation that satisfies the non-negative constraint and maximum principles even for anisotropic medium, possesses element-wise species balance property, and provides physically meaningful numerical solutions without node-to-node oscillations even on coarse computational grids. Numerical h-convergence is performed on a series of hierarchical meshes, and the proposed methodology performed well. It is noteworthy that four-node quadrilateral meshes performed better than three-node triangular meshes.

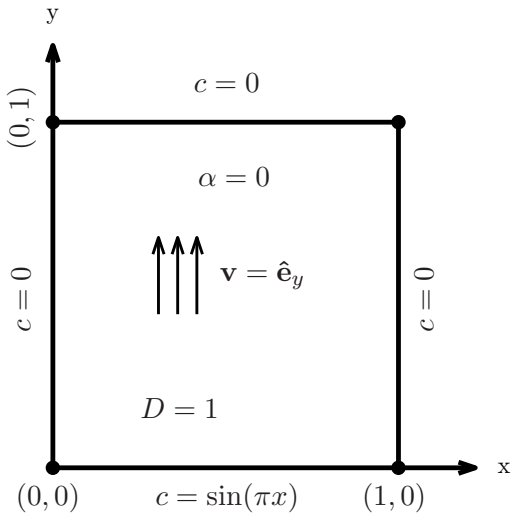

FIGURE 10. Numerical h-convergence study: A pictorial description of the two-dimensional boundary value problem used in the convergence analysis.

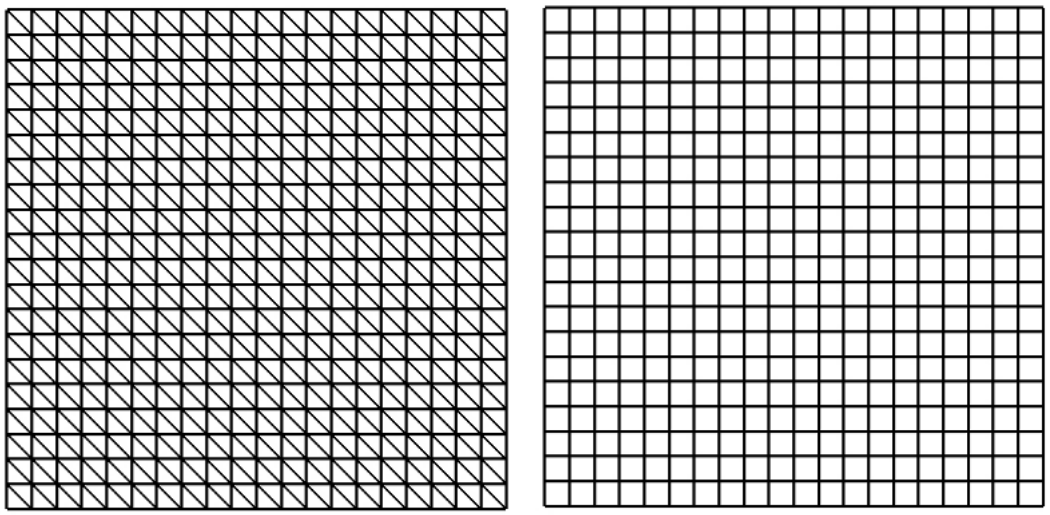

FIGURE 11. Numerical h-convergence study: This figure shows the typical three-node triangular and four-node quadrilateral meshes used in the numerical convergence study. The meshes shown in the figure have 21 nodes along each side of the computational domain. A series of hierarchical computational meshes is employed in the study: 11×11, 21×21, 41×41, 81×81, and 161×161 meshes.

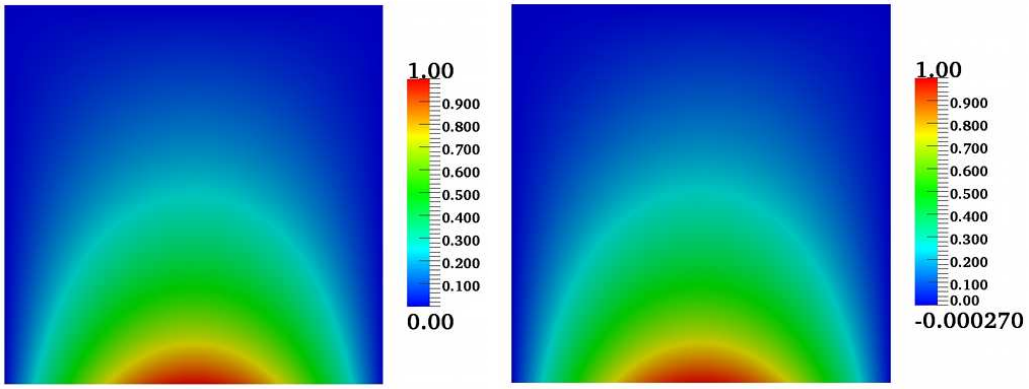

(a) Concentration: No constraints (b) Concentration: Local mass balance

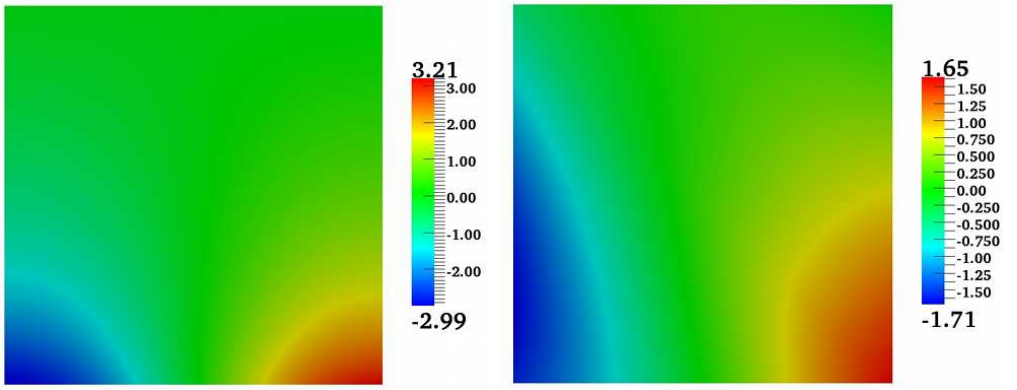

(c) Flux (x-component): No constraints (d) Flux (x-component): Local mass balance

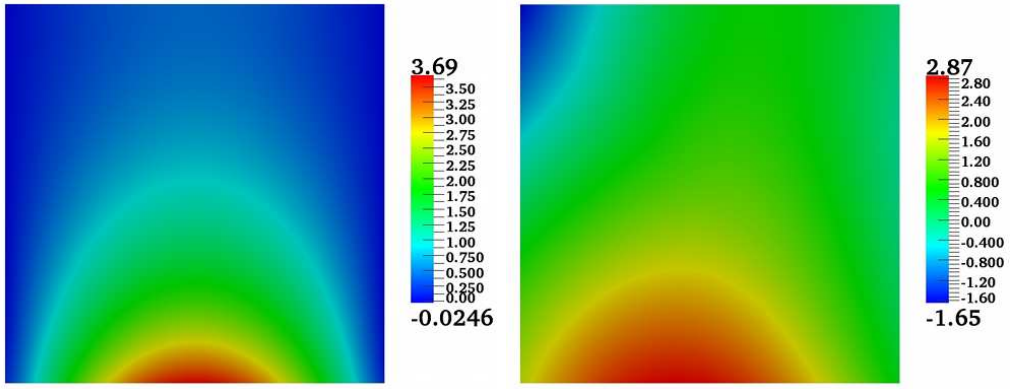

(e) Flux (y-component): No constraints (f) Flux (y-component): Local mass balance

FIGURE 12. Numerical h-convergence study: This figure shows the concentration and flux profiles for stabilized least-squares finite element method for T3-mesh with 161 nodes on each side of the domain. The numerical results obtained are very similar to that of the primitive least-squares. The concentration and flux profiles match with the analytical solution when there are no mass balance constraints. But when local mass balance is enforced as a constraints one obtains *negative values* for concentration. The flux profile for stabilized least-squares with local mass balance constraints differ considerably as compared to analytical solution.

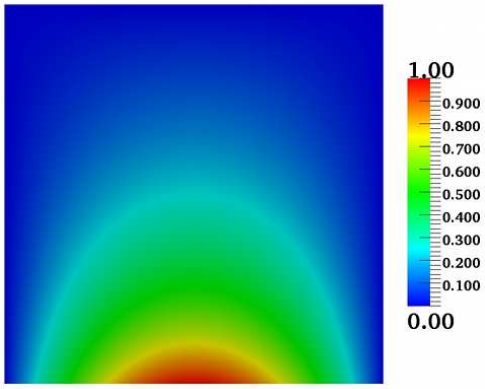

(a) Concentration: No constraints

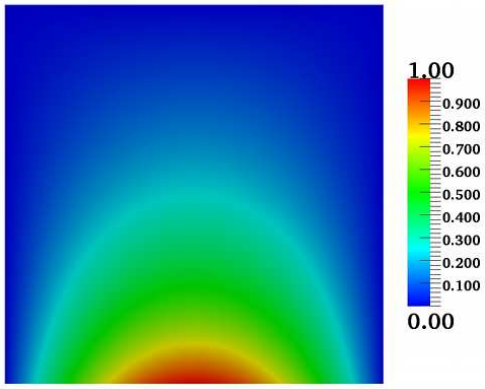

(b) Concentration: Local mass balance

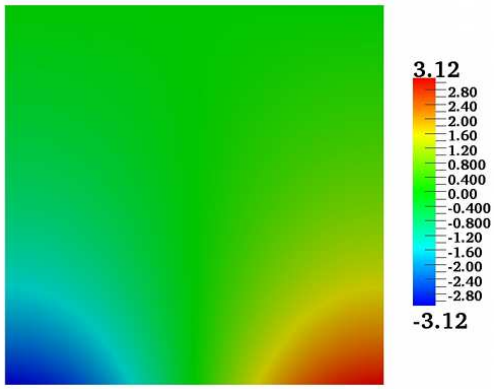

(c) Flux (x-component): No constraints

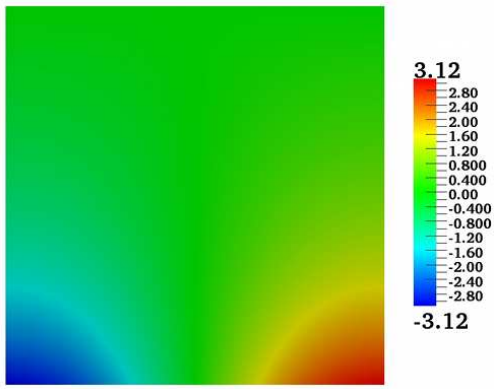

(d) Flux (x-component): Local mass balance

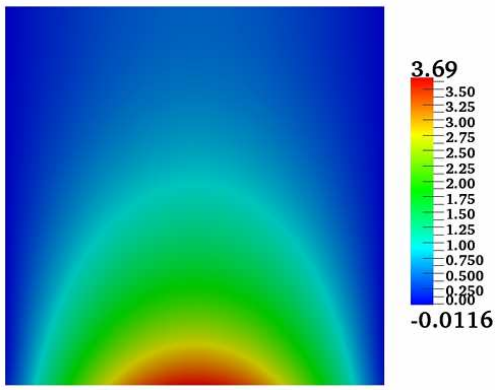

(e) Flux (y-component): No constraints

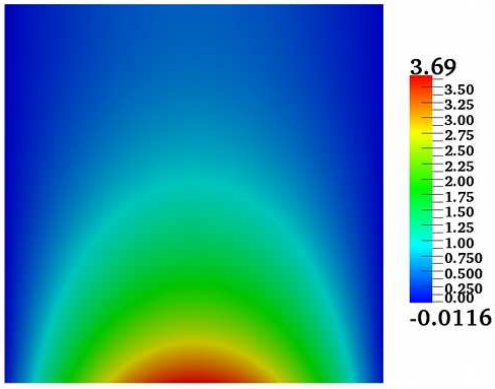

(f) Flux (y-component): Local mass balance

FIGURE 13. Numerical h-convergence study: This figure shows the concentration and flux profiles for stabilized least-squares finite element method. In this case, we use Q4-mesh with 161 nodes on each side to perform the numerical simulation. This formulation based on the Q4-element is able to predict the nature of the analytical solution both qualitatively and quantitatively. There are no violation of the non-negative constraint when one enforces the local mass balance constraints.

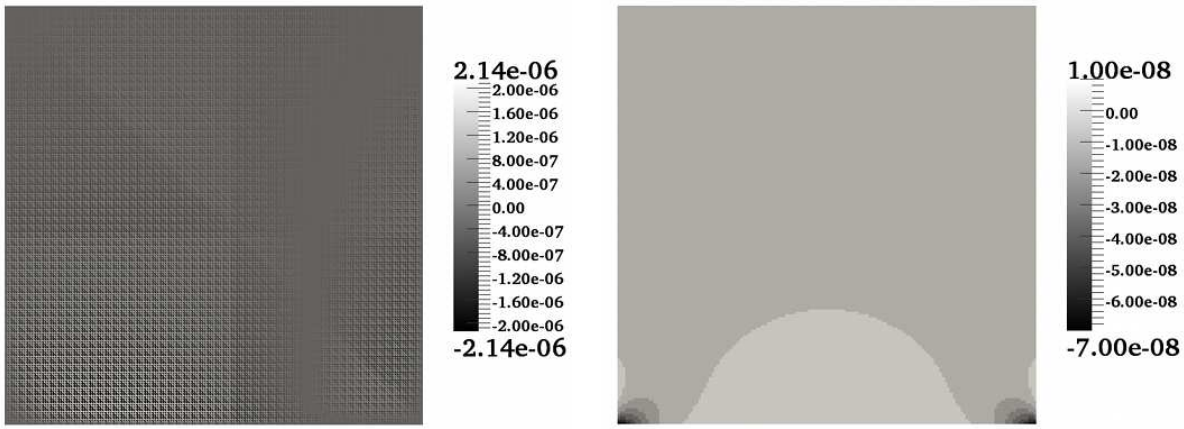

FIGURE 14. Numerical h-convergence study: This figure provides information in regards to the error incurred in satisfying local mass balance for stabilized least-squares functional. The left figure shows the error for T3-mesh while the right figure shows the error for Q4-mesh. One can observe that the maximum and minimum values of error in local mass balance for T3-mesh is much bigger than that of Q4-mesh.

A Report on Research Task #4.3

Mesh restrictions on T3 element to satisfy maximum principles for heterogeneous anisotropic diffusion

11. INTRODUCTION AND MOTIVATION

Diffusion-type equations are commonly encountered in various branches of engineering, sciences, and even in economics [**27, 54, 67, 69, 91, 9, 87**]. These equations have been well-studied in Applied Mathematics, and several properties and estimates have been derived [**32, 79**]. Numerous numerical formulations have been proposed and their performance have been analyzed both theoretically and numerically [**37, 34, 47, 46, 17, 18, 25, 26, 59**]. Several sophisticated software packages have been developed to solve these type of equations [**3, 5, 4**]. Special solvers for solving the resulting discrete equations have also been proposed and studied adequately [**90, 41**].

This paper concerns with numerical solutions. Despite the aforementioned advances, it should be noted that a numerical solution will always lose some mathematical properties that the exact solution possess. In particular, the aforementioned numerical formulations do not satisfy comparison principles, maximum principles, and the non-negative constraint. There are two possible routes to satisfy maximum principles and the non-negative constraint under the finite element method. The first approach is to employ optimization-based methodologies to explicitly enforce the desirable properties as constraints. Some notable works in this direction are presented in references [**75, 73, 74**]. One of the main advantages of these methods is that there is no need to place restrictions on the mesh. But this comes with an additional computational cost. Although it has been shown that the additional computational cost is less than 10% [**74**].

The second approach is to place restrictions on the mesh to meet maximum principles and the non-negative constraint. Ciarlet and Raviart [**24**] have shown that numerical solutions based on the single-field Galerkin finite element formulation, in general, does not converge *uniformly*. It should be, however, noted that the single-field Galerkin formulation is a converging scheme. Ciarlet and Raviart have also shown that a sufficient condition for single-field Galerkin formulation to converge uniformly for *isotropic* diffusion is to employ a well-centered three-node triangular elements with low-order interpolation. The obvious advantage of the second approach is that one can use the single-field Galerkin formulation without any modification. The drawback is that an appropriate computational mesh may not exist because of the required restrictions on the shape and size of the finite element. For example, it is a herculean task (sometimes impossible) to generate a well-centered triangular mesh for any given two-dimensional domain [**93**]. Note that requiring a mesh to be well-centered is a more stringent requirement than requiring the mesh to be Delaunay.

11.1. Main contributions and outline of the report. *Herein, we shall focus on the second approach. In particular, we shall derive sufficient conditions for restrictions on the three-node triangle finite elements to meet comparison principles, maximum principles, and the non-negative constraint in the case of heterogeneous anisotropic diffusion.* The remainder of this research report is organized as follows. In Section 12, we shall present the governing equations for anisotropic diffusion and associated comparison principle, maximum principle, and the non-negative constraint. In Section 13, we shall present discrete versions of the comparison principle and maximum principle. We then derive restrictions on the mesh for three-node triangle element to meet maximum principles and comparison principles for heterogeneous anisotropic diffusion. Conclusions are drawn in Section 14.

12. ANISOTROPIC DIFFUSION EQUATION AND ASSOCIATED MATHEMATICAL PRINCIPLES

12.1. Anisotropic diffusion equation. Let $\Omega \subset \mathbb{R}^{nd}$ be a bounded open domain, where "*nd*" denotes the number of spatial dimensions. The boundary of the domain is denoted by $\partial\Omega$, which is assumed to be piecewise smooth. Mathematically, $\partial\Omega := \overline{\Omega} - \Omega$, where a superposed bar denotes the set closure. A spatial point is denoted by $\mathbf{x} \in \overline{\Omega}$. The gradient and divergence operators are, respectively, denoted by grad$[\cdot]$ and div$[\cdot]$. Let $c(\mathbf{x})$ denote the concentration field. The boundary is divided into two parts: Γ^{D} and Γ^{N} such that $\Gamma^{\mathrm{D}} \cup \Gamma^{\mathrm{N}} = \partial\Omega$ and $\Gamma^{\mathrm{D}} \cap \Gamma^{\mathrm{N}} = \emptyset$ for well-posedness. Γ^{D} is that part of the boundary on which Dirichlet boundary condition is prescribed (i.e., the concentration is prescribed), and Γ^{N} is the part of the boundary on which the Neumann boundary condition is prescribed (i.e., the flux is prescribed). For uniqueness of the solution, we shall assume that meas $\left(\Gamma^{\mathrm{D}}\right) > 0$. The governing equations take the following form:

$$-\mathrm{div}\left[\mathbf{D}(\mathbf{x})\mathrm{grad}[c(\mathbf{x})]\right] = f(\mathbf{x}) \quad \text{in } \Omega \tag{12.1a}$$

$$c(\mathbf{x}) = c^{\mathrm{p}}(\mathbf{x}) \quad \text{on } \Gamma^{\mathrm{D}} \tag{12.1b}$$

$$-\mathbf{n}(\mathbf{x}) \cdot \mathbf{D}(\mathbf{x})\mathrm{grad}[c(\mathbf{x})] = q^{\mathrm{p}}(\mathbf{x}) \quad \text{on } \Gamma^{\mathrm{N}} \tag{12.1c}$$

where $\mathbf{n}(\mathbf{x})$ is the unit outward normal to the boundary, $f(\mathbf{x})$ is the prescribed volumetric source, $\mathbf{D}(\mathbf{x})$ is the anisotropic diffusivity tensor, $c^{\mathrm{p}}(\mathbf{x})$ is the prescribed concentration, and $q^{\mathrm{p}}(\mathbf{x})$ is the prescribed flux. Physics of the problem demands that the diffusivity tensor be symmetric. That is,

$$\mathbf{D}^{\mathrm{T}}(\mathbf{x}) = \mathbf{D}(\mathbf{x}) \quad \forall \mathbf{x} \in \Omega \tag{12.2}$$

In addition, the diffusivity tensor is assumed to be uniformly elliptic and bounded above. That is, there exists two real numbers $0 < \gamma_1 \leq \gamma_2 < +\infty$ such that we have

$$0 < \gamma_1 \boldsymbol{\xi} \cdot \boldsymbol{\xi} \leq \boldsymbol{\xi} \cdot \mathbf{D}(\mathbf{x})\boldsymbol{\xi} \leq \gamma_2 \boldsymbol{\xi} \cdot \boldsymbol{\xi} \quad \forall \boldsymbol{\xi} \in \mathbb{R}^{nd} \backslash \{\mathbf{0}\} \text{ and } \forall \mathbf{x} \in \Omega \tag{12.3}$$

From the theory of partial differential equations, it is well-known that the aforementioned boundary value problem satisfies the so-called maximum principles, the non-negative constraint, and comparison principles. We shall present the relevant results in the form of theorems without proofs. For complete details, see references [**32, 79**].

THEOREM 12.1 (A comparison principle). *Let* $\mathcal{L}[c] := -\mathrm{div}[\mathbf{D}(\mathbf{x})\mathrm{grad}[c]]$. *Let* $c_1(\mathbf{x})$, $c_2(\mathbf{x}) \in C^2(\Omega) \cap C^0(\overline{\Omega})$. *If* $\mathcal{L}[c_1] \geq \mathcal{L}[c_2]$ in Ω *and* $c_1(\mathbf{x}) \geq c_2(\mathbf{x})$ *on* $\partial\Omega$ *then we have*

$$c_1(\mathbf{x}) \geq c_2(\mathbf{x}) \quad \forall \mathbf{x} \in \overline{\Omega} \tag{12.4}$$

THEOREM 12.2 (A maximum principle and the non-negative condition). *Let* $c^{\mathrm{p}}(\mathbf{x}) \geq 0$ *on* $\partial\Omega$ *and* $\mathbf{D}(\mathbf{x})$ *be continuously differentiable. If* $c(\mathbf{x}) \in C^2(\Omega) \cap C^0(\overline{\Omega})$ *satisfies the differential inequality* $-\mathrm{div}[\mathbf{D}(\mathbf{x})\mathrm{grad}[c]] = f(\mathbf{x}) \geq 0$ *in* Ω*, then* $c(\mathbf{x})$ *satisfies the following conditions:*

$$\min_{\mathbf{x}\in\overline{\Omega}} c(\mathbf{x}) = \min_{\mathbf{x}\in\partial\Omega} c(\mathbf{x}) \tag{12.5}$$

$$c(\mathbf{x}) \geq 0 \quad \text{in } \overline{\Omega} \tag{12.6}$$

Various numerical formulations such as finite element methods, finite volume methods, and finite difference methods exist to solve these governing equations (12.1a)–(12.1c). It is well-known that the framework offered by finite element methods are successful in obtaining accurate numerical results for elliptic and parabolic partial differential equations. Among them single-field Galerkin formulation is a very popular method for self-adjoint operators because of its rich mathematical literature and amenability for computer implementation. Herein, we will outline the single-field Galerkin formulation and derive mesh restrictions based on this methodology. It should be noted that restrictions imposed on a mesh change as one alters the numerical formulation.

12.2. Single-field Galerkin formulation. We shall need the following function spaces to precisely write down the single-field Galerkin formulation:

$$\mathcal{C} := \left\{ c(\mathbf{x}) \in H^1(\Omega) \;\middle|\; c(\mathbf{x}) = c^{\mathrm{p}}(\mathbf{x}) \text{ on } \Gamma^{\mathrm{D}} \right\} \tag{12.7a}$$

$$\mathcal{W} := \left\{ w(\mathbf{x}) \in H^1(\Omega) \;\middle|\; w(\mathbf{x}) = 0 \text{ on } \Gamma^{\mathrm{D}} \right\} \tag{12.7b}$$

where $H^1(\Omega)$ is a standard Sobolev space [**32**]. Given two fields $a(\mathbf{x})$ and $b(\mathbf{x})$ on K, the standard L_2 inner product over K is denoted as follows:

$$(a; b)_K = \int_K a(\mathbf{x}) \cdot b(\mathbf{x}) \, \mathrm{d}K \tag{12.8}$$

The subscript for the inner product will be dropped if $K = \Omega$. The single-field Galerkin formulation for anisotropic diffusion equation reads as follows: Find $c(\mathbf{x}) \in \mathcal{C}$ such that we have

$$(\mathrm{grad}[w]; \mathbf{D}(\mathbf{x})\mathrm{grad}[c]) = (w(\mathbf{x}); f(\mathbf{x})) + (w(\mathbf{x}); q^{\mathrm{p}}(\mathbf{x}))_{\Gamma^{\mathrm{N}}} \quad \forall w(\mathbf{x}) \in \mathcal{W} \tag{12.9}$$

It is well-documented that the single-field Galerkin formulation violates the non-negative constraint and maximum principles on general computational grids [**24, 73, 75**]. The violation is more severe if the diffusion tensor is anisotropic. In the next section, by appealing to theory of nonnegative matrices [**12, 50, 94**], we shall derive sufficient conditions on T3 elements to satisfy comparison principles, maximum principles, and the non-negative constraint.

13. MESH RESTRICTIONS TO SATISFY COMPARISON AND MAXIMUM PRINCIPLES

13.1. Discrete equations. In this subsection, we will outline the discrete versions of the governing equations for anisotropic diffusion and the corresponding mathematical principles. To this end we use low-order finite elements to discretize the anisotropic diffusion equations (12.1a)–(12.1c) based on single-field Galerkin formulation (12.9). One of the important reasons for the use of low-order finite elements (linear simplicial elements) for anisotropic diffusion is that they play a prominent role in satisfying maximum principle. They are also of utmost importance in mesh generation of complex geometries, error analysis, and adaptive local mesh refinement. The low-order finite element discretization of anisotropic diffusion leads to a system of linear equations

given by $\boldsymbol{K}\boldsymbol{c} = \boldsymbol{f}$, where $\boldsymbol{K}$ is the stiffness matrix, $\boldsymbol{c}$ is the nodal concentration vector, and $\boldsymbol{f}$ is the volumetric source vector.

Based on this standard finite element methodology, we analyze the properties that the stiffness matrix inherits and has to possess from the continuous boundary value problem. From the equations (12.2) and (12.3), diffusivity tensor being symmetric and positive definite implies that the stiffness matrix $\boldsymbol{K}$ is also symmetric and positive definite. One of the most important property that the discrete system needs to have inorder to mimic the mathematical properties that continuous system possess is that the stiffness matrix $\boldsymbol{K}$ has to be a *monotone* matrix. This is a necessary and sufficient condition for the discrete equations to satisfy comparison principles, maximum principles, and to meet the non-negative constraint. On general computational grids, it is well-known that the stiffness matrix obtained via low-order finite element discretization of anisotropic diffusion *will not* be a monotone matrix. So one of the ways to make sure that the stiffness matrix belongs to the class of monotone matrices is that we impose restrictions on the element shape and size in a computational mesh. In next subsection, we will discuss on a subclass of monotone matrices which are easily amenable for deriving mesh restrictions.

13.2. Monotone matrices. The stiffness matrix $\boldsymbol{K}$ is said to be monotone if $\boldsymbol{K}^{-1}$ exists and $\boldsymbol{K}^{-1} \succeq \boldsymbol{0}$. This means that $\left(\boldsymbol{K}^{-1}\right)_{ij} \geq 0 \quad \forall i, j$. So in order to make sure that the stiffness matrix be monotone, we have to impose restrictions on $\boldsymbol{K}^{-1}$. This means we have to find a computational mesh such that $\left(\boldsymbol{K}^{-1}\right)_{ij} \geq 0 \quad \forall i, j$. In general, to get an explicit analytical formula for $\left(\boldsymbol{K}^{-1}\right)_{ij}$ is extremely difficult and not viable. Hence, it is not a feasible option to find mesh restrictions based on the condition that $\left(\boldsymbol{K}^{-1}\right)_{ij} \geq 0$. So a practicable route to obtain monotone stiffness matrices through mesh restrictions is to consider strictly diagonally dominant matrices, which form a subset to the class of monotone matrices [**94**, Section 3, Corollary 3.20 and Corollary 3.21]. The matrix $\boldsymbol{K}$ is said to be strictly diagonally dominant if it satisfies the following conditions:

(a) Positive diagonal entries: $\left(\boldsymbol{K}\right)_{ii} > 0$,
(b) Non-positive off-diagonal entries: $\left(\boldsymbol{K}\right)_{ij} \leq 0 \quad \forall i \neq j$, and
(c) Strict diagonal dominance of rows: $|\left(\boldsymbol{K}\right)_{ii}| > \sum_{i \neq j} |\left(\boldsymbol{K}\right)_{ij}| \quad \forall i, j.$

One should note that the above three conditions are sufficient but not necessary for the stiffness matrix to be monotone. The obvious advantage of considering strictly diagonally matrices is that there is no need to compute $\left(\boldsymbol{K}^{-1}\right)_{ij}$ explicitly because it is known aprior that these matrices are monotone. Hence, through the manipulation of the entries of the stiffness matrix we can derive the restrictions on the computational mesh to achieve strict diagonal dominance. We will now present the discrete versions of the comparison principle and maximum principle outlined in Theorems 12.1 and 12.2

THEOREM 13.1 (A discrete comparison principle). *A numerical formulation is said to possess a discrete comparison principle, if for any two finite-dimensional volumetric source vectors $\boldsymbol{f}_1$ and $\boldsymbol{f}_2$ which satisfy the relation $\boldsymbol{f}_1 \succeq \boldsymbol{f}_2$, then the finite-dimensional numerical solutions satisfy $\boldsymbol{c}_1 \succeq \boldsymbol{c}_2$.*

THEOREM 13.2 (A discrete maximum principle and the non-negative constraint). *A numerical formulation is said to possess a discrete maximum principle and meets the non-negativity constraint, if for any finite-dimensional volumetric source vector $\boldsymbol{f} \succeq \boldsymbol{0}$ and for a given Dirichlet boundary conditions vector $\boldsymbol{c}^{\mathrm{p}}(\mathbf{x}) \succeq \boldsymbol{0}$ on $\partial\Omega$, then the finite-dimensional numerical solution $\boldsymbol{c}(\mathbf{x})$ satisfies*

the following conditions:

$$\min_{\mathbf{x}\in\overline{\Omega}} \boldsymbol{c}\left(\mathbf{x}\right) = \min_{\mathbf{x}\in\partial\Omega} \boldsymbol{c}^{\mathrm{p}}\left(\mathbf{x}\right) \tag{13.1a}$$

$$\boldsymbol{c}\left(\mathbf{x}\right) \succeq \mathbf{0} \quad \forall \mathbf{x} \in \overline{\Omega} \tag{13.1b}$$

REMARK 13.3. *It should be noted that if a numerical formulation satisfies discrete comparison principle then it automatically obeys discrete maximum principle and non-negativity constraint. This can be shown by constructing a volumetric source vector* $\boldsymbol{f}_2 \succeq \mathbf{0}$ *based on the monotone stiffness matrix* $\boldsymbol{K}$ *and the non-negative Dirichlet boundary conditions vector* $\boldsymbol{c}^{\mathrm{p}}\left(\mathbf{x}\right)$*. The explicit formula for* $\boldsymbol{f}_2$ *is given by* $\boldsymbol{f}_2 = \boldsymbol{K}\boldsymbol{c}^{\mathrm{p}}$*. Hence, this results in* $\boldsymbol{c}_2 = \boldsymbol{c}^{\mathrm{p}} \succeq \mathbf{0}$*. So from the Theorem 13.1, it is evident that for any finite-dimensional numerical solution* $\boldsymbol{c}_1$ *we have the relation* $\boldsymbol{c}_1 \succeq \boldsymbol{c}_2 \succeq \boldsymbol{c}^{\mathrm{p}}$*. The non-negative constraint on the concentration vector* $\boldsymbol{c}_1$ *follows from the fact that* $\boldsymbol{c}^{\mathrm{p}} \succeq \mathbf{0}$*.*

REMARK 13.4. *In the continuous setting, the comparison principle implies the maximum principle and vice-versa. The maximum principle implies the non-negative constraint. In discrete setting, a numerical methodology may inherit one or more of discrete versions of these principles, and in some cases, none. Here are some of the examples:*

(i) The single-field Galerkin formulation for anisotropic diffusion on general computational grids does not possess any of the discrete versions of the comparison principle, the maximum principle or the non-negative constraint.

(ii) Le Potier's method [**84**] *and Lipnikov et al.* [**62, 63**] *satisfy the non-negative constraint but does not possess the discrete version of the comparison principle and the maximum principle.*

(iii) The optimization-based methods based on low-order finite elements [**64, 75, 73**] *satisfies the non-negative constraint and possess a discrete version of the maximum principle. However, the methods do not inherit the comparison principle (a counterexample is shown in the Reference* [**74**, Section 4, Figure 1]*).*

(iv) The single-field Galerkin formulation for isotropic diffusion based on well-centered triangular meshes possess discrete versions of all the three principles (the comparison principle, the maximum principle, and the non-negative constraint).

13.3. Sufficient conditions on local stiffness matrix. In this subsection, we will obtain sufficient conditions that insures the local stiffness matrix for a T3 element to be weakly diagonally dominant. We will employ low-order Lagrange finite elements to derive the local stiffness matrix. The reason for using low-order finite elements is that the shape functions for these elements are monotonic and do not change their sign within the element [**75, 73**]. Note that this reasoning will not hold for higher-order Lagrange finite elements as the shape functions for these elements can change their sign within the element and hence *need not* satisfy the discrete maximum principle (for more details see Reference [**80**]). Once we make sure that all of the local stiffness matrices are weakly diagonally dominant then the standard finite element assembly process guarantees that the global stiffness matrix is strictly diagonally dominant. After all if the stiffness matrix $\boldsymbol{K}$ is strictly diagonally dominant, from subsections 13.1–13.2, we are ascertained that the the nodal values for the concentration vector are non-negative. Thus we have non-negative solution everywhere in the T3 element which results in non-negativity on the whole computational domain.

A pictorial description of the T3 element on which we derive sufficient conditions is given in Figure 15. The mesh element PQR corresponds to an arbitrary T3 element of the computational mesh in (X, Y) coordinate system. Through a sequence of angle-preserving affine transformations

and scaling operations this arbitrary mesh element is transformed to an actual element ABC in (x, y) coordinate system. This transformation is composed of rigid body motion of the triangle PQR and homogeneous deformations of its sides. Based on the principles of continuum mechanics [**39, 38, 49**], we will now outline the corresponding mathematical equations for this transformation and scaling operations:

$$\mathbf{x} = \mathbf{Q}\mathbf{p} + \mathbf{c} \tag{13.2a}$$

$$\|\mathbf{u}_i\| = \lambda_i \|\mathbf{v}_i\| \quad \text{where } \lambda_i \in \mathbb{R}_+ \text{ and } i = \{1, 2, 3\} \tag{13.2b}$$

where $\mathbf{p}$ is the coordinates of a point in (X, Y) coordinate system, $\mathbf{x}$ is the coordinates of a point in (x, y) coordinate system, $\mathbf{c}$ is the translation vector, $\mathbf{Q}$ is a proper orthogonal transformation matrix, $\|\mathbf{v}_i\|$ is the length of a side of the triangle PQR, $\|\mathbf{u}_i\|$ represents the length of the transformed side of PQR, and λ_i relates the length of a side in PQR to that of the corresponding transformed side in ABC. Note that such type of transformation *does not* change the angles of the triangle PQR. Hence the angles and their orientation are preserved during such transformations.

Such transformations are needed due to the fact that we want to reduce the number of variables on which we derive mesh restrictions. By performing these type of transformations, we only need to consider the coordinates (a, b) to derive restrictions on the T3 element. But if we consider a general arbitrary mesh element given by triangle PQR, we need to consider all the coordinates of the triangle. This make the problem complicated and the derived mesh restrictions based on the arbitrary mesh element will be difficult to analyze and interpret. Important information such as the lower and upper bounds on the angles of the triangles of the computational mesh, which is need to generate *quality triangulations* might be difficult to deduce if one considers analyzing the arbitrary mesh element. Note that this is one of the most influential factors in generating triangular meshes. In our case, for two-dimensional domains, a *quality triangulation* means that one can obtain a lower bound on the angles of the triangles in the computational mesh [**93**]. If one does not preserve the angles during the transformation then it might result in small angles in the triangle PQR (needle-like or degenerate triangles) and hence achieving a quality triangular mesh is daunting. These needle-type triangles and the corresponding triangulations gives rise to highly ill-conditioned stiffness matrices and causes inherent difficulties in developing error estimates.

Our objective is to find the coordinates (a, b) such that the local stiffness matrix is weakly diagonally dominant for a given type of diffusivity tensor. The local stiffness matrix for anisotropic diffusion equation based on single-field Galerkin formulation is given by:

$$\boldsymbol{K}_e = \int_{\Omega_e} \boldsymbol{B}\boldsymbol{D}(\boldsymbol{x})\boldsymbol{B}^{\mathrm{t}} \, \mathrm{d}\Omega \tag{13.3}$$

where the matrix $\boldsymbol{B}$ in terms of the coordinates (a, b) is given as follows:

$$\boldsymbol{B} = \frac{1}{b} \begin{pmatrix} -b & (a-1) \\ b & -a \\ 0 & 1 \end{pmatrix} \tag{13.4}$$

Since the entries in the matrix $\boldsymbol{B}$ are constants. We have the local stiffness matrix $\boldsymbol{K}_e$ given as follows:

$$\boldsymbol{K}_e = \boldsymbol{B} \left(\int\limits_{\Omega_e} \boldsymbol{D}(\boldsymbol{x}) \, \mathrm{d}\Omega \right) \boldsymbol{B}^{\mathrm{t}} \tag{13.5}$$

In the subsequent subsections, we present various sufficient conditions through which we can find these coordinates (a, b) and glean information on the possible angles, corresponding shape and size of the triangle ABC.

13.3.1. *T3 element for heterogeneous isotropic diffusivity.* In this subsection, we consider the case where the diffusivity is isotropic and heterogeneous in the total domain. For this case, we show that the diffusivity *does not* have any influence on determining the coordinates (a, b). This means that the restrictions we obtain on the coordinates and the angles of the triangle ABC is independent of how the diffusivity is varying across the domain. The following is the local stiffness matrix for scalar heterogeneous isotropic diffusion:

$$\boldsymbol{K}_e = \frac{1}{b^2} \int\limits_{\Omega_e} D(\boldsymbol{x}) \, \mathrm{d}\Omega \begin{pmatrix} b^2 + (a-1)^2 & a - a^2 - b^2 & (a-1) \\ a - a^2 - b^2 & a^2 + b^2 & -a \\ (a-1) & -a & 1 \end{pmatrix} \tag{13.6}$$

where the integral of the diffusivity $D(\boldsymbol{x})$ over the actual T3 element Ω_e (triangle ABC) is given as follows:

$$\tilde{D} = \frac{1}{\mathrm{meas}(\Omega_e)} \int\limits_{\Omega_e} D(\boldsymbol{x}) \, \mathrm{d}\Omega \tag{13.7}$$

where $\mathrm{meas}(\Omega_e) = \frac{b}{2}$ is the area of the actual T3 element ABC is always positive. As the scalar diffusivity $D(\boldsymbol{x}) > 0$, so its definite integral over Ω_e which is $\tilde{D}$ is also greater than zero. Hence the simplified expression for the local stiffness matrix is given as follows:

$$\boldsymbol{K}_e = \frac{\tilde{D}}{2b} \begin{pmatrix} b^2 + (a-1)^2 & a - a^2 - b^2 & (a-1) \\ a - a^2 - b^2 & a^2 + b^2 & -a \\ (a-1) & -a & 1 \end{pmatrix} \tag{13.8}$$

We shall now present the sufficient conditions so that the matrix $\boldsymbol{K}_e$ is weakly diagonally dominant:

Condition No-1. Positive diagonal entries: $(\boldsymbol{K}_e)_{ii} > 0 \quad \forall i = 1, 2, 3$. This restriction gives us the following inequalities:

$$(\boldsymbol{K}_e)_{11} = \frac{\tilde{D}}{2b} \left(b^2 + (a-1)^2 \right) > 0 \tag{13.9a}$$

$$(\boldsymbol{K}_e)_{22} = \frac{\tilde{D}}{2b} \left(a^2 + b^2 \right) > 0 \tag{13.9b}$$

$$(\boldsymbol{K}_e)_{33} = \frac{\tilde{D}}{2b} > 0 \tag{13.9c}$$

As $\tilde{D} > 0$ and $b > 0$, it is evident that all of the inequalities given by equations (13.9a)–(13.9c) are trivially satisfied. Hence this condition has no effect on obtaining restrictions on coordinates (a, b).

Condition No-2. Weak diagonal dominance of rows: $|\,(\boldsymbol{K}_e)_{ii}\,| \geq \sum_{i\neq j} |\,(\boldsymbol{K}_e)_{ij}\,| \quad \forall i,j$ where $i = 1,2,3$ and $j = 1,2,3$. This restriction gives the following inequalities:

$$\left(b^2 + (a-1)^2\right) \geq \left(a^2 + b^2 - a\right) + (1-a) \tag{13.10a}$$

$$\left(a^2 + b^2\right) \geq a + \left(a^2 + b^2 - a\right) \tag{13.10b}$$

$$1 \geq (1-a) + a \tag{13.10c}$$

Note that these inequalities (13.10a)–(13.10c) are trivially satisfied. Hence this condition has no influence on obtaining restrictions on triangle ABC.

Condition No-3. Non-positive off-diagonal entries: $(\boldsymbol{K}_e)_{ij} \leq 0 \quad \forall i \neq j$ where $i = 1,2,3$ and $j = 1,2,3$. This restriction gives the following inequalities:

$$(\boldsymbol{K}_e)_{ij} = \begin{cases} (\boldsymbol{K}_e)_{12} &= \frac{\tilde{D}}{2b}\left(a - a^2 - b^2\right) \leq 0 \\ (\boldsymbol{K}_e)_{13} &= \frac{\tilde{D}}{2b}\left(a - 1\right) \leq 0 \\ (\boldsymbol{K}_e)_{23} &= \frac{\tilde{D}}{2b}\left(-a\right) \leq 0 \end{cases} \qquad \forall i \neq j$$

using the fact that $\tilde{D} > 0$ and $b > 0$, and rearranging the above relations we get the following inequalities:

$$\left(a - \frac{1}{2}\right)^2 + b^2 \geq \left(\frac{1}{2}\right)^2 \tag{13.11a}$$

$$a \leq 1 \tag{13.11b}$$

$$a \geq 0 \tag{13.11c}$$

The region in which the coordinates (a,b) satisfy the above inequalities given by the equations (13.11a)–(13.11c) is shown in Figure 16. According to these inequalities (13.11a)–(13.11c), heterogeneity of the scalar diffusivity has *no role* in obtaining the feasible region for the coordinates (a,b). It is evident from the Figure 16 that the interior angles of the triangle ABC are either acute or atmost right-angle. Based on the sufficient conditions, one can notice that an obtuse-angled triangle is not possible. So in order to satisfy discrete comparison principle, discrete maximum principle, and non-negative constraint the triangulation of a given computational domain must contain acute-angled triangles or right-angled triangles. These three sufficient conditions show that well-centered or acute-angled triangulation inherit all the three discrete versions of the continuous properties of scalar heterogeneous isotropic diffusion equations.

13.3.2. *T3 element for heterogeneous anisotropic diffusivity.* In this subsection, we consider the case where the diffusivity $\mathbf{D}(\mathbf{x}) = \begin{pmatrix} D_{xx}(\boldsymbol{x}) & D_{xy}(\boldsymbol{x}) \\ D_{xy}(\boldsymbol{x}) & D_{yy}(\boldsymbol{x}) \end{pmatrix}$ is anisotropic and heterogeneous across the domain. For sake of brevity and ease of manipulations, we drop the symbol $(\boldsymbol{x})$ in the components of the diffusivity tensor. Note that the symbol '$\boldsymbol{x}$' in the components of $\boldsymbol{D}(\boldsymbol{x})$ is dropped for sake of convenience and *should not* be interpreted as though the diffusivity tensor is constant. As discussed in Section 12, the diffusivity tensor satisfies certain properties. Based on these equations (12.2) and (12.3), we derive various results related to $\boldsymbol{D}(\boldsymbol{x})$ that we will be using in deriving mesh restrictions.

LEMMA 13.5 (Necessary conditions on the components of anisotropic diffusivity tensor). *If $\boldsymbol{D}(\boldsymbol{x})$ is symmetric, uniformly elliptic, and bounded above. Then its components satisfy the following*

relations:

$$D_{xx} > 0 \tag{13.12a}$$

$$D_{yy} > 0 \tag{13.12b}$$

$$D_{xx}D_{yy} > D_{xy}^2 \tag{13.12c}$$

PROOF. Since $\boldsymbol{D}(\boldsymbol{x})$ is symmetric from Spectral Theorem [**44**, Section 79, Theorem 1], the eigenvalues of $\boldsymbol{D}(\boldsymbol{x})$ are real. According to the equation (12.3), $\boldsymbol{D}(\boldsymbol{x})$ is uniformly elliptic, and bounded above. Hence the eigenvalues are positive and bounded above. The eigenvalues in terms of D_{xx}, D_{xy}, and D_{yy} are given as follows:

$$\lambda_1 = \frac{(D_{xx} + D_{yy}) + \sqrt{(D_{xx} - D_{yy})^2 + 4D_{xy}^2}}{2} \tag{13.13a}$$

$$\lambda_2 = \frac{(D_{xx} + D_{yy}) - \sqrt{(D_{xx} - D_{yy})^2 + 4D_{xy}^2}}{2} \tag{13.13b}$$

Now using the fact that $\lambda_1 > 0$ and $\lambda_2 > 0$ we get the following relations:

$$D_{xx} + D_{yy} > 0 \tag{13.14a}$$

$$(D_{xx} + D_{yy})^2 > (D_{xx} - D_{yy})^2 + 4D_{xy}^2 \tag{13.14b}$$

On algebraic manipulations of the above equations results in the relations (13.12a)-(13.12c) which completes the proof. □

DEFINITION 13.6 (Positive linear maps). *Let $\mathcal{U}$ and $\mathcal{V}$ be two vector spaces defined over a field $\mathbb{K}$. A function $\Phi : \mathcal{U} \to \mathcal{V}$ is called a linear map if it satisfies the following conditions:*

$$\Phi[\boldsymbol{x} + \boldsymbol{y}] = \Phi[\boldsymbol{x}] + \Phi[\boldsymbol{y}] \quad \forall \boldsymbol{x}, \boldsymbol{y} \in \mathcal{U} \tag{13.15a}$$

$$\Phi[\alpha\boldsymbol{x}] = \alpha\Phi[\boldsymbol{x}] \quad \forall \boldsymbol{x} \in \mathcal{U}, \alpha \in \mathbb{K} \tag{13.15b}$$

Let $\mathbb{M}_n := \mathbb{M}_{n\times n}(\mathbb{R})$ be the set of all real matrices of size "$n \times n$" defined over a field of real number $\mathbb{R}$. This space of matrices $\mathbb{M}_n$ is a vector space[**44**]*. A linear map $\Phi : \mathbb{M}_n \to \mathbb{M}_k$ is called positive if $\Phi(\boldsymbol{A})$ is positive semi-definite whenever $\boldsymbol{A}$ is positive semi-definite and is strictly positive if $\Phi(\boldsymbol{A})$ is positive definite whenever $\boldsymbol{A}$ is positive definite* [**14**, Section 2.2].

THEOREM 13.7 (Strictly positive linear mapping of anisotropic diffusivity). *Let $\Phi[\bullet] := \int_{\Omega_e}[\bullet]\mathrm{d}\Omega$. Show that $\Phi[\bullet]$ is a linear map and $\Phi[\boldsymbol{D}(\boldsymbol{x})]$ is symmetric, uniformly elliptic, and bounded above.*

PROOF. From the definition 13.6, it is evident that $\Phi[\bullet]$ is a linear map and $\Phi[\boldsymbol{D}(\boldsymbol{x})]$ is symmetric. Note that from equation (12.3), the scalar $\boldsymbol{\xi} \cdot \mathbf{D}(\mathbf{x})\boldsymbol{\xi} > 0$ and $\mathrm{meas}(\Omega_e) > 0$. As it is well known that Lebesgue integration of a scalar for a strictly positive measure is always greater than zero [**89**]. Hence $\int_{\Omega_e} \boldsymbol{\xi} \cdot \mathbf{D}(\mathbf{x})\boldsymbol{\xi} > 0 \quad \forall \mathbf{x} \in \Omega_e$. Integrating the equation (12.3), over Ω_e result in the following relation:

$$0 < \gamma_1\boldsymbol{\xi} \cdot \boldsymbol{\xi} \leq \frac{1}{\mathrm{meas}(\Omega_e)} \int_{\Omega_e} \boldsymbol{\xi} \cdot \mathbf{D}(\mathbf{x})\boldsymbol{\xi} \leq \gamma_2\boldsymbol{\xi} \cdot \boldsymbol{\xi} \quad \forall \boldsymbol{\xi} \in \mathbb{R}^{nd}\backslash\{\mathbf{0}\} \text{ and } \forall \mathbf{x} \in \Omega_e \tag{13.16}$$

Since the vector $\boldsymbol{\xi}$ independent of $\boldsymbol{x}$ and Ω_e we can interchange the order of integration. This gives us the following equation:

$$0 < \gamma_1 \boldsymbol{\xi}\cdot\boldsymbol{\xi} \leq \frac{1}{\text{meas}(\Omega_e)}\boldsymbol{\xi}\cdot\Phi[\boldsymbol{D}(\boldsymbol{x})]\boldsymbol{\xi} \leq \gamma_2 \boldsymbol{\xi}\cdot\boldsymbol{\xi} \quad \forall \boldsymbol{\xi} \in \mathbb{R}^{nd}\backslash\{\mathbf{0}\} \text{ and } \forall \mathbf{x} \in \Omega_e \tag{13.17}$$

this shows that $\Phi[\boldsymbol{D}(\boldsymbol{x})]$ is a strictly positive linear map of $\boldsymbol{D}(\boldsymbol{x})$ and indeed preserves its properties. This completes the proof. □

Let us denote $\tilde{\boldsymbol{D}} := \frac{1}{\text{meas}(\Omega_e)}\Phi[\boldsymbol{D}(\boldsymbol{x})]$, $\epsilon := \frac{\tilde{D}_{yy}}{\tilde{D}_{xx}}$, and $\eta := \frac{\tilde{D}_{xy}}{\tilde{D}_{xx}}$. Note that the matrix components of $\tilde{\boldsymbol{D}}$ are constants. From Theorem 13.7 and Lemma 13.5, it is evident that $\tilde{D}_{xx} > 0$, $\tilde{D}_{yy} > 0$, and $\tilde{D}_{xx}\tilde{D}_{yy} > \tilde{D}_{xy}^2$. So from equation (13.12c), we have $\eta \in (-\sqrt{\epsilon}, \sqrt{\epsilon})$. These two non-dimensional quantities $\epsilon$and η govern the mesh restrictions that we impose on the coordinates (a, b). From equations (13.3) and (13.4), the stiffness matrix for anisotropic diffusivity tensor is given as follows:

$$\boldsymbol{K}_e = \begin{pmatrix} \frac{\tilde{D}_{xx}b^2 - 2\tilde{D}_{xy}b(a-1) + \tilde{D}_{yy}(a-1)^2}{2b} & -\frac{\tilde{D}_{xx}b^2 + \tilde{D}_{xy}(b-2ab) + \tilde{D}_{yy}a(a-1)}{2b} & \frac{-\tilde{D}_{xy}b + \tilde{D}_{yy}(a-1)}{2b} \\ -\frac{\tilde{D}_{xx}b^2 + \tilde{D}_{xy}(b-2ab) + \tilde{D}_{yy}a(a-1)}{2b} & \frac{\tilde{D}_{xx}b^2 - 2\tilde{D}_{xy}ab + \tilde{D}_{yy}a^2}{2b} & \frac{\tilde{D}_{xy}b - \tilde{D}_{yy}a}{2b} \\ \frac{-\tilde{D}_{xy}b + \tilde{D}_{yy}(a-1)}{2b} & \frac{\tilde{D}_{xy}b - \tilde{D}_{yy}a}{2b} & \frac{\tilde{D}_{yy}}{2b} \end{pmatrix} \tag{13.18}$$

We now present the sufficient conditions so that the matrix $\boldsymbol{K}_e$ is weakly diagonally dominant:

Condition-4: Positive diagonal entries: $(\boldsymbol{K}_e)_{ii} > 0 \quad \forall i = 1, 2, 3$, gives the following relations:

$$(\boldsymbol{K}_e)_{ii} = \begin{cases} (\boldsymbol{K}_e)_{11} &= \frac{\tilde{D}_{xx}b^2 - 2\tilde{D}_{xy}b(a-1) + \tilde{D}_{yy}(a-1)^2}{2b} > 0 \\ (\boldsymbol{K}_e)_{22} &= \frac{\tilde{D}_{xx}b^2 - 2\tilde{D}_{xy}ab + \tilde{D}_{yy}a^2}{2b} > 0 \\ (\boldsymbol{K}_e)_{33} &= \frac{\tilde{D}_{yy}}{2b} > 0 \end{cases}$$

As $\tilde{D}_{yy} > 0$, from $(\boldsymbol{K}_e)_{33} > 0$ we need to have $b > 0$. So rearranging the above relations we have the following restrictions:

$$(\boldsymbol{K}_e)_{11} = \left(b\sqrt{\tilde{D}_{xx}} - |a-1|\sqrt{\tilde{D}_{yy}}\right)^2 + 2b|a-1|\left(\sqrt{\tilde{D}_{xx}}\sqrt{\tilde{D}_{yy}} - \text{Sgn}\left[|a-1|\right]\tilde{D}_{xy}\right) > 0 \tag{13.19a}$$

$$(\boldsymbol{K}_e)_{22} = \left(b\sqrt{\tilde{D}_{xx}} - |a|\sqrt{\tilde{D}_{yy}}\right)^2 + 2b|a|\left(\sqrt{\tilde{D}_{xx}}\sqrt{\tilde{D}_{yy}} - \text{Sgn}\left[|a|\right]\tilde{D}_{xy}\right) > 0 \tag{13.19b}$$

$$(\boldsymbol{K}_e)_{33} = \frac{\tilde{D}_{yy}}{2b} > 0 \tag{13.19c}$$

where Sgn[•] is the standard signum function. From Lemma 13.5, it is evident that $\sqrt{\tilde{D}_{xx}}\sqrt{\tilde{D}_{yy}} > \tilde{D}_{xy}$. Hence equations (13.19a)-(13.19c) are trivially satisfied for $b > 0$ and for any abscissa a.

Condition-5: Non-positive off-diagonal entries: $(\boldsymbol{K}_e)_{ij} \leq 0 \quad \forall i \neq j$ where $i = 1, 2, 3$ and $j = 1, 2, 3$. This restriction gives the following relations:

$$(\boldsymbol{K}_e)_{ij} = \begin{cases} (\boldsymbol{K}_e)_{12} &= -\frac{\tilde{D}_{xx}b^2 + \tilde{D}_{xy}(b-2ab) + \tilde{D}_{yy}a(a-1)}{2b} \leq 0 \\ (\boldsymbol{K}_e)_{13} &= \frac{-\tilde{D}_{xy}b + \tilde{D}_{yy}(a-1)}{2b} \leq 0 \\ (\boldsymbol{K}_e)_{23} &= \frac{\tilde{D}_{xy}b - \tilde{D}_{yy}a}{2b} \leq 0 \end{cases}$$

using the paramters ϵ, η, and the fact that ordinate $b > 0$ we have the following inequalities:

$$\left(a - \frac{1}{2}\right)^2 + \left(\frac{b}{\sqrt{\epsilon}}\right)^2 - 2b\left(\frac{\eta}{\epsilon}\right)\left(a - \frac{1}{2}\right) \geq \left(\frac{1}{2}\right)^2 \tag{13.20a}$$

$$\frac{a-1}{b} \leq \frac{\eta}{\epsilon} \tag{13.20b}$$

$$\frac{a}{b} \geq \frac{\eta}{\epsilon} \tag{13.20c}$$

these inequalities dictate the feasible region for coordinates (a, b). For a given ϵ and by varying η which lies between $-\sqrt{\epsilon}$ and $\sqrt{\epsilon}$, we get different feasible regions for (a, b). Herein, we have choosen $\epsilon = 10$ and $\eta \in \{-1, 0, 1\}$. For these values, we have plotted the feasible region based on the inequalities (13.20a)-(13.20c). From figures 17, 18, and 19, the following can be inferred based on the feasible region:

- If $\eta = 0$ the possible T3 elements are either acute angled or right angled triangles.
- If either $\eta < 0$ or $\eta > 0$ then there is no restriction on the angles of the triangle.

Condition-6: Weak diagonal dominance of rows: $|(\boldsymbol{K}_e)_{ii}| \geq \sum_{i \neq j} |(\boldsymbol{K}_e)_{ij}| \quad \forall i, j$ where $i = 1, 2, 3$ and $j = 1, 2, 3$. This gives the following relations:

$$\left(b^2 - 2\eta b(a-1) + \epsilon(a-1)^2\right) \geq \left(b^2 + \eta(b - 2ab) + \epsilon a(a-1)\right) + (\eta b - \epsilon(a-1)) \tag{13.21a}$$

$$\left(b^2 - 2\eta ab + \epsilon a^2\right) \geq \left(b^2 + \eta(b - 2ab) + \epsilon a(a-1)\right)(\epsilon a - \eta b) \tag{13.21b}$$

$$\epsilon \geq (\eta b - \epsilon(a-1)) + (\epsilon a - \eta b) \tag{13.21c}$$

if Condition-1 and Condition-2 are satisfied then this condition is trivially satisfied.

14. CONCLUDING REMARKS

We have shown that a well-centered mesh (or acute-angled triangle) need not be sufficient or in some cases too restrictive to satisfy maximum principles and the non-negative constraint for *anisotropic* diffusion equation. This work will invaluable in two respects:

(i) It will give guide the existing users on the restrictions to be placed on the mesh to meet the maximum principles.

(ii) The presented study has clearly shown that placing restrictions on computational grids is not a viable approach to achieve physically meaningful non-negative solutions for highly anisotropic medium. We hope that this research note will motivate researchers to develop new methodologies to satisfy maximum principles and the non-negative constraint without any restricts on the mesh.

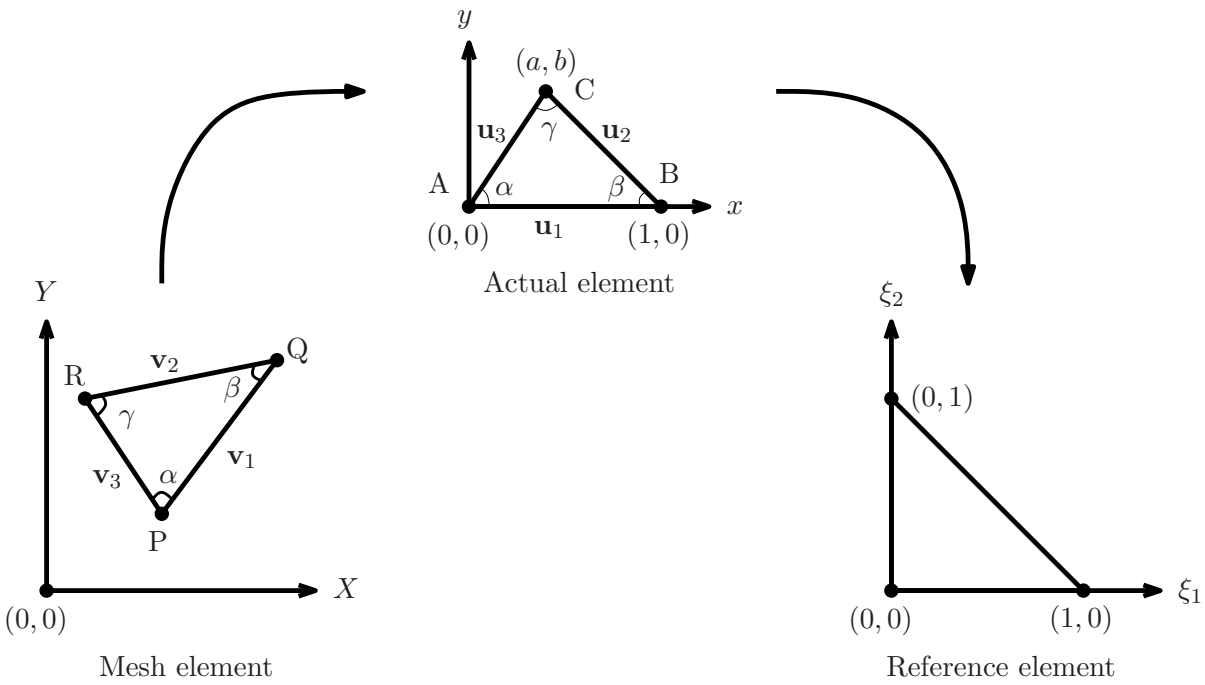

FIGURE 15. T3 element: A pictorial description of the mesh element, actual element, and reference element. The mesh element PQR corresponds to an arbitrary T3 element of the computational mesh in (X, Y) coordinate system. This mesh element PQR is transformed to an actual element ABC which is given in (x, y) coordinate system. Analysis is performed on the actual element ABC such that one obtains restrictions on coordinates (a, b). This is accomplished via imposing conditions on local stiffness matrix to be weakly diagonally dominant. Finally, after one obtains the coordinates (a, b), the actual element is transformed back to the original mesh element.

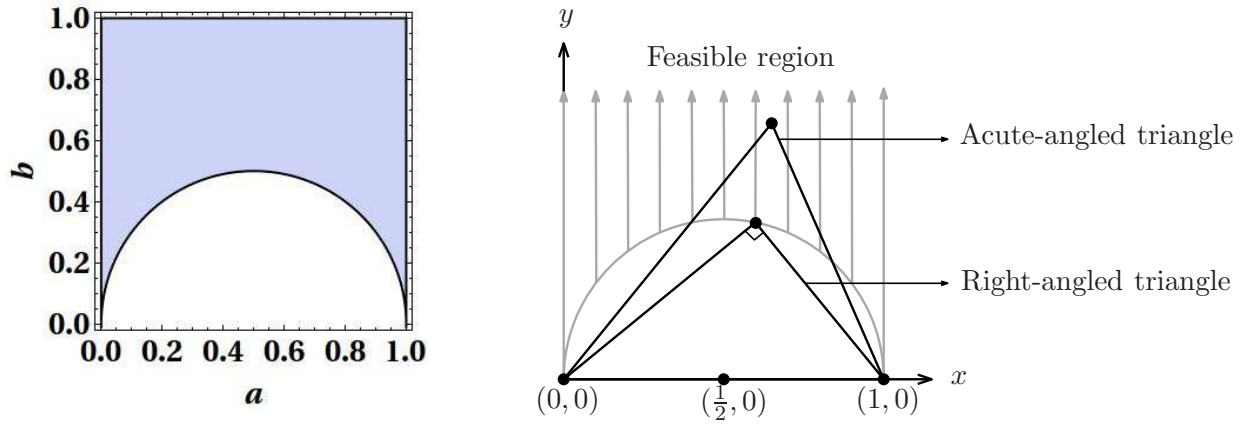

FIGURE 16. T3 element for heterogeneous isotropic diffusivity: A pictorial description of the feasible region (left figure) is shown in lightblue color. The right figure indicates that the point (a, b) can lie either on the circle with center $(\frac{1}{2}, 0)$ and radius $\frac{1}{2}$ or outside the circular region. The points within the circular region are unfeasible. This results in two possibilities for choosing a T3 element in the realm of the feasible region, which is either a right-angled triangle or a acute-angled triangle.

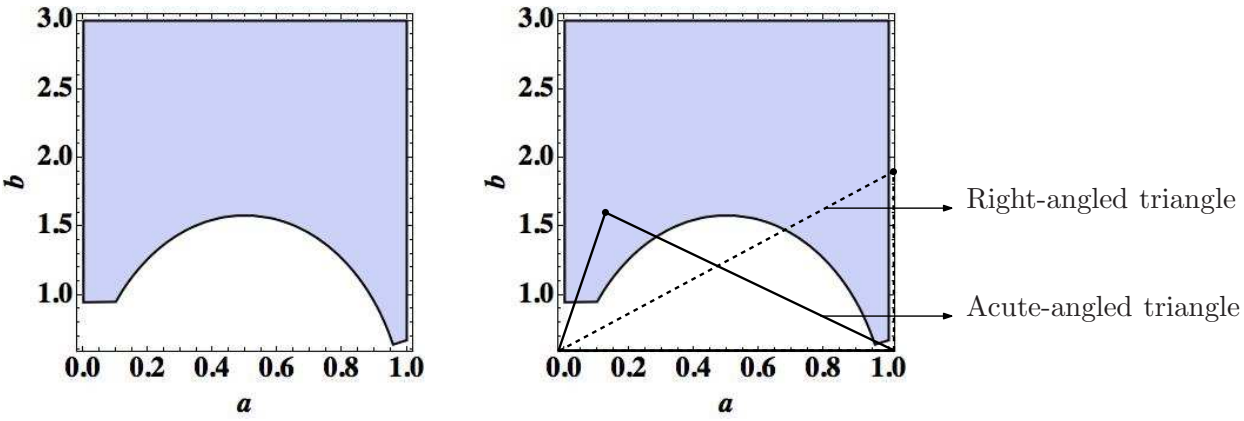

(a) Feasible region for (a, b)

(b) Possible T3 elements when $\tilde{D}_{xy} = 0$

FIGURE 17. T3 element for anisotropic diffusivity when $\tilde{D}_{xy} = 0$: A pictorial description of the feasible region (left figure) for the coordinates (a, b) is indicated in lightblue color. Analysis has been performed for the case when $\tilde{D}_{xy} = 0$. The numerical values for the two parameters which decide the feasible region are chosen to be $\epsilon = 10$ and $\eta = 0$. In this case, the right figure indicates that acute-angled and right-angled triangles are possible. As ϵ increases the coordinate b has to increase proportionally to satisfy the inequality given by the equation (13.20a). For higher values of ϵ, it is very difficult to find a suitable T3 element.

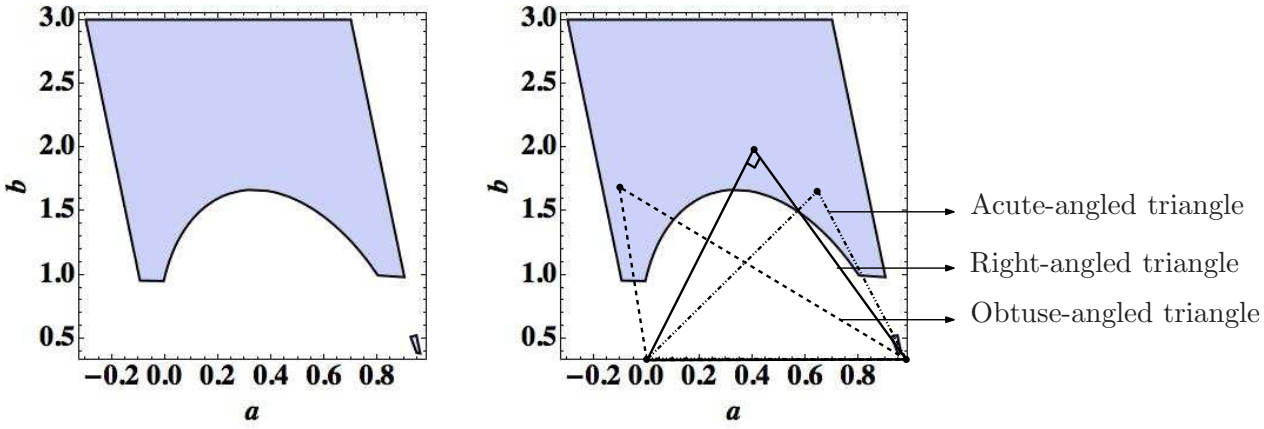

(a) Feasible region for (a, b) (b) Possible T3 elements when $\tilde{D}_{xy} < 0$

FIGURE 18. T3 element for anisotropic diffusivity when $\tilde{D}_{xy} < 0$: The left figure indicates the feasible region for the coordinates (a, b) in lightblue color. The right figure indicates that when $\tilde{D}_{xy} < 0$, angles in the T3 element can be acute-angle or right-angle or even obtuse-angle. In this case, we have chosen $\epsilon = 10$ and $\eta = -1$. For a fixed η as ϵ increases the value of coordinate b also increases. So it is a daunting task to find a viable T3 element.

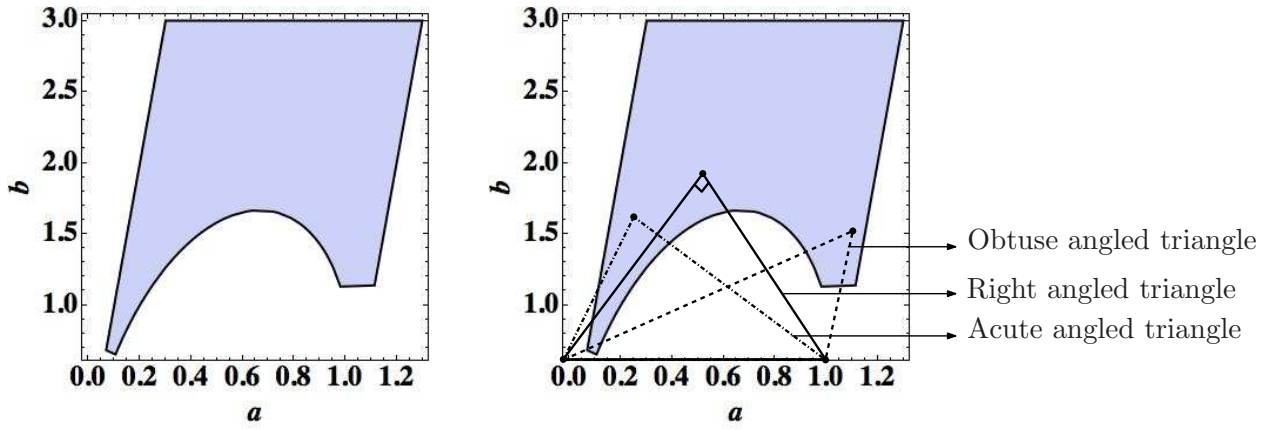

(a) Feasible region for (a, b) (b) Possible T3 elements when $\tilde{D}_{xy} > 0$

FIGURE 19. T3 element for anisotropic diffusivity when $\tilde{D}_{xy} > 0$: The left figure indicates the feasible region for the coordinates (a, b) in lightblue color. The right figure indicates that when $\tilde{D}_{xy} > 0$, angles in the T3 element can be acute-angle or right-angle or even obtuse-angle. In this case, we have chosen $\epsilon = 10$ and $\eta = 1$. For a fixed η as ϵ increases the value of coordinate b also increases. Finding a T3 element in such cases is nearly impossible.

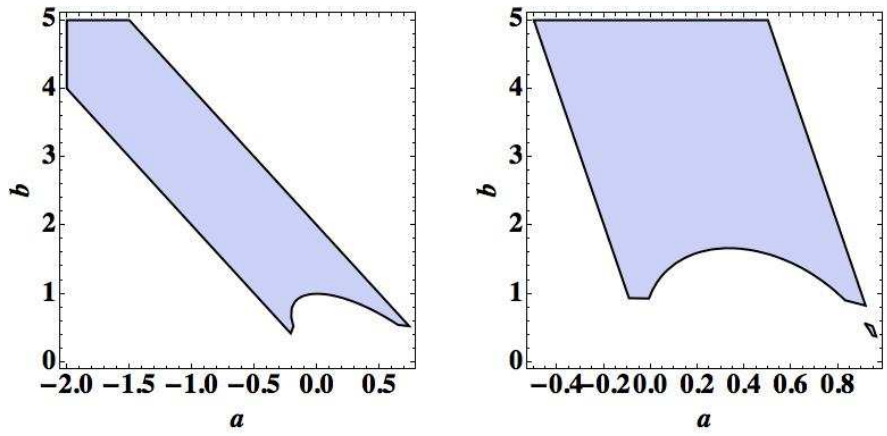

(a) $\epsilon = 2$ and $\eta = -1$ (b) $\epsilon = 10$ and $\eta = -1$

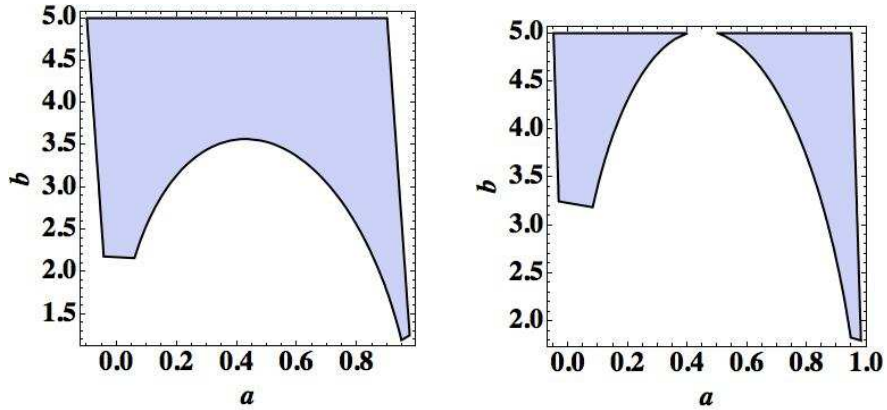

(c) $\epsilon = 50$ and $\eta = -1$ (d) $\epsilon = 100$ and $\eta = -1$

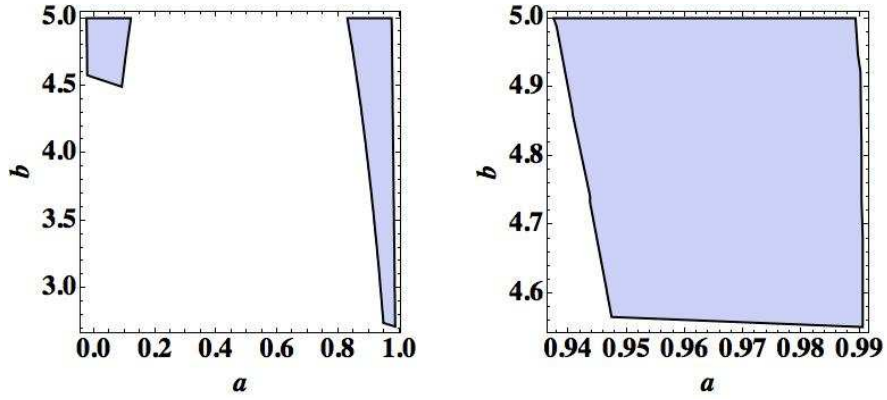

(e) $\epsilon = 200$ and $\eta = -1$ (f) $\epsilon = 500$ and $\eta = -1$

FIGURE 20. T3 element for fixed η and varying ϵ: A pictorial description of the feasible region (lightblue color) for a fixed η and varying ϵ. Analysis is performed for $\eta = -1$ and $\epsilon = \{2, 10, 50, 100, 200, 500\}$. It is evident there is a drastic variation in the feasible region as ϵ increases. Note that for higher values of ϵ it is very difficult to find a suitable T3 element which can mesh a given computational domain.

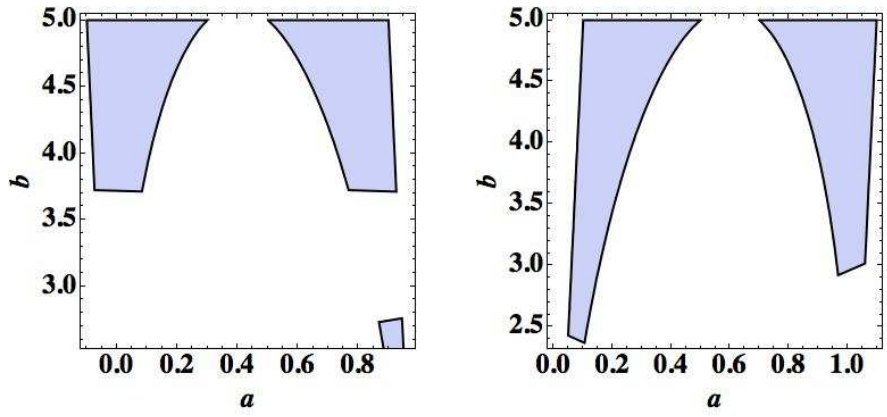

(a) $\epsilon = 100$ and $\eta = -2$

(b) $\epsilon = 100$ and $\eta = 2$

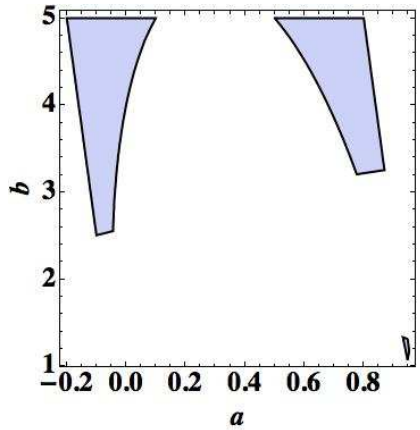

(c) $\epsilon = 100$ and $\eta = -4$

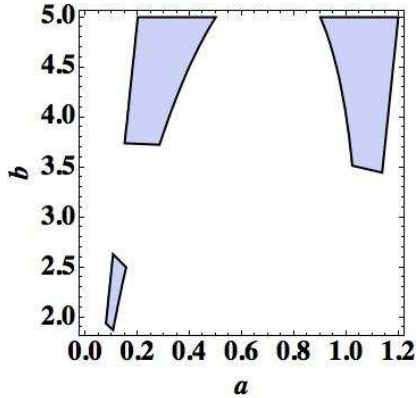

(d) $\epsilon = 100$ and $\eta = 4$

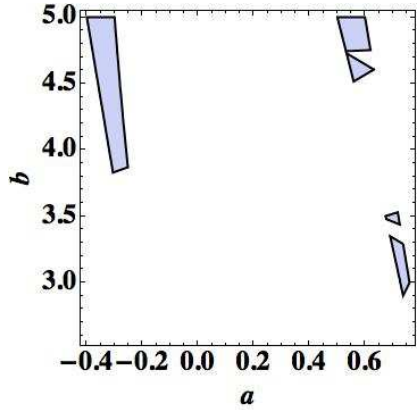

(e) $\epsilon = 100$ and $\eta = -8$

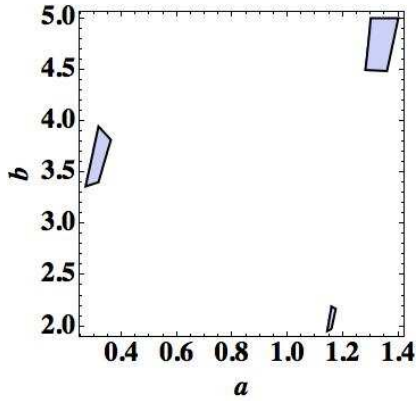

(f) $\epsilon = 100$ and $\eta = 8$

FIGURE 21. T3 element for fixed ϵ and varying η: A pictorial description of the feasible region (lightblue color) for a fixed ϵ and varying η. Analysis is performed for $\epsilon = 100$ and $\eta = \{-8, -4, -2, 2, 4, 8\}$. It is evident there is considerable variation in the feasible region as η changes. Also there is no fixed pattern on this variation about η.

Bibliography

[1] *Gmsh: A three-dimensional finite element mesh generator with pre- and post-processing facilities*. URL: http://www.geuz.org/gmsh/.

[2] *Tecplot 360: User's Manual*. URL: http://www.tecplot.com, Bellevue, Washington, USA, 2008.

[3] *ABAQUS/CAE/Standard, Version 6.8-3*. Simulia, Providence, Rhode Island, www.simulia.com, 2009.

[4] *ANSYS, Version 14.5*. ANSYS, Inc., Canonsburg, Pennsylvania, www.ansys.com, 2012.

[5] *COMSOL Multiphysics User's Guide, Version 4.3a*. COMSOL, Inc., Burlington, Massachusetts, www.comsol.com, 2012.

[6] *General Algebraic Modeling System (GAMS)*. Version 23.8, GAMS Development Corporation, Washington DC, USA, 2012.

[7] *MATLAB 2012a*. The MathWorks, Inc., Natick, Massachusetts, USA, 2012.

[8] B. M. Adams, W. J. Bohnhoff, K. R. Dalbey, J. P. Eddy, M. S. Eldred, D. M. Gay, K. Haskell, P. D. Hough, and L. P. Swiler. *DAKOTA, A Multilevel Parallel Object-Oriented Framework for Design Optimization, Parameter Estimation, Uncertainty Quantification, and Sensitivity Analysis: Version 5.2 User's Manual*. Sandia Technical Report SAND2010-2183, 2011.

[9] M. Aoki. *Modeling Aggregate Behavior and Fluctuations in Economics: Stochastic Views of Interacting Agents*. Cambridge University Press, Cambridge, UK, 2004.

[10] U. M. Ascher and L. R. Petzold. *Computer Methods for Ordinary Differential Equations and Differential-Algebraic Equations*. SIAM, Philadelphia, USA, 1998.

[11] R. G. Bartle and D. R. Sherbert. *Introduction to Real Analysis*. John Wiley & Sons, Inc., New Jersey, USA, 2011.

[12] A. Berman and R. J. Plemmons. *Nonnegative Matrices in the Mathematical Sciences*. Academic Press, New York, USA, 1979.

[13] M. Berzins. Modified mass matrices and positivity preservation for hyperbolic and parabolic PDEs. *Communications in Numerical Methods in Engineering*, 17:659–666, 2001.

[14] R. Bhatia. *Positive Definite Matrices*. Princeton Series in Applied Mathematics. Princeton University Press, Princeton, New Jersey, 2007.

[15] F. A. Bornemann. An adaptive multilevel approach to parabolic equations I. General theory and 1D implementation. *Impact of Computing in Science and Engineering*, 2:279–317, 1990.

[16] S. Boyd and L. Vandenberghe. *Convex Optimization*. Cambridge University Press, Cambridge, UK, 2004.

[17] E. Burman and A. Ern. Nonlinear diffusion and discrete maximum principle for stabilized Galerkin approximations of the convection-diffusion-reaction equation. *Computer Methods in Applied Mechanics and Engineering*, 191:3833–3855, 2002.

[18] E. Burman and A. Ern. Stabilized Galerkin approximation of convection-diffusion-reaction equations: Discrete maximum principle and convergence. *Mathematics of Computation*, 74:1637–1652, 2005.

[19] H. S. Carslaw and J. C. Jaeger. *Conduction of Heat in Solids*. Oxford University Press, New York, USA, second edition, 1986.

[20] C. Cattaneo. Sur une forme de l'équation de la chaleur éliminant le paradoxe d'une propagation instantanée. *Comptes Rendus*, 247:431–433, 1958.

[21] R. Chapko and R. Kress. Rothe's method for the heat equation and boundary integral equations. *Journal of Integral Equations and Applications*, 09:47–69, 1997.

[22] C. M. Chen and V. Thomee. The lumped mass finite element method for a parabolic problem. *Journal of the Australian Mathematical Society*, 26:329–354, 1985.

[23] J. Chung and G. M. Hulbert. A time integration algorithm for structural dynamics with improved numerical dissipation: The generalized-α method. *Journal of Applied Mechanics*, 60:371–375, 1993.

[24] P. G. Ciarlet and P-A. Raviart. Maximum principle and uniform convergence for the finite element method. *Computer Methods in Applied Methods and Engineering*, 2:17–31, 1973.

[25] R. Codina. Comparison of some finite element methods for solving the diffusion-convection-reaction equation. *Computer Methods in Applied Mechanics and Engineering*, 156:185–210, 1998.

[26] R. Codina. On stabilized finite element methods for linear systems of convection-diffusion-reaction equations. *Computer Methods in Applied Mechanics and Engineering*, 188:61–82, 2000.

[27] J. Crank. *The Mathematics of Diffusion*. Clarendon press, Oxford, second edition, 1975.

[28] E. L. Cussler. *Diffusion: Mass Transfer in Fluid Systems*. Cambridge University Press, Cambridge, UK, third edition, 2009.

[29] J. Donea and A. Huerta. *Finite Element Methods for Flow Problems*. John Wiley & Sons, Inc., Chichester, UK, 2003.

[30] J. Douglas and T. Dupont. Galerkin methods for parabolic equations. *SIAM Journal on Numerical Analysis*, 07:575–626, 1970.

[31] M. A. T. Elshebli. Discrete maximum principle for the finite element solution of linear non-stationary diffusion-reaction problems. *Applied Mathematical Modeling*, 32:1530–1541, 1998.

[32] L. C. Evans. *Partial Differential Equations*. American Mathematical Society, Providence, Rhode Island, USA, 1998.

[33] I. Farago, R. Horvath, and S. Korotov. Discrete maximum principle for linear parabolic problems solved on hybrid meshes. *Applied Numerical Mathematics*, 53:249–264, 2005.

[34] L. P. Franca, S. L. Frey, and T. J. R. Hughes. Stabilized finite element methods: I. Application to the advective-diffusive model. *Computer Methods in Applied Mechanics and Engineering*, 95:253–276, 1992.

[35] L. P. Franca, A. Nesliturk, and M. Stynes. On the stability of residual-free bubbles for convection-diffusion problems and their approximation by a two-level finite element method. *Computer Methods in Applied Mechanics and Engineering*, 166:35–49, 1998.

[36] D. Gilbarg and N. S. Trudinger. *Elliptic Partial Differential Equations of Second Order*. Springer, New York, USA, 2001.

[37] P. M. Gresho and R. L. Sani. *Incompressible Flow and the Finite Element Method: Advection-Diffusion*, volume 1. John Wiley & Sons, Inc., Chichester, UK, 2000.

[38] M. E. Gurtin. *An Introduction to Continuum Mechanics*. Academic Press, San Diego, USA, 1981.

[39] M. E. Gurtin. *Topics in Finite Elasticity*. SIAM, Philadelphia, USA, 1981.

[40] M. E. Gurtin and A. C. Pipkin. A general theory of heat conduction with finite speed. *Archive for Rational Mechanics and Analysis*, 31:113–126, 1968.

[41] W. Hackbusch. *Multi-Grid Methods and Applications*. Springer Series in Computational Mathematics. Springer-Verlag, New York, USA, 2003.

[42] E. Hairer, C. Lubich, and M. Roche. *The Numerical Solution of Differential-Algebraic Systems by Runge-Kutta Methods*. Lecture Notes in Mathematics. Springer-Verlag, New York, USA, 1989.

[43] E. Hairer and G. Wanner. *Solving Ordinary Differential Equations II: Stiff and Differential-Algebraic Problems*. Springer-Verlag, New York, USA, 1996.

[44] P. R. Halmos. *Finite-Dimensional Vector Spaces*. Springer-Verlag, New York, USA, 1993.

[45] I. Harari. Stability of semidiscrete formulations for parabolic problems at small time steps. *Computer Methods in Applied Mechanics and Engineering*, 193:1491–1516, 2004.

[46] G. Hauke. A simple subgrid scale stabilized method for the advection-diffusion-reaction equation. *Computer Methods in Applied Mechanics and Engineering*, 191:2925–2947, 2002.

[47] G. Hauke and A. G. Olivares. Variational subgrid scale formulations for the advection-diffusion-reaction equation. *Computer Methods in Applied Mechanics and Engineering*, 190:6847–6865, 2001.

[48] P. Herrera and A. Valocchi. Positive solution of two-dimensional solute transport in heterogeneous aquifers. *Ground Water*, 44:803–813, 2006.

[49] G. A. Holzapfel. *Nonlinear Solid Mechanics*. John Wiley & Sons, Inc., Chichester, UK, 2000.

[50] R. A. Horn and C. R. Johnson. *Topics in Matrix Analysis*. Cambridge University Press, Cambridge, UK, 1991.

[51] R. Horvath. Sufficient conditions of the discrete maximum-minimum principle for parabolic problems on rectangular meshes. *International Journal of Computers and Mathematics with Applications*, 55:2306–2317, 2008.

[52] P. W. Hsieh and S. Y. Yang. On efficient least-squares finite element methods for convection-dominated problems. *Computer Methods in Applied Mechanics and Engineering*, 199:183–196, 2009.

[53] T. J. R. Hughes. *The Finite Element Method: Linear Static and Dynamic Finite Element Analysis*. Prentice-Hall, Englewood Cliffs, New Jersey, USA, 1987.

[54] W. H. Hundsdrofer and J. G. Verwer. *Numerical Solution of Time-Dependent Advection-Diffusion-Reaction Equations*. Springer-Verlag, New York, USA, 2007.

[55] J. Ignaczak and M. O. Starzewski. *Thermoelasticity with Finite Wave Speeds*. Oxford Science Publications, New York, USA, 2009.

[56] T. Ikeda. *Maximum Principle in Finite Element Models for Convection-Diffusion Phenomena*. Lecture notes in numerical and applied analysis. North-Holland Publishing Company, New York, USA, 1983.

[57] F. Ilinca and J. F. Hetu. Galerkin gradient least-squares formulations for transient conduction heat transfer. *Computer Methods in Applied Mechanics and Engineering*, 191:3073–3097, 2002.

[58] K. E. Jansen, C. H. Whiting, and G. H. Hulbert. A generalized-α method for integrating the filtered Navier-Stokes equations with a stabilized finite element method. *Computer Methods in Applied Mechanics and Engineering*, 190:305–319, 2000.

[59] V. John and E. Schmeyer. Finite element methods for time-dependent convection-diffusion-reaction equations with small diffusion. *Computer Methods in Applied Mechanics and Engineering*, 198:475–494, 2008.

[60] J. Lang and A. Walter. An adaptive Rothe method for nonlinear reaction-diffusion systems. *Applied Numerical Mathematics*, 13:135–146, 1993.

[61] E. E. Levi. Sull' equazione del calore. *Annali di Matematica Pura ed Applicata*, 14:187–264, 1908.

[62] K. Lipnikov, M. Shashkov, D. Svyatskiy, and Y. Vassilevski. Monotone finite volume schemes for diffusion equations on unstructured triangular and shape-regular polygonal meshes. *Journal of Computational Physics*, 227:492–512, 2007.

[63] K. Lipnikov, D. Svyatskiy, and Y. Vassilevski. Interpolation-free monotone finite volume method for diffusion equations on polygonal meshes. *Journal of Computational Physics*, 228:703–716, 2009.

[64] R. Liska and M. Shashkov. Enforcing the discrete maximum principle for linear finite element solutions for elliptic problems. *Communications in Computational Physics*, 3:852–877, 2008.

[65] J. C. Maxwell. On the dynamical theory of gases. *Philosophical Transactions of Royal Society of London*, A157:26–78, 1866.

[66] R. McOwen. *Partial Differential Equations: Methods and Applications*. Prentice Hall, New Jersey, USA, 1996.

[67] Z. Mei. *Numerical Bifurcation Analysis for Reaction-Diffusion Equations*. Springer-Verlag, New York, USA, 2000.

[68] A. Mizukami. Variable explicit finite element methods for unsteady heat conduction equations. *Computer Methods in Applied Mechanics and Engineering*, 59:101–109, 1986.

[69] K. W. Morton. *Numerical Solution of Convection-Diffusion Problems*, volume 12 of *Applied Mathematics and Mathematical Computation*. Chapman & Hall, London, UK, 1996.

[70] M. K. Mudunuru and K. B. Nakshatrala. A framework for coupled deformation-diffusion analysis with application to degradation/healing. *International Journal for Numerical Methods in Engineering*, 89:1144–1170, 2012.

[71] COMSOL Multiphysics. Version 4.3 a. *COMSOL Inc, Burlington, MA*, 2012.

[72] T. Munson, J. Sarich, S. Wild, S. Benson, and L. C. McInnes. TAO 2.0 Users Manual. Technical Report ANL/MCS-TM-322, Mathematics and Computer Science Division, Argonne National Laboratory, 2012. http://www.mcs.anl.gov/tao.

[73] H. Nagarajan and K. B. Nakshatrala. Enforcing the non-negativity constraint and maximum principles for diffusion with decay on general computational grids. *International Journal for Numerical Methods in Fluids*, 67:820–847, 2011.

[74] K. B. Nakshatrala, M. K. Mudunuru, and A. J. Valocchi. A numerical framework for diffusion-controlled bimolecular-reactive systems to enforce maximum principles and non-negative constraint. *Available on arXiv:1210.5290*, 2012.

[75] K. B. Nakshatrala and A. J. Valocchi. Non-negative mixed finite element formulations for a tensorial diffusion equation. *Journal of Computational Physics*, 228:6726–6752, 2009.

[76] L. Nirenberg. A strong maximum principle for parabolic equations. *Communications on Pure and Applied Mathematics*, 6:167–177, 1953.

[77] M. N. Ozisik. *Heat Conduction*. John Wiley & Sons, Inc., New York, USA, second edition, 1993.

[78] J.-S. Pang. Methods for quadratic programming: A survey. *Computers and Chemical Engineering*, 5:583–594, 1983.

[79] C. V. Pao. *Nonlinear Parabolic and Elliptic Equations*. Springer-Verlag, New York, USA, 1993.

[80] G. S. Payette, K. B. Nakshatrala, and J. N. Reddy. On the performance of high-order finite elements with respect to maximum principles and the non-negative constraint for diffusion-type equations. *International Journal for Numerical Methods in Engineering*, 91:742–771, 2012.

[81] L. Petzold. Differential/algebraic equations are not ODEs. *SIAM Journal on Scientific and Statistical Computing*, 3:367–384, 1982.

[82] M. Picone. Maggiorazione degli integrali delle equazioni totalmente paraboliche alle derivate parziali del secondo ordine. *Annali di Matematica Pura ed Applicata*, 7:145–192, 1929.

[83] G. Porru and S. Serra. Maximum principles for parabolic equations. *Journal of the Australian Mathematical Society*, 56:41–52, 1994.

[84] C. Le Potier. Finite volume monotone scheme for highly anisotropic diffusion operators on unstructured triangular meshes. *Comptes Rendus Mathematique*, 341:787–792, 2005.

[85] M. H. Protter and H. F. Weinberger. *Maximum Principles in Differential Equations*. Springer-Verlag, New York, USA, 1999.

[86] E. Rank, C. Katz, and H. Werner. On the importance of the discrete maximum principle in transient analysis using finite element methods. *International Journal for Numerical Methods in Engineering*, 19:1771–1782, 1983.

[87] B. M. Roehner. *Hidden Collective Factors in Speculative Trading: A Study in Analytical Economics*. Springer-Verlag, Heidelberg, Germany, second edition, 2009.

[88] E. Rothe. Zweidimensionale parabolische randwertaufgaben als grenzfall eindimensionaler randwertaufgaben. *Mathematische Annalen*, 102:650–670, 1930.

[89] W. Rudin. *The Principles of Mathematical Analysis*. McGraw-Hill, New York, USA, third edition, 1976.

[90] Y. Saad. *Iterative Methods for Sparse Linear Systems*. SIAM, Philadelphia, USA, 2003.

[91] R. Taylor and R. Krishna. *Multicomponent Mass Transfer*. Wiley Series in Chemical Engineering. John Wiley & Sons Inc., New York, USA, 1993.

[92] H. R. Thomas and Z. Zhou. An analysis of factors that govern the minimum time step size to be used in the finite element analysis of diffusion problems. *Communications in Numerical Methods in Engineering*, 14:809–819, 1998.

[93] E. Vanderzee, A. N. Hirani, D. Guoy, and E. A. Ramos. Well-centered triangulation. *SIAM Journal on Scientific Computing*, 31:4497–4523, 2010.

[94] R. S. Varga. *Matrix Iterative Analysis*, volume 27 of *Springer Series in Computational Mathematics*. Springer-Verlag, Berlin, Heidelberg, second revised and expanded edition, 2009.

[95] Y. Ye and E. Tse. An extension of Karmarkar's projective algorithm for convex quadratic programming. *Mathematical Programming*, 44:157–179, 1989.

Task 4: Mathematical and Computational Modeling of Deterioration Process

Senior personnel
Dr. Kalyana Babu Nakshatrala (***e-mail:*** knakshatrala@uh.edu)
Dr. Kaspar J. Willam (***e-mail:*** kwillam@uh.edu)
University of Houston, Houston, Texas 77204.

Covering Period: October 1, 2013 through September 30, 2014
Date of Report: October 20, 2014

ID #: RPA-12-3545, Yearly Report Y2

SUMMARY & PLANS

The following are the completed research tasks.

(I) ***Deriving mesh restrictions to meet maximum principles:*** We completely finished this aspect of the research in the second year, which was started towards the end of the first year. This research is about deriving mesh restrictions to meet maximum principles and the non-negative constraint for advection-diffusion and linear reactions. [**Status:** Finished. The paper is available on arXiv.]

(II) ***Numerical methodology for transient diffusion equation to meet maximum principles and the non-negative constraint:*** One of main tasks on the numerical modeling front is to the develop numerical methodologies for satisfying maximum principles and the non-negative constraint for transient problems.

(a) We *finished* the development of a robust methodology for linear transient diffusion equations. The research is also submitted for review to an international journal. [**Status:** Finished. The paper will soon be placed on arXiv.]

(b) In the second year, we started developing non-negative methodologies for *semi-linear* diffusion-type equations. We completed the theoretical aspects, and we are in process of generating numerical results. This will be finished in the first quarter of third year, and will be submitted to a journal. For sake of brevity of the yearly report, we did not include these results in this report.

(c) In the third year, we will develop non-negative formulations for steady-state and transient *quasilinear* diffusion-type equations.

(III) ***On achieving element-wise species balance and enforcing maximum principles for advection-diffusion-reaction equations:*** This is research is one of the main ingredients of the computational modeling of degradation of materials. A robust predictive framework for advective-diffusive-reactive systems is vital to predict the various degradation mechanisms. This part of the research has been started in the first year, and will continue to the early part of the third year. We are currently working on to numerical challenges posed by choatic advection, which can arise in, for example, moisture degradation mechanism. The duration of the research topic should be a reflection of the transformative nature of the research. This will also be completed by the end of first quarter in the third year.

(IV) ***A chemo-thermal-deformation model for degradation of materials/structures:*** We have been developing a hierarchy of mathematical models to model various mechanisms of degradation. The models will account for coupled chemo-thermal-deformation response, which is crucial for mathematical modeling of degradation of materials. As discussed in our proposal, this mathematical model in consistently derived using mechanics and thermodynamics principles. In particular, the model will satisfy the second law of thermodynamics, which is not the case with some of the current models for degradation. In the fourth quarter of second year, the effect of degradation on stress concentration is studied. To this end, a plate with a circular hole subjected to uniaxial tension is considered. This problem is classical and well-studied in the absence of degradation. However, it not addressed in the literature how degradation affects the stress concentration, and the distribution of stresses and strains. In the next quarter, we will calibrate the model using the hygrothermal data published in the literature on concrete.

Invited Talks

I1. **Rice University:** "*Importance of non-negative solutions in degradation modeling, groundwater modeling, and reactive transport*," Graduate seminar, Department of Civil and Environmental Engineering, February 7, 2014.

I2. M.K. Mudunuru, and K.B. Nakshatrala, "*Why need physics-compatible numerical formulations for flow and transport in subsurface and material modeling?*," **Indian Institute of Science (IISc)**, July 30, 2014.

I3. J. Chang, and K.B. Nakshatrala, "*A locally conservative finite element formulation and its parallel implementation in PETSc*," **Los Alamos National Laboratory**, August 4, 2014.

Conferences Talks

C1. S. Karimi, and K. B. Nakshatrala, "**Monolithic multi-time-step coupling methods for second-order transient systems**," *17th US National Congress of Theoretical and Applied Mechanics*, Michigan State University, June 15–20, 2014.

C2. M. K. Mudunuru, and K. B. Nakshatrala, "**On mesh restrictions for mixed formulations for mixed formulations for anisotropic diffusion equation in high contrast heterogeneous media**," *17th US National Congress of Theoretical and Applied Mechanics*, Michigan State University, June 15–20, 2014.

C3. J. Chang, and K. B. Nakshatrala, "**Computational performance of locally conservative methods for large-scale flow and transport through porous media**," *17th US National Congress of Theoretical and Applied Mechanics*, Michigan State University, June 15–20, 2014.

C4a. S. Karimi, and K.B. Nakshatrala, "**On the development and performance of multi-time-step coupling methods for transient multi-scale problems**," *Experimental and Computational Nonlinear Dynamics* session, *51st SES Annual Technical Meeting*, Purdue University, October 1–3, 2014. [***Student poster competition***]

C4b. S. Karimi, and K.B. Nakshatrala, "**Monolithic multi-time-step coupling methods for transient problems in solid mechanics and transport**," *Experimental and Computational Nonlinear Dynamics* session, *51st SES Annual Technical Meeting*, Purdue University, October 1–3, 2014. [***Oral presentation***]

C5. J. Chang, and K.B. Nakshatrala, "**A methodology to ensure local mass conservation for porous media models under finite element formulations based on convex optimization**," *AGU Fall Meeting*, December 15–19, 2014. [***Poster presentation***]

C6. S. Karimi, and K.B. Nakshatrala, "**A monolithic multi-time-step computational framework for transient advective-diffusive-reactive**," *AGU Fall Meeting*, December 15–19, 2014. [***Poster presentation***]

C7. S. Karra, J. Chang, and K.B. Nakshatrala, "**On the performance of maximum-principle enforcing methods applied to large-scale subsurface problems**," *AGU Fall Meeting*, December 15–19, 2014. [***Poster presentation***]

C8. K.B. Nakshatrala, "**On enforcing maximum principles, comparison principles, monotone property, and the non-negative constraint for linear/nonlinear steady-state/transient diffusion-type equations**," *AGU Fall Meeting*, December 15–19, 2014.

Peer-Reviewed Conference Papers/Extended Abstracts

P1. M. K. Mudunuru, and K. B. Nakshatrala, "**On mesh restrictions for mixed formulations for mixed formulations for anisotropic diffusion equation in high contrast heterogeneous media**," *17th US National Congress of Theoretical and Applied Mechanics*, abstract number C-06-703, 2014.

P2. J. Chang, and K. B. Nakshatrala, "**Computational performance of locally conservative methods for large-scale flow and transport through porous media**," *17th US National Congress of Theoretical and Applied Mechanics*, abstract number C-06-523, 2014.

P3. S. Karimi, and K. B. Nakshatrala, "**Monolithic multi-time-step coupling methods for second-order transient systems**," *17th US National Congress of Theoretical and Applied Mechanics*, abstract number C-06-840, 2014.

Awards / Honors

A1. Saeed Karimi (a Ph.D. student under Dr. Kalyana B. Nakshatrala) got travel grant from the prestigious *Society of Industrial and Applied Mathematics* to attend 2015 SIAM Conference on Computational Science and Engineering (CSE15). He won the award based on the conference talk abstract on "*Monolithic multi-time-step coupling methods for transient systems*," S. Karimi, and K. B. Nakshatrala. The award consists of $650 and waiver of conference registration fee.

Mini-symposia organization at national/international conferences

M1. "*Continuum scale modeling of flow and reactive transport in porous media*," Organizers: S. Karra, and K.B. Nakshatrala, American Geophysical Union Fall Meeting, San Francisco, December 9–13, 2013.

M2. "*Continuum scale modeling of flow and reactive transport in porous media*," Organizers: S. Karra, and K.B. Nakshatrala, American Geophysical Union Fall Meeting, San Francisco, December 15–19, 2014.

M3. "*Modeling flow and transport in heterogeneous porous media*," Organizers: K.B. Nakshatrala (Chair), S. Karra, and H. Viswanathan, 13th US National Congress on Computational Mechanics, San Diego, California, July 26–30, 2014.

M4. "*Mathematical and numerical modeling of degradation of materials and structures*," Organizers: K.B. Nakshatrala (Chair), D.Z. Turner, K.J. Willam, and R. Ballarini, 13th US National Congress on Computational Mechanics, San Diego, California, July 26–30, 2014.

On modeling of material degradation due to moisture

Abstract

In this paper, we derive a chemical degradation model under small strain and isothermal conditions by appealing to the maximization of entropy production. In this process, we shall provide a thermodynamic status of the degradation model recently proposed by Mudunuru and Nakshatrala (IJNME, DOI: 10.1002/nme.3282, 2012). In order to illustrate the advantage of this model, the results obtained from this framework will be compared with that of metric-based meshes based on the standard Galerkin method. Furthermore, we shall study the behavior of degrading slabs under self-weight, which is a 3D problem. To crystalize ideas, we shall assume the degradation is due to moisture, which is a predominant degradation mechanism in slabs and nuclear containments. Employing this model, we shall solve various representative boundary value problems pertaining to moisture degradation, which provide valuable information on the structural response of building materials. We shall compare the behavior of an infinite degrading slab with the behavior of a finite-sized degrading slab. We shall highlight the limitations of typical semi-inverse solutions, which are commonly employed in practice. We shall also discuss the implication of the results from our study on degradation of slabs with respect to better design codes.

1. INTRODUCTION AND MOTIVATION

A robust infrastructure is vital for economic growth. Modeling infrastructural materials and the ability to predict their response in severe environmental conditions is of great importance to the infrastructure industry. Most of the well-known manifestations, such as "wear out " and "fracture", are related with a phenomenon called degradation of materials [**7**]. Degradation is a major, widespread, and an important engineering problem. There is a recent surge in research activities to develop new infrastructural materials that have better resistance to various degradation mechanisms. There is also a growing research interest to understand the general behavior of degrading structural members. For various types of infrastructure (e.g., transportation infrastructure, residential and commercial buildings), slab is one of the essential load bearing structural members. To give specific examples, slabs are used as the building blocks for highway pavements, floors and roofs of buildings, decks in bridges, and as walls in water tanks. Therefore, this paper will simulate one of the most typical degradation phenomenons, two-way coupled chemical degradation problem. Especially, we shall study the behavior of slabs subjected to degradation.

1.1. Main contributions and outline of the paper. The main contributions of this paper are as follows:

(i) We derived a chemical degradation model under small strain and isothermal conditions by appealing to the maximization of rate of entropy production. Many exisiting models (some of them not necessarily degradation models) will be special cases of the proposed degradation model. In this process, we shall provide a thermodynamic status of the degradation model proposed by [**30**].

(ii) We illustrated the performance of metric-based meshes in solving coupled deformation-diffusion problems in terms of matrix condition number, and the overall quality of solutions.

(iii) We illustrated that material degradation gives rise to secondary effects like bulging, which play an important in design considerations.

(iv) We illustrated the deficiencies of commonly employed semi-inverse methods in the prediction of deformations of degrading slabs. We showed that the behavior of an infinite slab (which is a common idealization made in obtaining analytical solutions) is qualitatively and quantitatively different from that of a finite-sized slab, especially in the presence of degradation.

(v) We are currently developing a computational framework to model unsteady motions of structures subject to matrial degradation. This research will be reported in the next quarter.

2. MATHEMATICAL MODELS FOR DEGRADATION AND THEIR THERMODYNAMIC STATUS

Let $\Omega \subset \mathbb{R}^{nd}$ be a bounded open domain, where "nd" denotes the number of spatial dimensions. Let $\partial\Omega$ denote the boundary of the domain, and a spatial point in Ω is denoted by $\mathbf{x}$. As we are concerned with linearized theory of degradation models, the unit outward normal to the boundary is denoted as $\widehat{\mathbf{n}}(\mathbf{x})$ (instead of $\widehat{\mathbf{n}}(\mathbf{x},t)$). The gradient and divergence operators with respect to $\mathbf{x}$ are, respectively, denoted as grad$[\cdot]$ and div$[\cdot]$. We shall denote the time by $t \in [0,\mathcal{I}]$, where $\mathcal{I}$ is the length of the time interval. In the view that degradation of a material will involve multiple coupled processes. We shall now define various physical and chemical quantities that are need to document the relevant balance laws and constitutive models.

Denote the temperature by $\vartheta(\mathbf{x},t)$ and the specific entropy by $\eta(\mathbf{x},t)$. The mass concentration of the chemical species [**10**] is denoted by $c(\mathbf{x},t)$, which is also referred to as mass fraction in some books [**38**]. The corresponding chemical potential is denoted by $\varkappa(\mathbf{x},t)$. The displacement, velocity, and acceleration of the solid are respectively, denoted by $\mathbf{u}(\mathbf{x},t)$, $\mathbf{v}(\mathbf{x},t)$, and $\mathbf{a}(\mathbf{x},t)$. The temperature, concentration, entropy, and chemical potential are scalar fields, while the displacement, velocity, and acceleration are all vector fields.

For the deformation problem, the boundary is divided into Γ_u^{D} and Γ_u^{N} such that $\Gamma_u^{\mathrm{D}} \cup \Gamma_u^{\mathrm{N}} = \partial\Omega$ and $\Gamma_u^{\mathrm{D}} \cap \Gamma_u^{\mathrm{N}} = \emptyset$. Γ_u^{D} is that part of the boundary on which displacement is prescribed and Γ_u^{N} is part of the boundary on which traction is prescribed. Similarly, for the transport problem, the boundary is divided into Γ_c^{D} and Γ_c^{N} such that $\Gamma_c^{\mathrm{D}} \cup \Gamma_c^{\mathrm{N}} = \partial\Omega$ and $\Gamma_c^{\mathrm{D}} \cap \Gamma_c^{\mathrm{N}} = \emptyset$. Γ_c^{D} is that part of the boundary on which concentration is prescribed and Γ_c^{N} is part of the boundary on which transport flux is prescribed. As for the thermal problem, the boundary is divided into $\Gamma_\vartheta^{\mathrm{D}}$ and $\Gamma_\vartheta^{\mathrm{N}}$ such that $\Gamma_\vartheta^{\mathrm{D}} \cup \Gamma_\vartheta^{\mathrm{N}} = \partial\Omega$ and $\Gamma_\vartheta^{\mathrm{D}} \cap \Gamma_\vartheta^{\mathrm{N}} = \emptyset$. $\Gamma_\vartheta^{\mathrm{D}}$ is that part of the boundary on which temperature is prescribed and $\Gamma_\vartheta^{\mathrm{N}}$ is part of the boundary on which heat flux is prescribed.

2.1. Balance laws for chemo-mechano degradation.

In chemo-mechano degradation problems, several balance laws should be obeyed. The following summarizes different balance laws in homogenized sense:

- Balance of mass and linear momentum for solid in the degrading body can be stated as follows:

$$\dot{\rho} + \rho \mathrm{div}[\mathbf{v}] = 0 \tag{2.1}$$

$$\rho\dot{\mathbf{v}} = \mathrm{div}[\mathbf{T}] + \rho\mathbf{b} \tag{2.2}$$

  where $\dot{(\,)}$ denotes the material time derivative [**18**], ρ is the density of the solid, $\mathbf{b}(\mathbf{x},t)$ is the specific body force, and $\mathbf{T}(\mathbf{x},t)$ is the Cauchy stress in the solid.

- As the system under consideration is open and the chemical species cannot taken partial stresses, we only have balance of mass for chemical species in the degrading body. This is given as follows:

$$\rho\dot{c} + \mathrm{div}[\mathbf{h}] = h \tag{2.3}$$

where $\mathbf{h}(\mathbf{x}, t)$ is the diffusive flux vector and $h(\mathbf{x}, t)$ is the volumetric source of the chemical species.
- The balance of energy for the degrading body takes the following form:

$$\rho\left(\frac{\partial A}{\partial \mathbf{E}_l} \cdot \dot{\mathbf{E}}_l + \vartheta\dot{\eta}\right) = \mathbf{T} \cdot \dot{\mathbf{E}}_l - \mathrm{div}[\mathbf{q}] - \mathrm{grad}[\varkappa] \cdot \mathbf{h} + q \tag{2.4}$$

where A is the specific Helmholtz potential, $\mathbf{E}_l$ is the linearized strain, η is the specific entropy, $\varkappa(\mathbf{x}, t)$ is the chemical potential, $\mathbf{q}(\mathbf{x}, t)$ is the heat flux vector, and $q(\mathbf{x}, t)$ is the volumetric heat source.
- Finally, the second law of thermodynamics in its reduced form is given as follows:

$$\rho\left(\frac{\partial A}{\partial \mathbf{E}_l} \cdot \dot{\mathbf{E}}_l\right) = \mathbf{T} \cdot \dot{\mathbf{E}}_l - \frac{1}{\vartheta}\mathrm{grad}[\vartheta] \cdot \mathbf{q} - \mathrm{grad}[\varkappa] \cdot \mathbf{h} - \zeta \tag{2.5}$$

where ζ is the rate of dissipation functional, which is always non-negative. Additionally, we have the following relations for chemical potential and specific entropy:

$$\varkappa := \frac{\partial A}{\partial c} \tag{2.6}$$

$$\eta := -\frac{\partial A}{\partial \vartheta} \tag{2.7}$$

2.2. A linearized two-way coupled chemical degradation model. We shall appeal to the axiom of *maximization of rate of entropy production* [**46**] to derive constitutive relations that satisfy the second law of thermodynamics *aprior*. To this end, we need to prescribe two scalar functionals: A functional to describe how the material stores energy and a functional to describe how the material dissipates energy. In our case, we shall specify '$\hat{A}(\mathbf{E}_l, c, \vartheta)$' the specific Helmholtz potential and '$\hat{\zeta}(\mathbf{E}_l, \vartheta, c, \dot{\mathbf{E}}_l, \mathrm{grad}[\vartheta], \mathrm{grad}[\varkappa])$' the rate of dissipation functional. Our model will be restricted to case when the degradation process is taking place very close to the equilibrium. Mathematically, this assumption takes the following form:

$$\epsilon := \left(\|\mathrm{grad}[\mathbf{u}]\|^2 + \left(\frac{\vartheta - \vartheta_{\mathrm{ref}}}{\vartheta_{\mathrm{ref}}}\right)^2 + \frac{l^2\|\mathrm{grad}[\vartheta]\|^2}{\vartheta_{\mathrm{ref}}^2} + \frac{l^2\|\mathrm{grad}[c]\|^2}{c_{\mathrm{ref}}^2}\right)^{1/2} \ll 1 \tag{2.8}$$

where ϑ_{ref} and c_{ref} are, respectively, the reference temperature and reference concentration, which will be problem specific. From the above *near equilibrium* assumption (based on equation (2.8)), it is evident that strain in the solid is linear and is defined as follows:

$$\mathbf{E}_l := \frac{1}{2}\left(\mathrm{grad}[\mathbf{u}] + \mathrm{grad}[\mathbf{u}]^{\mathrm{T}}\right) \tag{2.9}$$

Correspondingly, the specific Helmholtz potential for a linearized chemical degradation model is given as follows:

$$A = \hat{A}(\mathbf{E}_l, c, \vartheta) = \frac{1}{2\rho}\mathbf{E}_l \cdot \mathbb{C}(c)\mathbf{E}_l - \frac{1}{2}\frac{c_p}{\vartheta_{\text{ref}}}(\vartheta - \vartheta_{\text{ref}})^2 + \frac{1}{\rho}(\vartheta - \vartheta_{\text{ref}})\,\mathbf{M}_{\vartheta\mathbf{E}_l} \cdot \mathbf{E}_l + \frac{1}{\rho}(c - c_{\text{ref}})\,\mathbf{M}_{c\mathbf{E}_l} \cdot \mathbf{E}_l + \frac{1}{2}R_s\vartheta_{\text{ref}}(c - c_{\text{ref}})^2 \tag{2.10}$$

where $R_s = \frac{R}{M}$. R_s and R are,respectively, the specific gas constant and the universal gas constant. M is the molecular mass of chemical species, c_p is the coefficient of heat capacity, $\mathbf{M}_{\vartheta\mathbf{E}_l}$ is the anisotropic coefficient of thermal expansion (which is assumed to be independent of temperature, concentration, and strain), and $\mathbf{M}_{c\mathbf{E}_l}$ is the anisotropic coefficient of chemical expansion due to concentration (which is assumed to be independent of temperature, concentration, and strain).

REMARK 2.1. *In chemoelasticity and in modeling degradation of materials due to transport and reaction of chemical species, coefficient of chemical expansion* $\mathbf{M}_{c\mathbf{E}_l}$ *plays a vital role. It should be noted that induced-strains due to chemical expansivity will be significant in harsh environmental conditions and cannot be neglected [**39**]. Considerable inquest has been made in literature to experimentally measure* $\mathbf{M}_{c\mathbf{E}_l}$ *in ceramics [**6**, **8**, **29**], laminated and polymer composites [**9**, **12**, **39**], elastomers and biological materials [**19**, **24**, **31**], and concrete structures [**40**, **41**, **43**]. But seldom progress has been accomplished to develop constitutive models and computational frameworks for such chemoelastic materials or materials undergoing chemical-induced degradation. Herein, we shall take a step forward to address this issue.*

Furthermore, the rate of dissipation functional for a linearized chemical degradation model is taken as follows:

$$\begin{aligned}\zeta &= \hat{\zeta}(\mathbf{E}_l, \vartheta, c, \dot{\mathbf{E}}_l, \text{grad}[\vartheta], \text{grad}[\varkappa]) \\ &= \frac{1}{\vartheta}\text{grad}[\vartheta] \cdot \mathbf{D}_{\vartheta\vartheta}\text{grad}[\vartheta] + \frac{c}{R\vartheta_{\text{ref}}}\text{grad}[\varkappa] \cdot \mathbf{D}_{\varkappa\varkappa}\text{grad}[\varkappa]\end{aligned} \tag{2.11}$$

where $\mathbf{D}_{\vartheta\vartheta}$ is the anisotropic heat conduction, and $\mathbf{D}_{\varkappa\varkappa}$ is the anisotropic diffusivity tensor.

2.2.1. *Maximization of rate of entropy production.* Among various methodologies to derive constitutive relations [**28**], axiom of maximization of rate of entropy production put-forth by Ziegler [**46**] is an attractive and simple procedure. Using this procedure, constitutive equations can be generated by specifying $\hat{A}(\mathbf{E}_l, c, \vartheta)$ and $\hat{\zeta}(\mathbf{E}_l, \vartheta, c, \dot{\mathbf{E}}_l, \text{grad}[\vartheta], \text{grad}[\varkappa])$. Accordingly, the mathematical statement of the maximization of rate of entropy production can be written as follows:

$$\underset{\dot{\mathbf{E}}_l, \text{grad}[\vartheta], \text{grad}[\varkappa]}{\text{maximize}} \quad \hat{\zeta}(\mathbf{E}_l, \vartheta, c, \dot{\mathbf{E}}_l, \text{grad}[\vartheta], \text{grad}[\varkappa]) \tag{2.12a}$$

$$\text{subject to} \qquad \rho\left(\frac{\partial A}{\partial \mathbf{E}_l} \cdot \dot{\mathbf{E}}_l\right) = \mathbf{T} \cdot \dot{\mathbf{E}}_l - \frac{1}{\vartheta}\mathbf{q} \cdot \text{grad}[\vartheta] - \text{grad}[\varkappa] \cdot \mathbf{h} - \zeta \tag{2.12b}$$

Based on the method of Lagrange multipliers, the above constrained optimization problem can be written as follows :

$$\begin{aligned}\underset{\dot{\mathbf{E}}_l, \text{grad}[\vartheta], \text{grad}[\varkappa], \lambda}{\text{extremize}} \quad & \hat{\zeta}(\mathbf{E}_l, \vartheta, c, \dot{\mathbf{E}}_l, \text{grad}[\vartheta], \text{grad}[\varkappa]) \\ & + \lambda\left(\rho\left(\frac{\partial A}{\partial \mathbf{E}_l} \cdot \dot{\mathbf{E}}_l\right) - \mathbf{T} \cdot \dot{\mathbf{E}}_l + \frac{1}{\vartheta}\mathbf{q} \cdot \text{grad}[\vartheta] + \text{grad}[\varkappa] \cdot \mathbf{h} + \zeta\right)\end{aligned} \tag{2.13}$$

where λ is the Lagrange multiplier enforcing the constraint of (2.12b). Compute the partial derivative of this problem with respect to each variable, we can have the following equations:

$$\partial\dot{\mathbf{E}}_l: \quad \mathbf{T} = \rho\frac{\partial A}{\partial \mathbf{E}_l} + \left(\frac{1+\lambda}{\lambda}\right)\frac{\partial \zeta}{\partial \dot{\mathbf{E}}_l} \tag{2.14a}$$

$$\partial \mathrm{grad}[\vartheta]: \quad \frac{1}{\vartheta}\mathbf{q} = -\left(\frac{1+\lambda}{\lambda}\right)\frac{\partial \zeta}{\partial \mathrm{grad}[\vartheta]} \tag{2.14b}$$

$$\partial \mathrm{grad}[\varkappa]: \quad \mathbf{h} = -\left(\frac{1+\lambda}{\lambda}\right)\frac{\partial \zeta}{\partial \mathrm{grad}[\varkappa]} \tag{2.14c}$$

$$\partial\lambda: \quad \rho\left(\frac{\partial A}{\partial \mathbf{E}_l}\cdot\dot{\mathbf{E}}_l\right) - \mathbf{T}\cdot\dot{\mathbf{E}}_l + \frac{1}{\vartheta}\mathbf{q}\cdot\mathrm{grad}[\vartheta] + \mathrm{grad}[\varkappa]\cdot\mathbf{h} + \zeta = 0 \tag{2.14d}$$

The Lagrange multiplier can be obtained from these above equations:

$$\lambda = \left[\frac{\zeta}{\frac{\partial\zeta}{\partial\dot{\mathbf{E}}_l}\cdot\dot{\mathbf{E}}_l + \frac{\partial\zeta}{\partial\mathrm{grad}[\vartheta]}\cdot\mathrm{grad}[\vartheta] + \frac{\partial\zeta}{\partial\mathrm{grad}[\varkappa]}\cdot\mathrm{grad}[\varkappa]} - 1\right]^{-1} \tag{2.15}$$

If we assume that the rate of dissipation functional is a homogenous function of order 2, (2.15) can be rewritten as follows.

$$\frac{\partial\zeta}{\partial\dot{\mathbf{E}}_l}\cdot\dot{\mathbf{E}}_l + \frac{\partial\zeta}{\partial\mathrm{grad}[\vartheta]}\cdot\mathrm{grad}[\vartheta] + \frac{\partial\zeta}{\partial\mathrm{grad}[\varkappa]}\cdot\mathrm{grad}[\varkappa] = 2\zeta \tag{2.16}$$

Since $\lambda = -2$, the constitutive relations take the following form:

$$\mathbf{T} = \rho\frac{\partial A}{\partial \mathbf{E}_l} + \frac{1}{2}\frac{\partial\zeta}{\partial\dot{\mathbf{E}}_l} = \mathbb{C}(c)\mathbf{E}_l + (\vartheta-\vartheta_{\mathrm{ref}})\mathbf{M}_{\vartheta\mathbf{E}_l} + (c-c_{\mathrm{ref}})\mathbf{M}_{c\mathbf{E}_l} \tag{2.17a}$$

$$\mathbf{q} = -\frac{\vartheta}{2}\frac{\partial\zeta}{\partial\mathrm{grad}[\vartheta]} = -\mathbf{D}_{\vartheta\vartheta}\mathrm{grad}[\vartheta] \tag{2.17b}$$

$$\mathbf{h} = -\frac{1}{2}\frac{\partial\zeta}{\partial\mathrm{grad}[\varkappa]} = -\frac{c}{R_s\vartheta_{\mathrm{ref}}}\mathbf{D}_{\varkappa\varkappa}\mathrm{grad}[\varkappa] \tag{2.17c}$$

2.3. Status of the degradation model in [30]. The balance laws in this model should be checked. The specific entropy, Cauchy stress,chemical potential under the assumption of equation (2.8) can be written as follows:

$$\eta = -\frac{\partial A}{\partial\vartheta} = \frac{c_p}{\vartheta_{\mathrm{ref}}}\{\vartheta-\vartheta_{\mathrm{ref}}\} + \frac{1}{\rho}\mathbf{M}_{\vartheta\mathbf{E}_l}\cdot\mathbf{E}_l \tag{2.18}$$

$$\mathbf{T} = \rho\frac{\partial A}{\partial\mathbf{E}_l} = \mathbb{C}(c)\mathbf{E}_l + (c-c_{\mathrm{ref}})\mathbf{M}_{c\mathbf{E}_l} \tag{2.19}$$

$$\varkappa = \frac{\partial A}{\partial c} = \frac{1}{\rho}\mathbf{M}_{c\mathbf{E}_l}\cdot\mathbf{E}_l + R_s\vartheta_{\mathrm{ref}}(c-c_{\mathrm{ref}}) \tag{2.20}$$

Since the solid is linear elastic, the balance of mass for solid (2.1) stands automatically in steady state. The balance of linear momentum can be written as follows:

$$\rho\dot{\mathbf{v}} = \mathrm{div}[\mathbb{C}(c)\mathbf{E}_l + (c-c_{\mathrm{ref}})\mathbf{M}_{c\mathbf{E}_l}] + \rho\mathbf{b} \tag{2.21}$$

The balance of species (2.3) can be written as follows:

$$\rho\dot{c} + \mathrm{div}[\mathbf{h}] = h \tag{2.22}$$

The balance of energy can be written as follows under the assumption of equation (2.8) :

$$\rho\vartheta\frac{c_p}{\vartheta_{\text{ref}}}\dot{\vartheta}+\vartheta\mathbf{M}_{\vartheta\mathbf{E}_l}\cdot\dot{\mathbf{E}}_l-c\text{grad}[c]\cdot\mathbf{D}_{\varkappa\varkappa}\text{grad}[\varkappa]=q \tag{2.23}$$

The isothermal assumption can be taken based on the equation (2.24), that is:

$$q=-c\text{grad}[c]\cdot\mathbf{D}_{\varkappa\varkappa}\text{grad}[\varkappa] \tag{2.24}$$

Therefore, the steady-state governing equation for this model can be written as follows:

$$\text{div}[\mathbb{C}(c)\mathbf{E}_l]+\rho\mathbf{b}(\mathbf{x})=0 \tag{2.25}$$

$$\text{div}[\mathbf{h}(\mathbf{x})]=h(\mathbf{x}) \tag{2.26}$$

2.4. Constitutive specifications in the model [30]. The first and second invariants of the strain tensor are defined as follows.

$$I_{\mathbf{E}_l}=\text{tr}[\mathbf{E}_l] \tag{2.27a}$$

$$II_{\mathbf{E}_l}=\sqrt{\frac{2}{3}(3\text{tr}[\mathbf{E}^2{}_l]-(\text{tr}[\mathbf{E}_l])^2)} \tag{2.27b}$$

Since the solid is assumed to be linear elastic, the Cauchy stress, which depends on the concentration and position, takes the following form:

$$\mathbf{T}_c=\lambda(\mathbf{x},c)I_{\mathbf{E}_l}\mathbf{I}+2\mu(\mathbf{x},c)\mathbf{E}_l \tag{2.28}$$

where $\mathbf{I}$ is the second-order tensor, and the Lamé parameters are given by the following expressions:

$$\lambda(\mathbf{x},c)=\lambda_0(\mathbf{x})--\lambda_1(\mathbf{x})\frac{c}{c_{\text{ref}}} \tag{2.29a}$$

$$\mu(\mathbf{x},c)=\mu_0(\mathbf{x})--\mu_1(\mathbf{x})\frac{c}{c_{\text{ref}}} \tag{2.29b}$$

where λ_0 and μ_0 are the lamé parameters of materials with c_{ref}. λ_1 and μ_1 are the parameters that account for the effect of diffusion on deformation. Since this is a degradation model, λ_1 and $\mu_1$are all positive.
The effect of deformation on diffusivity is modeled as follows.
When tensile strain is predominant:

$$\mathbf{D}=\mathbf{D}_0+(\mathbf{D}_T-\mathbf{D}_0)\left(1-\exp[\eta_T I_{\mathbf{E}_l}]\right)+(\mathbf{D}_S-\mathbf{D}_0)\left(1-\exp[\eta_S II_{\mathbf{E}_l}]\right) \tag{2.30}$$

where η_T and η_S are non-negative parameters, $\mathbf{D}_0$, $\mathbf{D}_T$ and $\mathbf{D}_S$ are, respectively, the reference diffusivity tensors under no, tensile, and shear strains.
When compression is predominant:

$$\mathbf{D}=\mathbf{D}_0+(\mathbf{D}_C-\mathbf{D}_0)\left(1-\exp[\eta_C I_{\mathbf{E}_l}]\right)+(\mathbf{D}_S-\mathbf{D}_0)\left(1-\exp[\eta_S II_{\mathbf{E}_l}]\right) \tag{2.31}$$

where η_C is a non-negative parameter and $\mathbf{D}_C$ is the reference diffusivity tensor under compressive strains.

3. ON THE PERFORMANCE OF METRIC-BASED MESHES AND NON-NEGATIVE FORMULATIONS IN DEGRADATION MODELING

In solving chemical degradation problem, Newton Raphson and standard Galerkin method can produce negative concentration values, since the diffusivity tensor is anisotropic. Usually, there are two methods can be used to avoid this situation. The first one is to design a proper numerical scheme, and the other is to build a proper mesh [**25**]. In this section, several case studies will be done to show the performance of all these methods: the Newton Raphson method and the Galerkin method using the regular mesh and the metric-based mesh, as well as the non-negative formulation.

3.1. Plate with a square hole. The first case study is a bi-unit square plate with a hole of length $\frac{1}{9}$ under self-weight. The boundary condition for deformation subproblem is that the internal boundary is fixed, and external is traction free. For the diffusion subproblem, the concentration at the hole is maintained at 1, whereas at the boundary of the plate is 0. The tensile strain is assumed to be predominant, therefore equation (2.30) will be applied. $\mathbf{D}_0$, $\mathbf{D}_T$, and $\mathbf{D}_S$ have been chosen as follows.

$$\mathbf{D}_0 = \begin{pmatrix} \cos(\theta) & -\sin(\theta) \\ \sin(\theta) & \cos(\theta) \end{pmatrix} \begin{pmatrix} d_1 & 0 \\ 0 & d_2 \end{pmatrix} \begin{pmatrix} \cos(\theta) & \sin(\theta) \\ -\sin(\theta) & \cos(\theta) \end{pmatrix} \tag{3.1a}$$

$$\mathbf{D}_T = \begin{pmatrix} \cos(\theta) & -\sin(\theta) \\ \sin(\theta) & \cos(\theta) \end{pmatrix} \begin{pmatrix} d_1^T & 0 \\ 0 & d_2^T \end{pmatrix} \begin{pmatrix} \cos(\theta) & \sin(\theta) \\ -\sin(\theta) & \cos(\theta) \end{pmatrix} \tag{3.1b}$$

$$\mathbf{D}_S = \begin{pmatrix} \cos(\theta) & -\sin(\theta) \\ \sin(\theta) & \cos(\theta) \end{pmatrix} \begin{pmatrix} d_1^S & 0 \\ 0 & d_2^S \end{pmatrix} \begin{pmatrix} \cos(\theta) & \sin(\theta) \\ -\sin(\theta) & \cos(\theta) \end{pmatrix} \tag{3.1c}$$

The parameters are assumed as follows.

$$\begin{aligned} &\theta = \frac{\pi}{4},\ \eta_T = 1,\ \eta_S = 1,\ d_1 = 10000,\ d_2 = 1,\ d_1^T = 20000,\ d_2^T = 5,\ d_1^S = 15000,\ d_2^S = 2, \\ &\rho = 10^3,\ g = 10,\ c_{\text{ref}} = 1,\ \lambda_0 = 10^{10},\ \mu_0 = 2 \times 10^{10},\ \lambda_1 = 9 \times 10^{10},\ \mu_1 = 1.8 \times 10^{10} \end{aligned} \tag{3.2}$$

Two different kinds of mesh has been shown in Figure 1. The restriction on the metric-based mesh should be the inverse of the diffusivity tensor. However, the diffusivity tensor varies from element to element, since it depends on the strain, which is different for each element. Since it is difficult (or impossible) to apply the corresponding diffusivity tensor to each element, the mesh is generated based on the inverse of $\mathbf{D}_0$.

For the Newton Raphson method, the residual variations have been shown in Figure 4. It can be found that only the regular mesh can be used to solve this problem, since the metric-based mesh leads to high condition numbers. The concentration distribution results have been depicted in Figure 2. Table 1 shows the number of elements and nodes, the condition number of stiffness in both deformation and diffusion subproblems, the healing index, and the minimum concentration in all four methods. The healing index is the percentage of nodes with negative values. The variation of condition number of stiffness in deformation and diffusion subproblems with the iteration number have been described in Figure 3.

From above results, we can find out that, for the diffusion subproblem, although the healing index is reduced by the metric-based mesh, negative concentration values still exist. Moreover, the adapted mesh does not simulate the deformation problem very well. Not only the maximum displacement cannot be captured, but also the condition number of stiffness in deformation subproblem is much higher than the other methods.

TABLE 1. Square plate with hole: Comparison of four methods

Method	Mesh type	Number of elements	Number of nodes	Condition number of stiffness		Healing index	Minimum concentration
				Deformation subproblem	Diffusion subproblem		
Newton Raphson	Regular	1868	998	5504194221.99		29.46	-0.035
Standard Galerkin	Regular	1868	998	402360.54	807.06	29.75	-0.035
Standard Galerkin	Metric-based	2502	1395	5813905.18	1005.15	18.99	-0.02
Non-negative formulation	Regular	1868	998	400934.66	807.07	0	0

3.2. Plate with a circle hole. This is a very classical problem in material's mechanics. A bi-unit square plate with a circular hole with radius 0.2. For the deformation subproblem, the top and the bottom surfaces are subjected to uniaxial tension. For the diffusion subproblem, the concentration at the circular hole is maintained at 1, whereas at the boundary of the square plate is 0.

The tensile strain is assumed to be predominant, and then all the parameters are assumed as follows.

$$\theta = \frac{\pi}{3},\ \eta_T = 10,\ \eta_S = 1,\ d_1 = 2\times 10^5,\ d_2 = 1,\ d_1^T = 1\times 10^6,\ d_2^T = 2,\ d_1^S = 5\times 10^5,$$
$$d_2^S = 2,\ \rho = 1\times 10^3,\ g = 10,\ c_{\text{ref}} = 1,\ \lambda_0 = \mu_0 = 1\times 10^6,\ \lambda_1 = \mu_1 = 9\times 10^5 \tag{3.3}$$

The regular mesh and metric-based mesh for the plate have been depicted in 5. The restriction on the metric-based mesh is still the inverse of $\mathbf{D}_0$. Newton Raphson method cannot solve this problem using either regular mesh or metric-based mesh. The concentration distribution results have been described in Figure 6.

3.3. Concrete beam with cracks. Since there is always several cracks in the concrete beam in practice, we will study the behavior of a cantilever beam with several random generated cracks under self-weight. The length of the beam is 5.0 and the height is 2.0. For the beam, the boundary condition for deformation subproblem is that the left end of beam is fixed, and other edges are traction free. For the diffusion subproblem, the concentration at the left edge is maintained at 1, whereas at other sides of the beam is 0. As for the cracks, all the surfaces are traction free and diffusion flux free.

The tensile strain is assumed to be predominant, and then all the parameters are assumed as follows.

$$\theta = \frac{\pi}{3},\ \eta_T = 10,\ \eta_S = 10,\ d_1 = 1\times 10^{12},\ d_2 = 1,\ d_1^T = 2\times 10^{12},\ d_2^T = 5,$$
$$d_1^S = 1.5\times 10^{12},\ d_2^S = 2,\ \rho = 2.4\times 10^3,\ g = 10,\ c_{\text{ref}} = 1,$$
$$\lambda_0 = 10^{10},\ \mu_0 = 2\times 10^{10},\ \lambda_1 = 9\times 10^{10},\ \mu_1 = 1.8\times 10^{10} \tag{3.4}$$

The regular mesh and metric-based mesh for the beam have been depicted in 8. The restriction on the metric-based mesh is still the inverse of $\mathbf{D}_0$. Newton Raphson method cannot solve this

problem using either regular mesh or metric-based mesh. The concentration distribution results have been described in Figure 9.

TABLE 2. Concrete beam with cracks: Comparison of three methods

Method	Number of elements	Number of nodes	Condition number of stiffness		Healing index	Minimum concentration
			Deformation subproblem	Diffusion subproblem		
Standard Galerkin	924	514	736183.57	9472.80	49.22	-0.0645
Metric-based mesh	10506	5863	115979203.94	12726536.93	16.60	-0.0249
Non-negative formulation	924	514	741879.48	9472.80	0	0

From the above results, we can see that: first, the negative concentration area in the Galerkin method using regular mesh is extended in this case. Although the metric-based mesh reduced the area effectively, the negative concentration values still exist. Second, the maximum displacements in Galerkin method using metric-based mesh are smaller than those obtained by non-negative formulation. Last but not least, the number of elements and nodes in metric-based mesh is much bigger than the regular mesh, which implies the computational complexity of Galerkin method using the metric-based mesh.

4. CONCLUDING REMARKS

In this paper, a chemical degradation under small strain and isothermal condition is derived, which provides a thermodynamic status of the degradation model proposed by Mudunuru and Nakshatrala. Since there are two methods to avoid the negative concentration generated by the standard Galerkin method, we compare the performance of this non-negative formulation with the Galerkin method based on metric-based mesh. Furthermore, we extend the non-negative formulation to 3D problem. The behavior of degrading slabs under self-weight is analyzed. The analytical solution has been obtained by semi-inverse method for an infinite degrading slab, whereas the numerical solution has been obtained for a finite-sized slab. The comparison between them has been conducted. From the results, we can conclude as follows.

(i) The metric-based mesh can reduce the negative concentration values effectively, however, they still exist.
(ii) The Galerkin method based on metric-based mesh cannot simulate the deformation subproblem very well.
(iii) The analytical solution can not simulate the materials with isotropic or anisotropic diffusivity appropriately.
(iv) The assumption of zero displacement in x and y directions is another significant limitation of the semi-inverse method. For large structures in reality, especially the anisotropic materials, the deformations along x and y directions can not be ignored.
(v) The deformation in z direction is not uniformly distributed on the plane, as the analytical solution assumed. Moreover, the maximum deformation can occur on the edge of the slab.

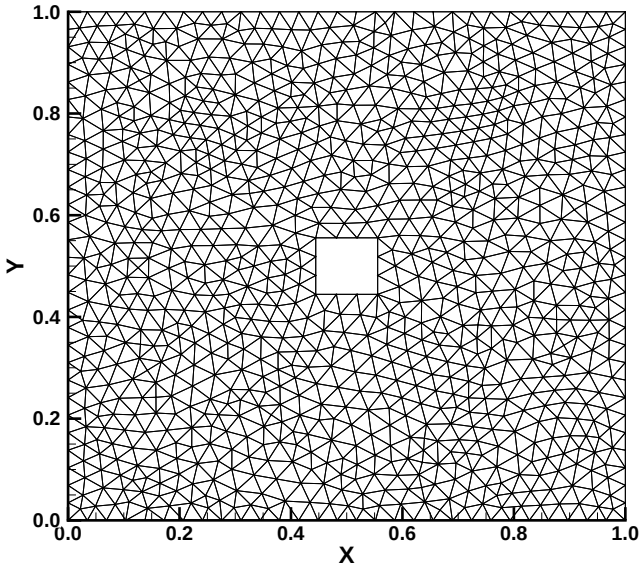

(a) The regular mesh.

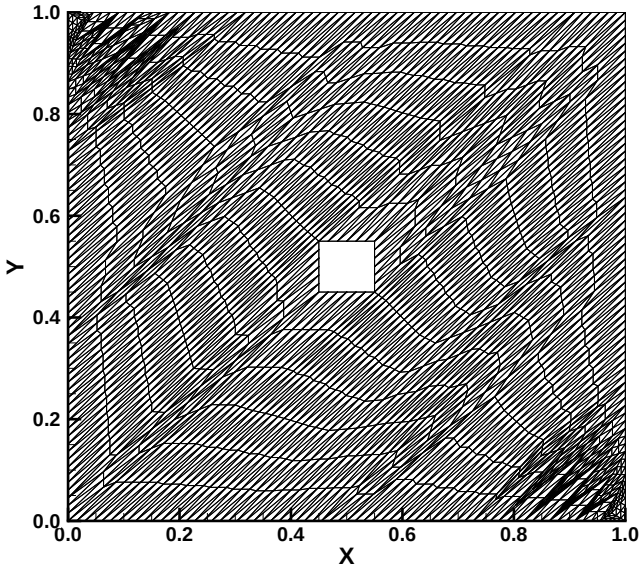

(b) The metric-based mesh.

FIGURE 1. Square plate with a hole: This figure shows the computational meshes employed in the numerical simulation. The regular mesh is a Delaunay-type mesh generated using Gmsh [**1**]. The metric-based mesh is generated using FreeFem++ corresponding to the diffusivity tensor given by equation (3.1a).

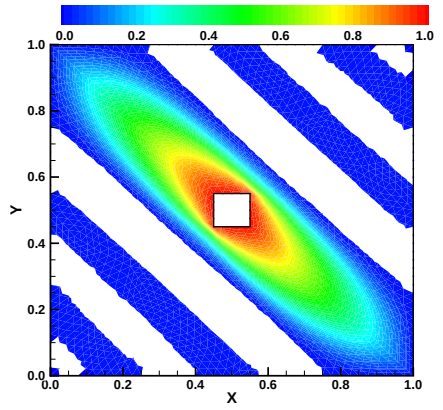

(a) Newton Raphson method using the regular mesh.

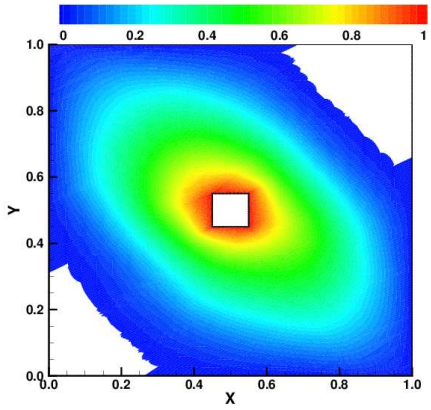

(b) Newton Raphson method using the metric-based mesh.

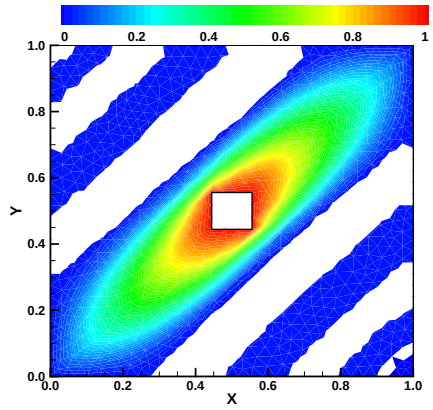

(c) Galerkin formulation using the regular mesh.

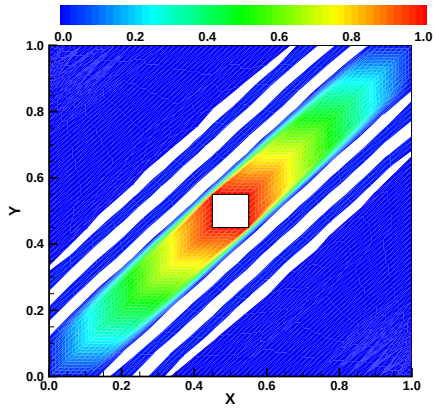

(d) Galerkin formulation using the metric-based mesh.

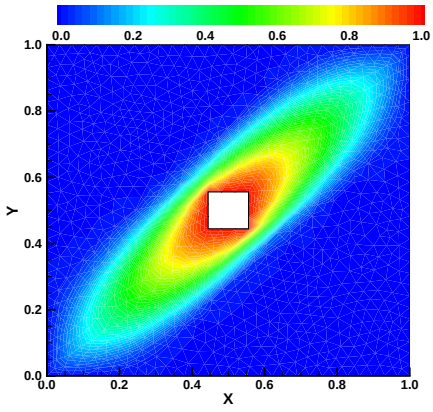

(e) Non-negative formulation using the regular mesh.

FIGURE 2. Square plate with a hole: This figure compares the concentration profiles obtained using the Newton Raphson method, Galerkin formulation and the non-negative formulation. The computational meshes (the regular and metric-based meshes) are shown in Figure 1.

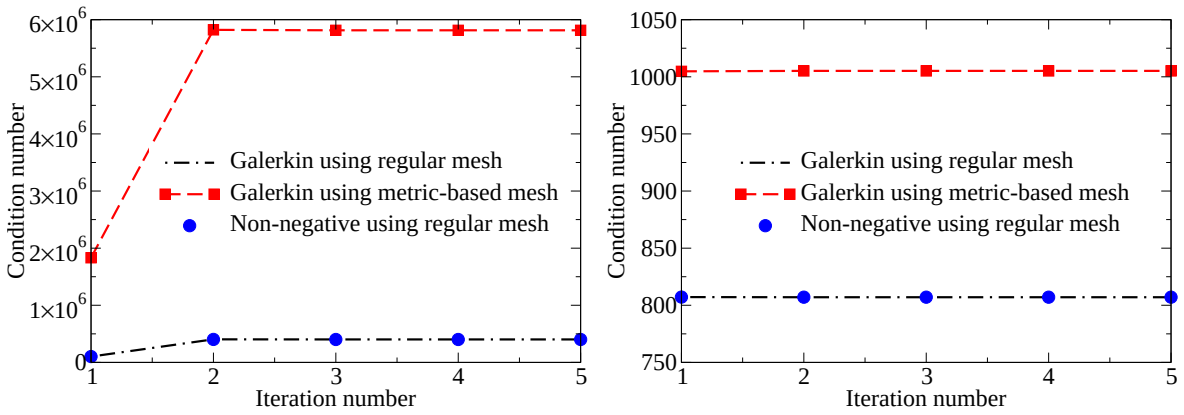

(a) Deformation subproblem

(b) Diffusion subproblem

FIGURE 3. Square plate with a hole: The variation of condition number with iterations for deformation and diffusion subproblems under the Galerkin formulation and the non-negative formulation. From this figure, it evident that metric-based meshed give rise to matrices with large condition numbers, particularly for the deformation subproblem. This substantiates one of the main conclusions of this paper: *metric-based meshes, which work well for anisotropic diffusion equations, may not produce accurate results for the deformation subproblem.*

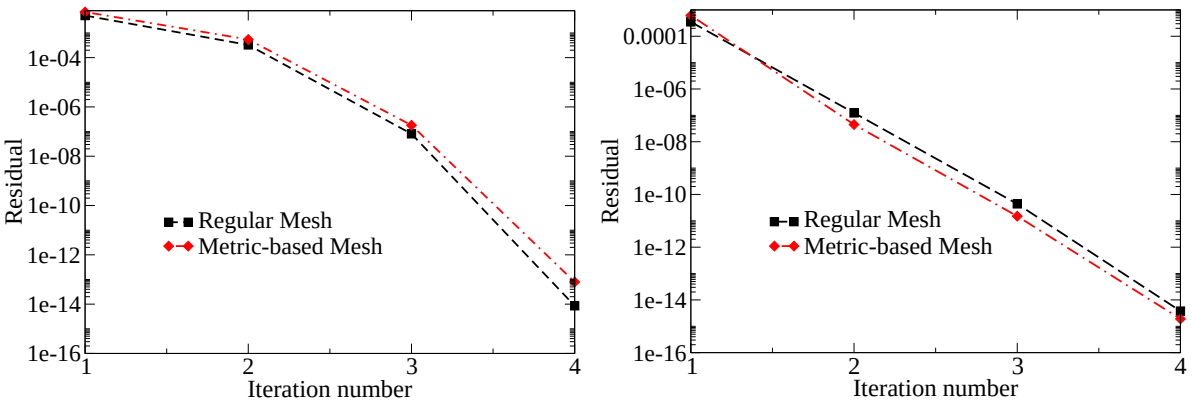

(a) Square plate with square hole.

(b) Square plate with circle hole.

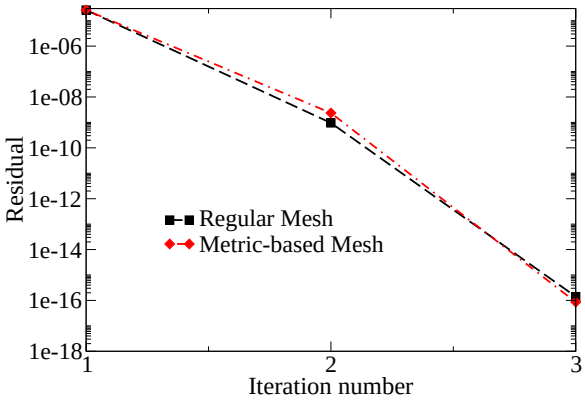

(c) Concrete beam with cracks.

FIGURE 4. This figure compares the residual obtained using the Newton Raphson method. The computational meshes (the regular and metric-based meshes) are shown in Figure 1, Figure 5, and Figure 8.

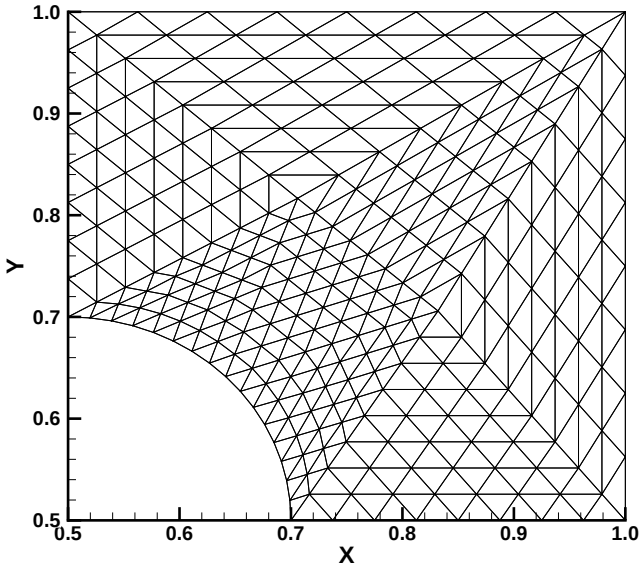

(a) The regular mesh.

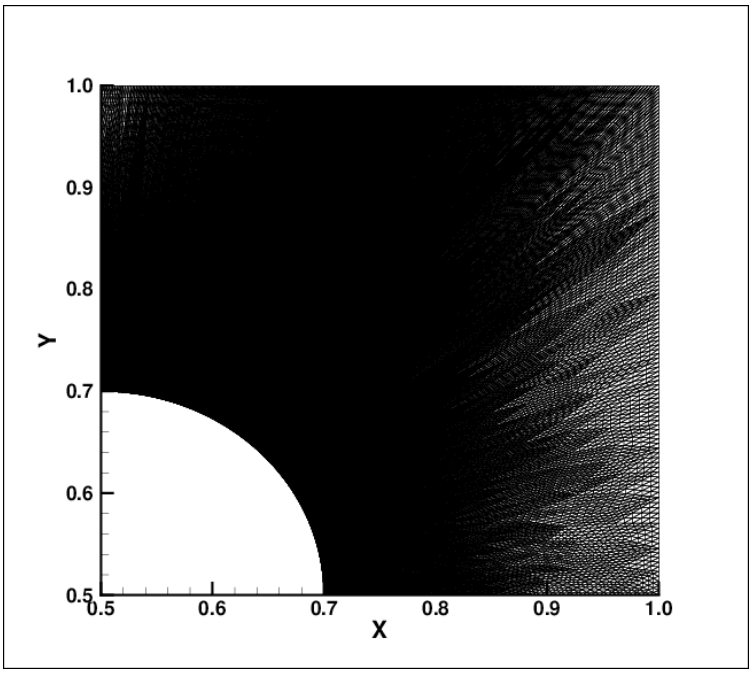

(b) The metric-based mesh.

FIGURE 5. Plate with a circular hole: This figure shows the computational meshes employed in the numerical simulation. The regular mesh is a Delaunay-type mesh generated using Gmsh [**1**]. The metric-based mesh is generated using FreeFem++ corresponding to the diffusivity tensor given by equation (3.1a).

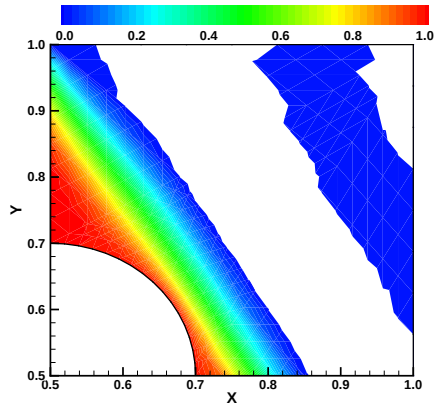

(a) Newton Raphson method using the regular mesh.

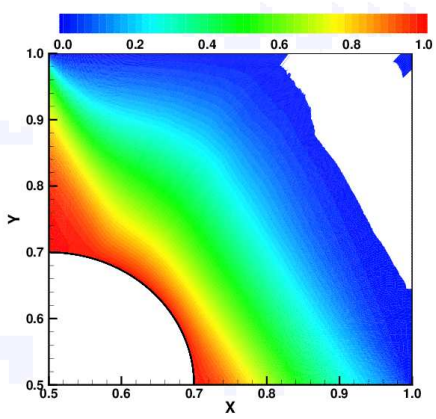

(b) Newton Raphson using the metric-based mesh.

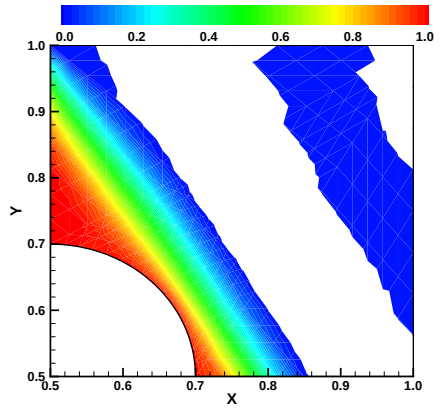

(c) Galerkin formulation using the regular mesh.

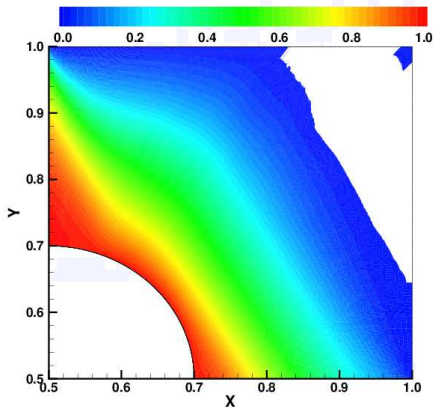

(d) Galerkin formulation using the metric-based mesh.

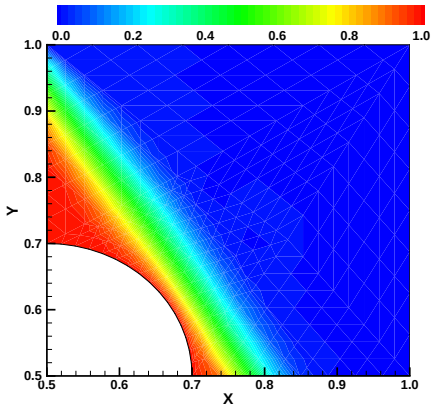

(e) Non-negative formulation using the regular mesh.

FIGURE 6. Plate with a circular hole: This figure compares the concentration profiles obtained using the Galerkin formulation and the non-negative formulation. The computational meshes (the regular and metric-based meshes) are shown in Figure 5.

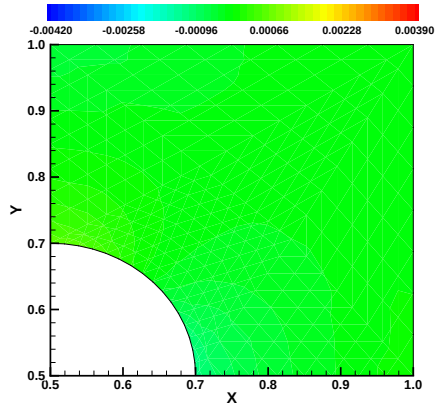

(a) Strain: Without degradation.

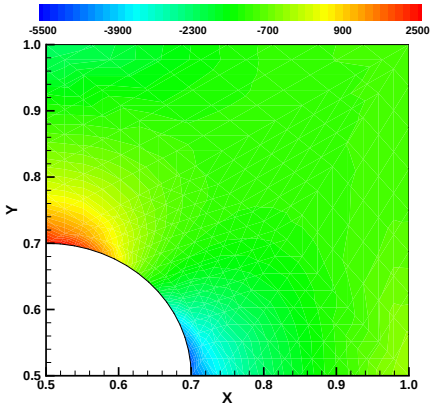

(b) Stress: Without degradation.

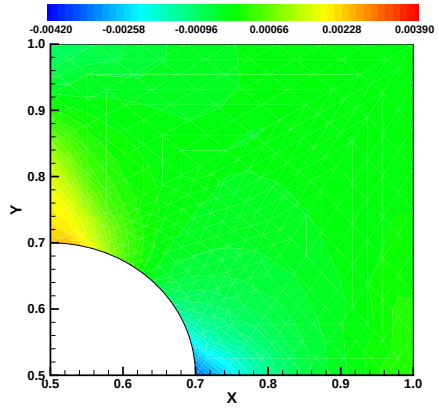

(c) Strain: Galerkin formulation using the regular mesh.

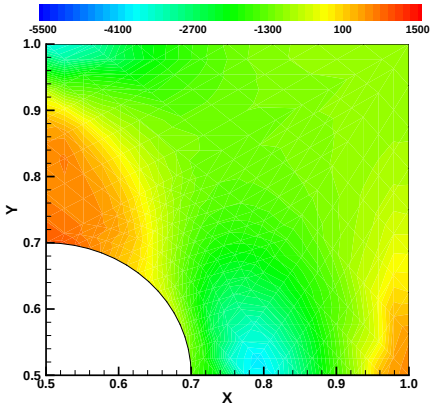

(d) Stress: Galerkin formulation using the regular mesh.

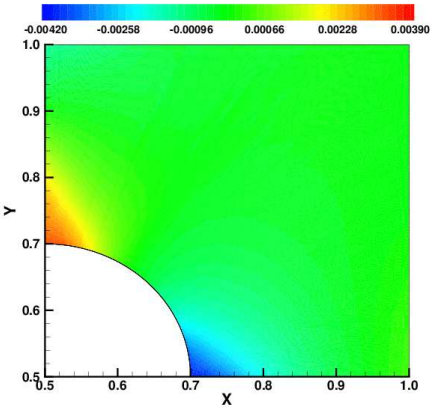

(e) Strain: Galerkin formulation using the metric-based mesh.

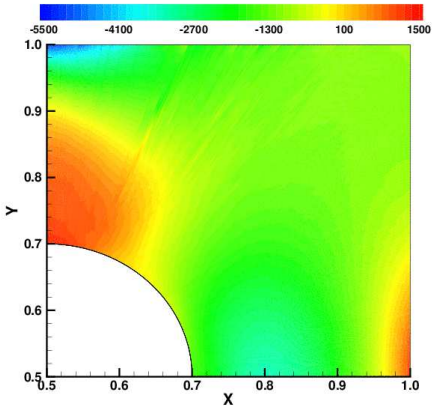

(f) Stress: Galerkin formulation using the metric-based mesh.

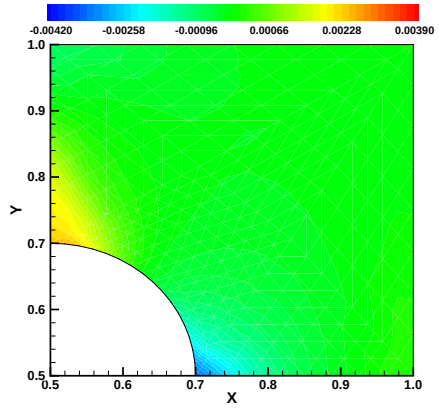

(g) Strain: Newton Raphson method using the regular mesh.

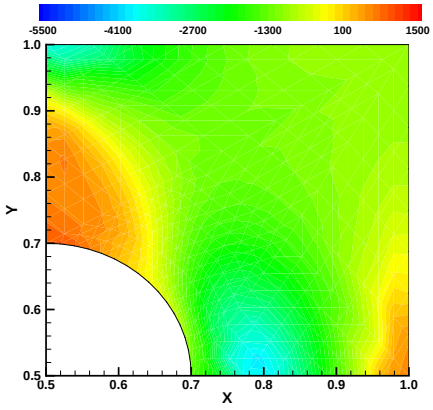

(h) Stress: Newton Raphson method using the regular mesh.

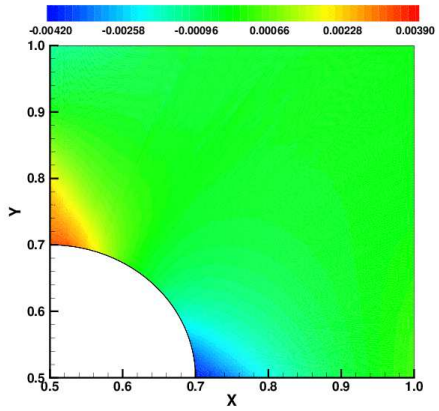

(i) Strain: Newton Raphson using the metric-based mesh.

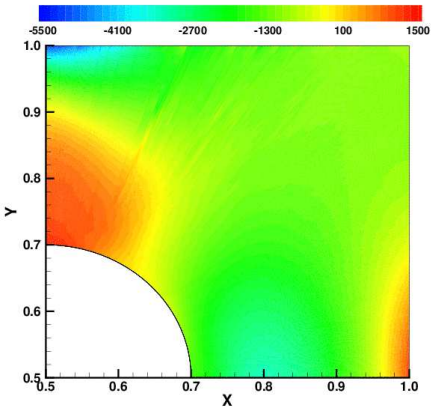

(j) Stress: Newton Raphson using the metric-based mesh.

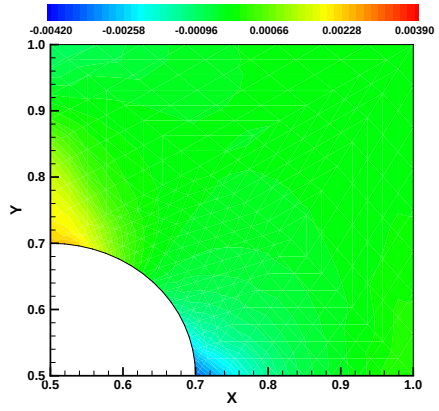

(k) Strain: Non-negative formulation using the regular mesh.

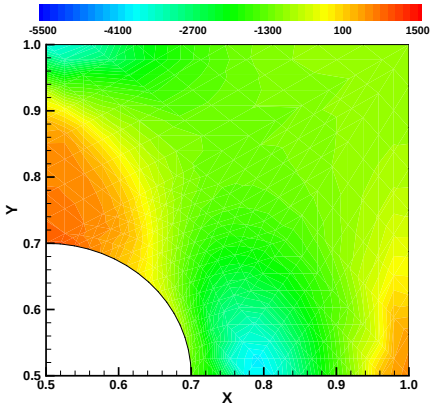

(l) Stress: Non-negative formulation using the regular mesh.

FIGURE 7. Plate with a circular hole: This figure compares the contours of trace of stress obtained using the Galerkin formulation and the non-negative formulation. The computational meshes (the regular and metric-based meshes) are shown in Figure 5.

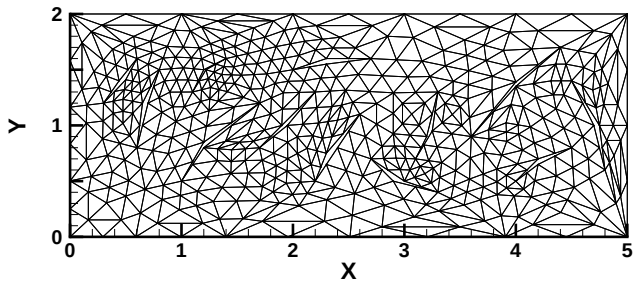

(a) The regular mesh.

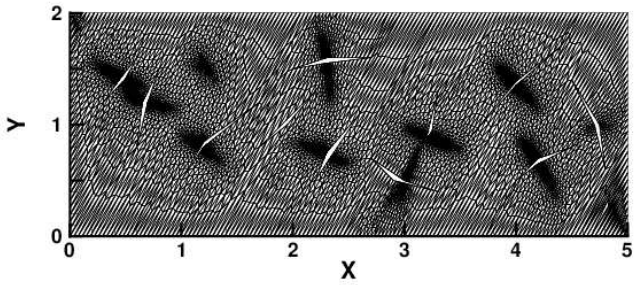

(b) The metric-based mesh.

FIGURE 8. Concrete beam with cracks: This figure shows the computational meshes employed in the numerical simulation. The regular mesh is a Delaunay-type mesh generated using Gmsh [**1**]. The metric-based mesh is generated using FreeFem++ corresponding to the diffusivity tensor given by equation (3.1a).

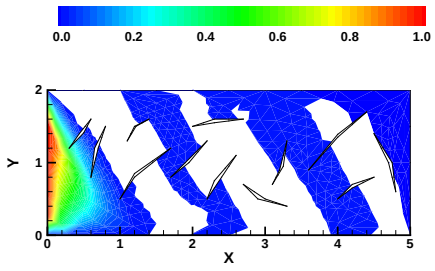

(a) Newton Raphson method using the regular mesh.

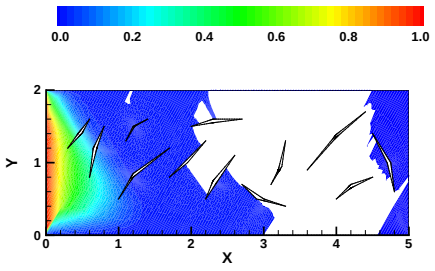

(b) Galerkin formulation using the metric-based mesh.

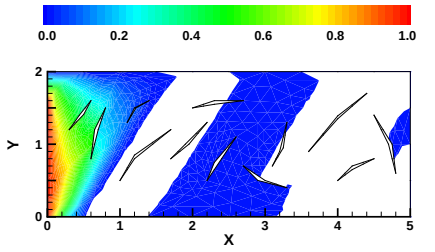

(c) Galerkin formulation using the regular mesh.

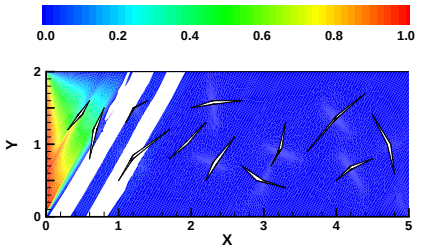

(d) Galerkin formulation using the metric-based mesh.

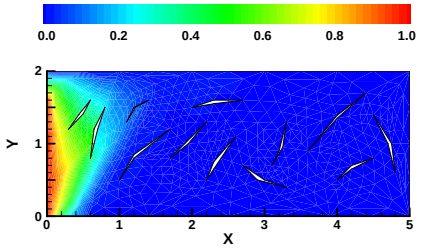

(e) Non-negative formulation using the regular mesh.

FIGURE 9. Concrete beam with cracks: This figure compares the concentration profiles obtained using the Galerkin formulation and the non-negative formulation. The computational meshes (the regular and metric-based meshes) are shown in Figure 8.

On mesh restrictions to satisfy maximum principles, comparison principles, and the non-negative constraint for a general linear second-order elliptic equation

Research highlights

- Various versions of discrete comparison principles and their relationship to discrete maximum principles and non-negative constraint are discussed.
- Necessary and sufficient conditions on stiffness matrix $\boldsymbol{K}$ to satisfy discrete weak and strong comparison principles for a general linear uniformly elliptic partial differential equation are constructed.
- A general relationship between various discrete comparison principles, discrete maximum principles, and non-negative constraint within the context of mesh restrictions, numerical formulations, and post-processing methods are discussed.
- Various important aspects of numerical solution spaces pertinent to different discrete properties are provided.
- Pros and cons of using nonobtuse, acute, well-centered triangulations for heterogeneous isotropic diffusivity and anisotropic $\mathcal{M}$-uniform meshes (which are constructed based on a *Riemannian metric tensor* depending on the components of anisotropic diffusivity tensor) for heterogeneous anisotropic diffusivity to satisfy various discrete properties are discussed in detail.
- Finally, two different methodologies are proposed to extend the numerical framework of a general linear second-order elliptic partial differential equation to a general semilinear and quasilinear second-order elliptic partial differential equations of monotone type.

Abstract

In this research report, we derive restrictions for three-node triangular (T3) element and a four-node quadrilateral (Q4) element to satisfy comparison principles, maximum principles, and the non-negative constraint for a general linear second-order elliptic equation under the standard single-field Galerkin formulation. It is well-known that an acute-angled triangle or (in some cases) a right-angled triangle is sufficient to satisfy the discrete weak maximum principle for *isotropic* diffusion. Herein, we show that this condition can be either too restrictive or not sufficient to satisfy various discrete maximum principles, discrete comparison principles, and the non-negative constraint for a general linear second-order elliptic equation. We shall also pictorially show that the feasible region for T3 and Q4 elements to satisfy various discrete principles is based on a metric tensor whose components are a function of anisotropic diffusivity tensor, velocity field, and linear reaction coefficient with respect to a suitable coordinate system. Finally, we critically review some of the recent developments in the field of discrete maximum principles, derive new results, and shed light on to the possible future developments on this research area.

5. INTRODUCTION AND MOTIVATION

Diffusion-type equations are commonly encountered in various branches of engineering, sciences, and even in economics [**14**]. These equations have been well-studied in Applied Mathematics, and several properties and estimates have been derived [**15**,**35**]. Numerous numerical formulations have been proposed and their performance has been analyzed both theoretically and numerically (e.g.,

see [**17**]). Several sophisticated software packages, such as ABAQUS [**2**], ANSYS [**3**], COMSOL [**4**], and MATLAB's PDE Toolbox [**5**], have been developed to solve these types of equations. This report is concerned with numerical solutions for anisotropic advection-diffusion-reaction equations. Despite the aforementioned advances, it should be noted that a numerical solution always loses some mathematical properties that the exact solution possesses. In particular, the aforementioned software packages and popular numerical formulations do not satisfy the so-called discrete comparison principles (DCP), discrete maximum principles (DMP), and the non-negative constraint (NC).

5.1. Mesh restrictions and time step constraints. The first approach is to place restrictions on the mesh to meet maximum principles and the non-negative constraint. For isotropic homogeneous diffusivity, Ciarlet and Raviart [**13**] have shown that numerical solutions based on the single-field Galerkin finite element formulation, in general, does not converge *uniformly*. It should however be noted that the single-field Galerkin formulation is a converging scheme. Ciarlet and Raviart have also shown that a sufficient condition for single-field Galerkin formulation to converge uniformly for *isotropic* diffusion is to employ a well-centered three-node triangular elements with low-order interpolation. The obvious advantage of this approach is that one can use the single-field Galerkin formulation without any modification. The drawback is that an appropriate computational mesh may not exist because of the required restrictions on the shape and size of the finite element. For example, it is a herculean task (sometimes impossible) to generate a well-centered triangular mesh for any given two-dimensional domain [**42**]. Note that requiring a mesh to be well-centered is a more stringent requirement than requiring the mesh to be Delaunay. In the scientific literature one can find numerous commercial and open-source mesh generators that produce premium quality structured and unstructured meshes for various complicated domains. For example, see the survey report by Owen [**34**], which accounts for more than 70 unstructured mesh generation software products. However, the use of these mesh generators in the area of numerical analysis and engineering, in particular, to construct mesh restrictions for diffusion-type equations to satisfy DCPs, DMPs, and NC is hardly known.

5.2. Non-negativity, monotone, and monotonicity preserving numerical formulations. The second approach is mainly concerned with developing new innovative numerical methodologies based on certain *physical and variational principles* so that they satisfy DCPs, DMPs, and NC. Broadly, these methods can be classified into the following three categories:

- *Non-negative formulations*: A numerical method belongs to the class of non-negative formulations if the resulting numerical solution satisfies certain DMPs and NC.
- *Monotone formulations*: A numerical method is said to be monotone if the resulting numerical solution satisfies certain DMPs, DCPs, and NC.
- *Monotonicity preserving formulations*: A numerical formulation is said to monotonicity preserving if the resulting numerical solution does not exhibit spurious oscillations within itself.

It is evident from the above set of definitions that a non-negative formulation need not satisfy a monotone condition and a monotone numerical method may not be monotonicity preserving. A general relationship between non-negative formulations, monotone formulations, and monotonicity preserving formulations is pictorially described in Figure 10.

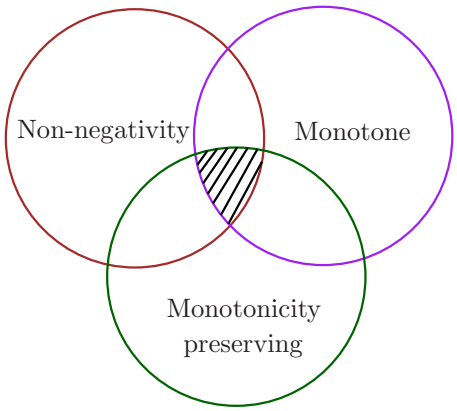

FIGURE 10. Non-negativity, monotone, and monotonicity preserving numerical formulations: A pictorial description of various class of numerical formulations satisfying certain discrete properties. The shaded region in the Venn diagram represents a set of formulations for which the numerical solutions obeys all the three important properties. Typically, designing a numerical methodology so that it falls in to the shaded region category is still an open problem.

5.3. Post-processing methods. The third approach is post-processing (PP) based methods. In literature, there are various types of PP methods which can be used to recover certain discrete properties for diffusion type equations. Some of the research works in this direction include

- Local and global remapping/repair methods (e.g., see [**23**]
- Constrained monotonic regression based methods [**11**].
- Cutoff methods (also known as the clipping methods) [**22**, **27**].
- A combination of remapping/repair methods and cutoff methods [**44**, **45**].

It needs to be emphasized that *a posterior cutoff analysis* is a serious variational crime. In general, this method is neither conservative nor satisfies DMPs and DCPs. The primary objective of this method is to cutoff the values of a numerical solution if it is less than a given number (which is the cutoff value). Hence, it is called as the cutoff method. In case of highly anisotropic diffusion problems and for distorted meshes this method predicts erroneous numerical results [**32**, **33**]. By specifying the cutoff value to be zero, it is always guaranteed to satisfy NC through this methodology. In addition, if nature of the solution is known aprior, then one can also prevent undershooting and overshooting of the numerical solution by chopping off those values.

Herein, we shall focus on the first approach. In particular, we shall derive sufficient conditions for restrictions on the three-node triangle finite elements to meet comparison principles, maximum principles, and the non-negative constraint in the case of heterogeneous anisotropic advection-diffusion-reaction equations.

6. LINEAR SECOND-ORDER ELLIPTIC EQUATION AND ASSOCIATED MATHEMATICAL PRINCIPLES

Let $\Omega \subset \mathbb{R}^{nd}$ be a open bounded domain, where "nd" denotes the number of spatial dimensions. The boundary of the domain is denoted by $\partial\Omega$, which is assumed to be piecewise smooth. Mathematically, $\partial\Omega := \overline{\Omega} - \Omega$, where a superposed bar denotes the set closure. A spatial point is denoted by $\mathbf{x} \in \overline{\Omega}$. The gradient and divergence operators with respect to $\mathbf{x}$ are, respectively,

denoted by grad[·] and div[·]. Let $c(\mathbf{x})$ denote the concentration field. We shall assume that Dirichlet boundary condition is prescribed (i.e., the concentration is prescribed) on the entire boundary. The remainder of this paper deals with the following boundary value problem, which is written in terms of a general linear second-order differential operator in *divergence form*:

$$\mathcal{L}[c] := -\text{div}\left[\mathbf{D}(\mathbf{x})\text{grad}[c(\mathbf{x})]\right] + \mathbf{v}(\mathbf{x}) \cdot \text{grad}[c(\mathbf{x})] + \alpha(\mathbf{x})c(\mathbf{x}) = f(\mathbf{x}) \quad \text{in } \Omega \tag{6.1a}$$

$$c(\mathbf{x}) = c^{\text{p}}(\mathbf{x}) \quad \text{on } \partial\Omega \tag{6.1b}$$

where $\mathcal{L}$ denotes the second-order linear differential operator, $f(\mathbf{x})$ is the prescribed volumetric source, $\alpha(\mathbf{x})$ is the linear reaction coefficient, $\mathbf{v}(\mathbf{x})$ is the velocity vector field, $\mathbf{D}(\mathbf{x})$ is the anisotropic diffusivity tensor, and $c^{\text{p}}(\mathbf{x})$ is the prescribed concentration. Physics of the problem demands that the diffusivity tensor (which is a second-order tensor) be symmetric. That is,

$$\mathbf{D}^{\text{T}}(\mathbf{x}) = \mathbf{D}(\mathbf{x}) \quad \forall \mathbf{x} \in \Omega \tag{6.2}$$

REMARK 6.1. *In mathematical analysis, the divergence form is a suitable setting for energy methods. However, some studies on maximum principles do employ the nondivergence form, which can be written as follows:*

$$\mathcal{L}[c] = \sum_{i,j=1}^{nd} (\mathbf{P})_{ij} \frac{\partial^2 c}{\partial x_i \partial x_j} + \sum_{i=1}^{nd} (\mathbf{q})_i \frac{\partial c}{\partial x_i} + r(\mathbf{x})c \tag{6.3}$$

where the coefficient $(\mathbf{P})_{ij}$, $(\mathbf{q})_i$, *and* $r(\mathbf{x})$, *which can be related to the physical quantities such as the diffusivity tensor, velocity field, and linear reaction coefficient. It should be, however, noted that the nondivergence form exists irrespective of differentiability of the diffusivity tensor. If* $\mathbf{D}(\mathbf{x})$ *is continuously differentiable, then there exists a one-to-one correspondence between the divergence form and the nondivergence form. In such cases, the operator* $\mathcal{L}$ *in the divergence form given by equation* (6.1a) *can be put into the following nondivergence form [**15**, Chapter 6]:*

$$\mathcal{L}[c] = -\mathbf{D}(\mathbf{x}) \cdot \text{grad}\left[\text{grad}[c(\mathbf{x})]\right] + (\mathbf{v}(\mathbf{x}) - \text{div}\left[\mathbf{D}(\mathbf{x})\right]) \cdot \text{grad}[c(\mathbf{x})] + \alpha(\mathbf{x})c(\mathbf{x}) \tag{6.4}$$

where we have used the following identity in combination with equation (6.2) *to obtain equation* (6.4)

$$\text{div}\left[\mathbf{D}^{\text{T}}(\mathbf{x})\text{grad}[c(\mathbf{x})\right] = \mathbf{D}(\mathbf{x}) \cdot \text{grad}\left[\text{grad}[c(\mathbf{x})]\right] + \text{div}\left[\mathbf{D}(\mathbf{x})\right] \cdot \text{grad}[c(\mathbf{x})] \tag{6.5}$$

Based on the nature of the coefficients and connectedness of the physical domain, different versions of maximum and comparison principles exist in the mathematical literature [**15**,**16**,**36**,**37**]. As stated earlier in this paper, we shall restrict ourselves to the boundary value problem given by the equations (6.1a)–(6.1b). Further analysis pertaining to Neumann boundary conditions and mixed boundary conditions within the context of maximum principles, comparison principles, and the non-negative constraint is beyond the scope of this paper.

We shall say that the operator $\mathcal{L}$ is *elliptic* at a point $\mathbf{x} \in \Omega$ if

$$0 < \lambda_{\min}(\mathbf{x})\boldsymbol{\xi} \cdot \boldsymbol{\xi} \leq \boldsymbol{\xi} \cdot \mathbf{D}(\mathbf{x})\boldsymbol{\xi} \leq \lambda_{\max}(\mathbf{x})\boldsymbol{\xi} \cdot \boldsymbol{\xi} \quad \forall \boldsymbol{\xi} \in \mathbb{R}^{nd} \backslash \{\mathbf{0}\} \tag{6.6}$$

where $\lambda_{\min}(\mathbf{x})$ and $\lambda_{\max}(\mathbf{x})$ are, respectively, the minimum and maximum eigenvalues of $\mathbf{D}(\mathbf{x})$. The operator $\mathcal{L}$ is said to be *strictly elliptic* if there exists a constant λ_0 such that

$$0 < \lambda_0 \leq \lambda_{\min}(\mathbf{x}) \quad \forall\, \mathbf{x} \in \Omega \tag{6.7}$$

and *uniformly elliptic* if

$$0 < \frac{\lambda_{\max}(\mathbf{x})}{\lambda_{\min}(\mathbf{x})} < +\infty \quad \forall\, \mathbf{x} \in \Omega \tag{6.8}$$

In the studies on maximum principles, it is common to impose the following restrictions on the velocity field $\mathbf{v}(\mathbf{x})$ and the reaction coefficient $\alpha(\mathbf{x})$:

$$\alpha(\mathbf{x}) \geq 0 \quad \forall\, \mathbf{x} \in \Omega \tag{6.9a}$$

$$\alpha(\mathbf{x}) - \frac{1}{2}\mathrm{div}\,[\mathbf{v}(\mathbf{x})] \geq 0 \quad \forall\, \mathbf{x} \in \Omega \tag{6.9b}$$

$$0 \leq \frac{|(\mathbf{v}(\mathbf{x}))_i|}{\lambda_{\min}(\mathbf{x})} \leq \beta_0 < +\infty \quad \forall\, \mathbf{x} \in \Omega \quad \text{and} \quad \forall\, i = 1, \cdots, nd \tag{6.9c}$$

where β_0 is a bounded non-negative constant. If $(\mathbf{D})_{ij}$ and $(\mathbf{v})_i$ are continuous in Ω, then the operator $\mathcal{L}$ is uniformly elliptic for any bounded subdomain $\Omega^{'} \subset\subset \Omega$ (which means that $\Omega^{'}$ is *compactly embedded* in Ω) and the condition given in equation (6.9c) holds. The restrictions given in equation (6.9b) can be relaxed in some situations (e.g., see references [**21**,**26**]). But the constraint on $\alpha(\mathbf{x})$ given by equation (6.9a) cannot be relaxed. If $\alpha(\mathbf{x}) < 0$ then equation (6.1a) is referred to as Helmholtz-type equation, which does not posses a maximum principle. From the theory of partial differential equations, it is well-known that the aforementioned boundary value problem given by equations (6.1a)–(6.1b) satisfies the so-called (weak and strong) comparison principles, (weak and strong) maximum principles, and the non-negative constraint. For future reference and for completeness, we shall briefly outline the main results. For a more thorough mathematical treatment, one could consult references [**15**, **16**, **35**].

THEOREM 6.2 (`Continuous weak and strict weak maximum principles`). *Let $\mathcal{L}$ be a uniformly elliptic operator satisfying the conditions given by equations* (6.9a)–(6.9c)*. In addition, let $\mathbf{D}(\mathbf{x})$ be continuously differentiable. Suppose that $c(\mathbf{x}) \in C^2(\Omega) \cap C^0(\overline{\Omega})$ satisfies the differential inequality $\mathcal{L}[c] \leq 0$ in Ω, then the maximum of $c(\mathbf{x})$ in $\overline{\Omega}$ is obtained on $\partial\Omega$. That is, $c(\mathbf{x})$ possesses the weak maximum principle (*wMP*), which can be written as follows:*

$$\max_{\mathbf{x}\in\overline{\Omega}} [c(\mathbf{x})] \leq \max \left[0, \max_{\mathbf{x}\in\partial\Omega} [c(\mathbf{x})]\right] \tag{6.10}$$

*Moreover, if $\alpha(\mathbf{x}) = 0$, then we have the strict weak maximum principle (*WMP*):*

$$\max_{\mathbf{x}\in\overline{\Omega}} [c(\mathbf{x})] = \max_{\mathbf{x}\in\partial\Omega} [c(\mathbf{x})] \tag{6.11}$$

PROOF. For a proof see references [**15**, **16**]. □

Several results pertaining to mesh restrictions are provided in the next set of figures. More results can found in the forthcoming paper.

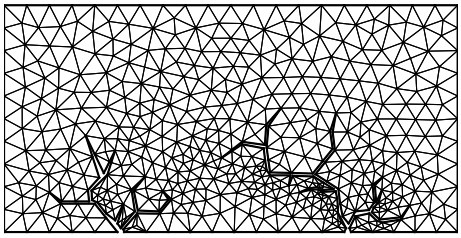

(a) Delaunay-Voronoi mesh: $Nv = 539$ and $Nele = 906$

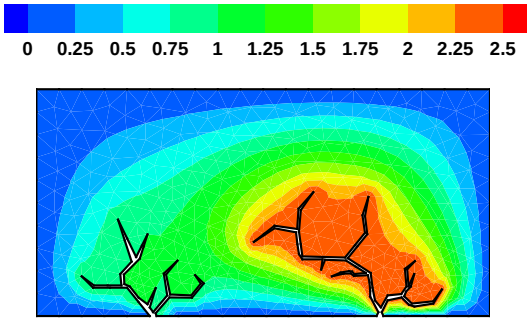

(b) $\mathbf{v} = (0, 0)$ and $\alpha = 0$

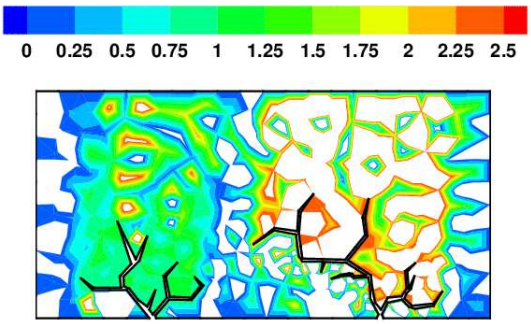

(c) $\mathbf{v} = (0.1, 1.0)$ and $\alpha = 0$

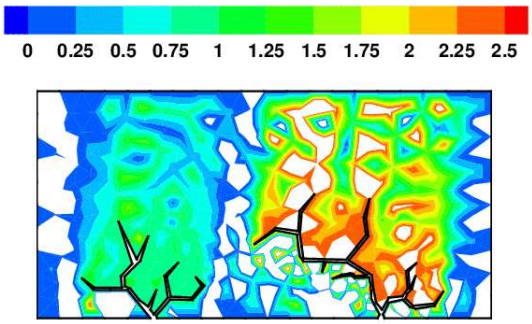

(d) $\mathbf{v} = (0.1, 1.0)$ and $\alpha = 1.0$

FIGURE 11. Test problem # 1: The top left figure shows a coarse triangulation used in the numerical study. The top right figure and the bottom two figures show the concentration profiles obtain for various values of velocity field and linear-reaction coefficient using this mesh. The white region in the figures indicate the area in which the value of concentration is negative and also violated the maximum constraint. The coarse Delaunay-Voronoi mesh obtained using the open source mesh generator Gmsh [**1**], satisfies NC and DMPs in case of pure diffusion. But this is not true for AD and ADR cases. In such scenarios, it produces unphysical values for concentration field. Moreover, the % of nodes that have violated the NC and maximum constraint is also very high.

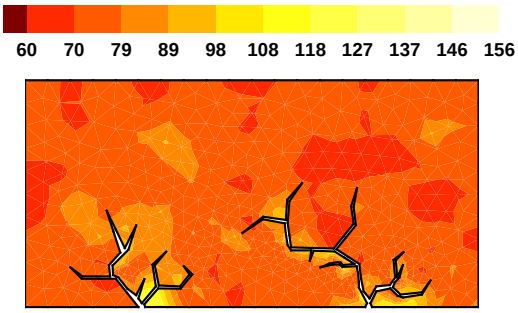

(a) Element maximum angles: $Nv = 539$ and $Nele = 906$

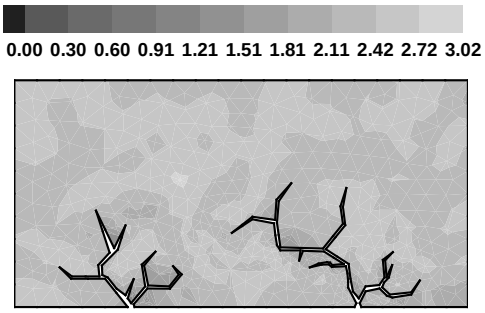

(b) Delaunay-type condition: $\mathbf{v} = (0, 0)$ and $\alpha = 0$

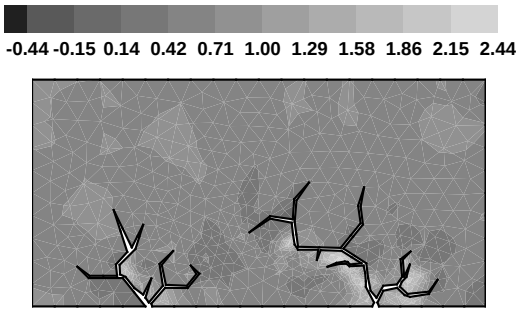

(c) Delaunay-type condition: $\mathbf{v} = (0.1, 1.0)$ and $\alpha = 0$

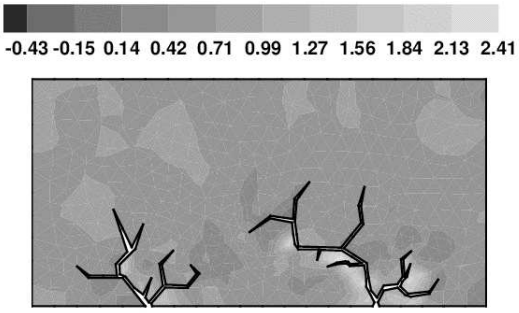

(d) Delaunay-type condition: $\mathbf{v} = (0.1, 1.0)$ and $\alpha = 1.0$

FIGURE 12. Test problem # 1: The top left figure shows the maximum angle possible in each element of the mesh. The top right figure and the bottom two figures show the *element maximum generalized Delaunay-type condition*, which is a weaker condition as compared to the *element maximum anisotropic nonobtuse angle condition*.

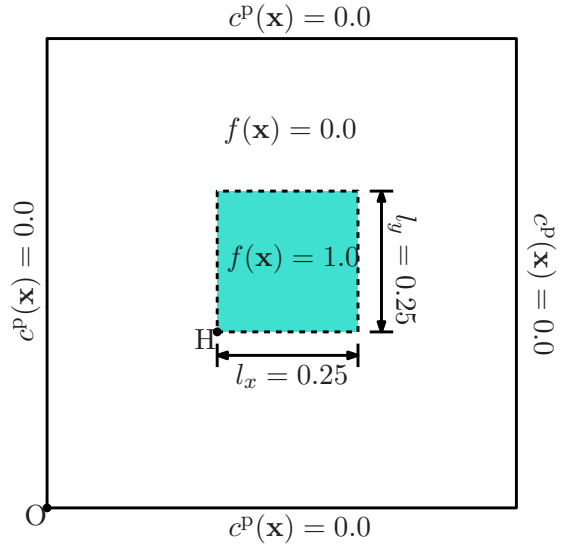

FIGURE 13. Test problem # 2: The computational domain under consideration is a bi-unit square with one of its vertices at origin $\mathrm{O} = (0, 0)$. Homogeneous Dirichlet boundary conditions are prescribed on all sides of the square. The volumetric source $f(\mathbf{x})$ is zero inside the domain except for the square region (including the boundaries) at vertex $\mathrm{H} = (0.375, 0.375)$. In this region, $f(\mathbf{x})$ is equal to unity. Herein, we assume that the velocity vector field and linear reaction coefficient are equal to zero everywhere in the computational domain.

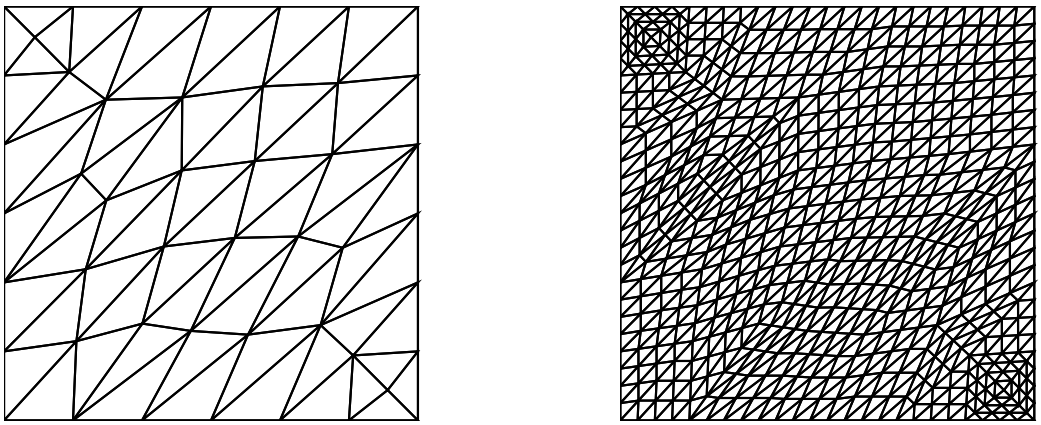

(a) Background mesh: $Nv = 47$ and $Nele = 68$

(b) Anisotropic triangulation: $Nv = 593$ and $Nele = 1088$

FIGURE 14. Test problem # 2: The left figure shows the background mesh on which BAMG operates to give an anisotropic triangulation, which is shown in the right figure. As the ratio of the minimum eigenvalue of anisotropic diffusivity tensor to its maximum is 0.1, which is not very high, so the resulting triangulation consists of a mixture of skinny and normal triangles.

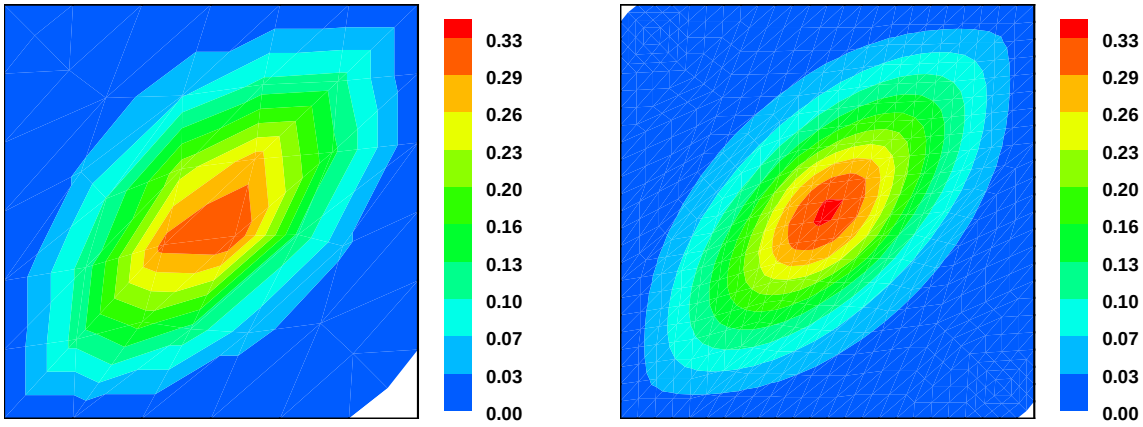

(a) Background mesh: $\mathbf{v} = (0, 0)$ and $\alpha = 0$ (b) Anisotropic triangulation: $\mathbf{v} = (0, 0)$ and $\alpha = 0$

FIGURE 15. Test problem # 2: This figure shows the concentration profile for pure anisotropic diffusion. Numerical simulations are performed based on the background mesh and anisotropic triangulation as shown in the Figure 14. The white region in the figures depicts the area in which the value of concentration is negative. As the mesh generator BAMG did not converge in `MaxIters`, the resulting mesh still violates the non-negative constraint. The minimum concentration and the percentage of nodes that have violated the non-negative constraint on the background mesh is about -4.8×10^{-5} and 2.13%. Correspondingly, these values on the anisotropic triangulation is around -1.35×10^{-8} and 0.34%. But it should be noted that this violation based on the anisotropic triangulation is very low as compared to that of the numerical results obtained using the background mesh.

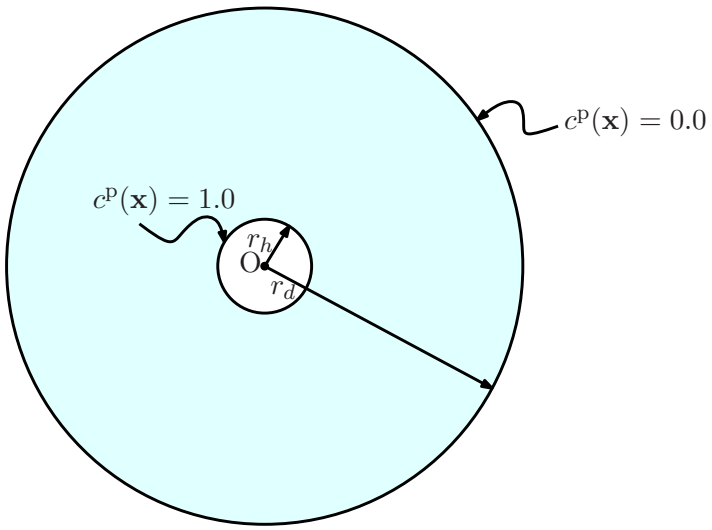

FIGURE 16. Test problem # 3: A pictorial description of the computational domain with relevant boundary conditions. The circular hole and the circular domain are centered at origin $\mathrm{O} = (0, 0)$. The radius of the circular hole and the circular domain are given by $r_h = 0.1$ and $r_d = 1.0$. Numerical simulations are performed for four different cases of velocity field and linear reaction coefficient, which are given by $\mathbf{v}(\mathbf{x}) = (0.0, 0.0)$ and $\alpha(\mathbf{x}) = 0.0$, $\mathbf{v}(\mathbf{x}) = (1.5, 1.0)$ and $\alpha(\mathbf{x}) = 1.0$, $\mathbf{v}(\mathbf{x}) = (5.0, 0.5)$ and $\alpha(\mathbf{x}) = 1.0$, and $\mathbf{v}(\mathbf{x}) = (0.0, 0.0)$ and $\alpha(\mathbf{x}) = 1000$.

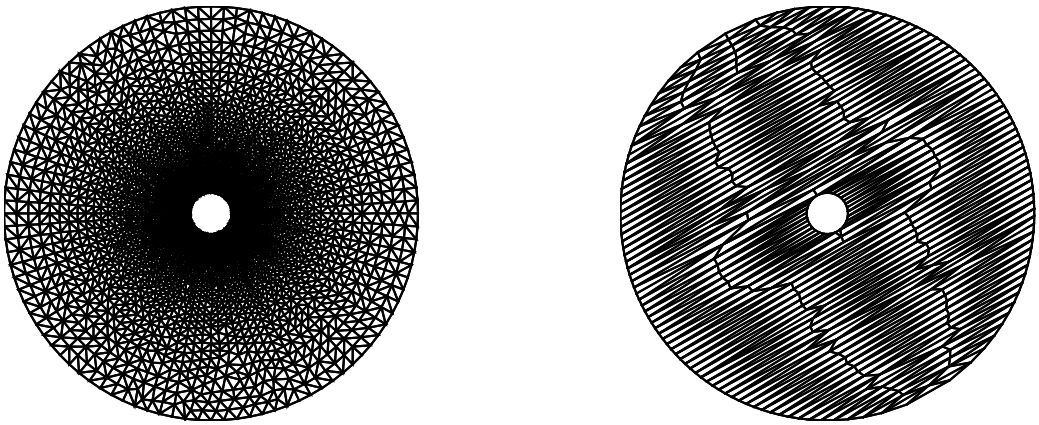

(a) Background mesh: $Nv = 5079$ and $Nele = 9918$ (b) Anisotropic triangulation: $Nv = 297$ and $Nele = 436$

FIGURE 17. Test problem # 3: The left figure shows the background mesh and the right figure shows the anisotropic triangulation obtained using BAMG for all the four cases. For this test problem, we obtain skinny triangles as the ratio of the minimum eigenvalue of $\mathbf{D}(\mathbf{x})$ to its maximum is 0.001, which is related to the aspect ratio of the sides of the triangle in the anisotropic mesh. Moreover, it is evident that the triangles in the mesh are aligned and oriented along the principal axis of the eigenvectors of the diffusivity tensor.

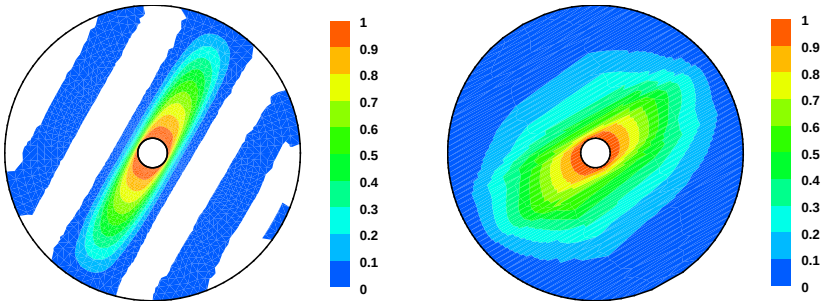

(a) Background mesh: $\mathbf{v} = (0, 0)$ and $\alpha = 0$

(b) Anisotropic triangulation: $\mathbf{v} = (0, 0)$ and $\alpha = 0$

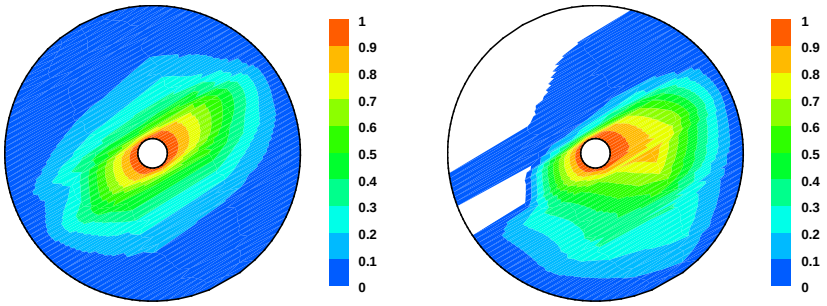

(c) Anisotropic triangulation: $\mathbf{v} = (1.5, 1.0)$ and $\alpha = 1.0$

(d) Anisotropic triangulation: $\mathbf{v} = (5.0, 0.5)$ and $\alpha = 1.0$

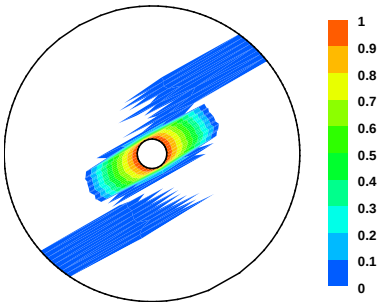

(e) Anisotropic triangulation: $\mathbf{v} = (0, 0)$ and $\alpha = 1000$

FIGURE 18. Test problem #3: This figure shows the concentration profiles for four different cases based on the background and anisotropic meshes shown in Figure 17. The white region in the figures (circular annulus) shows the area in which the value of concentration is negative. The minimum concentration and the percentage of nodes that have violated the non-negative constraint for the background mesh is about -1.67×10^{-2} and 30.28%. As the anisotropic mesh is coarse and the Algorithm did not converge in `MaxIters` for the advection-dominated advection-diffusion-reaction and reaction-dominated diffusion-reaction problems, the resulting mesh not only violates the non-negative constraint and but also produces spurious oscillations. The minimum concentration and the percentage of nodes that have violated the non-negative constraint for the case when $\mathbf{v} = (5.0, 0.5)$ and $\alpha = 1.0$ is about -1.78×10^{-1} and 13.47%, where as for the case when $\mathbf{v} = (0.0, 0.0)$ and $\alpha = 1000$ is around -2.79×10^{-1} and 20.54%. From these values, it is evident that the extent of this violation is very high for the reaction-dominated diffusion-reaction problems.

Bibliography

[1] *Gmsh: A three-dimensional finite element mesh generator with pre- and post-processing facilities*. URL: http://www.geuz.org/gmsh/.

[2] *ABAQUS/CAE/Standard, Version 6.8-3*. Simulia, Providence, Rhode Island, www.simulia.com, 2009.

[3] *ANSYS, Version 14.5*. ANSYS, Inc., Canonsburg, Pennsylvania, www.ansys.com, 2012.

[4] *COMSOL Multiphysics User's Guide, Version 4.3a*. COMSOL, Inc., Burlington, Massachusetts, www.comsol.com, 2012.

[5] *MATLAB 2012a*. The MathWorks, Inc., Natick, Massachusetts, USA, 2012.

[6] S. B. Adler. Chemical expansivity of electrochemical ceramics. *Journal of the American Ceramic Society*, 84:2117–2119, 2001.

[7] A. W. Batchelor, L. N. Lam, and M. Chandrasekaran. *Materials Degradation and Its Control by Surface Engineering*. Imperial College Press, London, UK, third edition, 2003.

[8] E. Blond and N. Richet. Thermomechanical modelling of ion–conducting membrane for oxygen separation. *Journal of the European Ceramic Society*, 28:793–801, 2008.

[9] H. Bouadi and C. T. Sun. Hygrothermal effects on the stress field of laminated composites. *Journal of Reinforced Plastics and Composites*, 8:40–54, 1989.

[10] R. M. Bowen. Theory of mixtures. In A. C. Eringen, editor, *Continuum Physics*, volume III. Academic Press, New York, 1976.

[11] O. Burdakov, I. Kapyrin, and Y. Vassilevski. Monotonicity recovering and accuracy preserving optimization methods for postprocessing finite element solutions. *Journal of Computational Physics*, 231:3126–3142, 2012.

[12] L. W. Cai and Y. Weitsman. Non–Fickian moisture diffusion in polymeric composites. *Journal of Composite Materials*, 28:130–154, 1994.

[13] P. G. Ciarlet and P-A. Raviart. Maximum principle and uniform convergence for the finite element method. *Computer Methods in Applied Methods and Engineering*, 2:17–31, 1973.

[14] J. Crank. *The Mathematics of Diffusion*. Clarendon press, Oxford, second edition, 1975.

[15] L. C. Evans. *Partial Differential Equations*. American Mathematical Society, Providence, Rhode Island, USA, 1998.

[16] D. Gilbarg and N. S. Trudinger. *Elliptic Partial Differential Equations of Second Order*. Springer, New York, USA, 2001.

[17] P. M. Gresho and R. L. Sani. *Incompressible Flow and the Finite Element Method: Advection-Diffusion*, volume 1. John Wiley & Sons, Inc., Chichester, UK, 2000.

[18] M. E. Gurtin. *An Introduction to Continuum Mechanics*. Academic Press, San Diego, USA, 1981.

[19] C. A. Harper. *Handbook of Plastics, Elastomers, & Composites*. McGraw–Hill, New York, USA, fourth edition, 2002.

[20] F. Hecht, S. Auliac, O. Pironneau, J. Morice, A. L. Hyaric, and K. Ohtsuka. *FreeFem++*. URL: http://www.freefem.org/ff++/, third edition, 2014. Version 3.26-2.

[21] W. Huang. Sign-preserving of principal eigenfunctions in P1 finite element approximation of eigenvalue problems of second-order elliptic operators. *arXiv:1306.1987*, 2013.

[22] C. Kreuzer. A note on why enforcing discrete maximum principles by a simple a posteriori cutoff is a good idea. *arXiv:1208.3958*, 2012.

[23] M. Kucharik, M. Shashkov, and B. Wendroff. An efficient linearity-and-bound-preserving remapping method. *Journal of Computational Physics*, 188:462–471, 2003.

[24] W. M. Lai, J. S. Hou, and V. C. Mow. A triphasic theory for the swelling and deformation behaviors of articular cartilage. *Journal of Biomechanical Engineering*, 113:245–258, 1991.

[25] X. Li and W. Huang. An anisotropic mesh adaptation method for the finite element solution of heterogeneous anisotropic diffusion problems. *Journal of Computational Physics*, 229(21):8072–8094, 2010.

[26] C. Lu, W. Huang, and J. Qiu. Maximum principle in linear finite element approximations of anisotropic diffusion-convection-reaction problems. *arXiv:1201.3564*, 2012.

[27] C. Lu, W. Huang, and E. S. V. Vleck. The cutoff method for the numerical computation of nonnegative solutions of parabolic PDEs with application to anisotropic diffusion and lubrication-type equations. *Journal of Computational Physics*, 242:24–36, 2013.

[28] G. A. Maugin. *The Thermomechanics of Nonlinear Irreversible Behaviours: An Introduction*. World Scientific Publishing Company, New Jersey, USA, 1998.

[29] A. N. Morozovska, E. A. Eliseev, A. K. Tagantsev, S. L. Bravina, L. Q. Chen, and S. V. Kalinin. Thermodynamics of electromechanically coupled mixed ionic–electronic conductors: Deformation potential, Vegard strains, and flexoelectric effect. *Physical Review B*, 83:195313(10), 2011.

[30] M. K. Mudunuru and K. B. Nakshatrala. A framework for coupled deformation-diffusion analysis with application to degradation / healing. *International Journal for Numerical Methods in Engineering*, DOI: 10.1002/nme.3282, 2011.

[31] E. R. Myers, W. M. Lai, and V. C. Mow. A continuum theory and an experiment for the ion–induced swelling behavior of articular cartilage. *Journal of Biomechanical Engineering*, 106:151–158, 1984.

[32] H. Nagarajan and K. B. Nakshatrala. Enforcing the non-negativity constraint and maximum principles for diffusion with decay on general computational grids. *International Journal for Numerical Methods in Fluids*, 67:820–847, 2011.

[33] K. B. Nakshatrala, M. K. Mudunuru, and A. J. Valocchi. A numerical framework for diffusion-controlled bimolecular-reactive systems to enforce maximum principles and non-negative constraint. *Journal of Computational Physics*, 253:278–307, 2013.

[34] S. J. Owen. A survey of unstructured mesh generation technology. In *7th International Meshing Roundtable, Sandia National Laboratory*, pages 239–267, 1998.

[35] C. V. Pao. *Nonlinear Parabolic and Elliptic Equations*. Springer-Verlag, New York, USA, 1993.

[36] P. Pucci and J. Serrin. The strong maximum principle revisited. *Journal of Differential Equations*, 196:1–66, 2004.

[37] P. Pucci and J. Serrin. *The Maximum Principle*. Birkhäuser Verlag, Basel, Switzerland, 2007.

[38] P. A. C. Raats. *Rational Thermodynamics*, chapter Applications of the theory of mixtures in soil physics, Appendix 5D, pages 326–343. Springer, 1984.

[39] G. C. Sih, J. G. Michopoulos, and S. C. Chou. *Hygrothermoelasticity*. Martinus Nijhoff Publishers, Dordrecht, The Netherlands, 1986.

[40] R. N. Swamy, editor. *The Alkali–Silica–Reaction in Concrete*. CRC Press, New York, USA, 2003.

[41] J. F. Ulm, O. Coussy, L. Kefei, and C. Larive. Thermo–chemo–mechanics of ASR expansion in concrete structures. *Journal of Engineering Mechanics*, 126:233–242, 2000.

[42] E. Vanderzee, A. N. Hirani, D. Guoy, and E. A. Ramos. Well-centered triangulation. *SIAM Journal on Scientific Computing*, 31:4497–4523, 2010.

[43] R. Černy and P. Rovnaníková. *Transport Processes in Concrete*. CRC Press, New York, USA, 2002.

[44] S. Wang, G. Yuan, Y. Li, and Z. Sheng. Discrete maximum principle based on repair technique for diamond type scheme of diffusion problems. *International Journal for Numerical Methods in Fluids*, 70:1188–1205, 2012.

[45] X. Zhao, Y. Chen, Y. Gao, C. Yu, and Y. Li. Finite volume element methods for nonequilibrium radiation diffusion equations. *International Journal for Numerical Methods in Fluids*, DOI: 10.1002/fld.3838, 2013.

[46] H. Ziegler. *An Introduction to Thermomechanics*. North Holland Publishing Company, Amsterdam, Netherlands, 1983.

Task 4: Mathematical and Computational Modeling of Deterioration Process

Senior personnel
Dr. Kalyana Babu Nakshatrala (***e-mail:*** knakshatrala@uh.edu)
University of Houston, Houston, Texas 77204.
Doctoral students
Can Xu & Maruti Mudunuru
Covering Period: October 1, 2014 through September 30, 2015

Date of Report: October 20, 2015
ID #: RPA-12-3545, Yearly Report Y3

Conferences talks / posters

C1a. S. Karimi, and K.B. Nakshatrala, "**On the development and performance of multi-time-step coupling methods for transient multi-scale problems**," *Experimental and Computational Nonlinear Dynamics* session, *51st SES Annual Technical Meeting*, Purdue University, October 1–3, 2014. [***Student poster competition***]

C1b. S. Karimi, and K.B. Nakshatrala, "**Monolithic multi-time-step coupling methods for transient problems in solid mechanics and transport**," *Experimental and Computational Nonlinear Dynamics* session, *51st SES Annual Technical Meeting*, Purdue University, October 1–3, 2014. [***Oral presentation***]

C2. J. Chang, and K.B. Nakshatrala, "**A methodology to ensure local mass conservation for porous media models under finite element formulations based on convex optimization**," *AGU Fall Meeting*, December 15–19, 2014. [***Poster presentation***]

C3. S. Karimi, and K.B. Nakshatrala, "**A monolithic multi-time-step computational framework for transient advective-diffusive-reactive**," *AGU Fall Meeting*, December 15–19, 2014. [***Poster presentation***]

C4. S. Karra, J. Chang, and K.B. Nakshatrala, "**On the performance of maximum-principle enforcing methods applied to large-scale subsurface problems**," *AGU Fall Meeting*, December 15–19, 2014. [***Poster presentation***]

C5. K.B. Nakshatrala, "**On enforcing maximum principles, comparison principles, monotone property, and the non-negative constraint for linear/nonlinear steady-state/transient diffusion-type equations**," *AGU Fall Meeting*, December 15–19, 2014. [***Poster presentation***]

C6a. S. Karimi[(s,*)], and K.B. Nakshatrala, "**Monolithic multi-time-step coupling methods for first and second-order transient systems**," *SIAM Conference on Computational Science & Engineering (CSE15)*, March 14–18, 2015. [***Poster presentation***]

C6b. S. Karimi[(s,*)], and K.B. Nakshatrala, "**Monolithic multi-time-step coupling methods for transient systems**," *SIAM Conference on Computational Science & Engineering (CSE15)*, March 14–18, 2015. [***Oral presentation***]

C7. J. Chang[(s,*)], K.B. Nakshatrala, and L. Johnsson, "**A comparative study on the computational efficiency of locally conservative finite element methods for subsurface flows**," *High Performance Computing in Fluid Flow* symposium, *The 18th International Conference on Finite Elements in Flow Problems (FEF 2015)*, Taipei, Taiwan, March 16–18, 2015. [***Oral presentation***]

C8. J. Chang[(s,*)], K.B. Nakshatrala, and S. Karra, "**Large-scale optimization-based nonnegative computational framework for diffusion equations: Parallel implementation and performance studies**," *PETSc Conference and Tutorial*, Argonne National Laboratory, Chicago, June 15-18, 2015.

C9. S. Karimi[(s,*)], and K.B. Nakshatrala, "**On lattice Boltzmann methods for flow and transport problems in porous media**," 13$^{\text{th}}$ *US National Congress on Computational Mechanics*, San Diego, July 26–30, 2015. [***Student poster competition & oral presentation***]

C10. J. Chang[(s,*)], K.B. Nakshatrala, and L. Johnsson, "**A comparative study on the computational efficiency of locally conservative finite element methods for subsurface flows**," 13$^{\text{th}}$ *US National Congress on Computational Mechanics*, San Diego, July 26–30, 2015. [***Student poster competition & oral presentation***]

C11. K.B. Nakshatrala, C. Xu[(s)], and M.K. Mudunuru[(s,*)], "**On designing staggered coupling algorithms for modeling degradation of materials**," 13$^{\text{th}}$ *US National Congress on Computational Mechanics*, San Diego, July 26–30, 2015. [***Oral presentation***]

C12. M. Shaboeui[(s,*)], and K.B. Nakshatrala, "**A posteriori error estimation techniques to verify numerical solutions in porous media models**," *ASME International Mechanical Engineering Congress & Exposition* Conference, Houston, November 13–19, 2015. [***Oral presentation***]

C13. C. Xu[(s,*)], and K.B. Nakshatrala, "**Chemical degradation of hyperelastic solids: Mathematical model and coupling algorithms**," *ASME International Mechanical Engineering Congress & Exposition* Conference, Houston, November 13–19, 2015. [***Oral presentation***]

C14. J. Chang[(s,*)], K.B. Nakshatrala, and S. Karra, "**Enhanced predictive capabilities of large-scale subsurface flow and transport**," *ASME International Mechanical Engineering Congress & Exposition* Conference, Houston, November 13–19, 2015. [***Oral presentation***]

C15. M.K. Mudunuru[(s,*)], M. Shabouei[(s)], and K.B. Nakshatrala, "**On local and global species conservation errors for nonlinear ecological models and chemical reacting flows**," *ASME International Mechanical Engineering Congress & Exposition* Conference, Houston, November 13–19, 2015. [***Oral presentation***]

C16. M.K. Mudunuru[(s,*)], M. Shabouei[(s)], and K.B. Nakshatrala, "**A locally conservative non-negative finite element formulation for anisotropic advective-diffusive-reactive systems**," *AGU Fall Meeting*, December 14-18, 2015. [***Poster presentation***]

Mini-symposia organization at national/international conferences

M1. "*Continuum scale modeling of flow and reactive transport in porous media*," Organizers: S. Karra, and K.B. Nakshatrala, American Geophysical Union Fall Meeting, San Francisco, December 15–19, 2014.

M2. "*Modeling flow and transport in heterogeneous porous media*," Organizers: K.B. Nakshatrala (Chair), S. Karra, and H. Viswanathan, **13th US National Congress on Computational Mechanics**, San Diego, California, July 26–30, 2015.

M3. "*Mathematical and numerical modeling of degradation of materials and structures*," Organizers: K.B. Nakshatrala (Chair), D.Z. Turner, K.J. Willam, and R. Ballarini, **13th US National Congress on Computational Mechanics**, San Diego, California, July 26–30, 2015.

M4. "*Advances in forward and inverse modeling of coupled Thermo-Hydro-Geomechanical-Chemical processes in porous media*," Organizers: D. Bau, S. Karra, S. Teatini, and K.B. Nakshatrala, **American Geophysical Union Fall Meeting**, San Francisco, December 14–18, 2015. [*AGU executive committee has accepted our proposal for the mini-symposium.*]

Accepted / published peer-reviewed papers

P1. M. K. Mudunuru[(s,*)], and K. B. Nakshatrala, "**On enforcing maximum principles and achieving element-wise species balance for advection-diffusion-reaction equations under the finite element method**," Accepted in the *Journal of Computational Physics*, 2015. [*An e-print of the paper is available on arXiv: 1506.06099.*]

P2. K. B. Nakshatrala, H. Nagarajan, and M. Shabouei, "*A numerical methodology for enforcing maximum principles and the non-negative constraint for transient diffusion equations*," Accepted in *Communications in Computational Physics*, 2015. [*An e-print is available on arXiv.*]

P3. M.K. Mudunuru[(s,*)], M. Shabouei[(s)], and K.B. Nakshatrala, "**On local and global species conservation errors for nonlinear ecological models and chemical reacting flows**," Paper number IMECE2015-52760, *ASME International Mechanical Engineering Congress & Exposition* Conference, 2015.

Journal papers under review

P4. M. K. Mudunuru[(s,*)], and K. B. Nakshatrala, "**On mesh restrictions to satisfy comparison principles, maximum principles, and the non-negative constraint: Recent developments and new results**," *under review*, 2015. [*An e-print of the paper is available on arXiv: 1502.06164.*]

Journal papers close to submission

P5. C. Xu[(s)], M. K. Mudunuru[(s)], and K. B. Nakshatrala, "**Material degradation due to moisture and temperature. Part 1: Mathematical model, analysis, and analytical solutions**," *under preparation*, 2015.

P6. C. Xu[(s)], and K. B. Nakshatrala, "**Material degradation due to moisture and temperature. Part 2: Computational framework, and numerical solutions**," *under preparation*, 2015.

P7. M. K. Mudunuru[(s,*)], and K. B. Nakshatrala, "**Numerical formulations for steady-state and transient semi-linear reaction-diffusion equations, and their structure preserving properties**," *under preparation*, 2015.

A summary of the research accomplishments

(1) **Mesh restrictions to meet the non-negative constraint:** This part of the research work has been ***completed*** entirely. A complete report has also been written on this topic, and submitted to a journal. An e-print of the report is available on arXiv: 1502.06164.

(2) **An optimization-based methodology to meet maximum principles and the non-negative constraint:** This part of the work has been ***completed*** entirely. A complete report has also been written on this topic, and submitted to a journal, which has been accepted in the prestigious Journal of Computational Physics. An e-print of the report is available on arXiv: 1506.06099.

(3) **Quantifying conservation errors under numerical formulations for nonlinear reactions:** This part of the research is also ***complete***. This work has been accepted for publication as a conference paper in *ASME 2015 International Mechanical Engineering Congress & Exposition conference*.

(4) **Non-negative formulations for nonlinear transport-reactions equations:** We are currently extending the non-negative formulations that we have developed for diffusion-type and advection-diffusion equations to nonlinear transport-reactions equations.

(5) **A thermomechanics-based constitutive model for thermal and moisture degradation:** We have split this research into two parts. The first part of the research deals with *Mathematical model, analysis, and analytical solutions*. The second part deals with *Computational framework, and numerical solutions*. We have made lot of progress on this topic. Some preliminary results have also been reported in couple of earlier quarterly reports. In the next few months, we will finish both the parts. Two manuscripts are under preparation.

Material degradation due to moisture and temperature: Mathematical model, analysis, and analytical solutions

Abstract. The mechanical response, serviceability, and load bearing capacity of materials and structural components can be adversely affected due to external stimuli, which include exposure to a corrosive chemical species, high temperatures, temperature fluctuations (i.e., freezing-thawing), cyclic mechanical loading, just to name a few. It is, therefore, of paramount importance in several branches of engineering – ranging from aerospace engineering, civil engineering to biomedical engineering – to have a fundamental understanding of degradation of materials, as the materials in these applications are often subjected to adverse environments. Due to recent advancements in material science, new materials like fiber-reinforced polymers and multi-functional materials that exhibit high ductility have been developed and have been widely used; for example, as infrastructural materials or in medical devices (e.g., stents). The traditional small-strain approaches of modeling these materials will not be adequate. In this paper, we study degradation of materials due to an exposure to chemical species and temperature under large-strain and large-deformations. In the first part of our research work, we present a consistent mathematical model with firm thermodynamic underpinning. We then obtain semi-analytical solutions of several canonical problems to illustrate the nature of the quasi-static and unsteady behaviors of degrading hyperelastic solids.

1. INTRODUCTION AND MOTIVATION

Material and structural degradation is a major wide-spread problem in infrastructure and various other real-life applications. Most of the well-known manifestations, such as "wear out" and "fracture" are related to the phenomenon of degradation [Batchelor et al., 2003]. Virtually, every material degrades when subjected to hostile environment and external stimuli. Importance of this phenomena has triggered a surge in research to develop more resistible materials. Consequently, understanding the general behavior of degrading materials has attracted the interest of researchers. A fundamental study of degradation is crucial to several branches of engineering: aerospace, mechanical, civil, and biomedical. Due to recent advancements in material science, new materials like fiber-reinforced polymers and multi-functional materials that exhibit high ductility have been developed. They have been widely used; for example, as infrastructural materials or in medical devices (e.g., stents). Traditional small-strain assumption to model these materials will not be adequate.

Herein, we develop a coupled continuum mathematical model for thermal and chemical-induced degradation of hyperelastic solids. It should be emphasized that elasticity is an idealization. There is no material whose response is perfectly elastic. But there are situations in which the response of certain materials under normal conditions can be idealized to be hyperelastic. For example, large blood arteries, and rock. Many of these materials function in hostile environments, and are constantly subjected to adverse external stimuli. One often is interested in the unsteady response of the bodies made of hyperelastic materials subject to degradation/healing and/or aging. The application areas in mind are the response of high performance cementitious materials (which undergo large strains and large deformations) and several important coupled deformation-transport processes in biomechanics and biomedicine.

1.1. Degradation mechanisms. The reason that more and more research has been conducted on degradation is that Degradation not only reduces the durability of materials but also

alters material properties. For instance, material damage can induce anisotropy in thermal conductivity and diffusivity. Some degradation factors and consequence of concrete structures have been listed in the following table.

TABLE 1. Primary degradation factors that can impact safety- related concrete structures [Naus, 2007]

	Degradation factor	Primary manifestation
Physical processes	cracking	reduced durability
	salt crystallization	cracking/loss material
	freezing and thawing	cracking/scaling/disintegration
	abrasion/erosion/cavitation	section loss
	thermal exposure/thermal cycling	cracking/spalling/strength loss
	vibration	cracking
	settlement	cracking/spalling/misalignment
Chemical processes	efflorescence/leaching	increased porosity
	sulfate attack	volume change/cracking
	delayed ettringite formation	volume change/cracking
	acids/bases	disintegration/spalling/leaching
	alkali-aggregate reactions	disintegration/cracking
	aggressive water	disintegration/loss material
	phosphate	surface deposits

There are many mechanisms that can result in the degradation of materials. In general, the degradation mechanisms can be divided into four catalogs: mechanical processes, chemical reactions, biological degradation [Gu et al., 1998], and radiation [Kaplan, 1989]. For mechanical processes, the performance of materials can be affected adversely by fatigue [Jung et al., 2000], pressure loading [Rajagopal et al., 2007], and swelling of solid mixtures [Buonsanti et al., 2011]. Examples of chemical degradation include humid and alkaline effects [Björk et al., 2003], exposure to chlorides and carbon-dioxide [Glasser et al., 2008], and calcium leaching [Gawin et al., 2009]. The coupling effects between these mechanisms can have a significant impact on the rate of deterioration of materials and structures. Therefore, developing an appropriate and general model of material degradation is very useful to predict the life span of a given structure. A comprehensive understanding degradation of materials not only plays a pivotal role in improving the reliability of existing infrastructure, but also has a tremendous impact on the economy. We shall assume that predominant degradation mechanisms are moisture and temperature. To this end, we propose a general three-way strongly coupled degradation model based on a thermodynamic framework. The three-way coupling is between mechanical, thermal and transport phenomena.

A material is said to be undergoing thermal degradation at a spatial point $\mathbf{x} \in \Omega$ if the available isothermal density is lower than the reference available isothermal power at that particular point. That is,

$$\left.\frac{dA}{dt}\right|_{\vartheta>\vartheta_{\text{ref}}} \leqslant \left.\frac{dA}{dt}\right|_{\vartheta=\vartheta_{\text{ref}}} \quad \text{for } \mathbf{x} \in \Omega \tag{1.1}$$

Similarly, the chemical/moisture degradation can be defined as follows.

$$\left.\frac{dA}{dt}\right|_{c>c_{\text{ref}}} \leqslant \left.\frac{dA}{dt}\right|_{c=c_{\text{ref}}} \quad \text{for } \mathbf{x} \in \Omega \tag{1.2}$$

where A denotes the specific Helmholtz potential of the material.

Numerical research has been done on thermal degradation. Some of them focus on the effect of thermal degradation on the performance of the materials, where the thermal conductivity is a function only depends on temperature. For instance, the interaction of thermal and mechanical damage processes in heterogeneous concrete materials has been examined in [Willam et al., 2005], the behavior of one-way reinforced concrete slabs exposed to fire has been invested in [Allam et al., 2013], and effective thermal properties has been predicted in particular composites in a micro mechanical model [Khan and Muliana, 2010; Khan et al., 2011].

On the other hand, experiments have been done to show the effect of an environment of alkalinity and humidity on concrete slabs of different components [Björk et al., 2003]. Several moisture damage mechanisms occurring within asphalt pavement have been listed in [Cho and Kim, 2010], and corresponding experiments have been done to show consequences. However, no model based on thermodynamics or empiricism is proposed in [Björk et al., 2003; Cho and Kim, 2010]. The thermal and moisture effects on structural stiffness and damping of laminated composites are investigated in [Bouadi and Sun, 1990]. An empirical model is established, but the transferability is an issue. A variety of experiments have been done to show the relation between the fluid-induced internal damage and anomalous fluid absorption in polymeric composites [Weitsman and Guo, 2002; Weitsman, 2006]. Analytical diffusion models based on equivalent diffusivity and capillary action have been presented. The overall damage parameter is used to simulate the effect of micro-cracks on diffusivity, which is hardly tell the effect of non-uniform deformation.

It is apparent that none of the mentioned paper of thermal or chemical degradation above have a proper thermodynamic basis.

1.2. Thermodynamics of chemo-thermo-mechano degradation. Typically, there are two approaches to build a thermodynamically-consistent degradation model. The first one is based on the theory of the internal variable, such as micro-cracks [Weitsman, 1987], damage parameter [Grasberger and Meschke, 2004]. A theoretical model is presented to investigate the mechano-chemical coupling involved in the adhesion of thin-shell structures in [Springman and Bassani, 2009]. The adhesive traction is used to simulate the coupled effect between chemical and mechanical problems. However, it cannot be a general case for other structures. Moreover, this model involves the multi-scale modeling approach, which require attentions to more issues such as the interdependence between the overall adhesive state and effective adhesive properties.

The other is to investigate the dependence of material properties on concentration of chemical species. The main disadvantage of the first approach is that it is difficult (or sometimes impossible) to measure the internal variables through experimentation. However, the second approach can circumvent this drawback. Moreover, the degradation parameters based on the second approach have a physical basis as compared to the first method. Therefore, we shall use the second approach to construct a thermodynamically- consistent degradation model in which all the damage parameters can be measured in experiments. Several studies have been conducted for this approach. The material moduli of linearized elastic bodies at a particular location is assumed to depend on the concentration of fluid at the location in [Muliana et al., 2009; Darbha and Rajagopal, 2009].

Others studies the effect of strain on thermal conductivity. Dating back to 1970s, people started to study the thermal conductivity of polymer solid under large strain [Picot and Debeauvais, 1975; Peng and Landel, 1975]. Bhowmick and Shenoy [Bhowmick and Shenoy, 2006] presented a method to model the effect of uniform pressure on the thermal conductivity, Xiaobo Li et al. [Li et al., 2010] studied the strain effects on the thermal conductivity of nano structures, and the thermal conductivity of metal degradation due to torsional fatigue has been shown in [Naderi and Khonsari, 2011]. A deformation-dependent diffusion model in composite media at finite strains is developed in [Klepach and Zohdi, 2014]. However, all of them are one-way coupled models. Some fully two-way coupled chemical degradation models have been developed [Karra and Rajagopal, 2012; Mudunuru and Nakshatrala, 2012]. The proposed model in this paper shall recover the model developed by Mudunuru and Nakshatrala [Mudunuru and Nakshatrala, 2012] since the degradation problem should be considered in an open system and not in a closed one [Karra and Rajagopal, 2012].

1.3. Objectives and scope of the paper. The main contributions of this paper are as follows:

(i) We derive a general chemo-thermo-mechano degradation model by appealing to the maximization of dissipation, which is capable of providing a thermodynamic status of many existing models. It will be shown that many popular models are special cases of the proposed mathematical model. For example, the small-strain moisture degradation model proposed in [Mudunuru and Nakshatrala, 2012] will be shown to be a special case of the proposed model. This also illustrates the thermodynamics basis of the degradation model in [Mudunuru and Nakshatrala, 2012], which is not addressed earlier.

(ii) A systematic mathematical analysis is performed on the proposed model, which includes showing that the unsteady solutions under the proposed degradation model are bounded. The analysis will take into account large/finite deformations, and the stability will be established in the sense of Lyapunov.

(iii) We will calibrate the proposed degradation model with existing experimental data sets. These calibration and validation studies will illustrate that the proposed constitutive model can be used with confidence in studying various brittle and quasi-brittle materials like ceramics, glass fibers and concrete.

(iv) Last but not the least, semi-analytical solutions to several canonical problems are presented, which can be valuable for developing better design and safety codes.

2. NOTATION, PRELIMINARIES, AND BALANCE LAWS

Let us consider a body $\mathfrak{B}$. The body occupies a reference configuration $\Omega_0(\mathfrak{B}) \subset \mathbb{R}^{nd}$, where "*nd*" denotes the number of spatial dimensions. A point in the reference configuration is denoted by $\mathbf{p} \in \Omega_0(\mathfrak{B})$. We shall denote the time by $t \in [0, \mathcal{T}]$, where $\mathcal{T}$ is the length of the time interval of interest. Due to motion, the body occupies different spatial configurations with time. We shall denote the configuration occupied by the body at time t as $\Omega_t(\mathfrak{B}) \subset \mathbb{R}^{nd}$. A corresponding spatial point will be denoted as $\mathbf{x} \in \Omega_t(\mathfrak{B})$. The gradient and divergence operators with respect to $\mathbf{p}$ are, respectively, denoted by Grad[$\bullet$] and Div[$\bullet$]. Similarly, the gradient and divergence operators with respect to $\mathbf{x}$ are, respectively, denoted by grad[$\bullet$] and div[$\bullet$].

The motion of the body is mathematically described by the following invertible mapping:

$$\mathbf{x} = \boldsymbol{\varphi}(\mathbf{p}, t) \tag{2.1}$$

The displacement vector field can then be written as:

$$\mathbf{u} = \mathbf{x} - \mathbf{p} = \boldsymbol{\varphi}(\mathbf{p}, t) - \mathbf{p} \tag{2.2}$$

The velocity vector field is defined as:

$$\mathbf{v} = \dot{\mathbf{x}} := \frac{\partial \boldsymbol{\varphi}(\mathbf{p}, t)}{\partial t} \tag{2.3}$$

where a superposed dot indicates the material/total time derivative, which is the derivative with respect to time holding the reference coordinates fixed. The gradient of motion (which is also referred to as the deformation gradient) is defined as:

$$\mathbf{F} = \mathrm{Grad}[\mathbf{x}] \equiv \frac{\partial \boldsymbol{\varphi}(\mathbf{p}, t)}{\partial \mathbf{p}} = \mathbf{I} + \mathrm{Grad}[\mathbf{u}] \tag{2.4}$$

where $\mathbf{I}$ denotes the second-order identity tensor. The corresponding right Cauchy-Green tensor is denoted by:

$$\mathbf{C} = \mathbf{F}^{\mathrm{T}}\mathbf{F} \tag{2.5}$$

where $(\bullet)^{\mathrm{T}}$ denotes the transpose of a second-order tensor. The velocity gradient with respect to $\mathbf{x}$ and the symmetric part of the velocity gradient are, respectively, defined as follows:

$$\mathbf{L} := \mathrm{grad}[\mathbf{v}] \equiv \dot{\mathbf{F}}\mathbf{F}^{-1} \tag{2.6}$$

$$\mathbf{D} := \frac{1}{2}\left(\mathbf{L} + \mathbf{L}^{\mathrm{T}}\right) \tag{2.7}$$

The Green-St. Venant strain tensor is defined as:

$$\mathbf{E} = \frac{1}{2}(\mathbf{C} - \mathbf{I}) = \frac{1}{2}\left(\mathrm{Grad}[\mathbf{u}] + \mathrm{Grad}[\mathbf{u}]^{\mathrm{T}} + \mathrm{Grad}[\mathbf{u}]^{\mathrm{T}}\mathrm{Grad}[\mathbf{u}]\right) \tag{2.8}$$

In those situations in which the following assumption holds:

$$\max_{\mathbf{p}\in\Omega_0(\mathfrak{B}),t\in\mathbb{R}} \sqrt{\|\boldsymbol{\varphi}(\mathbf{p}, t) - \mathbf{p}\|^2 + \|\mathrm{Grad}[\mathbf{u}]\|^2} \ll 1 \tag{2.9}$$

one is justified to employ the following linearized strain tensor:

$$\mathbf{E}_l = \frac{1}{2}\left(\mathrm{Grad}[\mathbf{u}] + \mathrm{Grad}[\mathbf{u}]^{\mathrm{T}}\right) \approx \frac{1}{2}\left(\mathrm{grad}[\mathbf{u}] + \mathrm{grad}[\mathbf{u}]^{\mathrm{T}}\right) \tag{2.10}$$

where $\| \bullet \|$ denotes the Frobenius norm [Antman, 1995].

Since we will be dealing with processes in addition to the mechanical deformation, we need to introduce quantities other than the ones that are associated with the kinematics. We will denote the temperature by ϑ and the specific entropy by η. The mass fraction of the chemical species is denoted by c and the corresponding chemical potential is denoted by $\varkappa$. The temperature, mass fraction of chemical species, entropy, and chemical potential are all scalar fields, while the displacement, velocity, and acceleration are vector fields. In some situations, it may be needed to explicitly indicate the functional dependence of these quantities. We employ a standard notation, which will be illustrated through the temperature field. The temperature in terms of reference coordinates and spatial coordinates will be denoted as follows:

$$\vartheta = \tilde{\vartheta}(\mathbf{p}, t) = \hat{\vartheta}(\mathbf{x}, t) \tag{2.11}$$

2.1. Balance laws. For our study, we shall consider the thermodynamic system to be the entire degrading body. Moreover, we shall assume that this thermodynamic system to be an open system. That is, heat and mass transfers can occur across the boundary of the system. We now present the balance laws that govern the evolution of the chosen system.

The *balance of mass of the solid* in the degrading body takes the following form:

$$\dot{\rho} + \rho \operatorname{div}[\mathbf{v}] = 0 \tag{2.12}$$

where ρ is the density of the solid in the deformed configuration $\Omega_t(\mathfrak{B})$. The *balance of a chemical species*, which is being transported in the degrading body, can be mathematically written as:

$$\rho \dot{c} + \operatorname{div}[\mathbf{h}] = h \tag{2.13}$$

where $\mathbf{h}$ is the mass transfer flux vector in the deformed configuration, and h is the volumetric source of the chemical species in the deformed configuration. We assume that the chemical species cannot take partial stresses, which is a reasonable assumption in the degradation of materials due to small concentrations of moisture. One can handle large moisture contents by introducing partial stresses and using the theory of interacting continua (which is often referred to mixture theory) [Bowen, 1976]. We do not address such issues, as our focus is degradation due to small concentrations of moisture or chemicals. The *balance of linear momentum of the solid* can be written as:

$$\rho \dot{\mathbf{v}} = \operatorname{div}[\mathbf{T}] + \rho \mathbf{b} \tag{2.14}$$

where $\mathbf{b}$ is the specific body force, and $\mathbf{T}$ is the Cauchy stress in the solid. Assuming that there is supply of internal couples, the *balance of angular momentum of the solid* reads:

$$\mathbf{T} = \mathbf{T}^{\mathrm{T}} \tag{2.15}$$

Assuming that the balance of linear momentum (i.e., equation (2.14)) holds, the *balance of energy of the system* (i.e., the first law of thermodynamics) can be written as:

$$\rho \frac{\mathrm{d}}{\mathrm{d}t} (A + \vartheta \eta) = \mathbf{T} \bullet \mathbf{D} - \operatorname{div}[\varkappa \mathbf{h}] + \varkappa h - \operatorname{div}[\mathbf{q}] + q \tag{2.16}$$

where A is the specific Helmholtz potential, $\mathbf{q}$ is the heat flux vector in the deformed configuration, and q is the volumetric heat source in the deformed configuration. In our study, we assume that the Helmholtz potential A to depend on $\mathbf{F}$, c, and ϑ. We also have the following relations for the chemical potential and specific entropy:

$$\varkappa := +\frac{\partial A}{\partial c} \tag{2.17}$$

$$\eta := -\frac{\partial A}{\partial \vartheta} \tag{2.18}$$

Assuming the balance of chemical species to hold, we then have the following:

$$\rho \left(\frac{\partial A}{\partial \mathbf{F}} \mathbf{F}^{\mathrm{T}} \bullet \mathbf{D} + \vartheta \dot{\eta} \right) = \mathbf{T} \bullet \mathbf{D} - \operatorname{div}[\mathbf{q}] - \operatorname{grad}[\varkappa] \bullet \mathbf{h} + q \tag{2.19}$$

The *localized version of the second law of thermodynamics in the deformed configuration* takes the following form:

$$\rho \left(\frac{\partial A}{\partial \mathbf{F}} \mathbf{F}^{\mathrm{T}} \bullet \mathbf{D} \right) = \mathbf{T} \bullet \mathbf{D} - \frac{1}{\vartheta} \operatorname{grad}[\vartheta] \bullet \mathbf{q} - \operatorname{grad}[\varkappa] \bullet \mathbf{h} - \rho \zeta \tag{2.20}$$

where ζ is the specific rate of dissipation functional, which is non-negative. The above equation is a stronger version than the second law of thermodynamics, which is a global law and not a local

one. The second law of thermodynamics does *not* assert that the rate of entropy production be non-decreasing at *each and every point* in the system/body.

2.2. The maximization of rate of dissipation. Among the various methodologies to derive constitutive relations (e.g., see [Maugin, 1998]), the axiom of maximization of rate of dissipation put-forth by Ziegler [Ziegler, 1983] is an attractive procedure. Herein, we extend this procedure to the open thermodynamic system under consideration. We obtain the constitutive relations using the maximization of dissipation hypothesis, which needs the prescription of two functionals – the Helmholtz potential and the dissipation functional. We assume the functional dependence of the Helmholtz potential and the dissipation functional to be $\hat{A}(\mathbf{F}, c, \vartheta)$ and $\hat{\zeta}(\mathbf{D}, \operatorname{grad}[\vartheta], \operatorname{grad}[\varkappa]; \mathbf{F}, \vartheta, c)$.

The mathematical statement of maximization of rate of dissipation can be written as follows:

$$\underset{\mathbf{D},\operatorname{grad}[\vartheta],\operatorname{grad}[\varkappa]}{\text{maximize}} \quad \rho\zeta = \rho\hat{\zeta}(\mathbf{D}, \operatorname{grad}[\vartheta], \operatorname{grad}[\varkappa]; \mathbf{F}, \vartheta, c) \tag{2.21a}$$

$$\text{subject to} \qquad \rho\left(\frac{\partial A}{\partial \mathbf{F}}\mathbf{F}^{\mathrm{T}} \bullet \mathbf{D}\right) = \mathbf{T} \bullet \mathbf{D} - \frac{1}{\vartheta}\operatorname{grad}[\vartheta] \bullet \mathbf{q} - \operatorname{grad}[\varkappa] \bullet \mathbf{h} - \rho\zeta \tag{2.21b}$$

Using the method of Lagrange multipliers, the above constrained optimization problem is equivalent to the following unconstrained optimization problem:

$$\begin{aligned}\underset{\mathbf{D},\operatorname{grad}[\vartheta],\operatorname{grad}[\varkappa],\Lambda_t}{\text{extremize}} \quad & \rho\hat{\zeta}(\mathbf{D}, \operatorname{grad}[\vartheta], \operatorname{grad}[\varkappa]; \mathbf{F}, \vartheta, c) \\ & + \Lambda_t\left(\rho\left(\frac{\partial A}{\partial \mathbf{F}}\mathbf{F}^{\mathrm{T}} \bullet \mathbf{D}\right) - \mathbf{T} \bullet \mathbf{D} + \frac{1}{\vartheta}\operatorname{grad}[\vartheta] \bullet \mathbf{q} + \operatorname{grad}[\varkappa] \bullet \mathbf{h} + \rho\zeta\right)\end{aligned} \tag{2.22}$$

where Λ_t is the Lagrange multiplier enforcing the constraint (2.21b). The first-order optimal conditions give rise to the following relations:

$$\mathbf{T} = \rho\frac{\partial A}{\partial \mathbf{F}}\mathbf{F}^{\mathrm{T}} + \left(\frac{1+\Lambda_t}{\Lambda_t}\right)\rho\frac{\partial \zeta}{\partial \mathbf{D}} \tag{2.23a}$$

$$\frac{1}{\vartheta}\mathbf{q} = -\left(\frac{1+\Lambda_t}{\Lambda_t}\right)\rho\frac{\partial \zeta}{\partial \operatorname{grad}[\vartheta]} \tag{2.23b}$$

$$\mathbf{h} = -\left(\frac{1+\Lambda_t}{\Lambda_t}\right)\rho\frac{\partial \zeta}{\partial \operatorname{grad}[\varkappa]} \tag{2.23c}$$

$$\rho\left(\frac{\partial A}{\partial \mathbf{F}}\mathbf{F}^{\mathrm{T}} \bullet \mathbf{D}\right) - \mathbf{T} \bullet \mathbf{D} + \frac{1}{\vartheta}\operatorname{grad}[\vartheta] \bullet \mathbf{q} + \operatorname{grad}[\varkappa] \bullet \mathbf{h} + \rho\zeta = 0 \tag{2.23d}$$

The above equations can be obtained by taking (Gâteaux) variation of the objective function in equation (2.35) with respect to $\mathbf{D}$, $\operatorname{grad}[\vartheta]$, $\operatorname{grad}[\varkappa]$ and Λ_t, respectively. By straightforward manipulations on equations (2.23a)–(2.23d), the Lagrange multiplier Λ_t can be explicitly calculated as follows:

$$\Lambda_t = \left[\frac{\zeta}{\frac{\partial \zeta}{\partial \mathbf{D}} \bullet \mathbf{D} + \frac{\partial \zeta}{\partial \operatorname{grad}[\vartheta]} \bullet \operatorname{grad}[\vartheta] + \frac{\partial \zeta}{\partial \operatorname{grad}[\varkappa]} \bullet \operatorname{grad}[\varkappa]} - 1\right]^{-1} \tag{2.24}$$

If the rate of dissipation functional ζ is a homogeneous functional of order 2 with respect to $\mathbf{D}$, $\operatorname{grad}[\vartheta]$ and $\operatorname{grad}[\varkappa]$, we then have

$$\frac{\partial \zeta}{\partial \mathbf{D}} \bullet \mathbf{D} + \frac{\partial \zeta}{\partial \operatorname{grad}[\vartheta]} \bullet \operatorname{grad}[\vartheta] + \frac{\partial \zeta}{\partial \operatorname{grad}[\varkappa]} \bullet \operatorname{grad}[\varkappa] = 2\zeta \tag{2.25}$$

which further implies that $\Lambda_t = -2$. The constitutive relations under $\Lambda_t = -2$ will simplify to:

$$\mathbf{T} = \rho\frac{\partial A}{\partial \mathbf{F}}\mathbf{F}^{\mathrm{T}} + \frac{1}{2}\rho\frac{\partial \zeta}{\partial \mathbf{D}} \tag{2.26a}$$

$$\mathbf{q} = -\frac{\vartheta}{2}\rho\frac{\partial \zeta}{\partial \mathrm{grad}[\vartheta]} \tag{2.26b}$$

$$\mathbf{h} = -\frac{1}{2}\rho\frac{\partial \zeta}{\partial \mathrm{grad}[\varkappa]} \tag{2.26c}$$

REMARK 2.1. *It should be emphasized that the dissipation functional need not be a homogeneous functional of order two in terms of* $\mathbf{F}$*,* c *and* ϑ*. The maximization of the rate of dissipation certainly does not require such an assumption. However, we shall make such an assumption, as it is convenient and the resulting constitutive relations can still model the desired degradation mechanisms.*

2.3. Governing equations in the reference configuration. Since we are also interested in developing a computational framework and obtaining numerical solutions, it will be convenient to write the balance laws in the reference configuration. To this end, we introduce:

$$J \equiv \det[\mathbf{F}] \tag{2.27}$$

where $\det[\bullet]$ denotes the determinant. The balance of mass in the reference configuration can be written as:

$$\rho_0 = J\rho \tag{2.28}$$

where ρ_0 is the density of the undeformed solid. The balance of chemical species in the reference configuration can be rewritten as:

$$\rho_0\dot{c} + \mathrm{Div}[\mathbf{h}_0] = h_0 \tag{2.29}$$

where $\mathbf{h}_0 = J\mathbf{F}^{-1}\mathbf{h}$ is the diffusive flux vector in the reference configuration and $h_0 = Jh$ is the volumetric source in the reference configuration. The balance of linear momentum in the reference configuration takes the following form:

$$\rho_0\dot{\mathbf{v}} = \mathrm{Div}[\mathbf{P}] + \rho_0\mathbf{b} \tag{2.30}$$

where $\mathbf{P} = J\mathbf{T}\mathbf{F}^{-\mathrm{T}}$ is the first Piola-Kirchhoff stress. The balance of angular momentum in the reference configuration takes the following form:

$$\mathbf{P}\mathbf{F}^{\mathrm{T}} = \mathbf{F}\mathbf{P}^{\mathrm{T}} \tag{2.31}$$

In the reference configuration, the balance of energy can be written as:

$$\rho_0\left(\frac{\partial A}{\partial \mathbf{F}} \bullet \dot{\mathbf{F}} + \vartheta\dot{\eta}\right) = \mathbf{P} \bullet \dot{\mathbf{F}} - \mathrm{Div}[\mathbf{q}_0] - \mathrm{Grad}[\varkappa] \bullet \mathbf{h}_0 + q_0 \tag{2.32}$$

where $\mathbf{q}_0 = J\mathbf{F}^{-1}\mathbf{q}$ is the heat flux vector in the reference configuration and $q_0 = Jq$ is the volumetric heat source in the reference configuration. In the reference configuration, the second law can be rewritten as:

$$\rho_0\left(\frac{\partial A}{\partial \mathbf{F}} \bullet \dot{\mathbf{F}}\right) = \mathbf{P} \bullet \dot{\mathbf{F}} - \frac{1}{\vartheta}\mathrm{Grad}[\vartheta] \bullet \mathbf{q}_0 - \mathrm{Grad}[\varkappa] \bullet \mathbf{h}_0 - \rho_0\zeta_0 \tag{2.33}$$

where $\zeta_0 = \zeta$ is the non-negative rate of dissipation functional in the reference configuration.

2.3.1. *Maximization of rate of dissipation in the reference configuration.* The mathematical statement of maximization of rate of dissipation can be written as follows:

$$\underset{\dot{\mathbf{F}},\mathrm{Grad}[\vartheta],\mathrm{Grad}[\varkappa]}{\text{maximize}} \quad \rho_0\zeta_0 = \tilde{\zeta}(\dot{\mathbf{F}},\mathrm{Grad}[\vartheta],\mathrm{Grad}[\varkappa];\mathbf{F},\vartheta,c) \tag{2.34a}$$

$$\text{subject to} \quad \rho_0\left(\frac{\partial A}{\partial \mathbf{F}} \bullet \dot{\mathbf{F}}\right) = \mathbf{P}\bullet\dot{\mathbf{F}} - \frac{1}{\vartheta}\mathrm{Grad}[\vartheta]\bullet\mathbf{q}_0 - \mathrm{Grad}[\varkappa]\bullet\mathbf{h}_0 - \rho_0\zeta_0 \tag{2.34b}$$

Using the method of Lagrange multipliers, one can obtain the following equivalent unconstrained optimization problem:

$$\begin{aligned}\underset{\dot{\mathbf{F}},\mathrm{Grad}[\vartheta],\mathrm{Grad}[\varkappa],\Lambda_0}{\text{extremize}} \quad & \rho_0\tilde{\zeta}(\dot{\mathbf{F}},\mathrm{Grad}[\vartheta],\mathrm{Grad}[\varkappa];\mathbf{F},\vartheta,c) \\ & + \Lambda_0\left(\rho_0\left(\frac{\partial A}{\partial \mathbf{F}} \bullet \dot{\mathbf{F}}\right) - \mathbf{P}\bullet\dot{\mathbf{F}} + \frac{1}{\vartheta}\mathrm{Grad}[\vartheta]\bullet\mathbf{q}_0 + \mathrm{Grad}[\varkappa]\bullet\mathbf{h}_0 + \rho_0\zeta_0\right)\end{aligned} \tag{2.35}$$

where Λ_0 is the Lagrange multiplier enforcing the constraint given by equation (2.34b). The first-order optimality conditions give rise to the following constitutive relations:

$$\mathbf{P} = \rho_0\frac{\partial A}{\partial \mathbf{F}} + \left(\frac{1+\Lambda_0}{\Lambda_0}\right)\rho_0\frac{\partial \zeta_0}{\partial \dot{\mathbf{F}}} \tag{2.36a}$$

$$\frac{1}{\vartheta}\mathbf{q}_0 = -\left(\frac{1+\Lambda_0}{\Lambda_0}\right)\rho_0\frac{\partial \zeta_0}{\partial \mathrm{Grad}[\vartheta]} \tag{2.36b}$$

$$\mathbf{h}_0 = -\left(\frac{1+\Lambda_0}{\Lambda_0}\right)\rho_0\frac{\partial \zeta_0}{\partial \mathrm{Grad}[\varkappa]} \tag{2.36c}$$

$$\rho_0\left(\frac{\partial A}{\partial \mathbf{F}} \bullet \dot{\mathbf{F}}\right) - \mathbf{P}\bullet\dot{\mathbf{F}} + \frac{1}{\vartheta}\mathrm{Grad}[\vartheta]\bullet\mathbf{q}_0 + \mathrm{Grad}[\varkappa]\bullet\mathbf{h}_0 + \rho_0\zeta_0 = 0 \tag{2.36d}$$

Similar to the derivation presented earlier in the context of current configuration, the Lagrange multiplier Λ_0 can be explicitly calculated as follows:

$$\Lambda_0 = \left[\frac{\zeta_0}{\frac{\partial\tilde{\zeta}}{\partial\dot{\mathbf{F}}}\bullet\dot{\mathbf{F}} + \frac{\partial\zeta_0}{\partial\mathrm{Grad}[\vartheta]}\bullet\mathrm{Grad}[\vartheta] + \frac{\partial\zeta_0}{\partial\mathrm{Grad}[\varkappa]}\bullet\mathrm{Grad}[\varkappa]} - 1\right]^{-1} \tag{2.37}$$

If the rate of dissipation functional in the reference configuration ζ_0 is a homogeneous functional of order 2, we have

$$\frac{\partial \zeta_0}{\partial \dot{\mathbf{F}}}\bullet\dot{\mathbf{F}} + \frac{\partial \zeta_0}{\partial \mathrm{Grad}[\vartheta]}\bullet\mathrm{Grad}[\vartheta] + \frac{\partial \zeta_0}{\partial \mathrm{Grad}[\varkappa]}\bullet\mathrm{Grad}[\varkappa] = 2\zeta_0 \tag{2.38}$$

which further implies that $\Lambda_0 = -2$. The constitutive relations under $\Lambda_0 = -2$ take the following form:

$$\mathbf{P} = \rho_0\frac{\partial A}{\partial \mathbf{F}} + \frac{1}{2}\rho_0\frac{\partial \zeta_0}{\partial \dot{\mathbf{F}}} \tag{2.39a}$$

$$\mathbf{q}_0 = -\frac{\vartheta}{2}\rho_0\frac{\partial \zeta_0}{\partial \mathrm{Grad}[\vartheta]} \tag{2.39b}$$

$$\mathbf{h}_0 = -\frac{1}{2}\rho_0\frac{\partial \zeta_0}{\partial \mathrm{Grad}[\varkappa]} \tag{2.39c}$$

3. A GENERAL CONSTITUTIVE MODEL FOR CHEMO-THERMO-MECHANO DEGRADATION

We will develop the proposed constitutive model by appealing to the maximization of rate of dissipation. Under the maximization of rate of dissipation hypothesis, the constitutive relations can be obtained by prescribing two functional – the Helmholtz potential and the dissipation functional. Philosophically, the Helmholtz potential quantifies the way in which the material stores energy, whereas the dissipation functional quantifies the way in which the material dissipates energy. For our proposed chemo-thermo-mechano degradation model, we prescribe the following functional forms for the specific Helmholtz potential and the rate of dissipation functional:

$$A = \hat{A}(\mathbf{F}, c, \vartheta) = \frac{1}{\rho_0}\psi - \frac{1}{2}\frac{c_p}{\vartheta_{\text{ref}}}\left\{\vartheta - \vartheta_{\text{ref}}\right\}^2 - \frac{1}{\rho_0}\left\{\vartheta - \vartheta_{\text{ref}}\right\}\mathbf{M}_{\vartheta\mathbf{E}} \bullet \mathbf{E} + d_{\vartheta c}\left\{\vartheta - \vartheta_{\text{ref}}\right\}\left\{c - c_{\text{ref}}\right\} - \frac{1}{\rho_0}\left\{c - c_{\text{ref}}\right\}\mathbf{M}_{c\mathbf{E}} \bullet \mathbf{E} + \frac{R_s\vartheta_{\text{ref}}}{2}\left\{c - c_{\text{ref}}\right\}^2 \tag{3.1}$$

$$\zeta = \hat{\zeta}(\mathbf{D}, \text{grad}[\vartheta], \text{grad}[\varkappa]; \mathbf{F}, \vartheta, c) = \frac{c_p}{\vartheta}\text{grad}[\vartheta] \bullet \mathbf{D}_{\vartheta\vartheta}\text{grad}[\vartheta] + \frac{1}{\vartheta}\text{grad}[\vartheta] \bullet \mathbf{D}_{\vartheta\varkappa}\text{grad}[\varkappa] + \frac{1}{\vartheta}\text{grad}[\varkappa] \bullet \mathbf{D}_{\varkappa\vartheta}\text{grad}[\vartheta] + \frac{1}{R_s\vartheta_{\text{ref}}}\text{grad}[\varkappa] \bullet \mathbf{D}_{\varkappa\varkappa}\text{grad}[\varkappa] \tag{3.2}$$

where $R_s = R/M$. R_s and R denote the specific vapor constant and the universal vapor constant respectively, M is the molecular mass of chemical species. ϑ_{ref} and c_{ref} are the specified reference temperature and reference mass concentration, which depend on the underlying boundary value problem. We denote c_p as the coefficient of heat capacity, $d_{\vartheta c}$ as the thermo-chemo coupled parameter, $\mathbf{M}_{\vartheta\mathbf{E}}$ as the anisotropic coefficient of thermal expansion (which is assumed to be independent of temperature, concentration, and strain), and $\mathbf{M}_{c\mathbf{E}}$ as the anisotropic coefficient of chemical expansion due to concentration (which is also assumed to be independent of temperature, concentration, and strain). Both $\mathbf{M}_{\vartheta\mathbf{E}}$ and $\mathbf{M}_{c\mathbf{E}}$ are assumed to be symmetric. $\mathbf{D}_{\vartheta\vartheta}$ is the anisotropic thermal conductivity tensor and $\mathbf{D}_{\varkappa\varkappa}$ is the anisotropic diffusivity tensor. $\mathbf{D}_{\vartheta\varkappa}$ corresponds to the anisotropic Soret effect tensor, which characterizes the transport of chemical species caused by temperature gradient. Similarly, $\mathbf{D}_{\varkappa\vartheta}$ is the Dufour effect tensor, which represents the heat flow caused by a concentration gradient.

REMARK 3.1. *In chemo-thermo-elasticity and in modeling degradation of materials due to transport and reaction of chemical species, coefficient of chemical expansion* $\mathbf{M}_{c\mathbf{E}}$ *and thermo-chemo coupling parameter* $d_{\vartheta c}$ *play a vital role (see [Sih et al., 1986, Chapter-5] and references therein). Induced-strains due to chemical expansivity will be significant in harsh environmental conditions and cannot be neglected [Sih et al., 1986]. Considerable inquest has been made in literature to experimentally measure* $\mathbf{M}_{c\mathbf{E}}$ *in ceramics [Adler, 2001; Morozovska et al., 2011; Blond and Richet, 2008], laminated and polymer composites [Sih et al., 1986; Bouadi and Sun, 1989; Cai and Weitsman, 1994], elastomers and biological materials [Harper, 2002; Myers et al., 1984; Lai et al., 1991], and concrete structures [Ulm et al., 2000; Černy and Rovnaníková, 2002; Swamy, 2003]. However, adequate progress has not been made yet to develop constitutive models and computational frameworks for such chemo-thermo-elastic materials or materials undergoing chemical-induced degradation. Herein, we shall take a step forward to address this issue.*

REMARK 3.2. *It should be noted that in the absence of electrical and magnetic fields, all of the above tensors are symmetric [Bowen, 1976; Coussy, 2004; Jarkova et al., 2001]. Moreover, from*

the Onsager reciprocal relations (which was put-forth by Onsager in 1930s [Onsager, 1931a,b]) we have the following relationship between the Soret effect tensor and the Dufour effect tensor.

$$\mathbf{D}_{\vartheta\varkappa} = \mathbf{D}_{\varkappa\vartheta} \tag{3.3}$$

Additionally, physics demands that the tensors $\mathbf{D}_{\vartheta\vartheta}$ and $\mathbf{D}_{\varkappa\varkappa}$ are positive definite.

REMARK 3.3. *Note that the specific Helmholtz potential and correspondingly the dissipation functional for diffusion can also be modelled using the following expressions:*

$$A_c = R_s\vartheta_{\text{ref}}c\{\ln[c] - 1\} \tag{3.4}$$

$$\zeta_c = \frac{c}{R_s\vartheta_{\text{ref}}}\text{grad}[\varkappa] \bullet \mathbf{D}_{\varkappa\varkappa}\text{grad}[\varkappa] \tag{3.5}$$

Both equations (3.1)–(3.2) *and* (3.4)–(3.5) *result in similar partial differential equation structure for modeling Fickian diffusion.*

Under the proposed model, the specific entropy and chemical potential take the following form:

$$\eta = -\frac{\partial A}{\partial\vartheta} = -\frac{1}{\rho_0}\frac{\partial\psi}{\partial\vartheta} + \frac{c_p}{\vartheta_{\text{ref}}}\{\vartheta - \vartheta_{\text{ref}}\} + \frac{1}{\rho_0}\mathbf{M}_{\vartheta\mathbf{E}} \bullet \mathbf{E} - d_{\vartheta c}\{c - c_{\text{ref}}\} \tag{3.6}$$

$$\varkappa = \frac{\partial A}{\partial c} = \frac{1}{\rho_0}\frac{\partial\psi}{\partial c} + R_s\vartheta_{\text{ref}}\{c - c_{\text{ref}}\} - \frac{1}{\rho_0}\mathbf{M}_{c\mathbf{E}} \bullet \mathbf{E} + d_{\vartheta c}\{\vartheta - \vartheta_{\text{ref}}\} \tag{3.7}$$

From equations 2.26a–2.26c, we have the constitutive relations in deformed configuration as:

$$\mathbf{T} = \rho\frac{\partial A}{\partial\mathbf{F}}\mathbf{F}^{\text{T}} = \frac{1}{J}\frac{\partial\psi}{\partial\mathbf{F}}\mathbf{F}^{\text{T}} - \frac{1}{J}\{\vartheta - \vartheta_{\text{ref}}\}\mathbf{F}\mathbf{M}_{\vartheta\mathbf{E}}\mathbf{F}^{\text{T}} - \frac{1}{J}\{c - c_{\text{ref}}\}\mathbf{F}\mathbf{M}_{c\mathbf{E}}\mathbf{F}^{\text{T}} \tag{3.8a}$$

$$\mathbf{q} = -\frac{\vartheta}{2}\rho\frac{\partial\hat{\zeta}}{\partial\text{grad}[\vartheta]} = -\rho c_p\mathbf{D}_{\vartheta\vartheta}\text{grad}[\vartheta] - \frac{\rho}{2}\mathbf{D}_{\vartheta\varkappa}\text{grad}[\varkappa] - \frac{\rho}{2}\mathbf{D}_{\varkappa\vartheta}\text{grad}[\varkappa] \tag{3.8b}$$

$$\mathbf{h} = -\frac{1}{2}\rho\frac{\partial\hat{\zeta}}{\partial\text{grad}[\varkappa]} = -\frac{\rho}{R_s\vartheta_{\text{ref}}}\mathbf{D}_{\varkappa\varkappa}\text{grad}[\varkappa] - \frac{\rho}{2\vartheta}\mathbf{D}_{\vartheta\varkappa}\text{grad}[\vartheta] - \frac{\rho}{2\vartheta}\mathbf{D}_{\varkappa\vartheta}\text{grad}[\vartheta] \tag{3.8c}$$

The rate of dissipation functional for the degradation model in the reference configuration is taken as follows:

$$\begin{aligned}\zeta &= \tilde{\zeta}(\dot{\mathbf{F}}, \text{Grad}[\vartheta], \text{Grad}[\varkappa]; \mathbf{F}, \vartheta, c)\\ &= \frac{c_p}{\vartheta}\text{Grad}[\vartheta] \bullet \overline{\mathbf{D}}_{\vartheta\vartheta}\text{Grad}[\vartheta] + \frac{1}{\vartheta}\text{Grad}[\vartheta] \bullet \overline{\mathbf{D}}_{\vartheta\varkappa}\text{Grad}[\varkappa]\\ &+ \frac{1}{\vartheta}\text{Grad}[\varkappa] \bullet \overline{\mathbf{D}}_{\varkappa\vartheta}\text{Grad}[\vartheta] + \frac{1}{R_s\vartheta_{\text{ref}}}\text{Grad}[\varkappa] \bullet \overline{\mathbf{D}}_{\varkappa\varkappa}\text{Grad}[\varkappa]\end{aligned} \tag{3.9}$$

where $\overline{\mathbf{D}}_{\alpha\beta} = \mathbf{F}^{-1}\mathbf{D}_{\alpha\beta}\mathbf{F}^{-T}$, α and β represent ϑ or $\varkappa$. Correspondingly, the constitutive relations in the reference configuration take the following form:

$$\mathbf{P} = \rho_0\frac{\partial A}{\partial\mathbf{F}} = \frac{\partial\psi}{\partial\mathbf{F}} - \{\vartheta - \vartheta_{\text{ref}}\}\mathbf{F}\mathbf{M}_{\vartheta\mathbf{E}} - \{c - c_{\text{ref}}\}\mathbf{F}\mathbf{M}_{c\mathbf{E}} \tag{3.10a}$$

$$\mathbf{q}_0 = -\frac{\vartheta}{2}\rho_0\frac{\partial\tilde{\zeta}}{\partial\text{Grad}[\vartheta]} = -\rho_0 c_p\overline{\mathbf{D}}_{\vartheta\vartheta}\text{Grad}[\vartheta] - \frac{\rho_0}{2}\overline{\mathbf{D}}_{\vartheta\varkappa}\text{Grad}[\varkappa] - \frac{\rho_0}{2}\overline{\mathbf{D}}_{\varkappa\vartheta}\text{Grad}[\varkappa] \tag{3.10b}$$

$$\mathbf{h}_0 = -\frac{1}{2}\rho_0\frac{\partial\tilde{\zeta}}{\partial\text{Grad}[\varkappa]} = -\frac{\rho_0}{R_s\vartheta_{\text{ref}}}\overline{\mathbf{D}}_{\varkappa\varkappa}\text{Grad}[\varkappa] - \frac{\rho_0}{2\vartheta}\overline{\mathbf{D}}_{\vartheta\varkappa}\text{Grad}[\vartheta] - \frac{\rho_0}{2\vartheta}\overline{\mathbf{D}}_{\varkappa\vartheta}\text{Grad}[\vartheta] \tag{3.10c}$$

3.1. Constitutive specifications for the degradation model. The following hyperelastic material models will be employed in this paper:

$$\psi = \frac{\lambda}{2}(\mathrm{tr}[\mathbf{E}])^2 + \mu\mathbf{E}\bullet\mathbf{E} \qquad \text{St. Venant-Kirchhoff model} \tag{3.11a}$$

$$\psi = \frac{\kappa}{2}(\ln[J])^2 + \mu\mathbf{E}\bullet\mathbf{E} \qquad \text{Modified St. Venant-Kirchhoff model} \tag{3.11b}$$

$$\psi = \frac{\mu}{2}(\mathrm{tr}[\mathbf{C}]-3) + \mu\ln[J] + \frac{\lambda}{2}(\ln[J])^2 \qquad \text{Neo-Hookean model} \tag{3.11c}$$

where ψ is the stored strain energy density functional, λ and μ are the Lamé parameters, and $\kappa = \lambda + \frac{2\mu}{3}$ is the bulk modulus. Recall that $J = \det[\mathbf{F}]$. The Lamé parameters in the degrading model are given by the following expressions:

$$\lambda(\mathbf{x}, c) = \lambda_0(\mathbf{x}) - \lambda_1(\mathbf{x})\frac{c}{c_{\mathrm{ref}}} - \lambda_2(\mathbf{x})\frac{\vartheta}{\vartheta_{\mathrm{ref}}} \tag{3.12a}$$

$$\mu(\mathbf{x}, c) = \mu_0(\mathbf{x}) - \mu_1(\mathbf{x})\frac{c}{c_{\mathrm{ref}}} - \mu_2(\mathbf{x})\frac{\vartheta}{\vartheta_{\mathrm{ref}}} \tag{3.12b}$$

where λ_0 and μ_0 are the Lamé parameters of the virgin material. λ_1 and μ_1 are the parameters that account for the effect of concentration of chemical species on degradation of solid. λ_2 and μ_2 are the parameters that account for the temperature effect on the degrading solid. It should be noted that λ_1, μ_1, λ_2, and μ_2 are all positive. Furthermore, these parameters are constrained such that the bulk modulus and shear modulus are strictly positive.

3.1.1. *Deformation dependent diffusivity.* The effect of deformation on diffusivity is modeled as follows: When tensile and shear strains are predominant, we have the following constitutive model

$$\begin{aligned}\mathbf{D}_{\varkappa\varkappa} = \mathbf{D}_0 &+ (\mathbf{D}_T - \mathbf{D}_0)\,\frac{(\exp[\eta_T I_{\mathbf{E}}]-1)}{(\exp[\eta_T E_{\mathrm{ref}T}]-1)} + (\mathbf{D}_S - \mathbf{D}_0)\,\frac{(\exp[\eta_S II_{\mathbf{E}}]-1)}{(\exp[\eta_S E_{\mathrm{ref}S}]-1)} \\ &+ (\mathbf{D}_{MS} - \mathbf{D}_0)\,\frac{(\exp[\eta_{MS} III_{\mathbf{E}}]-1)}{(\exp[\eta_{MS} E_{\mathrm{ref}MS}]-1)}\end{aligned} \tag{3.13}$$

where $I_{\mathbf{E}}$, $II_{\mathbf{E}}$, and $III_{\mathbf{E}}$ are the first, second, and third invariants of the Green–St-Venant strain tensor. These are defined as follows:

$$I_{\mathbf{E}} := \mathrm{tr}[\mathbf{E}] \tag{3.14a}$$

$$II_{\mathbf{E}} := \sqrt{2\,\mathrm{dev}[\mathbf{E}]\bullet\mathrm{dev}[\mathbf{E}]} = \sqrt{\frac{2}{3}(3\mathrm{tr}[\mathbf{E}^2] - (\mathrm{tr}[\mathbf{E}])^2)} \tag{3.14b}$$

$$III_{\mathbf{E}} := \det\left[\frac{1}{II_{\mathbf{E}}}\mathrm{dev}[\mathbf{E}]\right] \tag{3.14c}$$

where $\mathrm{dev}[\mathbf{E}] := \mathbf{E} - \frac{1}{3}\mathrm{tr}[\mathbf{E}]\mathbf{I}$ is the deviatoric part of $\mathbf{E}$. These invariants are used to model the effect of dilation, magnitude of distortion, and mode of distortion on the diffusivity of the solid. η_T, η_S, and η_{MS} are non-negative parameters. $E_{\mathrm{ref}T}$, $E_{\mathrm{ref}S}$, and $E_{\mathrm{ref}MS}$ are reference measures of the tensile strain, shear strain, and mode of shear strain respectively. $\mathbf{D}_0$, $\mathbf{D}_T$, $\mathbf{D}_S$, and $\mathbf{D}_{MS}$ are, respectively, the reference diffusivity tensors under no strain, tensile strain, and shear strain.

When compression and shear strains are predominant, deformation dependent diffusivity is modeled as follows:

$$\mathbf{D}_{\varkappa\varkappa} = \mathbf{D}_0 + (\mathbf{D}_0 - \mathbf{D}_C)\,\frac{(\exp[\eta_T I_{\mathbf{E}}] - 1)}{(\exp[\eta_T E_{\mathrm{ref}T}] - 1)} + (\mathbf{D}_S - \mathbf{D}_0)\,\frac{(\exp[\eta_S II_{\mathbf{E}}] - 1)}{(\exp[\eta_S E_{\mathrm{ref}S}] - 1)} + (\mathbf{D}_{MS} - \mathbf{D}_0)\,\frac{(\exp[\eta_{MS} III_{\mathbf{E}}] - 1)}{(\exp[\eta_{MS} E_{\mathrm{ref}MS}] - 1)} \tag{3.15}$$

where η_C is a non-negative parameter, $E_{\mathrm{ref}C}$ is a reference measure of the compression strain, and $\mathbf{D}_C$ is the reference diffusivity tensor under compressive strain.

REMARK 3.4. *In [Mudunuru and Nakshatrala, 2012], a constitutive model has been developed for deformation dependent diffusivity based on small-strain assumption. However, it should be noted that the model proposed by the authors is a special case and is obtained by linearizing the equations* (3.13) *and* (3.15)*. This model is developed based on the experimental evidence that the relative diffusion rate varies exponentially with respect to the trace of strain [McAfee, 1958a,b]. In this paper, we will take a step further to calibrate these materials parameters according to the experimental data for finite strains based on the model given by equations* (3.13) *and* (3.15)*. It should be noted that the model proposed in [Mudunuru and Nakshatrala, 2012] is a special case of the model given by equations* (3.13) *and* (3.15)*.*

REMARK 3.5. *Note that deformation dependent diffusivity given by equations* (3.13) *and* (3.15) *can be constructed using a different set of invariants of a given strain tensor. This invariants can be either principal or Hencky type [Lurie, 1990; sek and Kruisová, 2006; Criscione et al., 2000] based on the nature of material and associated experimental data. The proposed framework can accommodate such models with minor modifications.*

In case of transversely isotropic materials with fibers running along the direction $\mathbf{M}_{tf}$*, the following invariants are needed to model deformation dependent diffusivity in addition to the invariant set given by equations* (3.14a)–(3.14c)

$$IV_{\mathbf{E}} := \mathbf{M}_{tf} \bullet \mathbf{E}\mathbf{M}_{tf} \tag{3.16a}$$

$$V_{\mathbf{E}} := \mathbf{M}_{tf} \bullet \mathbf{E}^2\mathbf{M}_{tf} \tag{3.16b}$$

For more details on selection of invariants for transversely isotropic or orthotropic materials see [Lurie, 1990; Holzapfel, 2000; Ogden, 1997].

3.1.2. *Deformation dependent thermal conductivity.* The effect of deformation of the solid on thermal conductivity is modeled as follows [Bhowmick and Shenoy, 2006]:

$$\mathbf{D}_{\vartheta\vartheta} = \mathbf{K}_{0\vartheta}(1 + I_{\mathbf{E}})^{-\delta} \tag{3.17}$$

where δ is a non-negative parameter. $\mathbf{K}_{0\vartheta}$ is the reference conductivity tensors under no strain. Based on molecular dynamics simulations, Bhowmick and Shenoy [Bhowmick and Shenoy, 2006] suggested that δ to be 9.59 and $\mathbf{K}_{0\vartheta} = 4.61\vartheta^{-1.45}$ (for certain brittle-type materials). For various other ductile or brittle-type materials, these parameters can be determined by experiments or can be constructed using Lennard-Jones potential in molecular dynamics.

REMARK 3.6. *Due to the lack of experimental data, we assume that Dufour and Soret tensors do not depend on the deformation of solid. However, it should be noted that the proposed thermodynamic and computational framework can accommodate deformation dependent Dufour and Soret tensors with minor modifications (whenever such an experimental evidence is available).*

3.1.3. *Status of the degradation model in [Mudunuru and Nakshatrala, 2012].* The small-strain chemo-mechano degradation model proposed in [Mudunuru and Nakshatrala, 2012] is a special case of the proposed chemo-thermo-mechano degradation, and can be obtained under a plethora of assumptions. These assumptions include steady-state response, small strains, and isothermal conditions with negative volumetric heat source in the entire degrading body. One also needs to neglect chemo-thermo, chemo-mechano, and thermo-mechano couplings. Moreover, the functional forms of the specific Helmholtz potential and rate of dissipation functional need to be:

$$A = \frac{1}{\rho_0}\psi + \frac{R_s\vartheta_{\text{ref}}}{2}\{c - c_{\text{ref}}\}^2 \tag{3.18}$$

$$\zeta = \frac{1}{R_s\vartheta_{\text{ref}}}\text{grad}[\varkappa] \bullet \mathbf{D}_{\varkappa\varkappa}\text{grad}[\varkappa] \tag{3.19}$$

where the stored strain energy density functional is given by:

$$\psi = \hat{\psi}(\mathbf{E}_l, c) = \frac{\lambda(c)}{2}\text{tr}[\mathbf{E}_l]^2 + \mu(c)\mathbf{E}_l \bullet \mathbf{E}_l \tag{3.20}$$

Under the small strain assumption given by equation 2.9, the Cauchy stress, chemical potential, and mass transfer flux vector can be written as:

$$\mathbf{T} = \rho_0\frac{\partial A}{\partial \mathbf{E}_l} = \lambda(c)\text{tr}[\mathbf{E}_l]\mathbf{I} + \mu(c)\mathbf{E}_l \tag{3.21}$$

$$\varkappa = \frac{\partial A}{\partial c} = R_s\vartheta_{\text{ref}}\{c - c_{\text{ref}}\} \tag{3.22}$$

$$\mathbf{h} = -\frac{1}{2}\rho_0\frac{\partial\hat{\zeta}}{\partial\text{grad}[\varkappa]} = -\frac{\rho_0}{R_s\vartheta_{\text{ref}}}\mathbf{D}_{\varkappa\varkappa}\text{grad}[\varkappa] \tag{3.23}$$

The balance of chemical species and the balance of linear momentum for the solid are given by equations (2.13) and (2.14). Under the isothermal condition, the balance of energy simplifies to the following expression:

$$q = -\frac{\rho_0}{R_s\vartheta_{\text{ref}}}\text{grad}[\varkappa] \bullet \mathbf{D}_{\varkappa\varkappa}\text{grad}[\varkappa] \tag{3.24}$$

which means that q needs to be non-positive in order to maintain the isothermal condition.

3.2. Non-dimensional parameters to measure the strength of coupling. The evolution equations for the linearized chemo-thermo-mechano non-degrading and degrading materials are given follows:

$$\rho_0\dot{\mathbf{v}} = \text{div}[\lambda(c,\vartheta)\text{tr}[\mathbf{E}_l]\mathbf{I} + \mu(c,\vartheta)\mathbf{E}_l - \{\vartheta - \vartheta_{\text{ref}}\}\mathbf{M}_{\vartheta\mathbf{E}} - \{c - c_{\text{ref}}\}\mathbf{M}_{c\mathbf{E}}] + \rho_0\mathbf{b} \tag{3.25a}$$

$$\rho_0 R_s\vartheta_{\text{ref}}\dot{c} = \rho_0 R_s\vartheta_{\text{ref}}\text{div}[\mathbf{D}_{\varkappa\varkappa}\text{grad}[c]] + \rho_0\text{div}[(d_{\vartheta c}\mathbf{D}_{\varkappa\varkappa} + R_s\mathbf{D}_{\varkappa\vartheta})\,\text{grad}[\vartheta]] + R_s\vartheta_{\text{ref}}h \tag{3.25b}$$

$$\begin{aligned}\rho_0 c_p\dot{\vartheta} = {}& \frac{\rho_0}{R_s}\text{div}[\big(c_p R_s\mathbf{D}_{\vartheta\vartheta} + 2R_s d_{\vartheta c}\mathbf{D}_{\varkappa\vartheta} + d_{\vartheta c}^2\mathbf{D}_{\varkappa\varkappa}\big)\,\text{grad}[\vartheta]] + q + \vartheta_{\text{ref}}d_{\vartheta c}h \\ & + \text{div}[(\rho_0\vartheta_{\text{ref}}d_{\vartheta c}\mathbf{D}_{\varkappa\varkappa} + \rho_0 R_s\vartheta_{\text{ref}}\mathbf{D}_{\varkappa\vartheta})\,\text{grad}[c]] - \vartheta_{\text{ref}}\mathbf{M}_{\vartheta\mathbf{E}} \bullet \dot{\mathbf{E}}_l\end{aligned} \tag{3.25c}$$

where the Onsager reciprocal relation given by equation (3.3) has been used to obtain (3.25b) and (3.25c). Based on equations (3.25a)–(3.25c), the measure of strength of thermomechanical, chemo-mechanical, and chemo-thermomechanical coupling for non-degrading linearized elastic materials

are given by the following non-dimensional parameters

$$\mathcal{E}_{tm} = \frac{m_{\vartheta\mathbf{E}}^2 \vartheta_{\text{ref}}}{\rho_0 c_p(\lambda_0 + 2\mu_0)} \qquad \text{Thermomechanical coupling} \tag{3.26a}$$

$$\mathcal{E}_{cm} = \frac{m_{c\mathbf{E}}^2}{\rho_0 R_s \vartheta_{\text{ref}}(\lambda_0 + 2\mu_0)} \qquad \text{Chemomechanical coupling} \tag{3.26b}$$

$$\mathcal{E}_{ct} = \frac{R_s d_{\vartheta c} + R_s^2 \mathcal{S}_\vartheta}{d_{\vartheta c}^2 + 2R_s d_{\vartheta c}\mathcal{S}_\vartheta + R_s c_p \mathcal{L}\text{e}} \qquad \text{Chemo-thermo coupling} \tag{3.26c}$$

$$\mathcal{E}_{ctm} = \frac{\mathcal{E}_{tm}}{\mathcal{E}_{cm}} \qquad \text{Chemo-thermomechanical coupling} \tag{3.26d}$$

where $\mathcal{L}\text{e} := \frac{D_{\vartheta\vartheta}}{D_{\varkappa\varkappa}}$ is the standard Lewis number [Sih et al., 1986; Taylor and Krishna, 1993; Cussler, 2009]. $\mathcal{S}_\vartheta := \frac{D_{\varkappa\vartheta}}{D_{\varkappa\varkappa}}$ is called the Ludwig-Soret number [Platten and Legros, 1984; Platten, 2006].

REMARK 3.7. *Note that there are some materials which have high value of $m_{c\mathbf{E}}$. For instance, in certain ceramics, $m_{c\mathbf{E}}$ is 10 times higher than $m_{\vartheta\mathbf{E}}$. In those cases, chemoelasticity play a predominant role.*

To derive these non-dimensional quantities, we have taken $\mathbf{M}_{c\mathbf{E}} = m_{c\mathbf{E}}\mathbf{I}$ and $\mathbf{M}_{\vartheta\mathbf{E}} = m_{\vartheta\mathbf{E}}\mathbf{I}$. In addition, relevant transport and thermal coefficients are assumed to be constants, which is the case for isotropic materials. Similar non-dimensional numbers can be constructed for anisotropic materials by choosing an appropriate norm. In case of degradation, in addition to $\mathcal{E}_{tm}$, $\mathcal{E}_{cm}$, $\mathcal{E}_{ct}$, and $\mathcal{E}_{ctm}$, the following non-dimensional parameters determine which degradation process dominates

$$\mathcal{E}_{\vartheta\mathbf{E}_l} = \frac{\lambda_1 + 2\mu_1}{\lambda_0 + 2\mu_0} \qquad \text{Thermo-mechano degradation} \tag{3.27a}$$

$$\mathcal{E}_{\varkappa\mathbf{E}_l} = \frac{\lambda_2 + 2\mu_2}{\lambda_0 + 2\mu_0} \qquad \text{Chemo-mechano degradation} \tag{3.27b}$$

$$\mathcal{E}_{\vartheta\varkappa\mathbf{E}_l} = \frac{\mathcal{E}_{\vartheta\mathbf{E}_l}}{\mathcal{E}_{\varkappa\mathbf{E}_l}} \qquad \text{Chemo-thermo-mechano degradation} \tag{3.27c}$$

It should be noted that these non-dimensional parameters are of paramount importance in determining whether the underlying problem is strongly coupled or weakly coupled. For instance, the following provide the range of these parameters for various materials:

- For metals such as steel, we have $\mathcal{E}_{tm} \sim \mathcal{O}(10^{-2})$.
- For infrastructural materials such as standard cementitious concrete mixtures, we have $\mathcal{E}_{tm} \sim \mathcal{O}(10^{-3})$, $\mathcal{E}_{cm} \sim \mathcal{O}(10^{-2})$, $\mathcal{E}_{ct} \sim \mathcal{O}(10^{1})$, and $\mathcal{E}_{ctm} \sim \mathcal{O}(10^{-1})$.
- For brittle materials such as glass, $\mathcal{E}_{tm} \sim \mathcal{O}(10^{-4})$.
- For epoxy-based polymeric composites, we have $\mathcal{E}_{tm} \sim \mathcal{O}(10^{-3})$, $\mathcal{E}_{cm} \sim \mathcal{O}(10^{-4})$, $\mathcal{E}_{ct} \sim \mathcal{O}(10^{-2})$, and $\mathcal{E}_{ctm} \sim \mathcal{O}(10^{1})$.

The order of the dimensionless parameters given by equations (3.26a)–(3.26d) are estimated based on the values provided by Table 2.

REMARK 3.8. *It should be noted that the non-dimensional parameters given by equations* (3.26a)–(3.26d) *and* (3.27a)–(3.27c) *provide a foundation for demarcating linearized and finite strain theories. If the non-dimensional numbers (which form the basis for chemo-thermo-mechanical coupling) are small (generally in the order of* 10^{-2} *or less), then it is justified to use the linearized theory.*

TABLE 2. Summary of typical (average) material parameters for steel [Totten et al., 2002], glass [Groza et al., 2007], concrete [Nawy, 2008], and epoxy-based polymer composites (EPC) [Sih et al., 1986] at $\vartheta_{\text{ref}} = 300\,\text{K}$. The specific vapor constant R_s is equal to $461.5\,\text{J}\,\text{kg}^{-1}\text{K}^{-1}$ [Cussler, 2009].

Parameter	Steel	Concrete	Glass	EPC
ρ_0 $(\text{kg}\,\text{m}^{-3})$	7860	2400	2320	2700
c_p $(\text{J}\,\text{kg}^{-1}\text{K}^{-1})$	420	880	840	1300
$m_{\vartheta\mathbf{E}}$ $(\text{J}\,\text{m}^{-3}\text{K}^{-1})$	8.56×10^6	1.22×10^6	0.52×10^6	0.42×10^6
$m_{c\mathbf{E}}$ $(\text{J}\,\text{m}^{-3})$	N/A	7.14×10^8	N/A	14×10^6
λ_0 (GPa)	185	14	26.2	1.4
μ_0 (GPa)	79.3	21	26.2	1.4
$D_{\vartheta\vartheta}$ $(\text{m}^2\text{s}^{-1})$	4.55×10^{-6}	0.8×10^{-7}	4.58×10^{-7}	2.53×10^{-5}
$D_{\varkappa\varkappa}$ $(\text{m}^2\text{s}^{-1})$	1×10^{-12}	4×10^{-7}	7.26×10^{-13}	1.42×10^{-6}
$D_{\varkappa\vartheta}$ $(\text{m}^2\text{s}^{-1})$	N/A	3.32×10^{-7}	N/A	1.02×10^{-6}
$d_{\vartheta c}$ $(\text{J}\,\text{kg}^{-1}\text{K}^{-1})$	N/A	N/A	N/A	1.37×10^3
$\mathcal{L}\text{e}$	4.55×10^6	0.2	6.31×10^5	17.82
$\mathcal{S}_\vartheta$	N/A	0.805	N/A	0.718
$\mathcal{E}_{tm}$	1.94×10^{-2}	3.78×10^{-3}	5.29×10^{-4}	3.6×10^{-3}
$\mathcal{E}_{cm}$	N/A	2.74×10^{-2}	N/A	1.25×10^{-4}
$\mathcal{E}_{ct}$	N/A	2.11	N/A	5.83×10^{-2}
$\mathcal{E}_{ctm}$	N/A	1.37×10^{-1}	N/A	2.88×10^1

In all other cases, finite strain chemo-thermo-mechano degradation model has to be used. In addition, it should be noted that within the context of thermoelasticity, we recover the non-dimensional parameter proposed by Armero and Simo [Armero and Simo, 1992].

4. SEMI-ANALYTICAL SOLUTIONS TO CANONICAL PROBLEMS

In this section, we shall appeal to semi-inverse methods to obtain solutions to some popular canonical boundary value problems [Ogden, 1997]. Incompressible neo–Hookean chemo-thermo-mechano degradation model is consider here. Similar analysis can be performed for other compressible and incompressible chemo-mechano, thermo-mechano, and chemo-thermo-mechano degradation models. Coordinate system under consideration is either spherical or cylindrical. In all the problems discussed below, we assume concentration and temperature are only a function of time t and radius r (which is a current configuration variable). This assumption is often made because the underlying problem has either cylindrical or spherical symmetry. We also assume that the volumetric sources corresponding to temperature and concentration are equal to zero. In this paper, as we are mainly interested in degradation of solid due to temperature and transport of chemical species, we shall neglect Dufour effect, Soret effect, thermo-chemo coupling parameter $d_{\vartheta c}$, and anisotropic coefficient of thermal and chemical expansions. In order to reduce the complexity of finding solutions based on semi-inverse method for deformation sub-problem, we shall neglect the inertial effects and body forces.

Based on these assumptions, the governing equations for transport sub-problem reduce to the following partial differential equations in r and t in cylindrical coordinates:

$$\rho\frac{\partial c}{\partial t} + \frac{1}{r}\frac{\partial r h_r}{\partial r} = 0 \tag{4.1a}$$

$$c(r = r_i, t) = c_i \tag{4.1b}$$

$$c(r = r_o, t) = c_o \tag{4.1c}$$

$$c(r, t = 0) = c_0 \tag{4.1d}$$

where h_r is the mass transfer flux in the radial direction. Similarly, the governing equations for thermal sub-problem in cylindrical coordinates are given as follows:

$$\rho\vartheta\frac{\partial \eta}{\partial t} + \frac{1}{r}\frac{\partial r q_r}{\partial r} = -\frac{\partial \varkappa}{\partial r}h_{\mathrm{r}} \tag{4.2a}$$

$$\vartheta(r = r_i, t) = \vartheta_i \tag{4.2b}$$

$$\vartheta(r = r_o, t) = \vartheta_o \tag{4.2c}$$

$$\vartheta(r, t = 0) = \vartheta_0 \tag{4.2d}$$

where q_r is the heat flux in the radial direction.

In spherical coordinates, the governing equations for transport sub-problem are given as follows:

$$\rho\frac{\partial c}{\partial t} + \frac{1}{r^2}\frac{\partial r^2 h_r}{\partial r} = 0 \tag{4.3a}$$

$$c(r = r_i, t) = c_i \tag{4.3b}$$

$$c(r = r_o, t) = c_o \tag{4.3c}$$

$$c(r, t = 0) = c_0 \tag{4.3d}$$

Similarly, the governing equations for thermal sub-problem in spherical coordinates are given as follows:

$$\rho\vartheta\frac{\partial \eta}{\partial t} + \frac{1}{r^2}\frac{\partial r^2 q_r}{\partial r} = -\frac{\partial \varkappa}{\partial r}h_{\mathrm{r}} \tag{4.4a}$$

$$\vartheta(r = r_i, t) = \vartheta_i \tag{4.4b}$$

$$\vartheta(r = r_o, t) = \vartheta_o \tag{4.4c}$$

$$\vartheta(r, t = 0) = \vartheta_0 \tag{4.4d}$$

Another quantity of interest in material degradation is the extent of damage at a particular location or along the cross-section of the degrading body. In case of incompressible neo-hookean chemo-thermo-mechano degradation model, this quantity can be defined as follows:

$$\mathcal{D}_\mu(\mathbf{x}, t) := \frac{\mu}{\mu_0} = 1 - \left(\frac{\mu_1 c}{\mu_0 c_{\mathrm{ref}}}\right) - \left(\frac{\mu_2 \vartheta}{\mu_0 \vartheta_{\mathrm{ref}}}\right) \tag{4.5}$$

For virgin material, $\mathcal{D}_\mu = 1$. If $\mathcal{D}_\mu$ approaches zero, then the material has degraded the most. In addition, equation (4.5) also provides the following information:

- Amount of degradation at a given location and time,
- The parts of the body that suffered extensive damage, and
- The effect of temperature and moisture (or concentration of chemical species) on the mechanical properties of materials.

4.1. Bending of a degrading beam. Herein, we shall consider pure bending of a degrading beam. At time $t = 0$, a finite degrading beam is suddenly bent by an action of pure end moments. For $t > 0$, the centerline of the beam becomes a sector of a circle of radius r_c. This centerline is held fixed for all the time. Subsequently, the stresses in the degrading beam are allowed to relax. In addition, it is assumed that the material remains isotropic with respect to the reference configuration throughout the degradation process. These assumptions enable us to employ the counterpart of universal deformations (also known as semi-inverse method) [Ogden, 1997] to study such degrading beams.

A pictorial description of the initial boundary value problem is shown in Figure 3. In the reference configuration, the degrading beam is defined as follows:

$$-L \leq X \leq L, \qquad -W \leq Y \leq W, \qquad -H \leq Z \leq H \tag{4.6}$$

where (X, Y, Z) are the Cartesian coordinates in the reference configuration. We assume that the deformation in the current configuration is described as follows:

$$r = \sqrt{\frac{2X}{\alpha} + \beta} \qquad \theta = \frac{Y}{\gamma} \qquad z = Z \tag{4.7}$$

where (r, θ, z) are the cylindrical polar coordinates in the current configuration. When $X = 0$, we have $\beta = r_c^2$. It should be noted that α and γ are all unknown time-dependent parameters. These unknowns are evaluated from the incompressibility constraint, traction boundary conditions, and pure end moments. To reduce the complexity in finding semi-analytical solutions, we shall assume r_c is given. The faces $X = -L$ and $X = L$ are subjected to ambient atmospheric pressure 'p_{atm}'. Upon deformation, the corresponding deformed faces r_i and r_o are maintained at p_{atm}, where $r_i = \sqrt{r_c^2 - 2\gamma L}$ and $r_o = \sqrt{r_c^2 + 2\gamma L}$ are the inner and outer radius of the degrading beam. This gives the following traction boundary conditions:

$$T_{rr}(X = -L, t) = T_{rr}(X = L, t) = p_{\text{atm}} \tag{4.8}$$

The deformation gradient $\mathbf{F}$, right Cauchy-Green tensor $\mathbf{C}$, and left Cauchy-Green tensor $\mathbf{B}$ for the degrading beam are given as follows:

$$\mathbf{F} = \begin{pmatrix} \frac{1}{\alpha r} & 0 & 0 \\ 0 & \frac{r}{\gamma} & 0 \\ 0 & 0 & 1 \end{pmatrix} \qquad \mathbf{C} = \mathbf{B} = \begin{pmatrix} \frac{1}{\alpha^2 r^2} & 0 & 0 \\ 0 & \frac{r^2}{\gamma^2} & 0 \\ 0 & 0 & 1 \end{pmatrix} \tag{4.9}$$

Using the condition of incompressibility, we have $\alpha\gamma = 1$. The Cauchy stress tensor for incompressible neo–Hookean chemo-thermo-mechano degradation model is given as follows:

$$\mathbf{T} = -p\mathbf{I} + \mu(c, \vartheta)\mathbf{B} \tag{4.10}$$

The governing equations (balance of linear momentum) in cylindrical coordinates for deformation sub-problem are given as follows:

$$\frac{\partial T_{rr}}{\partial r} + \frac{1}{r}\frac{\partial T_{\theta r}}{\partial \theta} + \frac{\partial T_{zr}}{\partial z} + \frac{T_{rr} - T_{\theta\theta}}{r} = 0 \tag{4.11a}$$

$$\frac{\partial T_{r\theta}}{\partial r} + \frac{1}{r}\frac{\partial T_{\theta\theta}}{\partial \theta} + \frac{\partial T_{z\theta}}{\partial z} + \frac{2T_{r\theta}}{r} = 0 \tag{4.11b}$$

$$\frac{\partial T_{rz}}{\partial r} + \frac{1}{r}\frac{\partial T_{\theta z}}{\partial \theta} + \frac{\partial T_{zz}}{\partial z} + \frac{T_{rz}}{r} = 0 \tag{4.11c}$$

For incompressible degrading neo-Hookean material, the non-zero components of the Cauchy stress tensor are given as follows:

$$T_{rr} = -p + \frac{\mu(c,\vartheta)\gamma^2}{r^2} = -p + \frac{\mu(c,\vartheta)\gamma^2}{2\gamma X + r_c^2} \tag{4.12a}$$

$$T_{\theta\theta} = -p + \frac{\mu(c,\vartheta)r^2}{\gamma^2} = -p + \frac{\mu(c,\vartheta)\left(2\gamma X + r_c^2\right)}{\gamma^2} \tag{4.12b}$$

$$T_{zz} = -p + \mu(c,\vartheta) \tag{4.12c}$$

The balance of linear momentum given by equation (4.11a)–(4.11c) reduces to the following

$$\frac{\partial T_{rr}}{\partial r} + \frac{T_{rr} - T_{\theta\theta}}{r} = 0 \tag{4.13}$$

$$\frac{\partial p}{\partial \theta} = 0 \tag{4.14}$$

$$\frac{\partial p}{\partial z} = 0 \tag{4.15}$$

From (4.14) and (4.15), we have $p = p(r,t)$. Using equations (4.13), (4.7), (4.8), (4.12a), and (4.12b), we have the following non-linear equation in γ

$$T_{rr}(X=-L,t) - T_{rr}(X=L,t) = \int_{-L}^{L} \frac{\mu(c(X,t),\vartheta(X,t))\left(\gamma^4 - \left(2\gamma X + r_c^2\right)^2\right)}{\gamma\left(2\gamma X + r_c^2\right)^2} dX = 0 \tag{4.16}$$

where $c(X,t)$ and $\vartheta(X,t)$ are evaluated from the values of $c(r,t)$ and $\vartheta(r,t)$. From (4.16), $\gamma|_{t=0}$ is given as follows:

$$\gamma|_{t=0} = \sqrt{-2L^2 + \sqrt{4L^4 + r_c^4}} \tag{4.17}$$

which is the case for homogeneous neo-Hookean material. Once c, ϑ, and γ are known, the Lagrange multiplier $p = p(r,t)$ enforcing the incompressibility constraint can evaluated from (4.13) and (4.8) as follows:

$$p(r,t) = p_{\text{atm}} + \frac{\mu(c,\vartheta)\gamma^2}{r^2} - \int_{r_i}^{r} \frac{\mu(c,\vartheta)\left(\gamma^4 - r^4\right)}{\gamma^2 r^3} dr \tag{4.18}$$

where $r_i = \sqrt{r_c^2 - 2\gamma L}$. The bending moment in the deformation sub-problem can be evaluated based on the following formula:

$$\begin{aligned} M_{\text{beam}}(t) &= \int_{A_{\text{cross}}} T_{\theta\theta}(r - r_{\text{neu}})\mathrm{d}A \\ &= 2H \int_{-L}^{L} T_{\theta\theta}(-\sqrt{r_c^2 + 2\gamma X_{\text{neu}}} + \sqrt{r_c^2 + 2\gamma X})\frac{\gamma}{\sqrt{r_c^2 + 2\gamma X}}\mathrm{d}X \end{aligned} \tag{4.19}$$

where $\mathrm{d}A = 2H\mathrm{d}r$. $r_{\text{neu}} = \sqrt{r_c^2 + 2\gamma X_{\text{neu}}}$ is the neutral axis location, and X_{neu} is the value at which $T_{\theta\theta} = 0$. As r_c is given, the parameter γ is bounded above and below as follows:

$$\frac{-r_c^2}{2L} < \gamma < \frac{r_c^2}{2L} \tag{4.20}$$

which can be used in finding the solution for the non-linear equation given by (4.16). It should be noted that $\gamma|_{t=0}$ satisfies the inequality given by (4.20).

The chemical potential and specific entropy are given as follows:

$$\varkappa = \frac{1}{\rho_0}\frac{\partial \psi}{\partial c} + R_s\vartheta_{\rm ref}\{c - c_{\rm ref}\} = -\frac{\mu_1}{2\rho_0 c_{\rm ref}}\left(\frac{\gamma^2}{r^2} + \frac{r^2}{\gamma^2} - 2\right) + R_s\vartheta_{\rm ref}\{c - c_{\rm ref}\} \tag{4.21a}$$

$$\eta = -\frac{1}{\rho_0}\frac{\partial \psi}{\partial \vartheta} + \frac{c_p}{\vartheta_{\rm ref}}\{\vartheta - \vartheta_{\rm ref}\} = \frac{\mu_1}{2\rho_0\vartheta_{\rm ref}}\left(\frac{\gamma^2}{r^2} + \frac{r^2}{\gamma^2} - 2\right) + \frac{c_p}{\vartheta_{\rm ref}}\{\vartheta - \vartheta_{\rm ref}\} \tag{4.21b}$$

From equations (4.21a)–(4.21b) and appealing to incompressibility condition, the mass transfer and heat transfer fluxes in radial direction can be written as follows:

$$h_{\rm r} = -\frac{\rho_0}{R_s\vartheta_{\rm ref}}D_{\varkappa\varkappa}\frac{\partial \varkappa}{\partial r} = \frac{\mu_1 D_{\varkappa\varkappa}}{R_s\vartheta_{\rm ref}c_{\rm ref}}\left(\frac{r}{\gamma^2} - \frac{\gamma^2}{r^3}\right) - \rho_0 D_{\varkappa\varkappa}\frac{\partial c}{\partial r} \tag{4.22a}$$

$$q_{\rm r} = -\rho_0 c_p D_{\vartheta\vartheta}\frac{\partial \vartheta}{\partial r} \tag{4.22b}$$

From equation (4.1a) and (4.2a), the final form for the governing equations for transport and thermal sub-problems for degrading beam are given as follows:

$$\rho_0\frac{\partial c}{\partial t} - \left(\frac{\rho_0 D_{\varkappa\varkappa}}{r} + \rho_0\frac{\partial D_{\varkappa\varkappa}}{\partial r}\right)\frac{\partial c}{\partial r} - \rho_0 D_{\varkappa\varkappa}\frac{\partial^2 c}{\partial r^2} = \omega\frac{\partial D_{\varkappa\varkappa}}{\partial r}\left(\frac{\gamma^2}{r^3} - \frac{r}{\gamma^2}\right) - 2\omega D_{\varkappa\varkappa}\left(\frac{1}{\gamma^2} + \frac{\gamma^2}{r^4}\right) \tag{4.23}$$

$$\left(\frac{\rho_0 c_p\vartheta}{\vartheta_{\rm ref}}\right)\frac{\partial \vartheta}{\partial t} - \left(\frac{\rho_0 c_p D_{\vartheta\vartheta}}{r} + \rho_0 c_p\frac{\partial D_{\vartheta\vartheta}}{\partial r}\right)\frac{\partial \vartheta}{\partial r} - \rho_0 c_p D_{\vartheta\vartheta}\frac{\partial^2 \vartheta}{\partial r^2} = \rho_0 R_s\vartheta_{\rm ref}D_{\varkappa\varkappa}\left(\frac{\partial c}{\partial r}\right)^2 + \frac{R_s\vartheta_{\rm ref}D_{\varkappa\varkappa}\omega^2}{\rho_0}\left(\frac{\gamma^2}{r^3} - \frac{r}{\gamma^2}\right)^2 + 2R_s\vartheta_{\rm ref}\omega D_{\varkappa\varkappa}\left(\frac{\gamma^2}{r^3} - \frac{r}{\gamma^2}\right)\frac{\partial c}{\partial r} \tag{4.24}$$

where $\omega = \frac{\mu_1}{R_s\vartheta_{\rm ref}c_{\rm ref}}$. In deriving (4.24), we have assumed that $\frac{\partial r}{\partial t} \ll \frac{\partial \vartheta}{\partial t}$ (in order to reduce the complexity in finding semi-analytical solutions). We take ρ_0, r_c, R_s, $\vartheta_{\rm ref}$, $c_{\rm ref}$, and D_0 as the reference quantities. These reference quantities give rise to the following non-dimensional quantities:

$$\overline{r} = \frac{r}{r_c},\ \overline{X} = \frac{X}{r_c},\ \overline{\gamma} = \frac{\gamma}{r_c},\ \overline{D}_{\varkappa\varkappa} = \frac{D_{\varkappa\varkappa}}{D_0},\ \overline{D}_{\vartheta\vartheta} = \frac{D_{\vartheta\vartheta}}{D_0} \tag{4.25}$$

$$\overline{\mu}_1 = \frac{\mu_1}{\rho_0 R_s\vartheta_{\rm ref}},\ \overline{\mu}_0 = \frac{\mu_0}{\rho_0 R_s\vartheta_{\rm ref}},\ \overline{c} = \frac{c}{c_{\rm ref}},\ \overline{\vartheta} = \frac{\vartheta}{\vartheta_{\rm ref}},\ \overline{t} = \frac{D_0 t}{r_c^2} \tag{4.26}$$

The above non-dimensionalization introduces the following non-dimensional parameters:

$$\overline{\omega} = \frac{\omega}{\rho_0 c_{\rm ref}} \tag{4.27}$$

$$\overline{\tau} = \frac{R_s c_{\rm ref}^2}{c_p} \tag{4.28}$$

Correspondingly, the non-dimensionalized governing equations for transport and thermal sub-problems for degrading beam are given as follows:

$$\frac{\partial \overline{c}}{\partial \overline{t}} - \left(\frac{\overline{D}_{\varkappa\varkappa}}{\overline{r}} + \frac{\partial \overline{D}_{\varkappa\varkappa}}{\partial \overline{r}}\right)\frac{\partial \overline{c}}{\partial \overline{r}} - \overline{D}_{\varkappa\varkappa}\frac{\partial^2 \overline{c}}{\partial \overline{r}^2} = \overline{\omega}\frac{\partial \overline{D}_{\varkappa\varkappa}}{\partial \overline{r}}\left(\frac{\overline{\gamma}^2}{\overline{r}^3} - \frac{\overline{r}}{\overline{\gamma}^2}\right) - 2\overline{\omega}\overline{D}_{\varkappa\varkappa}\left(\frac{1}{\overline{\gamma}^2} + \frac{\overline{\gamma}^2}{\overline{r}^4}\right) \tag{4.29}$$

$$\overline{\vartheta}\frac{\partial\overline{\vartheta}}{\partial\overline{t}}-\left(\frac{\overline{D}_{\vartheta\vartheta}}{\overline{r}}+\frac{\partial\overline{D}_{\vartheta\vartheta}}{\partial\overline{r}}\right)\frac{\partial\overline{\vartheta}}{\partial\overline{r}}-\overline{D}_{\vartheta\vartheta}\frac{\partial^2\overline{\vartheta}}{\partial\overline{r}^2}=\overline{\tau}\overline{D}_{\varkappa\varkappa}\left(\frac{\partial\overline{c}}{\partial\overline{r}}\right)^2+2\overline{\tau\omega}\overline{D}_{\varkappa\varkappa}\left(\frac{\overline{\gamma}^2}{\overline{r}^3}-\frac{\overline{r}}{\overline{\gamma}^2}\right)\frac{\partial\overline{c}}{\partial\overline{r}}+\overline{\tau}\overline{D}_{\varkappa\varkappa}\overline{\omega}^2\left(\frac{\overline{\gamma}^2}{\overline{r}^3}-\frac{\overline{r}}{\overline{\gamma}^2}\right)^2 \tag{4.30}$$

where $\frac{\partial\overline{D}_{\varkappa\varkappa}}{\partial\overline{r}}$ and $\frac{\partial\overline{D}_{\vartheta\vartheta}}{\partial\overline{r}}$ are given as follows:

$$\frac{\partial\overline{D}_{\varkappa\varkappa}}{\partial\overline{r}}=\eta_T\left(\overline{D}_T-\overline{D}_0\right)\frac{(\exp[\eta_T\overline{I}_{\mathbf{E}}]-1)}{(\exp[\eta_T E_{\mathrm{ref}T}]-1)}\frac{\partial\overline{I}_{\mathbf{E}}}{\partial\overline{r}}+\eta_S\left(\overline{D}_S-\overline{D}_0\right)\frac{(\exp[\eta_S\overline{II}_{\mathbf{E}}]-1)}{(\exp[\eta_S E_{\mathrm{ref}S}]-1)}\frac{\partial\overline{II}_{\mathbf{E}}}{\partial\overline{r}} \tag{4.31}$$

$$\frac{\partial\overline{D}_{\vartheta\vartheta}}{\partial\overline{r}}=-\left(\delta K_{0\vartheta}(1+\overline{I}_{\mathbf{E}})^{-\delta-1}\right)\frac{\partial\overline{I}_{\mathbf{E}}}{\partial\overline{r}} \tag{4.32}$$

where the first and second invariants, $\overline{I}_{\mathbf{E}}$ and $\overline{II}_{\mathbf{E}}$, are given as follows:

$$\overline{I}_{\mathbf{E}}=\frac{1}{2}\left(\frac{\overline{\gamma}^2}{\overline{r}^2}+\frac{\overline{r}^2}{\overline{\gamma}^2}-2\right) \tag{4.33}$$

$$\overline{II}_{\mathbf{E}}=\sqrt{\frac{1}{6}\left(\left(\frac{\overline{\gamma}^2}{\overline{r}^2}-1\right)^2+\left(\frac{\overline{r}^2}{\overline{\gamma}^2}-1\right)^2+\left(\frac{\overline{\gamma}^2}{\overline{r}^2}-\frac{\overline{r}^2}{\overline{\gamma}^2}\right)^2\right)} \tag{4.34}$$

The partial derivative of the first and second invariants with respect to $\overline{r}$ are given as follows:

$$\frac{\partial\overline{I}_{\mathbf{E}}}{\partial\overline{r}}=\frac{\overline{r}}{\overline{\gamma}^2}-\frac{\overline{\gamma}^2}{\overline{r}^3} \tag{4.35}$$

$$\frac{\partial\overline{II}_{\mathbf{E}}}{\partial\overline{r}}=\frac{1}{3\overline{II}_{\mathbf{E}}}\left(\frac{-\overline{\gamma}^2}{\overline{r}^3}\left(\frac{\overline{\gamma}^2}{\overline{r}^2}-1\right)+\frac{\overline{r}}{\overline{\gamma}^2}\left(\frac{\overline{r}^2}{\overline{\gamma}^2}-1\right)-\left(\frac{\overline{\gamma}^2}{\overline{r}^3}+\frac{\overline{r}}{\overline{\gamma}^2}\right)\left(\frac{\overline{\gamma}^2}{\overline{r}^2}-\frac{\overline{r}^2}{\overline{\gamma}^2}\right)\right) \tag{4.36}$$

Correspondingly, the non-dimensional equation to obtain $\overline{\gamma}$ at each time is given as follows:

$$\int_{-L/r_c}^{L/r_c}\frac{\overline{\mu}(\overline{c}(\overline{X},\overline{t}),\overline{\vartheta}(\overline{X},\overline{t}))\left(\overline{\gamma}^4-\left(2\overline{\gamma}\overline{X}+1\right)^2\right)}{\overline{\gamma}\left(2\overline{\gamma}\overline{X}+1\right)^2}d\overline{X}=0 \tag{4.37}$$

The non-linear equation (4.37) enables us to find $\overline{\gamma}$ at various $\overline{t}$ given $\overline{c}(\overline{X},\overline{t})$ and $\overline{\vartheta}(\overline{X},\overline{t})$. However, it should be noted that $\overline{c}(\overline{X},\overline{t})$ and $\overline{\vartheta}(\overline{X},\overline{t})$ are also a function of $\overline{\gamma}$ in case of strong coupling. This is because diffusivity and thermal conductivity depend on the invariants of strain $\overline{\mathbf{E}}$. Hence, the integral equation (4.37) and partial differential equations (4.29) and (4.30) are strongly coupled.

4.1.1. *Steady-state analysis for beam degradation.* In case of steady-state, we have $h_r r = C_1$ and $q_r r + \varkappa h_r r = C_2$, where C_1 and C_2 are integration constants. Equations (4.29) and (4.30) imply that $\overline{c}$ and $\overline{\vartheta}$ are the solutions of the following ODEs:

$$\overline{D}_{\varkappa\varkappa}\overline{r}\frac{d\overline{c}}{d\overline{r}}-\overline{D}_{\varkappa\varkappa}\overline{\omega}\left(\frac{\overline{\gamma}^2}{\overline{r}^2}-\frac{\overline{r}^2}{\overline{\gamma}^2}\right)+\overline{C}_1=0 \tag{4.38a}$$

$$\overline{D}_{\vartheta\vartheta}\overline{r}\frac{d\overline{\vartheta}}{d\overline{r}}+\overline{\tau}\left(\frac{\overline{w}}{2}\left(\frac{\overline{\gamma}^2}{\overline{r}^2}+\frac{\overline{r}^2}{\overline{\gamma}^2}-2\right)-\overline{c}+1\right)\overline{C}_1+\overline{C}_2=0 \tag{4.38b}$$

Assuming $\overline{D}_{\vartheta\vartheta}$ is independent of $\overline{\vartheta}$, the analytical solutions to the above set of ODEs are given as follows:

$$\overline{c} = \int \left(\overline{\omega} \left(\frac{\overline{\gamma}^2}{\overline{r}^3} - \frac{\overline{r}}{\overline{\gamma}^2} \right) - \frac{\overline{C}_1}{\overline{r}\overline{D}_{\varkappa\varkappa}} \right) \, \mathrm{d}\overline{r} \tag{4.39a}$$

$$\overline{\vartheta} = \int \left(-\frac{\overline{\tau}\overline{C}_1}{\overline{D}_{\vartheta\vartheta}} \left(\frac{\overline{w}}{2} \left(\frac{\overline{\gamma}^2}{\overline{r}^3} + \frac{\overline{r}}{\overline{\gamma}^2} - \frac{2}{\overline{r}} \right) - \frac{\overline{c}-1}{\overline{r}} \right) - \frac{\overline{C}_2}{\overline{r}\overline{D}_{\vartheta\vartheta}} \right) \, \mathrm{d}\overline{r} \tag{4.39b}$$

where the integration constants $\overline{C}_1$ and $\overline{C}_2$ are determined from the respective boundary conditions for the transport and thermal sub-problems. In case of weak coupling (where $D_{\vartheta\vartheta}$ and $D_{\varkappa\varkappa}$ are constants), a simplified form for $\overline{c}$ and $\overline{\vartheta}$ is given as follows:

$$\overline{c} = -\frac{\overline{\omega}}{2} \left(\frac{\overline{\gamma}^2}{\overline{r}^2} + \frac{\overline{r}^2}{\overline{\gamma}^2} \right) + B_1 \ln[\overline{r}] + A_1 \tag{4.40a}$$

$$\overline{\vartheta} = -\frac{\overline{\tau} B_1^2 \overline{D}_{\varkappa\varkappa}}{2\overline{D}_{\vartheta\vartheta}} \ln[\overline{r}]^2 + Z_1 \ln[\overline{r}] + Y_1 \tag{4.40b}$$

where the constants A_1, B_1, Y_1, and Z_1 are given in terms of the boundary conditions $\overline{c}_i$, $\overline{c}_o$, $\overline{\vartheta}_i$, and $\overline{\vartheta}_o$ as follows:

$$A_1 = \overline{c}_i - B_1 \ln[\overline{r}_i] + \frac{\overline{\omega}}{2} \left(\frac{\overline{\gamma}^2}{\overline{r}_i^2} + \frac{\overline{r}_i^2}{\overline{\gamma}^2} \right) \tag{4.41a}$$

$$B_1 = \frac{1}{\ln[\overline{r}_o] - \ln[\overline{r}_i]} \left(\overline{c}_o - \overline{c}_i - \frac{\overline{\omega}}{2} \left(\frac{\overline{\gamma}^2}{\overline{r}_i^2} + \frac{\overline{r}_i^2}{\overline{\gamma}^2} - \frac{\overline{\gamma}^2}{\overline{r}_o^2} - \frac{\overline{r}_o^2}{\overline{\gamma}^2} \right) \right) \tag{4.41b}$$

$$Y_1 = \overline{\vartheta}_i + \frac{\overline{\tau} B_1^2 \overline{D}_{\varkappa\varkappa}}{2\overline{D}_{\vartheta\vartheta}} \ln[\overline{r}_i]^2 - Z_1 \ln[\overline{r}_i] \tag{4.41c}$$

$$Z_1 = \frac{1}{\ln[\overline{r}_o] - \ln[\overline{r}_i]} \left(\overline{\vartheta}_o - \overline{\vartheta}_i - \frac{\overline{\tau} B_1^2 \overline{D}_{\varkappa\varkappa}}{2\overline{D}_{\vartheta\vartheta}} \left(\ln[\overline{r}_i]^2 - \ln[\overline{r}_o]^2 \right) \right) \tag{4.41d}$$

4.1.2. *Quasistatic analysis for beam degradation.* Herein, we shall use the method of horizontal lines [Rothe, 1930; Picard and Leis, 1980] and shooting method [Heath, 2005] to obtain numerical solutions to equations (4.29) and (4.30). In the method of horizontal lines, the time is discretized first followed by spatial discretization. The time interval of interest $[0, \overline{\mathcal{I}}]$ is divided into N non-overlapping subintervals such that $\Delta\overline{t} = \frac{\overline{\mathcal{I}}}{N}$ and $\overline{t}_n = n\Delta\overline{t}$. $\overline{t}_n$ is called the integral time level, where $n = 0, 1, 2, \cdots, N$. $\Delta\overline{t}$ is the time-step, which is assumed to be uniform. Employing the method of horizontal lines with backward Euler time-stepping scheme, we obtain the following ODEs at each time-level for equations (4.29) and (4.30)

$$\begin{aligned} \frac{d^2\overline{c}^{(n+1)}}{d\overline{r}^2} + \left(\frac{1}{\overline{r}^{(n)}} + \left(\frac{1}{\overline{D}_{\varkappa\varkappa}^{(n)}} \right) \left. \frac{d\overline{D}_{\varkappa\varkappa}}{d\overline{r}} \right|_{\overline{t}=\overline{t}_n} \right) \frac{d\overline{c}^{(n+1)}}{d\overline{r}} - \frac{\overline{c}^{(n+1)}}{\overline{D}_{\varkappa\varkappa}^{(n)} \Delta\overline{t}} = 2\overline{\omega} \left(\frac{1}{\left(\overline{\gamma}^{(n)}\right)^2} + \frac{\left(\overline{\gamma}^{(n)}\right)^2}{\left(\overline{r}^{(n)}\right)^4} \right) \\ - \frac{\overline{c}^{(n)}}{\overline{D}_{\varkappa\varkappa}^{(n)} \Delta\overline{t}} - \left(\frac{\overline{\omega}}{\overline{D}_{\varkappa\varkappa}^{(n)}} \right) \left(\left. \frac{d\overline{D}_{\varkappa\varkappa}}{d\overline{r}} \right|_{\overline{t}=\overline{t}_n} \right) \left(\frac{\left(\overline{\gamma}^{(n)}\right)^2}{\left(\overline{r}^{(n)}\right)^3} - \frac{\overline{r}^{(n)}}{\left(\overline{\gamma}^{(n)}\right)^2} \right) \end{aligned} \tag{4.42}$$

$$\frac{d^2\overline{\vartheta}^{(n+1)}}{d\overline{r}^2}+\left(\frac{1}{\overline{r}^{(n)}}+\left(\frac{1}{\overline{D}^{(n)}_{\vartheta\vartheta}}\right)\frac{d\overline{D}_{\vartheta\vartheta}}{d\overline{r}}\bigg|_{\overline{t}=\overline{t}_n}\right)\frac{d\overline{\vartheta}^{(n+1)}}{d\overline{r}}-\frac{\overline{\vartheta}^{(n)}\overline{\vartheta}^{(n+1)}}{\overline{D}^{(n)}_{\vartheta\vartheta}\,\Delta\overline{t}}=-\frac{\overline{\tau}\overline{D}^{(n)}_{\varkappa\varkappa}}{\overline{D}^{(n)}_{\vartheta\vartheta}}\left(\frac{d\overline{c}}{d\overline{r}}\bigg|_{\overline{t}=\overline{t}_n}\right)^2-\frac{\left(\overline{\vartheta}^{(n)}\right)^2}{\overline{D}^{(n)}_{\vartheta\vartheta}\,\Delta\overline{t}}$$
$$-\frac{2\overline{\tau}\overline{\omega}\overline{D}^{(n)}_{\varkappa\varkappa}}{\overline{D}^{(n)}_{\vartheta\vartheta}}\left(\frac{\left(\overline{\gamma}^{(n)}\right)^2}{\left(\overline{r}^{(n)}\right)^3}-\frac{\overline{r}^{(n)}}{\left(\overline{\gamma}^{(n)}\right)^2}\right)\frac{d\overline{c}}{d\overline{r}}\bigg|_{\overline{t}=\overline{t}_n}-\frac{\overline{\tau}\overline{D}^{(n)}_{\varkappa\varkappa}\overline{\omega}^2}{\overline{D}^{(n)}_{\vartheta\vartheta}}\left(\frac{\left(\overline{\gamma}^{(n)}\right)^2}{\left(\overline{r}^{(n)}\right)^3}-\frac{\left(\overline{r}^{(n)}\right)}{\left(\overline{\gamma}^{(n)}\right)^2}\right)^2 \tag{4.43}$$

where $\overline{c}^{(n)}=\overline{c}(\overline{r},\overline{t}=\overline{t}_n)$, $\overline{\vartheta}^{(n)}=\overline{\vartheta}(\overline{r},\overline{t}=\overline{t}_n)$, and $\overline{r}^{(n)}=\sqrt{2\overline{\gamma}^{(n)}\overline{X}+\overline{r}_c^2}$. Algorithm 1 describes a procedure to determine $\overline{c}(\overline{r},\overline{t})$, $\overline{\vartheta}(\overline{r},\overline{t})$, and $\overline{\gamma}$ at various times using an iterative non-linear numerical solution strategy. The following values are assumed for the non-dimensional parameters in the strong coupling simulations:

$$\begin{aligned}&\overline{L}=1,\ \overline{r}_c=1,\ \Delta\overline{t}=0.1,\ \overline{t}=2,\ \overline{\omega}=0.05,\ \overline{\tau}=0.5,\ \overline{c}_i=0,\frac{\vartheta_0}{\vartheta_{\text{ref}}}=0.5\\&\overline{c}_o=1,\ \overline{\vartheta}_i=0.5,\ \overline{\vartheta}_o=1,\ \overline{\mu}_0=1,\ \overline{\mu}_1=\overline{\mu}_2=0.4,\ \overline{D}_0=1,\ \overline{D}_T=2.0,\\&\overline{D}_S=1.5,\ \eta_T=\eta_S=1,\ E_{\text{ref}T}=E_{\text{ref}S}=1,\ \overline{K}_0=1,\ \delta=10\end{aligned} \tag{4.44}$$

In case of weak coupling, we have $\overline{D}_0$ as $\overline{D}^{(n)}_{\varkappa\varkappa}$ and $\overline{K}_0$ as $\overline{D}^{(n)}_{\vartheta\vartheta}$, respectively. It should be noted that these values are constructed based on the (brittle-type) material parameters such as glass, ceramics, and concrete.

Figure 4 shows the profile of $\overline{T}_{\theta\theta}$ as a function of the reference location of the cross-section at various instants of time (due to the application of bending moment). In Figure 5, the plot of bending moment at various instants of time for both three-way strong and weak coupling degradation model is shown. Figure 6 shows the plot of chemical potential as a function of the reference location of the cross-section at various instants of time. The extent of damage at various instants of time is shown in Figure 7. Initially at time $\overline{t}=0$ and when there is no degradation, the response is that of a homogeneous neo-Hookean material. *On the onset of degradation, the material ceases to be homogeneous*. As degradation progress, one can see that the tensile and compressive parts of the beam relax at a much faster rate than that of the material closer to the neutral axis. Furthermore, the region in the tension and compression relax faster in case of strong coupling as compared to weak coupling. In addition, from Figure 4 one can see that $\overline{T}_{\theta\theta}$ for strong coupling is considerably different from the weak coupling. This is because the degradation progress is dependent on the deformation, concentration of the diffusing chemical species, and temperature of the body.

As Figure 5 shows, moment relaxation is observed for both cases. However, in weak coupling the moment declines more than that in strong coupling case. Moreover, as moment decreases, the chemical potential increases. From Figure 7, it is apparent that for both strong and weak coupling, the beam has degraded considerably in the tensile region as compared to the compression region. Quantitatively, extent of damage towards the tension side is three times greater than that of the compressive side of the beam. Furthermore, $\mathcal{D}_\mu$ across the cross section is not monotonic for strongly coupled problem. However, in case of weakly coupled problem (for time $\overline{t}>0.1$), we observe that the extent of damage is monotonic. *Herein, the main observation is that neutral axis shifts further to the left*, similar to the phenomenon observed in viscoelastic solids [Kolberg and Wineman, 1997]. Moreover, in case of weak coupling for some instants of time *the maximum stress does not occur at either tensile or compressive sides of the beam after the onset of degradation*. This is of primal importance in regards to the calculation of failure loads/moments due to material

damage. Hence, a simple approach based on strength of materials or a more complex finite elasticity theory to calculate stresses without accounting for degradation will lead to erroneous results.

Algorithm 1 Pure bending of degrading beam (numerical methodology to find $\overline{\gamma}$, $\overline{c}$, and $\overline{\vartheta}$)

1: INPUT: Non-dimensional material parameters, non-dimensional boundary conditions, and non-dimensional initial conditions, `MaxIters`, tolerances $\epsilon_{\text{tol}}^{(\gamma)}$, $\epsilon_{\text{tol}}^{(c)}$, and $\epsilon_{\text{tol}}^{(\vartheta)}$.
2: Evaluate $\overline{\gamma}$ at $\overline{t} = 0$ based on equation (4.17). Use this as an initial guess for solving nonlinear equation given by (4.37) or guess $\overline{\gamma}$ based on equation (4.20).
3: **for** $n = 1, 2, \cdots, N$ **do**
4: **for** $i = 1, 2, \cdots$ **do**
5: **if** $i >$ `MaxIters` **then**
6: Solution did not converge in specified maximum number of iterations. EXIT.
7: **end if**
8: `Diffusion sub-problem`: Given $\overline{\gamma}^{(i)}$, solve equation (4.42) to obtain $\overline{c}^{(i+1)}$. Herein, we use shooting method to solve the ODEs.
9: `Heat conduction sub-problem`: Given $\overline{\gamma}^{(i)}$ and $\overline{c}^{(i+1)}$, solve equation (4.43) to obtain $\overline{\vartheta}^{(i+1)}$. Similarly, we use shooting method to solve the ODEs.
10: `Deformation sub-problem`: Given $\overline{c}^{(i+1)}$ and $\overline{\vartheta}^{(i+1)}$, solve for $\overline{\gamma}^{(i+1)}$ given by equation (4.37) using bisection method.
11: **if** $\|\overline{\gamma}^{(i+1)} - \overline{\gamma}^{(i)}\| < \epsilon_{\text{tol}}^{(\gamma)}$, $\|\overline{c}^{(i+1)} - \overline{c}^{(i)}\| < \epsilon_{\text{tol}}^{(c)}$, and $\|\overline{\vartheta}^{(i+1)} - \overline{\vartheta}^{(i)}\| < \epsilon_{\text{tol}}^{(\vartheta)}$ **then**
12: OUTPUT: $\overline{\gamma}^{(i+1)}$, $\overline{c}^{(i+1)}$, and $\overline{\vartheta}^{(i+1)}$. EXIT the inner loop.
13: **else**
14: Update the guess: $\overline{\gamma}^{(i)} \leftarrow \overline{\gamma}^{(i+1)}$.
15: **end if**
16: **end for**
17: **end for**

REMARK 4.1. *Based on a semi-inverse approach, [Rajagopal et al., 2007] have shown that pure bending of a polymer beam stress relaxes under degradation. However, their model is based on internal variables, which is difficult to calibrate experimentally. On the other hand, the proposed (and calibrated) chemo-thermo-mechano degradation model is able to predict stress relaxation and shift of neutral axis without appealing to internal variable framework.*

4.2. Inflation of a degrading spherical shell. Herein, we shall consider degradation of a spherical shell subjected to pressure loading. A pictorial description of the boundary value problem is similar to the one shown in Figure 1. The shell is subjected to an inner pressure p_i and an outer pressure p_o. Due to the spherical symmetric associated with the problem, spherical coordinates are used to analyze the inflation of degrading spherical shell. It should be noted that the problem under consideration has relevance to safety, reliability, and defect monitoring of degrading spherical structures (such as a tank shell and bearing structure) due to a pressure process system [Pietraszkiewicz and Szymczak].

In the reference configuration, consider a spherical body of inner radius R_i and outer radius R_o defined as follows:

$$R_i \leq R \leq R_o, \quad 0 \leq \Theta \leq \pi, \quad 0 \leq \Phi \leq 2\pi \tag{4.45}$$

where (R, Θ, Φ) are the spherical polar coordinates in the reference configuration. The surfaces $R = R_i$ and $R = R_o$ are subjected to different pressures p_i and p_o. Under inflation, the deformation in the current configuration is described as follows:

$$r_i \leq r = m(R) \leq r_o, \quad \theta = \Theta, \quad \phi = \Phi \tag{4.46}$$

where (r, θ, ϕ) are the spherical polar coordinates, r_i is the inner radius, and r_o is the outer radius in the current configuration. The deformation gradient, the left Cauchy-Green tensor, and the right Cauchy-Green tensor have the following matrix representations:

$$\mathbf{F} = \begin{pmatrix} \frac{dm}{dR} & 0 & 0 \\ 0 & \frac{m}{R} & 0 \\ 0 & 0 & \frac{m}{R} \end{pmatrix} \qquad \mathbf{C} = \mathbf{B} = \begin{pmatrix} \left(\frac{dm}{dR}\right)^2 & 0 & 0 \\ 0 & \frac{m^2}{R^2} & 0 \\ 0 & 0 & \frac{m^2}{R^2} \end{pmatrix} \tag{4.47}$$

Using the condition of incompressibility, we have $r = \sqrt[3]{R^3 + r_i^3 - R_i^3}$ such that $r_i \leq r \leq r_o$, where $r_o = \sqrt[3]{R_o^3 + r_i^3 - R_i^3}$. The governing equations (balance of linear momentum) in spherical coordinates for deformation sub-problem are given as follows:

$$\frac{\partial T_{rr}}{\partial r} + \frac{1}{r}\frac{\partial T_{\theta r}}{\partial \theta} + \frac{1}{r\sin(\theta)}\frac{\partial T_{\phi r}}{\partial \phi} + \frac{2T_{rr} - T_{\theta\theta} - T_{\phi\phi}}{r} = 0 \tag{4.48a}$$

$$\frac{\partial T_{r\theta}}{\partial r} + \frac{1}{r}\frac{\partial T_{\theta\theta}}{\partial \theta} + \frac{1}{r\sin(\theta)}\frac{\partial T_{\phi\theta}}{\partial \phi} + \frac{2T_{r\theta} + T_{\theta r} + (T_{\theta\theta} - T_{\phi\phi})\cot(\theta)}{r} = 0 \tag{4.48b}$$

$$\frac{\partial T_{r\phi}}{\partial r} + \frac{1}{r}\frac{\partial T_{\theta\phi}}{\partial \theta} + \frac{1}{r\sin(\theta)}\frac{\partial T_{\phi\phi}}{\partial \phi} + \frac{2T_{r\phi} + T_{\phi r} + (T_{\theta\phi} + T_{\phi\theta})\cot(\theta)}{r} = 0 \tag{4.48c}$$

From equation (4.47), the non-zero components of the Cauchy stress are given as follows:

$$T_{rr} = -p + \mu(c, \vartheta)\left(\frac{\mathrm{d}m}{\mathrm{d}R}\right)^2 = -p + \mu(c, \vartheta)\left(\frac{R^2}{r^2}\right)^2 \tag{4.49a}$$

$$T_{\theta\theta} = -p + \mu(c, \vartheta)\frac{r^2}{R^2} \tag{4.49b}$$

$$T_{\phi\phi} = -p + \mu(c, \vartheta)\frac{r^2}{R^2} \tag{4.49c}$$

The balance of linear momentum given by equation (4.48a)–(4.48c) reduces to the following:

$$\frac{\partial T_{rr}}{\partial r} + \frac{2T_{rr} - T_{\theta\theta} - T_{\phi\phi}}{r} = 0, \ \frac{\partial p}{\partial \theta} = 0, \ \frac{\partial p}{\partial \phi} = 0 \tag{4.50}$$

From the above equations, we have $p = p(r, t)$. Using equations (4.50), (4.46), (4.49a), (4.49b), and (4.49c), we have the following non-linear equation in r_i:

$$T_{rr}(R = R_i, t) - T_{rr}(R = R_o, t) = p_o - p_i = \int_{R_i}^{R_o} \frac{2\mu(c(R,t), \vartheta(R,t))\left(R^6 - \left(R^3 + r_i^3 - R_i^3\right)^2\right)}{\left(R^3 + r_i^3 - R_i^3\right)^{\frac{7}{3}}} \mathrm{d}R \tag{4.51}$$

Once c, ϑ, and r_i are known, the Lagrange multiplier $p = p(r,t)$ enforcing the incompressibility constraint can evaluated from (4.50) as follows:

$$p(r,t) = p_i + \mu(c,\vartheta)\left(\frac{R^2}{r^2}\right)^2 - \int_{R_i}^{R} \frac{2\mu(c,\vartheta)\left(R^6 - \left(R^3 + r_i^3 - R_i^3\right)^2\right)}{\left(R^3 + r_i^3 - R_i^3\right)^{\frac{7}{3}}}\mathrm{d}R \tag{4.52}$$

The chemical potential, specific entropy, heat transfer flux, and mass transfer flux in radial direction for the degrading shell are given as follows:

$$\varkappa = \frac{1}{\rho_0}\frac{\partial \psi}{\partial c} + R_s\vartheta_{\mathrm{ref}}\{c - c_{\mathrm{ref}}\} = -\frac{\mu_1}{2\rho_0 c_{\mathrm{ref}}}\left(\frac{R^4}{r^4} + 2\frac{r^2}{R^2} - 3\right) + R_s\vartheta_{\mathrm{ref}}\{c - c_{\mathrm{ref}}\} \tag{4.53a}$$

$$\eta = -\frac{1}{\rho_0}\frac{\partial \psi}{\partial \vartheta} + \frac{c_p}{\vartheta_{\mathrm{ref}}}\{\vartheta - \vartheta_{\mathrm{ref}}\} = \frac{\mu_1}{2\rho_0\vartheta_{\mathrm{ref}}}\left(\frac{R^4}{r^4} + 2\frac{r^2}{R^2} - 3\right) + \frac{c_p}{\vartheta_{\mathrm{ref}}}\{\vartheta - \vartheta_{\mathrm{ref}}\} \tag{4.53b}$$

$$h_{\mathrm{r}} = -\frac{\rho_0}{R_s\vartheta_{\mathrm{ref}}}D_{\varkappa\varkappa}\frac{\partial \varkappa}{\partial r} = \frac{2\mu_1 D_{\varkappa\varkappa}}{R_s\vartheta_{\mathrm{ref}}c_{\mathrm{ref}}}\left(\frac{r}{R^2} - \frac{R^4}{r^5}\right) - \rho_0 D_{\varkappa\varkappa}\frac{\partial c}{\partial r} \tag{4.53c}$$

$$q_{\mathrm{r}} = -\rho_0 c_p D_{\vartheta\vartheta}\frac{\partial \vartheta}{\partial r} \tag{4.53d}$$

From equation (4.3a) and (4.4a), the final form for the governing equations for transport and thermal sub-problems for degrading shell is given as follows:

$$\rho_0\frac{\partial c}{\partial t} - \left(\frac{2\rho_0 D_{\varkappa\varkappa}}{r} + \rho_0\frac{\partial D_{\varkappa\varkappa}}{\partial r}\right)\frac{\partial c}{\partial r} - \rho_0 D_{\varkappa\varkappa}\frac{\partial^2 c}{\partial r^2} = 2\omega\frac{\partial D_{\varkappa\varkappa}}{\partial r}\left(\frac{R^4}{r^5} - \frac{r}{R^2}\right) - 6\omega D_{\varkappa\varkappa}\left(\frac{1}{R^2} + \frac{R^4}{r^6}\right) \tag{4.54}$$

$$\left(\frac{\rho_0 c_p\vartheta}{\vartheta_{\mathrm{ref}}}\right)\frac{\partial \vartheta}{\partial t} - \left(\frac{2\rho_0 c_p D_{\vartheta\vartheta}}{r} + \rho_0 c_p\frac{\partial D_{\vartheta\vartheta}}{\partial r}\right)\frac{\partial \vartheta}{\partial r} - \rho_0 c_p D_{\vartheta\vartheta}\frac{\partial^2\vartheta}{\partial r^2} = \rho_0 R_s\vartheta_{\mathrm{ref}}D_{\varkappa\varkappa}\left(\frac{\partial c}{\partial r}\right)^2 + \frac{4R_s\vartheta_{\mathrm{ref}}D_{\varkappa\varkappa}\omega^2}{\rho_0}\left(\frac{r}{R^2} - \frac{R^4}{r^5}\right)^2 - 4R_s\vartheta_{\mathrm{ref}}\omega D_{\varkappa\varkappa}\left(\frac{r}{R^2} - \frac{R^4}{r^5}\right)\frac{\partial c}{\partial r} \tag{4.55}$$

Most of the non-dimensional quantities are same as that of the beam bending problem except for the following:

$$\overline{r} = \frac{r}{R_o},\ \overline{R} = \frac{R}{R_o},\ \overline{t} = \frac{D_0 t}{R_o^2} \tag{4.56}$$

The non-dimensionalized governing equations for transport and thermal sub-problems for degrading shell are given as follows:

$$\frac{\partial \overline{c}}{\partial \overline{t}} - \left(\frac{2\overline{D}_{\varkappa\varkappa}}{\overline{r}} + \frac{\partial \overline{D}_{\varkappa\varkappa}}{\partial \overline{r}}\right)\frac{\partial \overline{c}}{\partial \overline{r}} - \overline{D}_{\varkappa\varkappa}\frac{\partial^2 \overline{c}}{\partial \overline{r}^2} = 2\overline{\omega}\frac{\partial \overline{D}_{\varkappa\varkappa}}{\partial \overline{r}}\left(\frac{\overline{R}^4}{\overline{r}^5} - \frac{\overline{r}}{\overline{R}^2}\right) - 6\overline{\omega}\overline{D}_{\varkappa\varkappa}\left(\frac{1}{\overline{R}^2} + \frac{\overline{R}^4}{\overline{r}^6}\right) \tag{4.57}$$

$$\overline{\vartheta}\frac{\partial \overline{\vartheta}}{\partial \overline{t}} - \left(2\frac{\overline{D}_{\vartheta\vartheta}}{\overline{r}} + \frac{\partial \overline{D}_{\vartheta\vartheta}}{\partial \overline{r}}\right)\frac{\partial \overline{\vartheta}}{\partial \overline{r}} - \overline{D}_{\vartheta\vartheta}\frac{\partial^2 \overline{\vartheta}}{\partial \overline{r}^2} = \overline{\tau}\overline{D}_{\varkappa\varkappa}\left(\frac{\partial \overline{c}}{\partial \overline{r}}\right)^2 - 4\overline{\tau\omega}\overline{D}_{\varkappa\varkappa}\left(\frac{\overline{r}}{\overline{R}^2} - \frac{\overline{R}^4}{\overline{r}^5}\right)\frac{\partial \overline{c}}{\partial \overline{r}} + 4\overline{\tau\omega}^2\overline{D}_{\varkappa\varkappa}\left(\frac{\overline{r}}{\overline{R}^2} - \frac{\overline{R}^4}{\overline{r}^5}\right)^2 \tag{4.58}$$

The first and second invariants of $\overline{\mathbf{E}}$ for degrading shell are given as follows:

$$\overline{I}_{\mathbf{E}} = \frac{1}{2}\left(\frac{\overline{R}^4}{\overline{r}^4} + 2\frac{\overline{r}^2}{\overline{R}^2} - 3\right) = \frac{1}{2}\left(\frac{\overline{R}^2}{\overline{r}^2} - 2\frac{\overline{r}^2}{\overline{R}^2} + 1\right)\left(\frac{\overline{R}^2}{\overline{r}^2} - 1\right) \geq 0 \tag{4.59}$$

$$\overline{II}_{\mathbf{E}} = \sqrt{\frac{1}{3}\left(\left(\frac{\overline{R}^4}{\overline{r}^4} - 1\right)^2 + \left(\frac{\overline{r}^2}{\overline{R}^2} - 1\right)^2 - 2\left(\frac{\overline{R}^4}{\overline{r}^4} - 1\right)\left(\frac{\overline{r}^2}{\overline{R}^2} - 1\right)\right)} \tag{4.60}$$

The partial derivative of the first and second invariants with respect to $\overline{r}$ are given as follows:

$$\frac{\partial \overline{I}_{\mathbf{E}}}{\partial \overline{r}} = 2\left(\frac{\overline{r}}{\overline{R}^2} - \frac{\overline{R}^4}{\overline{r}^5}\right) \tag{4.61}$$

$$\frac{\partial \overline{II}_{\mathbf{E}}}{\partial \overline{r}} = \frac{1}{3\overline{II}_{\mathbf{E}}}\left(\frac{4\overline{R}^4}{\overline{r}^5} + \frac{2\overline{r}}{\overline{R}^2}\right)\left(\frac{\overline{r}^2}{\overline{R}^2} - \frac{\overline{R}^4}{\overline{r}^4}\right) \tag{4.62}$$

Correspondingly, the non-dimensional equations to obtain $\overline{r}_i$ at each time is given as follows:

$$\overline{p}_o - \overline{p}_i = \int_{\overline{R}_i}^{\overline{R}_o} \frac{2\overline{\mu}(\overline{c}(\overline{R},\overline{t}),\overline{\vartheta}(\overline{R},\overline{t}))\left(\overline{R}^6 - \left(\overline{R}^3 + \overline{r}_i^3 - \overline{R}_i^3\right)^2\right)}{\left(\overline{R}^3 + \overline{r}_i^3 - \overline{R}_i^3\right)^{\frac{7}{3}}} \mathrm{d}\overline{R} \tag{4.63}$$

Algorithm 2 describes a procedure to determine $\overline{c}(\overline{r},\overline{t})$, $\overline{\vartheta}(\overline{r},\overline{t})$, and $\overline{r}_i$ at various times using an iterative non-linear numerical strategy.

4.2.1. *Steady-state analysis for degrading shell.* In case of steady-state, we have $h_r r^2 = C_3$ and $q_r r^2 + \varkappa h_r r^2 = C_4$, where C_3 and C_4 are constants. This implies that $\overline{c}$ and $\overline{\vartheta}$ are the solutions of the following ODEs:

$$\overline{D}_{\varkappa\varkappa}\overline{r}^2\frac{\partial \overline{c}}{\partial \overline{r}} - 2\overline{D}_{\varkappa\varkappa}\overline{\omega}\left(\frac{\overline{r}^3}{\overline{R}^2} - \frac{\overline{R}^4}{\overline{r}^3}\right) + \overline{C}_1 = 0 \tag{4.64a}$$

$$\overline{D}_{\vartheta\vartheta}\overline{r}^2\frac{\partial \overline{\vartheta}}{\partial \overline{r}} + \overline{\tau}\left(\frac{\overline{w}}{2}\left(\frac{\overline{R}^4}{\overline{r}^4} + 2\frac{\overline{r}^2}{\overline{R}^2} - 3\right) - \overline{c} + 1\right)\overline{C}_1 + \overline{C}_2 = 0 \tag{4.64b}$$

Correspondingly, the analytical solution to the above set of ODEs are given as follows:

$$\overline{c} = \int 2\overline{\omega}\left(\frac{\overline{r}}{\overline{R}^2} - \frac{\overline{R}^4}{\overline{r}^5}\right) - \frac{\overline{C}_1}{\overline{r}^2\overline{D}_{\varkappa\varkappa}}\,\mathrm{d}\overline{r} \tag{4.65a}$$

$$\overline{\vartheta} = \int -\frac{\overline{\tau}\overline{C}_1}{\overline{D}_{\vartheta\vartheta}}\left(\frac{\overline{w}}{2}\left(\frac{\overline{R}^4}{\overline{r}^6} + 2\frac{1}{\overline{R}^2} - \frac{3}{\overline{r}^2}\right) - \frac{\overline{c}-1}{\overline{r}^2}\right) - \frac{\overline{C}_2}{\overline{r}\overline{D}_{\vartheta\vartheta}}\,\mathrm{d}\overline{r} \tag{4.65b}$$

For weak coupling (where $D_{\vartheta\vartheta}$ and $D_{\varkappa\varkappa}$ are constants), a simplified form of the analytical solutions for $\overline{c}$ and $\overline{\vartheta}$ is given as follows:

$$\overline{c} = \overline{\omega}\left(\frac{\overline{r}^2}{\overline{R}^2} + \frac{\overline{R}^4}{2\overline{r}^4}\right) + \frac{B_2}{\overline{r}} + A_2 \tag{4.66a}$$

$$\overline{\vartheta} = -\frac{\overline{\tau}B_2^2\overline{D}_{\varkappa\varkappa}}{2\overline{D}_{\vartheta\vartheta}\overline{r}^2} + \frac{Z_2}{\overline{r}} + Y_2 \tag{4.66b}$$

where A_2, B_2, Y_2, and Z_2 are constants, which can be decided by the boundary conditions.

$$A_2 = \overline{c}_i - \frac{B_2}{\overline{r}_i} - \overline{\omega}\left(\frac{\overline{r}_i^2}{\overline{R}^2} + \frac{8\overline{R}^4}{\overline{r}_i^4}\right) \tag{4.67a}$$

$$B_2 = \frac{\overline{r}_i\overline{r}_o}{\overline{r}_i - \overline{r}_o}\left(\overline{c}_o - \overline{c}_i - \overline{\omega}\left(\frac{\overline{r}_o^2}{\overline{R}^2} + \frac{8\overline{R}^4}{\overline{r}_o^4} - \frac{\overline{r}_i^2}{\overline{R}^2} - \frac{8\overline{R}^4}{\overline{r}_i^4}\right)\right) \tag{4.67b}$$

$$Y_2 = \overline{\vartheta}_i + \frac{\overline{\tau}B_2^2\overline{D}_{\varkappa\varkappa}}{2\overline{D}_{\vartheta\vartheta}\overline{r}_i^2} - \frac{Z_2}{\overline{r}_i} \tag{4.67c}$$

$$Z_2 = \frac{\overline{r}_i - \overline{r}_o}{\overline{r}_i\overline{r}_o}\left(\overline{\vartheta}_o - \overline{\vartheta}_i - \frac{\overline{\tau}B_2^2\overline{D}_{\varkappa\varkappa}}{2\overline{D}_{\vartheta\vartheta}}\left(\frac{1}{\overline{r}_i^2} - \frac{1}{\overline{r}_o^2}\right)\right) \tag{4.67d}$$

4.2.2. *Quasistatic analysis for degrading shell.* Employing method of horizontal lines with backward Euler time-stepping scheme, we obtain the following ODEs at each time-level for equations (4.57) and (4.58)

$$\begin{aligned}\frac{d^2\overline{c}^{(n+1)}}{d\overline{r}^2} + \left(\frac{2}{\overline{r}^{(n)}} + \left(\frac{1}{\overline{D}_{\varkappa\varkappa}^{(n)}}\right)\left.\frac{d\overline{D}_{\varkappa\varkappa}}{d\overline{r}}\right|_{\overline{t}=\overline{t}_n}\right)\frac{d\overline{c}^{(n+1)}}{d\overline{r}} - \frac{\overline{c}^{(n+1)}}{\overline{D}_{\varkappa\varkappa}^{(n)}\Delta\overline{t}} = 6\overline{\omega}\left(\frac{1}{\left(\overline{R}^{(n)}\right)^2} + \frac{\left(\overline{R}^{(n)}\right)^4}{\left(\overline{r}^{(n)}\right)^6}\right)\\ - \frac{\overline{c}^{(n)}}{\overline{D}_{\varkappa\varkappa}^{(n)}\Delta\overline{t}} - \left(\frac{2\overline{\omega}}{\overline{D}_{\varkappa\varkappa}^{(n)}}\right)\left(\left.\frac{d\overline{D}_{\varkappa\varkappa}}{d\overline{r}}\right|_{\overline{t}=\overline{t}_n}\right)\left(\frac{\left(\overline{R}^{(n)}\right)^4}{\left(\overline{r}^{(n)}\right)^5} - \frac{\overline{r}^{(n)}}{\left(\overline{R}^{(n)}\right)^2}\right)\end{aligned} \tag{4.68}$$

$$\begin{aligned}\frac{d^2\overline{\vartheta}^{(n+1)}}{d\overline{r}^2} + \left(\frac{2}{\overline{r}^{(n)}} + \left(\frac{1}{\overline{D}_{\vartheta\vartheta}^{(n)}}\right)\left.\frac{d\overline{D}_{\vartheta\vartheta}}{d\overline{r}}\right|_{\overline{t}=\overline{t}_n}\right)\frac{d\overline{\vartheta}^{(n+1)}}{d\overline{r}} - \frac{\overline{\vartheta}^{(n)}\overline{\vartheta}^{(n+1)}}{\overline{D}_{\vartheta\vartheta}^{(n)}\Delta\overline{t}} = -\frac{\overline{\tau}\overline{D}_{\varkappa\varkappa}^{(n)}}{\overline{D}_{\vartheta\vartheta}^{(n)}}\left(\left.\frac{d\overline{c}}{d\overline{r}}\right|_{\overline{t}=\overline{t}_n}\right)^2 - \frac{\left(\overline{\vartheta}^{(n)}\right)^2}{\overline{D}_{\vartheta\vartheta}^{(n)}\Delta\overline{t}}\\ + \frac{4\overline{\tau}\overline{\omega}\overline{D}_{\varkappa\varkappa}^{(n)}}{\overline{D}_{\vartheta\vartheta}^{(n)}}\left(\frac{\left(\overline{r}^{(n)}\right)}{\left(\overline{R}^{(n)}\right)^2} - \frac{\left(\overline{R}^{(n)}\right)^4}{\left(\overline{r}^{(n)}\right)^5}\right)\left.\frac{d\overline{c}}{d\overline{r}}\right|_{\overline{t}=\overline{t}_n} - \frac{4\overline{\tau}\overline{\omega}^2\overline{D}_{\varkappa\varkappa}}{\overline{D}_{\vartheta\vartheta}^{(n)}}\left(\frac{\left(\overline{r}^{(n)}\right)}{\left(\overline{R}^{(n)}\right)^2} - \frac{\left(\overline{R}^{(n)}\right)^4}{\left(\overline{r}^{(n)}\right)^5}\right)^2\end{aligned} \tag{4.69}$$

The boundary conditions for diffusion and heat conduction problems are the same as the beam bending problem. The other parameters are assumed in the strongly coupling simulations as follows:

$$\begin{aligned}&\overline{R}_o = 1,\ \overline{R}_i = 0.5,\ \Delta\overline{t} = 0.01,\ \overline{t} = 2,\ \overline{\omega} = 0.05,\ \overline{\tau} = 0.2,\ \overline{\mu}_0 = 1,\ \overline{\mu}_1 = 0.3,\ \overline{\mu}_2 = 0.4,\\ &\overline{D}_0 = 1,\ \overline{D}_T = 1.5,\ \overline{D}_S = 1.2,\ \eta_T = \eta_S = 1,\ E_{\mathrm{ref}T} = E_{\mathrm{ref}S} = 1,\ \overline{K}_0 = 1,\ \delta = 10\end{aligned} \tag{4.70}$$

In weakly coupling problem, we use $\overline{D}_0$, $\overline{K}_0$ as $\overline{D}_{\varkappa\varkappa}^{(n)}$ and $\overline{D}_{\vartheta\vartheta}^{(n)}$, respectively.

4.2.3. *A discussion on the behavior of degrading spherical shell.* Figure 8 shows the plot of $\overline{r}_i$ as a function of the inner pressure $\overline{p}_i$ for strongly and weakly coupled chemo-thermo-mechano degradation problem. For a given $\overline{p}_i$, one can see that $\overline{r}_i$ for weak coupling is larger than strong coupling. This is because in the weakly coupled problem degradation happens at a much faster rate as compared to the strongly coupled problem. The hoop stress '$\overline{T}_{\theta\theta}$' as a function of the reference location $\overline{t} = 1$ due to various inner pressures $\overline{p}_i$ is shown in Figure 9. Analysis is performed for a strongly coupled chemo-thermo-mechano degradation problem. As the pressure increases the hoop stress change sign. Furthermore, $\overline{T}_{\theta\theta}$ magnitude increases as the pressure loading increases. Figure

10 shows the chemical potential as a function of the reference location $\overline{t} = 0.1$ due to various inner pressures $\overline{p}_i$. One can see that chemical potential increases with $\overline{p}_i$.

Figure 11 shows the extent of damage as a function of the reference location at various instants of time due to inner pressure $\overline{p}_i = 0.5$. Analysis is performed for strongly coupled chemo-thermo-mechano degradation problem. At initial times, we have variable heat sinks in the entire body.Additionally, as $\overline{I}_{\mathbf{E}} \geq 0$ the thermal conductivity decreases due to increase in $\overline{I}_{\mathbf{E}}$. Hence for initial times, as $\overline{\vartheta} \leq \overline{\vartheta}_0$ the material damage is less than that of at time $\overline{t} = 0$. The extent of damage as a function of the reference location at $\overline{t} = 1$ for various inner pressures '$\overline{p}_i$' is shown in Figure 12. As the pressure increases, for the weakly coupled problem, the extend of damage decreases. This means that the body degrades faster as one increases the inflation pressure $\overline{p}_i$. However, this is not the case for the strongly coupled problem. One can see that the material degrades slowly in case of strong coupling as compared to weak coupling. In this particular case, thermo-mechano coupling dominates and play a vital role. As $\overline{I}_{\mathbf{E}} \geq 0$, the strain-dependent thermal conductivity decreases as the pressure loading increases. Hence, there is less damage in the material due to decrease in temperature values as compared to weakly coupled chemo-thermo-mechano degradation problem.

Algorithm 2 Inflation of a degrading spherical shell (numerical methodology to find $\overline{r}_i$, $\overline{c}$, and $\overline{\vartheta}$)

1: INPUT: Non-dimensional material parameters, non-dimensional boundary conditions, and non-dimensional initial conditions, `MaxIters`, tolerances $\epsilon_{\text{tol}}^{(r)}$, $\epsilon_{\text{tol}}^{(c)}$, and $\epsilon_{\text{tol}}^{(\vartheta)}$.
2: Evaluate $\overline{r}_i$ at $\overline{t} = 0$ based on equation (4.63).
3: **for** $n = 1, 2, \cdots, N$ **do**
4: **for** $j = 1, 2, \cdots$ **do**
5: **if** $j >$ `MaxIters` **then**
6: Solution did not converge in specified maximum number of iterations. EXIT.
7: **end if**
8: `Diffusion sub-problem`: Given $\overline{r}_i^{(j)}$, solve equation (4.68) to obtain $\overline{c}^{(j+1)}$. Herein, we use shooting method to solve the ODEs.
9: `Heat conduction sub-problem`: Given $\overline{r}_i^{(j)}$ and $\overline{c}^{(j+1)}$, solve equation (4.69) to obtain $\overline{\vartheta}^{(j+1)}$. Similarly, we use shooting method to solve the ODEs.
10: `Deformation sub-problem`: Given $\overline{c}^{(j+1)}$ and $\overline{\vartheta}^{(j+1)}$, solve for $\overline{r}_i^{(j+1)}$ given by equation (4.63) using bisection method.
11: **if** $\|\overline{r}_i^{(j+1)} - \overline{r}_i^{(j)}\| < \epsilon_{\text{tol}}^{(r)}$, $\|\overline{c}^{(j+1)} - \overline{c}^{(j)}\| < \epsilon_{\text{tol}}^{(c)}$, and $\|\overline{\vartheta}^{(j+1)} - \overline{\vartheta}^{(j)}\| < \epsilon_{\text{tol}}^{(\vartheta)}$ **then**
12: OUTPUT: $\overline{r}_i^{(j+1)}$, $\overline{c}^{(j+1)}$, and $\overline{\vartheta}^{(j+1)}$. EXIT.
13: **else**
14: Update the guess: $\overline{r}_i^{(j)} \leftarrow \overline{r}_i^{(j+1)}$.
15: **end if**
16: **end for**
17: **end for**

4.3. Torsional shear of a degrading cylinder. A pictorial description of the degrading cylindrical annulus of finite length is shown in Figure 13. The bottom of the cylinder is fixed and just after time $t = 0$, a twisting moment is applied. We analyze the material degradation and corresponding structural response due to the torsional shear for a prescribed angle of twist. Initially,

the body is a homogeneous neo-Hookean material and there is no transport of chemical species in the body. For time $t > 0$, the outer boundary of the cylinder is always exposed to moisture (or a diffusing chemical species). The inner surface of the degrading annular cylinder is held at zero concentration. This can be achieved by constructing a mechanism which continuously removes the moisture (or diffusing chemical species) from the inner boundary of the degrading cylinder. Hence, one can control the concentration of the moisture at both inner and outer surfaces. Similar type of initial and boundary conditions are enforced for the thermal counter part.

In a reference configuration, consider a closed cylindrical body of inner radius R_i, outer radius R_o, and height L defined as follows:

$$R_i \leq R \leq R_o \qquad 0 \leq \Theta \leq 2\pi \qquad 0 \leq Z \leq L \tag{4.71}$$

where (R, Θ, Z) are the cylindrical polar coordinates in reference configuration. Under torsional shear, the deformation in the current configuration is described as follows:

$$r = R \qquad \theta = \Theta + g(Z,t) \qquad z = \Lambda Z \tag{4.72}$$

The deformation gradient $\mathbf{F}$ for the degrading cylinder is given as follows:

$$\mathbf{F} = \begin{pmatrix} 1 & 0 & 0 \\ 0 & 1 & rg' \\ 0 & 0 & \Lambda \end{pmatrix} \tag{4.73}$$

where $g' := \frac{\partial g(Z,t)}{\partial Z}$. Using the condition of incompressibility we have $\Lambda = 1$. The right Cauchy-Green tensor $\mathbf{C}$ and left Cauchy-Green tensor $\mathbf{B}$ for the degrading cylinder are given as follows:

$$\mathbf{C} = \begin{pmatrix} 1 & 0 & 0 \\ 0 & 1 & rg' \\ 0 & rg' & 1 + (rg')^2 \end{pmatrix} \quad \mathbf{B} = \begin{pmatrix} 1 & 0 & 0 \\ 0 & 1 + (rg')^2 & rg' \\ 0 & rg' & 1 \end{pmatrix} \tag{4.74}$$

The non-zero components of the Cauchy stress $\mathbf{T}$ are given as follows:

$$T_{rr} = -p + \mu(c,\vartheta) \tag{4.75a}$$

$$T_{\theta\theta} = -p + \mu(c,\vartheta)\left(1 + \left(rg'\right)^2\right) \tag{4.75b}$$

$$T_{zz} = -p + \mu(c,\vartheta) \tag{4.75c}$$

$$T_{\theta z} = T_{z\theta} = \mu(c,\vartheta) rg' \tag{4.75d}$$

The balance of linear momentum given by equation (4.11a)–(4.11c) reduces to the following

$$-\frac{\partial p}{\partial r} + \mu(c,\vartheta) r \left(g'\right)^2 = 0 \tag{4.76}$$

$$-\frac{1}{r}\frac{\partial p}{\partial \theta} + \mu(c,\vartheta) r g'' = 0 \tag{4.77}$$

$$-\frac{\partial p}{\partial z} = 0 \tag{4.78}$$

Assuming periodicity, we have $\frac{\partial p}{\partial \theta} = 0$. This implies $g'' = 0$. Hence, $g(Z,t)$ takes the following form:

$$g(Z,t) = \Psi_1(t) Z + \Psi_2(t) \tag{4.79}$$

where Ψ_1 and Ψ_2 are evaluated based on the input data. As the bottom of the cylinder is fixed, we have $g(Z=0,t)=0$, which implies $\Psi_2(t)=0$. Correspondingly, the twisting moment to generate the required change in angle of twist per unit length given by equation (4.79) is evaluated as follows:

$$M(t) = 2\pi \int_{R_i}^{R_o} \mu(c(R,t),\vartheta(R,t))\Psi_1(t) R^3 \mathrm{d}R \tag{4.80}$$

The chemical potential, specific entropy, mass transfer flux, and heat transfer flux in radial direction are given as follows:

$$\varkappa = \frac{1}{\rho_0}\frac{\partial \psi}{\partial c} + R_s \vartheta_{\mathrm{ref}}\{c - c_{\mathrm{ref}}\} = -\frac{\mu_1 r^2 \Psi_1^2}{2\rho_0 c_{\mathrm{ref}}} + R_s \vartheta_{\mathrm{ref}}\{c - c_{\mathrm{ref}}\} \tag{4.81a}$$

$$\eta = -\frac{1}{\rho_0}\frac{\partial \psi}{\partial \vartheta} + \frac{c_p}{\vartheta_{\mathrm{ref}}}\{\vartheta - \vartheta_{\mathrm{ref}}\} = \frac{\mu_1 r^2 \Psi_1^2}{2\rho_0 \vartheta_{\mathrm{ref}}} + \frac{c_p}{\vartheta_{\mathrm{ref}}}\{\vartheta - \vartheta_{\mathrm{ref}}\} \tag{4.81b}$$

$$h_{\mathrm{r}} = -\frac{\rho_0}{R_s \vartheta_{\mathrm{ref}}} D_{\varkappa\varkappa}\frac{\partial \varkappa}{\partial r} = \frac{\mu_1 D_{\varkappa\varkappa} r \Psi_1^2}{R_s \vartheta_{\mathrm{ref}} c_{\mathrm{ref}}} - \rho_0 D_{\varkappa\varkappa}\frac{\partial c}{\partial r} \tag{4.81c}$$

$$q_{\mathrm{r}} = -\rho_0 c_p D_{\vartheta\vartheta}\frac{\partial \vartheta}{\partial r} \tag{4.81d}$$

From equations (4.1a) and (4.2a), the final form of the governing equations for transport and thermal sub-problems for degrading cylinder is given as follows:

$$\rho_0\frac{\partial c}{\partial t} - \left(\frac{\rho_0 D_{\varkappa\varkappa}}{r} + \rho_0\frac{\partial D_{\varkappa\varkappa}}{\partial r}\right)\frac{\partial c}{\partial r} - \rho_0 D_{\varkappa\varkappa}\frac{\partial^2 c}{\partial r^2} = -\omega\Psi_1^2\left(2D_{\varkappa\varkappa} + r\frac{\partial D_{\varkappa\varkappa}}{\partial r}\right) \tag{4.82}$$

$$\begin{aligned}\left(\frac{\rho_0 c_p \vartheta}{\vartheta_{\mathrm{ref}}}\right)\frac{\partial \vartheta}{\partial t} - \left(\frac{\rho_0 c_p D_{\vartheta\vartheta}}{r} + \rho_0 c_p\frac{\partial D_{\vartheta\vartheta}}{\partial r}\right)\frac{\partial \vartheta}{\partial r} - \rho_0 c_p D_{\vartheta\vartheta}\frac{\partial^2 \vartheta}{\partial r^2} &= \rho_0 R_s \vartheta_{\mathrm{ref}} D_{\varkappa\varkappa}\left(\frac{\partial c}{\partial r}\right)^2 \\ &+ \frac{R_s \vartheta_{\mathrm{ref}} D_{\varkappa\varkappa}\omega^2}{\rho_0} r^2 \Psi_1^4 - 2R_s \vartheta_{\mathrm{ref}}\omega D_{\varkappa\varkappa} r \Psi_1^2\frac{\partial c}{\partial r}\end{aligned} \tag{4.83}$$

Correspondingly, the non-dimensionalized governing equations for transport and thermal sub-problems are given as follows:

$$\frac{\partial \overline{c}}{\partial \overline{t}} - \left(\frac{\overline{D}_{\varkappa\varkappa}}{\overline{r}} + \frac{\partial \overline{D}_{\varkappa\varkappa}}{\partial \overline{r}}\right)\frac{\partial \overline{c}}{\partial \overline{r}} - \overline{D}_{\varkappa\varkappa}\frac{\partial^2 \overline{c}}{\partial \overline{r}^2} = -\overline{\omega}\overline{\Psi}_1^2\left(2\overline{D}_{\varkappa\varkappa} + \overline{r}\frac{\partial \overline{D}_{\varkappa\varkappa}}{\partial \overline{r}}\right) \tag{4.84}$$

$$\overline{\vartheta}\frac{\partial \overline{\vartheta}}{\partial \overline{t}} - \left(\frac{\overline{D}_{\vartheta\vartheta}}{\overline{r}} + \frac{\partial \overline{D}_{\vartheta\vartheta}}{\partial \overline{r}}\right)\frac{\partial \overline{\vartheta}}{\partial \overline{r}} - \overline{D}_{\vartheta\vartheta}\frac{\partial^2 \overline{\vartheta}}{\partial \overline{r}^2} = \overline{\tau}\overline{D}_{\varkappa\varkappa}\left(\frac{\partial \overline{c}}{\partial \overline{r}}\right)^2 - 2\overline{\tau}\overline{\omega}\overline{D}_{\varkappa\varkappa}\overline{r}\overline{\Psi}_1^2\frac{\partial \overline{c}}{\partial \overline{r}} + \overline{\tau}\overline{D}_{\varkappa\varkappa}\overline{\omega}^2\overline{r}^2\overline{\Psi}_1^4 \tag{4.85}$$

where $\overline{I}_{\mathbf{E}}$, $\overline{II}_{\mathbf{E}}$, $\frac{\partial \overline{I}_{\mathbf{E}}}{\partial \overline{r}}$, and $\frac{\partial \overline{II}_{\mathbf{E}}}{\partial \overline{r}}$ are given as follows:

$$\overline{I}_{\mathbf{E}} = \frac{1}{2}\overline{r}^2\overline{\Psi}_1^2 \tag{4.86}$$

$$\overline{II}_{\mathbf{E}} = \sqrt{\frac{1}{6}\left(3\overline{r}^2\overline{\Psi}_1^2 + 2\overline{r}^4\overline{\Psi}_1^4\right)} \tag{4.87}$$

$$\frac{\partial \overline{I}_{\mathbf{E}}}{\partial \overline{r}} = \overline{r}\overline{\Psi}_1^2 \tag{4.88}$$

$$\frac{\partial \overline{II}_{\mathbf{E}}}{\partial \overline{r}} = \frac{1}{3\overline{II}_{\mathbf{E}}}\left(3\overline{r}\overline{\Psi}_1^2 + 4\overline{r}^3\overline{\Psi}_1^4\right) \tag{4.89}$$

where most of the non-dimensional quantities remain the same as that of the previous initial boundary value problems except the following:

$$\overline{R} = \frac{R}{R_o},\ \overline{\psi} = \psi R_o,\ \overline{t} = \frac{D_0 t}{R_o^2} \tag{4.90}$$

Correspondingly, the non-dimensional twisting moment $\overline{M}(\overline{t})$ is given as follows:

$$\overline{M}(\overline{t}) = 2\pi \int_{\overline{R}_i}^{\overline{R}_o} \overline{\mu}(\overline{c}(\overline{R},\overline{t}), \overline{\vartheta}(\overline{R},\overline{t}))\overline{\Psi}_1 \overline{R}^3 \mathrm{d}\overline{R} \tag{4.91}$$

Algorithm 3 describes a numerical solution procedure to determine $\overline{c}(\overline{r},\overline{t})$, $\overline{\vartheta}(\overline{r},\overline{t})$, and $\overline{M}(\overline{t})$ at various times for a given angle of twist per unit length.

4.3.1. *Steady-state and quasistatic response of degrading cylinder under torsional shear.* In case of steady-state, $\overline{c}$ and $\overline{\vartheta}$ are the solutions of the following ODEs:

$$\overline{D}_{\varkappa\varkappa}\overline{r}^2 \frac{d\overline{c}}{d\overline{r}} - \overline{D}_{\varkappa\varkappa}\overline{\omega r}\overline{\Psi}_1^2 + \overline{C}_1 = 0 \tag{4.92a}$$

$$\overline{D}_{\vartheta\vartheta}\overline{r}\frac{d\overline{\vartheta}}{d\overline{r}} + \overline{\tau}\left(\frac{\overline{\omega}}{2}\overline{r}^2\overline{\Psi}_1^2 - \overline{c} + 1\right)\overline{C}_1 + \overline{C}_2 = 0 \tag{4.92b}$$

where $\overline{C}_1$ and $\overline{C}_2$ are integration constants. Correspondingly, the analytical solutions to the above set of ODEs are given as follows:

$$\overline{c} = \int \left(\overline{\omega r}\overline{\Psi}_1^2 - \frac{\overline{C}_1}{\overline{r}\overline{D}_{\varkappa\varkappa}}\right)\mathrm{d}\overline{r} \tag{4.93a}$$

$$\overline{\vartheta} = \int \left(-\frac{\overline{\tau}\overline{C}_1}{\overline{D}_{\vartheta\vartheta}}\left(\frac{\overline{\omega}}{2}\overline{r}\overline{\Psi}_1^2 - \frac{\overline{c}-1}{\overline{r}}\right) - \frac{\overline{C}_2}{\overline{r}\overline{D}_{\vartheta\vartheta}}\right)\mathrm{d}\overline{r} \tag{4.93b}$$

For weak coupling (where $D_{\vartheta\vartheta}$ and $D_{\varkappa\varkappa}$ are constants), a simplified form of the analytical solutions for $\overline{c}$ and $\overline{\vartheta}$ is given as follows:

$$\overline{c} = \frac{\overline{\omega}}{2}\overline{r}^2\overline{\Psi}_1^2 + B_3\ln[\overline{r}] + A_3 \tag{4.94a}$$

$$\overline{\vartheta} = -\frac{\overline{\tau}B_3^2\overline{D}_{\varkappa\varkappa}}{2\overline{D}_{\vartheta\vartheta}}\ln[\overline{r}]^2 + Z_3\ln[\overline{r}] + Y_3 \tag{4.94b}$$

where A_3, B_3, Y_3, and Z_3 are constants, which are obtained by the corresponding boundary conditions for thermal and diffusion sub-problem. These are given as follows:

$$A_3 = \overline{c}_i - B_3\ln[\overline{r}_i] - \frac{\overline{\omega}}{2}\overline{r}_i^2\overline{\Psi}_1^2 \tag{4.95a}$$

$$B_3 = \frac{1}{\ln[\overline{r}_o] - \ln[\overline{r}_i]}\left(\overline{c}_o - \overline{c}_i - \frac{\overline{\omega}}{2}\left(\overline{r}_o^2\overline{\Psi}_1^2 - \overline{r}_i^2\overline{\Psi}_1^2\right)\right) \tag{4.95b}$$

$$Y_3 = \overline{\vartheta}_i + \frac{\overline{\tau}B_3^2\overline{D}_{\varkappa\varkappa}}{2\overline{D}_{\vartheta\vartheta}}\ln[\overline{r}_i]^2 - Z_3\ln[\overline{r}_i] \tag{4.95c}$$

$$Z_3 = \frac{1}{\ln[\overline{r}_o] - \ln[\overline{r}_i]}\left(\overline{\vartheta}_o - \overline{\vartheta}_i - \frac{\overline{\tau}B_3^2\overline{D}_{\varkappa\varkappa}}{2\overline{D}_{\vartheta\vartheta}}\left(\ln[\overline{r}_i]^2 - \ln[\overline{r}_o]^2\right)\right) \tag{4.95d}$$

For quasistatic analysis, method of horizontal lines with backward Euler time-stepping scheme is employed. This gives the following ODEs at each time-level:

$$\frac{d^2\overline{c}^{(n+1)}}{d\overline{r}^2}+\left(\frac{1}{\overline{r}^{(n)}}+\left(\frac{1}{\overline{D}^{(n)}_{\varkappa\varkappa}}\right)\left.\frac{d\overline{D}_{\varkappa\varkappa}}{d\overline{r}}\right|_{t=t_n}\right)\frac{d\overline{c}^{(n+1)}}{d\overline{r}}-\frac{\overline{c}^{(n+1)}}{\overline{D}^{(n)}_{\varkappa\varkappa}\Delta t}=2\overline{\omega}\left(\overline{\Psi}^{(n)}_1\right)^2$$
$$+\,\overline{\omega}\left(\overline{\Psi}^{(n)}_1\right)^2\frac{\overline{r}^{(n)}}{\overline{D}^{(n)}_{\varkappa\varkappa}}\left(\left.\frac{d\overline{D}_{\varkappa\varkappa}}{d\overline{r}}\right|_{t=t_n}\right)-\frac{\overline{c}^{(n)}}{\overline{D}^{(n)}_{\varkappa\varkappa}\Delta t} \tag{4.96}$$

$$\frac{d^2\overline{\vartheta}^{(n+1)}}{d\overline{r}^2}+\left(\frac{1}{\overline{r}^{(n)}}+\left(\frac{1}{\overline{D}^{(n)}_{\vartheta\vartheta}}\right)\left.\frac{d\overline{D}_{\vartheta\vartheta}}{d\overline{r}}\right|_{t=t_n}\right)\frac{d\overline{\vartheta}^{(n+1)}}{d\overline{r}}-\frac{\overline{\vartheta}^{(n)}\overline{\vartheta}^{(n+1)}}{\overline{D}^{(n)}_{\vartheta\vartheta}\Delta t}=-\frac{\overline{\tau}\overline{D}^{(n)}_{\varkappa\varkappa}}{\overline{D}^{(n)}_{\vartheta\vartheta}}\left(\left.\frac{d\overline{c}}{d\overline{r}}\right|_{t=t_n}\right)^2-\frac{\left(\overline{\vartheta}^{(n)}\right)^2}{\overline{D}^{(n)}_{\vartheta\vartheta}\Delta t}$$
$$+\,\frac{2\overline{\tau}\overline{\omega}\overline{D}^{(n)}_{\varkappa\varkappa}}{\overline{D}^{(n)}_{\vartheta\vartheta}}\overline{r}^{(n)}\left(\overline{\Psi}^{(n)}_1\right)^2\left.\frac{d\overline{c}}{d\overline{r}}\right|_{t=t_n}-\frac{\overline{\tau}\overline{D}^{(n)}_{\varkappa\varkappa}\overline{\omega}^2}{\overline{D}^{(n)}_{\vartheta\vartheta}}\left(\overline{r}^{(n)}\right)^2\left(\overline{\Psi}^{(n)}_1\right)^4 \tag{4.97}$$

The boundary conditions for diffusion and heat conduction problems are same as that of the previous boundary value problems. For numerical simulations, the non-dimensional parameters are assumed as follows:

$$\begin{aligned}&\overline{R}_o=1,\ \overline{R}_i=0.5,\ \Delta\overline{t}=0.1,\ \overline{t}=2,\ \overline{\omega}=0.05,\ \overline{\tau}=0.8,\ \overline{\mu}_0=1,\ \overline{\mu}_1=0.5,\ \overline{\mu}_2=0.2,\\ &\overline{D}_0=1,\ \overline{D}_T=1.5,\ \overline{D}_S=1.2,\ \eta_T=\eta_S=0.1,\ E_{\mathrm{ref}T}=E_{\mathrm{ref}S}=1,\ \overline{K}_0=1,\ \delta=10\end{aligned} \tag{4.98}$$

Figure 14 shows the twisting moment at various instants of time due to constant $\overline{\Psi}_1$, which is equal to 0.75. Analysis is performed for strongly coupled chemo-thermo-mechano degradation model. The concentration degradation material parameter $\overline{\mu}_1$ is varied from 0.1 to 0.5 while the thermal degradation parameter $\overline{\mu}_2$ is held fixed at 0.4. From this figure it is evident that as $\overline{\mu}_1$ increases the twisting moment required to keep the angle of twist unchanged, decreases. Reiterating, the torsional shear stress required to maintain a prescribed angular displacement decreases. To maintain a given angular displacement, lesser twisting moment is required if the material degrades at a faster pace. That is, *we observe moment relaxation due to material degradation and the body creep until a steady state is reached. In addition, one can see that moment relaxation depends on the geometry of the specimen. This aspect differentiates the stress relaxation due to degradation from the stress relaxation due to viscoelasticity.* Similar type of behaviour is observed when $\overline{\mu}_1$ is kept constant and $\overline{\mu}_2$ is varied. Figure 15 shows the chemical potential as a function of the reference location at $\overline{t}=1.0$ for various values of $\overline{\Psi}_1$. One can see that as $\overline{\Psi}_1$ increases, chemical potential, however, decreases, which is different from the degrading shell problem.

Figure 16 shows the extent of damage as a function of the reference location at $\overline{t}=1.0$ for various values of $\overline{\Psi}_1$. Based on the chosen set of non-dimensional parameters, thermal degradation dominates. As $\overline{\Psi}_1$ increases, the extent of damage near the inner radius R_i is not as profound as that of the outer radius R_o. Furthermore, as $\overline{I}_{\mathbf{E}}\geq 0$, and $\overline{I}_{\mathbf{E}}$ at R_o is greater than $\overline{I}_{\mathbf{E}}$ at R_i, $\mathcal{D}_\mu$ is much smaller at R_o as compared to R_i. This is because the thermal conductivity decreases as $R\longrightarrow R_o$. It should be noted that for low values of $\overline{\Psi}_1$, $\mathcal{D}_\mu$ is monotonic. However, for higher values of $\overline{\Psi}_1$, $\mathcal{D}_\mu$ ceases to be monotonic. Figure 17 shows the extent of damage as a function of the reference location at various instants of time for a given value of $\overline{\Psi}_1$. To perform numerical simulations, the values of $\overline{\mu}_1$ and $\overline{\mu}_2$ are taken to be equal to 0.5 and 0.2. Analysis is performed for strongly coupled chemo-thermo-mechano degradation model. From this figure it is clear that

for initial times, in certain locations, the material damage is less than that of at time $\overline{t} = 0$. This is because of the variable heat sinks in the entire body and decreasing thermal conductivity (due to increase in $\overline{I}_{\mathbf{E}}$). Similar type of behaviour is observed in degrading spherical shell problem. However, such a behavior lasts for a short time ($\overline{t} > 0.01$) as compared to the degrading shell problem. This is because the degradation due to moisture (or chemical concentration) dominates in this problem after $\overline{t} > 0.01$.

Algorithm 3 Torsional shear of a degrading cylinder (numerical methodology to find $\overline{M}$, $\overline{c}$, and $\overline{\vartheta}$)

1: INPUT: Non-dimensional material parameters, non-dimensional boundary conditions, and non-dimensional initial conditions.
2: **for** $n = 1, 2, \cdots, N$ **do**
3: `Diffusion sub-problem`: Given $\overline{\Psi}_1$, solve equation (4.96) to obtain $\overline{c}^{(n)}$. Herein, we use shooting method to solve the ODEs.
4: `Heat conduction sub-problem`: Given $\overline{\Psi}_1$ and $\overline{c}^{(n)}$, solve equation (4.97) to obtain $\overline{\vartheta}^{(n)}$. Similar to diffusion sub-problem, we use shooting method to solve the non-linear ODEs.
5: `Deformation sub-problem`: Given $\overline{c}^{(n)}$ and $\overline{\vartheta}^{(n)}$, solve for $\overline{M}^{(n)}$ given by equation (4.91).
6: **end for**

References

S. B. Adler. Chemical expansivity of electrochemical ceramics. *Journal of the American Ceramic Society*, 84:2117–2119, 2001.

S. M. Allam, H. M. F. Elbakry, and A. G. Rabeai. Behavior of one-way reinforced concrete slabs subjected to fire. *Alexandria Engineering Journal*, 52:749–761, 2013.

S. S. Antman. *Nonlinear Problems of Elasticity*. Springer-Verlag, New York, 1995.

F. Armero and J. C. Simo. A new unconditionally stable fractional step method for non-linear coupled thermomechanical problems. *International Journal of Numerical Methods in Engineering*, 35:737–766, 1992.

A. W. Batchelor, L. N. Lam, and M. Chandrasekaran. *Materials Degradation and Its Control by Surface Engineering*. Imperial College Press, London, third edition, 2003.

S. Bhowmick and V. B. Shenoy. Effect of strain on the thermal conductivity of solids. *The Journal of Chemical Physics*, 125:164513, 2006.

F. Björk, C. A. Eriksson, S. Karlsson, and F. Khabbaz. Degradation of components in flooring systems in humid and alkaline environments. *Construction and Building Materials*, 17:213–221, 2003.

E. Blond and N. Richet. Thermomechanical modelling of ion–conducting membrane for oxygen separation. *Journal of the European Ceramic Society*, 28:793–801, 2008.

H. Bouadi and C. T. Sun. Hygrothermal effects on the stress field of laminated composites. *Journal of Reinforced Plastics and Composites*, 8:40–54, 1989.

H. Bouadi and C. T. Sun. Hygrothermal effects on structural stiffness and structural damping of laminated composites. *Journal of Materials Science*, 25:499–505, 1990.

R. M. Bowen. Theory of mixtures. In A. C. Eringen, editor, *Continuum Physics*, volume III. Academic Press, New York, 1976.

M. Buonsanti, G. Leonard, and F. Scoppelliti. Equilibrium state of a binary granular solids mixture. *Applied Mechanics and Materials*, 52:389–392, 2011.

L. W. Cai and Y. Weitsman. Non–Fickian moisture diffusion in polymeric composites. *Journal of Composite Materials*, 28:130–154, 1994.

D. W. Cho and K. Kim. The mechanisms of moisture damage in asphalt pavement by applying chemistry aspects. *KSCE Journal of Civil Engineering*, 14:333–341, 2010.

O. Coussy. *Poromechanics*. John Wiley & Sons, Inc., New York, 2004.

J. C. Criscione, J. D. Humphrey, A. S. Douglas, and W. C. Hunter. An invariant basis for natural strain which yields orthogonal stress response terms in isotropic hyperelasticity. *Journal of the Mechanics and Physics of Solids*, 48:2445–2465, 2000.

E. L. Cussler. *Diffusion: Mass Transfer in Fluid Systems*. Cambridge University Press, Cambridge, third edition, 2009.

S. Darbha and K. R. Rajagopal. Unsteady motions of degrading or aging linearized elastic solids. *International Journal of Non-Linear Mechanics*, 44:478–485, 2009.

D. Gawin, F. Pesavento, and B. A. Schrefler. Modeling deterioration of cementitious materials exposed to calcium leaching in non-isothermal conditions. *Computer Methods in Applied Mechanics and Engineering*, 198:3051–3083, 2009.

F. P. Glasser, J. Marchand, and E. Samson. Durability of concrete degradation phenomena involving detrimental chemical reactions. *Cement and Concrete Research*, 38:226–246, 2008.

S. Grasberger and G. Meschke. Thermo-hygro-mechanical degradation of concrete: From coupled 3D material modeling to durability–oriented multifield structural analyses. *Materials and Structures*, 37:244–256, 2004.

J. R. Groza, J. F. Shackelford, E. J. Laverina, and M. T. Powers, editors. *Materials Processing Handbook*. CRC Press, Boca Raton, Florida, 2007.

J. D. Gu, T. E. Ford, N. S. Berke, and R. Mitchell. Biodeterioration of concrete by the fungus Fusarium. *International Biodeterioration & Biodegradation*, 41:101–109, 1998.

C. A. Harper. *Handbook of Plastics, Elastomers, & Composites*. McGraw–Hill, New York, fourth edition, 2002.

M. T. Heath. *Scientific Computing–An Introductory Survey*. McGraw-Hill, New York, USA, second edition, 2005.

G. A. Holzapfel. *Nonlinear Solid Mechanics*. John Wiley & Sons, Inc., Chichester, 2000.

E. Jarkova, H. Pleiner, H. W. Müller, A. Fink, and H. R. Brand. Hydrodynamics of nematic ferrofluids. *The European Physical Journal E*, 5:583–588, 2001.

Y. G. Jung, I. M. Peterson, D. K. Kim, and B. R. Lawn. Lifetime-limiting strength degradation from contact fatigue in dental ceramics. *Journal of Dental Research*, 79:722–731, 2000.

M. F. Kaplan. *Concrete Radiation Shielding: Nuclear Physics, Concrete Properties, Design and Construction*. John Wiley and Sons Inc., New York, 1989.

S. Karra and K. R. Rajagopal. Degradation and healing in a generalized neo-hookean solid due to infusion of a fluid. *Mechanics of Time-Dependent Materials*, 16:85–104, 2012.

K. A. Khan and A. H. Muliana. Effective thermal properties of viscoelastic composites having field-dependent constituent properties. *Acta Mechanica*, 209:153–178, 2010.

K. A. Khan, R. Barello, A. H. Muliana, and M. Lévesque. Coupled heat conduction and thermal stress analyses in particulate composites. *Mechanics of Materials*, 43:608–625, 2011.

D. Klepach and T. I. Zohdi. Strain assisted diffusion: Modeling and simulation of deformation-dependent diffusion in composite media. *Composites Part B: Engineering*, 56:413–423, 2014.

R. Kolberg and A. Wineman. Response of beams of non-linear viscoelastic materials exhibiting strain-dependent stress relaxation. *International Journal of Non-linear Mechanics*, 32:863–883, 1997.

W. M. Lai, J. S. Hou, and V. C. Mow. A triphasic theory for the swelling and deformation behaviors of articular cartilage. *Journal of Biomechanical Engineering*, 113:245–258, 1991.

X. Li, K. Maute, M. L. Dunn, and R. Yang. Strain effects on the thermal conductivity of nanostructures. *Physical Review B*, 81:245–318, 2010.

A. I. Lurie. *Nonlinear Theory of Elasticity*. North Holland Series in Applied Mathematics and Mechanics, Elsevier Science, Netherlands, 1990.

G. A. Maugin. *The Thermomechanics of Nonlinear Irreversible Behaviours: An Introduction*. World Scientific Publishing Company, New Jersey, USA, 1998.

K. B. McAfee. Stress-enhanced diffusion in glass I. Glass under tension and compression. *Journal of Chemical Physics*, 28:218–226, 1958a.

K. B. McAfee. Stress-enhanced diffusion in glass II. Glass under shear. *Journal of Chemical Physics*, 28:226–229, 1958b.

A. N. Morozovska, E. A. Eliseev, A. K. Tagantsev, S. L. Bravina, L. Q. Chen, and S. V. Kalinin. Thermodynamics of electromechanically coupled mixed ionic–electronic conductors: Deformation potential, Vegard strains, and flexoelectric effect. *Physical Review B*, 83:195313, 2011.

M. K. Mudunuru and K. B. Nakshatrala. A framework for coupled deformation-diffusion analysis with application to degradation/healing. *International Journal for Numerical Methods in Engineering*, 89:1144–1170, 2012.

A. Muliana, K. R. Rajagopal, and S. C. Subramanian. Degradation of an elastic composite cylinder due to the diffusion of a fluid. *Journal of Composite Materials*, 43:1225–1249, 2009.

E. R. Myers, W. M. Lai, and V. C. Mow. A continuum theory and an experiment for the ion–induced swelling behavior of articular cartilage. *Journal of Biomechanical Engineering*, 106: 151–158, 1984.

M. Naderi and M. M. Khonsari. On the characterization of thermal-conductivity degradation during torsional fatigue. *International Journal of Thermophysics*, 32:693–703, 2011.

D. J. Naus. Primer on durability of nuclear power plant reinforced concrete structures–A review of pertinent factors. Technical report, Oak Ridge National Laboratory (ORNL), NUREG/CR–6927, 2007.

E. G. Nawy, editor. *Concrete Construction Engineering Handbook*. CRC Press, Boca Raton, Florida, USA, 2008.

R. W. Ogden. *Nonlinear Elastic Deformations*. Dover publications, New York, 1997.

L. Onsager. Reciprocal relations in irreversible processes. i. *Physical Review*, 37:405, 1931a.

L. Onsager. Reciprocal relations in irreversible processes. ii. *Physical Review*, 38:2265, 1931b.

S. T. Peng and R. F. Landel. Induced anisotropy of thermal conductivity of polymer solids under large strains. *Journal of Applied Polymer Science*, 19:49–68, 1975.

R. Picard and R. Leis. Some remarks on the horizontal line method. *Mathematical Methods in the Applied Sciences*, 2:471–479, 1980.

J. J. C. Picot and F. Debeauvais. Molecular orientation effects on thermal conductivity of polydimethylsiloxane under shearing strain. *Polymer Engineering & Science*, 15:373–380, 1975.

W. Pietraszkiewicz and C. Szymczak, editors. *Shell Structures: Theory and Applications*. Proceedings of the 8th SSTA Conference. Taylor & Francis Group, London, UK.

J. K. Platten. The Soret effect: A review of recent experimental results. *Journal of Applied Mechanics*, 73:5–15, 2006.

J. K. Platten and J. C. Legros. *Convection in Liquids*. Springer-Verlag, Berlin, Heidelberg, 1984.

K. R. Rajagopal, A. R. Srinivasa, and A. S. Wineman. On the shear and bending of a degrading polymer beam. *International Journal of Plasticity*, 23:1618–1636, 2007.

E. Rothe. Zweidimensionale parabolische randwertaufgaben als grenzfall eindimensionaler randwertaufgaben. *Mathematische Annalen*, 102(1):650–670, 1930.

J. Plešek and A. Kruisová. Formulation, validation and numerical procedures for Hencky's elasticity model. *Computer and Structures*, 84:1141–1150, 2006.

G. C. Sih, J. G. Michopoulos, and S. C. Chou. *Hygrothermoelasticity*. Martinus Nijhoff Publishers, Dordrecht, The Netherlands, 1986.

R. M. Springman and J. L. Bassani. Mechano-chemical coupling in the adhesion of thin-shell structures. *Journal of the Mechanics and Physics of Solids*, 57:909–931, 2009.

R. N. Swamy, editor. *The Alkali–Silica–Reaction in Concrete*. CRC Press, New York, 2003.

R. Taylor and R. Krishna. *Multicomponent Mass Transfer*. Wiley Series in Chemical Engineering. John Wiley & Sons Inc., New York, 1993.

G. Totten, M. Howes, and T. Inoue, editors. *Handbook of Residual Stress and Deformation of Steel*. ASM International, Ohio, 2002.

J. F. Ulm, O. Coussy, L. Kefei, and C. Larive. Thermo–chemo–mechanics of ASR expansion in concrete structures. *Journal of Engineering Mechanics*, 126:233–242, 2000.

R. Černy and P. Rovnaníková. *Transport Processes in Concrete*. CRC Press, New York, USA, 2002.

Weitsman. Coupled damage and moisture-transport in fiber-reinforced, polymeric composites. *International Journal of Solids and Structures*, 23:1003–1025, 1987.

Y. J. Weitsman. Anomalous fluid sorption in polymeric composites and its relation to fluid-induced damage. *Composites Part A: Applied Science and Manufacturing*, 37:617–623, 2006.

Y. J. Weitsman and Y. J. Guo. A correlation between fluid-induced damage and anomalous fluid sorption in polymeric composites. *Composites Science and Technology*, 62:889–908, 2002.

K. Willam, I. Rhee, and Y. Xi. Thermal degradation of heterogeneous concrete materials. *Journal of Materials in Civil Engineering*, 17:276–285, 2005.

H. Ziegler. *An Introduction to Thermomechanics*. North Holland Publishing Company, Amsterdam, Netherlands, 1983.

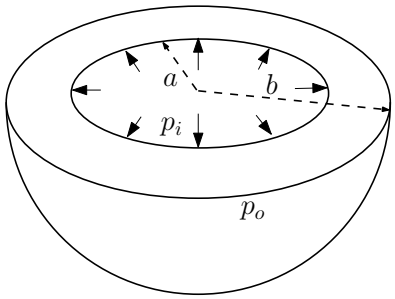

FIGURE 1. Calibration with experimental data: A pictorial description of the boundary value problem used for calibrating the proposed model with the experimental data.

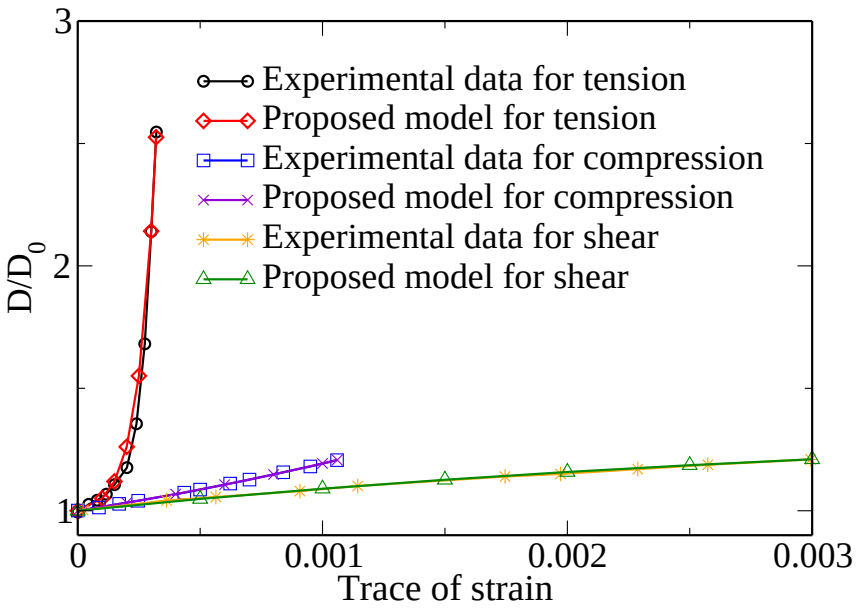

FIGURE 2. Calibration with experimental data: This figure compares the experimental data reported in [McAfee, 1958a,b] with the proposed constitutive model. The sample size is taken to be 3. The strain invariants are given by (3.14a)–(3.14b). A good agreement has been observed between the experimental data and the proposed constitutive model for the diffusivity under tensile, compressive, and shear strains.

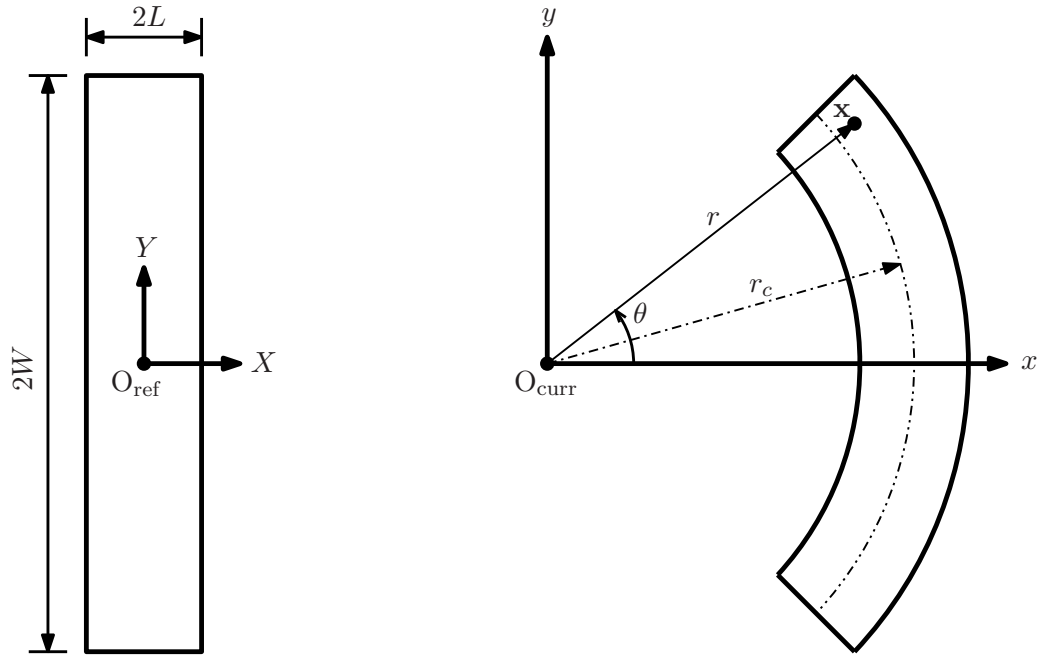

Reference configuration Current configuration

FIGURE 3. Bending of a degrading beam: A pictorial description of degrading beam in both reference and current configurations. Bending moment is applied at the two ends of the beam just after time $\overline{t} = 0$. $\mathrm{O}_{\mathrm{ref}}$ and $\mathrm{O}_{\mathrm{curr}}$ correspond to origin $(0, 0)$ in their respective configurations.

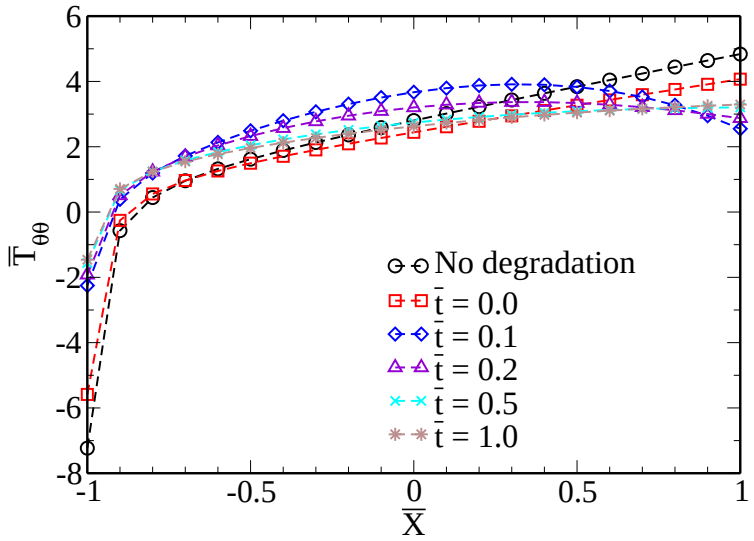

(a) Weak coupling: Chemo-thermo-mechano degradation

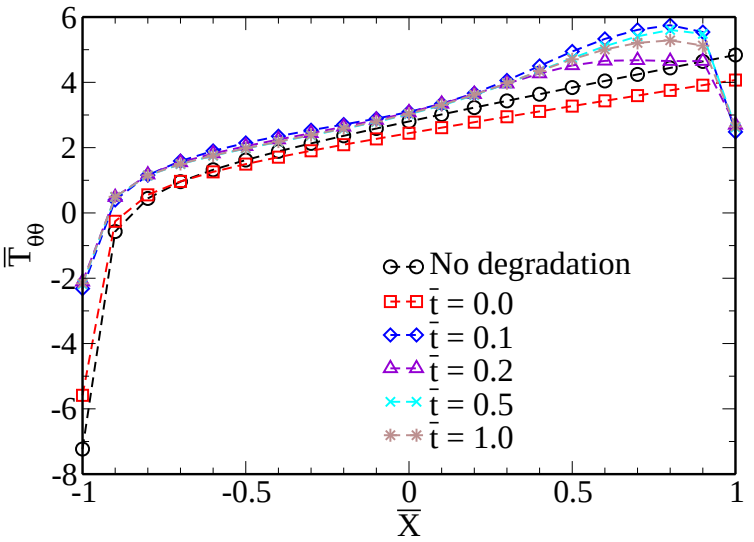

(b) Strong coupling: Chemo-thermo-mechano degradation

FIGURE 4. Bending of a degrading beam: This figure shows the plot of $\overline{T}_{\theta\theta}$ as a function of the reference location of the cross-section at various instants of time. The stress distribution is not linear, which is the case for finite deformation beam bending problem. Herein, we observe *stress-relaxation* for both weak and strong coupling. As degradation progress, one can see that neutral axis shifts further to the left. Furthermore, the tensile and compressive parts of the beam relax at a much faster rate than that of the material closer to the neutral axis.

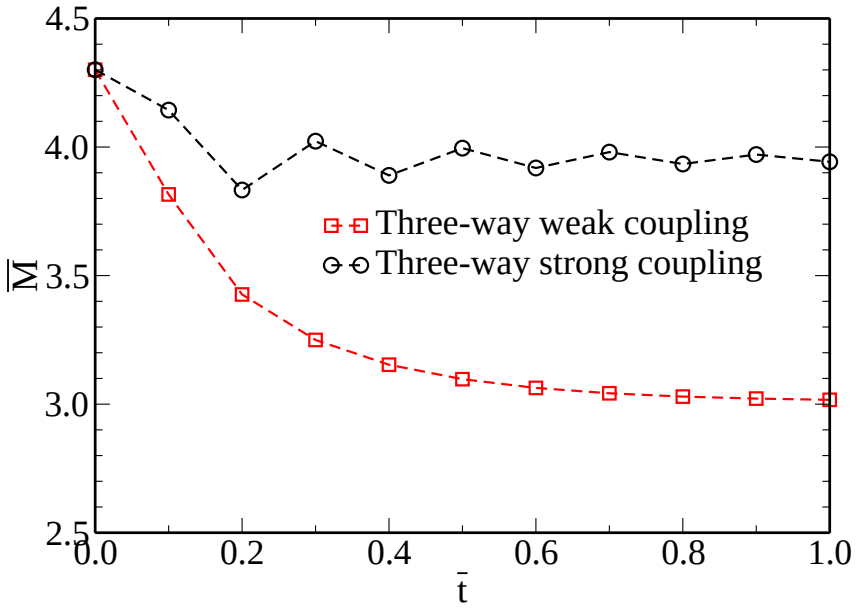

FIGURE 5. Bending of a degrading beam: This figure shows the plot of bending moment at various instants of time for both three-way strong and weak coupling degradation. Moment relaxation is observed for both cases, however, in weak coupling the moment declines more than that in strong coupling case.

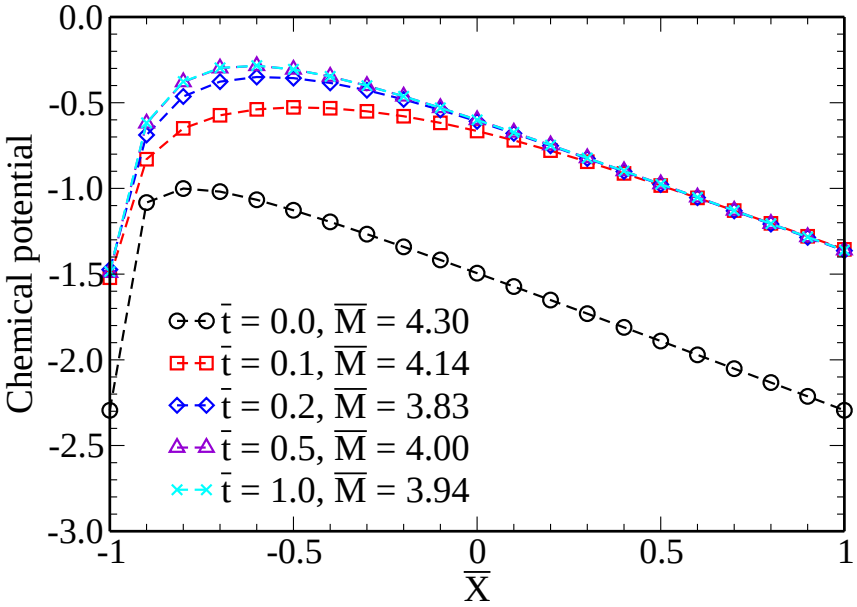

FIGURE 6. Bending of a degrading beam: This figure shows the plot of chemical potential as a function of the reference location of the cross-section at various instants of time. One can see that the chemical potential increases over time.

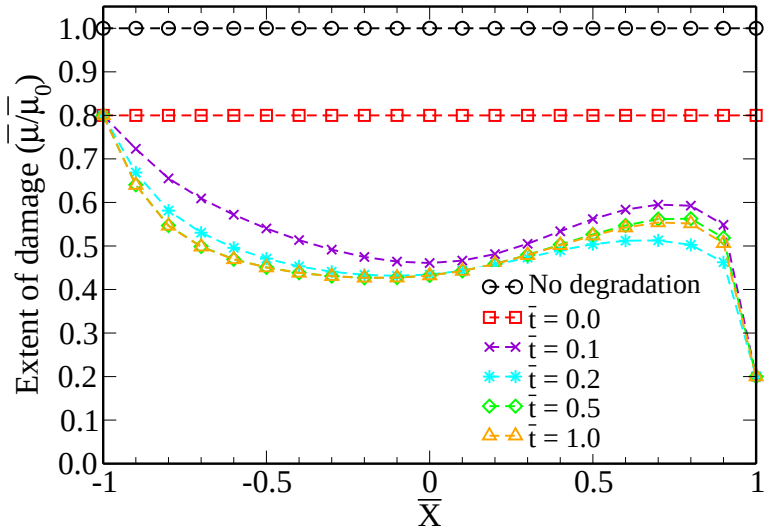

(a) Strong coupling: Chemo-thermo-mechano degradation

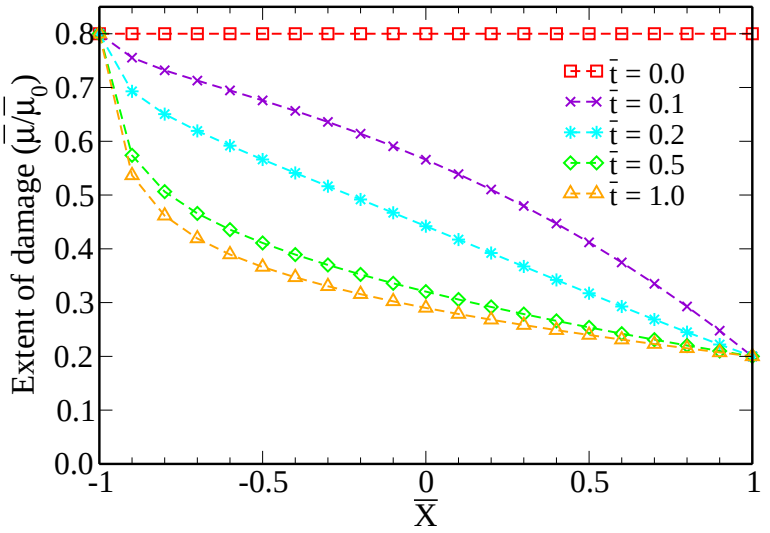

(b) Weak coupling: Chemo-thermo-mechano degradation

FIGURE 7. Bending of a degrading beam: This figure shows the extent of damage as a function of the reference location of the cross-section at various instants of time (due to the application of bending moment). Note that analysis is performed for both strongly coupled and weakly coupled chemo-thermo-mechano degradation. One can see that *a virgin beam which is initially homogeneous after degradation is not homogeneous anymore.* In addition, the extent of damage in tension side is higher than that of the compressive side of the beam.

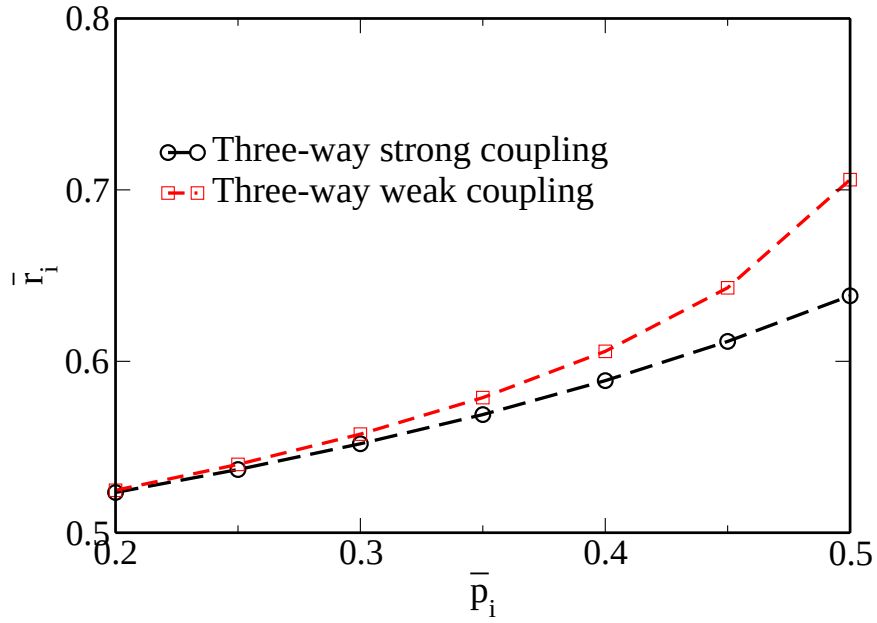

FIGURE 8. Inflation of a degrading spherical shell: This figure shows the plot of $\overline{r}_i$ as a function of the inner pressure $\overline{p}_i$ for strongly and weakly coupled chemo-thermo-mechano degradation problem. For a given $\overline{p}_i$, one can see that $\overline{r}_i$ for weak coupling is larger than strong coupling. This is because in the weakly coupled problem degradation happens at a much faster rate as compared to the strongly coupled problem.

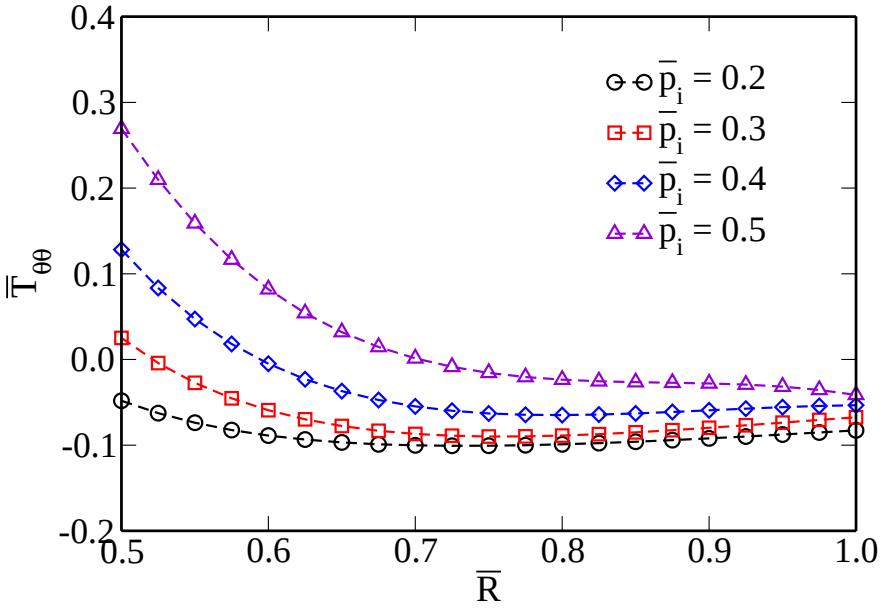

FIGURE 9. Inflation of a degrading spherical shell: This figure shows the hoop stress '$\overline{T}_{\theta\theta}$' as a function of the reference location $\overline{t} = 0.1$ due to various inner pressures $\overline{p}_i$. Analysis is performed for a strongly coupled chemo-thermo-mechano degradation problem. As the pressure increases the hoop stress change sign. Furthermore, $\overline{T}_{\theta\theta}$ magnitude increases as the pressure loading increases.

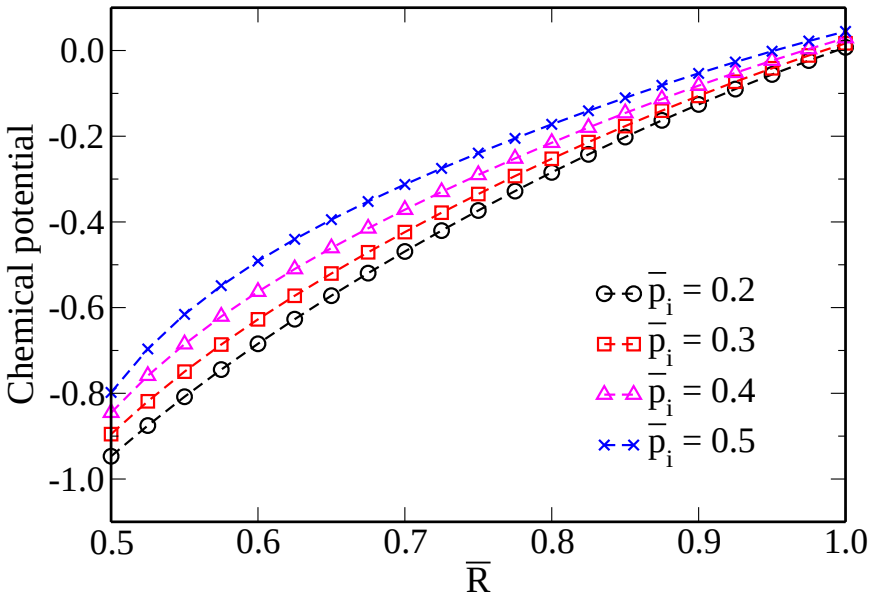

FIGURE 10. Inflation of a degrading spherical shell: This figure shows the chemical potential as a function of the reference location $\overline{t} = 0.1$ due to various inner pressures $\overline{p}_i$. One can see that chemical potential increases with $\overline{p}_i$.

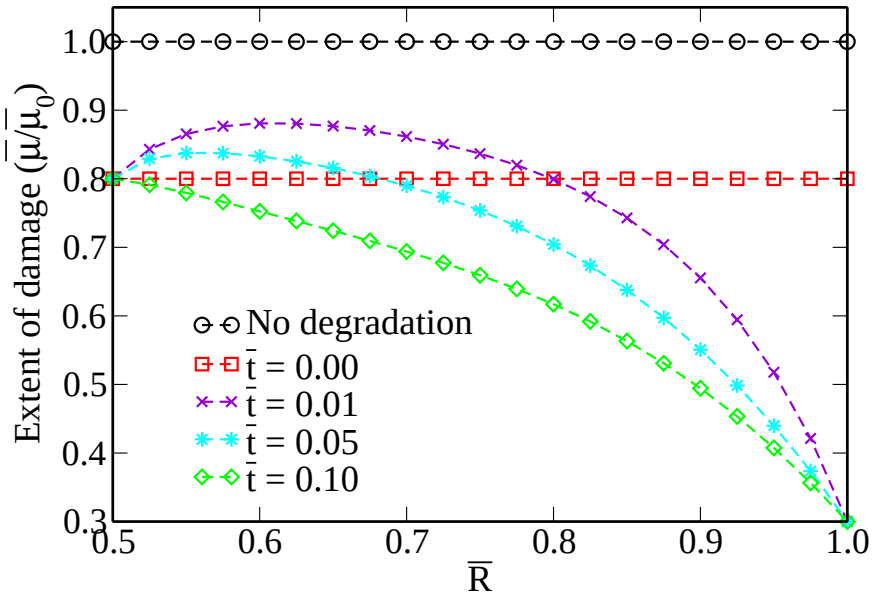

FIGURE 11. Inflation of a degrading spherical shell: This figure shows the extent of damage as a function of the reference location at various instants of time due to inner pressure $\overline{p}_i = 0.5$. Analysis is performed for strongly coupled chemo-thermo-mechano degradation problem. At initial times, we have variable heat sinks in the entire body. Additionally, as $\overline{I}_{\mathbf{E}} \geq 0$ the thermal conductivity decreases due to increase in $\overline{I}_{\mathbf{E}}$. Hence for initial times, as $\overline{\vartheta} \leq \overline{\vartheta}_0$ the material damage is less than that of at time $\overline{t} = 0$.

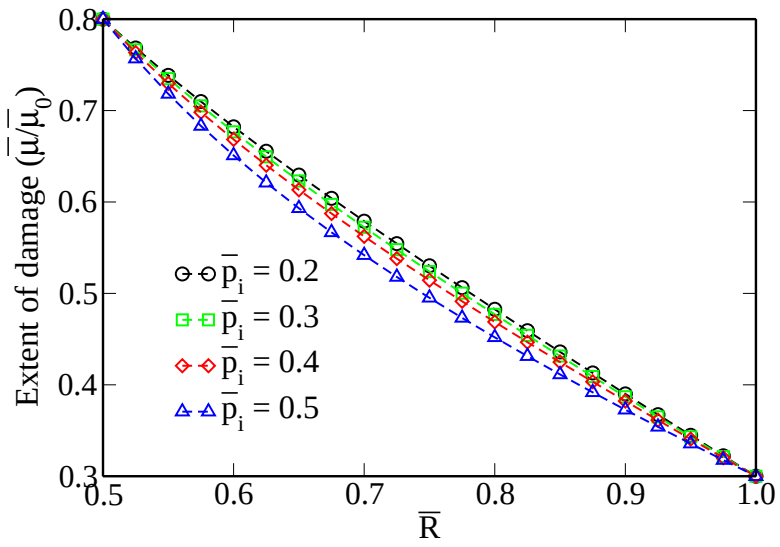

(a) Weak coupling: Chemo-thermo-mechano degradation

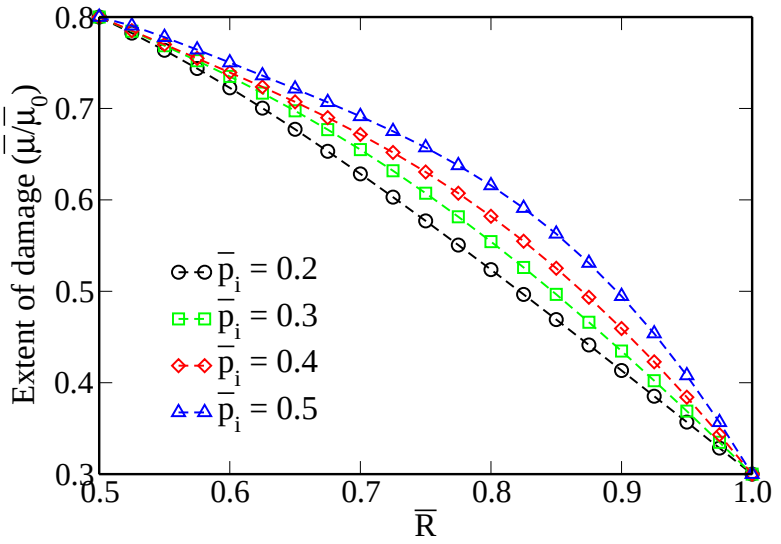

(b) Strong coupling: Chemo-thermo-mechano degradation

FIGURE 12. Inflation of a degrading spherical shell: This figure shows the extent of damage as a function of the reference location at $\overline{t} = 1$ for various inner pressures '$\overline{p}_i$'. As the pressure increases, for the weakly coupled problem, the extend of damage decreases. This means that the body degrades faster as one increases the inflation pressure $\overline{p}_i$. However, this is not the case for the strongly coupled problem. One can see that the material degrades slowly in case of strong coupling as compared to weak coupling. In this particular case, thermo-mechano coupling dominates and play a vital role. As $\overline{I}_{\mathbf{E}} \geq 0$, the strain-dependent thermal conductivity decreases as the pressure loading increases. Hence, there is less damage in the material due to decrease in temperature values as compared to weakly coupled chemo-thermo-mechano degradation problem.

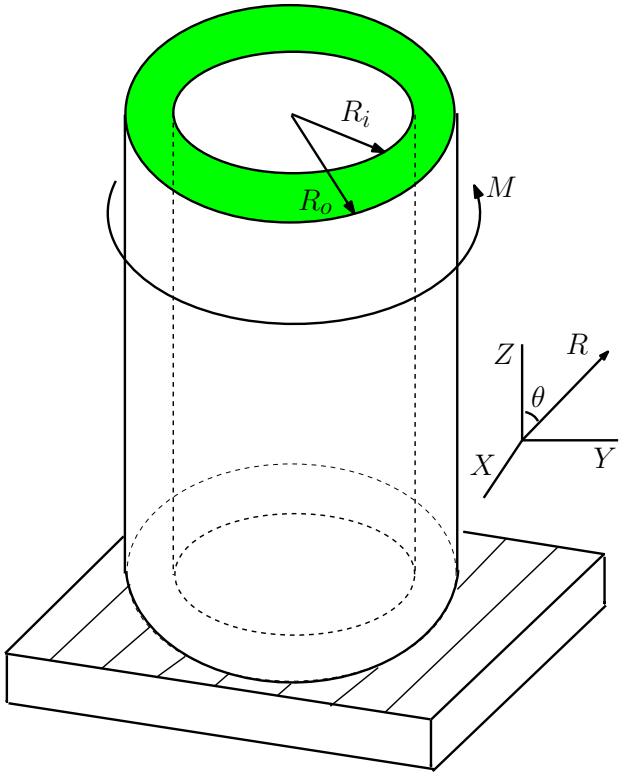

FIGURE 13. Torsional shear of a degrading cylinder: A pictorial description of the degrading cylinder under torsion in both reference and current configuration. R_i and R_o are the respective inner and outer radius of the cylinder. X, Y, and Z are the corresponding Cartesian coordinates in the reference configuration. The bottom of the cylinder is fixed and for $t \geq 0$ a twisting moment is applied.

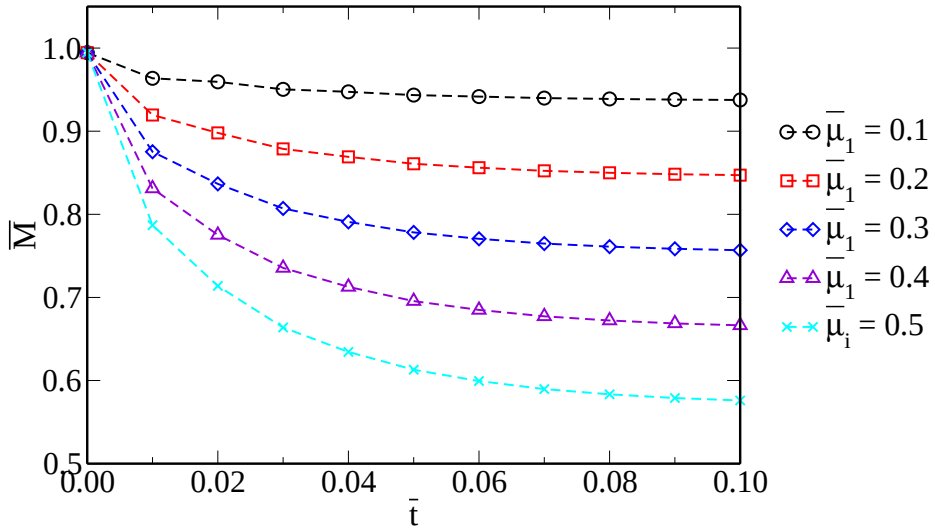

(a) Moment under different $\overline{\mu}_1$

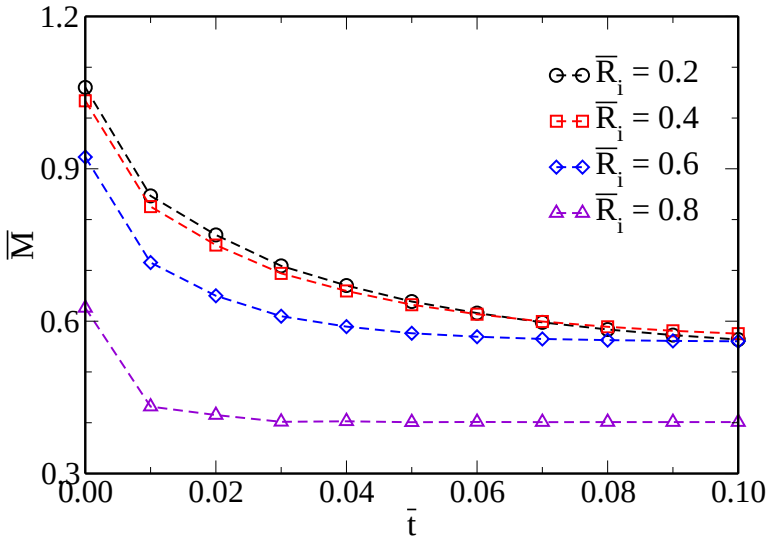

(b) Moment under different $\overline{R}_i$

FIGURE 14. Torsional shear of a degrading cylinder: This figure shows the twisting moment at various instants of time due to a given angle of twist per unit length of the cylinder, $\overline{\Psi}_1 = 0.75$. One can see that as $\overline{\mu}_1$ increases the twisting moment required to keep $\overline{\Psi}_1$ unchanged, decreases. Similar type of behaviour is observed when $\overline{\mu}_1$ is kept constant and $\overline{\mu}_2$ is varied. *Herein, the main observation is that moment relaxation not only depends on material degradation but also on the geometry of the degrading body.*

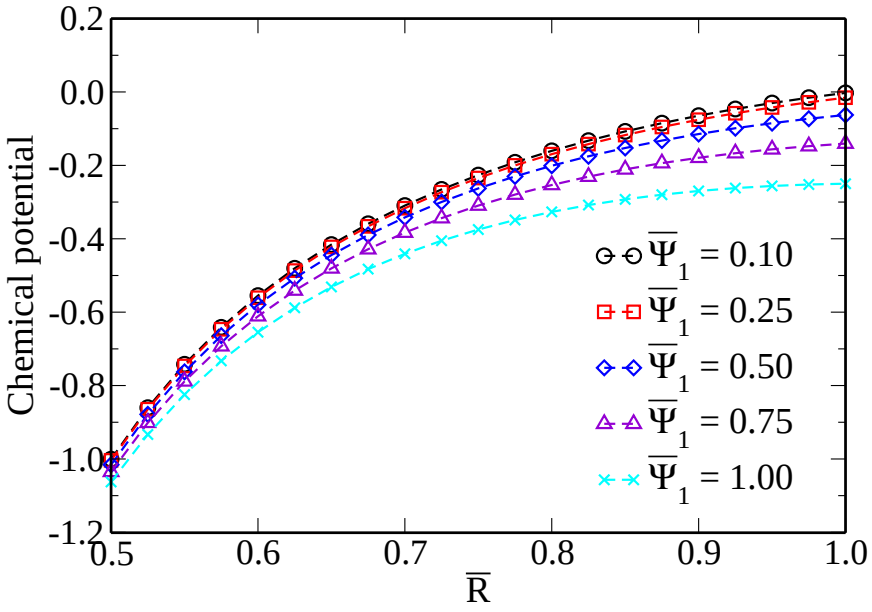

FIGURE 15. Torsional shear of a degrading cylinder: This figure shows the chemical potential as a function of the reference location at $\overline{t} = 1.0$ for various values of $\overline{\Psi}_1$. As $\overline{\Psi}_1$ increases, chemical potential, however, decreases.

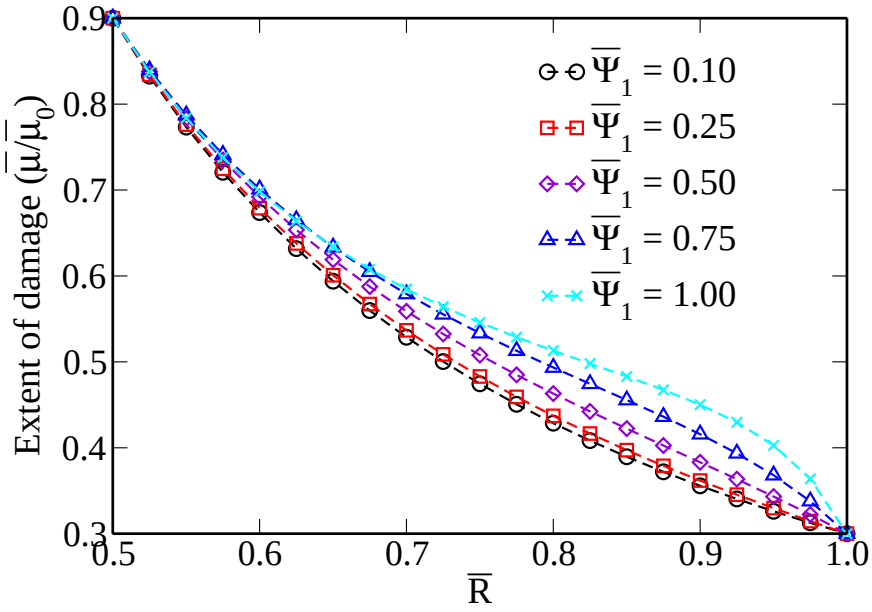

FIGURE 16. Torsional shear of a degrading cylinder: This figure shows the extent of damage as a function of the reference location at $\overline{t} = 1.0$ for various values of $\overline{\Psi}_1$. Herein, thermal degradation dominates. The extent of damage near the inner radius R_i is not as high as that of the outer radius R_o. It should be noted that for low values of $\overline{\Psi}_1$, $\mathcal{D}_\mu$ is monotonic. However, for higher values of $\overline{\Psi}$, $\mathcal{D}_\mu$ ceases to be monotonic.

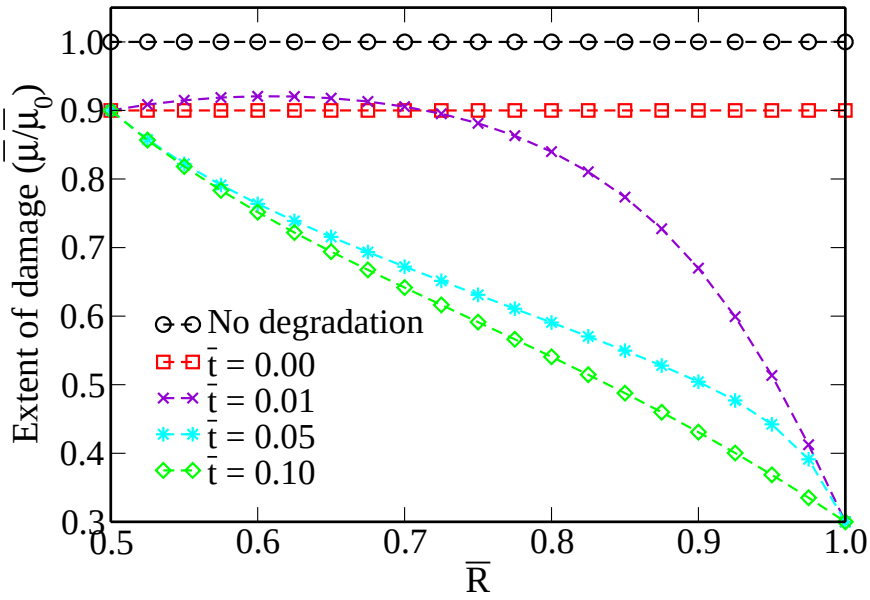

FIGURE 17. Torsional shear of a degrading cylinder: This figure shows the extent of damage as a function of the reference location at various instants of time for $\overline{\Psi}_1 = 0.75$. $\overline{\mu}_1 = 0.5$ and $\overline{\mu}_2 = 0.2$ are used in this case to for numerical simulations. Analysis is performed for strongly coupled chemo-thermo-mechano degradation. Note that $\overline{I}_{\mathbf{E}} \geq 0$. One can see that for initial times, the material damage is less than that of at $\overline{t} = 0$ in certain locations. This is because of the variable heat sinks in the entire body and decreasing thermal conductivity (due to increase in $\overline{I}_{\mathbf{E}}$). Similar type of behaviour is observed in degrading spherical shell problem. However, such a behavior lasts for a short while ($\overline{t} > 0.01$) as compared to the degrading shell problem. This is because the degradation due to moisture (or chemical concentration) dominates in this problem after $\overline{t} > 0.01$.